ULTRASONIC NONDESTRUCTIVE EVALUATION OF ARMOR CERAMICS

by

RAYMOND EDWIN BRENNAN IV

A dissertation submitted to the
Graduate School-New Brunswick
Rutgers, The State University of New Jersey
In partial fulfillment of the requirements
For the degree of
Doctor of Philosophy
Graduate Program in Materials Science and Engineering
Written under the direction of
Professor Richard A. Haber
And approved by

_____

_____

_____

_____

New Brunswick, New Jersey

October, 2007

ABSTRACT OF THE DISSERTATION

Ultrasonic Nondestructive Evaluation of

Armor Ceramics

By

Raymond Edwin Brennan IV

Dissertation Director:

Professor Richard A. Haber

Ceramic materials have been incorporated into armor systems to reduce their weight while providing high hardness, strength, and elastic response to stress. However, the presence of defects and flaws in armor ceramics can lead to ballistic failure. Nondestructive evaluation (NDE) techniques have been studied to locate and characterize defects and inhomogeneities in these materials.

High frequency ultrasound NDE has been explored for detecting and locating micron-range defects and identifying microstructural changes in dense armor ceramics such as silicon carbide (SiC). Ultrasound parameters such as transducer frequency have been analyzed to determine system conditions necessary for obtaining C-scan image maps based on differences in intensity of the collected ultrasound signals (reflected signal amplitudes) or transit time of ultrasound energy through materials (time-of-flight TOF). While TOF has have been used to evaluate changes in thickness, velocity, density, and acoustic impedance, reflected signal amplitude has been used to analyze attenuation, or loss, through a test specimen. Reflected signal amplitude and TOF C-scan imaging have

been useful for identifying and locating isolated defects and microstructural differences. Elastic property maps have been developed to plot differences in Poisson's ratio, elastic modulus, shear modulus, and bulk modulus.

Quantitative analysis techniques have been used to evaluate cumulative effects of reflected signal amplitude and TOF changes over scanned regions and their distributions over selected areas. Amplitude and TOF histogram curves, which have been characterized by area-under-the-curve values, full-width at half-maximum values, and critical tail regions, have provided a valuable means of sample comparison. Generally, more narrow distributions of amplitude and TOF values have corresponded to high density armor-grade samples, while broad distributions have indicated defects or inhomogeneous regions in the samples. In addition to developing techniques for determining individual defect size distributions within a bulk specimen, histogram simulations have been explored to study amplitude and TOF distribution trends by analyzing how the addition of defects of varying size, quantity, and acoustic impedance affect histogram characteristics. These data have been utilized to establish a representative materials fingerprint that provides defect input data which can be further quantified and applied to property, design, and performance modeling of armor ceramic materials.

ACKNOWLEDGEMENTS

I would like to acknowledge the U.S. Army Research Laboratory's Material Center of Excellence – Lightweight Materials for Vehicle Protection Program - under Cooperative Agreement No. W911NF-06-2-0007, and the Ceramic and Composite Materials Program, an NSF I/UCRC, under Agreement No. EEC-0436504 for funding the research presented in this dissertation.

I am especially grateful to my advisor and mentor, Professor Richard Haber, for his sage advice and perpetual encouragement each and every step of the way. Professor Haber believed in me even when I struggled to believe in myself, and this was the very type of support that helped fuel my accomplishments. I would also like to thank my exemplary thesis committee members, Professor Dale Niesz, Dr. James McCauley, and Professor George Sigel for their invaluable input, inspiring me to push the boundaries of what I thought was possible.

I would like to thank Dr. Mahesh Bhardwaj from the Ultran Group, the guru of ultrasound, for educating me on both the theoretical and practical aspects of ultrasound technology – teaching it as both an art and a science. Other Ultran Group members Thomas Eischeid, Michael Biviano, and Raghu Srivastra must certainly be thanked for not only their technical support, but also their friendship through the years. From the Army Research Laboratory, I would like to thank Dr. William Green, Dr. Ernie Chin, Dr. James Sands, Dr. Jerry LaSalvia, and Dr. Ryan McCuiston for their guidance on the armor-related aspects of this work. I would also like to thank Dr. Rich Palicka and Dr. Dan Ashkin from BAE/Cercom, Dr. Vimal Pujari from Saint Gobain, Dr. Bill Fisher

from Trex, Dr. Frank Anderson from CoorsTek, and Dr. Russ Yeckley from Kennametal for providing armor ceramic test specimens used in this work.

From the Department of Materials Science and Engineering at Rutgers University, I would like to acknowledge Professor Victor Greenhut, Professor Roger Cannon, and Professor Maneesh Chhowalla. Also from the Department of Materials Science and Engineering, I would like to thank the hardest working man in the business, John Yaniero, and the staff that just don't stop, especially Claudia Kuchinow.

You know I've got to shout out my colleagues and friends from the current and former conglomerate comprising the Haber Group, especially my two good friends Volkan and Anil, Cari, Navin, Dan, Steve, Andrew, Kevin, Vlad, Nestor, Chris, Laura R., Shawn, and of course, Laura Chirchillo.

My best friend, the love of my life, Asha, I couldn't have gotten through this without your endless support. You have always been there for me through thick and thin, and without that motivation, that inspiration, I wouldn't be the man I am today. For that, I will never stop thanking you.

My great friends throughout my time at graduate school, it's been a fun ride and I only hope we can keep it going as I leave the house that Rutgers built – Brad, Jessica, Susan, Bryan, Nader, Vahit, Ying Ma, Jen, Al, Doug, and too many more to name in the limited confines of this section.

My incredible friends outside of the department, for always providing an outlet to hang out, have fun, and live life to its fullest – Zack, Steve, Joe, David, Sarah, Gayatri, Nathan, and so many more.

I must also acknowledge the organizations I helped pioneer during my time as a graduate student. Da Chefs legacy will continue on and will never die – as it is was written and as it was meant to be. Autograph Empire will remain undefeated as its founders hang their hats on the hook of success. Rutgers Rarities will live in memories, as the spirits who hold onto the tradition await their next shining moment of glory.

I would like to thank my family – my dad, who happens to be my hero in life, the hardest working man on the planet who inspires me to do work. I am proud to call myself your son. To my mom, who takes encouragement to a higher plain, without whom I would not be where I am today. To my sister, Kelly, who is a great sister as well as a great friend.

I would also like to thank Almighty God and my Lord and Savior Jesus Christ through whom all things are possible.

To everyone who helped me along my path, you will not be forgotten.

TABLE OF CONTENTS

LIST OF TABLES

LIST OF FIGURES

1. Introduction

Armor is used to enhance personnel and vehicle survivability by defeating projectiles and fragments to prevent target perforation and structural failure [1]. Ceramic materials exhibit excellent armor performance against a variety of threats and lower weight as compared to metal alternatives. Armor ceramics and armor ceramic systems have eclipsed metal armor in most cases due to this reduction in weight, which provides a higher degree of mobility to the soldiers who utilize body armor and for the vehicles that are fitted with armor ceramic plates. In addition to the critical weight reduction, armor ceramics provide high hardness, high compressive strength, and high modulus, which are characteristics that enhance their ability to defeat a ballistic threat [1]. Just like any other manufactured product, it is crucial to implement a sufficient testing method to ensure the material integrity of the armor ceramic before it is applied in the field. In this case, the responsibility to provide a reliable product is even more vital since the end users are soldiers who protect the freedom of our country. They rely on armor ceramic and armor ceramic systems as a last line of defense. The overwhelming majority of current testing methods are destructive techniques that are applied to a relatively small sampling of armor ceramic materials. Since these destructively tested materials serve no use in the field, the results of quasi-static and ballistic testing must provide sufficient information about the integrity of the remaining untested components. However, making assumptions about the untested materials can be dangerous due to the degree of variability involved with the manufacture of a ceramic product and the critical nature of the application. The motivation for this research stems from a need for providing a nondestructive testing

method capable of achieving inspection of all armor ceramic materials from a batch before issuing them to the soldiers who rely on them for their survival.

During ballistic impact of a high velocity projectile with the surface of an armor ceramic, the projectile is blunted and a shock wave propagates from the site of impact. Ultimate failure is a function of the temporal and spatial interaction of macro-stresses within the ceramic materials at the microstructural and nanostructural scales including elastic and inelastic, or plastic, deformation, damage nucleation and evolution, and resulting failure from the macro-scale (top down) or from the nano-scale (bottom up). At the macro-scale, this involves formation of cone cracks, radial cracks, ring cracks, and a comminuted zone that leads to damage formation within grains and at grain boundaries. The presence of microstructural inhomogeneities and defects can influence all of these events. After sufficient damage is accumulated, the projectile begins to penetrate the armor ceramic and is further deformed and eroded until the kinetic energy of the event is used up. This armor ceramic failure can be attributed to and enhanced by the heterogeneity of the microstructure and the weakness of the interfaces due to the presence of impurities and voids [2]. These defects commonly include intergranular and intragranular porosity, inclusions due to contamination or the addition of sintering aids, microcracks, and gradients in grain size or density. The ballistic impact event affects a large volume of the armor ceramic which includes a wide range of these defects, from large isolated inclusions and pores to small microstructural inhomogeneities.

Nondestructive testing describes the methods that are used to examine an object, material, or system without impairing its future usefulness [3]. Common nondestructive testing techniques that are used to analyze advanced ceramic components and composites

include ultrasound, radiography, x-ray computed tomography, and acoustic emission [4]. After initial comparison and evaluation, ultrasound has been chosen for its potential to provide nondestructive, non-hazardous defect detection and property measurement of high density armor ceramic materials in a cost-effective manner. The ultrasound technique has capabilities of detecting and locating macroscale as well as microscale features in ceramic materials that may be detrimental to ballistic performance. This dissertation will examine the feasibility of utilizing ultrasound testing as a reliable method for nondestructively detecting and quantitatively evaluating bulk armor ceramic materials. The critical ultrasound parameters will be analyzed to determine the optimum conditions necessary for detection of micron-range and higher defects and features. The results will be used to provide input data that can be applied to armor ceramic property, design, and performance optimization.

A background on the history, fundamental principles, and relevant concepts of armor ceramics and ultrasound testing will first be presented. A method of attack will next be provided to describe the research plan in the context of meeting the objectives and achieving the goals set forth in the initial stages of this thesis work. An experimental procedure will be detailed to document the methodologies used. The results and discussion section will highlight important developments and novel techniques implemented for ultrasound nondestructive evaluation of armor ceramic materials. Finally, the outcome of the thesis work will be summarized in the conclusion section and ideas will be suggested for future considerations.

2. Background

The background section of this dissertation will focus on two topics including armor ceramics and ultrasound. A brief history of armor will be followed by a description of key armor ceramic properties and armor ceramic system components. Ballistic events, ceramic materials, and destructive testing methods will next be described before detailing the processing, properties, and critical defects common to silicon carbide armor ceramics. The ultrasound topic will include a history and a discussion of applications. Ultrasound fundamental concepts, equipment, capabilities, and advantages will also be described in great detail.

2.1. Armor Ceramics

Throughout recorded history, humans have used various forms of armor for protection against the threats of their respective time period. The evolution of armor materials has gradually progressed from animal hides, leather, and bone, to metals such as bronze and eventually steel, to the comparatively recent use of ceramic materials.

2.1.1. History of Armor

The use of armor is believed to have extended back beyond historical records when primitive warriors protected themselves with leather hides and helmets [5]. The first documented use of armor was by the Egyptians in 1500 BC, who sewed bronze scales or plates into cloth, but the heavy weight of the garments led to its early downfall [6]. The Assyrians next developed lamellar armor, or rectangular bronze plates sewn into garments, between 900 and 600 BC [6]. The ancient Greeks and later the Romans used bronze breastplates, back plates, and helmets for protection, and also developed the first form of mail, or chain link, which was metal fabric made of interwoven rings of iron or

steel [5-6]. In the 11th century, Chinese warriors wore layers of rhinoceros skin for protection and the Mongols used ox hides in a similar fashion in the 13th century [5]. In Europe, mail became the main defense for the body and limbs during the 12th and 13th centuries. Armor made of rigid plates, similar to those used by ancient Greeks and Romans, reappeared in Europe around 1250 [6]. The use of steel for plate armor became prevalent in the 14th century and evolved into its most popular form around 1450 as a suit of armor that protected knights in the European Middle Ages [5-6]. These suits of armor were composed of either large steel or iron plates that were linked by rivets [5]. During the 16th and 17th centuries in Western Europe, firearms and other weapons utilizing gunpowder became the standard, and body armor was losing popularity as it was not ready to meet the challenge of its latest threat [7].

It was not until the Civil War that body armor started to again gain momentum [7]. Even before the US military supported an official form of armor, peddlers traveled around Army camps selling vests and breastplates fitted with metallic ballistic material made up of steel plates [7]. Though numerous military authorities advocated the use of body armor during Word War I, it only reached a preliminary testing stage before it was eventually rejected [7]. Finally, during World War II, the next generation of ballistic vests known as flak jackets was introduced. In 1942, the Air Force issued these flak jackets, which were essentially heavy steel plates sewn into cloth, to pilots [7]. Next, the M12 vest, which was made up of aluminum plates and nylon cloth, was issued during the Korean War [7]. The improvement of flak jackets and vests made them lighter and better, as they were used in Vietnam, but although they were capable of stopping shrapnel, they could not stop bullets effectively [7]. It was not until the 1960's that the

modern form of bulletproof vests were developed with the onset of Kevlar and armor ceramic materials [7].

2.1.2. Armor Ceramic Properties

While the bulk of traditional armor materials were metal due to their high hardness and strength properties for protection against threats, one of the major disadvantages of using metallic armor, such as steel plates, was their heavy weight, which limited the amount that could be utilized for a given application. Armor ceramics were originally developed for personnel protection in the form of bulletproof vests and light vehicle protection in the form of helicopter seats in the 1960's to improve upon the shortcomings of commonly used steel armor [1,8]. Since the armor used in combat was required to be mobile, the motivation to develop armor ceramics was based on a need for lighter materials with comparable mechanical properties to metallic armor, whether the application was for armor plates worn by soldiers in protective vests or vehicle armor plates used to protect tanks. Advanced structural ceramic materials, which typically possessed densities of 4 g/cm^3 or less, had a distinct advantage over steel, which had a density of approximately 7 to 8 g/cm^3 [9]. By replacing metal armor with armor ceramics, the overall weight of an armored vehicle was reduced by as much as 60-70% [9]. In addition to a reduction in weight, it was also necessary for armor ceramics to meet the requirements to defeat ballistic threats.

Besides low density, properties that made ceramic materials ideal for armor applications included high hardness, high elastic, or Young's, modulus, high shear modulus, high bulk modulus, high material velocity, good abrasion, and high compressive strength [10-13]. While there were a multitude of advantages, not all of the

properties of ceramics were advantageous for use as armor. Ceramic materials were brittle and typically possessed low tensile strength, which limited their ballistic performance as compared to traditional steel armor [1]. For this reason, the armor ceramic component was incorporated into a multilayered armor system which exploited the high compressive strength of the ceramic material while offsetting the effect of low tensile strength [1]. The integration of the armor ceramic into an armor system will be further discussed as well as the importance of the aforementioned armor ceramic properties in relation to the ballistic event. The interaction between the high velocity projectile and the armor system and different types of ballistic threats will also be considered.

2.1.3. Armor Ceramic System Components

An armor ceramic system is generally composed of five separate layers including a cover layer, an armor ceramic ballistic layer, a bonding layer, a backing layer, and a protective layer [14-15]. The cover layer is the outermost layer, which provides abrasion protection and confines rubble through the front face after a ballistic impact event occurs [14]. As the sole visible layer of the armor system, it can also be camouflaged according to the surrounding environment. The armor ceramic layer is the main component for defeating the projectile, and its ideal properties have been mentioned and will be discussed in more detail. This component is the main focus of this dissertation. The bonding layer is often a rubber material that is utilized to minimize shock wave reflections through the system [14]. The backing layer is either a soft material such as a polymer composite or a hard material such as a metal that absorbs any additional kinetic energy that is not dissipated by the armor ceramic layer [14]. The protective layer

provides additional chemical protection in the case of failure of the other four layers. The two most important layers are the armor ceramic ballistic layer and the backing layer, as the others are secondary layers used for additional support. The description of a ballistic impact event will be discussed in terms of these two critical layers and their interaction with each other.

2.1.4. Ballistic Event

Armor ceramic materials are only as good as their ability to overcome a given threat. When a ballistic threat comes into contact with an armor ceramic, the result is what is referred to as a ballistic event. In this section, these interactions will be covered in terms of different types of ballistic threats, the relationship between the ballistic impact event and kinetic energy, the ballistic impact event stages, and the relationship between the ballistic event and armor properties.

2.1.4.1. Ballistic Threats

High velocity, or kinetic energy, projectiles can be classified into three different categories based on their caliber. Small-caliber projectiles typically include bullets and projectiles up to 7.62 mm, or 0.30 calibers, in size, projectile velocities less than 1,000 m/s, and length-to-diameter (L/D) ratios from about 1 to 5 [1]. These types of projectiles are typically fired from small arms or heavy machine guns [16]. They are often composed of either steel, which has a density of approximately 7.85 g/cm^3, or tungsten carbide, which has a higher density between 13.5 and 15.0 g/cm^3, and are sometimes composed of lead or tungsten alloy [1,16]. The nose shapes of these projectiles are either blunt or sharp, and the projectile energies tend to produce at total kinetic energy on the order of 10^3 to 10^4 Joules [1,16]. Medium-caliber threats are often long rod penetrators

between 20-140 mm in size with intermediate velocities between 1,300 and 1,600 m/s and high L/D ratios around 30:1 [1]. They are composed of metals such as tungsten sintered alloys or depleted uranium with high densities of approximately 18 g/cm^3, moderate toughness, and good ductility, making them resistant to shattering [1,16]. These projectiles often produce impacts with 10^6 Joules of kinetic energy [1]. Large-caliber threats include shaped-charge jets which exhibit high impact velocities and pressures on the target [1]. They possess tip velocities between 6,000 and 10,000 m/s with an additional tail velocity of 2,000 m/s that produces extremely high impact pressures on the order of 100 GPa [1]. These are more modern types of threats fired from weapons such as rocket-propelled grenades.

2.1.4.2. Ballistic Impact Event Relationship to Kinetic Energy

Small, medium, and large-caliber threats all exhibit a significant amount of kinetic energy and momentum upon impact with an armor ceramic system. The primary role of the armor ceramic component is to dissipate this kinetic energy, which can be achieved in three different ways. The first method is absorption of the kinetic energy as heat and deformation of the target material [11]. The second method is rebound, or deflection of the projectile off the face of the armor [11]. The third and most efficient method is gross deformation of the projectile which absorbs most of the kinetic energy during the destruction of the projectile and minimizes the momentum transfer [11]. The third method is the most common, and will be described in five stages that detail the occurrence of a ballistic event.

2.1.4.3. Ballistic Impact Event Stages

There are five major stages that dictate the response of an armor system to a ballistic impact from a high velocity projectile. They consist of (1) impact (2) pre-penetration (3) material failure (4) penetration and (5) momentum absorption [1]. The important events that occur during these stages are shown in the schematic in Figure 1.

Impact is the initial contact between the projectile and the armor system. Upon impact, the projectile is either blunted or fractures on the surface of the armor ceramic component, depending on the hardness of the projectile [16-17]. Meanwhile, ahead of the impact site, a shock wave is generated that propagates through the armor system [18].

During pre-penetration, the high compressive strength of the ceramic material overmatches the load produced by projectile impact, causing the projectile to dwell on the surface of the armor system [1,16]. At this time, the shock wave reflects off of the backing material, with a greater acoustic impedance mismatch between the materials resulting in a higher degree of wave reflection. These tensile wave reflections initiate a period of damage accumulation in the ceramic material as they meet the release waves which are generated from the rear of the projectile [16,18]. During shock wave propagation, large compressive stresses are also generated directly under the projectile, causing a damage zone, or comminuted, zone, which is also referred to as the Mescall zone [17,19]. In this comminuted zone, fine ceramic fragments are formed ahead and around the tip of the projectile [17-18]. This leads to fragmentation of the material as well as radial and cone crack formation and propagation [17,19]. These mechanisms increase the amount of damage in the ceramic material, significantly reducing its strength until failure occurs.

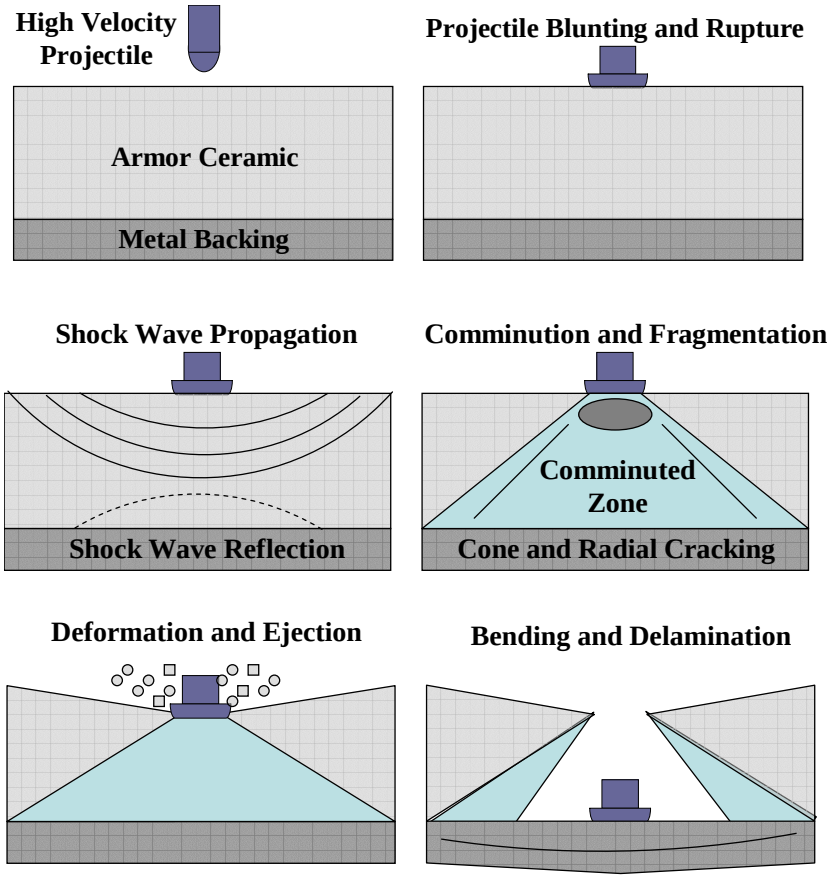

Figure 1. Ballistic impact and shock wave propagation event during high velocity projectile impact with armor ceramic supported by metal backing [10].

After sufficient damage is accumulated, the projectile begins to penetrate the armor ceramic. Under high stress and strain, the projectile moves through the comminuted zone due to the flow of comminuted material. The most important ceramic properties that prevent penetration of the projectile through the armor ceramic include the friction between comminuted granules, the strength of the comminuted material, and the compressive strength of intact material [17]. Depending on the caliber of the threat, there are several possible responses of the projectile during penetration. It can remain rigid, deform plastically if the projectile is a ductile metal, shatter and penetrate as a concentrated debris cloud, or erode [1]. The most common response is deformation and erosion until the kinetic energy of the event is used up [10]. Even though the ceramic material failed in the previous stage, it continues to offer sufficient resistance to erode the projectile and contribute to its fracture [1].

In the final ballistic event stage, any additional projectile momentum is absorbed by target deformation or elastic wave dissipation [1]. The backing material also catches any of the remaining projectile fragments or fractured ceramics that are pushed, or plugged, through the back of the ceramic material, a process that is sometimes referred to as capture [1].

2.1.4.4. Armor Property Relationship to Ballistic Event

While the importance of low density has been discussed as a motivation for the implementation of ceramic materials in armor systems, other critical properties that were touched upon briefly will be discussed in terms of their relationship to the ballistic impact event. High hardness, high compressive and tensile strength, high elastic properties, high

material velocity, and good abrasion are all properties that improve the ballistic performance of an armor ceramic material.

Armor ceramics require high impact strength and hardness in order to break up a sharp, hard projectile upon impact [11]. This implies that the ceramic should possess high hardness in addition to high compressive strength [11]. For the best results, the hardness of the ceramic component should be higher than the hardness of the projectile [20]. Another important property is high tensile strength, which was mentioned earlier that brittle ceramics do not often possess. However, the impact load transmitted through the ceramic during the ballistic event produces compressive stress on the backing layer and a corresponding tensile stress on the rear surface of the ceramic material layer due to shock wave propagation and tensile wave reflections, and this eventually leads to fracture [11]. Choosing a ceramic material and a backing layer material that promote high tensile strength will resist this type of fracture [11]. High elastic properties including elastic, shear, and bulk moduli are also important. Elastic, or Young's, modulus is a measure of the stiffness of a given material and is related to the rate of change of stress with an applied strain [21]. Shear modulus is a measure of the rigidity of a given material and is related to the rate of change of shear stress with an applied strain [21]. Bulk modulus, or incompressibility, is a measure of the resistance to uniform compression and is related to the pressure change due to a change in volume [21]. High elastic property values prevent large deformations in ceramic materials by reducing the amount of stress that a high velocity projectile can inflict on the material [12]. Another important property is a high material velocity, which indicates the ability of a ceramic material to dissipate energy from the impact area [20]. It is also believed that abrasion is an important mechanism for

defeating a projectile, since the fracture region in the ceramic material spreads from the point of impact, generating sharp fragments that can further promote abrasion or erosion of the projectile [11].

Another factor that is critical for ballistic performance of an armor ceramic material is the presence of defects. Ceramic materials are inherently brittle when they are subjected to tensile stresses due to their atomic bonding and lack of adequate dislocation mobility to support bulk plasticity, as opposed to most metals [1,22]. This lack of metal-like ductility makes the mechanical response of ceramic materials sensitive to microstructural defects, which can range in size from sub-nanometers to hundreds of micrometers [1]. The tensile and compressive stresses caused by the shock wave and reflected tensile waves activate pre-existing defects in the ceramic component of an armor system, causing the damage that leads to penetration of the projectile. These defects are weak points in the ceramic material that are exploited by the applied stress of the ballistic impact event, causing additional damage to occur. With a greater amount of accumulated damage, there is a greater chance that the armor ceramic system will fail. Therefore, as a first step, improvements in armor ceramic performance require an elimination or reduction in the size of pre-existing microstructural defects [1]. Armor ceramic defects are one of the focal points of this dissertation, and will be further addressed in terms of specific types, origins, and characterization.

2.1.5. Armor Ceramic Materials

Common polycrystalline ceramic materials used for armor applications include aluminum nitride (AlN), aluminum oxide (Al_2O_3), aluminum oxynitride (ALON), boron carbide (B_4C), silicon carbide (SiC), silicon nitride (Si_3N_4), and titanium diboride (TiB_2),

with SiC, B_4C, and Al_2O_3 most frequently utilized for body and vehicular armor [18]. All of the listed materials have densities less than 4.5 g/cm^3, high hardness values, high compressive and tensile strengths, good abrasive properties, high material velocities, and good elastic properties to high stress values [11]. A property comparison of steel and common armor ceramic materials is given in Table I [23-30]. Boron carbide is commonly used for personnel protection in the form of plate inserts as well as in aircraft, ship, and armored land vehicle panels and seats [31]. For protection against more lethal medium and high-caliber threats such as heavy machine guns and medium cannons, hot pressed silicon carbide is typically the material of choice [31-32].

2.1.6. Armor Ceramic Processing and Related Defects

The presence of defects in armor ceramic materials has been discussed in terms of its detrimental effect on ballistic performance. The origin of microstructural defects such as pores, inclusions, large grains, and microcracks, can be traced back to the processing of the materials. By pinpointing the origin of these defects, improvements can be made to the specific processing step to minimize their occurrence and improve the final product.

General ceramic processing, which is also utilized for fabrication of armor ceramic materials, can be divided into four distinct stages including powder processing, mixing, forming, and densification. These four stages and the common defects associated with each one are shown in Figure 2. The first stage of powder processing involves the preparation of the starting powders, during which time the initial particle size and particle size distribution are chosen. Possible issues that can occur during the stage include contamination and poor particle size distribution, which can later lead to

defects such as pores, inclusions, and unwanted second phases. If a smaller particle size is used for ceramic manufacturing, a fine-crystalline microstructure can be achieved for higher densification [20]. A smaller particle size, good particle distribution, and higher powder content of the starting powder can also result in higher hardness, elastic modulus, and material velocity properties [20].

The second stage of mixing involves the homogeneous addition of processing aids and sintering aids to the starting powders. Possible issues that may occur include poor mixedness and excess second phase addition which can later lead to defects such as inclusions, agglomerates, and unwanted second phases. Materials with a higher content of processing or sintering aids tend to have a larger average particle size and less microstructural uniformity [20].

The third stage of forming involves processing the starting powders or slurry into a sample of desired shape and dimensions. Common forming methods include pressing, casting, or extrusion. Possible issues that may occur during this stage include poor mixedness or poor powder or slurry distribution causing density gradients, and these can later lead to defects such as cracks, laminations, and voids.

The fourth stage of forming involves densification, which can either be pressureless or pressure-assisted. Pressureless sintering can be divided into categories of solid state sintering, liquid phase sintering, or reaction bonding. During this stage, variations in the percentage of second phase or non-uniform density distributions can result in defects such as open or closed pores, large grains, or uncontrolled phase generation. During the cool-down period from exposure to high temperatures, each individual grain wants to contract, but there is resistance from neighboring grains, which

results in the build-up of residual stresses at grain boundaries and junctions of multiple intersecting grains [1]. Since the magnitude of residual stresses increases with grain size, microcracking may occur with large grain size.

A more specific example of typical armor ceramic processing is provided. Armor ceramic materials are normally produced using powder processing routes in which micron-sized ceramic powders are pressed into green bodies that are less than 60% dense [1]. Armor ceramic materials are commonly densified using pressureless sintering techniques or hot-pressing, in which high uniaxial pressure is applied while the material is slowly heated [11]. Temperatures on the order of approximately 2000^{o}C are used for densification, and for hot-pressing, the applied pressure typically ranges from 0-200 MPa to achieve a 98-100% theoretical density [1]. Sintering additives are often used during the mixing stage to decrease the densification temperature [1].

Material	Density [g/cm^3]	Knoop Hardness [GPa]	Tensile Strength [MPa]	Fracture Toughness [MPa m$^{1/2}$]	Velocity [m/s]	Poisson's Ratio	E [GPa]
SiC (sint)	3.16	19.1	525	3.1	11,820	0.16	415
SiC (hp)	3.21	24.5	600	5.2	12,100	0.17	430
Al_2O_3	3.98	15.2	510	3.5	11,000	0.23	416
AlN	3.25	13.5	325	4.5	10,700	0.23	320
B_4C	2.51	28.4	470	3.5	14,090	0.18	456
TiB_2	4.50	26.5	285	6.2	11,400	0.11	565
Si_3N_4	3.24	14.7	720	6.1	11,000	0.27	290
Steel	7.80	6.0	1,800	50.0	5,850	0.28	200

Table I. Average physical, mechanical, and acoustic property comparison of common armor ceramic materials to properties of steel [20-27].

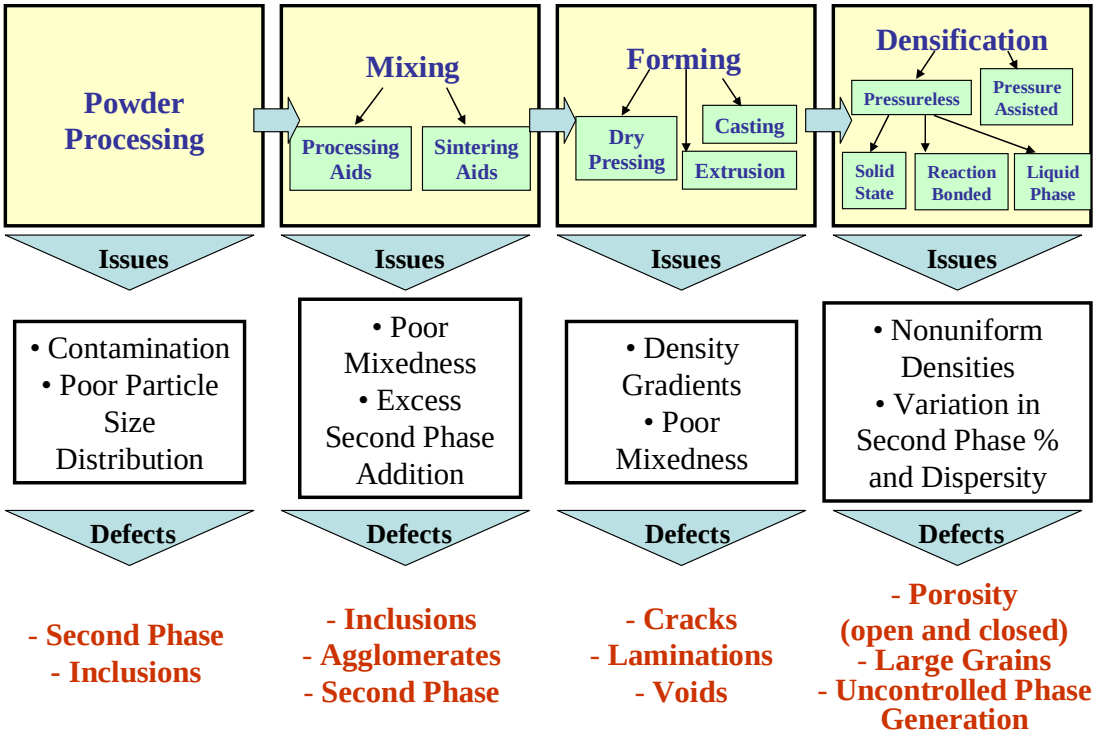

Figure 2. Armor ceramic processing step chart with related issues and resulting defects that commonly occur at each step.

2.1.7. Destructive Testing of Armor Ceramics

Presently, the most common method for evaluating armor ceramic ballistic integrity is destructive testing. A combination of static and ballistic testing on a limited number of samples from a batch is often conducted to form assumptions about similar plates from the same batch [2,19,33-42]. By this method, there is no direct testing of the plates that are used in the field. Destructive testing of a few armor plates from a production lot is not necessarily indicative of the performance of the remaining untested plates. Microstructural defects that could prove detrimental to the performance of the armor ceramics could be present, but these flaws cannot be detected without proper testing of individual plates. Destructive testing also incurs additional cost to the manufacturer. Armor ceramic materials that undergo ballistic or static testing are destroyed and rendered useless, leading to the eradication of potentially usable products. For this reason, the development of a nondestructive method for manufactured part inspection is particularly crucial for personnel and vehicular armor.

Some of the more common types of destructive tests can be categorized as mechanical tests, plate impact tests, penetration tests, or perforation tests. Mechanical test data are typically quasi-static or Hopkinson bar uniaxial compression data, which describe the stress state at failure and the average strain rate [43]. Plate impact tests investigate material behavior at high pressures and high strain rates, and the diagnostic measurements are used to construct a Hugoniot curve [43]. In this type of testing, compressive stresses are produced and transferred into the material in the form of a stress pulse [43]. If the stress pulse is high enough, the elastic limit, or Hugoniot Elastic Limit (HEL) of the material will be exceeded, resulting in permanent plastic deformation [43].

Ballistic penetration tests determine projectile and armor ceramic characteristics in relation to impact velocity [43]. Figure 3 includes images of ballistic penetration testing of an armor ceramic plate [44]. Included in this category, the Depth-of-Penetration (DOP) test is one of the most widely used ballistic tests for evaluation of armor ceramic materials [43]. In this test, a ceramic tile is placed on a steel target and projectile impact results in penetration and perforation of the tile [43]. This penetration is known as residual penetration and is used to determine the ceramic ballistic mass efficiency [43]. Perforation tests are ballistic tests in which targets including an armor ceramic front layer and metallic backing layer are shot at and perforated by small-caliber threats [43]. In the popular V50 test, the projectile velocity at which the probability of penetration through the backing is 50% is measured [45]. These properties are defined by the residual projectile characteristics and ballistic velocity limits [43].

Another issue with these destructive tests is that they test only a small relative volume of the armor ceramic plate. As shown in Figure 4, estimated effective volumes of various destructive tests are provided [46]. Two types of bend bar tests are estimated to test volumes of 12 mm^3 and 96 mm^3, respectively, while ring-on-ring methods test an estimated volume of 400 mm^3 and V50 techniques test an estimated volume of 15,000 mm^3 [46]. Compared to a standard armor plate with a length and width of 4-inches by 4-inches, and a thickness of 2-inches which has a volume of almost 524,400 mm^3, the effective volumes of the destructive tests are extremely small [46-47]. It is important to improve upon the problems with destructive testing of armor ceramics to test a large effective volume of each armor plate that is applied in the field in order to ensure sufficient material integrity.

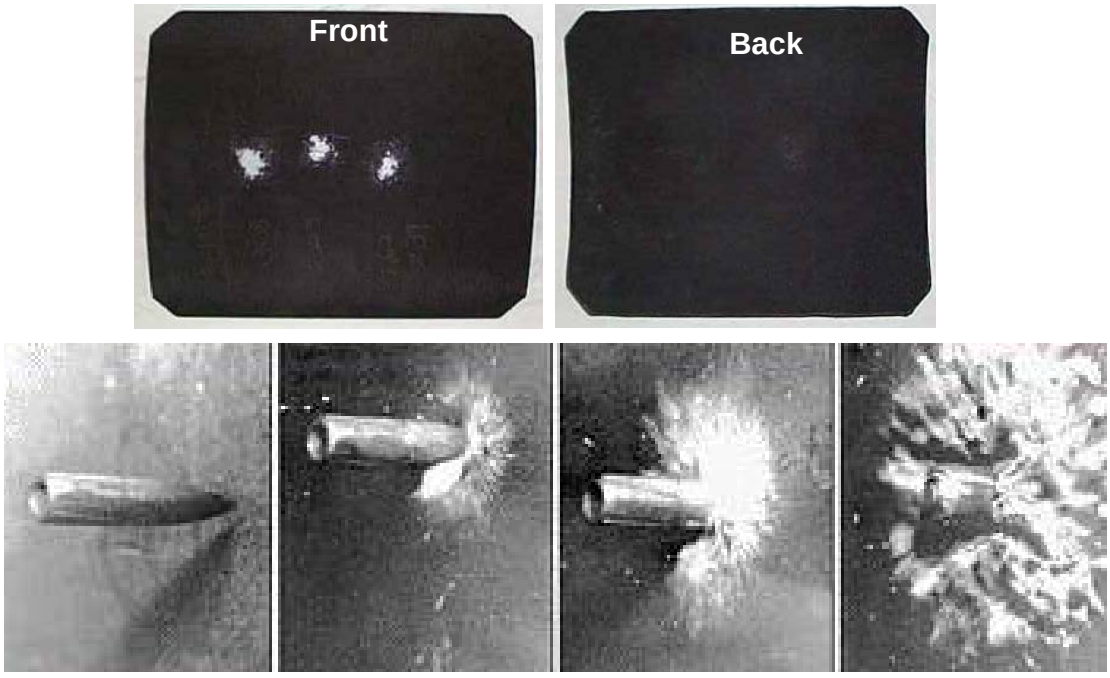

Figure 3. Armor ceramic plates shot from 25 yards with .3006 armor-piercing rounds [34].

(a)

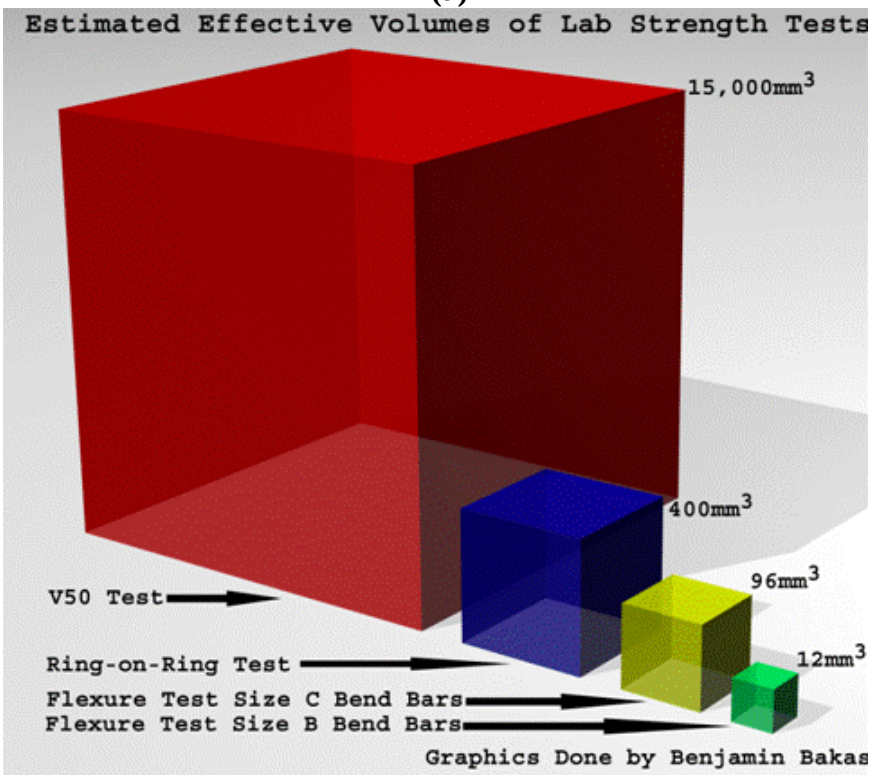

(b)

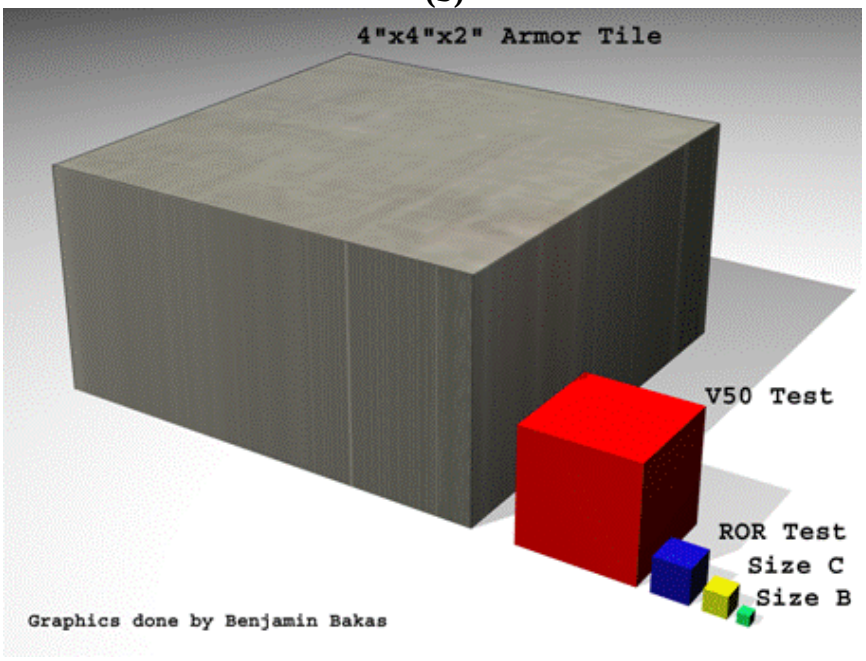

Figure 4. (a)Effective volume comparison of common mechanical and destructive tests (b) Effective volume comparison of tests to armor ceramic tile [37].

2.1.8. Silicon Carbide Armor Ceramics

One of the most commonly used armor ceramic materials is silicon carbide (SiC), which demonstrates high properties and ballistic performance while exhibiting a low density. As the main armor ceramic of interest in this dissertation, silicon carbide processing methods and properties and their relationship to defects will be discussed.

2.1.8.1. Silicon Carbide Processing and Properties

Silicon carbide is utilized in a multitude of ceramic applications that require low density, high strength, low thermal expansion, high thermal conductivity, high hardness, high elastic properties, good abrasion, high thermal shock resistance, good creep resistance, and high chemical inertness. Some commonly reported values of SiC include its high hardness value, with Knoop hardness ~2150-2950 kg/mm^2 or 31 GPa, as it is often used as an effective abrasive material [24]. The hardness varies depending on the crystallographic direction and impurities present [24]. Hot pressed SiC also has a tensile strength ~600 MPa, a compressive strength ~2480 MPa, a fracture toughness of ~ 5.2 $MPa \cdot m^{1/2}$, an elastic modulus between ~430 GPa and ~500 GPa, and a longitudinal material velocity between ~12,000 m/s and 12,200 m/s [24,43]. Unlike most metals with high strength and hardness, SiC has a low density value of ~3.16 g/cm^3 for sintered SiC and ~3.20 g/cm^3 for hot pressed SiC, with a theoretical density of ~3.22 g/cm^3 [24].

Many of these properties have been mentioned with regard to their critical importance for armor ceramic applications. The properties of SiC are a result of its spatial tetrahedral distribution of covalent interatomic bonds, which contributes to a low mobility of dislocations and macroscopic brittleness [24,48-51]. The high degree of covalency of Si-C bonds is around 87%, and this is the source of intrinsically high

strength in sintered SiC materials [52]. However, due to these highly covalent bond characteristics, which result in a low surface energy and a low diffusivity, it is difficult to sinter these materials to full density without the use of pressure and/or sintering additives [17,46]. These factors must be considered in the preparation of SiC armor ceramic materials.

Silicon carbide is derived from a powder or grain prepared by the carbon reduction of silica, and the technique by which it is produced has changed very little from its original preparation in 1891 by E.G. Acheson, an assistant to Thomas Edison [24,48]. On an industrial scale, SiC is manufactured most frequently by using this Acheson method, in which two solid electrodes are connected with graphite powder, a mixture of silica and coke is packed in the surrounding areas, and the assembly is electrically heated at 2700^{o}C [48]. The carbothermal reduction of silica (SiO_2) is accomplished by the reaction [46,48-49]:

$$SiO_2\,(s) + 3C\,(s) \rightarrow SiC\,(s) + 2CO\,(g) \qquad (1)$$

This process is used to produce the starting powder, which may contain impurities such as SiO_2, Fe_2O_3, and other oxides [46]. Depending on the reaction time and temperature, the resulting powder will be in the form of either a fine powder or a large mass, which must ground to the proper size [24]. After further crushing, milling, and separating the powder into submicron size for sintering preparation, additional treatments such as heating to oxidize the carbon or washing with hydrofluoric acid to remove SiO_2 may also be conducted [24].

It has been perceived by Ray et al. that armor ceramic materials used for high-speed impact protection should have a very small grain size and be as homogeneous as

possible [45]. However, the mechanical properties of SiC are not only influenced by grain size, but also by the grain boundary characteristics which are determined by the selection of sintering aids and densification conditions [10].

2.1.8.2. Silicon Carbide Sintering Additives

The two most common sintering additives for SiC processing are boron and carbon. Boron carbide (B_4C) and amorphous boron are often used as sources of boron, which is typically added between 0.3 and 0.5 weight percent [46,53]. Phenolic resin and carbon black are common sources of carbon, which is typically added in amounts between 1.0 and 6.0 weight percent [46,53]. In general, the purpose of adding boron is to create atomic vacancies and enhance sintering kinetics while carbon addition reduces the densification-inhibiting silica layer, which is an essential requirement for sintering [17,54]. The kinetic effects of the addition of boron and carbon will be discussed briefly.

Poor sintering of SiC is caused by the high degree of energy required to migrate defects in its structure, leading to poor volume diffusion and grain boundary diffusion [52]. In 1975, Prochazka et al. proposed that during sintering of submicron powders of covalently bonded solids, densification is prevented by a high ratio of grain boundary surface energies, γ_{GB}, to solid-vapor surface energies, γ_{SV} [55]. A pore surrounded by three grains can shrink to closure if the equilibrium dihedral angle is greater than 60^o or the γ_{GB}/γ_{SV} ratio is less than three, and the equation that relates these parameters is given by [55]:

$$\gamma_{GB} = 2\gamma_{sv}\left(\frac{\cos\theta}{2}\right) \tag{2}$$

Hausner et al. determined that a high grain boundary to surface energy ratio, γ_{GB}/γ_{SV}, inhibits the densification process [52]. Since the γ_{GB} is high in SiC due to strong

directionality of the Si-C bonds, it is necessary to reduce this factor and enhance γ_{SV} in order to maximize densification [55]. The addition of boron and carbon promotes sintering by enhancing grain boundary diffusion while reducing surface diffusion [52]. Added boron diffuses through the SiC and segregates selectively along the grain boundaries, decreasing γ_{GB} and therefore reducing γ_{GB}/γ_{SV} [55]. The surface of SiC has a tendency to adsorb impurities such as SiO_2, which subsequently lowers γ_{SV} and increases γ_{GB}/γ_{SV} [55]. The addition of excess carbon removes these thin layers of SiO_2 that form on the SiC powder, causing an increase in γ_{SV} and a decrease γ_{GB}/γ_{SV}, thereby promoting the densification process [55]. These sintering additives are critical for achieving full density for SiC armor ceramics.

2.1.8.3. Silicon Carbide Densification

Along with the addition of sintering additives, high sintering temperatures between 1800^{o}C and 2200^{o}C are also used to enhance densification [56]. Densification methods for preparation of SiC ceramics can be divided into pressureless sintering and hot pressing techniques.

Hot pressing can be described as sintering under the application of external pressure [57]. The applied mechanical pressure can increase the driving pressure for densification by acting against the internal pore pressure without increasing the driving force for grain growth [57]. For this reason, SiC armor ceramics are typically hot-pressed to obtain full density without increasing the grain size. In 1986, it was even demonstrated by Kriegesman et al. that by hot pressing SiC between 1900^{o}C and 2300^{o}C with pressures ranging from 100-400 MPa, dense SiC parts were fabricated without the use of sintering aids [55]. In a common modern use of the hot pressing technique for

producing armor ceramics, large slabs of SiC are fabricated in a batch process that uses high temperatures between 1900^{o}C and 2300^{o}C and high pressures between 10 MPa and 200 MPa [58]. After fabricating the slabs, four by four-inch ballistic tiles are cut and surface ground until final production specifications are met [58]. Some disadvantages of hot pressing are that it is an expensive and slow batch process that is limited to the production of simple shapes [55,58].

While the majority of high-performance SiC materials for armor applications have traditionally been fabricated using hot pressing, pressureless sintering is more desirable from a manufacturing standpoint because it allows production of large, complex-shaped parts, offers good mass productivity, and is more cost-effective [31,52]. However, unlike the hot pressing example in which dense SiC was produced without the use of sintering additives, boron and carbon sintering aids are required for fabricating high density SiC via pressureless sintering. The pressureless sintering kinetics were described during the discussion of sintering additives.

An early example of pressureless sintering was reported by Prochazka in 1975 who synthesized SiC with additions of 0.5 wt% boron and 1 wt% C while sintering to temperatures between 2050^{o}C and 2150^{o}C to achieve densities of 96% [55]. The effect of sintering times was also reported in terms of microstructural evolution by Aslan et al., who fabricated SiC by pressureless sintering at 2160^{o}C [59]. While equiaxed grains with an average grain size of 4.6 micrometers were found at 10 minutes, further annealing caused grain growth to an average size of 5.2 micrometers, and the grain morphology increased to an aspect ratio of 2 - 3 at 30 minutes. At 45 minutes, grains became more elongated, and beyond 90 minutes, large SiC platelets with lengths between 15 and 105

micrometers and aspect ratios around 9 were measured [59]. The changes in grain size and grain morphology are important for sintering, but are not critical during hot pressing.

Liquid phase sintering is another form of pressureless sintering in which metal and metal oxide sintering aids such as aluminum are applied [46]. The sintering aids can react with each other or the SiO_2 in the SiC powder to form a liquid phase that promotes densification by dissolving and reprecipitating SiC onto undissolved grains [46]. Liquid that does not dissolve into the SiC forms a grain boundary phase that dictates the mechanical properties [46]. In one example, liquid phase sintering was used to obtain greater than 95% densities at temperatures below 2000^{o}C [52].

2.1.8.4. Silicon Carbide Defects

While SiC is one of the strongest ceramic materials, its high strength can be limited by the presence of a variety of defects. There are many possible causes of microstructural defects during processing of SiC, which can occur during the general powder processing, mixing, forming, and densification steps described earlier. Common defects found in SiC include isolated pores, low density regions, large grains, inclusions, and variations in grain boundary compositions due to nonuniform distribution of impurities [53]. Two categories of defects include those with normal distributions and sizes such as small isolated pores and large grains and anomalous defects that include pores, inclusions, or porous areas with sizes much larger than the grain size [46,53]. Anomalous defects are low probability critical defects that usually occur in low volume percentages and are not generally detected [46,53].

During the powder processing stage for SiC, defects such as impurities and agglomerates can be introduced. SiC powder generally has free carbon as one of the

contaminants due to the nature of the reactions used to form it [60]. Metallic impurities such as iron are also commonly introduced during this stage [10]. These impurities often segregate in small, well-dispersed pockets along the SiC grain boundaries [10]. Improved powder processing can significantly reduce the presence of isolated pores, large grains, and inclusions by ensuring good particle size distribution and high purity of the starting powders [53]. Microstructural quality can be improved by improving both chemical and physical uniformity of the body [53]. Sieving and sedimentation techniques can be applied to the raw powder to remove hard agglomerates and coarse inclusions and to reduce the critical flaw size [53,61].

Addition of sintering aids such as boron and carbon during the mixing step leads to dense, fine-grained microstructures and high sintered body strength, but can also result in the formation of agglomerates and second phases at the grain boundaries that remain in the final material and negatively affect its mechanical properties, especially at high temperatures [46,52,56]. These second phases include the liquid phases formed by sintering aids, which create weak intergranular bonds by filling triple points and pores, leading to intergranular fracture [46]. Unreacted carbon can form amorphous carbon and graphitic inclusions that contain remnants of other sintering additives such as boron and alumina [46]. The carbon inclusions are usually intergranular, appearing at triple points where they trap other additives and impurities [46]. Boron and aluminum additives dissolve into the SiC until the solubility limit is reached and they form second phases within the SiC grains and at the grain boundaries [46]. The chemical inhomogeneities caused by excess amounts of sintering aids can give rise to localized density variations [53]. One way of reducing the probability of these types of defects is increasing the

mixedness of the sintering additives while another is to determine the proper amounts of additives that are necessary so that excess amounts are not added [53].

The forming process for SiC is important since defects are often introduced during this stage that may remain in the product even after successful sintering [60]. During the forming stage, dry pressing is a method used to make simple shapes, but processing-related agglomerates are commonly encountered [61]. Improper mixing in the previous stage leads to pore clusters that later form crack-like voids at the cluster-matrix interface due to differential sintering [61]. These clusters are critical fracture flaws that originate in the dry-pressing process [61]. A narrow range of these flaws between 100 and 150 micrometers for common dry-pressed specimens has been reported by Hurst et al. [61].

Densification is a critical stage in which the final microstructure and, therefore, the presence of microstructural defects will be determined. Formation of intragranular and intergranular flaws along the grain boundaries and at triple grain junctions occurs for densification any less than 100% theoretical. Pressureless sintering firing conditions, such as the sintering time effects described earlier, can create SiC with coarse elongated grain structures that cause intergranular cracking. This coarse microstructure will introduce additional intergranular porosity and also serve as stress concentrators from which cracks can form [46]. During hot pressing, temperatures of 2000^{o}C and higher are much greater than the melting points of metallic impurities so metallic melts can be expected that result in large inclusions which act as strength-limiting flaws [10].

Work by Bakas et al. has utilized high resolution field emission scanning electron microscopy (FESEM) on ballistically-tested hot pressed SiC armor samples to identify a

variety of defects [46]. The motivation for the work stemmed from reports of unexplained variability in DOP tests from seemingly identical armor ceramic material from the same production run and, therefore, manufactured under the same conditions [46]. The belief was that this type of tile-to-tile and possibly lot-to-lot variability may have been caused by the presence of anomalous defects in the materials that showed poor ballistic performance [46]. The defects that were found on the fracture surfaces of bend bars, ring-on-ring samples, and the ballistically tested armor fragments were most commonly carbonaceous and alumina inclusions [46]. The majority of defects fell within the ~20-80 μm range, with a common defect size of ~50 μm, while several large anomalous inclusions on the order of ~300-500 μm were also found [46]. Some FESEM images of defects from both of these size ranges are shown in Figure 5. These anomalous, critical defects found in SiC are not easily detectable within the bulk using common destructive and ballistic testing methods, and could prove to be detrimental to the performance of the armor ceramics. For this reason, there is a need to detect and identify any microstructural defects and inhomogeneities within armor ceramic materials before utilizing them in the field.

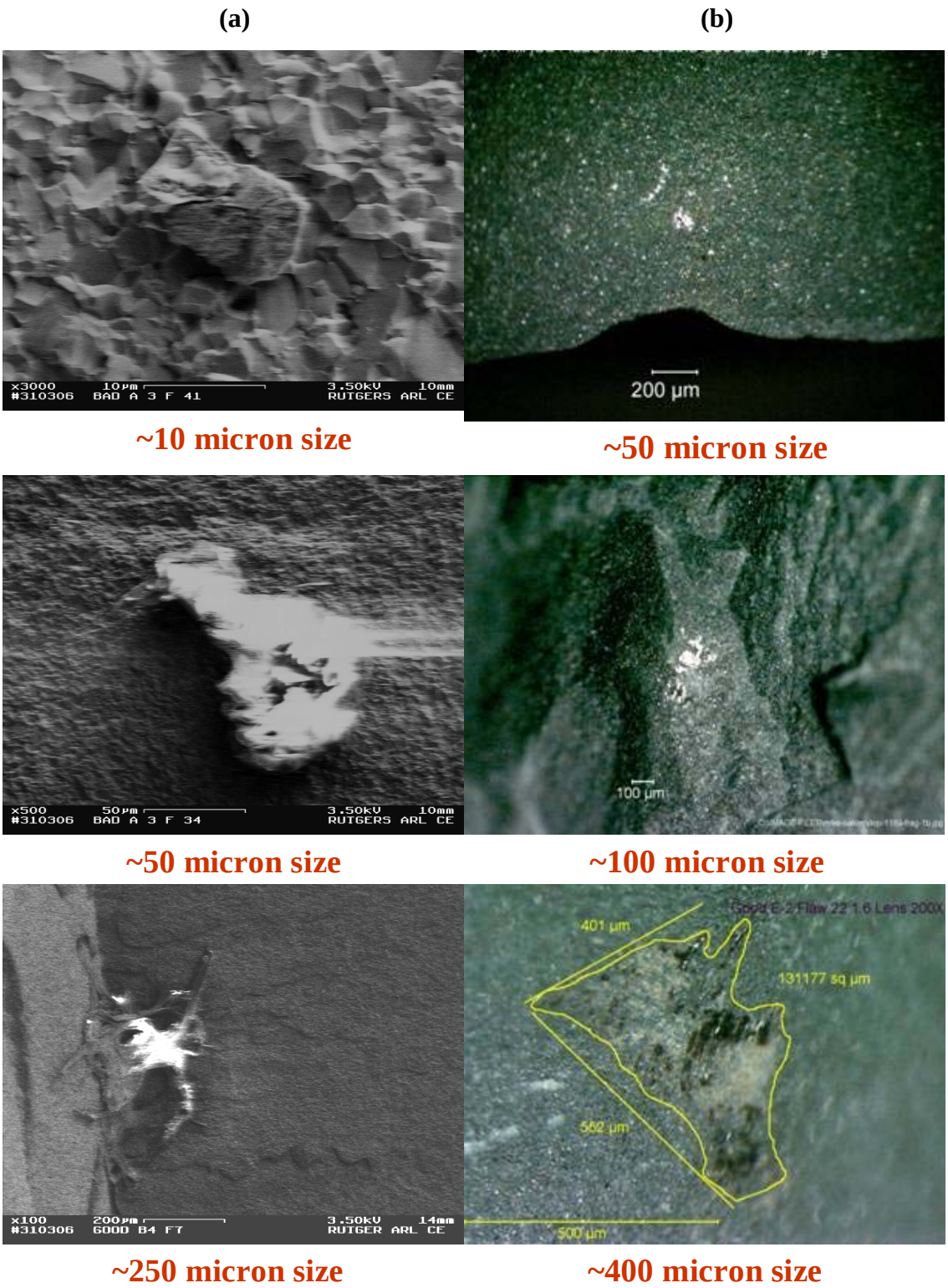

Figure 5. (a) Carbonaceous defects and (b) alumina defects of various sizes found on the fracture surfaces of ballistically tested SiC armor ceramics [37].

2.2. Ultrasound

Ultrasound is defined as sound generated above the audible human hearing range. Since the audible range falls between frequencies of 20 Hertz (Hz) and 20 kilohertz (kHz), ultrasound includes any sound wave with a frequency greater than 20 kHz. While ultrasound behaves in a similar manner to audible sound, it has a much shorter wavelength and, therefore, can be reflected off of very small surfaces, such as defects within bulk materials, making it useful for nondestructive testing [62].

2.2.1. Introduction to Ultrasound

In order to effectively describe the fundamentals and principles of ultrasound with respect to its applications for nondestructive evaluation of armor ceramics, a brief history will first be provided. This will be followed by a discussion of acoustic wave properties and material interactions, and a description of necessary equipment for generating ultrasound signals used for image mapping. Defect detection parameters will also be discussed and ultrasound advantages given to justify the use of ultrasonic testing as a viable nondestructive technique.

2.2.1.1. History of Ultrasound

Ultrasonics, in general, follows principles of acoustics so its early development can be traced back to roots in acoustics. The philosophy of ultrasound dates back as far as the 6th century BC, when Pythagoras performed experiments on vibrating strings, which led to a tuning system known as the sonometer [63]. In the 4th Century BC, Aristotle added to the philosophy by correctly assuming that sound waves resonate in air through motion of the air itself [63]. In 1st Century BC, architect Vitruvius determined the correct mechanism for movement of sound waves and applied it to acoustic design of

theaters [63]. In the 6th Century AD, Roman philosopher Boethius was the first to suggest that the human perception of pitch is related to physical property of frequency [63].

Transitioning from heavy philosophical reasoning to more concrete scientific evidence, Galileo Galilei (1564-1642) is said to have initialized modern study of acoustics. He elevated the study of vibrations and the correlation between pitch and frequency of the sound source to scientific standards [63]. Galileo discovered the general principles of sympathetic vibrations, or resonance, by conducting experiments with a pendulum and relating the frequency of vibrations to the length of the pendulum [64]. Other major scientific developments followed over the next few centuries.

French mathematician Marin Mersenne studied the vibration of stretched strings and developed a series of three laws that provided the basis for modern musical acoustics in 1636 [63]. English physicist Robert Hooke first produced a sound wave of known frequency using a rotating cog wheel as a measuring device. Felix Savart further developed the concept of using a large, toothed cog wheel for research on the lower frequency limit of hearing, a device that is commonly known as Savart's disk [63]. In the late 17th and early 18th centuries, detailed studies of the relationship between frequency and pitch in stretched strings were carried out by French physicist Joseph Sauveur, who came up with many acoustic terms that are still used today, including the actual term "acoustics" for the study of sound [63]. In 1794, an Italian biologist named Lazzaro Spallanzani was credited for the discovery of high frequency ultrasound when he demonstrated that the ability of bats to navigate accurately in the dark was due to echo reflections from high frequency inaudible sound [63]. In 1822, Swiss physicist Daniel

Colladen used an underwater bell to successfully estimate the speed of sound in the waters of Lake Geneva [63]. Very high frequency sound waves above the limit of human hearing were generated by English scientist Francis Galton in 1876 through his invention, the Galton whistle [63]. In the late 1800's, physicists were also working towards defining fundamental physics of the transmission, propagation, and refraction of sound vibrations, or waves. One of the most notable was Lord Rayleigh in England, whose "Theory of Sound" published in 1877, first described the sound wave as a mathematical equation [65]. Another breakthrough in high frequency echo-sounding techniques came in 1880, when brothers Pierre and Jacques Curie discovered the piezoelectric effect in which an electrical potential was produced when mechanical pressure was exerted on a quartz crystal, and reciprocally, a mechanical stress could be achieved in response to a difference in voltage [65]. This made it possible for the generation and reception of ultrasound in the frequency range of megahertz (MHz), or millions of cycles per second, and its application to echo-sounding devices [65].

With the development of ultrasound principles and early devices, practical applications of the technology were soon to follow. This started with the use of acoustic waves for determining distance. Colladen's use of underwater devices had pioneered the idea of measuring distance underwater using sound waves, which brought about the term SONAR, or Sound Navigation and Ranging [65]. In the early 1900's, lightships used a system that combined an underwater gong and a foghorn on deck. Since the crews aboard oncoming ships could hear both sounds, they were able to time the difference between them and determine their approximate distance from the lightship [65]. Underwater detection systems were developed for submarine navigation in World War I,

and gained particular interest after the sinking of the Titanic in 1912 [65]. That same year, Alexander Belm in Vienna developed an underwater echo-sounding device and Lewis Richardson filed a British patent for underwater echo ranging [65]. The first functioning echo ranging device was patented in the US in 1914 by Reginald Fessenden, and was capable of detecting an iceberg from two miles away, but could not precisely determine its direction [63].

Soon after, the concept of sonography was further applied to flaw detection in solids. In 1928, Sergei Sokolov proposed a technique for detecting irregularities in metals [63]. His work utilized a transmission technique for detecting metal flaws by varying ultrasonic energy across a medium. Due to poor resolution, he suggested the more practical idea of a reflection method, but the equipment for accomplishing this was not available until the 1940's. When the proper technology did become available, Floyd Firestone, Donald Sproule, and Adolf Trost applied the ideas of Sokolov to develop equipment that implemented an evolution from ultrasound transmission techniques to pulse-echo ultrasound reflection techniques for flaw detection in metals [63,65]. These devices set the tone for present day applications in ultrasound defect detection.

It was in the 1940's that the use of ultrasound expanded to its most common modern application in the field of medicine, which initially started with uses in therapy rather than diagnostics. The destructive ability of high intensity ultrasound was noted for its affect on schools of fish in the sea, and was later applied in 1944 by Lynn and Putnam, who successfully used ultrasound waves to destroy brain tissues in animals [63]. For more useful therapeutic medical applications, William Frye and Russell Myers used high intensity ultrasound to destroy parts of the basal ganglia in patients with Parkinson's

disease, Peter Lidstrom induced ablation of frontal lobe tissue in patients to alleviate pain from carcinomatosis, and Jerome Gersten applied the use of high intensity ultrasound to treatment of patients with rheumatic arthritis [63]. In the mid to late 1940's, lower intensity medical ultrasound began to take off as a diagnostic tool. Karl Dussik began experimentation on echo imaging of the brain, in which the first attempt at combining ultrasound with scanning and mapping was attempted [65]. These developments led to extensive studies of ultrasonic medical imaging in the United States and Japan starting in 1948 [65]. George Ludwig began inspection of animal tissue using flaw detector equipment used previously for SONAR applications. He continued the study of acoustic differences in different materials in order to detect gallstones in the human body. From that point forward, heavy research was conducted on the application of ultrasound as a method for detection of tumors, breast masses, and other anomalies in the body [65]. In the late 1950's and early 1960's, the work of Ian Donald in Scotland determined that clear ultrasonic echoes could be obtained from the fetal head, and with further experimentation, the diagnostic study of pregnancy from beginning to end became possible [63,65]. While a more detailed history of medical ultrasound can be found in the references, the focus of this work is concentrated on flaw detection in elastic solids.

Ultrasonic Nondestructive Evaluation (NDE) in the early days was primarily used for the detection of defects. It was hypothesized that a structure should not develop macroscopic defects during its lifetime, and if they were detected, the component should be removed from operation. In the early 1970's, several technological improvements led to major changes in the field. The first was the advancement in high frequency ultrasound technology that led to the ability to detect small flaws, which caused more

parts to be rejected despite the fact that the probability of component failure had not changed. The next was the emergence of fracture mechanics, which enabled the prediction of whether a crack of given size would fail under a particular load, and the study of fatigue, which was able to predict the growth rate of cracks under cyclic loading. These studies enabled a damage-tolerant design, or acceptance of structures containing defects if their sizes and characteristics were not of a critical nature. In addition to detection, quantitative information about flaw properties became important for predicting and determining the differences between components [66]. These underlying principles of ultrasound NDE have been well established and serve as the basis for current work that is being applied to evaluation of armor ceramics.

2.2.1.2. Ultrasound Applications

Based on the brief history of ultrasound provided, it is evident that there are a vast number of ultrasound applications in industrial and medical fields. These applications indicate an even wider range of scientific technologies and topics to which ultrasound can be applied. While the inclusion of a complete listing of ultrasound applications would not be plausible, a comprehensive list of major applications in industry and medicine is provided.

In the field of medicine, the most common application is ultrasonography, or medical sonography, in which ultrasound is used to scan internal parts of the body and provide a visual imaging display [67]. It is used to visualize the size, structure, and presence of any pathological lesions in muscles, tendons, and many internal organs [68]. Ultrasonography is often used for the detection of tumors or abnormal fluids in the body [67]. Obstetric sonography is one of the most common applications, used for the

visualization of the fetus during routine and emergency prenatal care [68]. In pelvic ultrasound, the uterus, ovaries, urinary bladder, or prostate are imaged [68]. In abdominal ultrasound, the organs of the abdomen such as the pancreas, aorta, inferior vena cava, liver, gall bladder, bile ducts, kidneys, and spleen are imaged. Ultrasound probes can be utilized for detection of small objects in the eyes that will enable removal by a surgeon [67]. Other medical fields in which ultrasonography is applied include cardiology, endocrinology, gastroenterology, gynecology, ophthalmology, urology, musculoskeletaltendon analysis, and vascular and intravascular analysis [68].

Ultrasound can also be used in surgical and therapeutic medical applications. As a surgical tool, high intensity focused ultrasound can be applied to the body for local heat absorption which is useful for destroying tissue in the brain, tumors in the breast, and cancers in the prostate and other organs [67]. Lithotripsy is a technique that uses focused ultrasound to break up kidney stones so that they can pass from the body [67]. Ultrasound can also assist in surgeries when attached to a vibrating saw for smooth cutting of bone and tissue [67]. Therapeutically, ultrasound waves are used create heat or agitation in localized regions of the body [68]. Phacoemulsification is a technique that uses ultrasound for the treatment of cataracts [68]. It can be applied by physical therapists for the treatment of muscle strains and injuries [68]. It can also be used to treat arthritic joints and for the cancer treatment [67].

Another medical application is Doppler ultrasound, in which continuous ultrasound is applied to measure the rate of a heartbeat or blood flow in the body [67]. It is used in the study of fetal hearts and the detection of blood flow blockages [67].

In addition to medical applications, there are many industrial applications of ultrasound as well. The most common is nondestructive testing, in which defects and flaws are detected and located [67]. Ultrasound imaging can be further applied for mapping defects in a solid. This application is most relevant to this thesis, in which armor ceramic bulk defects are detected, located, mapped, and evaluated. Ultrasonic cleaning uses a bath solution irradiated with high intensity ultrasound for cleaning machine parts [67]. In addition to the use of heat absorption for this application, cavitation, or the collapse and expansion of microbubbles on the surface of the parts, is produced to enhance the cleaning process [67]. Ultrasonic drilling, soldering, and welding are also applications in which ultrasonic oscillations are used to produce either heat or motion to drive the device [67,69]. Homogenization and emulsification in liquid systems can be accomplished by using high intensity ultrasound to produce cavitation [67]. While the vast majority of these applications utilize high intensity ultrasound for applying heat or motion to disturb the test specimen, low intensity ultrasound, which is used for nondestructive testing applications, can be used in a number of ways. Generally speaking, in addition to nondestructive testing, low intensity ultrasound can be used to measure properties such as flow, temperature, density, porosity, pressure, dynamic force, vibration, acceleration, viscosity in fluids, phase, microstructure, thickness, position, composition, anisotropy and texture, grain size, stress and strain, and elastic properties, among other things [70-71]. While it is not within the scope of this section to describe the application of ultrasound to each of these properties in great detail, those that are of interest to armor ceramics, including density, porosity, microstructure, thickness,

position, grain size, stress and strain, and elastic properties will be addressed throughout the text.

2.2.2. Ultrasound Fundamentals

The fundamental unit on which ultrasound is based is the acoustic, or sound, wave. Propagation of an acoustic wave through a material results in particle motion, and the interactions between the wave and the material are the basis for ultrasound testing from which acoustic and elastic properties can be determined. The acoustic impedance of the material as well as the refraction, mode conversion, and attenuation of sound waves as they interact with the material are important principles that will be covered in this section.

2.2.2.1. Wave Propagation and Particle Motion

Simply put, an acoustic wave is a pattern of disturbance caused by the movement of energy traveling through a medium as it propagates away from the source of sound [72]. The source is an object that causes the vibration [72]. Ultrasonic vibrations travel in the form of waves, similar to the way light travels [62]. However, unlike optical waves which can travel in a vacuum, ultrasound requires an elastic medium, such as a liquid or a solid, to propagate [62].

There are several important parameters that characterize the behavior and properties of an acoustic wave. The time required to complete a full wave cycle is known as the period, T, and is measured in seconds [62]. The frequency of the wave, f, is defined as the number of oscillations of a given particle per second [73], and is measured in inverse seconds, or Hertz. Within a given wave it is the same for all particles [73]. The relationship between period and wavelength is given by the equation:

$$f = \frac{1}{T} \tag{3}$$

demonstrating that the frequency and period are inversely proportional. The wavelength is the distance between two planes in which the particles are in the same state of motion [73], and is typically measured in microseconds, μs. The velocity of wave propagation is represented by the speed of sound over a given condition, and is measured in meters per second. Velocity is a characteristic of the material and is constant for a given material with a specified frequency and wavelength [73]. The wavelength is directly proportional to the velocity and the period of the wave and inversely proportional to the frequency of the wave, as given in the equations [62]:

$$\lambda = \frac{c}{f} \tag{4}$$

or

$$\lambda = c \cdot T \tag{5}$$

These equations will be discussed in more detail later as critical components of ultrasound evaluation.

All materials are comprised of atoms which may be forced into vibrational motion about their equilibrium positions [66]. Sound waves propagate in a material due to the vibrations or oscillatory motions of particles within that material [66]. As opposed to x-ray technology which uses electromagnetic waves, acoustic waves used for ultrasonic testing are mechanical waves that interact with the particles in the medium [73]. As the waves pass through the material, the particles oscillate back and forth about their equilibrium positions, but it is the disturbance which travels and not the individual particles in the medium [74]. The particles themselves remain in place and oscillate

about their positions of rest [73]. When a material is not stressed in tension or compression beyond its elastic limit, its individual particles perform what are known as elastic oscillations [66]. The acoustic waves travel by exerting oscillating pressure on particles of the medium, generally corresponding to the frequency of the incident wave [75]. When the particles of a medium are displaced from their equilibrium positions, internal restoration forces arise [66]. It is these elastic restoring forces between particles combined with inertia of the particles that lead to the oscillatory motion of the entire medium [66]. In a solid medium in which particles are tightly held together, oscillation of one particle generates corresponding vibrations in the adjacent particle and so on, completing the mechanism of ultrasound propagation [75]. Each individual particle is influenced by the motion of its nearest neighbor and both inertial and elastic restoring forces act upon each particle [66]. If all material particles are excited collectively in step with the sinusoidal oscillations, all particles in the first plane are forced to oscillate with the same amplitude, or width of oscillation, and frequency, or number of oscillations per second [73]. Elastic forces then transmit the oscillations to particles in the second plane and vibratory motion is transmitted to the third plane and so on [73]. In an elastic material, the motion requires a certain period of time to be transmitted, and there is a lag in phase between the planes that are excited [73]. This phase shift of oscillations creates alternating compression and expansion zones in which the particles are closer together and farther apart, respectively [73]. These zones travel at constant velocity and uniform intervals, and this is what is known as an elastic wave [73]. The overall pattern of disturbance of the elastic wave creates outward movement in a wave pattern, like waves

in the ocean [72]. The elastic wave carries the sound energy through the medium in all directions and with less intensity as it moves further from the source [72].

The particle oscillations that occur in an elastic medium can be compared to the motion of a small mass attached to a spring that is pulled down once and released [73]. This can be further visualized by imagining the entire body of the medium consisting of individual particles that are kept in position by elastic forces represented by a series of connected springs as shown in Figure 6 [73]. The oscillations of the springs are sinusoidal in nature and can be depicted as a function of time by a sine wave [73].

A mass on a spring has a single resonant frequency determined by its spring constant, k, and its mass, m [66]. The spring constant is the restoring force of a spring per unit length [66]. Within the elastic limit of any material there is a linear relationship between the displacement of a particle and the force attempting to restore the particle to its equilibrium position [66]. This linear dependency is described by Hooke's Law [66]. In terms of the spring model as depicted in Figure 7, Hooke's Law states that the restoring force due to a spring is proportional to the length that the spring is stretched, and acts in the opposite direction [66]. It is written as:

$$F = -k \cdot x \tag{6}$$

where F is the force, k is the spring constant, and x is the amount of particle displacement [66]. The spring is applying a force to the particle that is equal and opposite to the force pulling down on the particle [66]. According to Newton's Second Law, the force applied to a particle will be balanced by the mass, m, and acceleration, a, of the particle, represented by the equation [66]:

$$F = m \cdot a \tag{7}$$

Since Hooke's Law states that the applied force will be balanced by a force in the opposite direction that is dependent on the amount of displacement and the spring constant, the expression can be written as [66]:

$$m \cdot a = -k \cdot x \tag{8}$$

Since the mass and spring constant are constants for any given material, the only variables are acceleration and displacement, which are directly proportional [66]. If the displacement of a particle increases, so does its acceleration [66]. The time it takes a particle to move and return to its equilibrium position is independent of the force applied [66]. When all other variables and conditions such as pressure and temperature are held constant within a given material, sound travels at the same speed no matter how much force is applied [62,66]. Although the speed of sound is constant in a given material, it is different in different materials because the mass of atomic particles and the spring constants are different [66]. The speed of ultrasound and its mode of propagation are directly dependent on the composition and physical characteristics of the medium through which it is transmitted [75]. The mass of the particles is related to the density of the material and the spring constant is related to the elastic constants of the material [66]. These relationships allow ultrasonic testing to directly measure densities and elastic properties in an isotropic solid, which will be discussed later in greater detail.

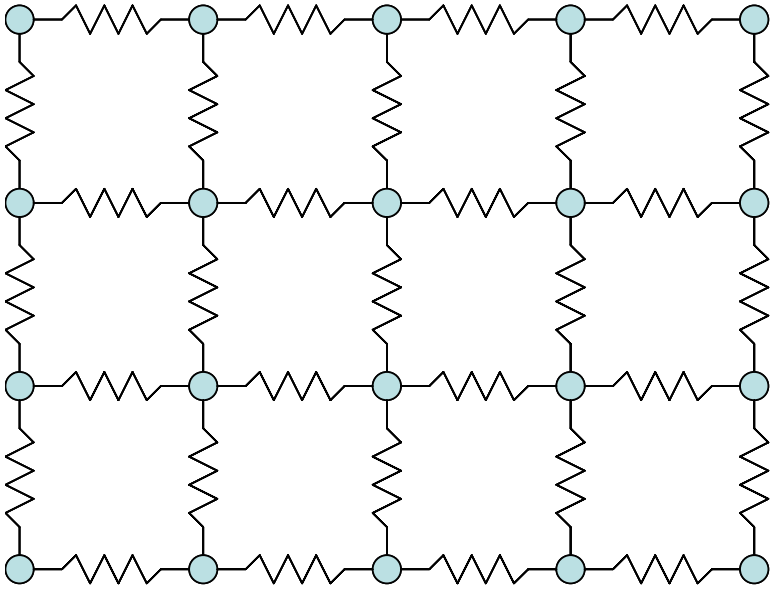

Figure 6. Individual particles represented by series of connected springs used for demonstrating concept of acoustic wave interaction with material.

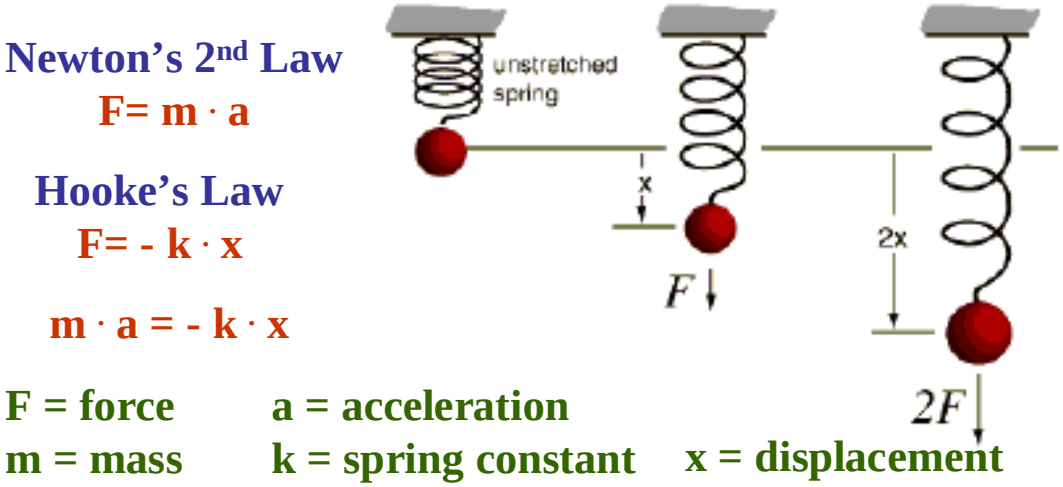

Figure 7. Spring model used for demonstrating Hooke's Law and equations for demonstrating relationship with Newton's Second Law [52].

In air, sound travels by the compression and expansion of air molecules in the direction of travel [66]. However, in solids, molecules can support vibrations in other directions, and therefore, a number of different types of sound waves are possible [66]. Acoustic waves can propagate in four principal modes that are based on the way the particles oscillate [66]. Sound can propagate as longitudinal waves, shear waves, surface waves, and in thin materials as plate waves [66]. Longitudinal and shear waves are the two modes of propagation most widely used in ultrasonic testing [66]. These are shown in Figure 8 in terms of the direction of particle motion and wave propagation. A longitudinal wave is a compression wave in which the particle motion occurs in the same direction as the propagation of the wave [62]. These types of waves are thought of as the true "sound waves" because like the traditional audible sound waves which transmit oscillations from a source of acoustic energy through the air to our ears [73], they are also compressional in nature [25]. They are sometimes known as density waves because their particle densities fluctuate as they move [66]. Longitudinal waves can be generated in both liquids and solids because their energy travels through atomic structures by a series of compression and expansion movements [66]. In transverse or shear waves the particles oscillate at right angles transverse to the direction of propagation [66]. Shear waves require an acoustically solid material for effective propagation and, therefore, are not effectively propagated in materials such as liquids or gases [66]. Shear waves are relatively weak compared to longitudinal waves [66]. In fact, shear waves are usually generated in materials using some of the energy from longitudinal waves [66]. Surface or Rayleigh waves travel along the surface of relatively thick solid materials, penetrating to a depth of one wavelength [66]. Their particle motion has an elliptical orbit [66]. Plate

waves occur in materials where the thickness is less than one wavelength of the ultrasound and have very complex vibrations [62].

2.2.2.2. Acoustic Impedance

Impedance is frequently used in electrical and mechanical applications to describe energy transfer characteristics at various boundaries [76]. The acoustic impedance, or sound resistance [73], denoted by Z, is a material property defined as the product of its density, ρ, and sound velocity, c according to the equation:

$$Z = \rho \cdot c \tag{9}$$

Acoustic impedance determines the passage of sound between two different materials [73] by describing its reflection and transmission characteristics [25]. Acoustic waves are reflected at boundaries where there is a difference in acoustic impedance between materials on each side of the boundary [66]. This difference in Z is commonly referred to as the impedance mismatch [66]. The greater the impedance mismatch, the higher the percentage of energy that will be reflected at the interface or boundary between one medium and another [66]. The amount of reflection of the acoustic waves, described by the reflection coefficient, R, and amount of transmission of the acoustic waves, described by the transmission coefficient, T, can be calculated from the following equations, in which the acoustic wave is being sent from one medium with acoustic impedance Z_1 into a second medium with acoustic impedance Z_2 [25]:

$$R = \frac{(Z_2 - Z_1)^2}{(Z_2 + Z_1)^2} \tag{10}$$

$$T = \frac{4Z_1Z_2}{(Z_2 + Z_1)^2} \tag{11}$$

Multiplying the reflection and transmission coefficients by 100 yields the amount of energy that is reflected and transmitted, respectively, as a percentage of the original energy [66]. Since the amount of reflected energy and transmitted energy must equal the total amount of incident energy [66], the sum of reflection and transmission coefficients is always 100, so by determining one of the values, subtraction by 100 will provide the value of the other. These principles are shown in the schematic in Figure 9.

The reflection and transmission coefficients are critical parameters that can be used in several ways. When it is desirable to couple the maximum amount of sound energy into a specimen, as it is for ultrasonic inspection of a material, acoustic impedance matching can be achieved by minimizing the difference between Z values. This will provide maximum transmission of acoustic energy through the material boundary. On the other hand, the degree of acoustic impedance mismatch between different boundaries in polycrystalline materials can aid in the detection of flaws and defects. A greater mismatch will result in a larger reflection of acoustic energy, making it easier to detect inhomogeneities within a bulk sample. However, a close match between Z values between the bulk material and a defect or flaw will cause a smaller reflection and make it more difficult to detect. For this reason, acoustic impedance is a material property that is critical for ultrasonic inspection of materials.

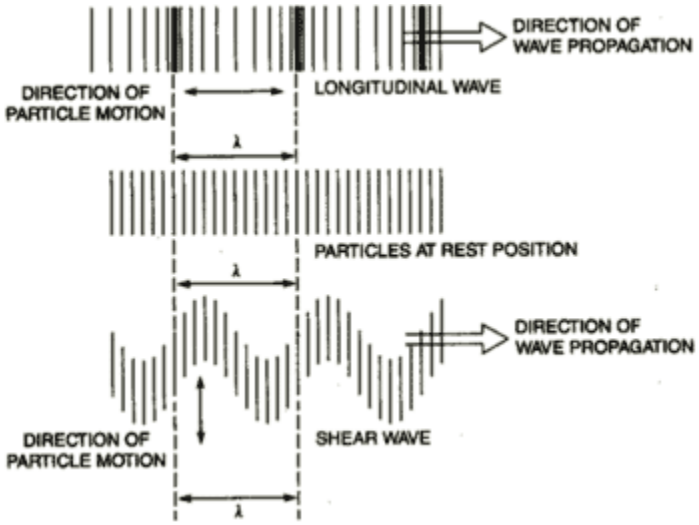

Figure 8. Schematics of longitudinal and shear wave in relation direction of wave propagation and direction of particle motion [52].

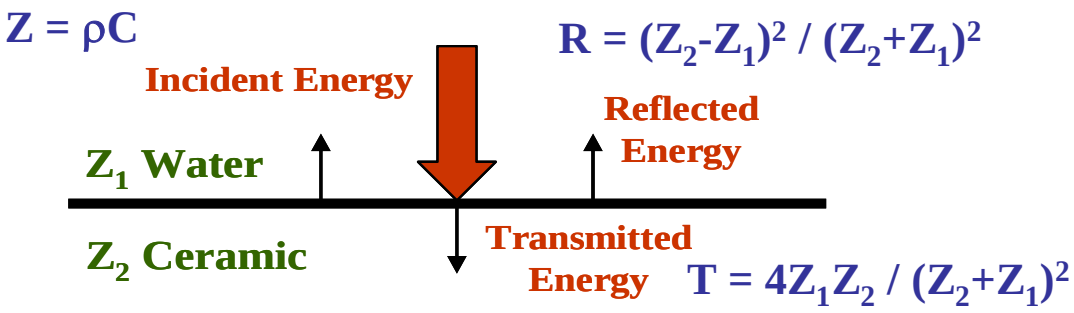

Figure 9. Schematic of reflection and transmission of incident acoustic energy at a material boundary in which there is an acoustic impedance mismatch.

2.2.2.3. Refraction and Mode Conversion

The reflection and transmission of acoustic waves described during the explanation of acoustic impedance assumed that the acoustic waves were passing from one interface to the next in a direction normal to the second interface. However, when an acoustic wave passes through an interface between two materials at an oblique angle, both reflected and refracted waves are produced [66]. This is the same phenomenon that occurs in optics with the reflection and refraction of light, which is why objects viewed across an interface appear to be shifted relative to their actual location [66]. An analogy can be made to viewing a stick that is halfway in the water, as it appears to be disjointed at the air-water interface and its direction appears to change [25].

Refraction occurs when the ultrasonic wave changes direction and velocity as it crosses a boundary between different materials [25]. As mentioned previously, the velocity of sound in each material is directly dependent on the composition and physical characteristics, or density and elastic properties, of each medium [75]. If acoustic waves are traveling in one material and enter a second material with higher velocity, the portion of the wave in the second material is moving faster than the portion in the first material, causing the wave to bend [66]. The ratio between wave speed in one material and wave speed in a second material is called the index of refraction [25]. The relationship between the angles and the waves can be described by Snell's Law, given by the equation:

$$\frac{\sin\theta_1}{c_1} = \frac{\sin\theta_2}{c_2} \tag{12}$$

in which θ_1 is the angle of incidence, θ_2 is the angle of refraction, c_1 is the velocity of sound in the first material, and c_2 is the velocity of sound in the second material

[25,66,77]. This principle is demonstrated in Figure 10. The larger the difference between the two materials, the more sound that is refracted [66]. It should also be noted that the angle of incidence θ_1 is the same as the angle as the reflection because the two waves are traveling in the same material and have the same velocities [66].

When refraction occurs in a solid material due to the transmission of sound waves into the material at an angle, one mode of wave propagation can be transformed into another [66]. This is referred to as mode conversion, and it occurs when a wave encounters an interface between materials of different acoustic impedance and the incident angle is not normal to the interface [66]. For example, when a longitudinal wave hits an interface at an angle, some of the energy can cause particle movement in the transverse direction and create a shear wave [66]. One common occurrence is for a solid material in water, in which case mode conversion occurs when the longitudinal wave in the water is converted into a shear wave in the material [25]. The shear wave is not refracted as much as the longitudinal wave because it travels slower [66]. Therefore, the velocity difference between the incident longitudinal wave and the shear wave is not as great as it is between the incident and refracted longitudinal waves [66]. When a longitudinal wave is reflected inside the material, the shear wave is reflected at a smaller angle than the reflected longitudinal wave [66]. This is also due to the fact that the shear velocity is less than the longitudinal velocity within a given material [66].

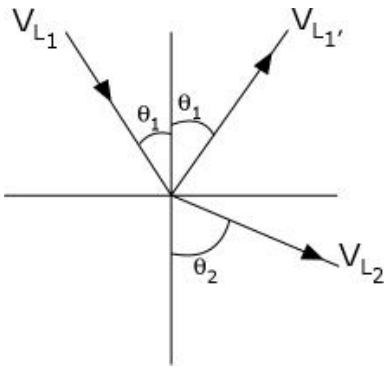

V_{L1} is longitudinal wave in Material 1
V_{L2} is longitudinal wave in Material 2
$V_{L1'}$ is reflected longitudinal wave
θ_1 is incident angle = reflected angle
θ_2 is refracted angle

Figure 10. Schematic of incident longitudinal wave entering second material at an angle to demonstrate reflected waves, refracted waves, and Snell's Law [52].

2.2.2.4. Attenuation of Ultrasonic Waves

When sound travels through a medium, its intensity decreases with distance [66]. In an ideal material, the sound pressure, which is indicated by the signal amplitude, is only reduced by spreading of the sound wave [66]. Natural materials, on the other hand, produce effects which further weaken the sound [66,73]. These factors include scattering and absorption, and their combined effect is referred to as attenuation [73]. Attenuation is generally defined as the reduction in strength of a signal. Ultrasonically, it can be described as the loss in acoustic energy that occurs between two points of travel. Therefore, ultrasonic attenuation is specifically defined as the decay rate of an acoustic wave as it propagates through a material [66], and it is responsible for the loss of acoustic energy due to scattering and absorption.

Absorption is the conversion of sound energy to other forms of energy [66]. It accounts for the conversion of mechanical energy to heat energy as the acoustic wave front passes through the material [76]. This energy is permanently lost [76] and, therefore, is of little consequence to inspection of materials since it provides no additional information about the material itself.

Scattering is the reflection of sound in directions other than its original direction of propagation [66]. It results from the fact that the material is not strictly homogeneous, but contains acoustic interfaces in which there are different densities or sound velocities [73]. Scattering can result from reflections at grain boundaries, small cracks, and other material inhomogeneities [76]. These inhomogeneities can be as pronounced as genuine material flaws that were unintentionally added during processing and forming or intentional flaws that were added as a sintering aid or a second phase [73]. They can also

be as subtle as anisotropic differences in randomly oriented grains that have different elastic properties and sound velocities in different directions [73]. Grain scattering losses occur on a microstructural level because small crystalline grains in a material (such as a ceramic or metal) scatter the incident wave in many directions, resulting in a net loss of amplitude with distance in the propagation direction [78].

Attenuation is generally expressed in terms of sound pressure of an acoustic wave in the form of the exponential function [73,76]:

$$P = P_o e^{-\alpha \cdot L} \tag{13}$$

where P_0 is the initial sound pressure level at a source or reference location, P is the sound pressure level at a second reference location, α is the attenuation coefficient in Nepers per unit length, where a Neper is a dimensionless quantity, and L is the distance of travel from the original source to the second reference location [76].

Another common equation for attenuation relates it to the intensity, or amplitude, of the acoustic wave. It is expressed in the same way, except the sound pressure is replaced by the amplitude of the propagating wave. In this instance:

$$A = A_o e^{-\alpha \cdot L} \tag{14}$$

where A_0 is the amplitude of the propagating wave at some location, A is the reduced amplitude after the wave has traveled a distance L from the initial location, and α is the attenuation coefficient expressed in Nepers per unit length [66]. By taking the natural log of both sides of the equation, the expression:

$$\alpha \cdot L = \ln\left(\frac{A_o}{A}\right) \tag{15}$$

is obtained. Ultrasound attenuation is typically expressed in units of decibels (dB) as opposed to Nepers because decibels are based on a logarithmic scale and are convenient to use when the magnitude of amplitude varies over a very large range [76]. This conversion is obtained by applying the logarithm to base 10 and multiplying by 20 to get [73]:

$$\alpha \cdot L = 20 \ln\left(\frac{A_0}{A}\right) dB \tag{16}$$

With this equation, the attenuation can be expressed in decibels per unit length, which is commonly in meters, or dB/m. This provides a more compatible scale for expressing acoustic loss in a material.

2.2.3. Ultrasound Equipment

There are several critical components necessary for generating acoustic waves in order to perform ultrasound testing. These include the ultrasonic transducer, which is the main component responsible for generating acoustic waves, the pulser-receiver, which drives the transducer and collects the resulting acoustic waves, the oscilloscope, which displays the collected signal data, and scanning equipment, which is used for mechanically manipulating the transducer over the desired area. These components comprise a comprehensive system for ultrasound evaluation of armor ceramics.

2.2.3.1. Ultrasound Transducer

The description of ultrasound equipment begins with the heart of the system – the ultrasound transducer. In general, a transducer is a device that converts one form of energy to another by accepting an input of energy in one form and producing an output of energy in some other form, with a known, fixed relationship between the input and output. Specifically, an ultrasonic transducer converts electrical energy into mechanical

energy in the form of sound, and mechanical energy back into electrical energy [62]. The conversion of electrical pulses to mechanical vibrations and the conversion of returned mechanical vibrations back into electrical pulses is the basis of ultrasonic testing [25]. Materials that are capable of this type of energy conversion are referred to as piezoelectric materials.

Three of the most common examples of materials that exhibit piezoelectric properties are quartz, lithium sulfate, and polarized ceramics [25]. Quartz crystals are known for their electrical and thermal stability, with resistance to wear and aging, insolubility in most liquids, and high mechanical strength, but they have low electromechanical conversion efficiency, or ability to effectively convert electrical to mechanical energy and vice versa [25]. Therefore, these are the least efficient piezoelectric materials for generating ultrasound. Lithium sulfate crystals have good damping properties and moderate conversion efficiency, making them the good receivers of ultrasound, but they cannot be used at temperatures above 165^{o}F [25]. Polarized ceramic materials such as barium titanate ($BaTiO_3$), lead zirconate titanate (PZT), and lead magnesium niobate-lead titanate (PMN-PT) have the highest conversion efficiency of the three, making them the most efficient generators of ultrasound energy [25]. Despite their disadvantage of exhibiting low mechanical strength, polarized piezoelectric ceramics are the most common materials used for transducer fabrication [25]. Due to their unique ability to convert mechanical to electrical and electrical to mechanical energy, piezoelectric materials are utilized as the active element in the transducer, one of the three major parts of the transducer structure, which also includes the backing material and the wear plate as shown in Figure 11.

The active element is basically a piece of polarized piezoelectric material with electrodes attached to each of its opposite faces [66], and the most common shape of the piezoelectric ceramic is a thin disk. When an electric field is applied across the material, the polarized molecules will align themselves with the electric field, resulting in induced dipoles within the molecular or crystal structure of the material, as shown in the schematic in Figure 12 [66]. This causes a proportional change in the thickness of the disk which, depending on the polarity of the electric field, will either cause it to expand or contract [76]. This phenomenon is known as the inverse piezoelectric effect. An increase in the field strength may cause further contraction or expansion of the disk, and conversely, a reduction in strength will relax it [76]. Piezoelectric materials also have the ability to perform the opposite function in converting a mechanical pulse into an electrical signal [76]. Permanently polarized materials such as quartz or $BaTiO_3$ will produce an electric field when the material changes dimensions as a result of an imposed mechanical force [66]. This phenomenon is known as the piezoelectric effect [66].

The properties of the piezoelectric disk used in the active element are also vital for a number of reasons. Besides the advantage of higher electromechanical conversion efficiency, polarized piezoelectric ceramics operate at low voltages and typically have temperature capabilities up to approximately $300^{o}C$ [66]. They also exhibit a great deal of flexibility, since they can be cut in a variety of manners to produce different wave modes, such as the longitudinal and shear types discussed previously [62]. The ability to cut piezoelectric ceramics into desired shapes and sizes is also important because of its effect on transducer frequency. The frequency is dictated by the thickness of the piezoelectric disk active element, with a uniform disk producing a single frequency in the

device [25]. A thinner active element will produce a higher transducer frequency. A thin element vibrates with a wavelength that is twice the thickness, so piezoelectric crystals are cut to a thickness that is one-half of the required wavelength [79]. For this reason, high frequency transducers are more difficult and expensive to produce because the elements are extremely thin and fragile. This relationship is described in Table II [25].

A second component of the transducer, the backing material supporting the crystal, has a great influence on the damping characteristics of the transducer [66]. It is a highly attenuative, high density material that is used to control the vibration of the transducer by absorbing the energy radiating from the back face of the active element [62]. The backing material serves two purposes. First, by controlling crystal dampening, it also controls the shape and duration of the output pulse [78]. Second, it acts as a filter by attenuating the energy on the back side of the crystal so unwanted reflections will not be received [25].

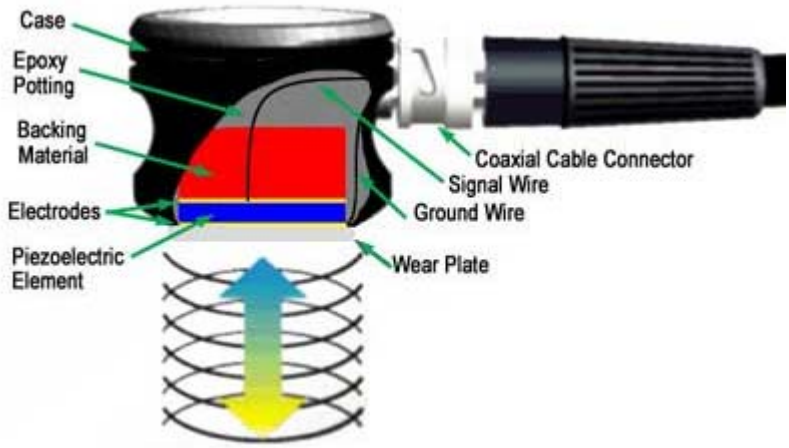

Figure 11. Schematic of ultrasound transducer containing piezoelectric active element, backing material, wear plate, and electrical connections [52].

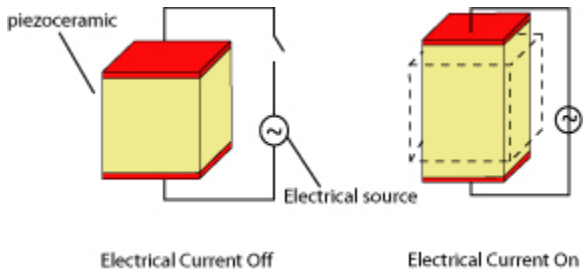

Figure 12. Schematic of inverse piezoelectric effect in which electrical voltage is applied to electroded piezoelectric material causing mechanical displacement [52].

Crystal Frequency (MHz)	Crystal Thickness (in)
0.20	0.500
0.50	0.200
1.00	0.100
2.25	0.050
5.00	0.020
10.00	0.010
15.00	0.007
20.00	0.006
25.00	0.005

Table II. Inverse relationship between piezoelectric crystal frequency and thickness [22].

A third component of the transducer, the wear plate, protects the fragile front face of the piezoelectric disk active element from the testing environment [62]. For this reason, the wear plate must be durable and corrosion resistant [62]. In order to get as much energy out of the transducer as possible, a matching layer can be incorporated into the wear plate to act as an acoustic impedance matching layer between the active element and the face of the transducer [66]. Optimal impedance matching is achieved by sizing the matching layer so that its thickness is one-quarter of the desired wavelength [66]. This keeps waves that are reflected within the matching layer in phase to minimize wave interference when they exit the layer [66].

While acoustic impedance matching is critical between the internal components of the transducer for maximizing the amount of generated ultrasound energy, it is also vital for transmitting ultrasound energy into the material being inspected for the same reason. The acoustic transmission material or layer located between the wear plate and the specimen being tested is referred to as the coupling agent or coupling medium. Coupling agents facilitate the transmission of ultrasonic energy from the transducer into the specimen and are generally necessary because the acoustic impedance mismatch between air and solids is large [66]. An acoustic impedance mismatch of this magnitude reflects most or all of the acoustic energy so that very little is transmitted into the test material [66]. The coupling agent displaces the air and makes it possible to get more sound energy into the test specimen so that a usable ultrasonic signal can be obtained [66]. Standard coupling agents include fluid materials such as water, oil, and glycerin. Table III shows acoustic impedance values of some common coupling agents in addition to common armor ceramic materials and related defect materials [23,25,26,75,80].

Materials	Density (g/cm^3)	Longitudinal Velocity (m/s)	Acoustic Impedance ($^x10^5$ $g/cm^2 \cdot s$)
Air	-	330	0.0004
Water	1.00	1,480	1.5
Oil	0.88	1,700	1.5
Glycerin	1.26	1,900	2.4
Carbon	1.47	2,250	6.3
Iron	7.69	5,900	45.4
Steel	7.80	5,850	45.6
SiC (sintered)	3.16	11,820	37.5
SiC (hot pressed)	3.21	12,100	39.0
Al_2O_3 (sintered)	3.98	10,600	43.0
AlN (hot pressed)	3.26	10,700	35.0
B_4C (sintered)	2.51	14,090	35.4
Si_3N_4 (sintered)	3.05	11,000	33.5
TiB_2 (sintered)	4.50	11,400	51.3
WC (sintered)	15.8	9,500	114.0
Al_2O_3 (green)	-	1,600	2.4
WC (green)	-	1,400	2.8

Table III. Density, longitudinal velocity, and Z values of various materials [20, 22-24, 59, 63].

Transducers can be categorized as either contact or immersion transducers based on the desired measurements and coupling agents used. Contact transducers are used for direct contact inspections with the test specimen, and their active elements are protected in a rugged casing to withstand sliding contact with a variety of materials [66]. They are designed to be easy to grip and often have replaceable wear plates to lengthen their lifetimes [66]. In contact testing, a thin film of oil, glycerin, or water is generally used [66]. Contact transducers can be further classified as either longitudinal or shear transducers, based on the type of motion generated in the active element when it is excited by an electrical pulse [78]. In longitudinal transducers, the crystal is excited in a mode that causes its thickness to expand and contract normal to the surface [78]. For transmitting longitudinal waves, commercially available fluids such as water, oil, or glycerin are typically used between the transducer and test surface [78]. In shear wave transducers, the crystal is excited in a transverse motion [78]. Since ordinary fluids do not support shear waves, special highly viscous shear wave coupling agents are necessary to allow transfer of this type of energy [78].

In contrast to contact transducers, immersion transducers do not contact the component directly [66]. Instead, they operate in a liquid environment and all of their connections are watertight [66]. They usually have an acoustic impedance matching layer that helps transmit more sound energy into the water and, in turn, into the component being inspected [66]. For immersion testing, both the transducer and sample are immersed in the coupling medium, which is typically water [66]. The internal construction of an immersion transducer is similar to that of a contact transducer, with two differences [78]. The external connector of an immersion transducer is typically the

UHF type which can be attached to a search tube and mechanically scanned to allow precise control over transducer motion. The other difference is that in immersion testing, the wear plate is called a quarter-wavelength plate and is specifically designed to allow efficient transfer of energy from the crystal to the water [78].

Immersion testing has a distinct advantage over contact testing because the water provides a source of constant coupling [78]. This input energy can be precisely controlled while manipulating or moving the transducer, unlike in contact testing where it is difficult to maintain constant contact with the part while moving the transducer, and there is a large variability in input energy [78]. In contact testing, however, the energy transfer into the part is considerably better since a large percentage of the energy that strikes the interface between the water and the part in immersion testing is reflected into the fluid [78]. Another advantage of immersion ultrasound testing is its ability to be easily applied to automated scanning applications due to the mobility of the transducer in the coupling medium of water [62]. This will be discussed in more detail throughout the text. Yet another advantage of immersion testing is its compatibility with transducer focusing [62].

Immersion transducers are available in three different configurations based on the desired degree of focus, including unfocused, or flat, spherically, or spot, focused, and cylindrically, or line, focused [62]. Focusing can be accomplished by either the addition of a lens or by curving the element itself [62]. In its most common form, a focused immersion transducer uses an acoustic lens between the crystal and the water to concentrate the acoustic energy into a narrower region [78].

2.2.3.2. Other Ultrasound Equipment

Besides the transducer, there are several other components of an ultrasound system that are important for performing ultrasound testing, including the pulser-receiver, oscilloscope, and scanning frame. It has been repeatedly mentioned that ultrasound transducers operate on the piezoelectric effect of mechanical to electrical energy conversion and vice versa. The device that supplies the electrical energy to the transducer and receives the signal reflections is referred to as the pulser-receiver, which is composed of a pulser section and a receiver section. The pulser section of the instrument is the driver of the system which generates electrical pulses of controlled energy that are very short, with durations of ~0.1 microseconds, highly repetitive, at ~1 millisecond apart, and have high amplitudes on the order of several hundred volts [78]. The way this works is that a bank of capacitors is charged periodically, then discharged across the plated faces of the piezoelectric crystal [78]. The amount of capacitance and frequency of discharge, or pulse repetition rate, are controlled by settings on the front panel of the pulser-receiver [78]. The pulse repetition frequency (PRF) setting normally runs at rates that range from 200 to 10,000 pulses per second [78]. These electrical pulses are reconverted into short mechanical ultrasonic pulses that drive the ultrasonic transducer which is in contact with the test specimen [66]. In the receiver section, voltage signals produced by the transducer, which represent the received ultrasonic pulses, are amplified [66]. Gain settings on the pulser-receiver control the degree of amplification [78]. The amplified radio frequency (RF) signals are displayed as voltage versus time traces on a standard oscilloscope [78]. The oscilloscope is triggered in synchronization with the PRF of the pulser-receiver [78].

Additional equipment is required for ultrasound scanning, including a motion controller, x-y scanning frame, and stage. If the test specimen is placed on the stage in a fixed position, the transducer, which is attached to the x-y scanning frame can be incrementally and mechanically manipulated in the x and y directions. By programming the scanning frame to raster over the test specimen in a controlled fashion, boundaries can be set up for ultrasound scanning over a selected area. Collection of the x-position, y-position, and scanning parameter will provide input for ultrasound mapping.

2.2.4. Ultrasound Beam and Sound Field Parameters

Up to this point, ultrasound has been discussed in terms of the propagation of an individual acoustic wave through a material. However, an ultrasound transducer does not only transmit a single acoustic wave, but rather a multitude of acoustic waves, which is collectively referred to as an ultrasound beam. It is the interaction of this beam with the material under inspection that determines the ultrasound results. Since the collection of acoustic waves that form the ultrasound beam are more complex than an individual acoustic wave, other parameters must be considered, and these will be discussed in the following sections. The beam transmitted into the test specimen comprises what is known as a sound field, which is characterized by the properties of multiple waves. In a transducer, the sound does not originate from a single point, but from many points along the surface of the active piezoelectric element [66]. Since an electrical pulse produces a large number of waves that are transmitted into the test specimen simultaneously, wave interaction and wave interference become critical for inspection, and must be addressed. From this point forward, ultrasound beam and sound field properties and characteristics will be discussed instead of individual acoustic waves.

2.2.4.1. Wave Interference and Near Field-Far Field Regions

When waves interact, they are superimposed on one another, and the amplitude of the sound pressure or particle displacement at any point of interaction is the sum of the amplitudes of the two individual waves [66,77]. Interacting waves that originate from the same point are described as in-phase when the peaks and valleys of one wave are exactly aligned with those of the other [66]. In this case, the two waves combine by an additive effect in which the displacement is double that of either wave acting alone [66]. Interacting waves that originate from the same point are described as out-of-phase when the peaks of one wave are exactly aligned with the valleys of the other wave [66]. In this case, the two waves cancel each other out [66]. When two waves are not completely in-phase or out-of-phase, the resulting wave is the sum of the wave amplitudes for all points along the wave [66].

For two interacting waves that do not originate from the same point, their interaction can be compared to dropping a stone into a pool of water and visualizing the waves radiating out from the source with a circular wave front [66]. If two stones are dropped a short distance apart into the water, their waves will radiate out from the source and interact with each other [66]. At every point where the waves interact, the amplitude of the particle displacement is the combined sum of the amplitudes of the particle displacement of the individual waves [66]. This is the same way that an ultrasound transducer should be viewed, since the waves propagate out from the transducer face with a circular wave front as well [66]. Where the waves interact, there are areas of destructive or constructive interference, referred to as nodes [66]. Wave interference results in diffraction patterns that break the acoustic waves up into high and low-energy

bands [25]. The resulting sound field can be divided into two separate zones which are shown in schematics in Figure 13 for both planar and focused transducers. Near the face of the transducer, there are extensive fluctuations or nodes referred to as interference fields, in which the sound field is very uneven [25,66]. This is known as the near field, or Fresnel, zone [66]. Away from the transducer, the sound field is more uniform in the region known as the far field, or Fraunhofer, zone [66]. In the far field, the beams spread out in a pattern originating from the center of the transducer [66]. Although the wave front in the far field is also non-uniform, at some distance central to the face of the transducer, a uniform and intense wave field develops [66].

The near and far fields can be visually depicted by observing the beam profile, which provides the shape of the ultrasound beam as shown in Figure 14. In the near field, the beam has a complex shape that narrows [62]. Convergence occurs due to the multiple constructive and destructive interference patterns of the acoustic waves [81]. In contrast, the beam diverges in the far field. This can be described by visualizing a typical transducer with a circular face and the sound field described as a cylindrical mass in front of the transducer [66]. The ultrasound beam energy does not retain its cylindrical shape, but spreads out when it enters the far field region, a phenomenon known as beam spread and sometimes referred to as beam divergence or ultrasonic diffraction [66].

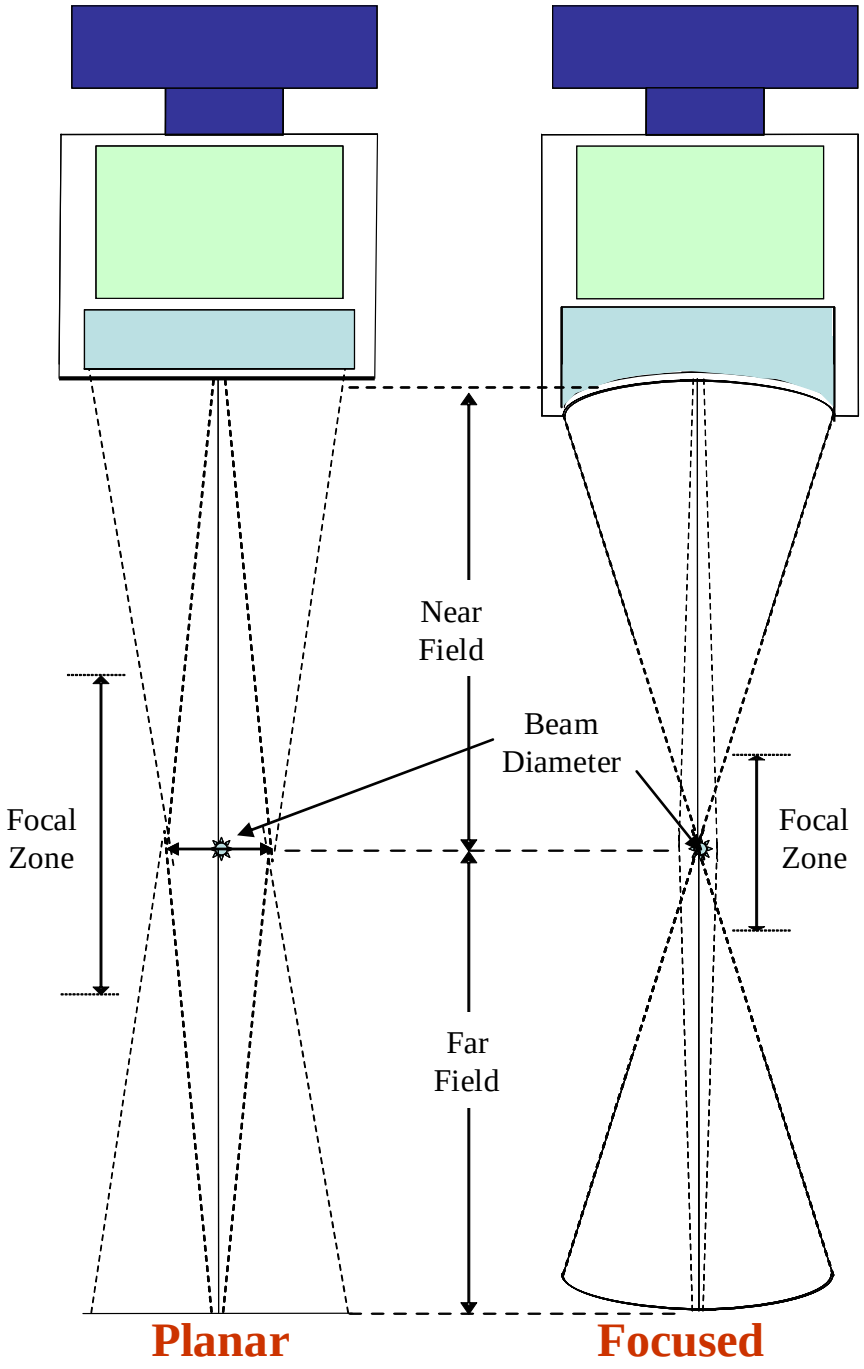

Figure 13. Schematic of planar and focused transducer configurations demonstrating near/far field relationship as well as focal zone and beam diameter differences.

(a)

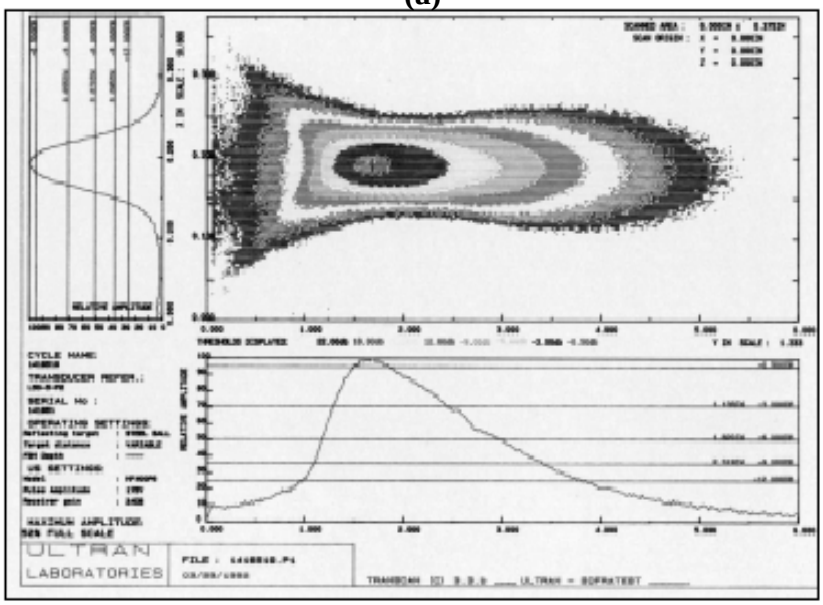

(b)

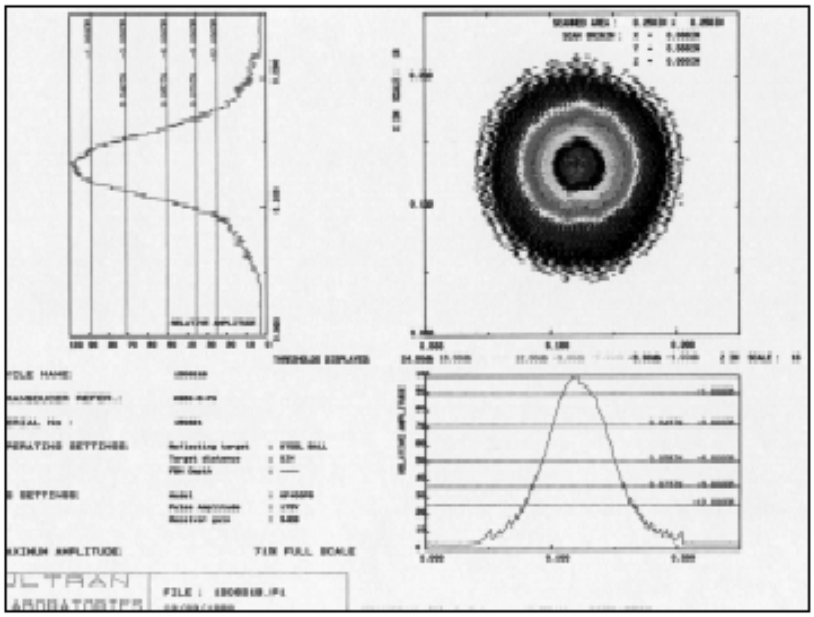

Figure 14. Characterization of (a) cross-section and (b) front view of ultrasound beam energy profile [80].

2.2.4.2. Beam Spread

Beam spread is the measure of the whole angle from side to side of the main lobe of the sound beam in the far field [66]. Beam divergence is a measure of the angle from one side of the sound beam, making it one-half of the beam spread [66]. Beam spread occurs due to the fact that the vibrating particles of the material through which the wave is traveling do not always transfer all of their energy in the direction of wave propagation [66]. Waves propagate through the transfer of energy from one particle to another in the medium, and if the particles are not directly aligned in the direction of wave propagation, some of the energy will get transferred off at an angle [66]. While constructive and destructive interference fill the sound field with fluctuation in the near field, at the start of the far field, the beam strength is always greatest at the center of the beam and diminishes as it spreads outward [66].

Beam spread is determined by the frequency and diameter of the transducer [66]. The beam spread angle can be measured by using the equation:

$$\sin\left(\frac{\alpha}{2}\right) = \frac{0.514c}{f \cdot D} \tag{17}$$

or

$$\sin\alpha = \frac{1.22\lambda}{D} \tag{18}$$

where α is the half angle beam spread from the center of the acoustic axis to the point where the sound pressure has decreased by one-half, or -6 dB, c is the sound velocity in the medium, f is the initial transducer frequency, D is the transducer diameter, and λ is the wavelength [25,62,66,81]. From this equation, it can be noted that the beam spread is inversely proportional to frequency and transducer diameter. Since the minimization of

beam spread is desirable, higher frequency, larger diameter ultrasound transducers are preferred.

2.2.4.3. Near Field – Far Field Transition

The transition between the near and far fields occurs at a distance, N, and is referred to as the natural focus of a flat, or unfocused, transducer [66]. The near/far field distance is significant because amplitude variations and fluctuations that characterize the near field change to a smoothly declining amplitude at this point [66]. The area just beyond the near field is where the sound wave is well-behaved and at its maximum strength, making it ideal for ultrasound inspection [66]. The near field distance is a function of the transducer frequency, element diameter, and sound velocity of the material, as shown in the equations:

$$N = \frac{D^2 \cdot f}{4c} \tag{19}$$

or

$$N = \frac{D^2}{4\lambda} \tag{20}$$

where N is near field distance, D is active element diameter, f is frequency, c is velocity, and λ is the wavelength [62]. According to the equation, the near-field distance increases with increasing transducer frequency [25].

2.2.5. Defect Sensitivity and Resolution

Some basic wave principle discussions and descriptions of a system for generating acoustic waves have been provided as a background introduction to the main goal of this thesis – the detection, resolution, and analysis of micron-range defects, flaws, and material inhomogeneities in high density, high material velocity, armor ceramic

materials. Sensitivity and resolution are two terms that are used in ultrasonic inspection to describe the ability of a technique to locate defects and flaws [66]. Sensitivity is a term that is used to describe defect detectability, or the ability to locate small discontinuities [66]. Resolution is a term that is used to describe the ability of a system to locate discontinuities that are either in close proximity to each other within the material or located near the surface of the test specimen [66].

There are several major factors that indicate the defect sensitivity of an ultrasound system. One is the interaction between the initial transducer frequency and the corresponding wavelength of the acoustic wave. Another related factor is the interaction between the transducer frequency and the effect of attenuation. The degree of attenuation can be a function of either the frequency of the transducer, the nature of the test specimen itself, or a combination of the two. Yet another factor that must be considered for determining sensitivity is the acoustic impedance coupling between the transducer, coupling agent, and test specimen as well as the mismatch between the bulk material and defect. While the relationship among frequency, wavelength, and attenuation can also affect the defect resolution of a system, there are some transducer parameters that have a unique effect depending on the type of resolution under evaluation. The lateral resolution is dictated by the beam diameter, or beam width. The axial resolution is dictated by the pulse length, or pulse width. Another underlying system parameter that influences both the sensitivity and resolution is the signal-to-noise-ratio. These interactions will be addressed in relation to their affect on defect sensitivity and resolution.

2.2.5.1. Frequency Effect on Wavelength

One of the most critical parameters for determining sensitivity and resolution is the frequency of the transducer that is being used for ultrasound testing, since it will indicate the wavelength of the acoustic waves that are transmitted into the sample. This will dictate the detectable feature size limit, according to the equation:

$$f = \frac{c}{\lambda} \tag{21}$$

where f is the initial transducer frequency, c is the acoustic velocity of the material, and λ is the wavelength [25]. Since the frequency and wavelength are inversely proportional, a high frequency corresponds to a short wavelength and a low frequency corresponds to a long wavelength. Sensitivity generally increases at higher frequencies and shorter wavelengths [66]. The frequency and wavelength relationship is shown in Tables IV-VI for several materials with different longitudinal velocity values. Resolution also generally increases as the frequency increases [66]. It must also be noted that while the transducer frequency is described in terms of a single frequency, the actual ultrasound beam is composed of a band of frequencies. While a single frequency may be used to represent the central frequency or peak frequency of the transducer, it is not enough to describe the entire set of frequency characteristics. The full range of frequencies is described as the transducer bandwidth. Transducer bandwidth will be discussed in more detail later in this section.

Velocity [m/s]	Freq	λ	Limit (0.1λ)	Limit (0.5λ)
12,000	500 kHz	24mm	2.4mm	12mm
12,000	1 MHz	12mm	1.2mm	6mm
12,000	10 MHz	1.2mm	120µm	600µm
12,000	20 MHz	600µm	60µm	300µm
12,000	50 MHz	240µm	24µm	120µm
12,000	75 MHz	160µm	16µm	80µm
12,000	100 MHz	120µm	12µm	60µm
12,000	125 MHz	96µm	9.6µm	48µm

Table IV. Theoretical defect detection size limitation estimates for SiC.

Velocity [m/s]	Freq	λ	Limit (0.1λ)	Limit (0.5λ)
10,850	500 kHz	22mm	2.2mm	11mm
10,850	1 MHz	11mm	1.1mm	5.4mm
10,850	10 MHz	1.1mm	109µm	543µm
10,850	20 MHz	543µm	54µm	271µm
10,850	50 MHz	217µm	22µm	109µm
10,850	75 MHz	145µm	15µm	72µm
10,850	100 MHz	109µm	11µm	54µm
10,850	125 MHz	87µm	8.7µm	43µm

Table V. Theoretical defect detection size limitation estimates for Al_2O_3.

Velocity [m/s]	Freq	λ	Limit (0.1λ)	Limit (0.5λ)
5,900	500 kHz	12mm	1.2mm	5.9mm
5,900	1 MHz	5.9mm	590µm	3.0mm
5,900	10 MHz	590µm	59µm	295µm
5,900	20 MHz	295µm	30µm	148µm
5,900	50 MHz	118µm	12µm	59µm
5,900	75 MHz	79µm	7.9µm	40µm
5,900	100 MHz	59µm	5.9µm	30µm
5,900	125 MHz	47µm	4.7µm	24µm

Table VI. Theoretical defect detection size limitation estimates for iron.

2.2.5.2. Frequency Effect on Attenuation

While increasing the transducer frequency improves sensitivity and resolution, there are also adverse effects. As the wave frequency is increased, attenuation, or loss of the signal due to wave scattering, also increases. Experimental data showing the effect of attenuation on transducer frequency and relative density are shown in Figure 15 [82]. Increased attenuation will limit the depth of penetration into a specimen, since there will be a higher degree of attenuation over a thicker specimen. Since the depth of penetration into a material being evaluated is adversely affected by attenuation, a transducer must be chosen based on a tradeoff between the defect sensitivity and desired penetration into the test specimen. According to these trends, higher frequencies can be used to resolve small features at the expense of penetration depth due to increased attenuation. Lower frequencies can be used to achieve deeper penetration due to lower attenuation, but the sensitivity required to detect smaller features will be lost. Highly dense materials are relatively acoustically transparent over a wide range of frequencies, while porous and granular materials attenuate more rapidly at higher frequencies. For this reason, the type of material being examined and the type of inhomogeneities present will also have a direct influence on attenuation [83-85].

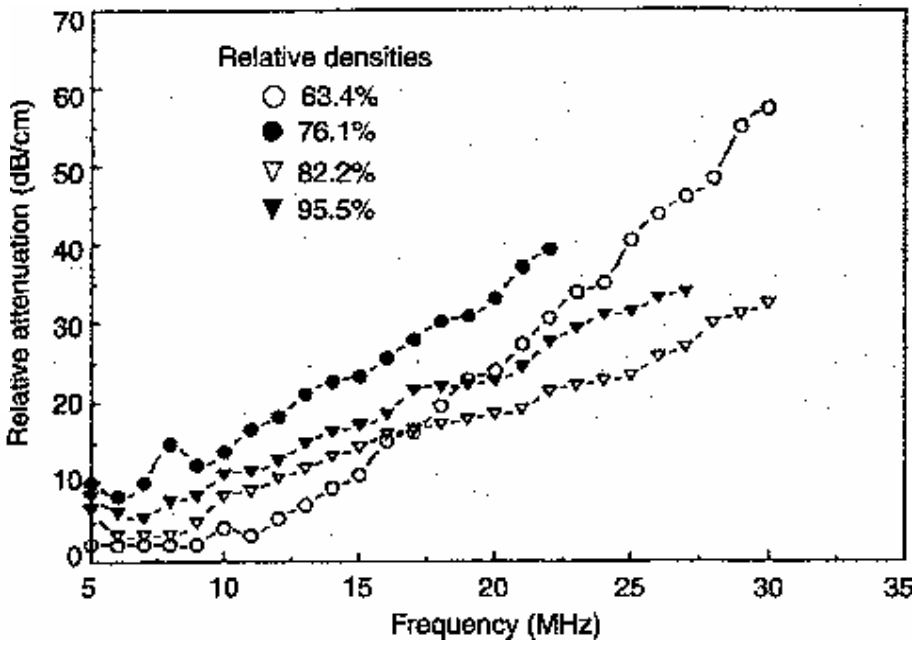

Figure 15. Attenuation effect at higher frequencies shown in terms of samples with increasing relative densities [82].

Attenuation is directly related to the amplitude, or intensity, of reflected ultrasound signals, which decrease with increasing attenuation. As described earlier, scattering and absorption, the two most influential causes of attenuation, set practical limitations to ultrasound testing of materials, but in different ways [73]. Absorption weakens the overall acoustic energy during inspection, reducing the transmitted energy and echoes from all reflections across the spectrum, whether they are from the back walls or from individual flaws [73]. This may be counterbalanced by increasing the transmitting voltage, enhancing the degree of amplification, or going to lower frequencies in which lower absorption is observed [73].

Scattering has a more pronounced effect, since it not only reduces the intensities of the echoes, but produces additional interfering echoes with varying wave characteristics [73]. In a worst case scenario, the interfering echoes from scattering can overshadow the true echoes [73]. This issue cannot be solved in the same way as the absorption problem, since the intensity of interfering echoes will also increase with increased transmitting voltage or amplification [73]. The only solution is to use lower frequencies in which the effect of attenuation is reduced [73]. However, this will also limit the degree of sensitivity to detection of small flaws [73]. For this reason, the frequency must be optimized to strike a balance between the degree of tolerable attenuation and the desired sensitivity to flaws.

2.2.5.3. Frequency Effect on Attenuation Due To Grain Scattering

While the attenuation described above accounts for macroscopic defects and features within a bulk sample, the microstructural effects of grain scattering on frequency must also be considered [78,86-88]. The frequency of the attenuation coefficient for

grain scattering depends strongly on the length of the wavelength, λ, relative to the average grain diameter, D, where V is the average volume of a grain [78]. There are three types of scattering based on this relationship, including Rayleigh, stochastic, and diffusion scattering [78]. Rayleigh scattering occurs when the wavelength is much longer than the average grain diameter ($\lambda >> D$), and the frequency variation is Vf^4, where f is the frequency. It was named for Lord Rayleigh, who first investigated it in connection with the scattering of light by dust particles in the sky [89]. Rayleigh demonstrated that the intensity of scattered radiation varies as the fourth power of frequency, which makes the sky appear blue [89]. The same relationship was found to hold true for acoustic waves scattering ultrasound energy in granular materials [89]. When the wavelength is similar to the average grain diameter ($\lambda \sim D$), stochastic scattering occurs in which the frequency dependence is Df^2. Diffusion scattering occurs when the wavelength is much shorter than the average grain diameter ($\lambda << D$), and the frequency dependence is 1/D.

In the frequency range commonly used for testing materials, the grain size is usually much smaller than the wavelength, and under these conditions, Rayleigh scattering occurs [73]. In the case of grain sizes of $1/1000^{th}$ to $1/100^{th}$ of the wavelength, scatter is for all practical purposes negligible [73]. It increases very rapidly however, approximately as the third power of the grain size, to make itself felt at sizes from $1/10^{th}$ to the full value of the wavelength [73]. For this reason, Rayleigh scattering is critical for dictating the microstructural characterization capabilities of ultrasound. During characterization of a fine-grained structure, an increase in frequency allows waves with shorter wavelengths to be transmitted into the material. When the frequency is high enough and the wavelength is short enough so that features on the order of the average

grain size fall within the range of $1/10^{th}$ to the full value of the wavelength, microstructural features can be detected. At low frequencies, these microstructural features would typically fall into the negligible range from $1/1000^{th}$ to $1/100^{th}$ of the wavelength.

On the other end of the spectrum, diffusion scattering is the reason why materials with a coarse grain structure are difficult to characterize. For materials with a large average grain size, the likelihood that the wavelength will be much shorter than the diameter of the coarse grains increases at higher frequencies, as the wavelength decreases. For ultrasonic inspection of materials with a coarse grain structure, lower frequencies are often required due to diffusion scattering. Just as in the case of Rayleigh scattering, the frequency must be optimized to effectively characterize the material under evaluation.

Much like attenuation due to grain scattering, attenuation due to absorption losses also exhibit frequency dependence. For these types of losses, the attenuation coefficient varies with the square of frequency, f^2 [78].

2.2.5.4. Acoustic Impedance Effect on Detection

The acoustic impedance value of the test specimen as compared to acoustic impedance values of any defects contained within the bulk also influences the probability of detection. As the acoustic impedance difference between the specimen and the defect increases, the amount of sound reflected by the defect increases and the amount transmitted through the defect decreases. These values can be calculated by using the equations for the reflection coefficient, R, and transmission coefficient, T, provided in the introduction to acoustic impedance. Since reflected signals are detected by the

transducer, a greater mismatch, and therefore a greater reflection of acoustic energy, will make it easier to detect the defect. Air has an extremely low acoustic impedance value close to zero, so if there are pores within a material, especially one with a high Z value, there is a high chance of detection. However, as the acoustic impedance mismatch between the specimen and the defect decreases, the amount of sound reflected by the defect is minimized and the amount transmitted through the defect increases, giving a low R value and a high T value. Defects that have Z values similar to the bulk are much more difficult to detect due to lower intensity reflected signals. A defect such as metal inclusion within the bulk of a ceramic material may be difficult to detect if the Z values match too closely. Acoustic impedance values of typical armor ceramic materials and related defects are shown in Table V. An example of the degree of reflection or transmission at different acoustic boundaries is demonstrated in the schematic in Figure 16 in which an immersed SiC matrix is evaluated in two locations. In the bulk location, the calculated percentage of original ultrasound energy that was received by the transducer in pulse-echo mode was 6.34%. In the location that placed the ultrasound beam in the path of a carbon defect, the calculated percentage of original ultrasound energy that was received by the transducer in pulse-echo mode was only 0.04%. This was a large difference in percentage of received ultrasound signal that influenced probability of detection.

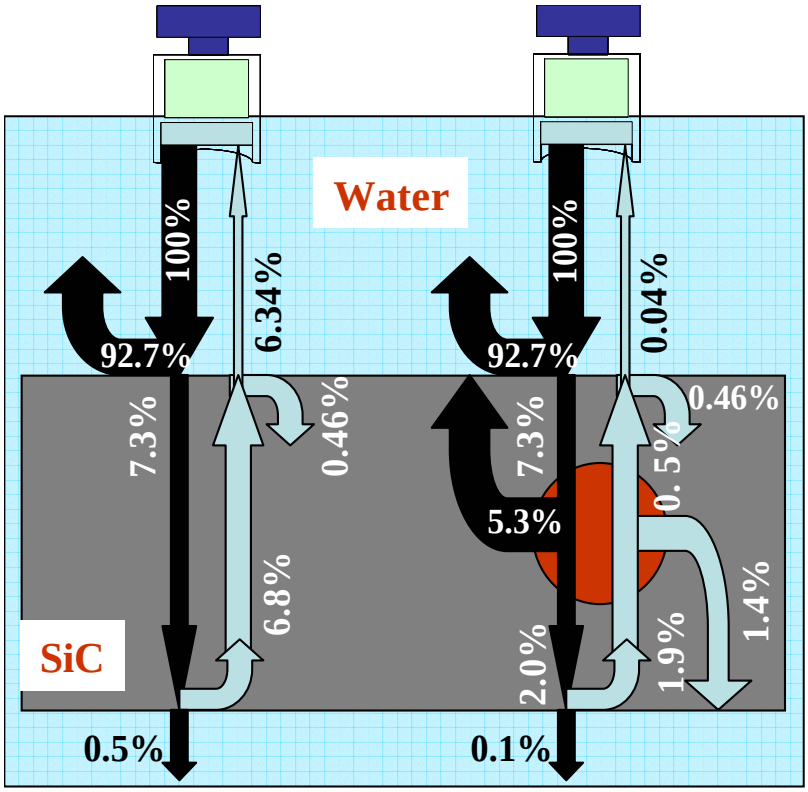

Figure 16. Schematic showing percentages of reflection and transmission of acoustic energy for SiC sample immersed in water. A homogeneous region on the left is compared to a region with a C defect on the right.

While acoustic impedance matching within the material is critical, matching between the transducer and the material must also be considered. This has been discussed in the context of a coupling medium or coupling agent which ideally provides a sufficient match between the transducer face and test specimen. However, there are improvements that can be made to maximize the amount of sound energy transmitted into the specimen. One strategy is to construct a transducer with an effective gradient of matching Z layers between the piezoelectric active element and the face of the transducer. Multiple matching layers enable maximum transmission of ultrasonic beam energy from the transducer to the sample surface. Optimization of the amount of ultrasound energy transferred into the test specimen will increase the chance that a defect will be detected, even if the acoustic impedance mismatch between the defect and the material is small.

2.2.5.5. Lateral Resolution and Beam Diameter

Lateral resolution is the ability to resolve two adjacent interfaces perpendicular to the ultrasound beam axis. The lateral resolution in an ultrasound beam varies with the beam width, or beam diameter, and is also affected by the focal length and area of the focal zone [90-91].

The main factor in determining the lateral resolution is the beam diameter of the transducer. An ideal transducer would have a perfectly narrow beam capable of transferring the maximum amount of ultrasonic energy into the test specimen. However, as described earlier, beam spread due to interference of multiple waves from the transducer face affects the shape of the beam, causing convergence of the beam in the near field and divergence in the far field. As shown in the schematic in Figure 13, even in a flat, unfocused transducer, there is a degree of natural geometrical focus which

creates a beam profile containing a region of minimum beam diameter. The distance from the face of the transducer to the point at which the beam diameter is minimized is referred to as the focal length. This is also the point in the sound field where the ultrasound beam is at its maximum amplitude and highest intensity [62]. In an unfocused transducer, this occurs at a distance that is approximately equal to the near-far field transition distance, N. The beam diameter (B_D) can be calculated using the equations:

$$B_D = \left(\frac{1.028 F_L \cdot c}{f \cdot D} \right) \tag{22}$$

or

$$B_D = 0.2568 D \cdot S_F \tag{23}$$

where F_L is focal length, c is velocity, f is frequency, D is transducer diameter, and S_F is normalized focal length, which has a value of one for a flat, unfocused transducer [62,92-93]. While the focal length describes a specific point, it is more common to refer to the entire area over which the ultrasound beam has the smallest diameter, and this is known as the focal zone [90]. The length of the focal zone (F_Z) can be calculated by the equation:

$$F_Z = N \cdot S_F{}^2 \left[\frac{2}{\left(1 + 0.5 S_F\right)} \right] \tag{24}$$

where N is the near-far field transition distance and S_F is the normalized focal length, which has a value of one for a flat, unfocused transducer [62].

The lateral resolution is approximately the same size as the beam width and the focal zone is the area over which the best lateral resolution can be achieved [90,94]. The sensitivity is also affected by the beam diameter at the point of interest, since a smaller beam diameter will result in a greater amount of energy reflected by a defect [94]. For

these reasons, it is desirable to minimize the beam diameter as much as possible. This can be achieved by increasing the frequency to reduce the beam diameter, but this also reduces the focal zone and, therefore, the range over which the minimum beam diameter is achieved [95].

2.2.5.6. Axial Resolution and Pulse Width, Bandwidth, Efficiency

The pulse width is a unit of time that corresponds to the initial frequency and its wavelength in the transducer. This factor is directly related to the sensitivity of defect detection, and is critical for determining the axial resolution, or ability to separate reflections from two closely spaced defects along the beam axis. The axial resolution is also sometimes referred to as depth resolution because of its ability to resolve defects along the axis of the ultrasound beam which penetrates through the thickness of the material. The pulse width indicates the resolution of two axial features in close proximity. A short pulse width is desirable for resolving ultrasound signals.

In this case, axial resolution is described as the ability of an ultrasonic wave to distinguish two closely lying planes such as the top and bottom surfaces of a thin material, the material surface and an internal defect close to the surface, or two defects in close proximity along the beam axis [96]. Time of flight (TOF) is the transit time of the ultrasound beam as it propagates from either the top to the bottom surface in the material, from the surface of the material to an internal defect close to the surface, or from one internal defect to another. While the behavior in all three cases is analogous, for the sake of simplification, in this case the TOF will be defined as the transit time from the top surface of the sample to an internal defect in close proximity. The relationship between

the TOF and pulse width determines the ability of the ultrasound transducer to resolve the internal defect in question.

The minimum thickness that an ultrasound wave can resolve in a given material (t_{min}) is given by the equation:

$$t_{\min} = \frac{n\lambda}{2} \tag{25}$$

where λ is the wavelength and n is the number of wavelengths of the interrogating wave [96]. The wavelength and frequency in this example will be expressed in units of time, where wavelength is the period of incident ultrasound, or 1/λ, as described in the previously defined equation. For example, at a frequency of 10 MHz, the period of 1λ = 100 ns, 2λ = 200 ns, 3λ = 300 ns, and so on, where each time period represents a pulse width [96]. If the TOF between the top surface of the material and the internal defect is 200 ns, the defect can be resolved by the 1λ 10 MHz ultrasonic wave [96]. However, the 2λ ultrasonic pulse is expected to yield poor to marginal axial resolution of the defect and the 3λ ultrasonic pulse will produce no resolution of the defect at all [96]. For this reason, a practical definition of resolution by ultrasound must contain a term that specifies the pulse width, such as the equation:

$$t_{\min} \geq p \tag{26}$$

where p is the actual width of the incident ultrasonic envelope [96]. To determine the optimum axial resolution in a given material, the equation:

$$p < M_{TOF} \tag{27}$$

can be used in which M_{TOF} is the known TOF from the surface of the test material to the internal defect [96]. Again, the same theory applied to the TOF between the top and

bottom surface of the material or the TOF between two internal defects in close proximity.

As evident in the example, at a specified ultrasonic frequency, the pulse width determines the suitability of axial resolution in a given material with respect to TOF of the propagating ultrasound wave in the material [96]. If the pulse width of incident ultrasound is large compared with the actual TOF in a given material, the resolution of the top and bottom surfaces of the material is not feasible [96]. This demonstrates that the most important parameter defining axial resolution is the width of the ultrasonic pulse [96].

In an ultrasound system, the pulse width is inversely proportional to the bandwidth of the transducer, which is defined as the width of the distribution of frequencies [97]. Therefore, a wider bandwidth will correspond to a shorter pulse width, which is desirable for improving the axial resolution [97]. When the frequency of a transducer is given by a single value, this represents the central frequency, while in actuality the bandwidth expresses the full range of frequencies associated with the transducer [66]. Highly damped transducers will respond to frequencies above and below the central frequency, and this broad bandwidth is characteristic of a transducer with short pulse width and improved axial resolution [66]. In contrast, less damped transducers will exhibit a narrower bandwidth and reduced axial resolution, but greater penetration depth [66]. Again, a tradeoff must be made between the desired axial resolution and the depth of penetration into the material.

The bandwidth can be expressed in terms of the efficiency, Q, which relates the energy stored in a system to the rate at which the energy is lost. The equation for Q is:

$$Q = \frac{f_r}{(f_1 - f_2)} \tag{28}$$

where f_r is the resonant frequency of the piezoelectric crystal in the transducer, f_1 is the frequency below f_r where the amplitude is equal to 0.707 the amplitude of f_r, and f_2 is the frequency above f_r where the amplitude is equal to 0.707 the amplitude of f_r [25]. The bandwidth is represented by (f_1 - f_2), and is inversely proportional to Q, making it proportional to the pulse width [25]. A transducer with a high Q value will respond to short voltage pulses with a relatively long lasting vibration, emitting ultrasound with a narrow bandwidth that is representative of nearly pure sound. This results in a longer pulse width and a higher signal-to-noise-ratio. On the other hand, a transducer with a low Q value will vibrate for only a short period of time, emitting a short ultrasound pulse with consisting of a broad range of frequencies. This results in a wide bandwidth which improves the axial resolution.

2.2.5.7. Transducer Focusing Factors

Up to this point, the sensitivity and resolution have been discussed in terms of flat, unfocused transducer evaluation. However, these factors can be improved by focusing the transducer. As touched upon earlier, acoustic lenses can be attached to the front surface of a transducer for focusing the ultrasound beam as shown in Figure 13 [25]. Factors such as the shape of the lens, radius of curvature of the lens, and depth of focus can affect the degree of improvement for sensitivity and resolution.

A focused transducer reduces the ultrasound beam diameter by restraining the beam to within narrow lateral dimensions at a specified depth. This improves the sensitivity to small defects and lateral resolution [81]. As the radius of curvature of the acoustic lens increases, the focal length, which is proportional to the beam diameter, also

increases [25]. The type of acoustic lens can also be important. Spherically focused transducers are used when improved resolution to small defects is required of when improved sensitivity at a specified distance is required for the test material [25]. Cylindrically focused transducers are used to shape the beam to conform to specific part geometry [25]. They are ideal for achieving improved resolution for detection of near surface flaws in curved objects [25]. Transducers can also be designed with various depths of focus [94]. With a narrow focus, the lateral resolution will be excellent at the focal depth, but deteriorate rapidly away from it [94]. Most transducers have a broader focus, which slightly compromises the resolution at the focus but gives better overall resolution over a greater depth range. These factors must be optimized to achieve a balance for ultrasound examination of the specific material under investigation [94].

The near/far field distance, N, is also an important consideration for transducer focusing. The transition distance, N, cannot be focused beyond its near field [25]. While transducers focused at > 0.6N produce little to no increase in sensitivity, those focused between 0.2N and 0.6N are ideal because they produce significant increases in sensitivity to small defects without significantly decreasing the ultrasonic energy [25]. Focusing lenses effectively shorten the near field by shifting the transition distance N closer to the transducer [25]. This can increase the reflected amplitude from defects near the focal point by shortening the focal length [25]. This technique can be used to obtain better near surface-resolution without increasing the transducer frequency [25]. This will thereby improve the axial resolution, which was described earlier with regard to the proximity of the surface of a test specimen and its near-surface defect. The disadvantage

is that sensitivity to defects in the far field is greatly decreased [25]. For these reasons, focusing properties must be carefully considered.

2.2.5.8. Signal-to-Noise Ratio

Sensitivity and resolution are both a function of the signal-to-noise ratio (SNR), which is the measure of how the signal from a defect compares to other background reflections categorized as noise [66]. A general rule is that an SNR value of three to one is often required as a minimum [66]. The signal-to-noise ratio encompasses many of the parameters that have been discussed in detail up to this point. It depends on factors such as the transducer frequency and bandwidth, the ultrasound path and distance, the transducer size and focal properties, the interface properties, the defect location with respect to the initial beam, and the size, shape, orientation, and Z value of the defect [66]. A formula relating these factors is given as:

$$SNR = \left(\frac{16}{\rho \cdot c \cdot w_x \cdot w_y \cdot p} \right)^{1/2} \cdot \left(\frac{A_{defect}(f_o)}{FOM(f_o)} \right) \tag{29}$$

where ρ is the density of the material, c is the speed of sound in the material, w_x and w_y are the lateral beam widths at the depth of the defect, p is the pulse width, A_{defect} (f_0) is the scattering amplitude of the defect at the center frequency f_0, and FOM (f_0) is the noise figure of merit at the center frequency f_0 [66].

A high value of SNR is desirable to enable high sensitivity and resolution for ultrasound defect detection. According to the formulation, SNR is directionally proportional to defect size, increasing with the size of the defect, meaning that larger defects are easier to detect [66]. The SNR increases as the beam diameter decreases for a more focused beam, making it inversely proportional to transducer beam width [66]. The

SNR also increases as the pulse width decreases, making it inversely proportional to the duration of the pulse produced by a transducer [66]. As mentioned earlier, the pulse width is reduced at higher frequencies, broader bandwidths, and higher efficiencies, making SNR proportional to frequency and bandwidth and inversely proportional to efficiency. SNR decreases with high density and velocity, making it inversely proportional to material density and acoustic velocity [66]. The SNR formulation covers many important trends that are critical to describing defect sensitivity and resolution in terms of ultrasound evaluation.

2.2.5.9. Minimum Defect Detectability

An increase in the transducer frequency at a fixed material velocity results in a shortening of the wavelength of sound [66]. Shortening the wavelength also has a significant effect on increasing the probability of detecting a defect [66]. As a general rule, a feature must be larger than one-half of the wavelength of the acoustic wave in order to stand a reasonable chance of being detected as shown in Tables IV-VI [66]. However, it has also been shown that frequency is not the only factor affecting sensitivity and resolution, which dictate whether or not a defect will be detected. Ultrasound transducer beam and sound field parameters such as beam diameter, focal zone, focal length, pulse width, bandwidth, and efficiency can be altered to improve detection capabilities. All of these factors are associated with the degree of focus of the transducer and/or modification of transducer components or dimensions. Optimization of these parameters allows detection of a feature larger than one-tenth of the wavelength of the acoustic wave as the Rayleigh limit is approached. This theoretical detection limit is

shown for various materials in Tables IV-VI and the principles will be covered in more detail in the following sections in terms of defect detection size.

The beam diameter, or beam width, which is also sometimes referred to as the spot size, was discussed in terms of its affect on both sensitivity and resolution. By minimizing the beam size, defect evaluation in the focal zone can be optimized for improvement of the minimum defect sensitivity as well as the lateral resolution. The beam diameter (B_D) equation provided earlier can be rewritten to account for wavelength, λ, due to the relationship between frequency, velocity, and wavelength. In its modified form, the equation becomes:

$$B_D = 1.028\left(\frac{\lambda \cdot F_L}{D}\right) \tag{30}$$

where F_L is the focal length and D is the diameter of the transducer. Since the beam diameter is proportional to wavelength and focal length and inversely proportional to transducer diameter, minimizing the wavelength and focal length and increasing the transducer diameter can result in minimization of the beam diameter. Decreasing the focal length can lead to aberrations associated with refraction at the interface between the coupling medium, which is most likely water, and the test specimen [98]. Increasing the transducer diameter can lead to problems associated with transducer fabrication [98]. This leads back to minimization of the wavelength, which can be achieved by increasing the transducer frequency. Functionally, this can be accomplished by minimizing the thickness of the piezoelectric active element which controls the frequency of the transducer, but there are both manufacturing and frequency-dependent limitations. Inhomogeneities within the material under inspection scatter acoustic energy as the ultrasound beam propagates, leading to exponential decay described by attenuation and

the appearance of noise referred to as backscattering [98]. These scattering phenomena limit the ability to decrease the wavelength since attenuation and backscattering become more significant at higher frequencies, as described in detail previously [98]. Therefore, the reflected signals from defects become more attenuated and the competing noise tends to obscure them [98].

The beam diameter can be further analyzed by acknowledging that proper transducer focusing can lead to its minimization and that focusing is controlled by an acoustic lens. In lens optics, the numerical aperture, NA, is defined by the equations:

$$NA = \frac{D}{F_L} \tag{31}$$

or

$$NA = 2\sin\alpha \tag{32}$$

where α is one-half of the angular aperture of the lens. This means that the beam diameter can also be expressed in terms of NA by the equation:

$$B_D = \frac{1.028\lambda}{NA} \tag{33}$$

These relationships can be analyzed in terms of Rayleigh's wave theory in order to obtain a semi-empirical equation for determining minimum defect detectability.

A vast majority of reports assume the beam diameter equal to one wavelength, which means that the focal length is equal to the active diameter within the medium of transmission. In immersion testing, while the focal length is larger in water, it is reduced in the material due to high refraction. This makes detectability equal to Rayleigh's diffraction-limited resolution, which is much better than 0.1λ [99]. All of this is a derivative of the numerical aperture within a given wavelength. If a planar, unfocused

transducer is used, the numerical aperture can be determined by assuming the maximum pressure point at the near-far field transition. In this case, the detectability is better than the commonly reported value of 0.5λ [99]. This means that the minimum defect detection limits can be conservatively established as 0.5λ for a planar unfocused transducer and 0.1λ for a focused transducer given a fixed material velocity for the specimen under evaluation as shown in Tables IV-VI [99].

The semi-empirical equations are based on the assumption that the defect and the wave front are spherical for a focused transducer and a planar, unfocused transducer. The resulting detectability limits are conservative and can be improved dramatically with signal processing [99]. For a planar, unfocused transducer, the limit can be determined by the equation:

$$\varphi_{\min} = \left(\frac{0.003\lambda \cdot N}{D} \right)^{1/2} \tag{34}$$

where φ_{min} is the minimum detectable defect and N is the near-far field transition [99]. For a focused transducer, the limit can be determined by the equation:

$$\varphi_{\min} = K\left(\frac{0.003\lambda}{NA} \right)^{1/2} \tag{35}$$

where K is the proportionality constant which is always greater than one and depends on the SNR of the whole system as well as experimental errors [99]. In both cases, the diameter of the ultrasonic beam ultimately determines how small a discontinuity is detected. For the focused transducer, this is (λ / NA), and for the planar, unfocused transducer, it is (λ N / D). These are semi-empirical relations in the sense that while they

are derivatives of Rayleigh's wave theory, they are also very practical, taking other factors such as SNR, experimental errors, and high frequency losses into account [99].

2.2.6. Ultrasound Testing

When evaluating a test specimen using an ultrasound system, the first step is to identify the reflected signals caused by acoustic impedance mismatches within the material. Reflected acoustic signals from the top and bottom surfaces of the material as well as any reflected signals from the bulk will be useful for characterizing the specimen, as shown in the schematic in Figure 17. Reflected signal characteristics such as amplitude intensity and position will aid in the detection and analysis of defects such as pores and inclusions. Techniques for identification and evaluation of reflected signals as well as relationships between these signals and various acoustic and elastic properties will be covered in this section with regard to both point analysis and imaging.

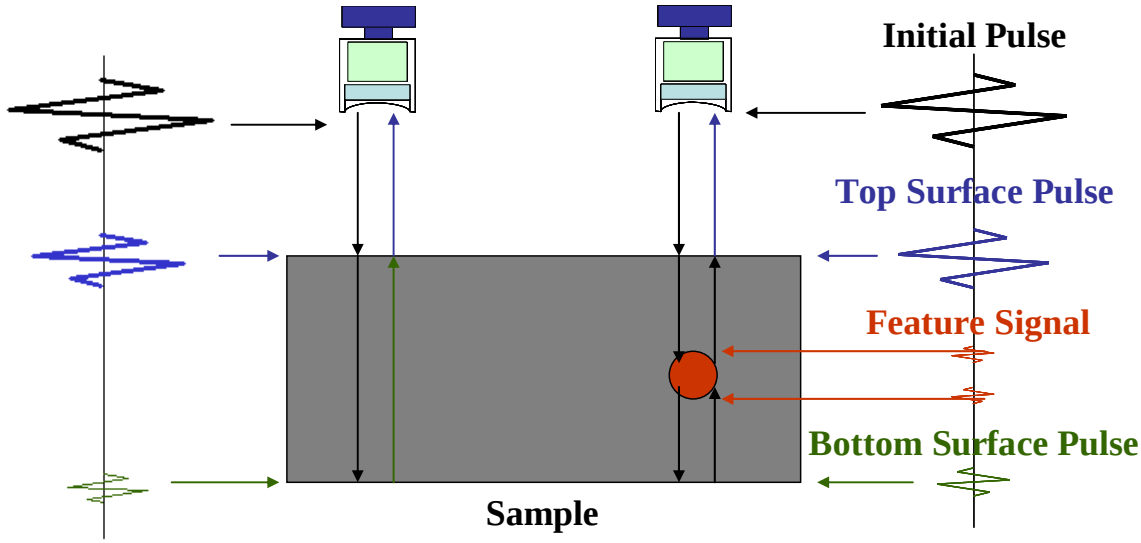

Figure 17. Schematic of common reflected signals due to acoustic impedance mismatch at various material boundaries.

2.2.6.1. Ultrasound Testing Methods and Transducer Configurations

In order to generate the desired signals, the basic order of operations is discussed in terms of the ultrasound equipment described previously. In an ultrasound system, the pulser portion of the pulser-receiver unit sends an initial electrical pulse to the ultrasonic transducer, and the piezoelectric active element in the transducer converts the pulse into acoustic waves via the inverse piezoelectric effect. The waves are transmitted through a coupling medium into the material that is being analyzed, and either transmit or reflect the ultrasonic energy, depending on the acoustic impedance differences between material boundaries [25]. For a larger acoustic impedance mismatch, more energy is reflected and less energy is transmitted into the material. When the reflected signals from the material are received and the piezoelectric active element converts the signals back into electrical waves via the piezoelectric effect, they are sent to the receiver portion of the pulser-receiver to amplify the signals. The amplified signals are displayed as a voltage versus time trace on an oscilloscope, which is used to identify the trigger signal from the transducer, the reflected signal from the top surface of the sample, the reflected signal from the bottom surface of the sample and any additional reflected signals and their echoes.

There are three main categories of ultrasonic transducer configurations that are commonly used for testing [78]. The first configuration involves a single transducer that is used as both the transmitting and receiving transducer, and this is referred to as the pulse-echo technique, which will be exclusively used in this work [78]. The second configuration, known as through-transmission, requires two transducers directly facing each other. The sample is placed between the transducers, and defects are detected by the

presence or absence of a signal picked up by the receiving transducer [78]. The third configuration, known as the pitch-catch method, also involves two transducers, but they are not directly across from each other. This technique is used specifically for samples from which either the top or bottom surface is inaccessible. In this case, the receiving transducer is placed in an accessible location to collect the signal [78].

2.2.6.2. Ultrasound Point Analysis and Imaging

The ultrasound tests are conducted using either contact testing in which the transducer is in direct contact with the test specimen, or immersion testing which is conducted in water. For contact testing, a thin layer of coupling agent is applied to the face of the transducer in order to provide acoustic impedance matching between the transducer and the sample. In immersion testing, both the transducer and test specimen are immersed in the coupling medium of water. These tests are either set up for single point analysis, which is most commonly performed using contact testing, or ultrasound imaging, which is most commonly performed using immersion testing.

For point analysis in contact mode, the reflected signals are collected over a single point at a fixed transducer position. For ultrasound imaging, the principles of point analysis are combined with the use of a scanning system, so that reflected signal variations can be analyzed over the entire area of the test specimen rather than just a few points. In this case, an immersion tank is set up in order to contain the specimen and the transducer in a coupling medium of water. The transducer is mounted to a scanning frame so that its position can be controlled in both the x and y directions. A manual z-positioning device is often set up for adjusting the position of the transducer relative to the sample. When the transducer is positioned at its optimum focal length, completely

perpendicular to the sample surface at an optimum tilt of 90^{o} relative to the sample surface, the signal amplitude is maximized. The signals are obtained in the same manner as described for point analysis, but in this case, the scan position is recorded in addition to the signal. As the transducer is mechanically manipulated over the selected sample area, the transducer collects the reflected signals at each (x, y) coordinate.

There are several inputs that are controlled before conducting the scan. The step size is dictated the smallest increment over which each data point is collected. The gated region or regions dictate which reflected signals are analyzed as the scan is run. Some examples of gated signals include selection of the top surface reflected signal to study the amplitude difference over the surface of the specimen, selection of the bottom surface reflected signal to study the degree of attenuation through the specimen, and selection of the region between the top and bottom surface reflected signals to study defects throughout the bulk of the specimen. The collected signals are assigned to a gray scale or color scale to represent changes in the variable of interest. The data are mapped by plotting points according to the assigned scale and (x, y) positions to produce an ultrasound image.

There are several important parameters involved with increasing the probability of detection of a feature during scanning including beam diameter, pulse width, step size, and acoustic impedance mismatch. By minimizing the transducer beam diameter at a given frequency, the probability of detection will increase as long as the defect size is greater than the theoretical detection limit. However, the closer the feature size is to the theoretical detection limit, the more difficult it is to distinguish. As mentioned previously, the beam diameter also dictates the lateral resolution for features that are in

close proximity. The smaller the pulse width, the higher the probability that two features along the beam axis can be resolved, as this parameter controls the axial resolution. When collecting an image, the step size is also critical since it dictates the pixel size of the image. Even if the transducer beam diameter and pulse width are sufficient for detecting a defect, it will not be detected if the step size is too large to distinguish it within the image. Another critical parameter is the acoustic impedance mismatch with the bulk material. A close match will minimize the ultrasound beam reflection and maximize the beam transmission through the feature. If the reflected signal is too small to detect due to a low acoustic impedance mismatch, the feature will not be resolved. All of these parameters must be considered and optimized in order to increase the probability that a defect or feature will be detected during ultrasound scan imaging.

2.2.6.3. A, B, and C-Scan Modes

There are three different ways to display the ultrasound signal information [76]. The first and most common is the A-scan, which is another name for the voltage verse time reading produced on the oscilloscope. The A-scan displays the amount of received ultrasonic energy as a function of time [66]. This type of scan can be performed by conducting point analysis of a specimen at any given position [76]. An example of an A-scan of the top and bottom surface reflected signals of a SiC armor ceramic material is shown in Figure 18. The B-scan is a cross-sectional profile view of the test specimen [66]. In this scan mode, the A-scan results are collected over either the x or the y dimension of the sample, and ultrasonic data representative of the cross-section of the selected area is displayed [76]. A schematic representation of a B-scan is shown in Figure 19. In the final type of ultrasound display, the transducer moves in raster-like

fashion so both x and y coordinates are collected in addition to the reflected signals. A time gate is set to consider only signals within the chosen time range, and this produces a two-dimensional downward view of defect response, referred to as a C-scan [76]. The C-scan is another name for the ultrasound image mapping described above, and is used to locate flaws and defects within a specimen based on acoustic differences. A schematic representation of the C-scan imaging technique is shown in Figure 20.

Another schematic representation of the reflected signals from an A-scan is shown from a microstructural standpoint in Figure 21. In this case, there are three examples of ultrasound beams and its corresponding reflections as it travels through an immersed material. In example A, the beam passes through the material and does not encounter any bulk defects. There are only two reflected signals in this case including the one at the water/material top surface interface and another at the material/water bottom surface interface. The attenuation of the ultrasound signal results in a lower bottom surface reflected signal amplitude that is not related to any bulk defects. In example B, the ultrasound beam encounters two triple point inclusions near the top surface and a pore near the bottom surface. This results in a total of five reflected signals including one from the water/material top surface interface, two from the material/inclusion interfaces, one from the material/pore interface, and the last from the material water bottom surface interface. The reflected signals were larger in amplitude for the pore with the greater Z mismatch as compared to the inclusions. The bottom surface reflected signal amplitude was also reduced as compared to example A due to the presence of the defects. In example C, the ultrasound beam encounters two pores and one triple point inclusion. In this case, the bottom surface reflected signal was even

lower than example B due to the higher loss of ultrasound energy from interaction with more pores in the bulk matrix. These schematic depictions represent common instances of what a high frequency ultrasound beam encounters on a microstructural level.

2.2.6.4. Measurement Domains

There are four different measurement domains that can be described to categorize the parameters and applications that are tested using ultrasound evaluation. In the time domain, the TOF values and material velocities of longitudinal and shear waves are used in application to density, thickness, defect detection, elastic and mechanical properties, among other things [75]. In the attenuation domain, fluctuations in reflected and transmitted signals at a given frequency and beam conditions are used in application to defect characterization, internal microstructure detection, and interface analysis [75]. In the frequency domain, the frequency-dependence of ultrasound attenuation is used to determine microstructure, grain size, grain boundary relationships, and porosity among other things [75]. In the image domain, TOF, velocity, and attenuation mapping are utilized for surface and internal imaging of defects, microstructure, density, velocity, and mechanical properties [75]. The only domain that will not be covered in this body of work is the frequency domain, since a single transducer with a fixed frequency will be used as opposed to the frequency variability required for operating in this domain.

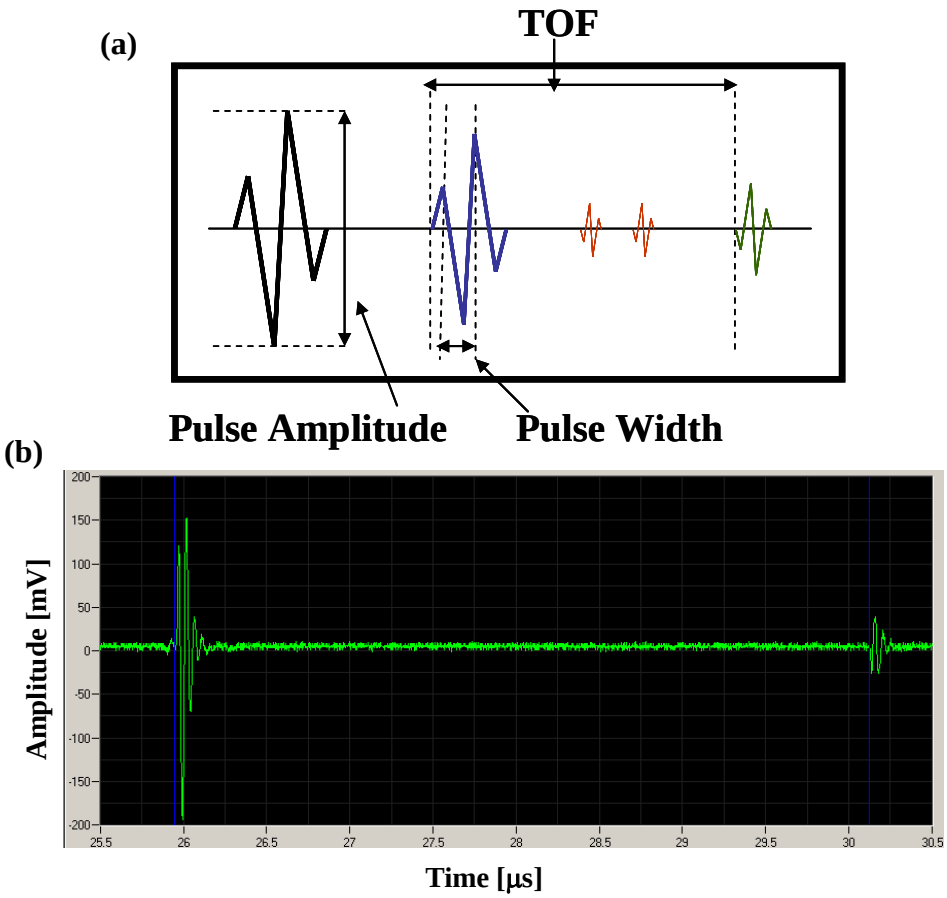

Figure 18. (a) Schematic of common A-scan signals and parameters and (b) actual top and bottom reflected signals from SiC sample.

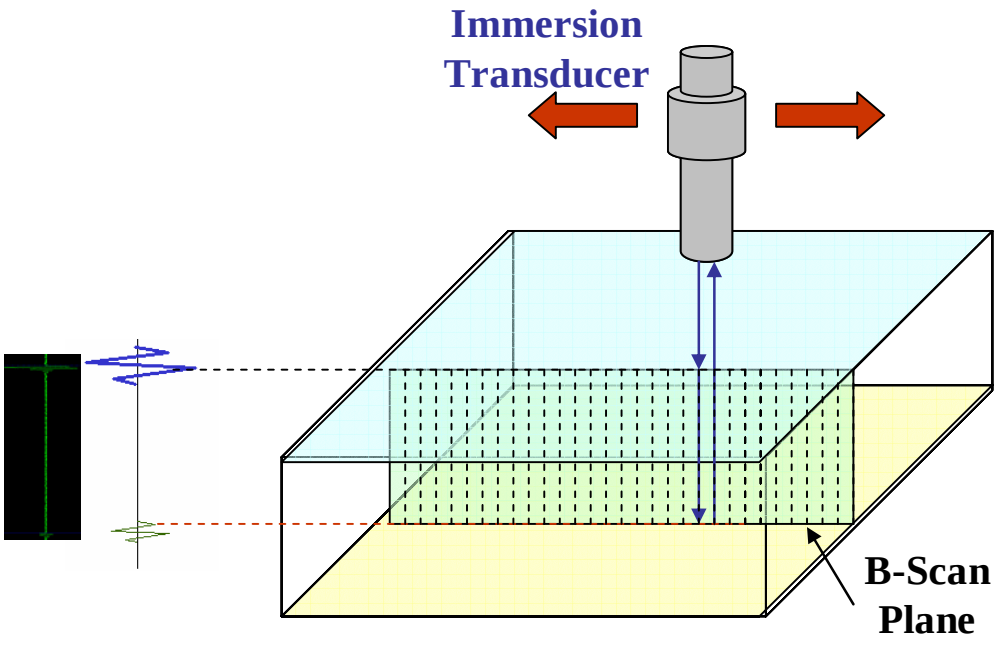

Figure 19. Schematic of B-Scan imaging of bulk test specimen for capturing cross-sectional plane in chosen location.

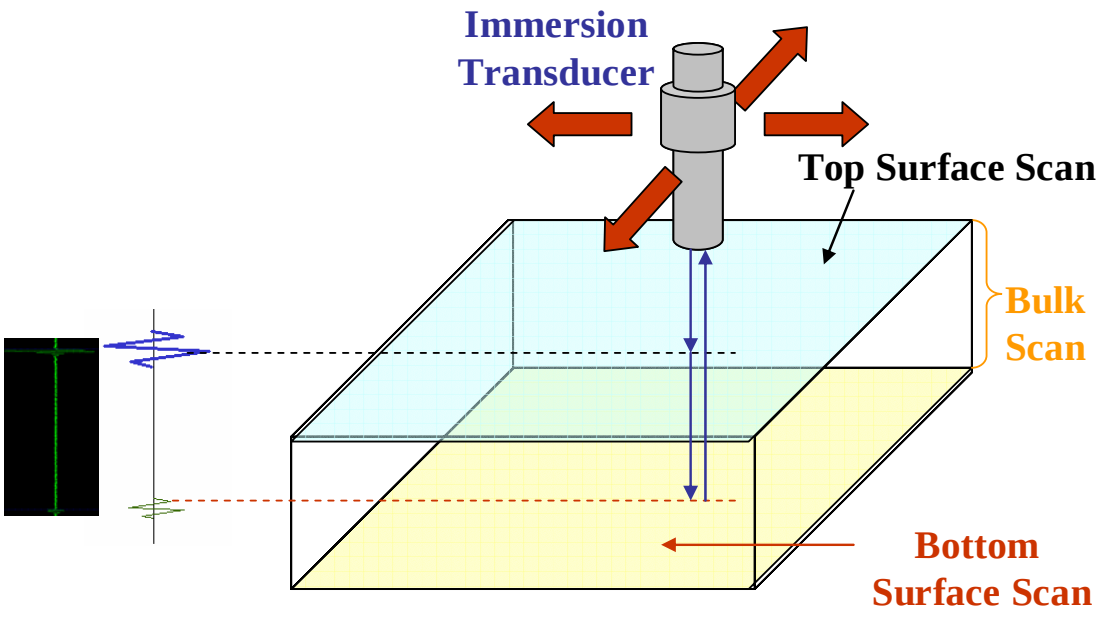

Figure 20. Schematic of C-Scan imaging of test specimen for collecting regional bulk ultrasound data.

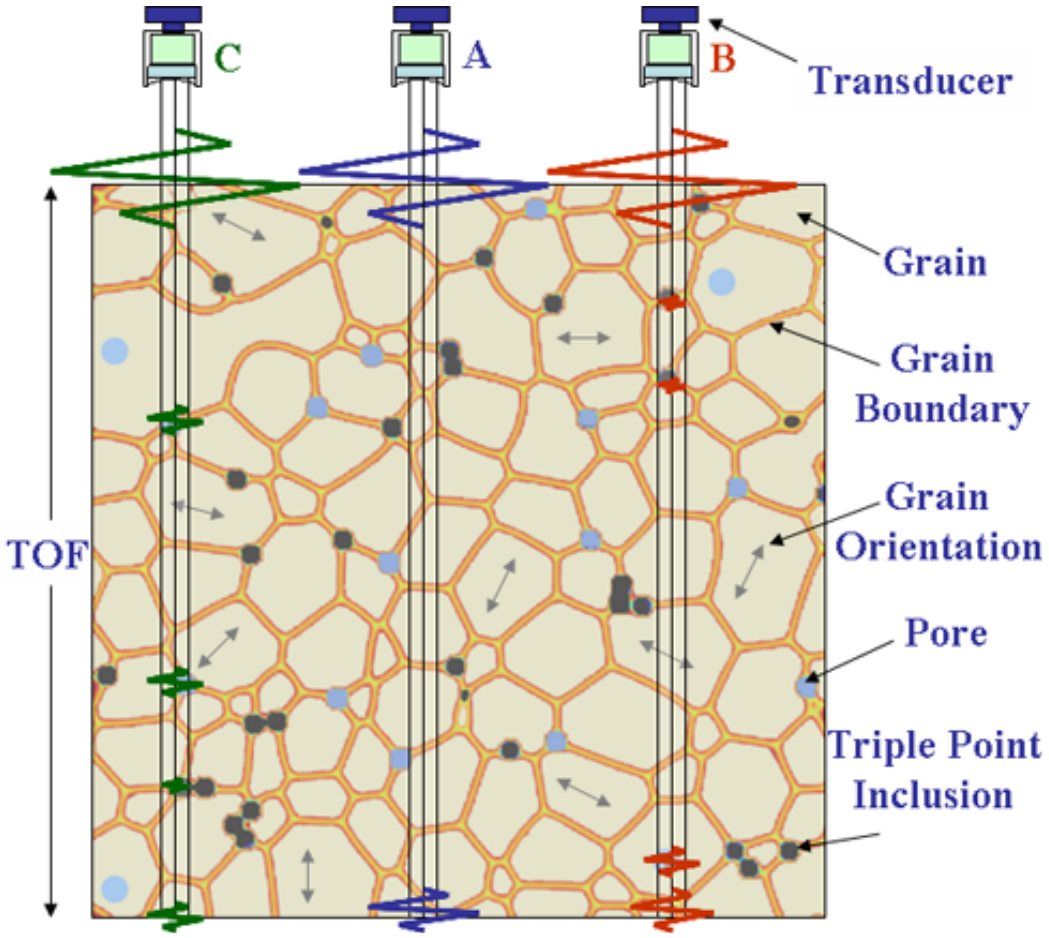

Figure 21. Schematic of ultrasound reflected signals on the microstructural level with A representing homogeneous region of material, and B and C representing interactions with pores and triple point inclusions. A reduction in the bottom surface reflected signal occurs in B and C.

2.2.6.5. TOF, Velocity, Acoustic Impedance, and Elastic Property Measurements

Time-of-flight (TOF) is a common parameter for ultrasound evaluation in the time domain. It was previously defined as the transit time between the top surface reflection and the bottom surface reflection. By using a simple relationship of distance equals rate times time, where time is TOF and distance is the known thickness, t, of the sample, the longitudinal, c_l, and shear, c_s, wave velocities can be determined using the equations [13,25]:

$$c_l = \frac{2t}{TOF_l} \tag{36}$$

or

$$c_s = \frac{2t}{TOF_s} \tag{37}$$

The factor of two is added for pulse-echo configuration as a round-trip time of travel since the same transducer is used for both transmitting and receiving the acoustic waves. If the through transmission configuration was used, in which one transducer transmits and the other receives, it would be multiplied by a factor of one. Material velocities of common armor ceramics, acoustic mediums, and defects can be found in Table IV. If the acoustic impedance, Z, of the specimen is known, the density, ρ, can also be determined from the equation [13,25]:

$$Z = \rho \cdot c_l \tag{38}$$

Before calculating the elastic properties, other useful variables that should be kept in mind are the density of the sample, ρ, and the gravitational acceleration, g, which is 9.81 m/s^2.

As mentioned earlier, the velocity of ultrasound and its mode of propagation are directly dependent on the composition and physical characteristics of the medium through which it is transmitted, where the mass of the particles is related to the density of the material and the spring constant is related to the elastic constants of the material [66,75]. Assuming isotropic conditions, the longitudinal, c_l, and shear, c_s, velocities can be used directly to calculate Poisson's ratio, elastic modulus, shear modulus, and bulk modulus [13,21,100].

Poisson's ratio, ν, which is the negative ratio of lateral and axial strains resulting from applied axial stress, can be calculated using the equation [13,21]:

$$\nu = \frac{1 - 2\left(\frac{c_s}{c_l}\right)^2}{2 - 2\left(\frac{c_s}{c_l}\right)^2} \tag{39}$$

Shear, or Young's modulus, E, which is the ratio of applied stress to the change in shape of a material, can be calculated by using the equation [21]:

$$E = \frac{{c_l}^2 \cdot \rho \cdot (1 - 2\nu) \cdot (1 + \nu)}{(1 - \nu)} \tag{40}$$

The shear modulus, G, which is the ratio of shear stress to shear strain, can be calculated by using the equation [21]:

$$G = \frac{E}{2 \cdot (1 + \nu)} \tag{41}$$

The bulk modulus, K, which is the ratio of the change in pressure acting on a volume to the fractional volume change, can be calculated by using the equation [21]:

$$K = \frac{E}{3 \cdot (1 - 2\nu)} \tag{42}$$

Good elastic properties are critical in armor ceramic materials that deal with the impact of high stress projectiles, so thickness and TOF measurements obtained from ultrasound evaluation are crucial, since they can be used to calculate a variety of elastic properties.

2.2.6.6. Time-of-Flight and Reflected Signal Amplitude Imaging

While TOF measurements can be used to evaluate changes in thickness, material velocity, density, and acoustic impedance in the time domain according to the equations, reflected signal amplitude scans can be used to analyze attenuation through a sample in the attenuation domain. Attenuation is directly related to the amplitude, or intensity, of the reflected ultrasound signals, which decreases proportionally with the degree of attenuation. Taking advantage of this phenomenon, microstructural features can be detected and evaluated by measuring the degree of attenuation caused by acoustic wave scattering [75]. Differences in reflected signal amplitude can be attributed to bulk material characteristics such as isolated defects and microstructural inhomogeneities.

When the reflected signals are gated, differences in either the TOF or reflected signal amplitude can be used for ultrasound image mapping. While the difference in amplitude intensity for the gated signal can be compared from point to point for amplitude imaging as shown in Figure 22, the difference in time between the gated top and bottom surface reflections can also used to determine the TOF differences over the scanned area as shown in Figure 23. The collected reflected signal amplitude data, in mV, or TOF data, in μs, are again assigned to a color scale or gray scale, which represent changes in the reflected signal amplitude or TOF over the gated regions. Depending on the assigned scale, one color shade difference represents a difference in voltage, commonly several mV, or fractions of a μs per shade. The data are mapped in relation to

both the assigned scales and the x and y positions of the points to produce an image map of the specimen. By examining ultrasound C-scan images of various armor ceramics, the reflected signal amplitude, attenuation, and TOF differences between samples can be compared and quantitatively analyzed to separate samples into categories based on defect percent, defect size, defect distribution, and defect location.

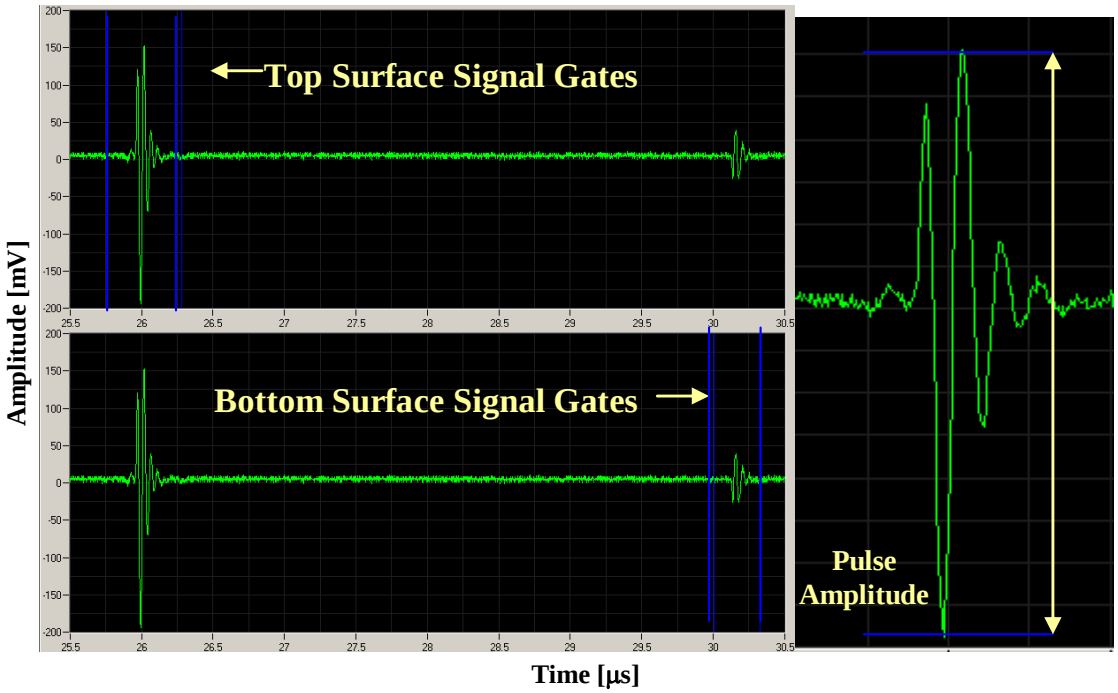

Figure 22. Reflected signal amplitude C-scan imaging method showing gating of top and bottom surface signals (left) and signal intensity (right).

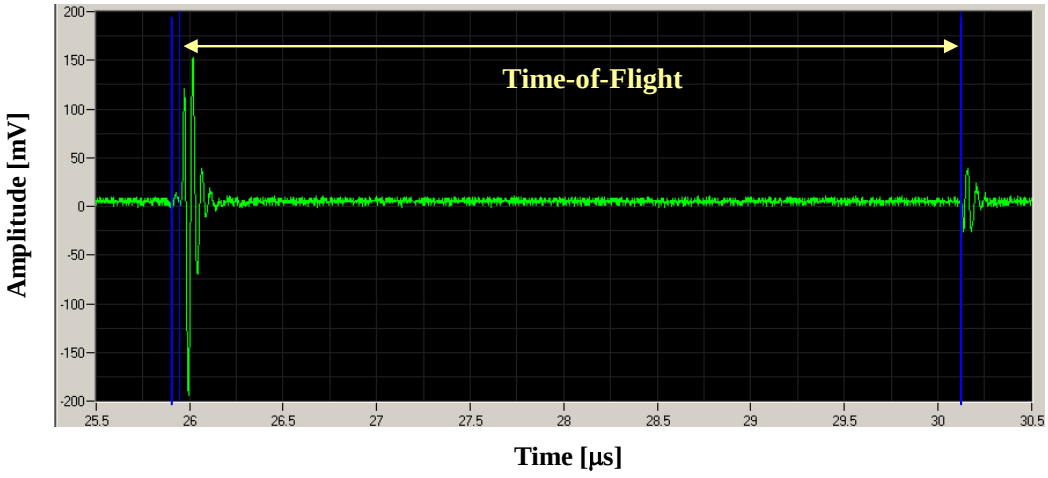

Figure 23. Time-of-flight C-scan imaging method in which both top and bottom reflected signals are gated and difference is measured.

2.2.7. Ultrasound Advantages

The advantages of ultrasound testing are that it is nondestructive, requires minimal sample preparation, and can be adapted to on-line manufacturing environments [75]. It is non-hazardous, unlike x-ray characterization methods, and can be used to test transparent or opaque materials [75]. It is sensitive to both surface and subsurface defects and only single-sided access is needed when pulse-echo techniques are used [66]. Ultrasound testing is also highly accurate in determining defect position and estimating size and shape, and the depth of penetration for flaw detection or measurement is superior to other nondestructive testing methods. When incorporated into the proper system, instantaneous ultrasound results can be provided and detailed images produced [66].

By investigating characteristics of ultrasonic waves transmitted through a material, a number of important properties can be obtained. Variations in material density cause corresponding variations in longitudinal, shear, and surface wave velocities, from which elastic properties can be determined [75]. Variations in particle size introduce scattering as a function of frequency-dependence of ultrasound attenuation, from which microstructure can be evaluated [75]. Anisotropic characteristics can be established by measuring direction-dependent velocities [75]. Manipulation of reflected or transmitted signals can be used for surface and internal imaging [75]. These characteristics make ultrasound testing useful for armor ceramic inspection.

No technique is without its disadvantages, however, and ultrasound testing is no exception. For example, the surface of the test specimen must be accessible to transmit ultrasound [66]. Testing normally requires a coupling medium to promote the transfer of sound energy into the specimen [66]. Materials that are rough, irregular in shape, curved,

very small, exceptionally thin, or inhomogeneous are often difficult to inspect [66]. Also, skill and training for ultrasound testing is more extensive than with some other nondestructive testing methods. The positive spin is that the listed disadvantages are primarily application-dependent or user-dependent issues. While other applications may be more difficult, ultrasound testing of armor ceramic plates is ideal since they are often large, polished specimens with parallel surfaces. In addition, skill can be obtained through effort, hard work, and proper training. By minimizing these limitations, a greater probability of success for ultrasonic testing of armor ceramics can be achieved.

2.2.8. Ultrasound Linear and Phased Arrays

While the transducers discussed up to this point have been single element transducers, there are alternative configurations that have helped to improve some of the aforementioned ultrasound disadvantages. By increasing the number and reducing the size of transducer elements, a linear array or phased array transducer can be assembled [101-102]. These smaller individual elements can be driven independently so that parameters such as array firing order, element selection, and pulse delay can be controlled. Linear and phased array transducers operate on the same principles. The main difference between these configurations is that a linear array typically consists of a single line of adjacent elements while a phased array consists of multiple lines of adjacent array in matrix form. For this reason, the phased array covers a larger area and a wider range of angles, giving it more flexibility and pulse sequencing options.

A linear or phased array transducer typically has up to 128 elements, but the main limitation to the number of elements is cost, as some larger linear arrays have utilized up to 512 elements spaced over 75-120 mm [103-104]. While the number of elements is not

limited theoretically, there are physical limitations to the element size, with a minimum of approximately 0.15 mm per element [104]. Since beam divergence is increased as the face of a transducer is reduced, the ultrasound beams produced from these narrow individual elements will rapidly diverge after traveling only a short distance [103]. The high degree of beam divergence leads to low sensitivity and poor lateral resolution if these small elements are driven one at a time [103]. In linear and pulse array transducers, however, adjacent elements are pulsed simultaneously, resulting in focused ultrasound beams [103]. By altering the simultaneous pulse times of these elements, the depth of focus can be controlled for evaluating the test specimen at different depths without changing the mechanical position of the transducer. Electronic focusing improves sensitivity and lateral resolution by increasing the amount of ultrasound energy in the focal zone [103]. Dynamic ultrasound beam control and beam steering can also be achieved by strategically pulsing individual elements at slightly different times. This enables control over the ultrasound beam angle, focal distance, and focal spot size [105]. Dynamic beam control is advantageous for inspecting components with complex shapes and for detecting defects of irregular shapes or multiple features along the perpendicular beam axis that would be difficult to detect using single element transduction. Electronic scanning can also be achieved using linear and phased array transducers by controlling the firing order of individual elements or groups of adjacent elements. This not only leads to faster inspection times, but also reduces the amount of mechanical transducer manipulation required for evaluating a large part.

The ultrasound linear and phased array transducer advantages of complex part inspection capabilities, large areal coverage, faster inspection times, detection of flaws

with various orientations, and simultaneous multi-angle and multi-depth inspections make it an intriguing choice. However, there are also disadvantages to these configurations in comparison to conventional single element transducers. Since it is more difficult to fabricate the smaller elements that make up the linear and phased arrays, the cost is much higher than a single element transducer. The large number of small elements also necessitates the use of more complex electronics for driving them individually. With a large number of elements, there is a greater risk that the dimensions of the elements will vary slightly, increasing the degree of error involved since the frequencies and other parameters may change for different elements. Current linear and phased array transducers are incapable of achieving frequencies higher than 20-25 MHz, which limits the detection of defects. The available array transducers are unable to detect defects and features in the micron-range that may be critical for armor ceramic ballistic performance. Due to the high cost and limited frequency capabilities of the linear and phased array transducers, single element transducers have been chosen for this work. As the fabrication methods improve for producing specialized linear and phased array transducers, it is believed that the transducer frequencies will increase and the costs will be reduced. If this is achieved in the future, these transducers will be ideal due to their advantages of faster inspection times of complex parts at multiple angles and depths.

3. Method of Attack

The main objective of this thesis work was to determine the feasibility of utilizing ultrasound C-scan imaging and quantitative analysis for nondestructive detection and evaluation of micron-range and larger features in high density bulk armor ceramics. Another objective was to develop a method for using ultrasound to establish a

representative materials fingerprint that would describe microstructural features including input data that could be quantified and applied to armor ceramic property, design, and performance optimization. These “features” and “inhomogeneities” are defined as differences in the bulk material as opposed to defects and flaws which are defined by their reduction of material properties. While “features” and “inhomogeneities” may or may not affect ballistic performance, “defects” and “flaws” are more likely to be detrimental to survivability of armor ceramics due to their influence on critical properties.

A number of tasks were designated to help meet these objectives. One task was to determine the limits and optimize the conditions necessary for nondestructively detecting 20 μm-size and larger inhomogeneities in bulk armor ceramics. Another task was to develop a quantitative analysis method for evaluation and comparison of bulk armor ceramic integrity. Another task was to develop a technique to analyze properties such as size, shape, and proximity of individual detected features to determine a defect size distribution. Another task was to develop a simulation technique to predict the effects and behavior of features of various sizes, distributions, volume percentages, and acoustic properties in a bulk armor ceramic matrix. These thesis objectives and tasks were applied to the development of a method of attack for addressing issues related to nondestructive evaluation of armor ceramic materials.

The method of attack that was chosen is summarized in this section. Since ultrasound testing and imaging was chosen as a new approach for armor ceramic material evaluation, an ultrasound system was put together at Rutgers University, and the optimum conditions were determined for conducting proper testing. A representative set of samples was necessary for determining the types of defects and features that could be

detected in commercial samples as well as samples fabricated with specific defects. The proper settings and parameters were also determined for conducting both contact point analysis and C-scan image mapping of the sample sets. For further evaluation of the point analysis and image data, both qualitative and quantitative methods of the data analysis were implemented and used for sample comparison. Evaluation of the same sample properties using other nondestructive methods, destructive methods, and microscopy were performed in order to correlate the ultrasound data. Additional simulation, modeling, and other novel evaluation techniques were also applied to extract the maximum amount data from the ultrasound results. These steps comprised the overall plan for approaching the thesis work, and were broken down into categories including the ultrasound system, test specimens, ultrasound point analysis and C-scan imaging, qualitative and quantitative analysis, ultrasound data correlation, and ultrasound simulation. These categories will be discussed in further detail in the following sections.

3.1. Ultrasound System

The first step toward conducting effective ultrasound nondestructive evaluation was to set up a functional system that could conduct proper point analysis and imaging. In order to accomplish this under a limited budget, a system was set up one component at a time by obtaining necessary equipment and assembling them into a fully functional unit. The items that were collected included a pulser-receiver, a remote pulser, an x-y scanning frame, an x-y motion controller, an immersion tank, a synapse card, an analog-to-digital (A/D) card with internal oscilloscope, and a series of ultrasonic transducers. Images of the ultrasound system and individual equipment are shown in Figure 24. A mechanical transducer holder was also built and fixed to the x-y scanning frame to

manually adjust the z-positioning and tilt in two directions of the ultrasonic transducer. A computer processing unit capable of efficient data collection was also utilized to run the synapse and A/D hardware, run the ultrasound analysis software, and to integrate the motion controller and pulser-receiver with the internal oscilloscope. The transducer series was chosen to provide a range of low to high frequencies and a selection of both focused and unfocused types to determine the optimum conditions for conducting scans of different materials. Further details of the equipment and their functions as a part of the system will be provided in the experimental section.

3.2. Samples

A set of representative samples was chosen to observe acoustic differences between a number of different samples. Differences in processing conditions were compared by ultrasonically testing SiC samples manufactured by different techniques including pressureless sintering and hot pressing. Differences in additive and second phase content were compared by ultrasonically testing sets of SiC samples that either contained or did not contain a known additive. Differences in the known presence of defects were compared by ultrasonically testing commercial armor ceramics in addition to samples with comparable material velocities and acoustic impedance values to which known defects and second phases were added. Further details of the samples and their analysis via ultrasound testing will be discussed in the results and discussion section.

Figure 24. Individual components of ultrasound system put together at Rutgers University including pulser-receiver, transducer, scanning frame and controllers for integrated operation.

3.3. Ultrasound Point Analysis and C-Scan Imaging

Two primary methods were chosen for ultrasound analysis of the various armor ceramic samples. The first was contact ultrasound for individual point analysis of the test specimens. In this method, contact transducers were utilized with a coupling medium of glycerin to improve acoustic impedance matching to the samples. The amplitude scans, or A-scans, were used to identify reflected ultrasound signals from the top surface, bottom surface, and from any defects located within the bulk of the samples. This method was used at several locations over each sample to collect longitudinal and shear TOF measurements and calculate material velocities and elastic properties at each point. This gave a general overview of individual acoustic and elastic properties before performing a full scan. The second method was ultrasound scanning for image map generation over a large sample area. In this method, an immersion setup was implemented with the x-y scanning frame, immersion tank, and ultrasonic immersion transducers to collect thousands of individual A-scans in order to look for changes in either reflected signal amplitude or TOF over the selected sample area. These reflected signal amplitude and TOF C-scan images were utilized to detect defects and compare samples, and will be discussed further in the experimental section.

3.4. Qualitative and Quantitative Analysis

After successfully collecting ultrasound point analysis data and image maps for the armor ceramic samples, it was important to present the data in a useful form for effective comparison among sample types and sample sets. By organizing and normalizing the raw reflected signal amplitude and TOF spatial data in a way that showed cumulative distribution trends, important sample comparisons could be made.

Qualitative analysis was conducted by visual analysis as well as imaging software that was capable of distinguishing regional differences over each C-scan image map. Quantitative analysis from point analysis data was collected by taking minimum values, maximum values, means, and standard deviations of thickness values, density values, longitudinal TOF values, shear TOF values, longitudinal velocities, shear velocities, acoustic impedance values, Poisson's ratios, elastic modulus values, shear modulus values, and bulk modulus values and comparing them among samples. Quantitative analysis from image maps was collected by plotting normalized reflected signal amplitude and TOF histograms from which cumulative defect distribution data could be extracted. Further analysis of critical tail regions representing areas of low reflected signal amplitude and high TOF were also conducted. Line scans, three-dimensional data maps, and amplitude distribution maps were also plotted to analyze the quantitative data in a number of forms. The combination of the qualitative and quantitative data was used to establish an ultrasound fingerprint at each individual frequency that could be used for further armor ceramic sample comparison.

3.5. Ultrasound Data Correlation

While ultrasound qualitative and quantitative data were collected, other methods were important for validating the data. Sample sets from which a history of ballistic testing had been collected were ultrasonically tested to correlate ultrasound and ballistic data. These and other methods of qualification were important for validation of the collected ultrasound data, as described in the results and discussion section.

3.6. Ultrasound Simulations

Quantitative analysis histogram data, which was used to provide information about cumulative distributions and isolate critical tail regions, served as the basis for ultrasound data simulations. Depending on the degree of difference within each sample, one or two-phase simulations were conducted. For samples with minimal occurrences or minimal acoustic impedance mismatch differences, one-phase simulations were conducted to study the effect of defect size and number of detectable defects. For samples with large inhomogeneous regions or second phases with large acoustic impedance mismatch, two-phase simulations were conducted in which peak deconvolution was utilized to study critical tail regions separately from the rest of the bulk. Further details of the application of these techniques are provided in the results and discussion section.

4. Experimental Procedure

The specific equipment and basic procedures for performing ultrasound point analysis via contact transduction and ultrasound C-scan image mapping via immersion transduction will be described in this section. These procedures will be utilized for the evaluation of armor ceramic samples in the results and discussion section. While this section will describe the basic procedures for conducting standard ultrasound testing, the development and application of specialized ultrasound techniques and methods will be detailed on an individual basis in the results and discussion section.

4.1. Ultrasound System Equipment

While some basic ultrasound system components were described in the ultrasound background section, the specific instruments and devices utilized for assembling the

ultrasound point analysis and scanning system at Rutgers University will be described here in greater detail. Besides the series of ultrasonic transducers which will be discussed in the next section, there were several critical components that were used for construction of the digital ultrasound scanning system at Rutgers. These included a pulser-receiver unit, a remote pulser, an x-y scanning frame, an x-y motion controller, an analog-to-digital (A/D) card, a synapse card, a computer processing unit, scanning software with oscilloscope functions, and image analysis software.

The pulser-receiver that was used was a JSR Synergetics Inc PR002A unit with a receiver bandwidth up to 200 MHz, a receiver attenuation control in 1 dB increments from 0 to 59 dB, a gain option of either 28 dB (low gain) or 49 dB (high gain), and a regulated -600VDC with an AC coupled positive external trigger [106]. The pulse trigger source could be used in either internal mode for continuous use or external mode for control during scanning. The pulse repetition rate ranged from 0 to 100 kHz. The remote pulser that was used was a JSR Synergetics Inc High Frequency 2.6-10-180DC100 unit which was compatible with the highest frequency transducers that were used [106]. The pulser-receiver had BNC ports for connecting the remote pulser, receiver input, receiver output, and sync/external trigger.

The x-y scanning frame was a Techno-Isel iMove Gantry III Cartesian Robot unit with servo motors, 200 mm Gantry clearance, a table size of 850 mm by 750 mm, and a usable x-y travel range of 500 mm by 540 mm [107]. The maximum speed capability of the unit was 2.4 m/s and the positional repeatability was ± 0.2 mm. The motion controller that was used for driving the servo motors of the x-y scanning frame was a Techno-Isel C-Series C10 iMove unit with two stepper drivers capable of linear

interpolation at rates of up to 10,000 steps per second and motions up to ± 8,000,000 steps. Each stepper motor amplifier, one controlling the x-direction and one controlling the y-direction, was capable of producing up to 2 AMPs at 44 Volts with protection against short circuits across phases, short circuits to ground, over and under voltage, and over-temperature. The x-y motion controller was connected to each servo motor using iMove controller cables with RS232 to AMP connectors. The C10 iMove controller also had a BNC synapse out connector on the back side of the unit.

The core computer unit was set up to handle the hardware including the A/D card and synapse card as well as the scanning and image analysis software. The computer itself was a 3.2 GHz Pentium 4 with 1 GB PC2700 SDRAM, nVidia GeForceMX400, and a 500W PSU. The A/D card was a CompuScope 8500 capable of sampling on analog input at speeds up to 500 MS/s with 8-bit resolution and storing up to 2 GigaSamples with the on-board acquisition memory [108]. It used a flash A/D converter which could take a new sample every two nanoseconds. The CompuScope 8500 card had a maximum sampling rate of 500 MHz and a signal-to-noise ratio (SNR) of 44 dB. The card had 1MΩ IN and EXT BNC connectors for data conversion. The synapse card was a Measurement Computing PCI-CTR05 five-channel counter-timer board. The function of the synapse was to act as an interfacing module between the x-y motion controller and the software to enable synchronization of the scanner control motors with the received ultrasound pulses to provide very accurate <0.01 mm scans. This technique was an improvement over conventional techniques that caused image shifts in the scans due to mistiming between the pulse collection and motor controls.

Two types of software were set up to handle ultrasound data collection and post-processing of the data and C-scan images. The iPass Core Infrastructure was developed by the Ultran Group as a Windows-based software package for handling amplitude scans and line scans as well as peak analysis in which gates could be selected for collecting the desired image map data [109]. The iPass software served as an internal oscilloscope for displaying the ultrasound signals in terms of time in microseconds (μs) along the x-axis and amplitude in millivolts (mV) along the y-axis. The iPass software was also designed to set up the scan settings such as the scan area, step size, and scan speed and relay the parameters to the x-y motion controller which controlled the x and y servo motors. For post-processing of the ultrasound data and images, the Windows-based iniView software analysis package, also developed by the Ultran Group, was utilized [109]. Some iniView functions included line scanning, amplitude distribution imaging, and regional scan selection to convert scanned areas to data sets that were used for further quantitative analysis evaluation.

4.2. Ultrasound System Equipment Integration

The individual ultrasound system components are integrated to form a cohesive unit for conducting either A-scan point analysis or C-scan image mapping. The way that the components worked together as a unit started with the ultrasound transducer of choice, which was mounted to the x-y scanning frame. This was accomplished by building a transducer mount that was fixed to the frame but could also be manipulated to manually adjust the z-positioning and tilt of the transducer in two directions. Depending on the type of transducer interface, it was connected to the remote pulser using either a BNC to BNC cable or a microdot to BNC cable. The remote pulser was connected to the

pulser-receiver in two locations including the high voltage “remote pulser” BNC connection and the “receiver input” BNC connection. While the “remote pulser” connection was used to send the high voltage pulse into the transducer, the “receiver input” connection was used to receive the analog signal from the transducer in pulse-echo configuration. From the pulser-receiver, the analog signal was sent through the “receiver output” connection through a BNC cable into the “1MΩ IN” input of the A/D card for conversion of the analog signal into digital form. The digital signals were read by the iPass software and displayed on the internal oscilloscope. While these connections enabled proper conversion of the ultrasound signals into a digital form that could be interpreted, the timing of the pulses still had to be addressed.

In order to ensure proper timing and synchronization of the pulses, a series of BNC connections was set up. The vital connection for ensuring proper timing was a T-connector that was used to integrate the A/D card, the synapse card, and pulser-receiver. The pulser-receiver connection was between the “Sync/External Trigger” connector and the T-connection on the A/D card. The synapse card connection was between the “Synapse Out” connector and the T-connection on the A/D card. The input of the synapse card was also connected by BNC cable to the back of the motion controller. In this way, motion controller sent a signal through the synapse which was sent to the T-connection. The T-connection sent the signal to the external trigger of the pulser-receiver to time the ultrasound pulses with the motion of the stage. All of this was synchronized by the synapse and interfaced with the iPass software using the A/D card.

Mechanically, the ultrasound transducer position was controlled by the x-y motion controller. The x-y motion controller was connected to the computer via an

RS232 connection, which read the commands input by the user on the iPass software. The input was sent from the motion controller through the iMove connector cables into the x and y servo motors of the x-y scanning frame, respectively. The motors controlled the x and y positions of the transducer which was mounted to the scanning frame as described earlier. For immersion scanning, a tank of deionized water was set up and the transducer manually positioned in the z-direction and both tilt-directions. By placing a test specimen into the immersion tank, the transducer could be rastered over the desired scan area in the coupling medium of water to collect the signals, which were displayed on the oscilloscope display of the iPass Core Infrastructure. The specific details of the software setup and physical sample setup will be discussed in the section on C-scan image mapping procedure.

4.3. Ultrasound System Transducers

A wide range of transducers was chosen to analyze armor ceramics under a variety of frequencies and conditions. All of the transducers that will be described were purchased from The Ultran Group in State College, Pennsylvania [109]. It was important to select transducers that were ideally suited to the type of material being evaluated in terms of acoustic series, frequency, and coupling mode. The selection of acoustic series was dependent on the material composition and test objectives. The W-series transducers were used for high resolution, M-series and λ-series transducers for extremely high resolution and detectability, VSP-series transducers for short pulse widths, and S-series transducers for shear wave measurements. Key properties for these transducer series are listed in Table VII. General W-series properties included a bandwidth between 50 and 100% at -6 dB, a pulse width between one and two periods, a sensitivity of -36 dB, and a

signal-to-noise ration (SNR) of 40 dB. General M-series properties included a bandwidth greater than 50% at -6 dB, a pulse width between two and three periods, a sensitivity of -50 dB, and an SNR of 30 dB. General λ-series planar (unfocused) transducer properties included a bandwidth between 100 and 150% at -6 dB, a pulse width between 1 and 1.5 periods, a sensitivity of -40 dB, and an SNR of 40 dB. General λ-series focused transducer properties included a bandwidth between 100 and 300% at -6 dB, a pulse width between 0.5 and 1 periods, a sensitivity of -40 dB, and an SNR of 40 dB. General VSP-series properties included a bandwidth between 100 and 150% at -6 dB, a pulse width between 0.5 and 1.5 periods, a sensitivity of -46 dB, and an SNR of 34 dB. General S-series properties included a bandwidth between 40 and 80% at -6 dB, a pulse width between two and four periods, a sensitivity of -40 dB, and an SNR of 30 dB. The series was indicated in the part number of each transducer that is described. The frequency selection was dependent on the material composition, microstructure, and texture. For the hard, fine-grain armor ceramics, ideal frequencies were selected between 10 MHz and >100 MHz. Lower frequency transducers were also selected for comparison purposes. The coupling mode selection was dependent on the material composition and desired contact with the material. Both contact and immersion transducers were utilized for point analysis or C-scan imaging, respectively, and the differences between these transducer types were described in the background section.

Transducer Series	Frequency Range	Bandwidth % @-6dB	Pulse Width (Periods)	Sensivity/SNR
W	<100 kHz to >25 MHz	50 to 100	1 to 2	-36 dB/40 dB
M	30 MHz to ~200 MHz	>50	2 to 3	-50 dB/30 dB
λ (planar)	1 MHz to >15 MHz	100 to 150	1 to 1.5	-40 dB/40 dB
λ (focused)	1 MHz to >15 MHz	100 to 300	0.5 to 1	-40 dB/40 dB
VSP	15 to 100 MHz	100 to 150	1 to 1.5	-46 dB/34 dB
S	<500 kHz to 100 MHz	40 to 80	2 to 4	-40 dB/30 dB

Table VII. Transducer series properties based on Ultran specifications for frequency range, bandwidth %, pulse width, and sensitivity [80].

In general, polarized ceramics and single crystals including PMN, PZT, and lithium niobate ($LiNbO_3$) were utilized as the active elements in the transducers, while the backing and damping materials were proprietary. The active elements used specifically for each individual transducer were also proprietary. The individual transducers that were chosen will be described.

For point analysis, four different contact transducers were used for evaluation. The first was a WC50-5 standard miniature longitudinal contact transducer with a standard side-mounted microdot co-axial connector, stainless steel housing, and hard protective face. This transducer had a nominal frequency of 5 MHz, an active diameter of 12.5 mm, and transducer dimensions of 16.0 mm in length and 17.8 mm in width. This was the lowest frequency contact transducer that was used for point analysis. The next longitudinal contact transducer was a VSP-50 very short pulse transducer with a top-mounted microdot co-axial connector and stainless steel housing. This was a broadband frequency transducer that was designed to have a very short pulse width, which has been mentioned in the background section to improve axial resolution. In this case, the pulse width was ~50 ns, the broadband frequency range was 5 to 30 MHz, and the active diameter was 4.5 mm. This transducer was used most often for point analysis because it provided sharp, high intensity ultrasound signals for accurate TOF and reflected signal amplitude measurement. The final longitudinal transducer was an MFD18-50 transducer with a top-mounted microdot co-axial connector and stainless steel housing. This M-series transducer had a nominal frequency of 50 MHz and a 4.7 mm active diameter. The one shear wave contact transducer that was utilized was an SFD18-25 transducer with a top-mounted microdot co-axial connector and stainless steel housing with a shear wave

vibration direction in the horizontal plane. This transducer had a nominal frequency of 25 MHz and an active diameter of 4.7 mm. These four transducers covered the frequency ranges and wave propagation modes necessary for conducting contact ultrasound point analysis.

For immersion testing and C-scan imaging, a series of eleven immersion transducers was used. Five of these were considered to be low frequency transducers <10 MHz that were used for comparison to the other six more ideally suited high frequency transducers with nominal frequencies between 10 MHz and 125 MHz. The five low frequency transducers were standard immersion transducers with top-mounted water-proof standard ultrahigh frequency (UHF) co-axial connectors and stainless steel cases. The first was a WS75-1 longitudinal planar immersion transducer with a nominal frequency of 1 MHz, an active diameter of 19.0 mm, an overall length of 25.0 mm, and an overall width of 21.0 mm. This was the lowest frequency immersion transducer that was used. The next was a WS50-2 longitudinal planar immersion transducer with a nominal frequency of 2 MHz, an active diameter of 12.5 mm, an overall length of 32.0 mm, and an overall width of 12.5 mm. The next was a WS50-2-P1.5 longitudinal focused immersion transducer which had the same frequency, active diameter, length, and width as the WS50-2, but also had an acoustic lens with a spherical point focus and focal length of 1.5 mm. The next was a WS50-5 longitudinal planar immersion transducer with a nominal frequency of 5 MHz, an active diameter of 25.0 mm, an overall length of 32.0 mm, and an overall width of 27.0 mm. The final low frequency transducer was a WS50-5-P3 longitudinal focused immersion transducer which had the same frequency, active diameter, length, and width as the WS50-5, but also had an acoustic

lens with a spherical point focus and focal length of 3.0 mm. While the higher frequency transducers were used most often for their high resolution and detectability capabilities, the lower frequency transducers were used for thicker samples and low density samples in which the degree of attenuation became a factor. They were also used to compare the types and sizes of defects that could be detected as compared to the higher frequency transducers.

The six high frequency transducers were primarily used for evaluation of the armor ceramic test specimens. All of these transducers had either a top-mounted or side-mounted microdot co-axial connector and were fixed to the x-y scanning frame using either a dummy UHF connector or a specially designed transducer holder that was fixed to the scanning frame. All of the transducers also had stainless steel cases. The first transducer was a WS25-10-P1.5 longitudinal focused immersion transducer which had a nominal frequency of 10 MHz, an active diameter of 6.3 mm, an overall length of 32.0 mm, and an overall width of 9.5 mm. The transducer also had an acoustic lens with a spherical point focus and focal length of 1.5 mm. The next was an LS25-10 λ-series longitudinal planar immersion transducer with a nominal frequency of 10 MHz, a broadband frequency range of 5 to 20 MHz, an active diameter of 6.3 mm, an overall length of 32.0 mm, and an overall width of 9.5 mm. The next was an LS18-15-P76 longitudinal focused immersion transducer with a nominal frequency of 15 MHz, a broadband frequency range of 8 to 30 MHz, an active diameter of 4.7 mm, an overall length of 32.0 mm, and an overall width of 9.5 mm. The transducer also had an acoustic lens with a spherical point focus and focal length of 76.0 mm. The next transducer was an MDS25-50-P150 longitudinal focused immersion transducer with a nominal frequency

of 50 MHz and an active diameter of 6.3 mm. The transducer also had an acoustically transparent optical quality clear fused silica glass acoustic lens with a spherical point focus and focal length of 150.0 mm. It should be mentioned that the long focal lengths of 76.0 mm and 150.0 mm measured for the focused transducers were based on examination of a perfect reflector in a medium of water. The optimum focal lengths were much shorter when evaluating a high velocity material such as an armor ceramic, and were adjusted according the material under evaluation. The next transducer was an MDS25-75 longitudinal planar immersion transducer with a nominal frequency of 75 MHz and an active diameter of 6.3 mm. The last and highest frequency transducer was an MDS12-125 longitudinal planar immersion transducer with a nominal frequency of 125 MHz and an active diameter of 3.2 mm. This set of longitudinal planar and focused transducers was primarily utilized for defect and microstructural feature detection in armor ceramic samples.

4.4. Point Analysis Evaluation Procedure

To conduct point analysis with a contact transducer such as the ones described above, there were several steps that needed to be taken. Initial preparation included measuring the thickness of the test specimen at each point at which the analysis was to be conducted and measuring the sample density by a technique such as the Archimedes method. As far as transducer set up, since all of the contact transducers had microdot co-axial connectors, they were connected to the remote pulser using a BNC-to-microdot cable. The test specimen, which could be a hot pressed SiC armor plate, for example, was placed on a flat surface. Glycerin [110] was used as the coupling medium of choice for improved acoustic impedance matching between the transducer face and the SiC

armor ceramic sample. A drop of glycerin was placed at each point where the analysis was conducted. The transducer face was positioned at the desired point of evaluation and physically pressed against the thin layer of glycerin on the surface of the sample. The more pressure placed on the contact transducer and the more perpendicular the transducer face was to the sample surface, the stronger the reflected ultrasound signals. The gain on the pulser receiver was adjusted to achieve the desired reflected signal parameters and the internal oscilloscope from the iPass program was used to display the reflected signals. This would result in a digital display of the reflected ultrasound signals in terms of amplitude in mV on the y-axis and time in μs on the x-axis. When a sufficient A-scan was obtained, the pulse trigger was switched to external mode on the pulser-receiver to capture a screen shot of the reflected signals. Typical reflected signals that were obtained using a longitudinal contact transducer included a top surface reflected signal due to an acoustic impedance mismatch between the transducer face and the SiC test specimen and a bottom surface reflected signal due to an acoustic impedance mismatch between the bottom of the sample and the flat surface it was resting on. Any reflected signals between the top and bottom surface signals would signify additional acoustic impedance mismatch within the bulk representing defects or inhomogeneities through that region of the sample. The gating function of the iPass software was used to measure the longitudinal TOF by placing the left side of the gate at the location where the top surface reflected signal was initiated and the right side of the gate at the location where the bottom surface reflected signal was initiated. A read out of the longitudinal TOF in μs was given, and the previously measured thickness value at the specific point was used to calculate the longitudinal velocity.

In order to determine the shear TOF, the SFD18-25 shear wave contact transducer was used, but the coupling medium was changed. In order to achieve the necessary shear signal, a more viscous coupling medium, in this case heat-treated honey, was used. There were also viscous solutions available for purchase that were intended for use as coupling agents for shear wave contact transduction. When pressing the transducer into the viscous coupling agent against the sample surface, good contact had to be made in order to achieve the resulting shear wave peak from the SiC test specimen. The gating function of iPass was again used to measure the time difference between the top surface signal reflection and the shear wave signal reflection to measure the shear TOF. By utilizing the previously measured thickness value and sample density as well as the measured longitudinal velocity from the identical point, acoustic and elastic properties could then be calculated using the previously described equations.

4.5. C-Scan Image Mapping Procedure

For immersion testing and C-scan image mapping, the transducer, test specimen, and iPass Cortex software were first set up. The iPass was set up by selecting the desired parameters to match the hardware and ultrasound system testing equipment. The iPass series 500G, input range of 1000 V, sampling rate of 500 MHz, and sampling depth of 32.77 μs were used as standard values. The positioning parameters were selected as linear motion for the iMove Gantry III x-y scanning frame. After the proper parameters were selected, the internal oscilloscope A-scan display was turned on. Again using the SiC armor ceramic plate example, the sample was placed into the immersion tank containing deionized water. The purity of the water was important to avoid any floating particulates that could have potentially interfered with ultrasound testing. After placing

the sample into the tank, a soft brush was used along the sample surfaces to remove any trapped air bubbles that formed when the sample was introduced to the water. The sample edges were placed on identical glass slides to prop the sample above the bottom surface of the tank. This was done to create a larger and more uniform acoustic impedance mismatch between the bottom of the sample and water instead of the bottom of the sample and the bottom of the immersion tank. By maximizing the degree of mismatch, the bottom surface reflected signal was optimized, which was especially important for working at high frequencies in which this signal would be closer to the noise floor.

The immersion transducer chosen for scanning was connected either top-mounted to the dummy UHF connector fixed to the x-y scanning frame or connected to an adaptor that was top-mounted to the dummy UHF connector. While the MDS25-50-P150 had a top-mounted UHF connector that could be connected directly, the other immersion transducers required one of two types of adaptors that fixed the transducer to the frame. The manual z-positioning was adjusted to lower the immersion transducer into the deionized water. The soft brush was again used to clean any trapped air bubbles off of the transducer face. The x-y motion controller and pulser-receiver were turned on to control the positioning of the transducer and enable activation of the ultrasound pulse, which was adjusted to the proper settings using the gain control. The positioning controls on the iPass were utilized to move the transducer over the center of the SiC test specimen in the x-direction and the y-direction. While observing the reflected signals using the iPass internal oscilloscope, the z-position was again changed to move the transducer to the proper distance away from the sample according to the optimum focal length. The z-

position was manually positioned further to get the reflected signals in the desired frame of time in μs. Next, the transducer tilt was adjusted in two directions until the transducer was perpendicular to the sample, indicated by maximum amplitude of the reflected ultrasound signals. After achieving proper z and tilt positioning of the transducer, the scanning region was set up.

Since the transducer was positioned near the center of the test specimen, it was first translated in the x-direction near the sample edge. Fine positioning adjustments were made until the signal disappeared. This value was set as the x-direction starting point. The transducer was next translated in the x-direction to the opposite sample edge and adjusted until the signal disappeared to set the x-direction stopping point. After bringing the transducer position back to the center, the same technique was used in the y-direction to set the y stopping and starting points and complete the setting of the full acquisition area. All of these values were programmed into the iPass software under the "positioning" tab, one of the four main tabs used for setting different parameters before conducting the scan. Also programmed under the "positioning" tab was the step size, or pixel size of the scan, which was typically 0.05 mm, 0.10 mm, or 0.20 mm, and the speed of the scan based on percentages up to 100% in each direction. While smaller step sizes were important for resolving microstructural differences, the file sizes and scan times increased due to the collection of a much greater number of data points, so this balance had to be considered.

Besides the "positioning" tab, parameters were also set under the "acquisition", "display", and "imaging" tabs. Under the "acquisition" tab, up to four gates could be set up at a time. Commonly, the first two gates were utilized, and they were adjusted in

terms of starting and ending positions in μs as well as threshold in mV. Gate 1 was set up to contain the top surface reflected signal while Gate 2 was set up to contain the bottom surface reflected signal. After setting up the desired gates, the "display" tab was selected to set up the A-scan parameters including the range of times in μs and range of amplitudes in mV that were displayed on the internal oscilloscope. The "imaging" tab was selected to determine the types of measurements to make using the gates and the ranges and types of palettes to use for display of each image. In order to select a bottom surface reflected signal amplitude scan, Gate 2 was selected for amplitude measurement in mV. In order to select a TOF scan, Gate 2 minus Gate 1 was selected for TOF measurement in μs. Typically, both of these settings were programmed to perform bottom surface reflected signal amplitude and longitudinal TOF scans simultaneously. The minimum and maximum palette values were set for the reflected signal amplitude scan in mV or dB and the longitudinal TOF scan in μs. Since these were set up on the oscilloscope in A-scan mode, several other points were examined to ensure that the signals would stay within the desired gates. If the reflected signal moved out of the gate for any reason, no data could be collected in that region. After setting up all of the scan parameters, the transducer was sent back to the home position and the scan was initialized. Each individual scan was saved with a file name that included the name of the sample, type of material, types of scans collected, gate positions and thresholds used, receiver attenuation used, and the step size used. After initiating the scan, the transducer was rastered over the pre-set acquisition area, collecting a number of reflected signal amplitude and/or TOF data points within the gates based on the step size that was input. The x and y positions of each data point were also collected for mapping each pixel

according to the pre-set palette. For typical ultrasound C-scan imaging of a four by four inch SiC armor plate at a step size of 0.20 mm, between 200,000 and 250,000 data points were collected in approximately 15 to 20 minutes to form both reflected signal amplitude and longitudinal TOF image maps. Each data point contained x-position, y-position, and either a reflected signal amplitude value in mV or a longitudinal TOF value in μs. In the next step, this large data set was qualitatively and quantitatively evaluated.

4.6. Quantitative Analysis Procedure

After collecting the ultrasound data, analysis was performed using several software programs, starting with the iniView image analysis software from The Ultran Group. After opening the file, a tab was selected to switch between the reflected signal amplitude C-scan image and the longitudinal TOF C-scan image since both were collected during the same scan. The palette was selected to qualitatively assess reflected signal amplitude or longitudinal TOF differences over the sample area. The statistics of the complete scan area including any collected background regions outside of the sample perimeter were displayed in terms of the minimum value, maximum value, average value, standard deviation value, and root mean square value. Rather than analyzing the statistics from the complete sample area including the background, a more representative area was selected using either the rectangular or circular selection tool, depending on the shape of the sample that was analyzed. The selection tool was dragged over the desired area, and the statistics of the selected region as well as the excluded region were displayed. These statistics were important for quantitative evaluation of the sample. In order to export the data for use with other statistical programs, the “export data” function was chosen and the selected area was exported as XLS data for direct compatibility with Microsoft Excel and

CSV text data that could be imported into other statistical analysis programs. Other useful iniView tools included the line scan feature, in which a line was drawn over the C-scan image and a graph was generated in terms of position on the line in the x-axis and reflected signal amplitude or longitudinal TOF in the y-axis. The pipette tool was used to select specific reflected signal amplitude or longitudinal TOF values from the scan directly, and by selecting a range of values, the image was re-plotted, showing only the values within the selected range. This was useful for identifying low reflected signal amplitude or high TOF regions over each sample. These and other features, which were not necessarily used for every scan collected, will be discussed on a more individual basis in the results and discussion section.

After collecting the XLS and CSV data from selected scan areas, Microsoft Excel was used to generate the initial quantitative analysis histogram data. First, the data were imported column-by-column into Excel, which was incapable of handling a single column of more than 65,536 data points. This was an issue for typical data sets of 200,000 to 250,000 points, a number that doubled and tripled as the step size was decreased. For this reason, the reflected signal amplitude or TOF data were input into Excel in data columns of 65,000 points each. Each column was sorted to observe minimum and maximum values, especially for high frequency scan images in which occasional data spikes would enter into the gates in the form of electromagnetic interference signals due to operation of the gated threshold close to the noise floor. If these extremely low (sometimes negative) or extremely high values were found, they were eliminated before performing further quantitative analysis because they were not representative of the test specimens. The data points from all the columns were then

selected and the “Histogram” function under “Data Analysis” under “Tools” was selected. This function separated the reflected signal amplitude values or TOF values into bins while determining the number of occurrences of each value, forming the histogram data set. When normalization of the data was required, the highest value in the desired column was determined and all of the values were divided by that value and multiplied by 100. This made it easier for comparison of samples that were on different scales so that they could be fit onto the same graphs and compared effectively. Next, the original or normalized columns were selected and the values were plotted into bar graphs.

For more advanced histogram plotting and quantitative analysis, the columns were imported into SigmaPlot 8.0 statistical analysis software. SigmaPlot was capable of handling the full data sets in a single column and was useful for 3D and other image plotting that will be discussed in the results and discussion section. After importing the histogram data, the majority of the points were zero points in which there were no occurrences of the values within those specific bins. The zero points were eliminated so that single points representing the histogram data could be plotted in terms of raw or normalized longitudinal TOF or reflected signal amplitude range on the x-axis and raw or normalized number of occurrences on the y-axis. After plotting the points, histogram curves were fit to the data using simple spline curve line and scatter to plot. SigmaPlot was also sometimes used to fit Gaussian or Lorentzian distributions to the data for comparison of the histogram curves to standard functions. In order to compare multiple normalized histogram curves to each other, plots were added and overlaid for direct comparison. For multiple curves, the amplitude or TOF ranges were adjusted and the curves from different samples color-coded and labeled. The histogram curves were

analyzed in terms of shape, distribution, and the presence of tail regions. The tail regions were critical regions of interest in that they would form at either maximum or minimum histogram curve values and represent the cumulative defect regions, for example. Tail properties were compared among samples for correlation to performance, which will be discussed further in the results and discussion section. For additional quantitative analysis, a SigmaPlot macro was used to calculate the area-under the curve for each histogram. The full-width at half maximum (FWHM) was also calculated for each curve. These quantitative values were used for further comparison of the samples, a technique which will be described in the results and discussion section. To obtain three-dimensional representations of changes in either reflected signal amplitude or TOF, the "Smooth 3D Data" option was selected under the "Transforms" menu and the raw x-position, y-position, and amplitude or TOF data were plotted in three dimensions. This 3D plot could be rotated to visually depict amplitude or TOF differences at various angles. By selecting the "Filled Contour" type of plot under "Contour Plot", the full C-scan image maps could also be created using SigmaPlot. This function will be discussed further in the results and discussion section.

While the basic quantitative analysis procedures have been described in this section, their application will be covered on a more individual basis with regard to specific armor ceramic test specimen evaluation in the following sections. Some other specialized procedures, including ultrasound fingerprint establishment, schematic representation mapping, 3D representation mapping, line scan evaluation, reflected signal amplitude distribution mapping, deconvolution tail analysis, elastic property mapping, individual defect size distribution evaluation, ultrasound simulation evaluation, and B-

scan image evaluation will be presented in the context of their corresponding application in the results and discussion section that follows.

5. Results and Discussion

Armor ceramic and ultrasound background as well as basic experimental procedures have been described up to this point. The following sections will cover the application of these concepts to ultrasound evaluation of armor ceramic materials. Armor ceramic test specimen analysis using both standard ultrasound characterization and novel ultrasound techniques will be described for comparison of armor materials with varying material integrity.

5.1. Test Specimens for Ultrasound Evaluation

Ultrasound testing and imaging was performed on a variety of test specimens. The three main categories of tested samples included hot pressed SiC, pressureless sintered SiC, and fabricated samples. A fourth category included non-SiC materials which were compared to the hot pressed and sintered SiC sample results. This unique collection of commercial and fabricated specimens enabled ultrasound image and data comparison for demonstrating variability among materials manufactured under either the same or different conditions.

The first classification of hot pressed samples included armor grade SiC plates that met manufacturing specifications and would be sold for application in the field. A second classification of hot pressed samples included SiC plates that either did not meet manufactured specifications or did not pass visual inspection and were pulled from the manufacturing line. One set of tested hot pressed SiC samples included plates from both of these classifications. While the samples were manufactured within the same batch

under the same processing conditions, only one of the specimens was considered acceptable according to predetermined specifications while the other two were red-flagged for either not meeting the density requirements or showing visible discolorations on the surface believed to be related to defects within the bulk. Another set of hot pressed samples included armor grade SiC plates with varying thicknesses.

The pressureless sintered SiC samples were commercial specimens that included three types. The first was a set of eight sintered SiC specimens from the same batch that were pressureless sintered with no additives. The second was a set of eight sintered SiC specimens from the same batch that were pressureless sintered with a TiB_2 additive. Variations in materials from the same batch as well as variations between the specimens with and without additives were ultrasonically tested and imaged. The third set of sintered SiC specimens included three samples that were manufactured under slightly different processing conditions. The uniqueness of these samples was that a history of ballistic performance data was collected from similar samples that originated from the same batches that they were fabricated from.

The third category of samples was fabricated by introducing features of known type, size, and distribution in order to test the detectability and resolution limits of the ultrasound equipment while confirming quantitative analysis results. A variety of different materials was used. One type was an epoxy matrix with WC spheres of different sizes and volume percentages which were used to look at the effect of high acoustic impedance mismatch within a bulk material. Alumina bulk materials were sintered with hollow polymer spheres of varying size and distribution that burned out to form pores within the Al_2O_3 matrix. Some additional hot pressed samples were

fabricated with various types of embedded defects of varying sizes that were used to simulate common defects found in commercial SiC armor ceramics. All of these samples were tested and imaged using ultrasound to detect the known features.

The final category included a series of samples that were mainly utilized for comparison to the test specimens in the other three categories. Hot pressed aluminum nitride, which is also used for armor applications, was analyzed as an alternative hot pressed material to compare to hot pressed SiC. Similarly, a set of pressureless sintered Al_2O_3 samples was tested ultrasonically to compare to the sintered SiC samples that were evaluated. The point analysis, ultrasound TOF and reflected signal amplitude imaging, and quantitative analysis data on these test specimens and sample sets will be discussed in detail.

5.2. SiC Test Specimens A, B, and C Hot Pressed Under the Same Conditions

Three hot pressed SiC specimens with varying material characteristics, identified as A, B, and C, were evaluated ultrasonically. While all three specimens were from the same batch and hot pressed under identical processing conditions, sample A was a high density armor grade SiC specimen, sample B had a suspected region of lower density according to the manufacturer, as marked on the sample surface, and sample C had a single discolored region, also marked on the sample surface, that was believed to be a defect. Sample A was an example of an armor plate that would be sold commercially, while samples B and C did not meet standard specifications and were red-flagged and pulled from the production line. The dimensions for sample A included a length of 101.60 mm, a width of 50.82 mm, and a thickness of 19.09 mm. The dimensions for sample B consisted of a length of 99.99 mm, a width of 82.76 mm, and a thickness of

12.78 mm. The dimensions for sample C included a length of 99.99 mm, a width of 99.99 mm, and a thickness of 12.78 mm. The densities for each sample were measured as 3.21 g/cm^3 for sample A, 3.18 g/cm^3 for sample B, and 3.19 g/cm^3 for sample C. The three hot pressed specimens were evaluated using reflected signal amplitude C-scan imaging and quantitative analysis as well as TOF C-scan imaging and quantitative analysis.

5.2.1. Reflected Signal Amplitude Evaluation of A, B, and C

The SiC specimens were evaluated for reflected signal amplitude variations using three ultrasound transducers of different frequencies including a 5 MHz (MDS25-5) transducer, a 50 MHz (MDS25-50) transducer, and 125 MHz (MDS12-125) transducer. Before performing ultrasound C-scan imaging, each specimen was immersed in de-ionized water, which was used as a coupling medium. The scan area was selected by choosing the x and y positions that would result in complete analysis of each specimen. Before performing the scans, it was confirmed that the bottom surface reflected signal could be detected at the highest frequency of 125 MHz for each specimen to ensure that penetration depth was not an issue. The bottom surface reflection signals were gated to evaluate the reflected signal amplitude changes through the bulk of each specimen. Ultrasound C-scan imaging was performed for each armor ceramic specimen at each of the three frequencies and the resulting data were analyzed both qualitatively and quantitatively.

The 5 MHz amplitude C-scans for the three SiC samples are shown in Figure 25. While there were slight variations over each individual C-scan image of ~1-10 mV, the scans appeared to be very similar, showing only minor reflected signal amplitude changes

over the full 0-75 mV range. Qualitatively, there were no major differences that could be determined among samples A, B, and C. The reflected signal amplitude ranges, averages, and standard deviations for the 5 MHz samples were compared in Table VIII to look for quantitative differences. The average amplitude values over the scanned areas were 48 mV, 54 mV, and 60 mV, while the average standard deviation values were 29 mV, 31 mV, and 31 mV, for A, B, and C, respectively. While the standard deviation values followed the expected trend of fewer amplitude differences for the armor grade specimen, sample A, the variations among the three samples were not significant enough at the lowest frequency of 5 MHz to categorize the specimens as qualitatively or quantitatively different. Ultrasound evaluation of the low frequency scans demonstrated that the three specimens were acoustically similar.

The results of the 50 MHz C-scan images, which were collected over an amplitude range of 0-150 mV, are shown in Figure 26. While the images appeared to be rather similar, there were some pronounced reflected signal amplitude variations detected at 50 MHz that could not be seen at 5 MHz. This was most evident in sample C, which contained a specific isolated feature with an amplitude value that was 15-20 mV higher than the amplitude values of the rest of the scanned specimen. This feature was singled out in the circled region and corresponded to the location of the discoloration that was red-flagged by the manufacturer. There were also several isolated features in sample C on the order of approximately 1 mm that had amplitude values that were 10-15 mV lower than the average amplitude of the rest of the scanned specimen. As shown in Table VIII, the average amplitude values for each sample were 112 mV, 99 mV, and 102 mV, while the average standard deviation values were 44 mV, 50 mV, and 49 mV, for A, B, and C,

respectively. Quantitatively, the standard deviation trends were similar to the results at 5 MHz, but qualitatively, the isolated features detected at the higher frequency of 50 MHz showed a vast improvement in sensitivity. Significant variations among the samples started to become apparent at this higher frequency.

At 125 MHz, the reflected signal amplitude differences among samples A, B, and C were most apparent, as shown in Figure 27. By performing C-scan imaging with this high frequency transducer, an increase in sensitivity and resolution was attained. Many features that could not be detected at 5 and 50 MHz were identified at 125 MHz. At the same time, the bottom surface reflected signal amplitude values were reduced to a range of 0-30 mV due to the higher degree of attenuation at the highest frequency. As shown in Table VIII, the average amplitude values for each sample were 21 mV, 19 mV, and 20 mV, while the average standard deviation values were 3.6 mV, 4.6 mV, and 5.9 mV, for A, B, and C, respectively. The trends were again consistent, with greater deviations for B and C as compared to the armor grade sample A. Sample A appeared to have the most homogeneous reflected signal amplitude distribution among the three samples, which was expected. Sample B showed the most pronounced qualitative differences. While the C-scan images at 5 and 50 MHz appeared to be relatively uniform, at 125 MHz, a large region of low reflected signal amplitude was found that bordered a large region of high reflected signal amplitude. The lower amplitude region showed agreement between the C-scan results and the manufacturer's identification of this area as a low density region, since a lower density region would mean a higher degree of porosity and therefore, a lower overall reflected signal amplitude. Based on the sharp regional change from low amplitude to high amplitude, it is possible that the low amplitude region was a result of a

process-related issue, such as an inhomogeneous density distribution within the bulk of the SiC compact. The C-scan results for sample B seemed to be consistent with this type of phenomenon. For sample C, the discoloration that was red-flagged by the manufacturer appeared as an isolated high amplitude defect. In addition, alternating bands of high and low amplitude were detected, with a high amplitude band that ran vertically through the center of sample C that was not detected at lower frequencies. The high reflected signal amplitude of this feature as compared to the rest of the bulk indicated that it was most likely a high density inclusion through which a greater amount of ultrasound energy was transmitted, resulting in an increase in bottom surface reflected signal intensity.

The features that were detected using the 125 MHz transducer were either undetected or poorly detected when using the lower frequency 5 MHz and 50 MHz transducers, demonstrating the importance of high frequency evaluation of bulk armor ceramic samples. Since the acoustic wavelengths at 125 MHz were much shorter and closer to the size of the microstructural features in the samples, detection of microstructural inhomogeneities was possible due to wave scattering effects from these small features. If a 5 MHz ultrasound comparison of the three samples had been made initially, it would have appeared as though the samples were equivalent and would perform equally well. If a 125 MHz ultrasound comparison of the three samples had been performed, samples B and C would have been questioned for their performance capability, since a higher number of isolated defects and low density regions in bulk armor ceramics were detected, increasing the probability that the specimens were not ballistically equivalent.

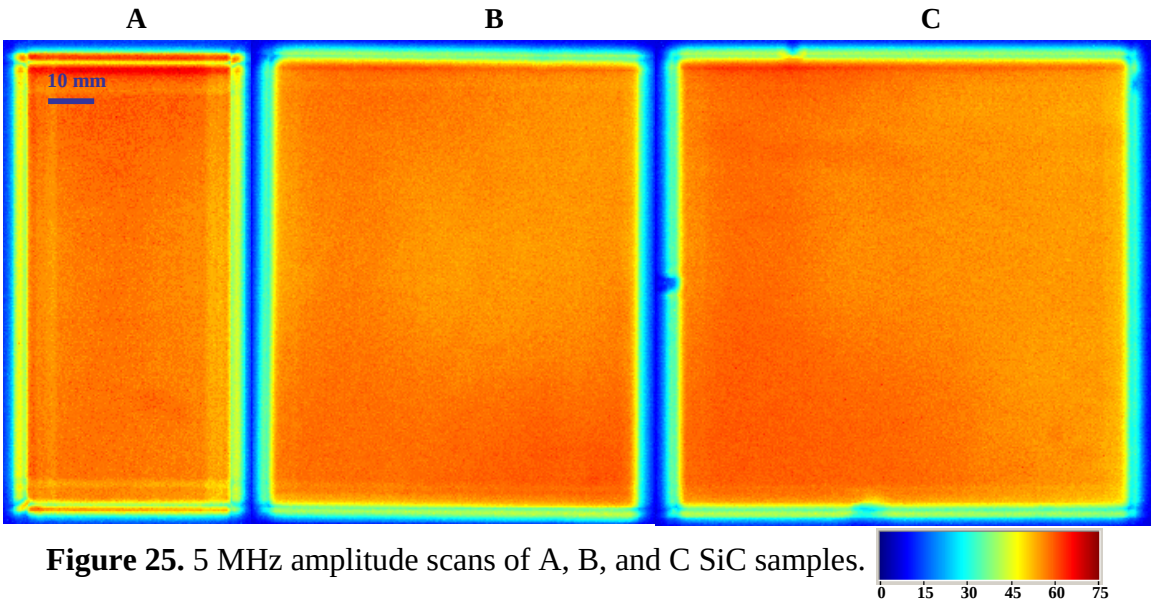

Figure 25. 5 MHz amplitude scans of A, B, and C SiC samples.

Sample	Frequency [MHz]	Min AMP [mV]	Max AMP [mV]	Avg AMP [mV]	StD AMP [mV]
A	**5**	9	80	48	29
A	**50**	9	156	112	44
A	**125**	9	30	21	3.6
B	**5**	9	94	54	31
B	**50**	9	148	99	50
B	**125**	9	38	19	4.6
C	**5**	9	98	60	31
C	**50**	8	147	102	49
C	**125**	9	36	20	5.9

Table VIII. Amplitude minimum, maximum, average and standard deviation values from samples A, B, and C at 5, 50, and 125 MHz frequencies.

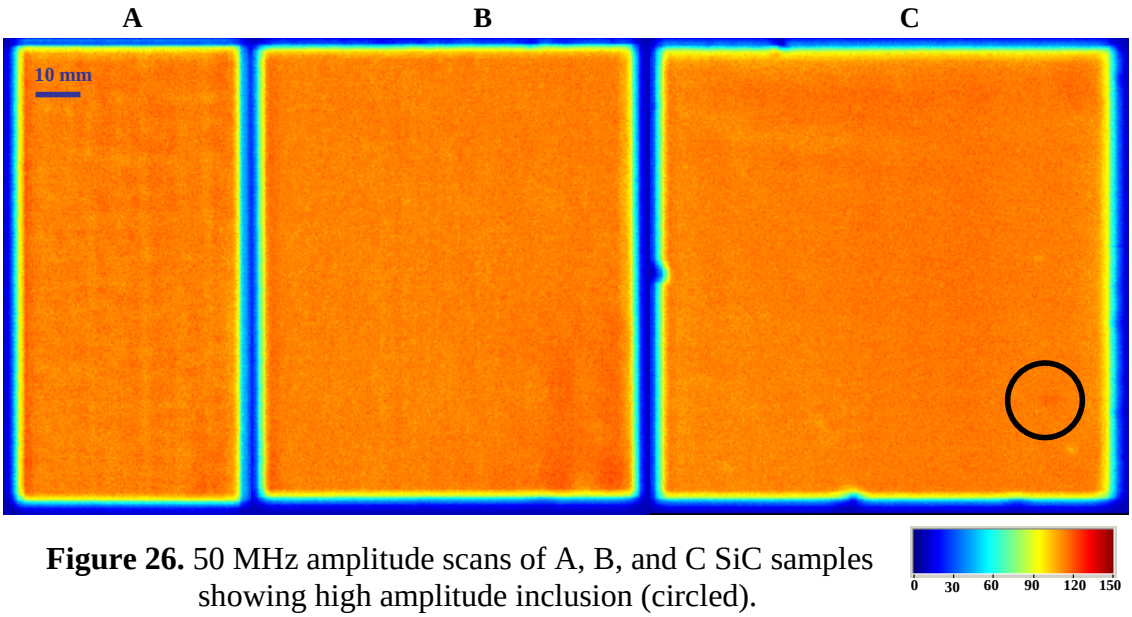

Figure 26. 50 MHz amplitude scans of A, B, and C SiC samples showing high amplitude inclusion (circled).

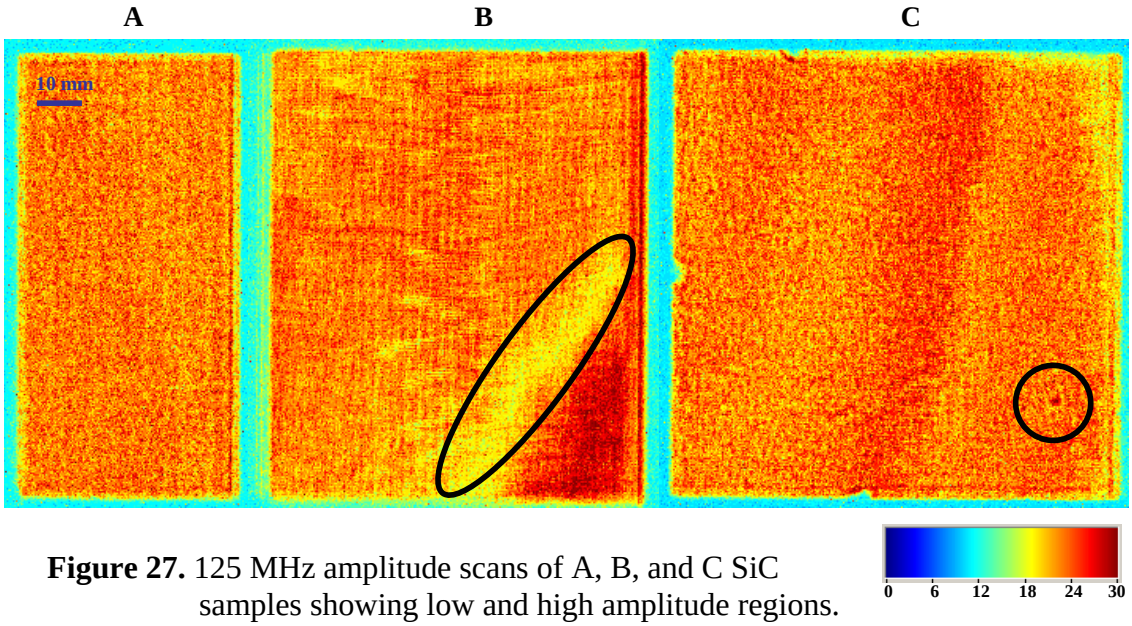

Figure 27. 125 MHz amplitude scans of A, B, and C SiC samples showing low and high amplitude regions.

5.2.2. Reflected Signal Amplitude Quantitative Analysis of A, B, and C

Normalized reflected signal amplitude histograms of each sample at each frequency were produced to quantitatively compare samples with and without significant defect regions. After normalizing the reflected signal amplitude data from each scan, histograms were plotted by collecting the number of occurrences of each amplitude (y-axis) over the full amplitude range (x-axis) of each scan. The left or right side, or tail, of each curve, which represented the lowest or highest normalized amplitude values, provided information about the cumulative area of isolated defects or defect regions in each specimen. The distribution of each curve indicated whether the range of normalized amplitudes for each scan was narrow or broad. A narrow curve represented a tight distribution of amplitude values and a smaller degree of variability over the sample, whereas a broad distribution indicated a wide range of amplitude values, and a greater presence of defects, lower density regions, and other inhomogeneities.

The data were compared at each frequency. For the 5 MHz amplitude histograms in Figure 28, the curves were very similar, all showing relatively narrow distributions. This was to be expected, since there were few detectable differences among the samples at this lower frequency and all of the scans appreared to be relatively homogeneous. At 50 MHz, there were more noticeable differences between the histograms, as shown in Figure 29. The armor grade sample A, indicated by the red curve, showed the most narrow distribution as compared to sample B with the lower density region (green curve) and sample C with the known defect (blue curve). These differences indicated a higher acoustic variance, which was to be expected since the amplitude ranges were much broader for these specimens. At 125 MHz, the differences among the curves were most

apparent, as shown in Figure 30. The normalized amplitude histogram curve from sample C appeared to show the broadest comparative amplitude range, followed by sample B. The shapes of the curves also changed to reflect minor differences in reflected signal amplitude, indicative of specific isolated defects, regions of varying density, and other microstructural inhomogeneties. The vast differences between the C-scans at the highest frequency, as shown in Figures 25-27, were also apparent in the quantitative histogram data. In order to reinforce this point, the areas under the normalized histogram curves and full-width at half-maximum values were collected and compared.

The area-under-the-curve (AUTC) and full-width at half-maximum (FWHM) data were utilized to assign values to each normalized histogram and test the theory that broader amplitude distributions reflected greater material changes. For the 5 MHz scans, the AUTC values did not follow the trend, with values of 583, 686, and 557 for samples A, B, and C, respectively. Since the scans and curves were so similar to each other at this low frequency they could not be distinguished from another. This reinforced the point that higher frequencies were required for effective comparison of bulk armor ceramics fabricated under the same processing conditions. The FWHM values at 5 MHz were very similar, but did follow the expected trend, as sample A had the smallest value of 6 representing the most narrow distribution while samples B and C each had a value of 7. At 50 MHz, the trend started to follow suit, as sample A showed the lowest AUTC value of 373, followed by sample B at 523, and sample C at 699. The AUTC values for B and C were significantly larger than for the narrow distribution of sample A. The FWHM values remained consistent, with a value of 2 for sample A, 3 for sample B, and 4 for sample C, the broadest distribution. The broadest amplitude distributions reflected the

greatest material differences and the largest area and FWHM values. The same trend followed for the 125 MHz histograms, with AUTC values of 1143 for A, 1262 for B, and 1445 for C and FWHM values of 2 for A, 3 for B, and 3 for C. The qualitative variations from both isolated defects and microstructural inhomogeneities resulted in a broadening of the normalized histogram curves for B and C as compared to A. The high amplitude tails on the right side of the B and C curves, representing the high reflected signal amplitude bulk features, were also more significant as compared to sample A. The trends that showed the differences between the three samples followed only at higher frequencies of 50 and 125 MHz, while the 5 MHz data were insufficient for providing the proper comparison. The normalized histogram quantitative analysis combined with AUTC and FWHM data provided an effective means of quantitative sample comparison.

The frequency comparison study of 5, 50, and 125 MHz ultrasound C-scan imaging of SiC specimens demonstrated that transducer frequency was a critical factor for proper reflected signal amplitude ultrasonic evaluation. While there were few observable differences among the three SiC armor ceramics at 5 MHz and minor variations at 50 MHz, 125 MHz scans showed drastic reflected signal amplitude differences from both large isolated defects and small microstructural inhomogeneities. The quantitative comparison of the three specimens, which presented the ultrasound data in normalized histogram form, confirmed the qualitative observations. At higher frequencies of 50 and 125 MHz, the histogram of sample A showed the most narrow distribution of the three samples, representing a more homogeneous distribution of reflected signal amplitude values. Samples B and C showed broader distributions as well as more pronounced tail regions that reflected the highest and lowest amplitude

occurrences. The AUTC and FWHM data supported these trends, as samples B and C had significantly higher values than sample A due to the broader overall distributions and larger tail regions.

Ballistic impact and shock wave events effect a large volume of each armor ceramic specimen. While common ballistic and quasi-static destructive testing techniques only test a small volume of material, ultrasonic nondestructive evaluation C-scan imaging cover a large volume of material, while testing the same specimens that are used directly in the field. The detection of isolated defects and microstructural inhomogeneities and the cumulative and distributed results obtained from quantitative evaluation of these features proved to be useful for armor ceramic comparison.

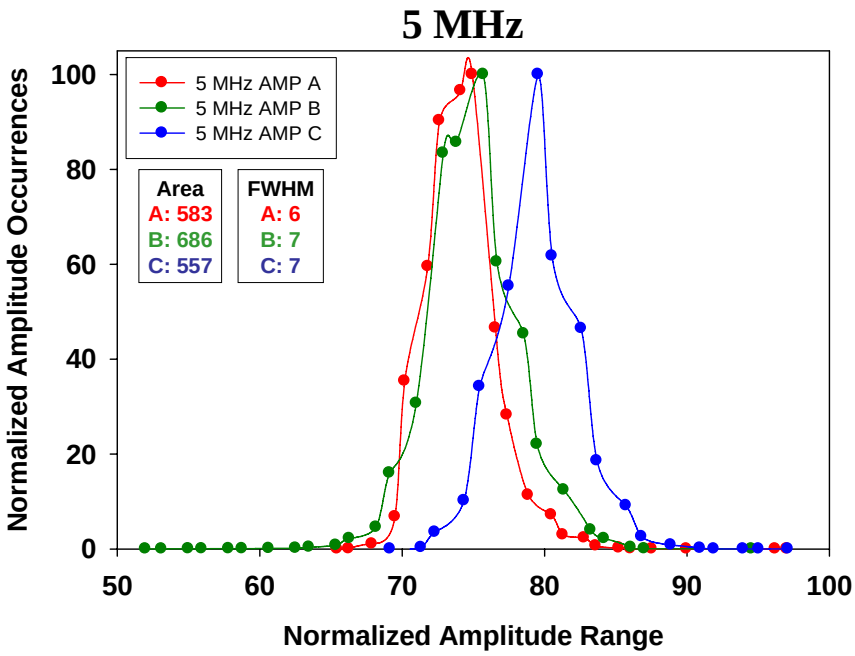

Figure 28. Normalized amplitude histogram comparison of A, B, and C at 5 MHz.

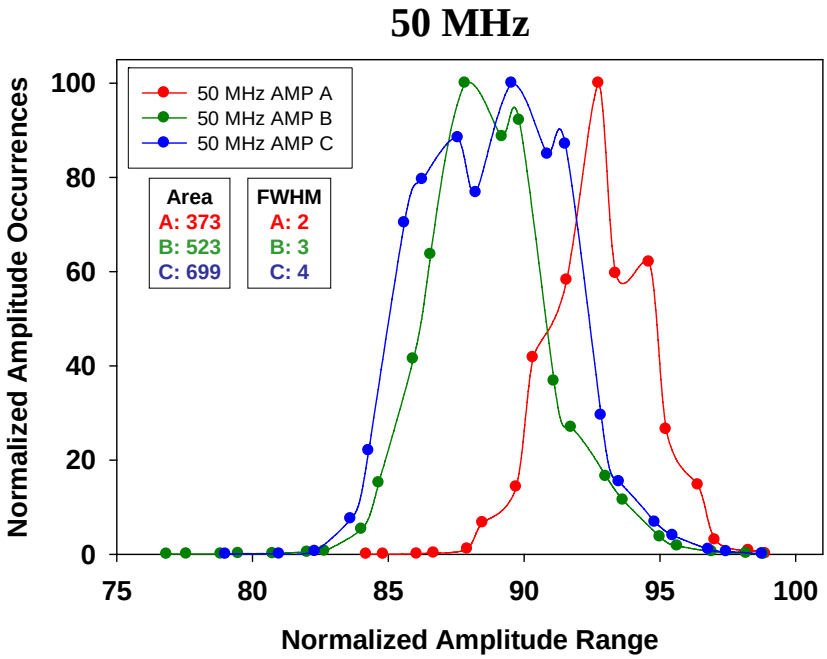

Figure 29. Normalized amplitude histogram comparison of A, B, and C at 50 MHz.

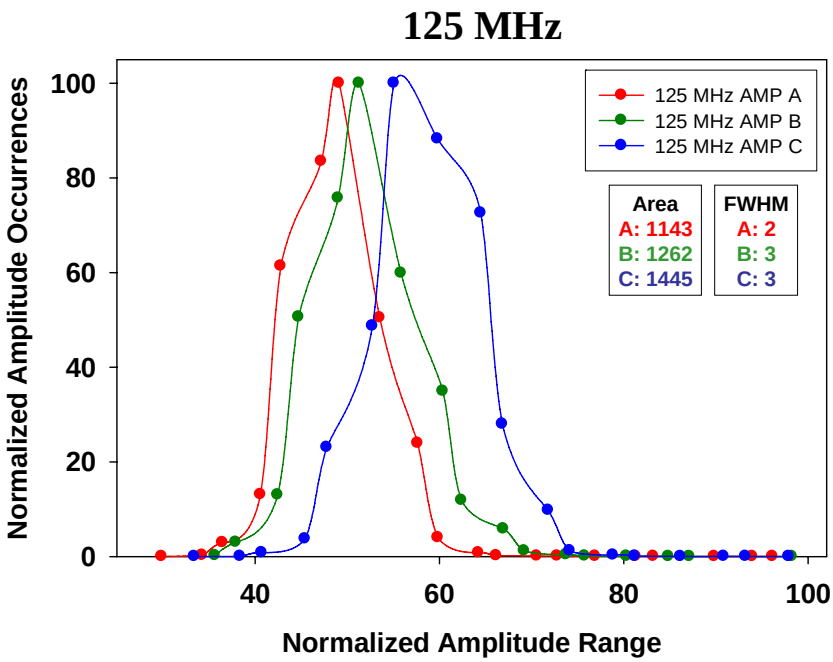

Figure 30. Normalized amplitude histogram comparison of A, B, and C at 125 MHz.

5.2.3. Point Analysis of A, B, and C

The hot pressed SiC test specimens were evaluated at nine separate points that covered different regions of the sample area, as shown in Figure 31. This analysis was performed to get a general idea of TOF, material velocity, and elastic property data trends across each sample. The values at each of the nine points for samples A, B, and C, which include measured thickness, bulk density, TOF_l, and TOF_s values as well as calculated c_l, c_s, ν, E, G, and K values which are shown in Tables IX, X, and XI.

The thickness at each point was first measured using an electronic caliper, and the average thickness values were found to be 19.07 mm for sample A, and 12.76 mm for samples B and C. As mentioned previously, the sample densities for A, B, and C were 3.21 g/cm^3, 3.18 g/cm^3, and 3.19 g/cm^3, respectively, according to Archimedes method. Ultrasound point analysis was conducted using a 50 MHz longitudinal contact transducer (VSP-50) and a 25 MHz shear contact transducer (SFD12-25) along with a glycerin coupling agent to measure TOF_l and TOF_s values across each sample. By using the longitudinal wave transducer to measure the difference in microseconds between the top surface reflected signal and the bottom surface reflected signal in the specimen, the longitudinal TOF was determined at each point as shown in Tables IX, X, and XI. By using the shear wave transducer to measure the difference between top and shear reflected signals, the shear TOF was determined at each point as shown in Tables IX, X, and XI. The top and bottom surface reflected signals used to calculate TOF_l at each point for sample A are shown in Figure 32. The average TOF_l values were found to be 3.127 μs, 2.095 μs, and 2.106 μs, and average TOF_s values were found to be 4.959 μs, 3.343 μs, and 3.357 μs for samples A, B, and C, respectively. The average c_l and c_s values

were found to be 12,197 m/s and 7,691 m/s for sample A, 12,175 m/s and 7,632 m/s for sample B, and 12,120 m/s and 7,602 m/s for sample C. The average elastic properties of ν, E, G, and K were 0.17, 444 GPa, 190 GPa, and 225 GPa, respectively, for sample A, 0.18, 436 GPa, 185 GPa, and 225 GPa, respectively, for sample B, and 0.18, 434 GPa, 185 GPa, and 223 GPa, respectively, for sample C. The measured values were comparable to reported values for hot pressed SiC found in the literature [24] as shown in Table XII.

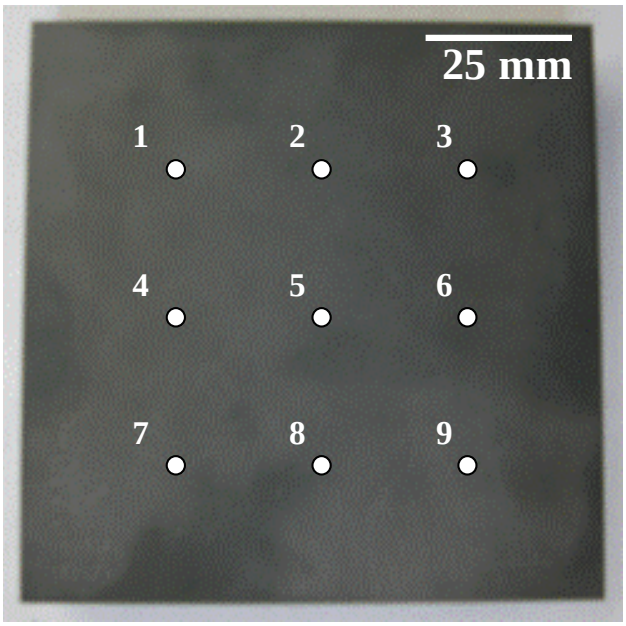

Figure 31. Point analysis positions under evaluation for sample C.

#	ρ (g/cc)	t (mm)	TOF_l (μs)	TOF_s (μs)	c_l (m/s)	c_s (m/s)	Z ($*10^5$ g/cm^{2}s)	ν	E (GPa)	G (GPa)	K (GPa)
1	3.21	19.07	3.127	4.959	12,197	7,691	39.2	0.17	444	190	225
2	3.21	19.07	3.127	4.959	12,197	7,691	39.2	0.17	444	190	225
3	3.21	19.07	3.127	4.959	12,197	7,691	39.2	0.17	444	190	225
4	3.21	19.07	3.127	4.959	12,197	7,691	39.2	0.17	444	190	225
5	3.21	19.07	3.127	4.959	12,197	7,691	39.2	0.17	444	190	225
6	3.21	19.07	3.127	4.959	12,197	7,691	39.2	0.17	444	190	225
7	3.21	19.07	3.127	4.959	12,197	7,691	39.2	0.17	444	190	225
8	3.21	19.07	3.127	4.959	12,197	7,691	39.2	0.17	444	190	225
9	3.21	19.07	3.127	4.959	12,197	7,691	39.2	0.17	444	190	225
Avg	**3.21**	**19.07**	**3.127**	**4.959**	**12,197**	**7,691**	**39.2**	**0.17**	**444**	**190**	**225**

Table IX. Point analysis data for sample A at nine different locations.

#	ρ (g/cc)	t (mm)	TOF_l (μs)	TOF_s (μs)	c_l (m/s)	c_s (m/s)	Z (*10^5 g/cm^{2}s)	ν	E (GPa)	G (GPa)	K (GPa)
1	3.18	12.76	2.095	3.341	12,181	7,638	38.7	0.18	437	186	225
2	3.18	12.76	2.095	3.341	12,181	7,638	38.7	0.18	437	186	225
3	3.18	12.76	2.095	3.341	12,181	7,638	38.7	0.18	437	186	225
4	3.18	12.76	2.095	3.341	12,181	7,638	38.7	0.18	437	186	225
5	3.18	12.76	2.095	3.341	12,181	7,638	38.7	0.18	437	186	225
6	3.18	12.75	2.095	3.341	12,172	7,632	38.7	0.18	436	185	224
7	3.18	12.76	2.095	3.341	12,181	7,638	38.7	0.18	437	186	225
8	3.18	12.75	2.094	3.340	12,178	7,632	38.7	0.18	436	185	225
9	3.18	12.75	2.100	3.357	12,143	7,596	38.6	0.18	433	184	224
Avg	**3.18**	**12.76**	**2.095**	**3.343**	**12,175**	**7,632**	**38.7**	**0.18**	**436**	**186**	**225**

Table X. Point analysis data for sample B at nine different locations.

#	ρ (g/cc)	t (mm)	TOF_l (μs)	TOF_s (μs)	c_l (m/s)	c_s (m/s)	Z (*10^5 g/cm^{2}s)	ν	E (GPa)	G (GPa)	K (GPa)
1	3.19	12.76	2.111	3.363	12,089	7,588	38.6	0.17	432	184	221
2	3.19	12.76	2.106	3.357	12,118	7,602	38.7	0.18	434	184	223
3	3.19	12.76	2.100	3.351	12,152	7,616	38.8	0.18	436	185	225
4	3.19	12.76	2.111	3.363	12,089	7,588	38.6	0.17	432	184	221
5	3.19	12.76	2.106	3.357	12,118	7,602	38.7	0.18	434	184	223
6	3.19	12.76	2.100	3.351	12,152	7,616	38.8	0.18	436	185	225
7	3.19	12.76	2.111	3.362	12,089	7,588	38.6	0.17	432	184	221
8	3.19	12.76	2.106	3.356	12,118	7,602	38.7	0.18	434	184	223
9	3.19	12.76	2.100	3.351	12,152	7,616	38.8	0.18	436	185	225
Avg	**3.19**	**12.76**	**2.106**	**3.357**	**12,120**	**7,602**	**38.7**	**0.18**	**434**	**184**	**223**

Table XI. Point analysis data for sample C at nine different locations.

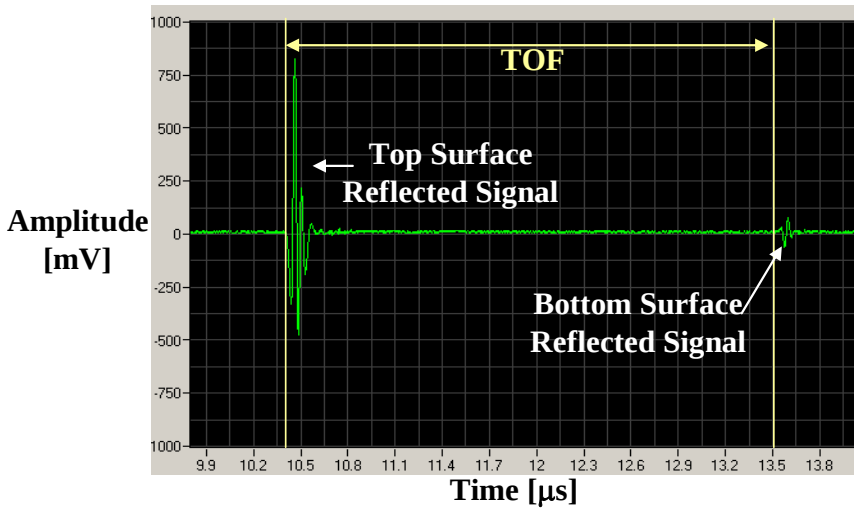

Figure 32. A-scan measurement of longitudinal TOF value from top and bottom reflected signals.

Sample	Frequency [MHz]	Min TOF [mV]	Max TOF [mV]	Avg TOF [mV]	StD TOF [μs]
A	5	3.312	3.322	3.316	0.00109
B	5	2.352	2.376	2.356	0.00319
C	5	2.356	2.376	2.367	0.00354
A	50	3.018	3.136	3.133	0.00108
B	50	2.110	2.150	2.130	0.00384
C	50	2.122	2.150	2.140	0.00311
A	75	3.104	3.110	3.106	0.00067
B	75	2.076	2.102	2.080	0.00409
C	75	2.080	2.100	2.090	0.00385

Table XII. TOF minimum, maximum, average, and standard deviation values from C-scanned areas at various frequencies.

Consistency trends across each sample were also evaluated. For sample A, the measured values were identical for all nine points, with no variation in either TOF_l or TOF_s. Since the thickness was the same at each point, the c_l, c_s, Z, ν, E, G, and K values were also identical at each point. For sample B, the values were consistent over the majority of the sample. The highest deviation occurred at point 9, in which the TOF_l increased slightly from an average of 2.095 μs to 2.100 μs and TOF_s increased slightly from an average of 3.343 μs to 3.357 μs. These higher TOF values led to lower longitudinal and shear velocities of 12,143 m/s and 7,496 m/s, respectively, as well as lower Z, E, G, and K values in this region as compared to the rest of the sample. For sample C, a TOF gradient was apparent. On the left side of the sample at points 1, 4, and 7, the TOF_l and TOF_s values were 2.111 μs and 3.363 μs, and they decreased to 2.106 μs and 3.357 μs in the center at points 2, 5, and 8, and to 2.100 μs 3.351 μs on the right side of the samples at points 3, 6, and 9. This gradient caused the c_l and c_s values to change from 12,089 m/s and 7,588 m/s on the left side to 12,152 m/s and 7,616 m/s on the right side. This also led to a slight increase in elastic properties from left to right with E values increasing from 426 GPa to 432 GPa and K values increasing from 221 GPa to 225 GPa. After point analysis trends were determined, TOF C-scan imaging was performed to look for similar property changes from a comprehensive map of more than 200,000 data points as opposed to a limited selection of nine individual data points.

5.2.4. TOF C-Scan Imaging of A, B, and C

Up to this point, ceramic armor samples A, B, and C were evaluated based on changes in reflected signal amplitude, which were dictated by the degree of attenuation, or loss, over the area of the sample. While some of the aforementioned factors that

caused attenuation included beam spreading, field effects, wave reflections from coupling agent mismatch, beam diffraction, and ultrasonic energy absorption, if the identical ultrasound scanning conditions were used, wave scattering became the dominant factor, and was utilized for detecting material inhomogeneities and defects. However, while it was easy to determine the overall change in attenuation, it was difficult to quantify the degree of attenuation caused solely by wave scattering. For this reason, the more quantifiable TOF parameter was evaluated in addition to collecting reflected signal amplitude data in order to develop a second type of ultrasound C-scan imaging that was directly related to elastic properties of the material.

As mentioned previously, TOF is the time it takes for an ultrasound signal to be transmitted through a sample. Since the two types of acoustic waves of interest for evaluation of bulk solid materials included longitudinal and shear waves, the TOF for each value was measured, denoted as TOF_l for longitudinal TOF and TOF_s for shear TOF. Again, by using a simple relationship of distance equals rate times time, where time was TOF and distance was the known thickness of the sample, longitudinal and shear material velocities were calculated using the Equations 36 and 37. These material velocity parameters have also been previously shown to be inversely proportional to the degree of porosity in a sample, as cited in several references [111-115]. Other related values that were calculated included elastic properties such as Poisson's ratio, elastic modulus, shear modulus, and bulk modulus from Equations 39-42. These were much more direct mathematical relationships than the reflected signal amplitude and attenuation relationships, in which many factors were involved that made them difficult

to quantify. For this reason, TOF values were used to calculate a variety of important material properties.

While this was an advantage of TOF C-scan imaging as compared to reflected signal amplitude C-scan imaging, the TOF technique was much more sensitive to the influence of surface voids and nonparallel surfaces. Since TOF measured the time for the ultrasound wave to travel through the sample, it varied as the transducer was scanned over a surface void or a nonparallel surface region, and this dominated the smaller TOF changes caused by bulk defects. In this case, reflected signal amplitude C-scan imaging was a more suitable technique, since minor nonparallel surface changes did not greatly influence attenuation. Both TOF and reflected signal amplitude C-scan imaging techniques evaluated defects in a similar manner. For TOF scans, if there was a bulk defect within the area being scanned, the time for the acoustic wave to travel through the sample, and therefore the TOF value, increased. The amount of time was dependent on the type of defect and its acoustic impedance value as compared to that of the sample bulk matrix. Since both techniques had their own unique advantages, both were important for comprehensive evaluation of armor ceramic materials.

Ultrasound TOF C-scan imaging was performed using samples A, B, and C, with all three specimens hot pressed under identical conditions. Two of the transducers utilized for obtaining TOF C-scan images, the 5 MHz (MDS25-5) and 50 MHz (MDS25-50), were the same ones used to obtain reflected signal amplitude C-scan images. However, instead of using the 125 MHz (MDS12-125) transducer due to the high degree of noise introduced into the TOF C-scan images, a lower frequency 75 MHz (MDS12-75) transducer was used to obtain the data.

TOF C-scan imaging was conducted at 5 MHz, 50 MHz, and 75 MHz to look for TOF variations in samples A, B, and C. The effect of transducer frequency on locating specific TOF differences was also evaluated. After identifying and gating the top and bottom reflected signals, samples A, B, and C were scanned at each frequency to pinpoint TOF variations. The TOF C-scan images for the three samples at each frequency are shown in Figures 33-35. The hot pressed samples were suitable for TOF evaluation because of their flat, parallel surfaces and fine surface finish. This enabled the collection of TOF image maps and data sets based on bulk differences with little influence from surface inhomogeneities.

The three samples were first imaged at the lowest frequency of 5 MHz, as shown in Figure 33. The TOF C-scan images of each of the samples analyzed at the lowest frequency appear to be almost identical. Upon careful visual analysis, there were slightly higher TOF regions in the bottom right corner of sample B and the left side of sample C while sample A appeared to be homogeneous. These slight TOF differences matched the point analysis trends in which point 9 in sample B showed a higher TOF as compared to the rest of the sample and points 1, 4, and 7 in sample C showed higher TOF values starting on the left side of the sample. The minimal variations in TOF were expected at 5 MHz due to theoretically lower detectability limits at lower frequencies. This was also consistent with the reflected signal amplitude data in which the 5 MHz scans showed the lowest variability due to an inability to detect smaller microstructural inhomogeneities. An area was selected from each sample to include the bulk data while avoiding the outer perimeter regions which were influenced by edge effect.

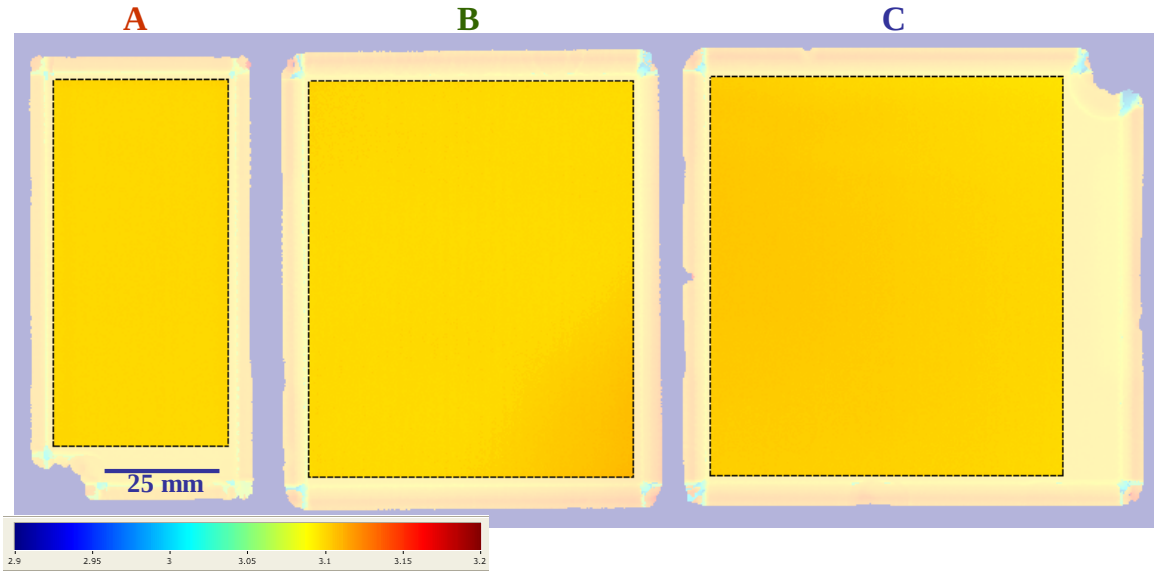

Figure 33. 5 MHz TOF scans of A, B, and C SiC samples.

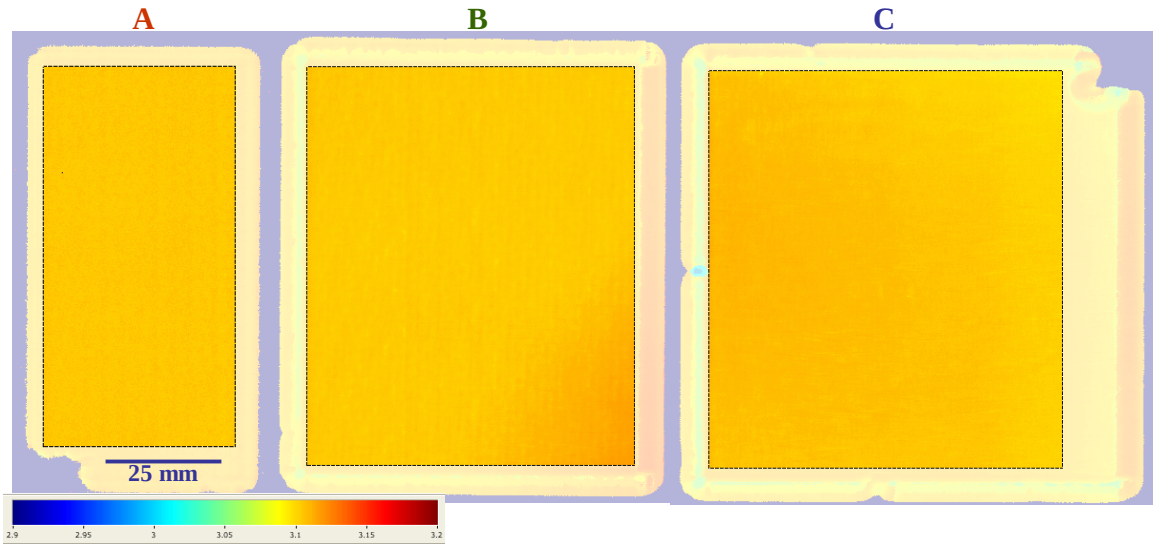

Figure 34. 50 MHz TOF scans of A, B, and C SiC samples.

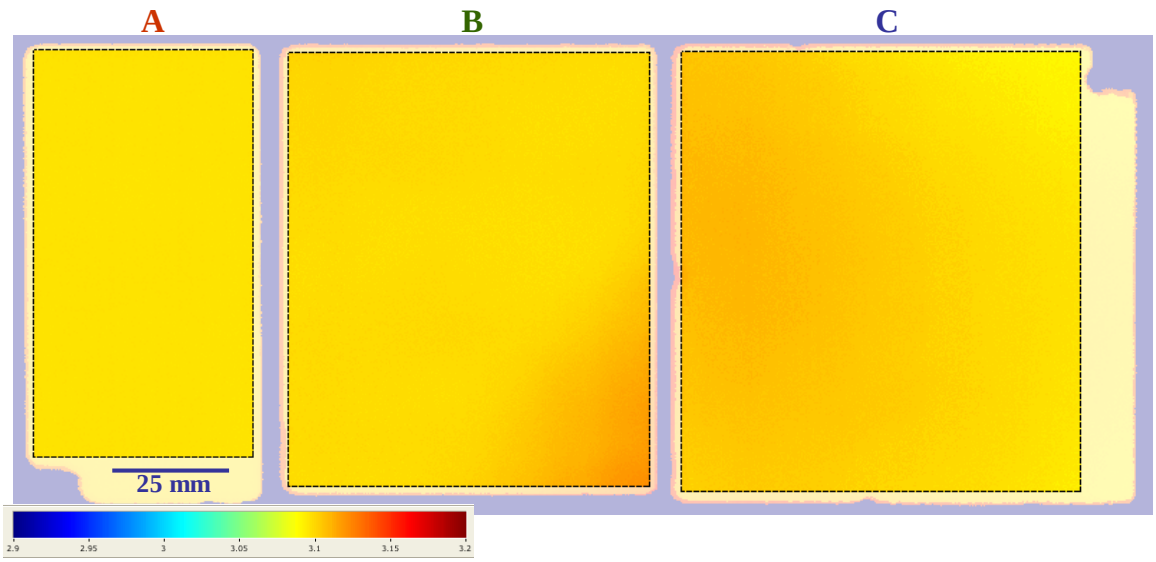

Figure 35. 75 MHz TOF scans of A, B, and C SiC samples.

Edge effect is a transducer phenomenon resulting from the collection of average values over the entire ultrasound beam. At the edge of the sample when the transducer is halfway over the sample and halfway over the immersion medium, an average is taken which results in the appearance of a gradient along the sample edge. This effect can be reduced by minimizing the ultrasound beam diameter so that the number of points collected over both the sample and the water is minimized. For the lower frequency transducer used in this study, the edge effect was prominent, so the area selections used for quantitative analysis avoided the sample edges. Since this also impacted the ability to detect near-edge defects in a sample, higher frequencies and transducer parameters that minimized the beam diameter were preferred for reduction of the edge effect.

The range of longitudinal TOF values for sample A at 5 MHz was between 3.312 μs and 3.322 μs with an average value of 3.316 μs and a standard deviation of 0.00109 μs. The range of values for sample B at 5 MHz was between 2.076 μs and 2.102 μs with an average value of 2.080 μs and a standard deviation of 0.00409 μs. The range of values for sample C at 5 MHz was between 2.080 μs and 2.100 μs with an average value of 2.090 μs and a standard deviation of 0.00385 μs. One noticeable difference was between the average point analysis values and the average TOF C-scan image values. This was due to the TOF measurements, which were conducted at the onset of each reflected signal for point analysis as opposed to the peak-to-peak differences that were gated during imaging. The more accurate point analysis data served as a correction factor, as the degree of variation stayed consistent during imaging. The greatest difference came at lower frequencies in which the peaks were broader. The longitudinal TOF values were much higher for sample A due to the greater thickness and, therefore, the longer time for

the acoustic waves to travel through the sample. Sample A also showed the smallest standard deviation of 0.00109 μs as compared to higher values of 0.00409 μs and 0.00385 μs for samples B and C, respectively. Despite the fact that the three sample areas appeared almost identical, sample A stood out as the most homogeneous in terms of TOF. The TOF minimum, maximum, average, and standard deviation values for each sample can be found in Table XII.

The samples were next evaluated using the 50 MHz transducer, as shown in Figure 34. The C-scan images at this frequency demonstrated a more succinct difference among the samples in terms of the high TOF trends described by the point analysis data. In addition, small regional TOF changes were also detected throughout each sample. These subtle differences contrasted the homogeneous regions consistently present at 5 MHz. However, the 50 MHz samples were also influenced by a significant edge effect that had to be accounted for. The average and standard deviation values of the selected areas were 3.133 μs and 0.00108 μs for sample A, 2.130 μs and 0.00384 μs for sample B, and 2.140 μs and 0.00311 μs for sample C, respectively. Once again, sample A had a significantly lower standard deviation as compared to B and C. Sample B had the highest standard deviation among the three samples due to the high TOF region in the bottom right corner in which the TOF went from an average value of 2.130 μs to a maximum value of 2.150 μs.

Finally, the samples were evaluated using the 75 MHz transducer, as shown in Figure 35. With the 75 MHz transducer, the edge effect was minimized to enable evaluation of a larger area which also improved the ability to detect near-edge defects. Again, the TOF differences at the highest frequency were most apparent, just as in the

case of the reflected signal amplitude trends. The reflected signal amplitude C-scan image maps, however, were much more sensitive to frequency differences, as each increase in transducer frequency enabled the detection of a whole new set of defects and features that could not be detected at lower frequencies. The average and standard deviation values for the selected areas were 3.106 μs and 0.00067 μs for sample A, 2.080 μs and 0.00409 μs for sample B, and 2.090 μs and 0.00385 μs for sample C, respectively. The degree of contrast at the highest frequency was readily apparent as sample A showed the lowest overall standard deviation of 0.00067 μs and sample B showed the highest overall standard deviation of 0.00409 μs. The trends remained the same at each frequency, as samples A, C, and B, in that order, consistently demonstrated the lowest to highest standard deviation values.

It must be kept in mind that while the smaller TOF variations did not drastically affect the sample properties, the higher TOF variations were significant. For example, the largest variation of TOF values within the same sample was for sample B at 50 MHz with a variation of 0.40 μs. This corresponded to a material velocity difference of 225 m/s between the high TOF region, which had a longitudinal velocity 11,870 m/s and the lower TOF region, which had a longitudinal velocity of 12,095 m/s. This also led to elastic property differences of E ~16 GPa, G ~7 GPa, and K ~8 GPa within the same sample. These are rather large variations considering all three samples were hot pressed under the same stringent manufacturing conditions. For this reason, it is believed that the variations were most likely related to varying processing conditions such as improper mixing, poor additive dispersion, or the introduction of contamination. The detection of such TOF differences, therefore, became critical, and with further analysis, the source of

the defects could be traced back to the related manufacturing step for further optimization.

5.2.5. TOF C-Scan Quantitative Analysis of A, B, and C

The same quantitative analysis approach that was utilized for obtaining reflected signal amplitude histograms was also applied for plotting TOF histograms. The reason for using histograms as the quantitative analysis tool of choice was the ability to look at a sample in terms of its cumulative property distribution. For the reflected signal amplitude histograms, the lower amplitude regions corresponding to higher attenuation in the sample were critical while in the TOF histograms, the higher TOF regions corresponding to lower material velocities were critical. It was important to determine the cumulative defect or inhomogeneity distribution for each sample because in the case of a ballistic event, the shock wave activates pre-existing defects within an armor ceramic material before penetration of the projectile [1,31]. A minimization of these defects will enable a higher resistance to penetration for the armor ceramic. In the first plot in Figure 36, the number of occurrences of each TOF value was plotted on the y-axis against the range of TOF values in μs along the x-axis. Since sample A was much thicker than samples B and C, this plot did not effectively demonstrate the difference between samples, as the histogram curve for sample A was around 3.2 μs while the other two overlapped at around 2.1 μs. In order to construct a histogram for better sample comparison, the TOF range on the x-axis was normalized. By normalizing the data, the histograms were placed on a level playing ground for direct comparison of integrity. For further quantification of the histogram curves, AUTC and FWHM values were also collected.

Figures 37-39 show the TOF histogram results for samples A, B, and C at each frequency. The AUTC and FWHM values for each sample are shown in Table XIII. The 5 MHz TOF normalized histograms in Figure 37 showed clear differences between the histogram curves of each sample. Sample A had a narrow distribution that was consistent with its homogeneous appearance and low standard deviation value. The shape of the curve was an approximate Gaussian distribution. The corresponding AUTC and FWHM values of 8.58 and 0.07, respectively, were much smaller than the values for B and C. This type of distribution in addition to the quantitative values appeared to be representative of an ideal armor ceramic material, as sample A was a high density, homogeneous sample with no detectable defects. Therefore, a narrow distribution with low AUTC and FWHM values was preferred. The histogram curve for Sample B showed a wider distribution than sample A, but not the widest distribution of the three samples. Instead, the distinguishing feature was a long tail region that was consistent with the high standard deviation values of sample B. The tail represented the high TOF values in the bottom right corner of the sample, but the rest of the sample was still relatively uniform. This was an example of a critical region in an otherwise high integrity sample. The AUTC and FWHM values for the sample were 19.02 and 0.22, which were both much greater than for sample A. However, the broadest distribution and highest area and FWHM values came from sample C. The area and FWHM values of 43.62 and 0.45 were more than twice that of sample B, and this was due to the TOF gradient of high to low values from the left side to the right side of the sample. Rather than a concentrated critical area as in sample B, sample C showed progressive changes over the entire sample area. While the bulk of sample C was wider, the overall width of sample B including the

tail covered a larger range, accounting for its higher standard deviation. Sample C exemplified a third distinct type of normalized histogram profile. It should be mentioned that despite the fact that the three samples appeared to be very similar at 5 MHz, the differences were quite apparent in the histogram data.

The 50 MHz TOF histograms are shown in Figure 38. The noticeable trends in the histogram curves were very similar to those at 5 MHz. Sample A again exhibited the narrowest distribution with an AUTC value of 11.49 and a FWHM value of 0.06. Sample B again showed a clear tail and had AUTC and FWHM values of 22.88 and 0.20, again covering the widest range of normalized TOF values. Sample C showed a broad distribution with an area of 29.08 and an FWHM value of 0.29, but the shape of the curve was very disjointed, as if there were two distinct regions of dominating TOF values. By observing the TOF C-scan image, it appeared as though there were two dominant TOF values that occur across the gradient, and this was most apparent when observing the quantitative data.

The same trends occurred for the 75 MHz TOF histograms shown in Figure 39. Sample A showed a narrow distribution with AUTC and FWHM values of 6.85 and 0.10. Sample B exhibited its familiar tail and had an AUTC value of 15.41 and an FWHM value of 0.18. Sample C showed a similar shape as in the 50 MHz histogram curve, though the distribution was much more even, almost bimodal. The AUTC and FWHM values for sample C were the highest of all the samples at 55.51 and 0.60. The histogram, AUTC, and FWHM trends were very consistent at all transducer frequencies, with the only major difference being the morphology of the histogram curve for sample C.

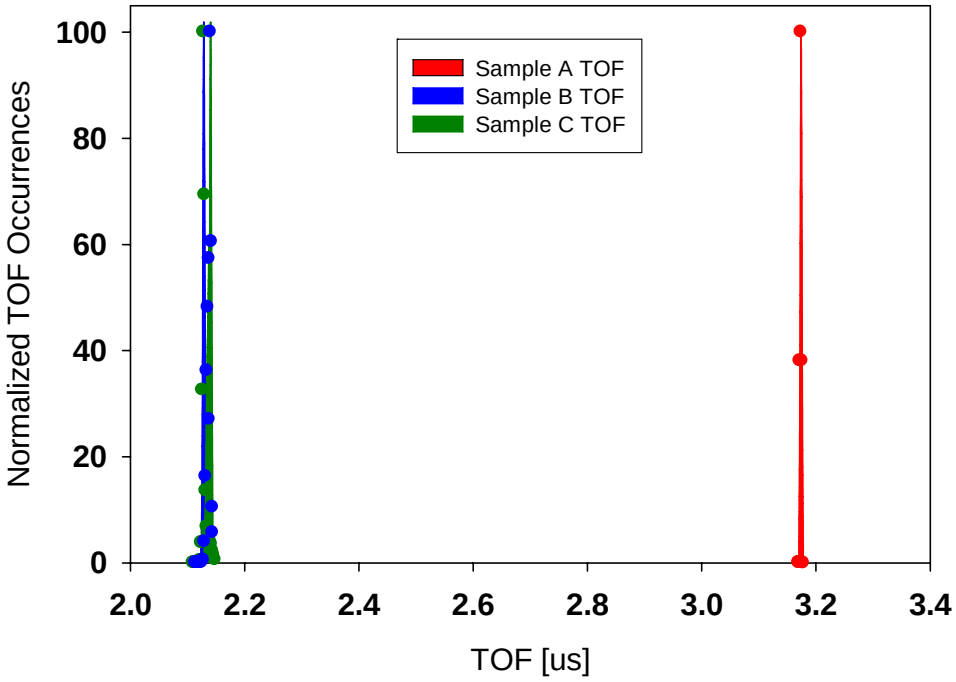

Figure 36. Raw TOF histogram curves prior to normalization which are heavily influenced by sample thickness.

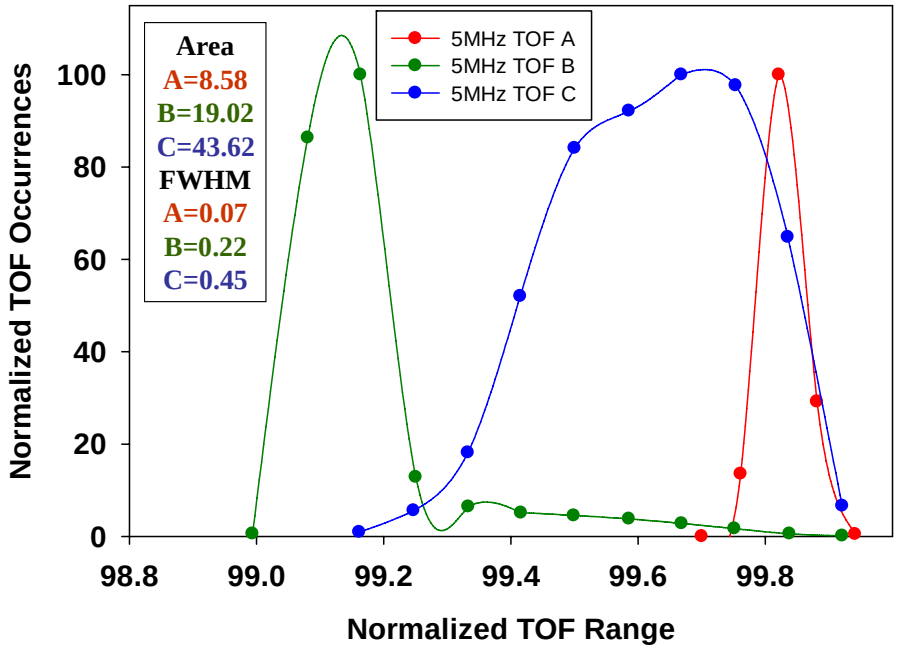

Figure 37. Normalized TOF histogram curves for samples A, B, and C at 5 MHz.

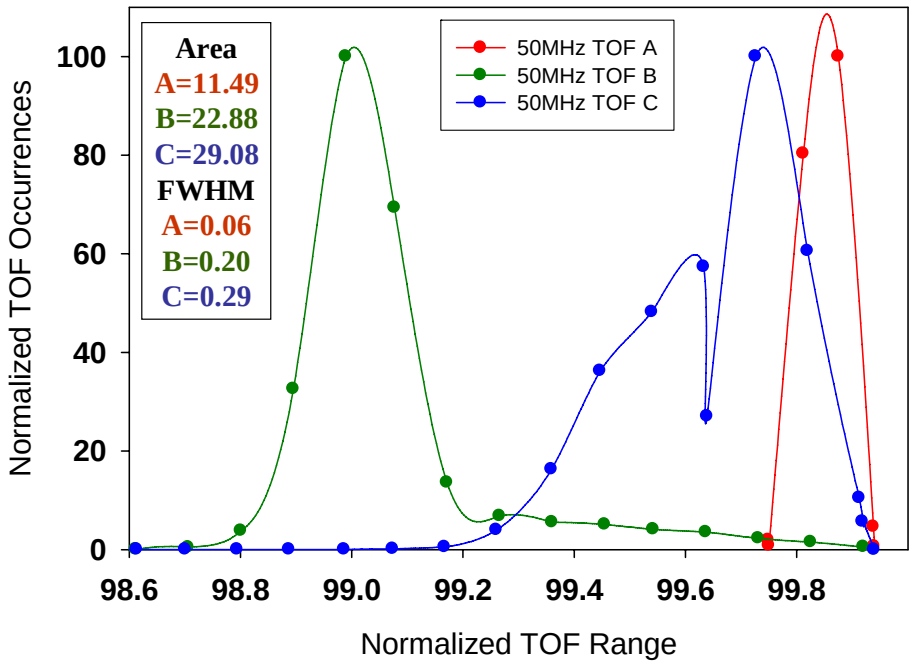

Figure 38. Normalized TOF histogram curves for samples A, B, and C at 50 MHz.

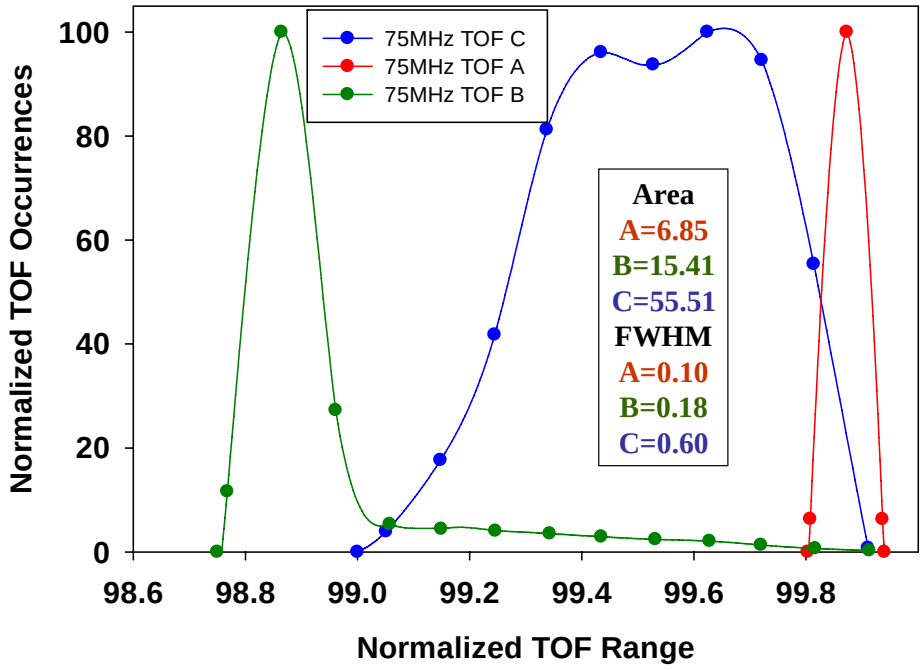

Figure 39. Normalized TOF histogram curves for samples A, B, and C at 75 MHz.

Sample	Frequency [MHz]	TOF Area	TOF FWHM	Velocity Area	Velocity FWHM
A	**5**	8.58	0.07	1050	10
B	**5**	19.02	0.22	2335	27
C	**5**	43.62	0.45	5318	55
A	**50**	11.49	0.06	964	12
B	**50**	22.88	0.20	2849	25
C	**50**	29.08	0.29	4187	35
A	**75**	6.85	0.10	840	10
B	**75**	15.41	0.18	1912	18
C	**75**	55.51	0.60	6769	40

Table XIII. TOF AUTC and FWHM values for samples A, B, and C at various frequencies.

In addition to collecting TOF histograms, velocity histograms were also obtained for all three samples at each frequency, as shown in Figures 40-42. Since TOF and velocity are inversely proportional, velocity histograms exhibited inverted curve shapes in comparison to their TOF counterparts. By converting the values, more property-friendly material velocity data were obtained for sample comparison since the effect of thickness differences was eliminated. The critical areas in this case were the lower velocities which corresponded to lower elastic properties. The same trends were evident for the velocity histograms. At 5 MHz, the quantitative values increased for samples A, B, and C, with AUTC values going from 1050 to 2335 to 5318 and FWHM values increasing from 10 to 27 to 45, respectively. At 50 MHz, the trend continued as AUTC values for A, B, and C increased from 964 to 2849 to 4187 and FWHM values increased from 12 to 25 to 35, respectively. At 75 MHz, the quantitative values increased for samples A, B, and C, with the lowest and highest AUTC values from 840 to 1912 to 6769 while FWHM values increased from 10 to 18 to 40, respectively. Both the TOF histogram and velocity histogram data were very consistent, following the trends closely.

The SiC sample set was very valuable for demonstrating three distinct types of armor ceramic materials, as they showed a significant degree of variability despite being manufactured in the same lot within the sample production line. Sample A, the highest density armor grade specimen which met manufacturing specifications, appeared to have the most homogeneous TOF distribution among the three samples. The TOF and velocity histograms showed the narrowest distribution and lowest AUTC and FWHM values compared to B and C. Sample B, which was red-flagged for not meeting the standard density requirements, proved to have a distinct area of higher TOF values which

corresponded to the tail region in the TOF and velocity histograms. Sample C, which was singled out due to a discoloration on the surface believed to be a defect, exhibited a previously unknown density gradient over the sample despite the fact that it had a higher overall density than sample B. The histograms were represented by broad bulk distributions that consistently exhibited the highest AUTC and FWHM values in both the TOF and velocity histograms. While samples B and C were pulled from the production line, there was no guarantee that other armor ceramic samples with similar bulk issues would not be overlooked. C-scan image maps and quantitative histogram data proved to be valuable tools for conducting this type of sample comparison. By implementing an ultrasound inspection step into the process, it is possible that hot pressed armor ceramic materials can be fully characterized before being used in their final applications.

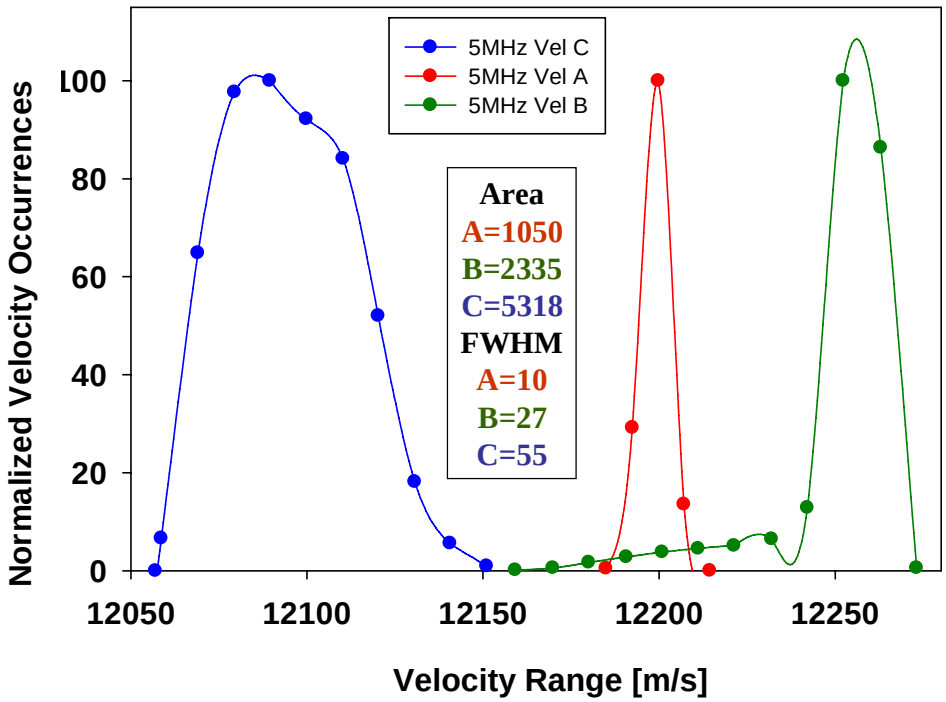

Figure 40. Velocity histogram curves for samples A, B, and C at 5 MHz.

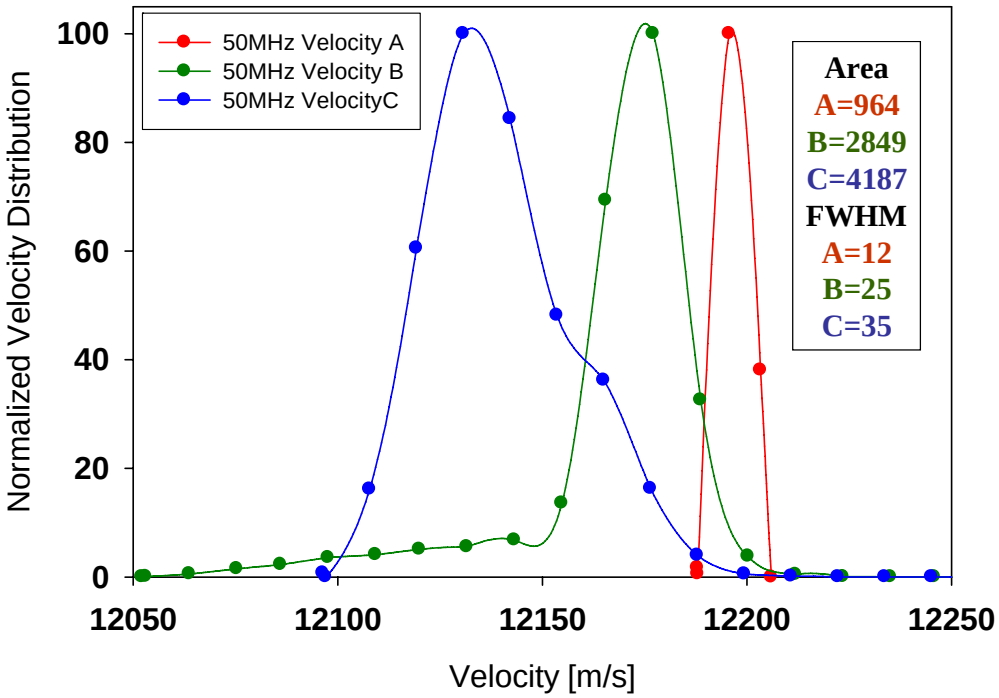

Figure 41. Velocity histogram curves for samples A, B, and C at 50 MHz.

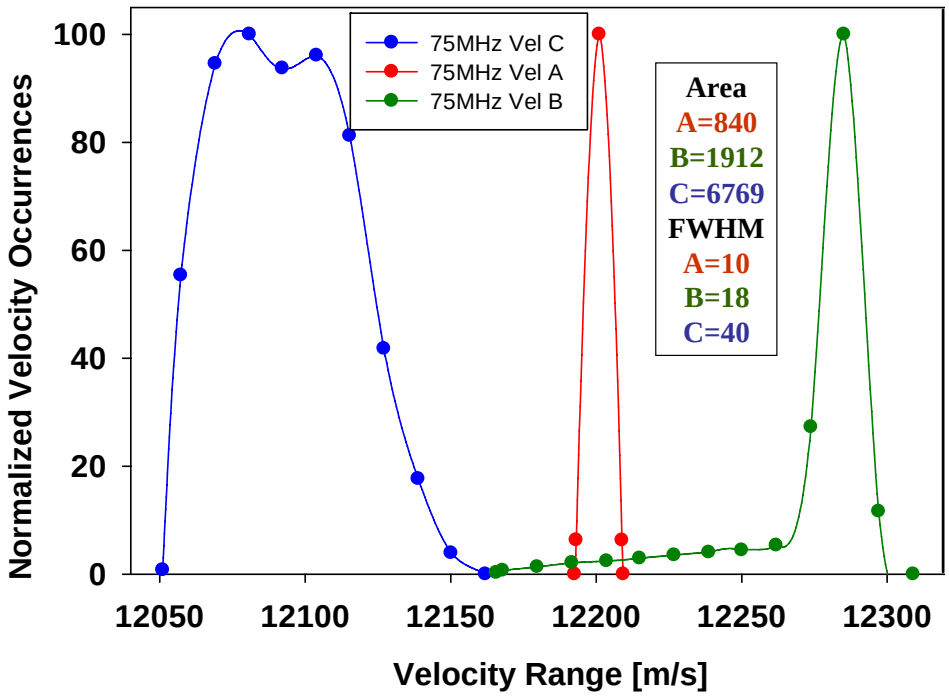

Figure 42. Velocity histogram curves for samples A, B, and C at 75 MHz.

5.3. SiC Test Specimens D and E Hot Pressed Under the Varying Conditions

Two SiC samples, D and E, were evaluated using ultrasonic methods. Sample D was a high density hot-pressed SiC armor grade plate with a length and width of 101.6 mm by 101.6 mm and an average thickness of 19.1 mm. The density of the sample was measured as 3.22 g/cc using the Archimedes method, which was comparable to the density of a hot-pressed SiC sample of 3.22 g/cc found in the literature [24]. Sample E was a high density hot-pressed SiC armor plate with a length and width of 101.7 mm by 101.7 mm, an average thickness of 50.9 mm, and a density of 3.22 g/cc. While sample D had a comparable thickness to sample A from the other set of hot pressed SiC samples, sample E was much thicker, so effect of penetration depth had to be taken into consideration. Samples D and E were also high density samples close to theoretical density, with slightly higher values than sample A.

Two types of ultrasound testing were again utilized to examine the hot pressed SiC samples. Point analysis was conducted using a longitudinal contact very short pulse 50 MHz transducer (VSP-50) that was placed at nine different locations to cover a wide area for each sample. The locations were the same as the point shown in Figure 31. Glycerin was used as the coupling agent. Figure 43 shows a reflected signal amplitude scan from the center of sample D at position five. Ultrasound C-scan imaging was conducted using the longitudinal immersion 75 MHz transducer (MDS-75) also used for TOF C-scan imaging of samples A, B, and C. Since sample E was more than 50 mm thick, a higher degree of attenuation due to the higher depth was a concern. For this reason, the receiver attenuation was optimized before imaging to ensure a sufficient signal-to-noise ratio for resolving the bottom surface reflected signal of specimen E,

which was expected to suffer from a higher degree of attenuation and, therefore, amplitude reduction. The 75 MHz transducer in this case was sufficient for handling a 30 dB receiver attenuation, or gain, which reduced the noise level while maintaining sufficient signal intensity for resolving both the top and bottom signal reflections for both samples. During immersion C-scan imaging, the samples were also placed on slides of equivalent thickness to create a boundary of water at the bottom surface of each sample to ensure a maximum bottom surface reflected signal.

5.3.1. Point Analysis of D and E

The SiC samples were first tested using the longitudinal 50 MHz contact transducer (VSP-50) to conduct point analysis. After designating the point positions and measuring thickness values, the A-scans were collected, as shown in Figure 43 for sample A. Longitudinal TOF values were measured as the difference between the top and bottom reflection signals in μs while shear TOF values were measured as the difference between the top surface reflected signal and the shear reflected signal, which was approximately 1.5-1.7 times the longitudinal TOF, also measured in μs [116]. The average collected data for samples D and E can be found in Tables XIV and XV, respectively, with the average values over the original nine points calculated for each property.

Sample D showed consistent values over all nine positions, as the thickness was measured as 19.07 mm, the longitudinal TOF was measured between 3.096 and 3.105 μs, and the shear TOF was measured between 4.919 and 4.927 μs. With average longitudinal and shear TOF values of 3.103 and 4.923 μs, the longitudinal and shear velocities were calculated as 12,290 and 7,750 m/s, respectively. Based on the sample density measured

by Archimedes method, the average Z value was calculated as 39.6 x 10^5 g/cm^2s and the average ν was 0.17. Elastic property average values were identical at all nine points, with E of 450 GPa, G of 190 GPa, and K of 230 GPa. These measured values compared favorably to reported values of hot pressed SiC samples including ν = 0.17, E = 430 GPa, G = 180 GPa, and K = 220 GPa found in the literature [24,43]. Sample E, which had the highest average thickness of the samples, at 50.92 mm, also showed consistent values over the nine points. The average TOF values of 8.322 μs for longitudinal and 13.115 μs for shear led to velocity values of 12,240 m/s for longitudinal and 7,770 m/s for shear. The longitudinal velocity was slightly lower than for sample A, which may have been attributed to the fact that sample E was nearly 2.7 times thicker. In general, for a thicker material, it is more difficult to maintain a higher longitudinal velocity since material homogeneities that can contribute to a reduction in velocity are measured over a longer ultrasound path for thicker samples. The elastic properties of sample E, which were 450 GPa, 190 GPa, and 220 GPa for E, G, and K, respectively, were comparable to those of sample D, both of which were hot pressed materials.

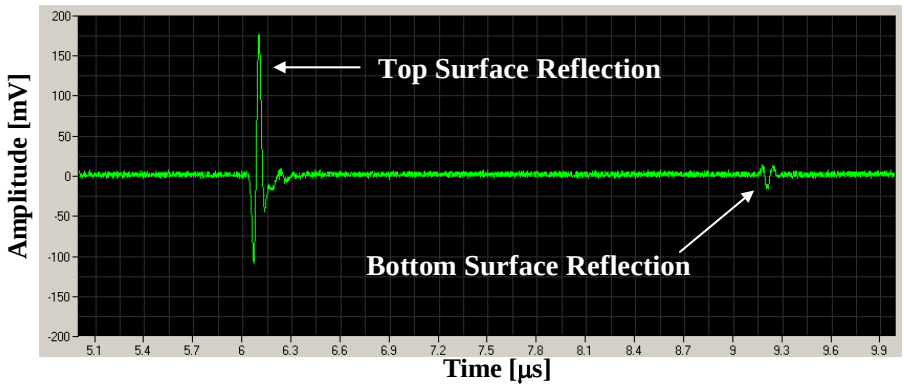

Figure 43. A-scan top and bottom surface reflected signals from sample D.

#	ρ (g/cc)	t (mm)	TOF_l (μs)	TOF_s (μs)	c_l (m/s)	c_s (m/s)	Z (*10^5 g/cm^{2}s)	ν	E (GPa)	G (GPa)	K (GPa)
1	3.22	19.07	3.105	4.927	12,280	7,740	39.6	0.17	450	190	230
2	3.22	19.07	3.105	4.919	12,280	7,750	39.6	0.17	450	190	230
3	3.22	19.07	3.096	4.919	12,320	7,750	39.7	0.17	450	190	230
4	3.22	19.07	3.096	4.927	12,320	7,740	39.7	0.17	450	190	230
5	3.22	19.07	3.105	4.919	12,280	7,750	39.6	0.17	450	190	230
6	3.22	19.07	3.105	4.919	12,280	7,750	39.6	0.17	450	190	230
7	3.22	19.07	3.105	4.927	12,280	7,740	39.6	0.17	450	190	230
8	3.22	19.07	3.105	4.919	12,280	7,750	39.7	0.17	450	190	230
9	3.22	19.07	3.105	4.927	12,280	7,740	39.6	0.17	450	190	230
Avg	**3.22**	**19.07**	**3.103**	**4.923**	**12,290**	**7,750**	**39.6**	**0.17**	**450**	**190**	**230**

Table XIV. Point analysis ultrasound data for sample D.

#	ρ (g/cc)	t (mm)	TOF_l (μs)	TOF_s (μs)	c_l (m/s)	c_s (m/s)	Z (*10^5 g/cm^{2}s)	ν	E (GPa)	G (GPa)	K (GPa)
1	3.22	50.93	8.322	13.115	12,240	7,770	39.4	0.16	450	190	220
2	3.22	50.93	8.322	13.115	12,240	7,770	39.4	0.16	450	190	220
3	3.22	50.92	8.322	13.115	12,240	7,770	39.4	0.16	450	190	220
4	3.22	50.92	8.323	13.115	12,240	7,770	39.4	0.16	450	190	220
5	3.22	50.92	8.322	13.115	12,240	7,770	39.4	0.16	450	190	220
6	3.22	50.93	8.322	13.115	12,240	7,770	39.4	0.16	450	190	220
7	3.22	50.93	8.322	13.115	12,240	7,770	39.4	0.16	450	190	220
8	3.22	50.92	8.322	13.115	12,240	7,770	39.4	0.16	450	190	220
9	3.22	50.92	8.322	13.115	12,240	7,770	39.4	0.16	450	190	220
Avg	**3.22**	**50.92**	**8.322**	**13.115**	**12,240**	**7,770**	**39.4**	**0.16**	**450**	**190**	**220**

Table XV. Point analysis ultrasound data for sample E.

5.3.2. TOF C-Scan Imaging of D and E

C-scan imaging was performed using the 75 MHz longitudinal immersion transducer to collect TOF data over the entire area of each SiC sample. The data were collected in addition to x and y positions of each point and the ranges were chosen based on a representation of approximately 95% of the maximum TOF value in μs for comparison purposes. The TOF C-scan images for each of the SiC samples are shown in Figures 44a and 44b. The minimum, maximum, average, and standard deviation TOF values are shown in Table XVI. A small population of data points scattered throughout each sample displayed TOF values close to zero due to electrical interference during C-scan imaging, but these were not factored into the data because they were not representative of the samples.

Sample D appeared to be the most homogeneous of the samples, with a standard deviation TOF value of 0.002 μs, the lowest value of the samples. The appearance of the C-scan was also consistent, with no detectable variation over the range from 2.950 to 3.108 μs. Sample E was also consistent over the majority of the sample with little variation, but there was a region on the left side of the sample with a higher average range of TOF values. When analyzed separately, the homogeneous region of the sample had an average of 8.320 μs with a standard deviation of 0.007 μs while the higher TOF region had an average of 8.390 μs and a standard deviation of 0.021 μs. This region increased the average TOF values for the overall sample, which had an average TOF of 8.323 μs and a standard deviation of 0.017 μs, making it the sample with the lowest homogeneity index value. This longer transit time was most likely the result of bulk

inhomogeneities that lengthened the transit time and, therefore, impeded the velocity of sound wave travel through the sample within that region.

5.3.3. TOF C-Scan Quantitative Analysis of D and E

The data points collected from the C-scan images were analyzed further to look for distribution trends for each sample that could be used for comparison of material integrity. Since the specimens were different in terms of thickness, the TOF values and homogeneity also varied, with values t ~19.07 mm and TOF ~ 3.11 μs for sample D, and t ~ 50.92 mm and TOF ~ 8.32 μs for sample E. For this reason, the number of TOF occurrences and the TOF range were normalized as shown in the plot in Figure 45. The AUTC and FWHM values were calculated for each curve for further quantitative comparison. In the fully normalized plot, sample D showed the most narrow distribution, which was expected due to the homogeneous nature of the C-scan image and point analysis data. The AUTC value was 11.1 and the FWHM value 0.2 for this sample. Sample E also showed a narrow distribution, but the higher TOF region in the sample appeared as a tail on the right side of the normalized histogram curve. The AUTC value of 21.3 was higher than for sample D due to the addition of the tail, but the FWHM, which took into account the bulk of the histogram curve, was very similar to sample A with a value of 0.3. The AUTC value was favorable for comparison of the histograms since it took the entire sample into account. The FWHM, on the other hand, focused on the distribution and did not take into account the features of minimum or maximum TOF values found the tails. This was evident in the comparison of samples D and E, which were almost identical in FWHM, but quite different in AUTC.

5.3.4. Material Velocity Data Analysis of D and E

The TOF values from the C-scan images were also converted to normalized velocity histograms by selecting an average thickness for each sample, calculating velocity values from the TOF data points, and plotting the data as histograms. Again, the number of velocity occurrences were normalized on the y-axis and plotted against the range of material velocity values, as shown in Figure 46. The velocity histogram plots demonstrated inverse characteristics as compared to their normalized TOF histogram counterparts, with the most homogeneous curve for sample D showing the narrowest distribution of velocity values. The sample AUTC value was calculated as 1369 and the FWHM as 13. Again, Sample E had a relatively narrow distribution, but the tail in this case was on the left side, representing a low velocity region, whereas for the TOF histogram the tail was on the right. The low velocity region may have been the result of a processing-related issue that resulted in a low density region. This may have led to an enhanced degree of porosity, a more likely possibility for sample E rather than D, since E was more than twice as thick and therefore more difficult to process.

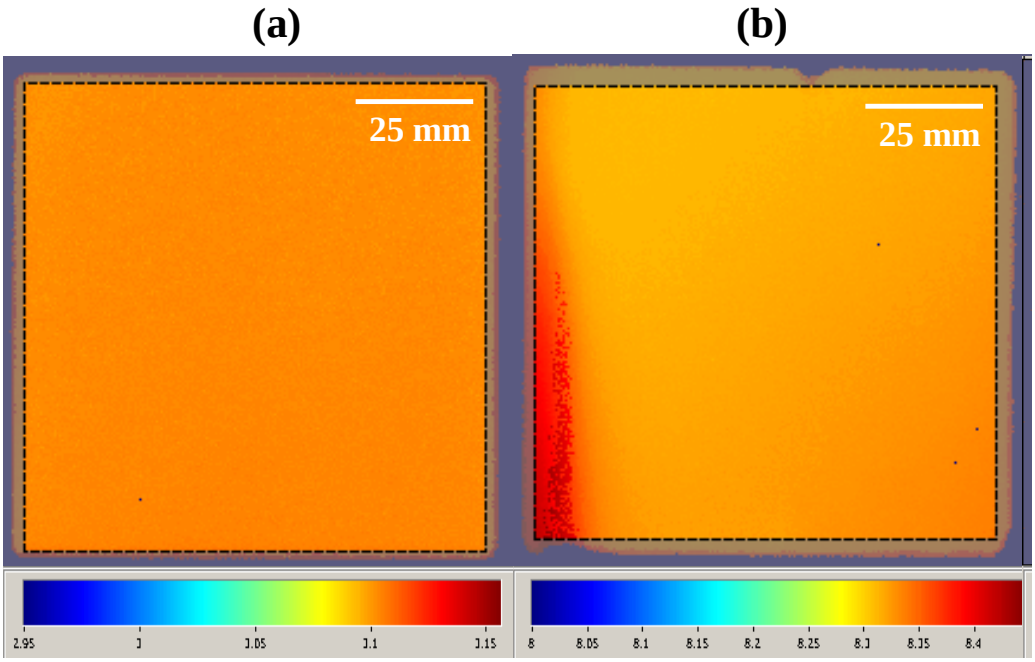

Figure 44. TOF C-scan images from samples D and E.

Sample	Type	Minimum	Maximum	Average	Standard Deviation
D	TOF	2.902	3.108	3.103	0.002
E	TOF	7.818	8.446	8.323	0.017
D	AMP	196	266	227	7.52
E	AMP	34	233	186	37.49

Table XVI. Minimum, maximum, average, and standard deviation Amplitude and TOF values for samples D and E.

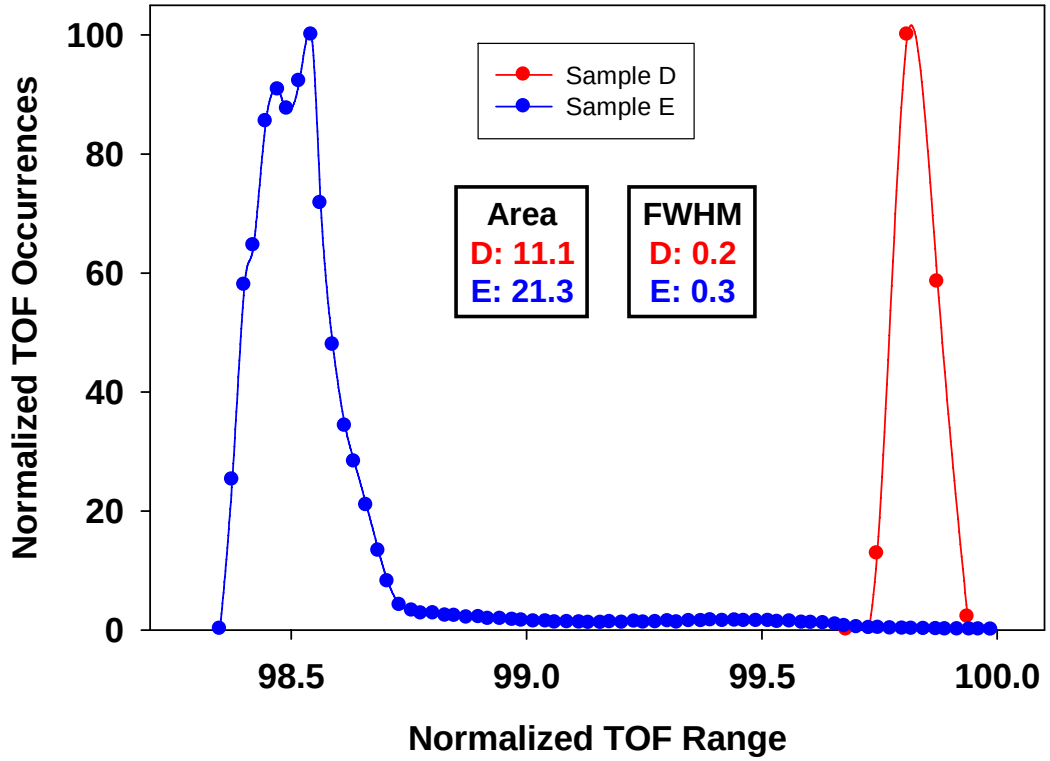

Figure 45. Normalized TOF histogram curves from samples D and E.

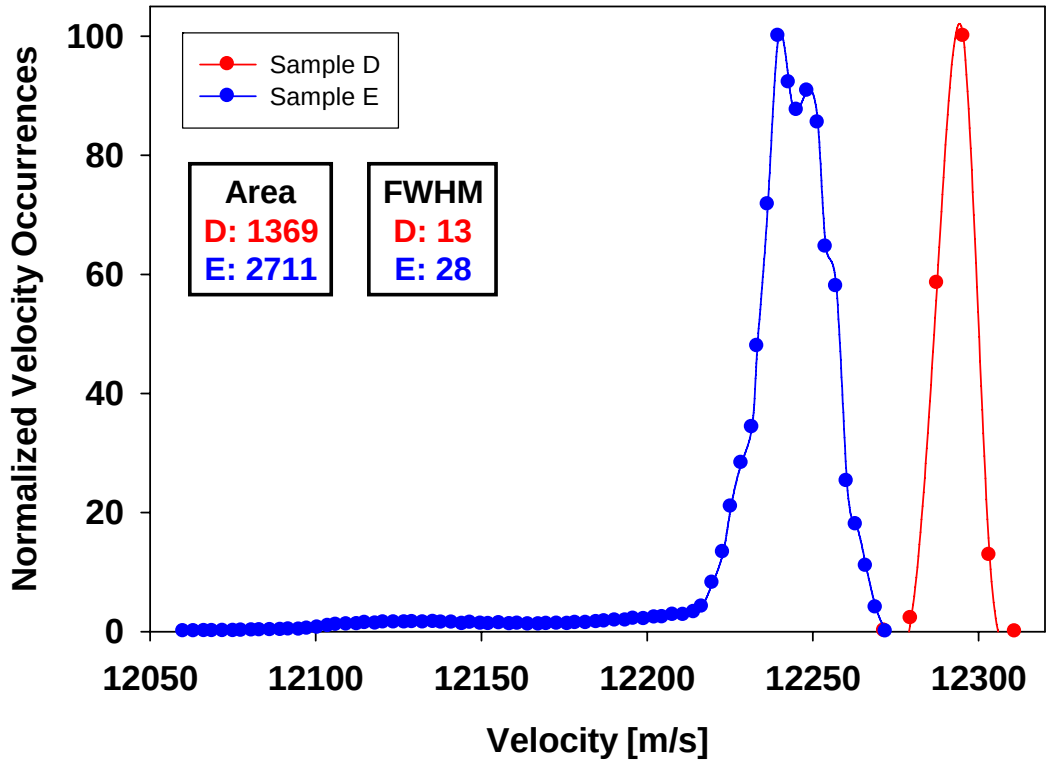

Figure 46. Velocity histogram curves from samples D and E.

5.3.5. Reflected Signal Amplitude C-Scan Imaging of D and E

The other C-scan imaging technique that was used to evaluate the specimens was based on monitoring reflected signal amplitude changes. The data were collected in addition to x and y positions for each point and plotted over a range determined by the minimum and maximum amplitude intensity values in mV for each scan. The reflected signal amplitude C-scan images are shown in Figures 47a and 47b. The ranges were chosen based on a representation from zero to the maximum amplitude value for comparison purposes. The minimum, maximum, average, and standard deviation amplitude values are shown in Table XVI. Since the samples were run under the same conditions but varied in thickness, the average amplitude values for each sample were significantly different. The thicker sample E had a higher degree of attenuation, or loss, of ultrasound energy on average due to the longer ultrasound path the sound wave traveled. This led to lower average reflected signal amplitude values for the thicker samples since they were all scanned under equal conditions, with sample E ~186 mV and sample D ~227 mV.

When observing the reflected signal amplitude C-scan images in Figures 47a and 47b, some of the same features found in the TOF images were identified, while others were more pronounced. Sample D was still the most homogeneous, with the lowest standard deviation of 7.52 mV, but minor variations were evident due to slight differences in the intensity of the bottom surface reflected signal. The reflected signal amplitude images appeared to be more sensitive to subtle microstructural changes than the TOF images. In sample E, the area of interest was the low amplitude region on the left side of the sample, which led to the highest standard deviation of 37.49 mV. In this

region there was a high degree of loss where the amplitude dropped to ~34 mV. Compared to the average of ~186 mV for the overall sample, the reflected signal amplitude in this region dropped ~152 mV, or the equivalent loss of ~44 dB. This region was more pronounced in the reflected signal amplitude C-scan due to a high degree of signal loss. As mentioned previously, it was believed that there was a processing-related issue that caused a high degree of attenuation in the region. The standard deviation values showed the same trends as in the TOF data, reflecting the overall amplitude changes shown in Table XVI. The most drastic change in reflected signal amplitude occurred from the high to low density regions in sample E while the most homogenous amplitude distribution was shown in sample D.

5.3.6. Reflected Signal Amplitude Quantitative Analysis of D and E

A more quantitative evaluation of the reflected signal amplitude data was achieved by plotting histograms in which the normalized amplitude occurrences were represented by the y-axis and the normalized amplitude range by the x-axis, as shown in Figure 48. For sample D, which had and AUTC value of 680 and a FWHM of 7, the distribution was more narrow than the other samples, which was consistent with the TOF and velocity results. For sample E, there was a very similar distribution of amplitude values as compared to sample D, but again, there was a long tail on the left representative of lower reflected signal amplitude data from the region on the left side of the sample. These curves resembled the velocity histograms in Figure 46. The AUTC value for sample E was 782 and the FWHM was 7. While the AUTC difference was in large part due to the tail, the FWHM was identical to that of sample D, meaning that the distribution

was the same for both hot-pressed samples, with the exception of the low amplitude tail region.

5.3.7. Further Analysis of Test Specimen E

As an additional test in response to the TOF and reflected signal amplitude C-scan imaging trends found in sample E, point analysis was conducted at three additional points in the region that was detected as a low TOF, high amplitude area. The point locations, designated as 10, 11, and 12, are shown in Figure 49. The data for these points are shown in Table XVII. While the same thickness values were once again measured as 50.92 and 50.93 mm, the TOF values increased and the velocity values decreased as the measurements were made. The TOF values increased from an average of 8.322 μs for the previously measured nine points to 8.364, 8.418, and 8.437 μs while the velocity values decreased from an average of 12,240 m/s to 12,180, 12,100, and 12,070 m/s for points 10, 11, and 12, respectively. These changes in TOF and velocity led to a slight decrease in some elastic properties, with the averages of bulk values dropping in ν and K from 0.16 and 220 GPa to 0.15 and 210 GPa for points 10, 11, and 12, respectively, but these changes were not very significant.

Another test was conducted to analyze both the bulk and high TOF regions from sample E in terms of density differences. For the hot pressed materials, samples D and E both had measured densities of 3.22 g/cm^3. Since the high TOF region detected by C-scan imaging in sample E was believed to be related to porosity, it was also thought that there should be a corresponding change in density. This test was conducted to determine the impact of the higher TOF region in terms of altering the overall density of sample E. The regions were isolated and evaluated based on separate TOF ranges, with the bulk

region represented by 8.30 to 8.33 μs and the high TOF region represented by 8.34 to 8.46 μs, as shown in Figure 50. The bulk region, which covered approximately 91.6% of the sample, had an average TOF of 8.319 μs while the high TOF region, which covered approximately 8.4%, had an average TOF of 8.396 μs. By using 50.92 mm as the average thickness, the average material velocities were calculated as 12,240 m/s for the bulk region and 12,130 m/s for the high TOF region. By utilizing average Z values from point analysis studies, which were 39.4 x 10^5 g/cm^{2}s for the bulk region and 39.0 x 10^5 g/cm^{2}s for the high TOF region, average densities were estimated from the aforementioned equation as 3.219 g/cm^3 and 3.215 g/cm^3, respectively. This corresponded to a density difference of 0.118% between the two regions. Since the high TOF region covered approximately 8.4% of the sample, the overall sample density was estimated as 3.219 g/cm^3. The TOF difference, which appeared to be quite significant in the C-scan image, related to only a minor change in density. This test demonstrated the sensitivity of ultrasound testing for detecting small changes in density between the two regions in sample E.

The full set of ultrasound data was consistent in establishing sample D as the most homogeneous with the narrowest distribution and the lowest AUTC and FWHM values. Sample E showed a similar distribution over the bulk of the sample, but a region in the bottom left corner was discovered with uncharacteristically higher TOF and lower amplitude. When point analysis was conducted within this region, the material velocity and elastic property values were also found to be lower. After conducting full ultrasound C-scan imaging and quantitative analysis of the hot pressed SiC samples A, B, C, D, and E, sintered SiC samples were evaluated for comparison.

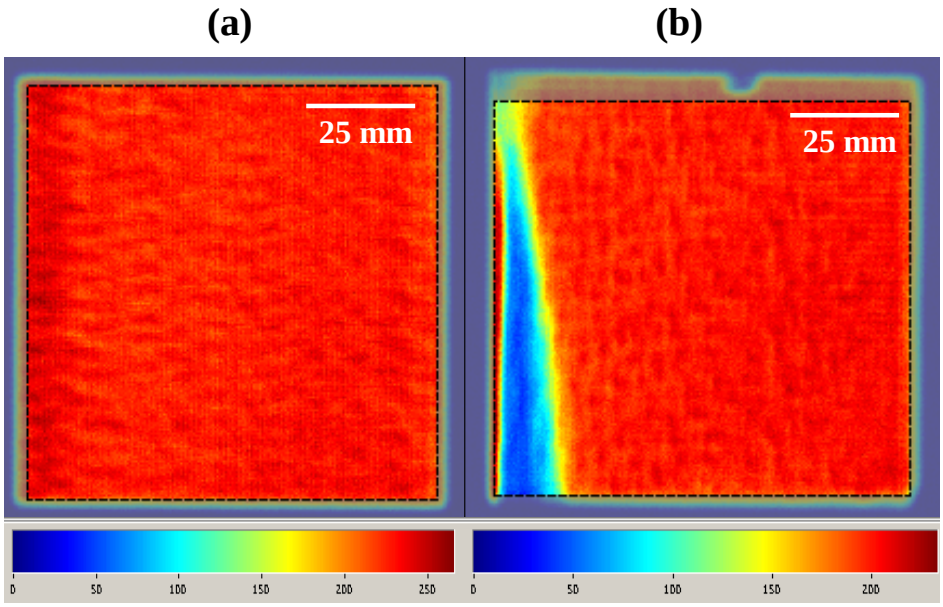

Figure 47. Reflected signal amplitude C-scan images from samples D and E.

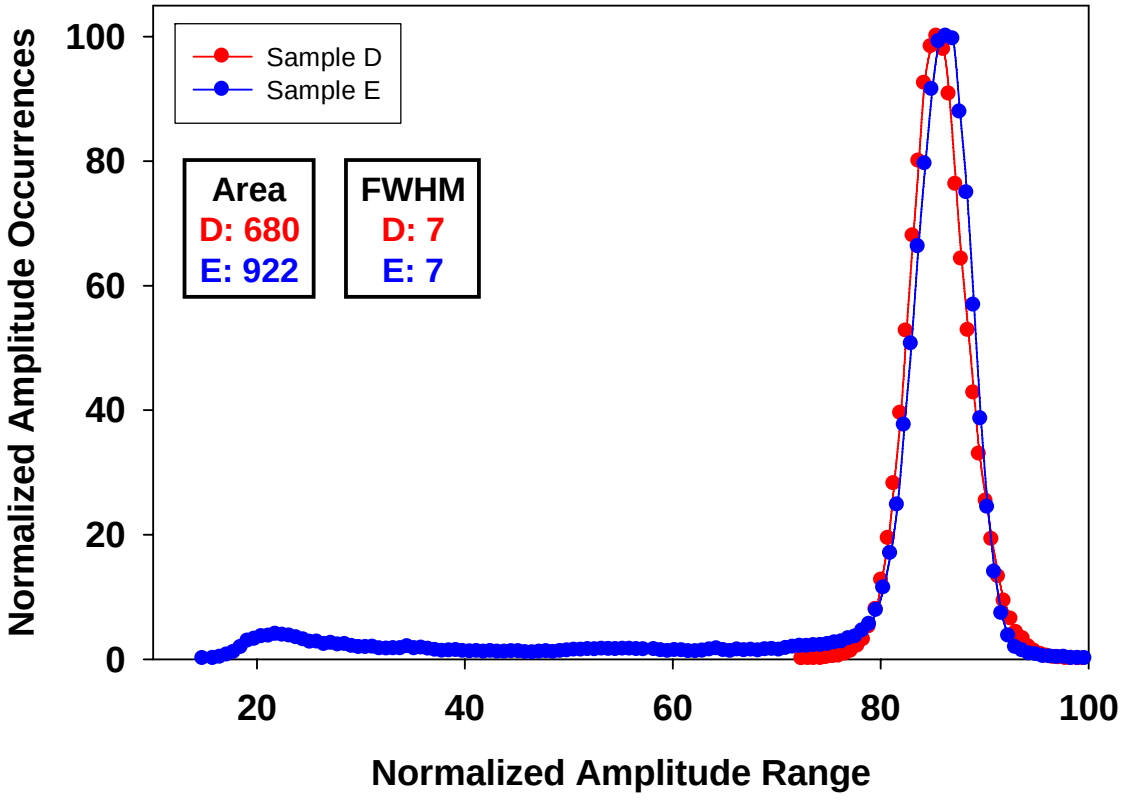

Figure 48. Reflected signal amplitude histogram curves from samples D and E.

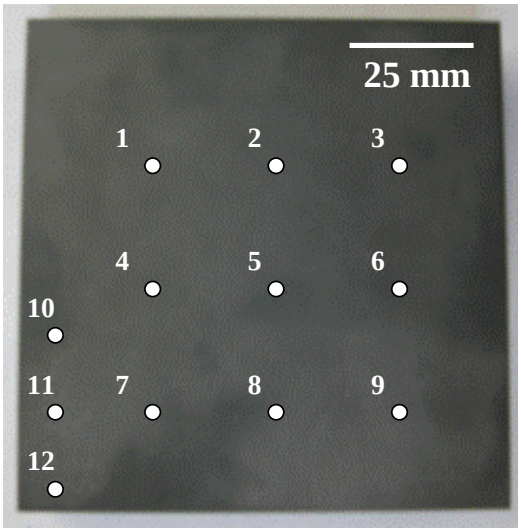

Figure 49. Additional point analysis positions for sample E.

#	ρ (g/cc)	t (mm)	TOF_l (μs)	TOF_s (μs)	c_l (m/s)	c_s (m/s)	Z (*10^5 g/cm^{2}s)	ν	E (GPa)	G (GPa)	K (GPa)
10	3.22	50.93	8.364	13.127	12,180	7,760	39.2	0.16	450	190	220
11	3.22	50.92	8.418	13.146	12,100	7,750	39.0	0.15	440	190	210
12	3.22	50.92	8.437	13.164	12,070	7,740	38.9	0.15	440	190	210
Avg	**3.22**	**50.92**	**8.406**	**13.146**	**12,120**	**7,750**	**39.0**	**0.15**	**440**	**190**	**210**

Table XVII. Additional point analysis evaluation data for sample E at points 10-12.

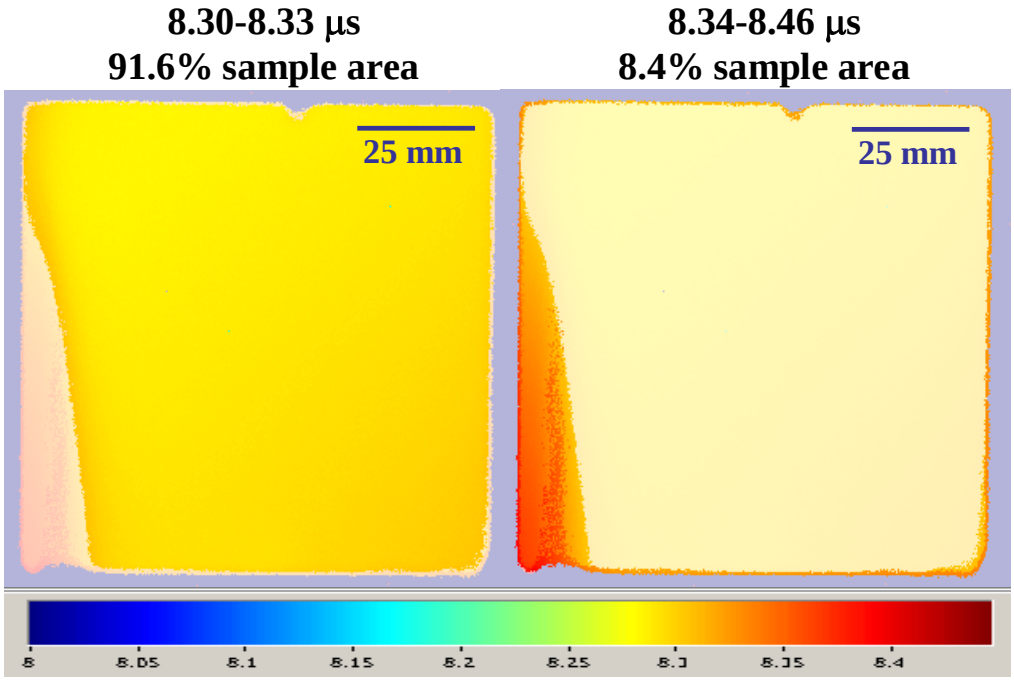

Figure 50. TOF distribution analysis for two ranges of values for sample E.

5.4. Sintered SiC Test Specimens SA1-SA8

A set of eight sintered SiC armor plates, denoted as SA1-SA8 with density values reported by the manufacturer between 3.160 and 3.170 g/cm^3. The manufactured plates had been cut to the same dimensions, with an average length and width of 101.6 mm and an average thickness of 7.82 mm. The Archimedes method was used to measure more precise density values for each sample.

Point analysis was performed using the longitudinal contact very short pulse 50 MHz transducer (VSP-50), which was placed at nine different locations to cover a wide set of regional areas for each sample, as shown in Figure 31. Figure 51 shows the A-scans for all the samples, which were recorded from the center of each sample at position five, as shown in Figure 31. Ultrasound C-scan imaging was conducted using longitudinal immersion 5 MHz (MDS-5), 75 MHz (MDS-75), and 125 MHz (MDS-125) transducers. The 5 MHz and 75 MHz transducers in this case were sufficient for handling a 30 dB receiver attenuation, or gain, which reduced the full wave spectrum to reduce the noise level while maintaining sufficient signal intensity for easily resolving both the top and bottom reflected signals. For the 125 MHz transducer, the receiver attenuation was lowered to 5 dB in order to resolve the bottom surface reflected signal while suppressing the noise enough so that it did not interfere drastically. Occasional noise signals present in the 125 MHz C-scan image results were identified and removed from quantitative analysis data since they were not representative of the bulk sample characteristics.

5.4.1. Point Analysis of SA1-SA8

The SiC samples were first tested using the longitudinal 50 MHz contact transducer to conduct point analysis at nine locations. After designating the point positions and measuring thickness values, the A-scans were collected for measurement of TOF values, as shown in Figure 51. Longitudinal TOF values were measured as the difference between the top and bottom surface reflected signals in μs while shear TOF values were measured as the difference between the top surface reflected signal and the shear reflected signal. The data for all eight samples at each of the nine measured points can be found in Tables XVIII-XXV, along with the average values calculated for each property. An overview of average values for each sample is presented in Table XXVI, including a comparison to reported National Institute of Standards and Technology [23] values for sintered SiC and a comparison to previously measured values for high density hot-pressed SiC samples.

Table XXVI shows a comparison of the average values among each of the eight samples, starting with the density, which was reported by the manufacturer. The range of densities went from 3.151 g/cm^3 to 3.171 g/cm^3, with an average density of 3.163 g/cm^3. This was comparable to reported values of 3.160 g/cm^3 found in the literature for a similar sintered SiC material [117]. The average thickness (t) ranged between 7.80 mm and 7.84 mm, with an overall average of 7.82 mm for the eight samples. A-scan data were measured from the center of each sample at position five to identify top and bottom surface reflected signals for determination of longitudinal and shear TOF values. The averages of all the samples combined were 1.309 μs for TOF_l and 2.504 μs for TOF_s. By applying the Equations 36 and 37, average velocity values were c_l = 11,950 m/s and c_s =

7,610 m/s, which were slightly higher than the NIST reported values [23] of c_l = 11,820 m/s and c_s = 7,520 m/s for a sintered SiC material with a density of 3.160 g/cm^3. The average acoustic impedance value of 37.8x10^5 g/cm^{2}s was also slightly higher than NIST reported value [23] of 37.4x10^5 g/cm^{2}s due to the higher average material velocity values for the eight samples. The average calculated values for the eight SiC samples were ν = 0.16, E = 430 GPa, G = 180 GPa, and K = 210 GPa, which compared favorably to NIST reported values [23] of 420 GPa, 180 GPa, and 200 GPa, respectively. They were also similar to the literature reported values of a similar sintered SiC material which had E = 416 GPa and G = 185 GPa [117]. The measured SA values were also compared to higher density hot pressed SiC values from previous studies and literature reported values, as shown in Table XXVI. The hot pressed samples showed higher values for c_l at 12,270 m/s, c_s at 7,760 m/s, Z at 39.5x10^5 g/cm^{2}s, and ν = 0.17, as expected due to the higher densities and resulting higher sound velocities through the samples. However, the elastic property values were very similar to the sintered SiC samples being analyzed, with E = 430 GPa, G = 180 GPa, and K = 220 GPa.

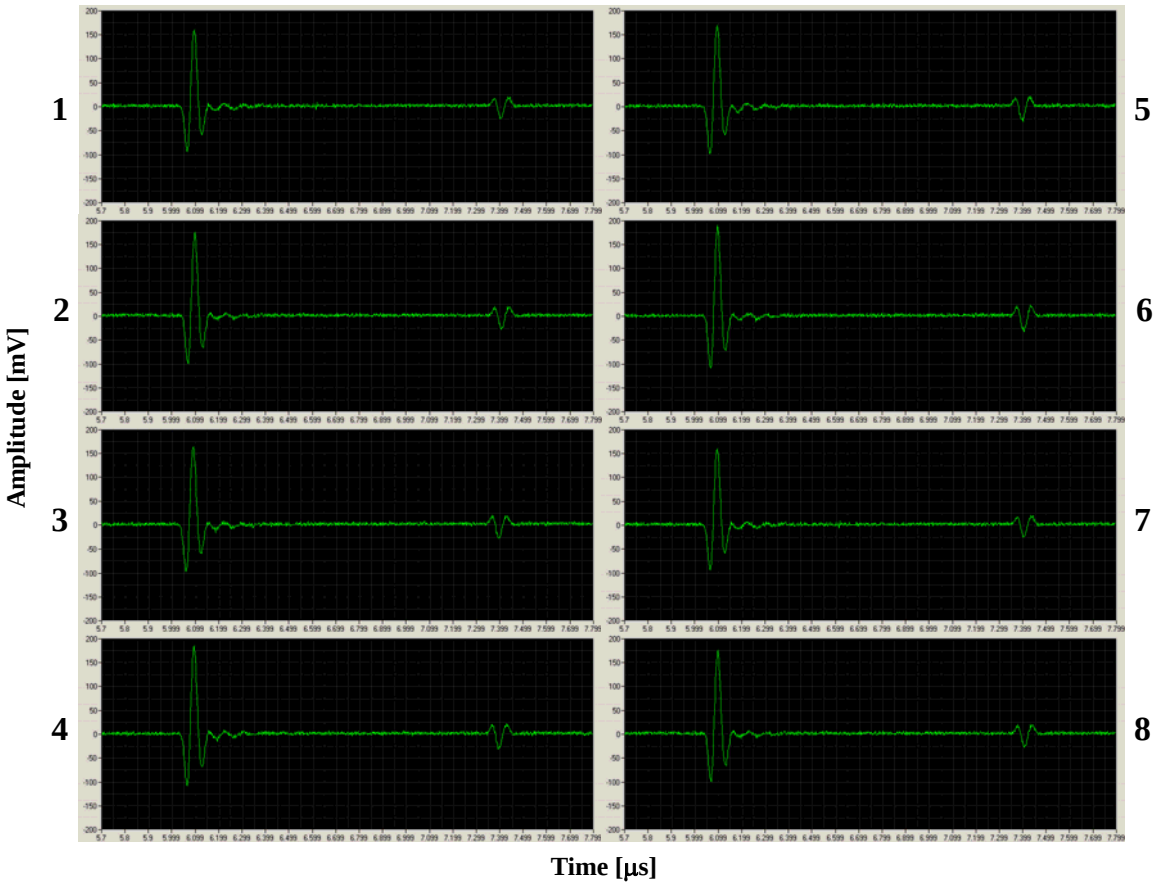

Figure 51. Position 5 top and bottom reflected signals for samples SA1-SA8.

#	ρ (g/cc)	t (mm)	TOF_l (μs)	TOF_s (μs)	c_l (m/s)	c_s (m/s)	Z (*10^5 g/cm^{2}s)	ν	E (GPa)	G (GPa)	K (GPa)
1	3.151	7.76	1.305	2.048	11,890	7,580	37.5	0.16	420	180	200
2	3.151	7.78	1.307	2.052	11,900	7,580	37.5	0.16	420	180	210
3	3.151	7.77	1.304	2.047	11,920	7,590	37.6	0.16	420	180	210
4	3.151	7.84	1.312	2.060	11,950	7,610	37.7	0.16	420	180	210
5	3.151	7.82	1.312	2.060	11,920	7,590	37.6	0.16	420	180	210
6	3.151	7.83	1.312	2.059	11,940	7,610	37.6	0.16	420	180	210
7	3.151	7.82	1.312	2.058	11,920	7,600	37.6	0.16	420	180	210
8	3.151	7.83	1.312	2.060	11,940	7,600	37.6	0.16	420	180	210
9	3.151	7.82	1.312	2.059	11,920	7,600	37.6	0.16	420	180	210
Avg	**3.151**	**7.81**	**1.310**	**2.056**	**11,920**	**7,600**	**37.6**	**0.16**	**420**	**180**	**210**

Table XVIII. Point analysis data for sample SA1.

#	ρ (g/cc)	t (mm)	TOF_l (μs)	TOF_s (μs)	c_l (m/s)	c_s (m/s)	Z (*10^5 g/cm^{2}s)	ν	E (GPa)	G (GPa)	K (GPa)
1	3.163	7.83	1.309	2.055	11,960	7,620	37.8	0.16	430	180	210
2	3.163	7.84	1.311	2.058	11,960	7,620	37.8	0.16	430	180	210
3	3.163	7.80	1.309	2.055	11,920	7,590	37.7	0.16	420	180	210
4	3.163	7.81	1.309	2.054	11,930	7,600	37.7	0.16	420	180	210
5	3.163	7.84	1.312	2.060	11,950	7,610	37.8	0.16	420	180	210
6	3.163	7.82	1.312	2.059	11,920	7,600	37.7	0.16	420	180	210
7	3.163	7.80	1.309	2.055	11,920	7,590	37.7	0.16	420	180	210
8	3.163	7.81	1.312	2.060	11,910	7,580	37.7	0.16	420	180	210
9	3.163	7.80	1.309	2.054	11,920	7,590	37.7	0.16	420	180	210
Avg	**3.163**	**7.82**	**1.310**	**2.057**	**11,930**	**7,600**	**37.7**	**0.16**	**420**	**180**	**210**

Table XIX. Point analysis data for sample SA2.

#	ρ (g/cc)	t (mm)	TOF_l (μs)	TOF_s (μs)	c_l (m/s)	c_s (m/s)	Z (*10^5 g/cm^{2}s)	ν	E (GPa)	G (GPa)	K (GPa)
1	3.163	7.82	1.310	2.057	11,940	7,600	37.8	0.16	420	180	210
2	3.163	7.80	1.313	2.061	11,880	7,570	37.6	0.16	420	180	200
3	3.163	7.76	1.302	2.044	11,920	7,590	37.7	0.16	420	180	210
4	3.163	7.83	1.310	2.057	11,950	7,610	37.8	0.16	430	180	210
5	3.163	7.85	1.309	2.055	11,990	7,640	37.9	0.16	430	180	210
6	3.163	7.77	1.304	2.047	11,920	7,590	37.7	0.16	420	180	210
7	3.163	7.80	1.312	2.060	11,890	7,570	37.6	0.16	420	180	210
8	3.163	7.79	1.312	2.059	11,880	7,570	37.6	0.16	420	180	200
9	3.163	7.76	1.299	2.039	11,950	7,610	37.8	0.16	420	180	210
Avg	**3.163**	**7.80**	**1.308**	**2.053**	**11,920**	**7,590**	**37.7**	**0.16**	**420**	**180**	**210**

Table XX. Point analysis data for sample SA3.

#	ρ (g/cc)	t (mm)	TOF_l (μs)	TOF_s (μs)	c_l (m/s)	c_s (m/s)	Z (*10^5 g/cm^2s)	ν	E (GPa)	G (GPa)	K (GPa)
1	3.164	7.80	1.296	2.035	12,040	7,670	38.1	0.16	430	190	210
2	3.164	7.83	1.305	2.049	12,000	7,640	38.0	0.16	430	180	210
3	3.164	7.82	1.310	2.057	11,940	7,600	37.8	0.16	420	180	210
4	3.164	7.81	1.305	2.048	11,970	7,630	37.9	0.16	430	180	210
5	3.164	7.83	1.304	2.047	12,010	7,650	38.0	0.16	430	190	210
6	3.164	7.85	1.307	2.052	12,010	7,650	38.0	0.16	430	190	210
7	3.164	7.80	1.309	2.055	11,920	7,600	37.7	0.16	420	180	210
8	3.164	7.84	1.299	2.039	12,070	7,690	38.2	0.16	430	190	210
9	3.164	7.83	1.302	2.044	12,030	7,660	38.1	0.16	430	190	210
Avg	**3.164**	**7.82**	**1.304**	**2.047**	**12,000**	**7,640**	**38.0**	**0.16**	**430**	**190**	**210**

Table XXI. Point analysis data for sample SA4.

#	ρ (g/cc)	t (mm)	TOF_l (μs)	TOF_s (μs)	c_l (m/s)	c_s (m/s)	Z (*10^5 g/cm^2s)	ν	E (GPa)	G (GPa)	K (GPa)
1	3.161	7.75	1.299	2.039	11,930	7,600	37.7	0.16	420	180	210
2	3.161	7.77	1.304	2.047	11,920	7,590	37.7	0.16	420	180	210
3	3.161	7.80	1.304	2.048	11,960	7,620	37.8	0.16	430	180	210
4	3.161	7.79	1.304	2.047	11,950	7,610	37.8	0.16	420	180	210
5	3.161	7.80	1.304	2.048	11,960	7,620	37.8	0.16	430	180	210
6	3.161	7.82	1.309	2.055	11,950	7,610	37.8	0.16	420	180	210
7	3.161	7.81	1.304	2.048	11,980	7,630	37.9	0.16	430	180	210
8	3.161	7.84	1.307	2.052	12,000	7,640	37.9	0.16	430	180	210
9	3.161	7.83	1.307	2.052	11,980	7,630	37.9	0.16	430	180	210
Avg	**3.161**	**7.80**	**1.305**	**2.048**	**11,960**	**7,620**	**37.8**	**0.16**	**430**	**180**	**210**

Table XXII. Point analysis data for sample SA5.

#	ρ (g/cc)	t (mm)	TOF_l (μs)	TOF_s (μs)	c_l (m/s)	c_s (m/s)	Z (*10^5 g/cm^2s)	ν	E (GPa)	G (GPa)	K (GPa)
1	3.161	7.84	1.307	2.052	12,000	7,640	37.9	0.16	430	180	210
2	3.161	7.85	1.312	2.060	11,970	7,620	37.8	0.16	430	180	210
3	3.161	7.85	1.310	2.057	11,980	7,630	37.9	0.16	430	180	210
4	3.161	7.85	1.312	2.060	11,970	7,620	37.8	0.16	430	180	210
5	3.161	7.85	1.312	2.060	11,970	7,620	37.8	0.16	430	180	210
6	3.161	7.82	1.310	2.056	11,940	7,610	37.7	0.16	420	180	210
7	3.161	7.82	1.309	2.054	11,950	7,610	37.8	0.16	420	180	210
8	3.161	7.84	1.309	2.055	11,980	7,630	37.9	0.16	430	180	210
9	3.161	7.80	1.307	2.051	11,940	7,610	37.7	0.16	420	180	210
Avg	**3.161**	**7.84**	**1.310**	**2.056**	**11,970**	**7,620**	**37.8**	**0.16**	**430**	**180**	**210**

Table XXIII. Point analysis data for sample SA6.

#	ρ (g/cc)	t (mm)	TOF_l (μs)	TOF_s (μs)	c_l (m/s)	c_s (m/s)	Z (*10^5 g/cm^2s)	ν	E (GPa)	G (GPa)	K (GPa)
1	3.171	7.81	1.310	2.057	11,920	7,590	37.8	0.16	420	180	210
2	3.171	7.85	1.315	2.065	11,940	7,600	37.9	0.16	430	180	210
3	3.171	7.84	1.315	2.064	11,920	7,600	37.8	0.16	420	180	210
4	3.171	7.83	1.310	2.057	11,950	7,610	37.9	0.16	430	180	210
5	3.171	7.84	1.312	2.059	11,950	7,620	37.9	0.16	430	180	210
6	3.171	7.86	1.312	2.060	11,980	7,630	38.0	0.16	430	180	210
7	3.171	7.80	1.307	2.052	11,940	7,600	37.8	0.16	420	180	210
8	3.171	7.84	1.312	2.060	11,950	7,610	37.9	0.16	430	180	210
9	3.171	7.83	1.310	2.057	11,950	7,610	37.9	0.16	430	180	210
Avg	**3.171**	**7.83**	**1.311**	**2.059**	**11,940**	**7,610**	**37.9**	**0.16**	**430**	**180**	**210**

Table XXIV. Point analysis data for sample SA7.

#	ρ (g/cc)	t (mm)	TOF_l (μs)	TOF_s (μs)	c_l (m/s)	c_s (m/s)	Z (*10^5 g/cm^2s)	ν	E (GPa)	G (GPa)	K (GPa)
1	3.168	7.79	1.302	2.044	11,970	7,620	37.9	0.16	430	180	210
2	3.168	7.83	1.312	2.060	11,940	7,600	37.8	0.16	420	180	210
3	3.168	7.84	1.312	2.060	11,950	7,610	37.9	0.16	430	180	210
4	3.168	7.81	1.307	2.051	11,950	7,620	37.9	0.16	430	180	210
5	3.168	7.83	1.312	2.059	11,940	7,610	37.8	0.16	420	180	210
6	3.168	7.85	1.312	2.060	11,970	7,620	37.9	0.16	430	180	210
7	3.168	7.83	1.307	2.052	11,980	7,630	38.0	0.16	430	180	210
8	3.168	7.86	1.315	2.064	11,950	7,620	37.9	0.16	430	180	210
9	3.168	7.85	1.312	2.060	11,970	7,620	37.9	0.16	430	180	210
Avg	**3.168**	**7.83**	**1.310**	**2.057**	**11,960**	**7,620**	**37.9**	**0.16**	**430**	**180**	**210**

Table XXV. Point analysis data for sample SA8.

#	ρ (g/cc)	t (mm)	TOF_l (μs)	TOF_s (μs)	c_l (m/s)	c_s (m/s)	Z (*10^5 g/cm^2s)	ν	E (GPa)	G (GPa)	K (GPa)
1	3.151	7.81	1.310	2.056	11,920	7,600	37.6	0.16	420	180	210
2	3.163	7.82	1.310	2.057	11,930	7,600	37.7	0.16	420	180	210
3	3.163	7.80	1.308	2.053	11,920	7,590	37.7	0.16	420	180	210
4	3.164	7.82	1.304	2.047	12,000	7,640	38.0	0.16	430	190	210
5	3.161	7.80	1.305	2.048	11,960	7,620	37.8	0.16	430	180	210
6	3.161	7.84	1.310	2.056	11,970	7,620	37.8	0.16	430	180	210
7	3.171	7.83	1.311	2.059	11,940	7,610	37.9	0.16	430	180	210
8	3.168	7.83	1.310	2.057	11,960	7,620	37.9	0.16	430	180	210
Avg	**3.163**	**7.82**	**1.309**	**2.054**	**11,950**	**7,610**	**37.8**	**0.16**	**430**	**180**	**210**
Rep	**3.16**	-	-	-	**11,820**	**7,520**	**37.4**	**0.16**	**420**	**180**	**200**
HP	**3.22**	-	-	-	**12,270**	**7,760**	**39.5**	**0.17**	**430**	**180**	**220**

Table XXVI. Average point analysis data for samples SA1-SA8 and comparison to reported sintered and hot pressed SiC

While these trends were apparent for the average values of the eight samples, Tables XVIII-XXV showed regional differences in thickness, TOF, velocity, and elastic properties for each individual sample. Most of these values were very consistent over each sintered SiC sample. The only noticeable differences came from slight thickness variations. Sample SA3, for example, had a slightly thinner region on the right side, which exhibited an average thickness of 7.76 mm as opposed to the rest of the sample, which had an average thickness of 7.82 mm, as shown in Table XX. Points three, six, and nine all had lower TOF values as a result, since the time for the acoustic wave to travel through this region was less than for the rest of the sample. However, the effect on the elastic property values was insignificant, as the values were quite consistent throughout the sample. Even the largest degree of difference among the samples, as exemplified in this case, did not significantly change the elastic properties, so the SiC plates were considered to be consistent both within the same sample and compared to the rest of the samples.

5.4.2. TOF C-scan Imaging of SA1-SA8

C-scan imaging was performed using the 5, 75, and 125 MHz longitudinal immersion transducers to collect TOF data over the area of each SiC sample. The TOF data were collected in addition to x and y positions of each point and the data ranges were chosen based on a representation of approximately 95% of the maximum value up to the maximum TOF in μs for comparison purposes. The TOF C-scan images for each of the SiC samples are shown in Figure 52 for samples SA1-SA4 and Figure 53 for samples SA5-SA8. The average and standard deviation TOF values for each sample are shown in Table XXVII. A small representation of data points peppered throughout each sample,

most notably in the 125 MHz scans, displayed TOF values close to zero due to electrical interference during C-scan imaging. These data points appeared more frequently in the 125 MHz scans because the thresholds of the gates were lowered to include the lower intensity bottom surface reflected signals, thus allowing more noise peaks into the scanned data. For this reason, the receiver attenuation was lowered to 5 dB, as mentioned previously, reducing the signal-to-noise ratio in the process. While some noise peaks were still present, the resulting interference data points were not factored in to the average, standard deviation, or quantitative analysis data because they were not representative of the bulk samples.

The TOF C-scan images in Figures 52 and 53 showed a visual depiction of the differences between the samples at all three frequencies. At 5 MHz, there were minor TOF differences across each sample. The largest differences could be found on the right side of SA3 and the left side of SA4, which were sample areas of lower average thickness. This was apparent when looking at Table XV, which showed below average thickness at points 3, 6, and 9 and Table XVI, which showed below average thickness points at 1, 4, and 7. Since unfocused low frequency transducers could not resolve defects smaller than millimeter-range according to the theoretical detection limits in Table IV, in this case 1.2 mm at 5 MHz, micron-range defects were not detected.

5MHz		
#	Average (μs)	Standard Deviation (μs)
1	1.297	.00444
2	1.299	.00370
3	1.294	.00602
4	1.294	.00609
5	1.293	.00342
6	1.296	.00402
7	1.298	.00472
8	1.300	.00435

75MHz		
#	Average (μs)	Standard Deviation (μs)
1	1.294	.00607
2	1.301	.01359
3	1.292	.00751
4	1.291	.00733
5	1.293	.01109
6	1.295	.00522
7	1.297	.00860
8	1.298	.00607

125MHz		
#	Average (μs)	Standard Deviation (μs)
1	1.301	.00547
2	1.303	.00733
3	1.298	.00714
4	1.297	.00673
5	1.296	.00513
6	1.300	.00467
7	1.303	.00723
8	1.304	.00569

Table XXVII. Average and standard deviation TOF C-scan image data for samples SA1-SA8 at various frequencies.

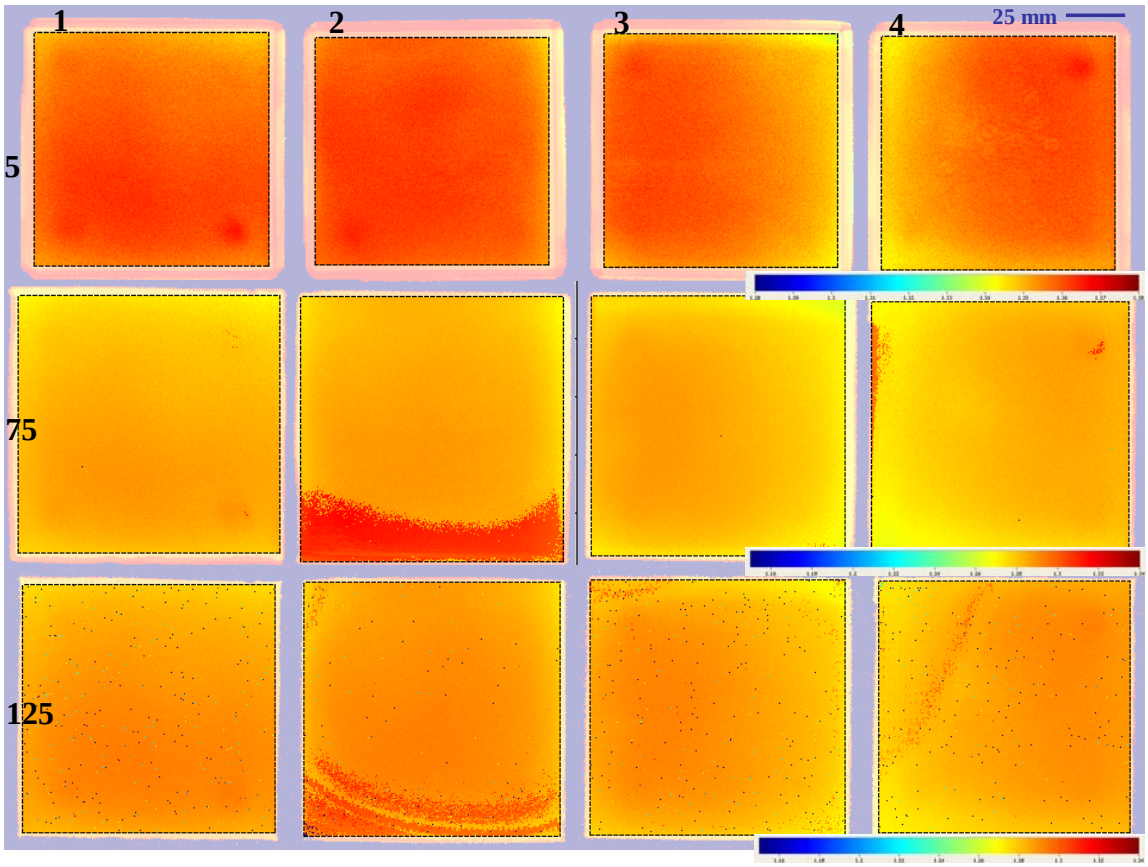

Figure 52. TOF C-scan image maps of SA1-SA4 at 5, 75, and 125 MHz.

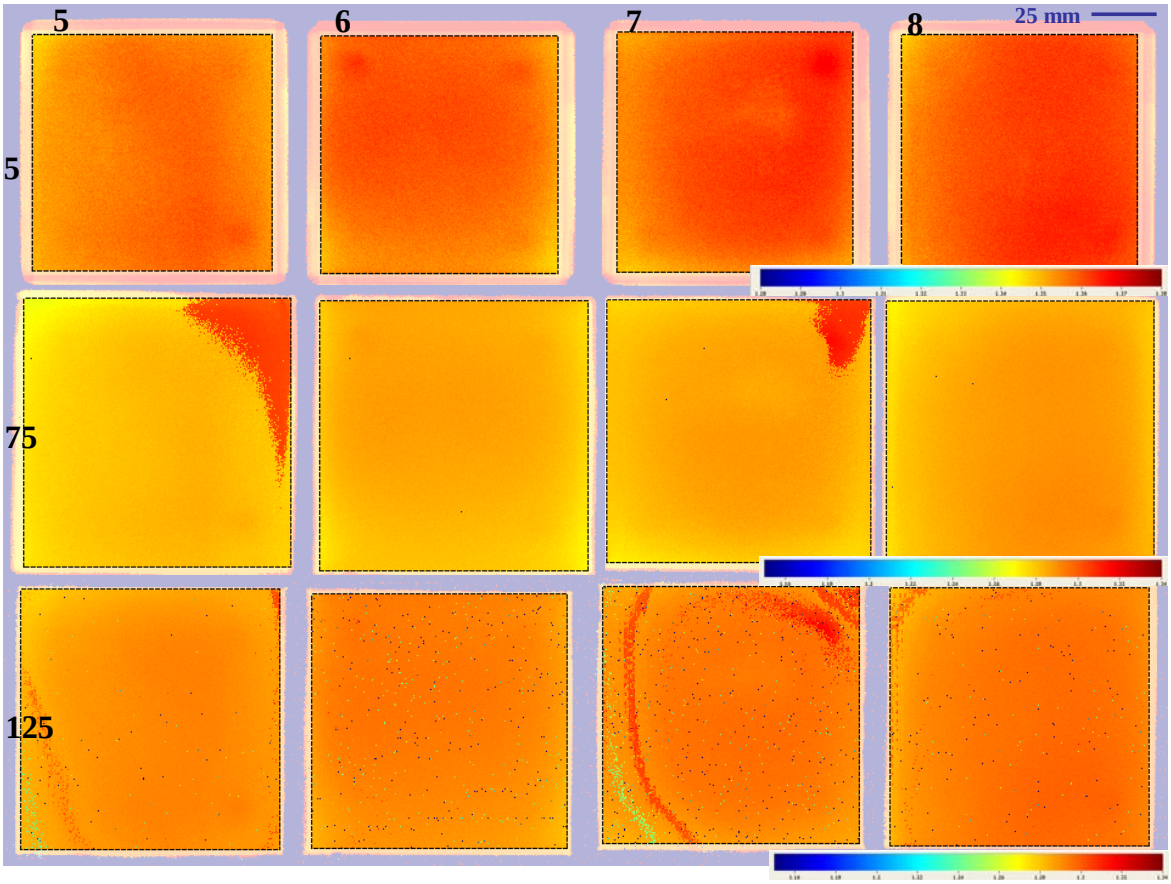

Figure 53. TOF C-scan image maps of SA5-SA8 at 5, 75, and 125 MHz.

Other interesting features detected at 5 MHz included ~5-10 mm circular regions of higher TOF which could be distinguished, especially in samples SA1, SA3, SA4, SA5, and SA6. These large features were found in the corners of the listed samples and were believed to be process-related. One reason for these large features that was discussed with the manufacturer was the use of spacers to separate the samples at the corner during the green state. These stacking configurations resulted in an increased amount of pressure at specific regions in the corners of the majority of the samples, and upon firing, led to density variations within these regions. At 75 MHz, in which the theoretical detection limit for a planar transducer was approximately 80 μm according to Table IV, the regional TOF differences were readily apparent. As mentioned previously, despite the increased attenuation for this higher frequency transducer, the bottom surface reflected signal was still very strong, as a 30 dB receiver attenuation, or gain, was sufficient for resolving the signal while drastically reducing the noise level. Samples SA2, SA5, and SA7 stood out, as they each showed higher TOF value regions that were not detected at 5 MHz. These regions were not caused by increased sample thickness, which would have been observed at 5 MHz, but rather bulk changes only detectable at higher frequencies. These large regions were again believed to be caused by process-related factors such as density variations from improper die filling during dry pressing. In addition to the large regions, SA1 and SA4 showed smaller regions of higher TOF that were believed to be attributed to individual defects. The defects for these two samples fell within the 5-10 mm circular regions detected in the 5 MHz scans. At 125 MHz, the increased attenuation played a role, since the receiver attenuation had to be reduced to 5 dB to resolve the bottom surface signal reflection, as mentioned earlier. However, the

specific TOF differences were recognized visually despite the interference points, which were scattered throughout each C-scan. As opposed to the large regions of higher TOF found in the 75 MHz scans, this higher frequency transducer showed specific bands within those regions that were reminiscent of process-related pressing patterns. These pressing patterns were evident in all of the samples except for SA1 and SA6. The greatest TOF differences in the patterns were found in SA2 and SA7, two of the samples with high TOF regions from the 75 MHz scans. The C-scan images appeared to show consistent visual trends at all frequencies, with more specific defect patterns becoming evident and apparent at higher frequencies.

The average and standard deviation values for these TOF C-scan images are listed in Table XXVII to provide numerical comparison in addition to visual comparison. As opposed to the average TOF values calculated using point analysis, the average TOF values from C-scan imaging data were lower by approximately 0.010-0.015 μs. This was a slight difference that corresponded to a material velocity variation between 3-4 m/s. The reason for the difference was the way the TOF was measured in each technique. For point analysis, the TOF was measured from the onset of the top surface reflection peak to the onset of the bottom surface reflection peak. This was more accurate than the C-scan TOF technique, which measured the position from the maximum intensity of the top surface reflection peak to the position from the maximum intensity of the bottom surface reflection peak. The standard deviation comparison of TOF data for each SiC sample was a good way to compare samples to one another using a single numerical value to determine how much the TOF range changed over the sample area. At 5 MHz, the standard deviation differences were most drastic for sample SA3 with a value of $6.02^{x}10^{-3}$

μs and sample 4 with a value of $6.09^{x}10^{-3}$ μs. This was expected due to the thinner regions on the right and left sides, respectively, which caused a decrease in TOF, and therefore, an increase in the overall standard deviation. The rest of the samples had standard deviation values that were very similar, ranging from 3.42 x 10^{-3} to 4.72 x 10^{-3} μs. At 75 MHz, samples SA2, SA5, SA7, which had large regions of high TOF, had the three highest standard deviation values of 13.6 x 10^{-3}, 11.1 x 10^{-3}, and 8.60 x 10^{-3} μs, respectively, while the rest of the samples ranged from 5.22 x 10^{-3} to 7.51 x 10^{-3} μs. At 125 MHz, samples SA2 and SA7, which appeared to exhibit the highest TOF pressing patterns, also had the highest standard deviations of 7.33 x 10^{-3} and 7.23 x 10^{-3} μs, respectively. The numerical standard deviation trends were consistent with the visual trends.

5.4.3. TOF and Material Velocity C-scan Quantitative Analysis of SA1-SA8

In a first attempt to quantify the data, the TOF values from the selected regions in Figures 52 and 53 were normalized in terms of the number of TOF occurrences on the y-axis while the TOF range on the x-axis remained the same. The histograms quantitatively depicted the cumulative TOF data for each sample and were observed for their shape, broadness of distribution, and tail properties. The AUTC and FWHM values were also calculated for each curve. Figures 54, 55, and 56 show the TOF histogram curves for all eight sintered SiC samples at each frequency including the calculated AUTC and FWHM values. Figures 57, 58, and 59 show the velocity histogram curves for all eight samples at each frequency including the calculated AUTC and FWHM values.

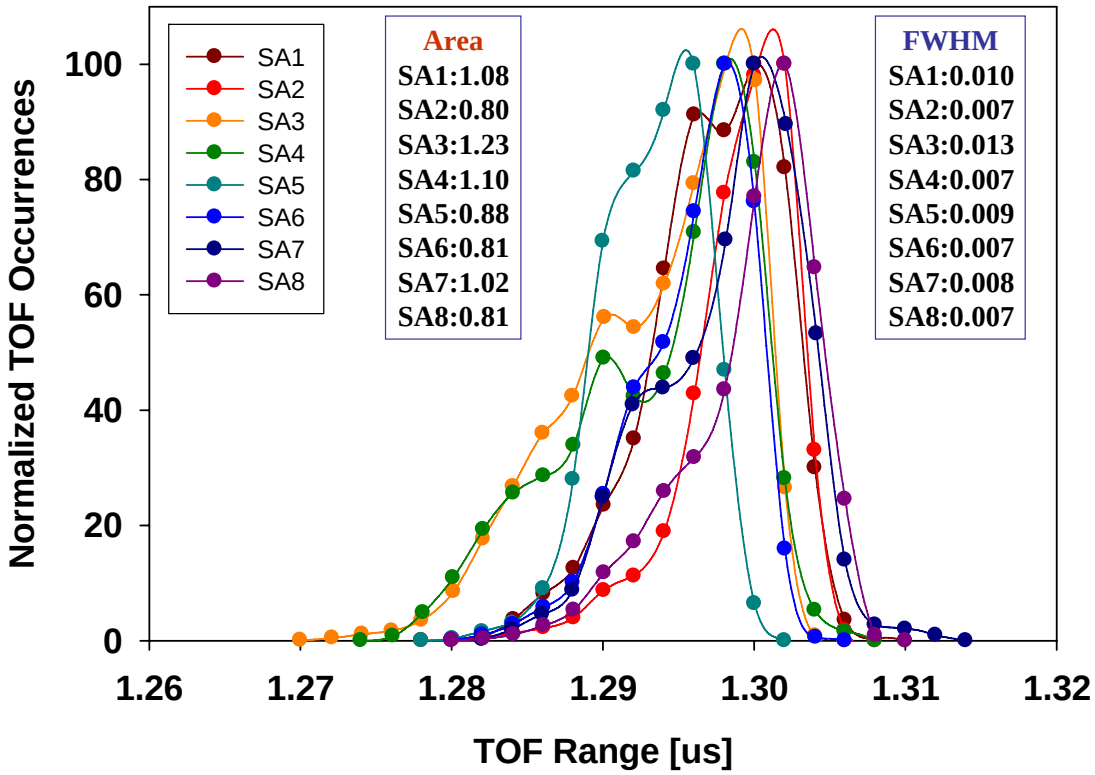

Figure 54. TOF histogram curves for SA1-SA8 at 5 MHz.

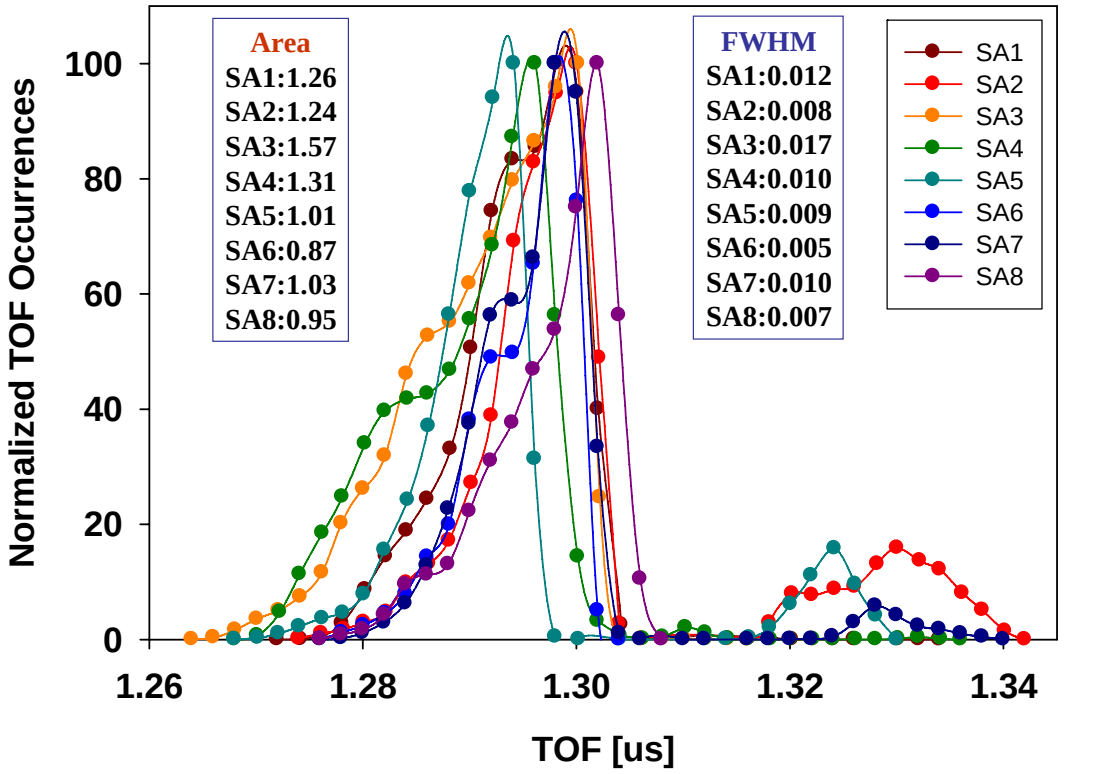

Figure 55. TOF histogram curves for SA1-SA8 at 75 MHz.

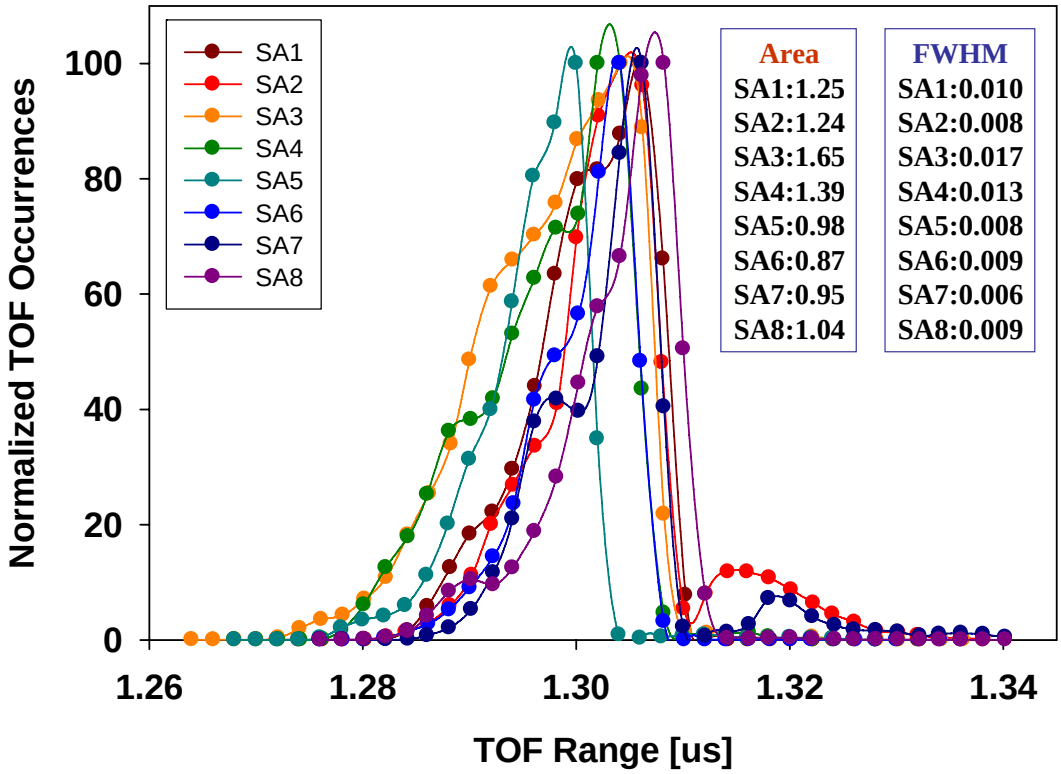

Figure 56. TOF histogram curves for SA1-SA8 at 125 MHz.

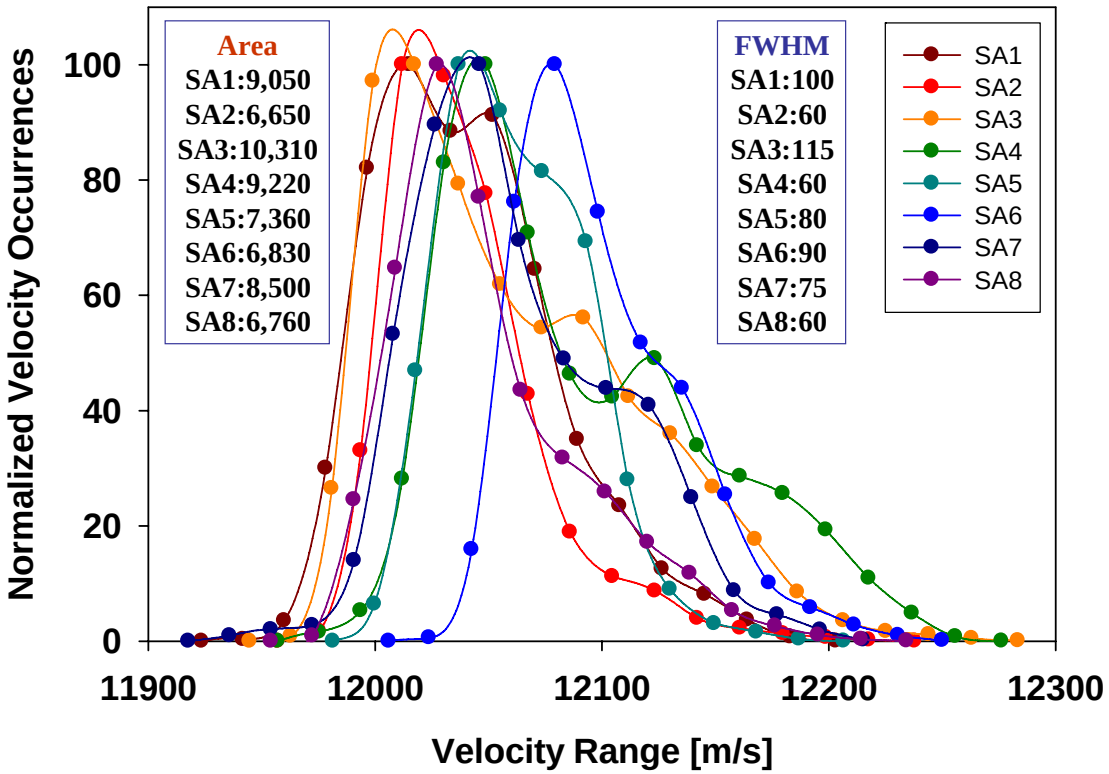

Figure 57. Velocity histogram curves for SA1-SA8 at 5 MHz.

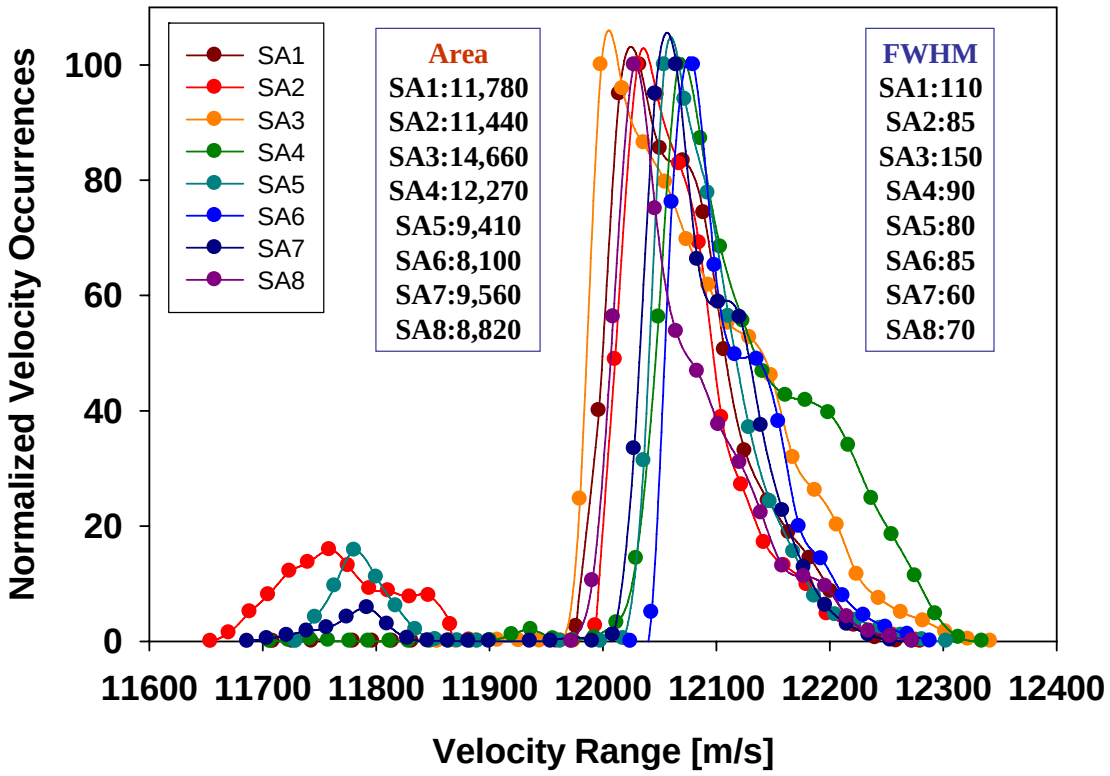

Figure 58. Velocity histogram curves for SA1-SA8 at 75 MHz.

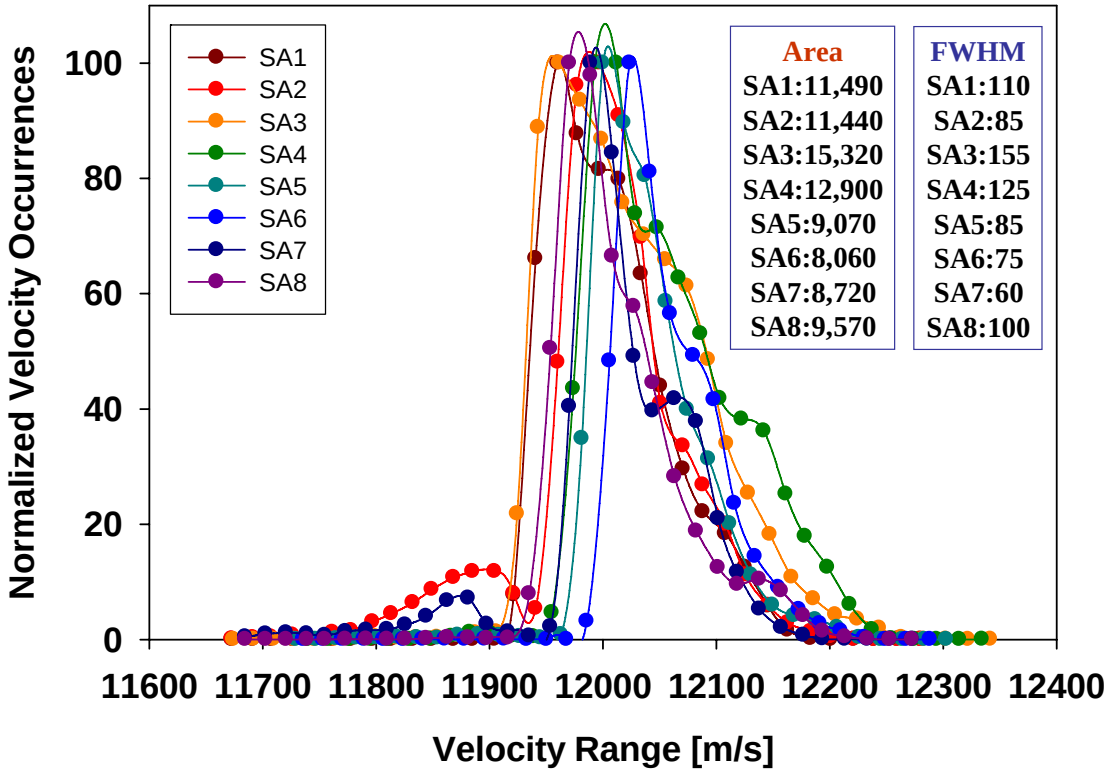

Figure 59. Velocity histogram curves for SA1-SA8 at 125 MHz.

For the 5 MHz TOF histograms in Figure 54, the curves were similar over the 1.27 to 1.31 μs range. The only features that stood out were the second peaks and wider distributions on the left side of the curves for SA3 and SA4. These were the two samples with the slightly thinner regions that caused lower TOF values in those areas. For this reason, the curves were broader at the lower end of the TOF spectrum from 1.27 to 1.29 μs. The AUTC values reflected an increase in histogram curve broadness as the distribution was wider in SA3 with an area of 1.23 and SA4 with an area of 1.10. The FWHM values also provided a means of comparison, but one that was highly dependent on peak broadness at a specific set of normalized TOF values. For example, while SA3 and SA4 that stood out with the highest AUTC values, only SA3 registered a high FWHM value while SA4 was among the lowest. Although both minor peaks on the left sides of the curves were similar, the one for SA3 happened to fall above 50% normalized TOF while SA4 fell below. Since FWHM values measured the broadness of the histograms along that line, the numbers were very different for these two curves. The AUTC values were found to be more reliable for sample comparison in this case. The velocity histogram curves for 5 MHz, as seen in Figure 57, showed the same trends as the TOF curves, but in the opposite direction. This was true for all velocity histogram curves, since TOF and velocity are inversely proportional. The lower TOF regions corresponded to higher material velocity values and the higher TOF regions corresponded to lower material velocity values. One observation was that sample SA6 had the highest peak velocity and one of the lowest FWHM values. Comparatively speaking, this would be considered the best out of the eight very similar sintered SiC materials, but this observation was made at 5 MHz where only large material inhomogeneities could be

detected. The AUTC and FWHM trends were the same, as SA3 and SA4 showed the highest AUTC values and SA3 exhibited a distinctly higher FWHM value than SA4 despite similar histogram curves.

For the 75 MHz TOF histograms in Figure 55, a new trend was found that was not present in the 5 MHz histograms. While the histograms seemed to maintain a similar curve shape at both frequencies between 1.26 and 1.31 μs, additional curves were found at higher TOF values between 1.32 and 1.34 μs for four of the samples at 75 MHz. These high TOF tails could not be distinguished at lower frequencies but were of vital interest for comparing material integrity among samples, since higher TOF values corresponded to lower material velocities and lower elastic properties. These regions were red-flagged as weak points in otherwise identical samples. Again, these regions were not a result of thickness differences in the samples, as they would have been apparent at 5 MHz if they were. Instead, they were bulk material changes that caused a variation in acoustic wave behavior within the same sample. The high TOF tails were observed for SA2, SA4, SA5, and SA7. These results were consistent with the high TOF regions in the C-scan images shown in Figure 52 and Figure 53. The area of each region corresponded to the area of each tail, with SA2 possessing the largest tail area and SA4 the smallest. The AUTC values did not correlate directly with the tail characteristics. While the tails influenced the overall AUTC values, they were not significantly large enough to dictate the final histogram AUTC values. SA5, which had no distinguishable tail, had the largest AUTC because it had the largest TOF distribution between 1.26 and 1.31 μs. The large TOF AUTC value for SA2 between 1.32 and 1.34 μs increased the overall AUTC, but the rest of the sample had a relatively narrow distribution between 1.26 and 1.31 μs. The FWHM

values were not at all influenced by the tails because none of the tail areas were large enough to reach the 50% normalized TOF range. This meant that the tails, which were the most influential factor for distinguishing similar SiC samples, needed to be considered separately from other quantitative data. SA2, SA5, and SA7, respectively, would be considered the most problematic samples according to this analysis. Again, the velocity curves in Figure 58 showed the inverse trends of the TOF curves. The tails corresponded to lower velocities between 11,650 and 11,850 m/s as opposed to the rest of the sample areas which were between 11,950 and 12,300 m/s. The order of importance for histogram comparison would be to first look for tail regions and evaluate their areas, next to evaluate the overall AUTC values, and finally to look for possible trends in FWHM data.

For the 125 MHz TOF histograms in Figure 56, the tails were still present, most significantly for SA2 and SA7. As was mentioned in the C-scan image evaluation, the highest frequency 125 MHz scans provided more detailed imaging of TOF variations in the SiC samples. While all of these differences were evident in the histogram data, the two that were most significant came from what appeared to be pressing patterns in SA2 and SA7. Again, the noise-related pixels scattered throughout the C-scan images were eliminated before constructing the histogram curves and did not influence the data. One difference between the tails at 125 MHz was that they were closer to the bulk distributions in the range of 1.31 and 1.33 μs as opposed to 1.32 and 1.34 μs for the 75 MHz scans. The 125 MHz transducer appeared to have picked up more minute TOF differences than the 75 MHz transducer. However, the AUTC results were still highly comparable for both frequencies. Once again, SA3 had the highest AUTC value of the

eight samples due to a broad bulk distribution of TOF values followed by SA4, SA1, and SA2. The FWHM values were also highest for SA3, SA4, and SA1 at both frequencies. SA6 had the lowest AUTC value with the narrowest distribution of TOF differences at 75 and 125 MHz, making it the most homogeneous sample under high frequency ultrasound evaluation. The velocity histograms for the 125 MHz scans in Figure 59 again showed the inverse trends of the TOF curves. The tails corresponded to lower velocities between 11,800 and 11,950 m/s as opposed to the rest of the sample areas which were between 11,950 and 12,250 m/s. After performing ultrasound quantitative histogram analysis using all three transducers on the same set of samples, it was determined that the frequency choice was dependent on the desired outcome. For thickness variations and millimeter-size defect evaluations, 5 MHz ultrasound analysis was sufficient. For bulk property evaluation in terms of significantly inhomogeneous regions and roughly 100 micron-size defect evaluation, 75 MHz was sufficient. For detailed bulk property evaluation in terms of specific microstructural inhomogeneity patterns and 50 micron-size defect evaluation, 125 MHz was sufficient, but some degree of loss in signal-to-noise ratio could be expected.

Based solely on nondestructive ultrasound analysis of the set of eight sintered SiC samples at high frequencies, SA6, the most homogeneous sample, would be expected to exhibit improved performance as compared to SA2 and SA6, which showed the greatest degree of TOF and velocity variability. The degree of difference between average and high TOF regions within the same sample could be used to quantify the effect of material inhomogeneities. For example, the average bulk region with TOF_l~1.290 μs and TOF_s~2.025 μs would have c_l~12,120 m/s with elastic properties of E~437 GPa, G~189

GPa, and K~213 GPa. The high TOF region with TOF_l~1.330 μs and TOF_s~2.088 μs would drop to c_l~11,760 m/s with elastic properties of E~411 GPa, G~177 GPa, and K~201 GPa. The elastic properties were reduced by approximately 6% in the high TOF regions which would make those specific regions more vulnerable in terms of performance. These values demonstrated the degree of loss that could be expected when comparing the average bulk regions from the SiC samples to those with higher TOF and low material velocity values.

5.4.4. Reflected Signal Amplitude C-Scan Imaging of SA1-SA8

Reflected signal amplitude C-scan imaging was used to evaluate the sintered SiC armor samples by monitoring amplitude changes in the bottom surface reflected signals. The reflected signal amplitude C-scan images for each of the SiC samples are shown in Figures 60 and 61. The average and standard deviation amplitude values are shown in Table XXVIII. It should also be pointed out that unlike in the TOF C-scan images, there were no observable occurrences of noise, at any of the frequencies, so no adjustments had to be made to eliminate data points that were not representative of the samples.

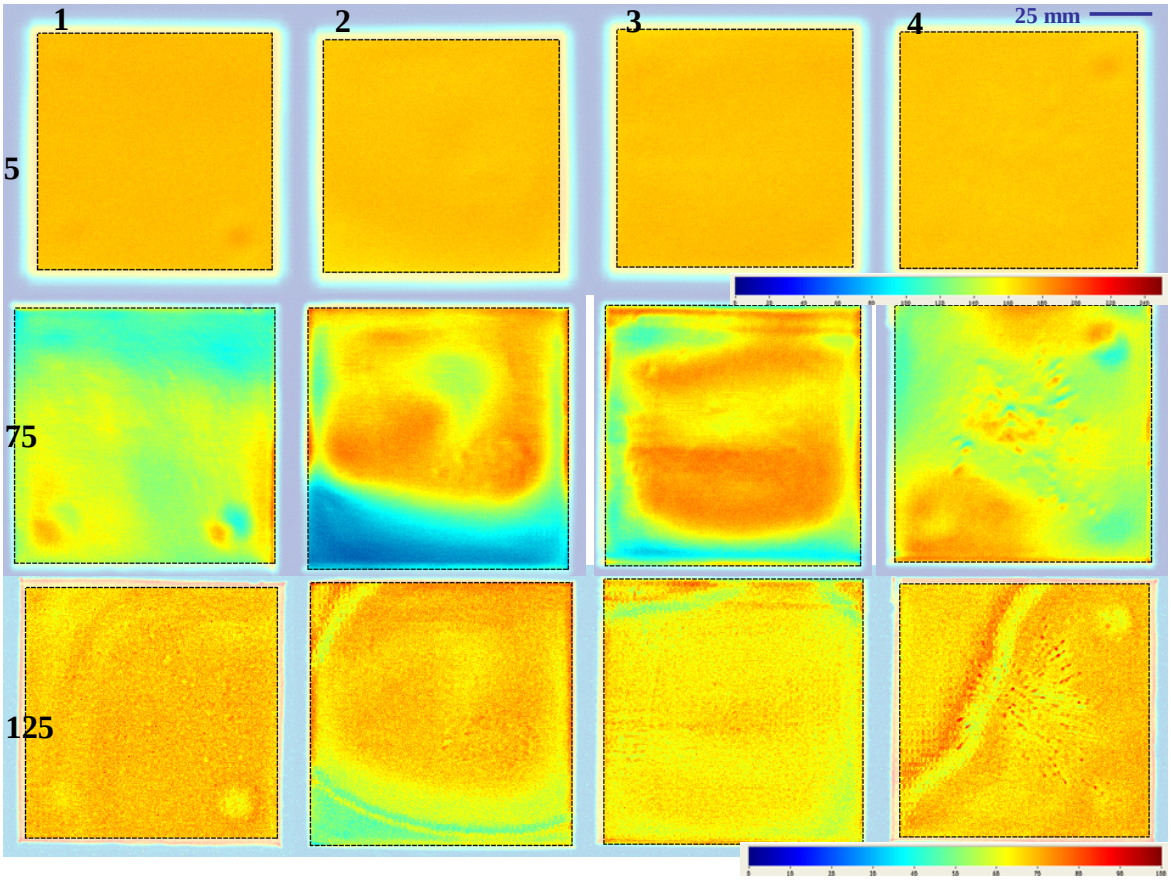

Figure 60. Reflected signal amplitude C-scan images of SA1-SA4 at 5, 75, and 125 MHz.

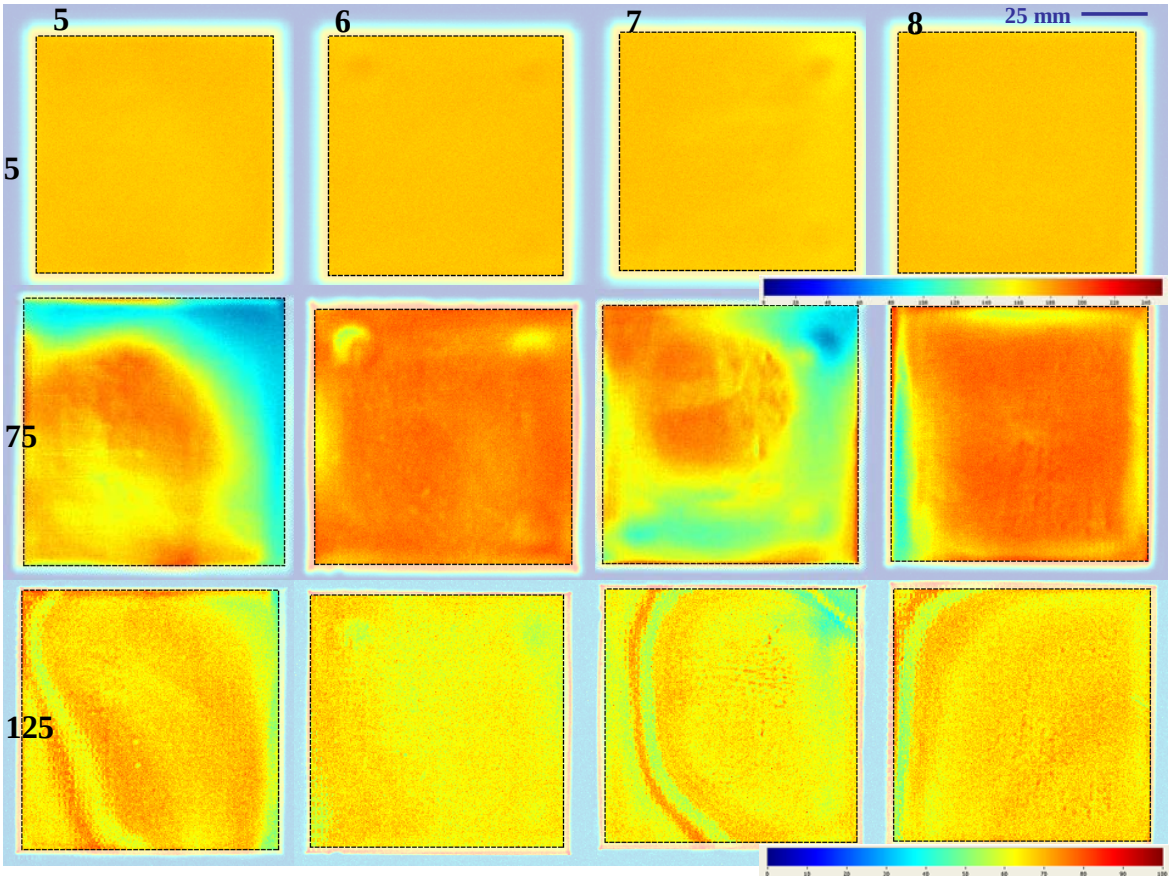

Figure 61. Reflected signal amplitude C-scan images of SA5-SA8 at 5, 75, and 125 MHz.

5MHz

#	Average (mV)	Standard Deviation (mV)
1	186	2.13
2	184	2.88
3	185	2.33
4	183	2.02
5	184	2.17
6	185	1.99
7	182	3.40
8	184	2.07

75MHz

#	Average (mV)	Standard Deviation (mV)
1	138	21.2
2	146	50.1
3	169	30.7
4	155	20.6
5	154	44.1
6	205	9.8
7	161	33.8
8	197	24.3

125MHz

#	Average (mV)	Standard Deviation (mV)
1	73.7	3.73
2	69.3	8.34
3	67.3	4.76
4	72.3	4.95
5	70.5	6.02
6	66.9	4.15
7	65.8	6.19
8	69.9	4.97

Table XXVIII. Average and standard deviation amplitude C-scan image data for samples SA1-SA8 at various frequencies.

At 5 MHz, there was very little variation among the eight samples over the 0-250 mV reflected surface amplitude range. Table XXVIII showed a very similar average range of amplitude values between 182-186 mV, an average difference of only 12 dB among the eight samples. While the TOF C-scan images were very sensitive to thickness differences such as those in SA3 and SA4, which directly affected the image data, the reflected signal amplitude images were not influenced by thickness. Instead, the only changes were due to amplitude or attenuation variations caused by scattering from material inhomogeneities or defects. While the thickness differences from TOF scans sometimes overshadowed other inhomogeneities, this was not a factor for reflected signal amplitude scans. Despite the small degree of variation among the 5 MHz scans, samples SA1, SA4, SA6, and SA7 did show amplitude differences identifying the 5-10 mm circular defects that were also found in the TOF C-scan images.

The 75 MHz reflected signal amplitude C-scan images showed a great deal of variation over the 0-250 mV range. The level of acoustic wave scattering resulting from inhomogeneities in the detectable size range at this frequency was enhanced, leading to detection of large variable regions at 75 MHz. When compared to the TOF C-scan images, the same high TOF regions that were identified in SA2, SA5, and SA7 matched the regions of lowest reflected signal amplitude. However, instead of a “black-and-white” contrast between two distinct regions as observed in the TOF scans, the amplitude scans showed more detailed variations corresponding to minor changes throughout each sample. The circular defects pointed out in other scans were also identified in greater detail. SA1 and SA3 exhibited not only a drop in amplitude where the defects occurred, but a high amplitude region next to each low amplitude region. This may have been due

to handling of the green samples before firing. It is believed that the plates may have been placed or stacked using spacers on or near the corners. If this were the case, more pressure would have been induced on the corners of the samples before firing, creating high density regions of high pressure next to circular low density regions of low pressure where the material was displaced from. In contrast, SA6 and SA7 showed only low amplitude circular regions indicative of bulk defects that may have been caused by a similar phenomenon. In order to put the degree of reflected signal amplitude loss into perspective, the average values of 146 mV for SA2, 154 mV for SA5, and 161 mV for SA7, as shown in Table XXIV, were compared to the regions with the highest degree of loss. The lowest recorded reflected signal amplitude values were 28 mV for SA2, 36 mV for SA5, and 45 mV for SA7, resulting in a drastic reduction in attenuation of 41 dB for each of the three samples with respect to the average. The standard deviation values from Table XXVIII were also highest for SA2 at 50.1 mV, SA5 at 44.1 mV, and SA7 at 33.8 mV with the lowest value at 9.8 mV for SA6. All of these trends were consistent with the TOF data.

In contrast to the 75 MHz results, the 125 MHz reflected signal amplitude images showed pressing patterns, defects, and other material inhomogeneities related to a lower level of wave scattering associated with the higher frequency. These images also showed much greater detail than their TOF counterparts. Pressing patterns were identified in each of the samples except for SA6, which may have been a large part of the reason why it was noted as the most homogeneous sample out of the eight. SA3, SA4, SA5, and SA8 all showed distinct patterns that could not be detected by ultrasound C-scan imaging under any of the other conditions that were tested. The circular defects of lower reflected

signal amplitude were detailed in SA1, SA4, SA6, and SA7. In addition, individual defects that were not detectable at other frequencies were also found. For example, in SA1, circular regions of both lower and higher amplitude as small as 75-125 μm were identified throughout the sample. The regions of higher reflected signal amplitude were most likely representative of high acoustic impedance inclusions as opposed to the lower reflected amplitude regions most likely representative of low acoustic impedance defects and pores. The most interesting defects detected at 125 MHz were in sample SA4, which showed a dispersion of ~100-200 μm high reflected signal amplitude inclusions throughout the center of the sample. These were only resolvable in the 125 MHz reflected signal amplitude C-scan images and to some degree, though not clearly, at 75 MHz. It was believed that these may have been small agglomerates or particulates of a high acoustic impedance material that were introduced to the sample as sintering additives.

5.4.5. Reflected Signal Amplitude Quantitative Analysis of SA1-SA8

A more quantitative evaluation of the reflected signal amplitude data was achieved by plotting amplitude histograms in which the normalized amplitude occurrences were graphed on the y-axis against the normalized amplitude range on the x-axis, as shown in Figures 62, 63, and 64. At 5 MHz, the C-scan images were very similar with little noticeable variability and the normalized amplitude histograms reflected this trend. The histogram curves were very similar for all eight samples, with SA2 and SA7 demonstrating slightly extended tails. Upon observation of the area and FWHM data, SA7 had the highest values of 388 and 3.5, respectively. While this sample stood out as the most different, the other samples demonstrated narrow ranges of 253 to 312 for area

and 2.2 to 2.9 for FWHM. This set of samples exhibited the lowest amount of normalized histogram variability.

At 75 MHz, the normalized amplitude histograms showed the highest degree of variation due to the drastic changes in reflected signal amplitude. Wide distributions and tails of significant area were present for most of the samples, especially SA2, SA3, SA5, and SA7. These histograms were much broader in comparison to SA6, which took up a much smaller region of the graph. Another interesting histogram curve was SA4, which had a significant region of high reflected signal amplitude occurrences on the right side of the curve due to an increased number of high signal amplitude defects through the center of the sample. According to the AUTC data, the highest values were those with large regions of low reflected signal amplitude, with SA7 highest at 3,590, SA5 next at 2,719, and SA2 next at 2,615. SA7 and SA5 also had the highest FWHM values of 38 and 20, respectively. The lowest AUTC value for SA6 was 698 followed by SA8 with 858. These were also the samples with the lowest FWHM values at 6 and 5, respectively. These trends were once again consistent with TOF histogram data trends.

At 125 MHz, the normalized amplitude histograms were not as broad as the ones obtained at 75 MHz. The 125 MHz reflected signal amplitude C-scan images revealed more microstructural inhomogeneities and defect regions than were present in the lower frequency and TOF data. Pressing patterns and 75-125 micron defects provided more detail of minor differences within the same samples and among different samples. One trend that remained consistent was that the three samples with the highest AUTC values were the same, with SA7 at 1,397, SA2 at 1,387, and SA5 at 1,326. SA7 and SA5 also exhibited two of the highest FWHM values at 13 and 10, respectively. The tail area for

SA2 remained distinguishable, but the detection of more specific pressing patterns and defects cut down on large low reflected signal amplitude regions, broadening the overall normalized histograms and reducing the tail regions. Sample SA6, which exhibited the lowest AUTC values at lower frequencies was characterized by reflected signal amplitude differences that were not previously detected. For this reason, sample SA1, which had the least distinguishable pressing pattern next to SA6, had the lowest area of 874 and the lowest FWHM of 8. The consistent trends under all conditions were that SA7, SA2, and SA5 would be red-flagged for their large sample variability and samples SA6 and SA1 showed the smallest degree of variation compared to the rest of the sample set.

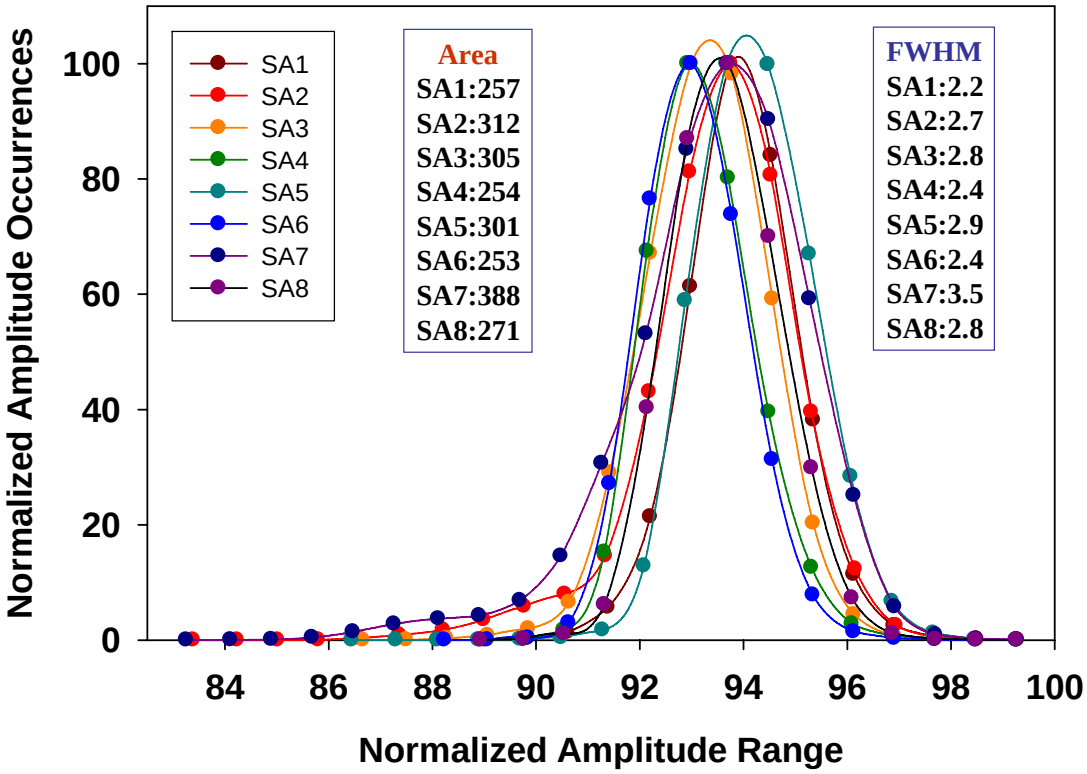

Figure 62. Amplitude histogram curves for SA1-SA8 at 5 MHz.

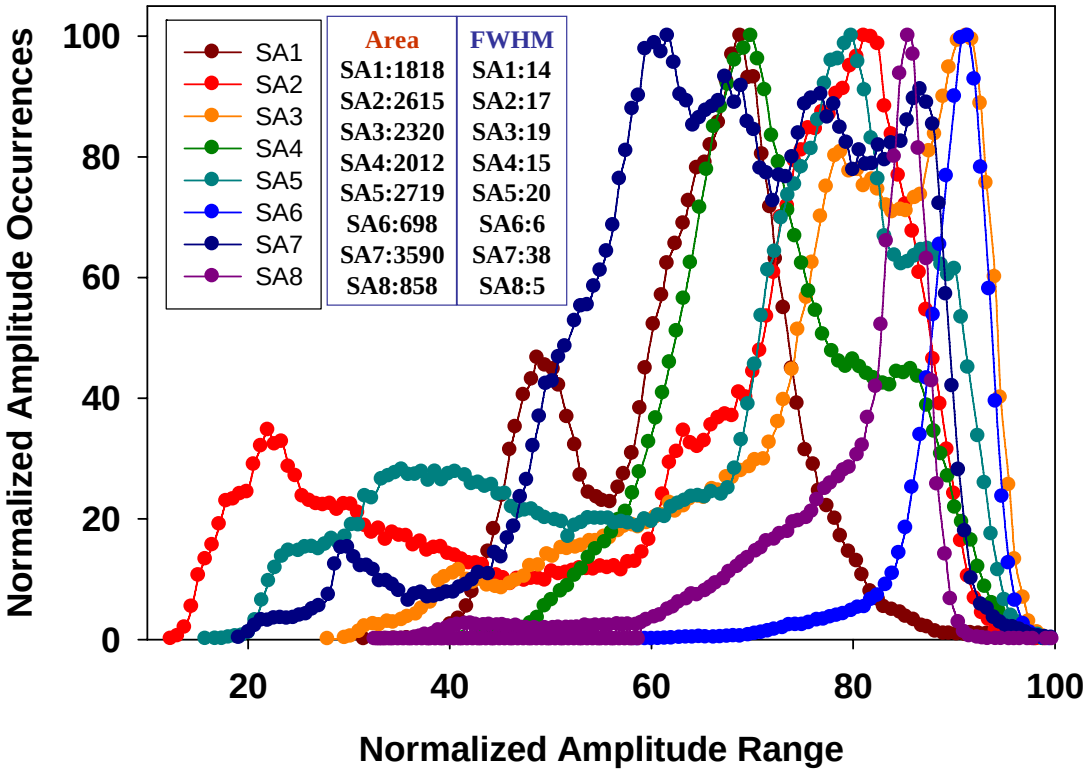

Figure 63. Amplitude histogram curves for SA1-SA8 at 75 MHz.

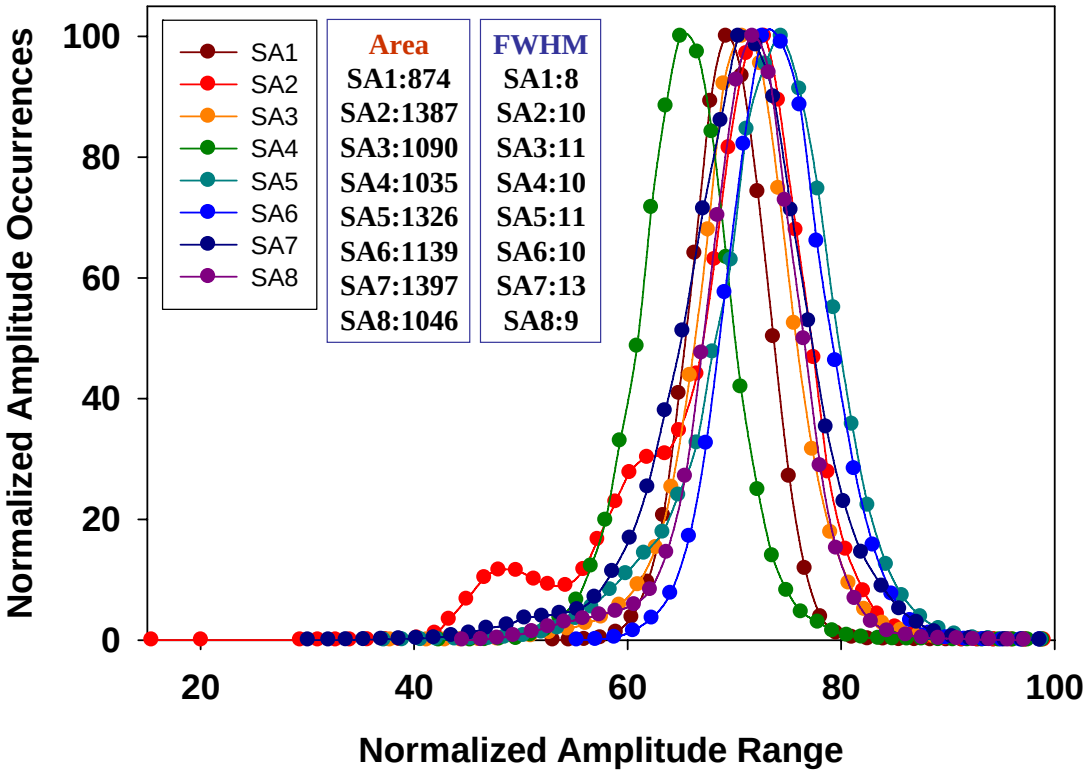

Figure 64. Amplitude histogram curves for SA1-SA8 at 125 MHz.

5.4.6. Schematics of Test Specimens SA1-SA8

The TOF and reflected signal ultrasound C-scan image data were utilized to put together schematics of general regions of interest detected throughout the eight SA SiC samples, as shown in Figures 65-68. The regions of interest were characterized by inhomogeneous TOF or reflected signal amplitude values as compared to the average values for each sample. Approximate areas were traced by overlaying scans of varying frequency (5, 75, 125 MHz) and type (TOF, amplitude) and outlining the regional patterns. The resulting areas were labeled accordingly. For example, a feature labeled AMP75 would identify a feature detected from a 75 MHz reflected signal amplitude scan while a feature labeled TOF125 would identify a feature detected by a 125 MHz TOF scan. The regions were separated in terms of degree of difference from the sample average, with red representing the largest change in TOF or amplitude, blue representing a subtle but definitive change in TOF or amplitude, and green representing an intermediate change in TOF or amplitude falling somewhere between the two. The features were categorized into six different types including (a) general regions of low amplitude (b) general regions of high TOF (c) large circle defects near the corners of several samples (d) pressing patterns due to subtle pressure gradients (detected only at highest frequency) (e) general regions containing large amounts of distinct inclusions and (f) isolated individual defects. Some regions were scan-specific, such as the pressing patterns and small isolated individual inclusions which were only detected by 125 MHz reflected signal amplitude scans. Many of the representative regions overlapped since the features were consistent among different scans, with amplitude features generally wider due to larger edge effects and features detected at higher frequencies more narrow and

detailed. For example, there were several cases in which a 75 MHz amplitude feature resembled a large general area of change whereas the same feature at 125 MHz resembled a narrower pattern over a more definitive area.

The schematics were evaluated sample by sample. Sample SA1 showed upper regions of low reflected signal amplitude as well as circle defects toward the bottom corners. Sample SA2 showed the largest and most inhomogeneous high TOF/low amplitude region at the bottom of the sample, as characterized by the red region. The amplitude region at 75 MHz encompassed the entire area while the TOF region at 75 MHz was not as wide. The 125 MHz amplitude scan showed more detailed pressing patterns within the area as opposed to the large definitive areas shown at 75 MHz. There were also various low amplitude regions with slight differences from the rest of the samples. Sample SA3 showed low amplitude pressing patterns near the perimeter of the sample. Sample SA4 was characterized by a distinct pressing pattern in addition to a unique region containing various inclusions in the center of the sample. A circle defect was also evident in the top right corner. Sample SA5 showed another significantly inhomogeneous high TOF region in the top corner as well as pressing patterns in the bottom left corner and isolated and circle defects in defined regions. Sample SA6 showed several low amplitude sections and a distinct isolated inclusion. Sample SA7 was the third sample to demonstrate an extreme high TOF region in the top right corner, which was surrounded by low amplitude and inclusion areas. Intermediate pressing patterns and low amplitude regions were also present on the left and bottom. Sample SA8 exhibited pressing patterns and low amplitude regions in addition to several sporadic inclusion areas. To summarize, the most inhomogeneous regions were in samples SA2,

SA5, and SA7, while large circle defects were present in SA1, SA4, and SA5, distinct pressing patterns existed in samples SA3, SA4, SA5, SA7, and SA8, and concentrated inclusion areas were evident in SA4, SA7, and SA8. The primary reason for preparing the images in this way was to provide a general idea of which regions, according to ultrasound testing, showed potential differences in properties and to examine the estimated degree of difference between features.

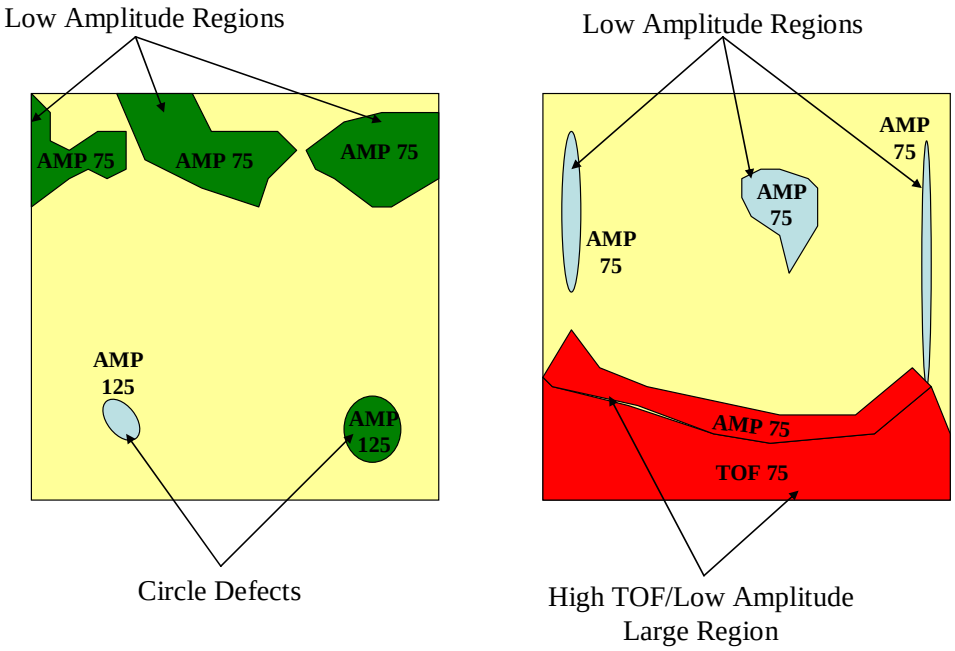

Figure 65. Schematic representations of samples SA1 and SA2.

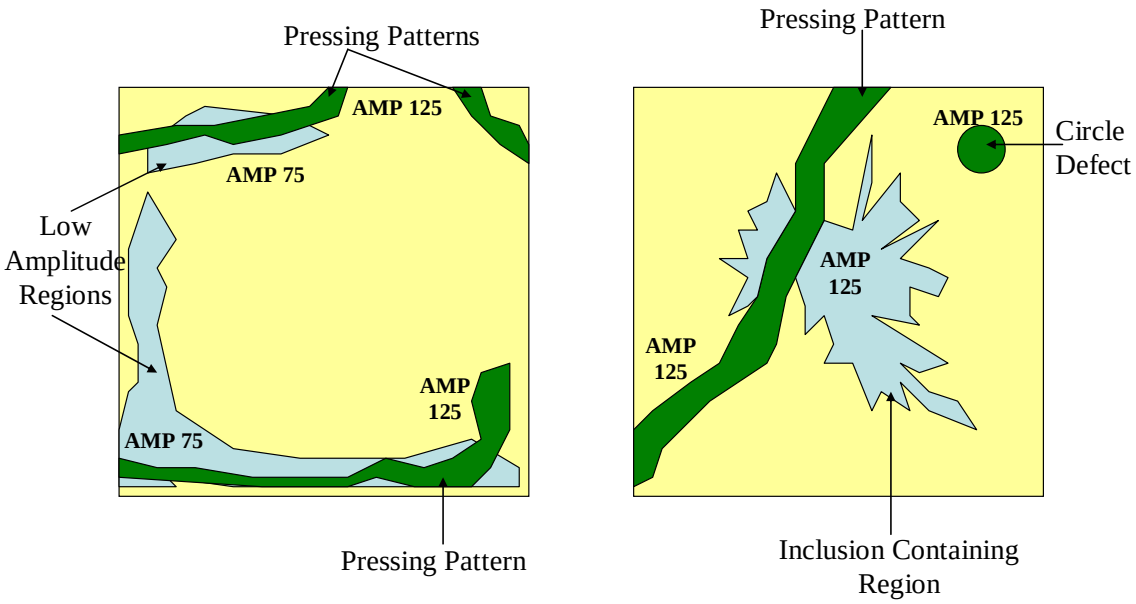

Figure 66. Schematic representations of samples SA3 and SA4.

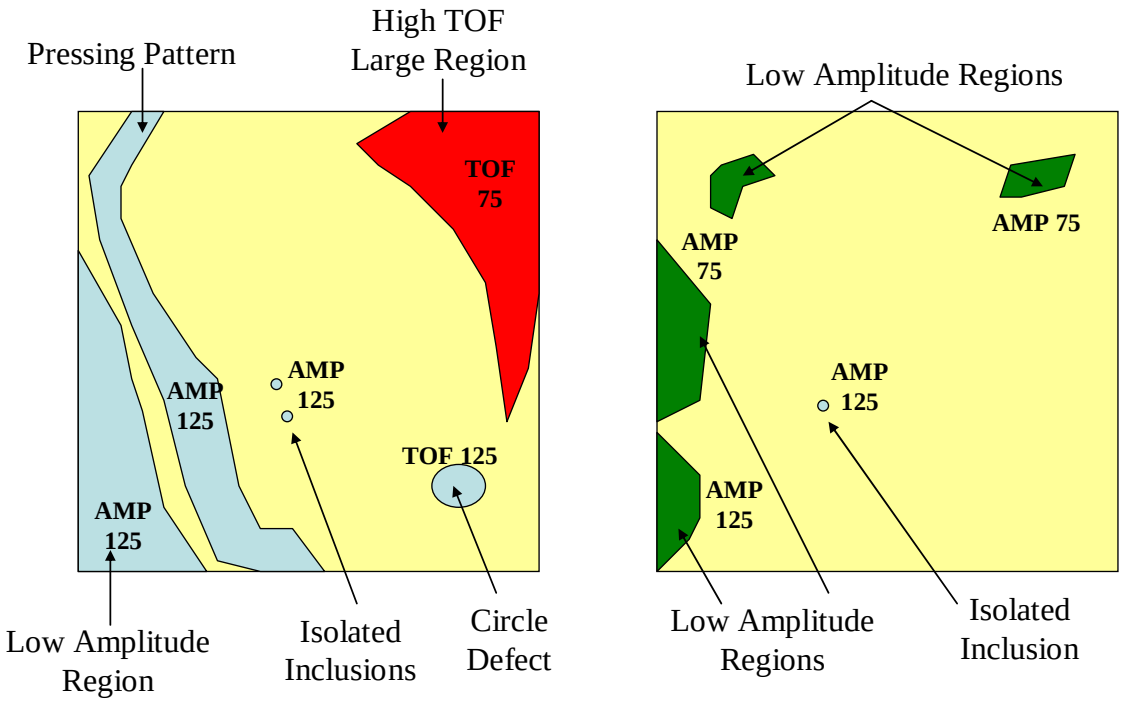

Figure 67. Schematic representations of samples SA5 and SA6.

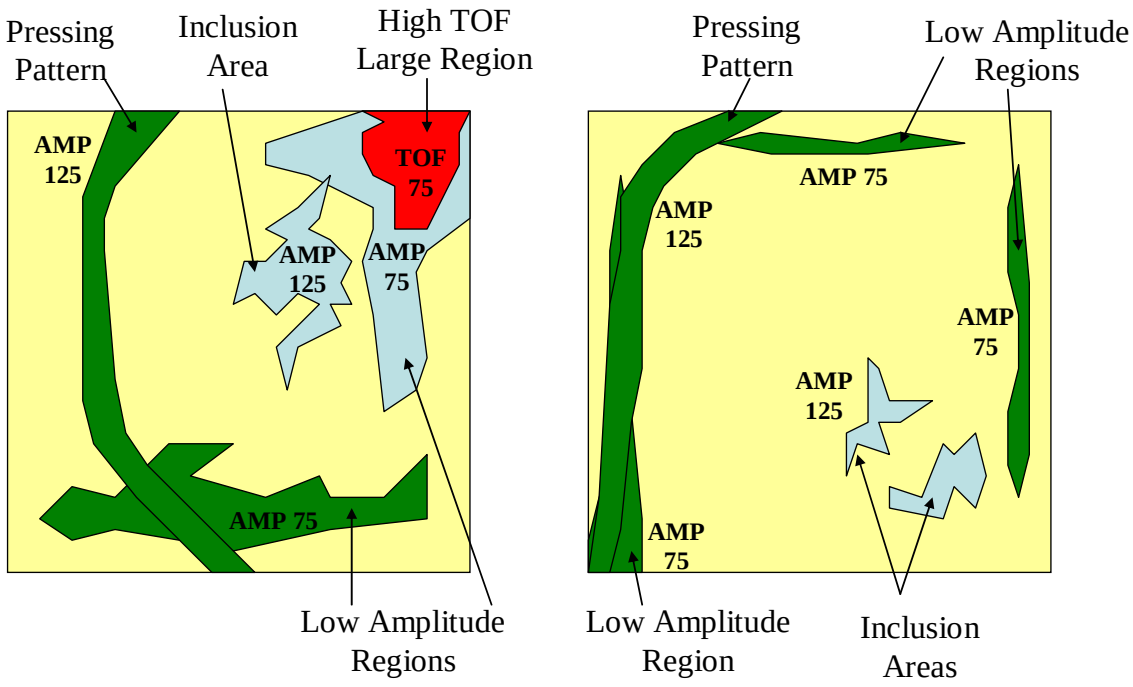

Figure 68. Schematic representations of samples SA7 and SA8.

5.4.7. Further Observations of Test Specimens SA1-SA8

It is important to note that this set of sintered SiC armor samples was manufactured under the same conditions with the expectation that they would come out the same in every case. While some of the differences seemed quantitatively large among the samples, they were still relatively small compared to samples fabricated under different conditions. The point analysis data were very similar among the samples, with elastic property values that showed little variation. This sample set was more of a challenge to find differences among samples, since every sample was considered to be very similar. In previous studies on hot pressed samples D and E, the variability was large for samples of different thickness. This study demonstrated the ability of nondestructive ultrasound characterization to find significant differences and trends among samples that were considered to be relatively the same.

It is also important to note that the TOF and amplitude C-scans were both useful for demonstrating the trends among the eight sintered SiC samples. Each individual technique was successful in identifying specific features that the other could not. The TOF data showed thickness differences as a result of uneven polishing that were not a factor in the amplitude data. The TOF data were also useful for calculating elastic property values that the reflected signal amplitude data could not provide directly. On the other hand, the reflected signal amplitude C-scan images showed more frequent occurrences of isolated defects and microstructural inhomogeneities due to scattering, especially at high frequencies, many of which could not be detected using TOF C-scan imaging. The major defects, regional differences, and quantitative trends were consistent for both the TOF and reflected signal amplitude images and quantitative data. This

emphasized the importance of utilizing both amplitude and TOF C-scan imaging for obtaining a full range of ultrasound data for sample comparison.

5.5. Sintered SiC Test Specimens ST1-ST8

A set of eight sintered SiC armor plates with density values reported by the manufacturer between 3.210 and 3.270 g/cm^3 was obtained for ultrasound evaluation. The manufactured plates had been cut to the same dimensions, with an average length and width of 101.6 mm and an average thickness of 7.65 mm. The Archimedes method was used to obtain more precise density values for each sample. As opposed to previously evaluated sintered SiC samples from the same manufacturer (SA), these samples (ST) contained additional processing additives. These TiB_2 additives, which had higher densities of 4.50 g/cm^3 (as compared to ~3.160 g/cm^3 for sintered SiC), lower material velocities of 11,400 m/s (as compared to ~11,820 m/s for sintered SiC), and higher acoustic impedance values of 51.3x10^5 g/cm^{2}s (as compared to 37.4^{x}10^5 g/cm^{2}s) than the SiC bulk, as reported in the literature, influenced the properties and ultrasound characteristics of the armor plates [118].

Again, point analysis was conducted using the longitudinal contact very short pulse 50 MHz transducer (VSP-50) which was placed at nine locations over each sample, as shown in Figure 31. Figure 69 shows the A-scans for all three samples, which were recorded from the center of each sample at position five. Ultrasound C-scan imaging was conducted using longitudinal immersion 5 MHz (MDS-5), 75 MHz (MDS-75), and 125 MHz (MDS-125) transducers. Occasional noise signals present in the 125 MHz C-scan image results were identified and removed from quantitative analysis data.

5.5.1. Point Analysis of ST1-ST8

The SiC samples were tested using the longitudinal 50 MHz contact transducer to conduct point analysis at the nine locations. The data for all eight samples at each of the nine measured points can be found in Tables XXIX-XXXVI, along with the average values calculated for each property. An overview of average sample values is presented in Table XXXVII, including a comparison to reported National Institute of Standards and Technology [23] values for sintered SiC and a comparison to previously measured values for high density hot-pressed SiC samples. Table XXXVII shows a comparison of the average values among each of the eight ST samples, starting with the density, which was reported by the manufacturer. The range of densities went from 3.195 g/cm^3 to 3.259 g/cm^3, with an average density among the samples of 3.231 g/cm^3. The density values of the ST samples were much higher than the previously evaluated SA samples, in which the average density value was 3.163 g/cm^3. This was due to the higher density of the additives in the ST samples. However, the average density value for the ST samples was lower than the reported value in the literature of a similar sintered SiC material containing 15% TiB_2 additive which had a density of 3.36 g/cm^3 [117,119]. The average thickness (t) of the ST samples ranged between 7.54 mm and 7.71 mm, with an overall average of 7.65 mm, compared to an average thickness of 7.82 mm for the SA samples. A-scan readings such as the ones shown in Figure 31, in which the center position five was analyzed to identify top and bottom surface reflected signals, were used to measure longitudinal and shear TOF values. The averages of all the samples were 1.341 μs for longitudinal TOF_l and 2.105 μs for shear TOF_s. Longitudinal and shear velocity values were calculated as c_l = 11,410 m/s and c_s = 7,260 m/s, which were lower than the NIST

reported values of c_l = 11,820 m/s and c_s = 7,520 m/s [23] for sintered SiC with a density of 3.16 g/cc. These values were also lower than SA measured values of c_l = 11,950 m/s and c_s = 7,610 m/s. The reason for this was believed to be the TiB_2 additives contained in the eight ST samples which increased the densities but lowered the material velocities as compared to sintered SiC samples without the addition of such additives. The average acoustic impedance (Z) value of 36.9 x 10^5 g/cm^{2}s was also lower than NIST reported value of 37.4 x 10^5 g/cm^{2}s [23] and the SA sample value of 37.8 x 10^5 g/cm^{2}s due to the lower material velocity values for the eight samples. The average calculated values for the eight ST samples were ν = 0.16, E = 390 GPa, G = 170 GPa, and K = 200 GPa, compared to NIST reported values of 420 GPa, 180 GPa, and 200 GPa [23], and the SA measured values of 430 GPa, 180 GPa, and 210 GPa, respectively. The ST elastic properties were compared to reported elastic properties from a similar sintered SiC material with 15% TiB_2 additive. For this material which had a higher density of 3.36 g/cm^3, values of E = 402 GPa and G = 181 GPa were reported [117]. The measured values of the sintered ST samples were also compared to higher density hot pressed SiC values from previous studies and literature reported values [23] as shown in Table XXXVII. The hot pressed samples showed higher values for c_l at 12,270 m/s, c_s at 7,760 m/s, Z at 39.5 x 10^5 g/cm^{2}s, and ν = 0.17, as expected due to the higher sound velocity through the samples.

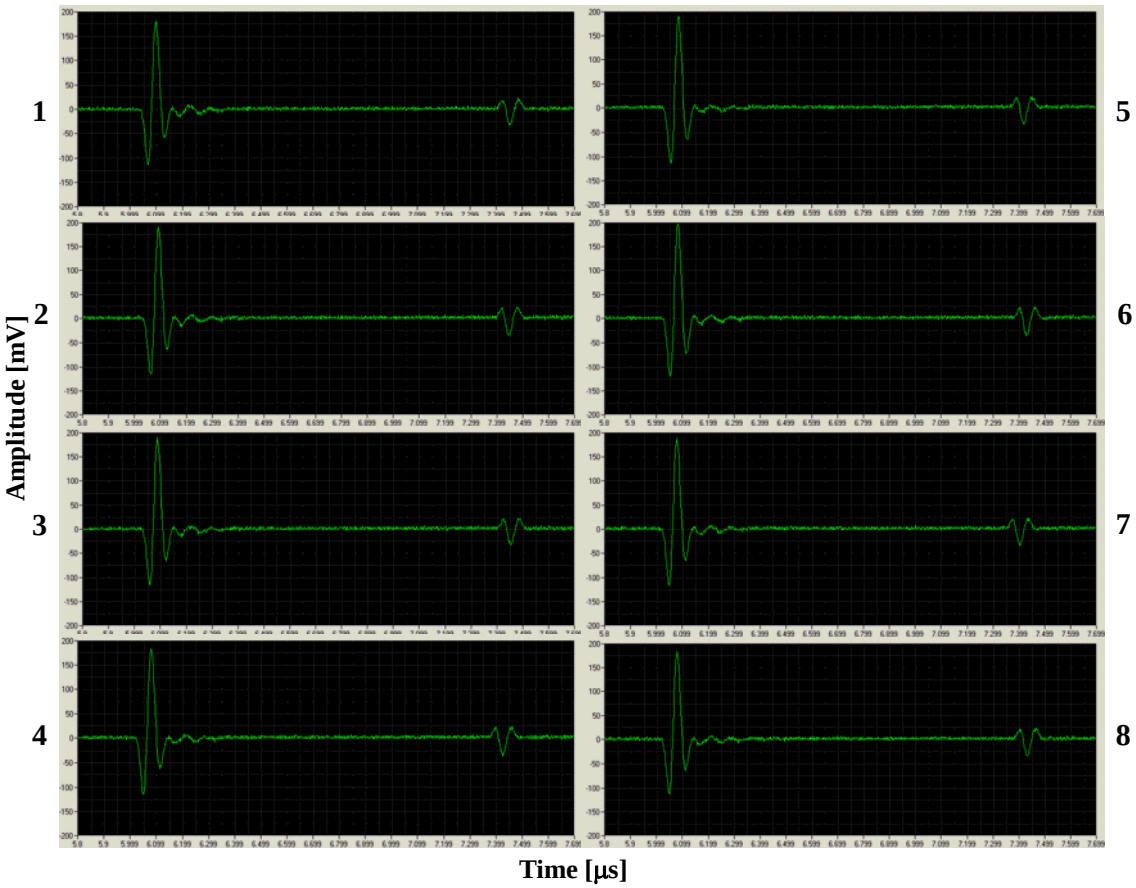

Figure 69. Position 5 top and bottom reflected signals for samples ST1-ST8.

#	ρ (g/cc)	t (mm)	TOF_l (μs)	TOF_s (μs)	c_l (m/s)	c_s (m/s)	Z (*10^5 g/cm^{2}s)	ν	E (GPa)	G (GPa)	K (GPa)
1	3.219	7.69	1.328	2.085	11,580	7,380	37.3	0.16	410	180	200
2	3.219	7.70	1.355	2.127	11,370	7,240	36.6	0.16	390	170	190
3	3.219	7.72	1.367	2.146	11,290	7,190	36.4	0.16	390	170	190
4	3.219	7.63	1.326	2.082	11,510	7,330	37.0	0.16	400	170	200
5	3.219	7.70	1.357	2.130	11,350	7,230	36.5	0.16	390	170	190
6	3.219	7.68	1.362	2.138	11,280	7,180	36.3	0.16	390	170	190
7	3.219	7.68	1.326	2.082	11,580	7,040	37.3	0.16	390	160	220
8	3.219	7.67	1.357	2.130	11,300	7,200	36.4	0.16	390	170	190
9	3.219	7.69	1.358	2.132	11,330	7,210	36.5	0.16	390	170	190
Avg	**3.219**	**7.68**	**1.348**	**2.117**	**11,400**	**7,220**	**36.7**	**0.16**	**390**	**170**	**200**

Table XXIX. Point analysis data for sample ST1.

#	ρ (g/cc)	t (mm)	TOF_l (μs)	TOF_s (μs)	c_l (m/s)	c_s (m/s)	Z ($*10^5$ g/cm^{2}s)	ν	E (GPa)	G (GPa)	K (GPa)
1	3.195	7.66	1.355	2.127	11,310	7,200	36.1	0.16	380	170	190
2	3.195	7.64	1.362	2.138	11,220	7,150	35.8	0.16	380	160	180
3	3.195	7.61	1.352	2.123	11,260	7,170	36.0	0.16	380	160	190
4	3.195	7.68	1.350	2.120	11,380	7,250	36.4	0.16	390	170	190
5	3.195	7.70	1.358	2.132	11,340	6,640	36.2	0.16	390	170	190
6	3.195	7.62	1.360	2.135	11,210	7,140	35.8	0.16	380	160	180
7	3.195	7.69	1.363	2.140	11,280	7,190	36.1	0.16	380	170	190
8	3.195	7.66	1.352	2.123	11,330	7,220	36.2	0.16	390	170	190
9	3.195	7.64	1.357	2.130	11,260	7,170	36.0	0.16	380	160	190
Avg	**3.195**	**7.66**	**1.357**	**2.130**	**11,290**	**7,130**	**36.1**	**0.16**	**380**	**170**	**190**

Table XXX. Point analysis data for sample ST2.

#	ρ (g/cc)	t (mm)	TOF_l (μs)	TOF_s (μs)	c_l (m/s)	c_s (m/s)	Z ($*10^5$ g/cm^{2}s)	ν	E (GPa)	G (GPa)	K (GPa)
1	3.221	7.70	1.380	2.167	11,160	7,110	35.9	0.16	380	160	180
2	3.221	7.76	1.373	2.156	11,300	7,200	36.4	0.16	390	170	190
3	3.221	7.77	1.372	2.154	11,330	7,210	36.5	0.16	390	170	190
4	3.221	7.67	1.368	2.148	11,210	7,140	36.1	0.16	380	160	190
5	3.221	7.76	1.365	2.143	11,370	7,240	36.6	0.16	390	170	190
6	3.221	7.70	1.355	2.127	11,370	7,240	36.6	0.16	390	170	390
7	3.221	7.69	1.338	2.101	11,490	7,320	37.0	0.16	400	170	200
8	3.221	7.67	1.330	2.088	11,530	7,350	37.2	0.16	400	170	200
9	3.221	7.66	1.326	2.081	11,550	7,360	37.2	0.16	400	170	200
Avg	**3.221**	**7.71**	**1.356**	**2.129**	**11,370**	**7,240**	**36.6**	**0.16**	**390**	**170**	**210**

Table XXXI. Point analysis data for sample ST3.

#	ρ (g/cc)	t (mm)	TOF_l (μs)	TOF_s (μs)	c_l (m/s)	c_s (m/s)	Z (*10^5 g/cm^2s)	ν	E (GPa)	G (GPa)	K (GPa)
1	3.230	7.69	1.333	2.093	11,540	7,350	37.3	0.16	400	170	200
2	3.230	7.65	1.326	2.082	11,540	7,350	37.3	0.16	400	170	200
3	3.230	7.61	1.331	2.090	11,440	7,280	36.9	0.16	400	170	190
4	3.230	7.72	1.341	2.105	11,510	7,330	37.2	0.16	400	170	200
5	3.230	7.68	1.345	2.112	11,420	7,270	36.9	0.16	400	170	190
6	3.230	7.62	1.340	2.104	11,370	7,240	36.7	0.16	390	170	190
7	3.230	7.66	1.360	2.135	11,260	7,180	36.7	0.16	380	170	190
8	3.230	7.68	1.355	2.127	11,340	7,220	36.6	0.16	390	170	190
9	3.230	7.63	1.353	2.124	11,280	7,180	36.4	0.16	390	170	190
Avg	**3.230**	**7.66**	**1.343**	**2.108**	**11,410**	**7,270**	**36.9**	**0.16**	**390**	**170**	**190**

Table XXXII. Point analysis data for sample ST4.

#	ρ (g/cc)	t (mm)	TOF_l (μs)	TOF_s (μs)	c_l (m/s)	c_s (m/s)	Z (*10^5 g/cm^2s)	ν	E (GPa)	G (GPa)	K (GPa)
1	3.257	7.63	1.328	2.085	11,490	7,320	37.4	0.16	400	170	200
2	3.257	7.59	1.316	2.066	11,530	7,350	37.6	0.16	410	180	200
3	3.257	7.57	1.301	2.043	11,640	7,410	38.0	0.16	410	180	200
4	3.257	7.72	1.350	2.120	11,440	7,280	37.3	0.16	400	170	200
5	3.257	7.67	1.324	2.079	11,590	7,380	37.7	0.16	410	180	200
6	3.257	7.61	1.312	2.060	11,600	7,390	37.8	0.16	410	180	200
7	3.257	7.74	1.355	2.127	11,420	7,280	37.2	0.16	400	170	200
8	3.257	7.72	1.346	2.135	11,470	7,230	37.4	0.16	400	170	200
9	3.257	7.61	1.314	2.063	11,580	7,380	37.7	0.16	410	180	200
Avg	**3.257**	**7.65**	**1.327**	**2.086**	**11,530**	**7,340**	**37.6**	**0.16**	**410**	**180**	**200**

Table XXXIII. Point analysis data for sample ST5.

#	ρ (g/cc)	t (mm)	TOF_l (μs)	TOF_s (μs)	c_l (m/s)	c_s (m/s)	Z (*10^5 g/cm^{2}s)	ν	E (GPa)	G (GPa)	K (GPa)
1	3.249	7.68	1.348	2.116	11,390	7,260	37.0	0.16	400	170	190
2	3.249	7.69	1.335	2.096	11,520	7,340	37.4	0.16	410	180	200
3	3.249	7.62	1.321	2.074	11,540	7,350	37.5	0.16	410	180	200
4	3.249	7.66	1.352	2.123	11,330	7,220	36.8	0.16	390	170	190
5	3.249	7.70	1.348	2.116	11,420	7,280	37.1	0.16	400	170	190
6	3.249	7.62	1.318	2.069	11,560	7,370	37.6	0.16	410	180	200
7	3.249	7.65	1.353	2.124	11,310	7,200	36.7	0.16	390	170	190
8	3.249	7.66	1.345	2.112	11,390	7,250	37.0	0.16	400	170	190
9	3.249	7.61	1.321	2.074	11,520	7,340	37.4	0.16	410	180	200
Avg	**3.249**	**7.65**	**1.338**	**2.100**	**11,440**	**7,290**	**37.2**	**0.16**	**400**	**170**	**190**

Table XXXIV. Point analysis data for sample ST6.

#	ρ (g/cc)	t (mm)	TOF_l (μs)	TOF_s (μs)	c_l (m/s)	c_s (m/s)	Z (*10^5 g/cm^{2}s)	ν	E (GPa)	G (GPa)	K (GPa)
1	3.259	7.50	1.331	2.090	11,270	7,180	36.7	0.16	390	170	190
2	3.259	7.56	1.326	2.082	11,400	7,260	37.2	0.16	400	170	190
3	3.259	7.52	1.311	2.058	11,470	7,310	37.4	0.16	400	170	200
4	3.259	7.53	1.328	2.085	11,340	7,220	37.0	0.16	390	170	190
5	3.259	7.60	1.324	2.079	11,480	7,310	37.4	0.16	400	170	200
6	3.259	7.55	1.311	2.058	11,520	7,340	37.5	0.16	410	180	200
7	3.259	7.50	1.306	2.050	11,490	7,320	37.4	0.16	400	170	200
8	3.259	7.54	1.307	2.052	11,540	7,350	37.6	0.16	410	180	200
9	3.259	7.57	1.301	2.043	11,640	7,410	38.0	0.16	420	180	200
Avg	**3.259**	**7.54**	**1.316**	**2.066**	**11,460**	**7,300**	**37.4**	**0.16**	**400**	**170**	**200**

Table XXXV. Point analysis data for sample ST7.

#	ρ (g/cc)	t (mm)	TOF_l (μs)	TOF_s (μs)	c_l (m/s)	c_s (m/s)	Z (*10^5 g/cm^2s)	ν	E (GPa)	G (GPa)	K (GPa)
1	3.220	7.60	1.357	2.130	11,200	7,140	36.1	0.16	380	160	190
2	3.220	7.63	1.352	2.123	11,290	7,190	36.3	0.16	390	170	190
3	3.220	7.62	1.350	2.120	11,290	7,190	36.4	0.16	390	170	190
4	3.220	7.66	1.350	2.120	11,350	7,230	36.5	0.16	390	170	190
5	3.220	7.68	1.357	2.130	11,320	7,210	36.4	0.16	390	170	190
6	3.220	7.62	1.350	2.120	11,290	7,190	36.4	0.16	390	170	190
7	3.220	7.63	1.324	2.079	11,530	7,340	37.1	0.16	400	170	200
8	3.220	7.63	1.323	2.077	11,530	7,350	37.1	0.16	400	170	200
9	3.220	7.60	1.314	2.063	11,570	7,370	37.2	0.16	410	170	200
Avg	**3.220**	**7.63**	**1.342**	**2.107**	**11,370**	**7,250**	**36.6**	**0.16**	**390**	**170**	**190**

Table XXXVI. Point analysis data for sample ST8.

#	ρ (g/cc)	t (mm)	TOF_l (μs)	TOF_s (μs)	c_l (m/s)	c_s (m/s)	Z (*10^5 g/cm^2s)	ν	E (GPa)	G (GPa)	K (GPa)
1	3.219	7.68	1.348	2.117	11,400	7,220	36.7	0.16	390	170	200
2	3.195	7.66	1.357	2.130	11,290	7,130	36.1	0.16	380	170	190
3	3.221	7.71	1.356	2.129	11,370	7,240	36.6	0.16	390	170	210
4	3.230	7.66	1.343	2.108	11,410	7,270	36.9	0.16	390	170	190
5	3.257	7.65	1.327	2.086	11,530	7,340	37.6	0.16	410	180	200
6	3.249	7.65	1.338	2.100	11,440	7,290	37.2	0.16	400	170	190
7	3.259	7.54	1.316	2.066	11,460	7,300	37.4	0.16	400	170	200
8	3.220	7.63	1.342	2.107	11,370	7,250	36.6	0.16	390	170	190
Avg	**3.231**	**7.65**	**1.341**	**2.105**	**11,410**	**7,260**	**36.9**	**0.16**	**390**	**170**	**200**
Rep	**3.16**	-	-	-	**11,820**	**7,520**	**37.4**	**0.16**	**420**	**180**	**200**
HP	**3.22**	-	-	-	**12,270**	**7,760**	**39.5**	**0.17**	**430**	**180**	**220**

Table XXXVII. Average point analysis data for samples ST1-ST8 and comparison to reported sintered and hot pressed SiC.

While these trends were apparent for the average values of the eight ST samples, Tables XXIX-XXXVI showed regional differences in thickness, TOF, velocity, and elastic properties for each individual sample. Most of these values were very consistent over each sintered SiC sample. The only noticeable differences came from slight thickness variations. Sample ST5, for example, had a slightly thinner region on the right side, which exhibited an average thickness of 7.60 mm as opposed to the rest of the sample, which had an average thickness of 7.70 mm, as shown in Table XXXIII. Points three, six, and nine all had lower TOF values as a result, since the time for the acoustic wave to travel through this region was less than for the rest of the sample. However, the effect on the elastic property values was less significant, as the values were quite consistent throughout the sample. Even the largest degree of difference between samples, as exemplified in this case, did not significantly change the elastic properties, so the SiC plates were considered to be consistent both individually and as compared to the rest of the samples.

5.5.2. TOF C-scan Imaging of ST1-ST8

C-scan imaging was performed using the 5, 75, and 125 MHz longitudinal immersion transducers to collect TOF data over the area of each ST sample. The TOF C-scan images for each of the SiC samples are shown in Figure 70 for samples 1-4 and Figure 71 for samples 5-8. The average and standard deviation TOF values for each sample are shown in Table XXXVIII. A number of data points scattered throughout the 125 MHz scans displayed individual TOF points close to zero, in most cases due to electrical interference during C-scan imaging. These data points were readily apparent in the 125 MHz scans because the thresholds of the gates were lowered to pick up the lower

intensity bottom surface signal reflection, thus allowing more noise peaks into the scanned data. While some noise peaks were still present, the resulting individual interference data points were not factored in to the average, standard deviation, or quantitative analysis data because they were not representative of the samples.

The TOF C-scan images in Figures 70 and 71 show a visual depiction of the differences between the samples at all three frequencies. At 5 MHz, there were only minor TOF differences across each sample. Since the planar low frequency transducer could not resolve defects smaller than millimeter-range according to the theoretical detection limits in Table IV, in this case 1.2 mm at 5 MHz, isolated defects were not detected. At 75 MHz, in which the theoretical detection limit for a planar transducer was approximately 80 μm according to Table IV, the regional TOF differences were readily apparent. As mentioned previously, despite the increased attenuation for this higher frequency transducer, the bottom surface reflected signal was still very strong, as the 30 dB receiver attenuation was sufficient for resolving the signal while drastically reducing the noise level. Samples ST2, ST4, ST7, and ST8 stood out, as they each showed isolated higher TOF regions that were not detected at 5 MHz. These regions were not caused by higher sample thickness, which would have been observed at 5 MHz, but by bulk changes only detectable at higher frequencies. These large regions were believed to be caused by process-related factors such as highly concentrated, inhomogeneous distributions of TiB_2 additives or low density regions from inhomogeneous dry pressing. Sample ST8 showed a significant loss of signal in the top left corner in which the intensity was reduced to the noise level. This region was red-flagged as a problem area for further evaluation. In addition to these regions, ST3 and ST5 demonstrated more

gradual changes in TOF over larger sample regions which were believed to reflect more of a change in thickness over the samples since they expanded over such wide areas. At 125 MHz, the increased attenuation played a role, since the receiver attenuation had to be reduced to 5 dB to resolve the bottom surface reflected signal, as mentioned earlier. However, the specific TOF differences could still be recognized visually despite the interference points and bands, which were scattered throughout each C-scan. As opposed to the large regions of higher TOF found in the 75 MHz scans, the 125 MHz transducer showed specific bands within those regions that were characteristic of process-related pressing patterns. These pressing patterns were especially evident in all of the samples except for ST3, ST7, and ST8 in which lower TOF values were identified in specific patterns. In addition, sample ST3 also showed a high loss region in the top left corner. For ST7, which showed a high TOF region at 75 MHz, specific pressing patterns were evident within the same region at 125 MHz. The greatest TOF differences in the patterns were shown in ST3, ST7, and ST8, two of the three samples with high TOF regions from the 75 MHz scans. The C-scan images appeared to show consistent visual trends at all frequencies, with more specific defect patterns becoming evident at higher frequencies.

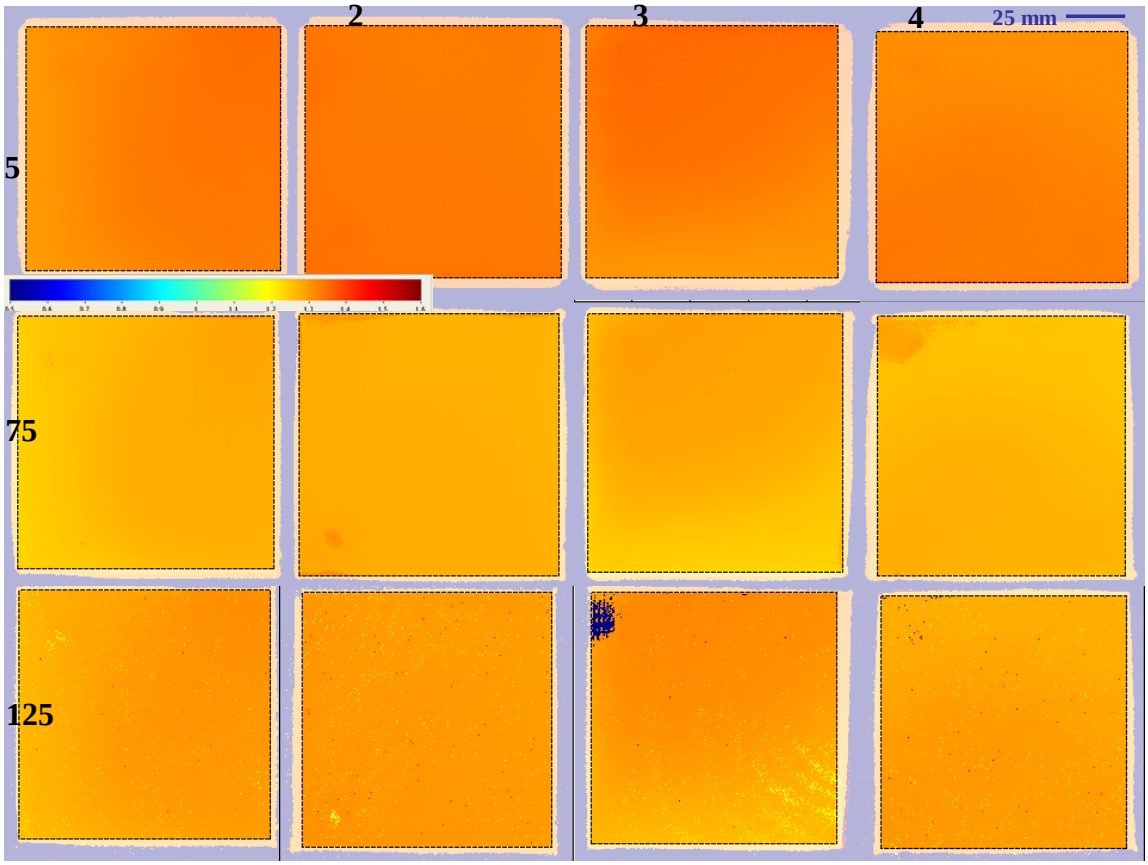

Figure 70. TOF C-scan image maps of ST1-ST4 at 5, 75, and 125 MHz.

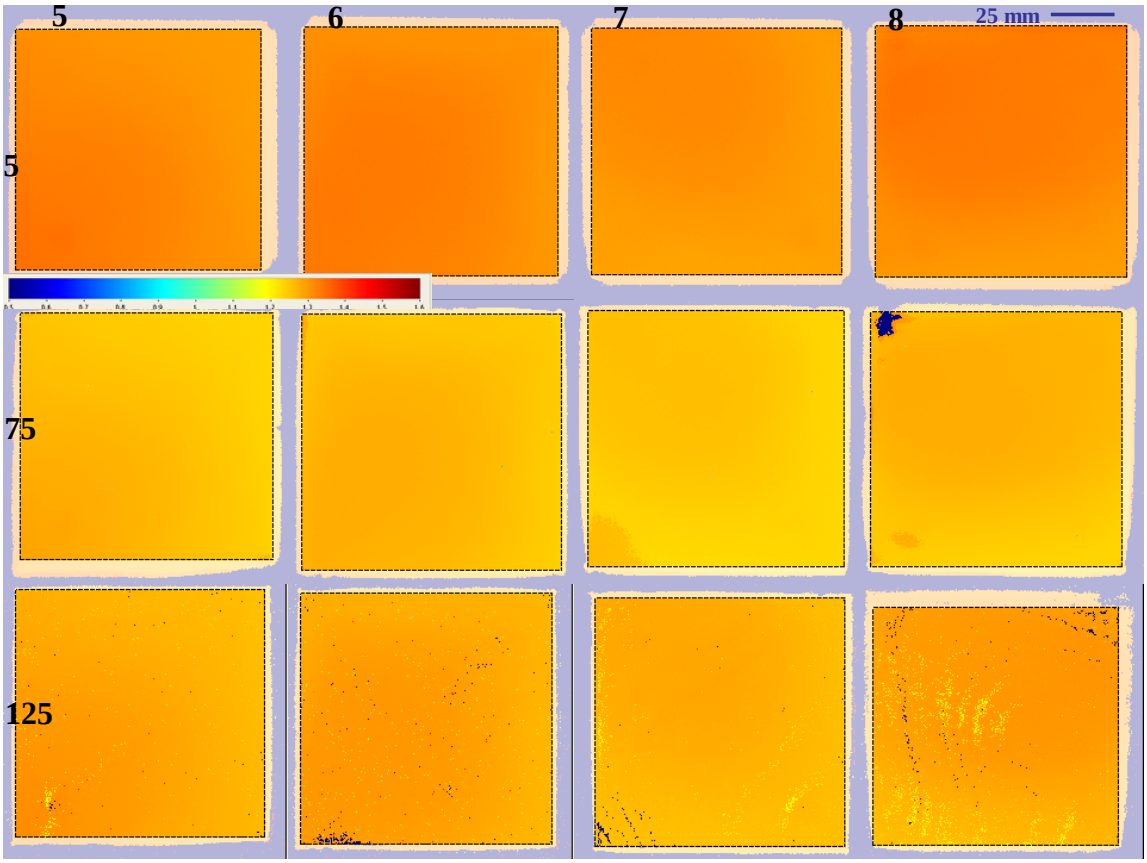

Figure 71. TOF C-scan image maps of ST5-ST8 at 5, 75, and 125 MHz.

5MHz

#	Average (µs)	Standard Deviation (µs)
1	1.412	0.0187
2	1.408	0.0045
3	1.419	0.0217
4	1.408	0.0118
5	1.397	0.0174
6	1.404	0.0139
7	1.381	0.0130
8	1.408	0.0168

75MHz

#	Average (µs)	Standard Deviation (µs)
1	1.333	0.0184
2	1.344	0.0067
3	1.339	0.0235
4	1.330	0.0119
5	1.319	0.0187
6	1.327	0.0150
7	1.303	0.0135
8	1.227	1.389

125MHz

#	Average (µs)	Standard Deviation (µs)
1	1.363	0.207
2	1.373	0.112
3	1.004	3.672
4	1.337	0.946
5	1.312	1.214
6	1.207	2.374
7	1.381	1.890
8	1.182	2.559

Table XXXVIII. Average and standard deviation TOF C-scan image data for samples ST1-ST8 at various frequencies.

The average and standard deviation values for the TOF C-scan images are listed in Table XXXVIII to provide numerical comparison in addition to visual comparison. As opposed to the average TOF values calculated using point analysis, the average TOF values from C-scan imaging data were lower by approximately 0.010-0.015 μs. This was a slight difference that corresponded to a material velocity variation between 3-4 m/s. The standard deviation values from the TOF data were utilized to compare samples to one another using a single numerical value to determine how much the TOF range changed over the sample area. At 5 MHz, the standard deviation difference was most drastic for sample ST3 which had a value of 21.7×10^{-3} μs. This was expected due to the thinner regions on the right and left sides, respectively, which caused a decrease in TOF, and therefore, an increase in the overall standard deviation. At 75 MHz, sample ST8 had a standard deviation value of 1.39 μs which was much greater than the other samples due entirely to the lost reflected signal in the upper left-hand corner. The other samples all had similar standard deviation values ranging from 6.7×10^{-3} for ST2 to 23.5×10^{-3} μs for ST3. At 125 MHz, the majority of samples had extremely high standard deviation values due to the wide range of values from interference points and bands. The variations in these values made it difficult to obtain a sufficiently accurate evaluation at this high frequency.

5.5.3. TOF and Material Velocity C-Scan Quantitative Analysis of ST1-ST8

In addition to analysis of the ST sample data, a comparison was also made between the data obtained for the ST and SA samples. Normalized histogram curves were collected and AUTC and FWHM values were calculated for each histogram curve for further quantitative comparison. Figures 72, 73, and 74 show the TOF histogram

curves for all eight sintered SiC samples at each frequency including the calculated AUTC and FWHM values. Figures 75, 76, and 77 show the velocity histogram curves for all eight samples at each frequency including the calculated AUTC and FWHM values.

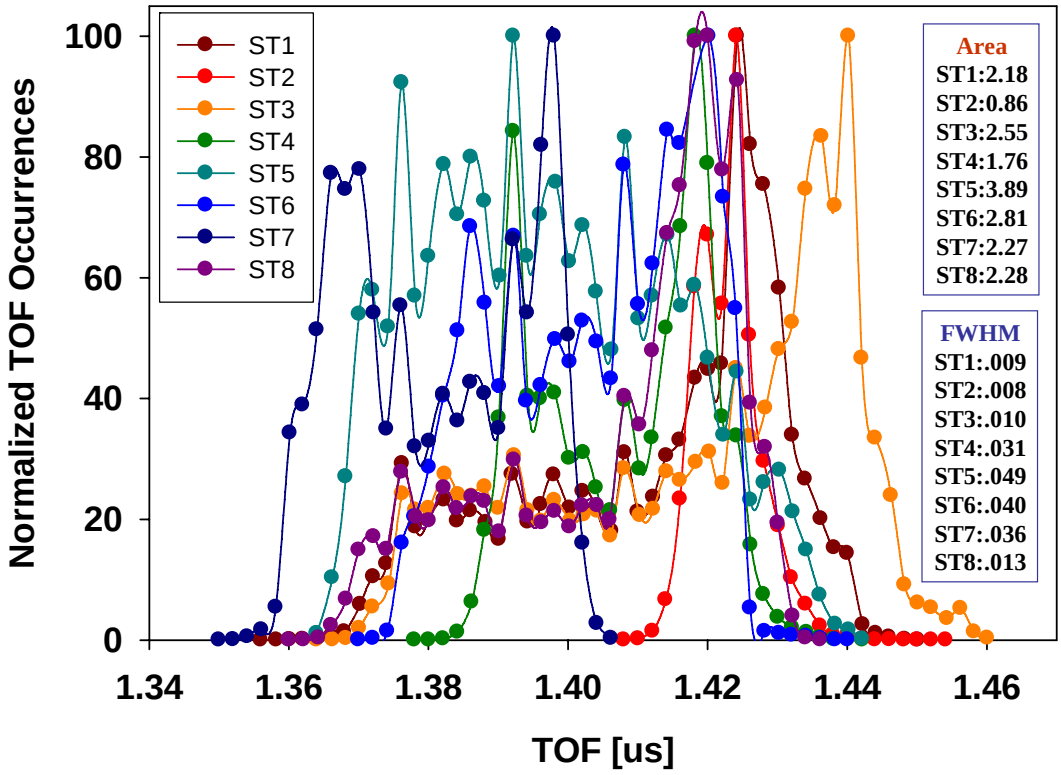

Figure 72. TOF histogram curves for ST1-ST8 at 5 MHz.

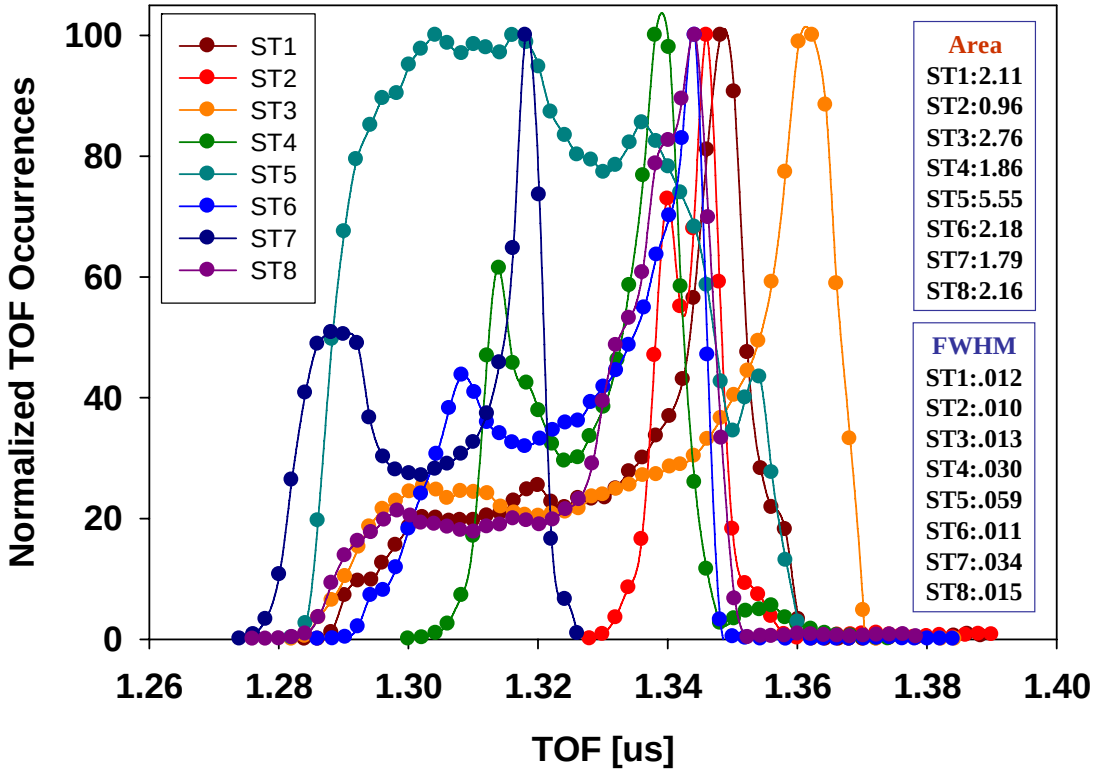

Figure 73. TOF histogram curves for ST1-ST8 at 75 MHz.

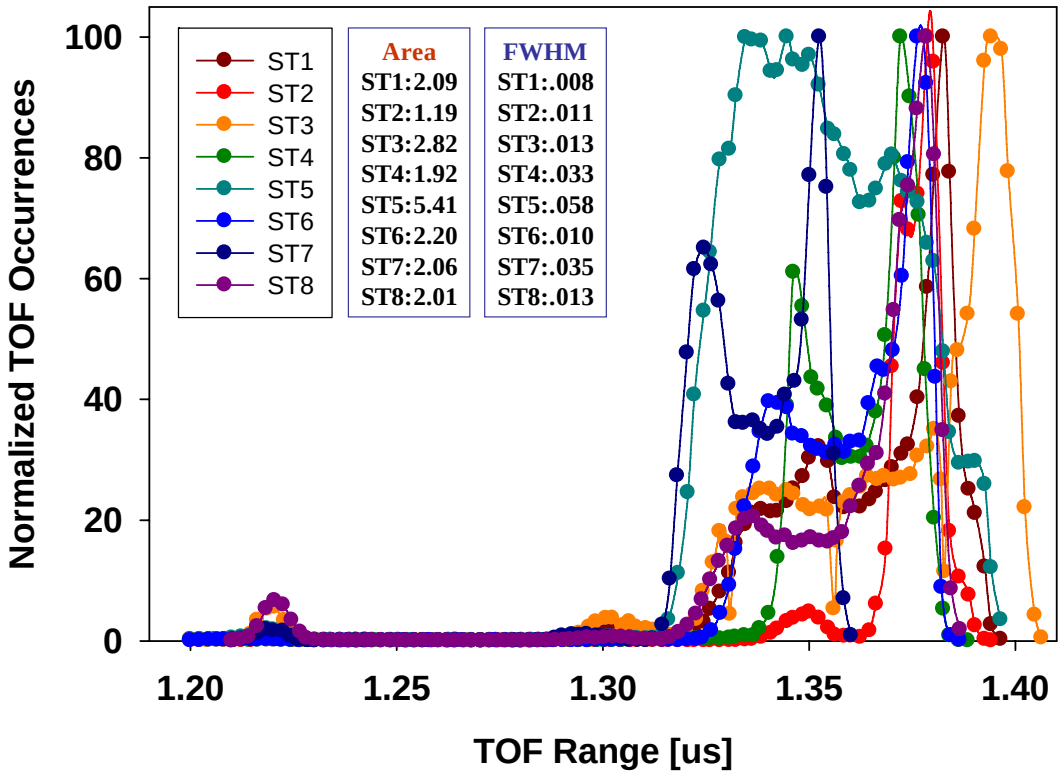

Figure 74. TOF histogram curves for ST1-ST8 at 125 MHz.

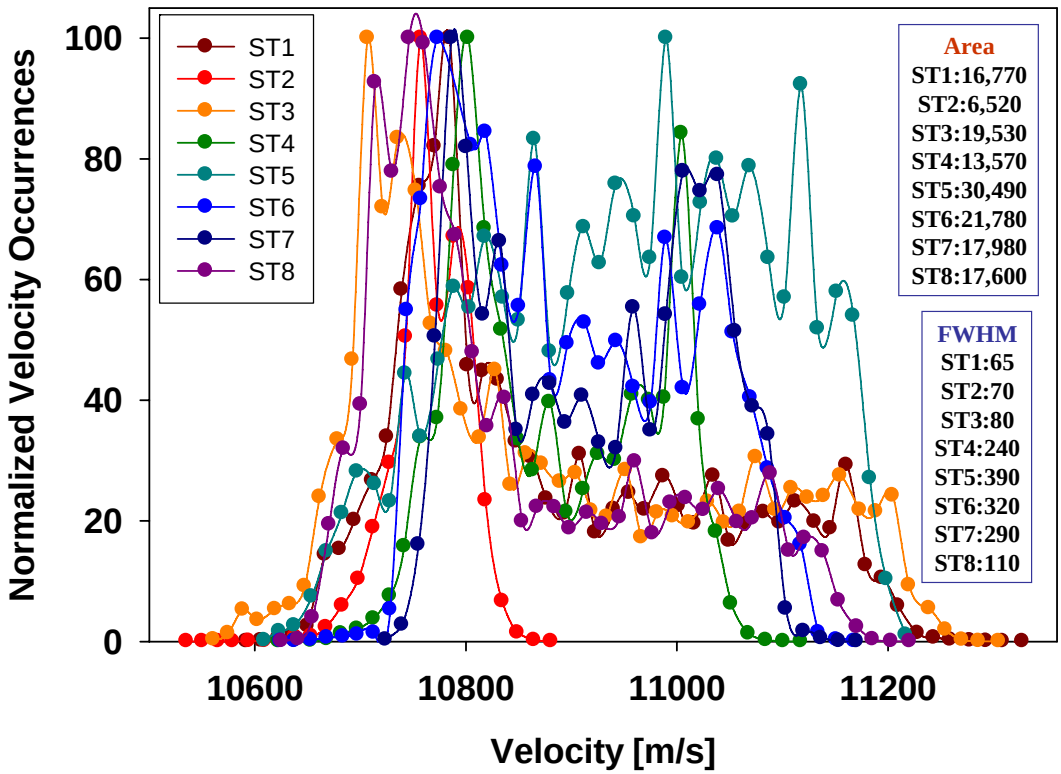

Figure 75. Velocity histogram curves for ST1-ST8 at 5 MHz.

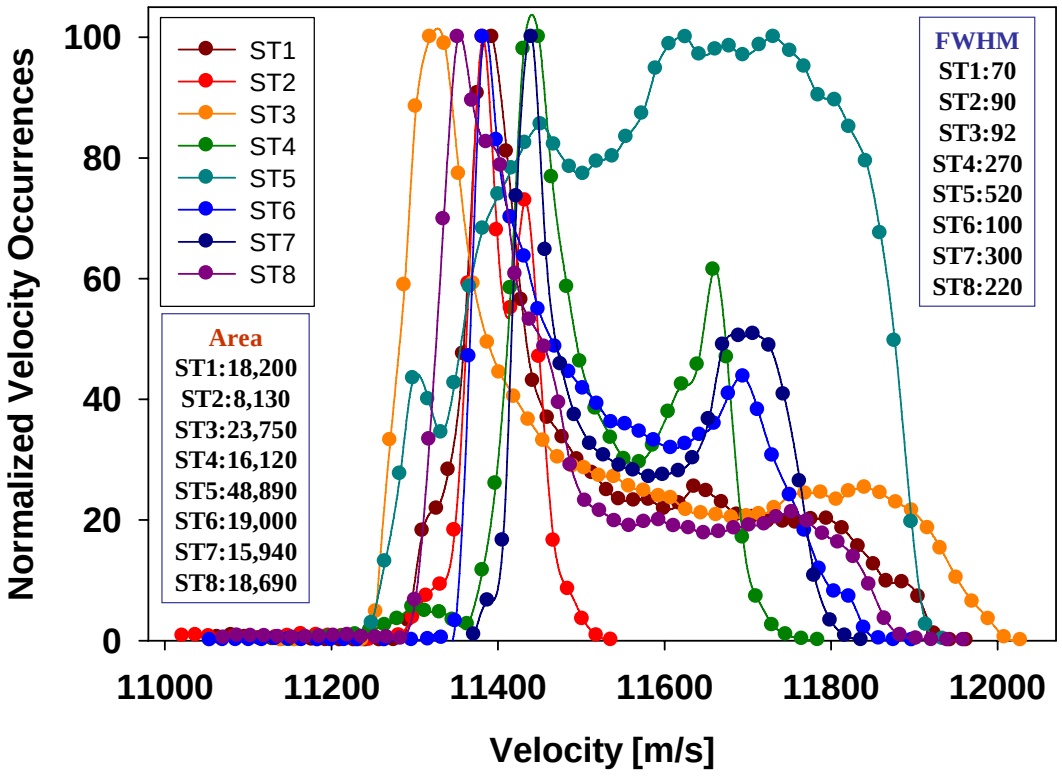

Figure 76. Velocity histogram curves for ST1-ST8 at 75 MHz.

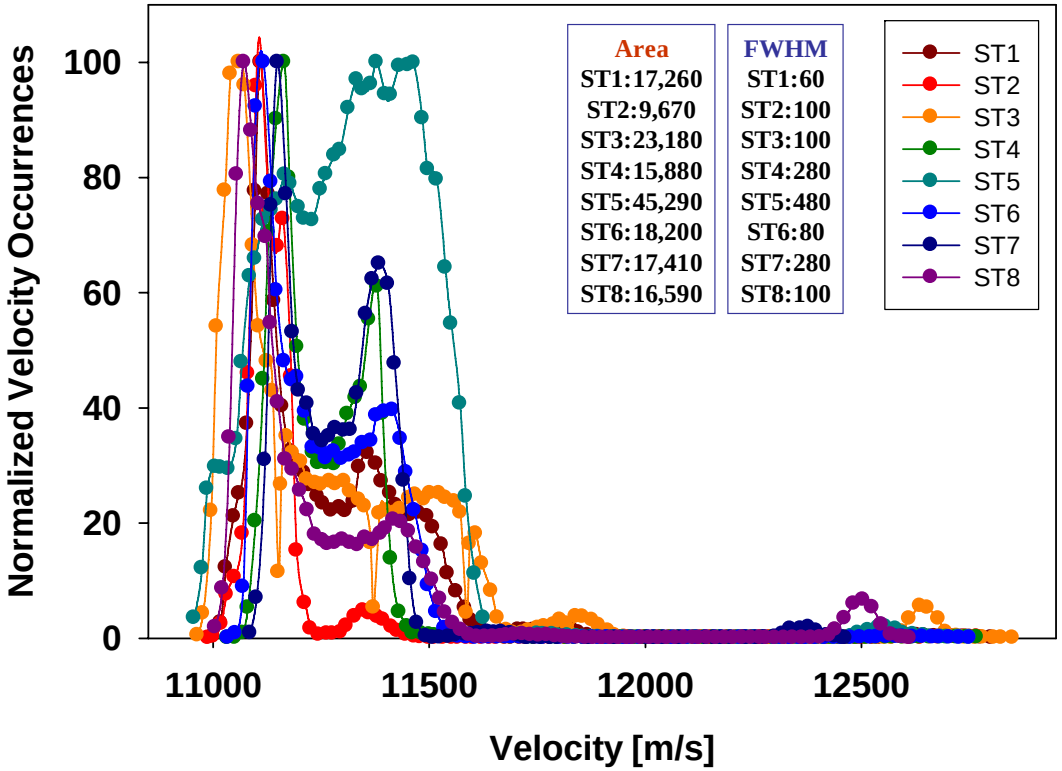

Figure 77. Velocity histogram curves for ST1-ST8 at 125 MHz.

For the 5 MHz TOF histograms in Figure 72, the histogram curves showed a great deal of variation over the range of 1.35 to 1.46 μs. The high degree of variability for the ST samples was much different than the previously evaluated SA samples, which exhibited a tight distribution over the 1.27 to 1.31 μs range. Not only was the distribution more narrow for the SA samples, but the average TOF data range was much lower despite the fact that these samples were thicker on average (7.82 mm) than the ST samples (7.65 mm). For this reason, the vast difference in TOF was believed to be due to the addition of TiB_2, which had a lower velocity (11,400 m/s) and, therefore, higher TOF than the SiC bulk. This would explain the increase in TOF range despite the lower average thickness. While there were no particularly distinguishing features among the TOF curves, some general trends were that samples ST1, ST3, and ST8 had long tails with low TOF values, sample ST2 had the most narrow comparative distribution, and the remaining samples were extremely variable, with randomly high distributions. The AUTC values reflected these drastic changes while the FWHM values also provided a means of comparison, but one that was very dependent on peak broadness at a specific set of normalized TOF values. The AUTC value for ST2, which had the most narrow distribution, was 0.86, which fell within the same range of the SA samples. However, the average AUTC value for the rest of the ST samples was 2.53, with a maximum value of 3.89 for ST5, compared to the highest SA AUTC value of 1.23 for SA3. The velocity histogram curves for 5 MHz, as seen in Figure 75, showed the same trends as the TOF curves, but in the reverse direction. While the 5 MHz data did not provide the most useful defect data due to its detectability limitations, the one clear trend was that the

distributions were much more variable for the ST samples containing the TiB_2 additive than they were for the previously tested SA samples.

For the 75 MHz TOF histograms in Figure 73, the data ranges were lower and more narrow (1.28 to 1.37 μs), but the general trend of large distinct tails and broad curve distributions was still present. While the peak values for the SA samples at 75 MHz fell between 1.29 and 1.30 μs, the peak values for the ST samples were between 1.32 and 1.36 μs, exhibiting generally higher TOF and lower velocity values due to the effect of the additive. The tails for the SA samples also exhibited smaller areas and were distinctly separate from their overall distributions whereas the ST samples had high area tails that were sometimes indistinguishable from the overall distribution. The most drastic case was ST5, which had an extremely wide TOF data range between 1.28 and 1.36 μs, with the highest overall AUTC value of 5.55. The next highest AUTC value was less than half of that value, at 2.76 for ST3. ST5 easily stood out as the sample with the widest distribution and the highest degree of variability, since it was so much different in size, shape, and properties than the other histogram curves. For the sake of comparison, the average AUTC and FWHM values for the ST samples were 2.42 and 0.023, respectively, while the values for the SA samples were much lower at 1.16 and 0.010, respectively. Since the only difference in fabrication and processing of the SA and ST samples was the TiB_2 additive, these major quantitative differences were believed to originate from this source. Again, the velocity curves in Figure 76 showed the inverse trends of the TOF curves. The ST samples had area values ranging from 8,130 for SA2 to 48,890 for ST5 while the SA sample values ranged from 8,100 for SA6 to 14,660 for SA3. As mentioned previously, the order of importance for histogram comparison would be to

first look for tail regions and evaluate their areas, next to evaluate the overall AUTC values, and finally to look for possible trends in FWHM data. The data consistently showed that the SA samples had smaller tails, lower AUTC values, and lower FWHM values than the ST samples and were therefore more homogeneously distributed.

For the 125 MHz TOF histograms in Figure 74, the distributions and histogram curve properties were similar to the 75 MHz data, but with one major difference. As opposed to the 75 MHz data, the 125 MHz data showed the presence of additional tails at much lower TOF values around 1.22 μs for several samples. Samples ST3, ST5, ST6, ST7, and ST8 all showed significant tail regions at that particular TOF value. The 125 MHz scans were more sensitive to these specific low TOF patterns due to the higher detectability and provided more detailed imaging of TOF variations. The tails were representative of bulk data from regions around 1.2 μs and should not be associated with the electrical interference regions that had a complete loss of signal, since these fell near 0.0 μs. These noise-related pixels scattered throughout the C-scan images were eliminated before constructing the histogram curves and did not influence the data. Due to the similarities between the histogram curves at 75 MHz and 125 MHz, the AUTC and FWHM values were highly comparable, and the small tail regions did not affect the overall values greatly. Once again, ST5 had the highest AUTC value of the eight ST samples due to a broad bulk distribution of TOF values followed by ST3 and ST6. ST2 had the lowest AUTC value with the narrowest distribution of TOF differences at 75 and 125 MHz, making it the most homogeneous sample under high frequency ultrasound evaluation. The velocity histograms for the 125 MHz scans in Figure 77 again showed inverse trends compared to the TOF curves. The tails that were only detected at 125

MHz corresponded to small regions of high velocity values between 12,400 and 12,600 m/s as opposed to the rest of the sample areas which were between 11,000 and 11,700 m/s. The histogram curve shapes and distributions remained consistent over all frequencies for the ST samples. For the 5 MHz evaluation, the data were much more variable, but the trends became clearer at 75 MHz. The 125 MHz analysis revealed the presence of low TOF/high velocity features that could not be detected at the other frequencies.

Based solely on nondestructive ultrasound quantitative analysis of the set of eight sintered SiC samples at high frequencies, SA2, the most homogeneous sample, would be believed to exhibit improved performance as compared to SA5, which showed the greatest degree of TOF and velocity variability.

5.5.4. Reflected Signal Amplitude C-Scan Imaging of ST1-ST8

The reflected signal amplitude data were collected in addition to x and y positions for each point and plotted over a range determined by the minimum and maximum amplitude intensity values in mV for each scan. The reflected signal amplitude C-scan images for each of the SiC samples are shown in Figures 78 and 79. The average and standard deviation amplitude values are shown in Table XXXIX. It should also be pointed out that unlike in the TOF C-scan images, there were no observable occurrences of noise, at any of the frequencies, so no adjustments had to be made to eliminate data points that were not representative of the samples.

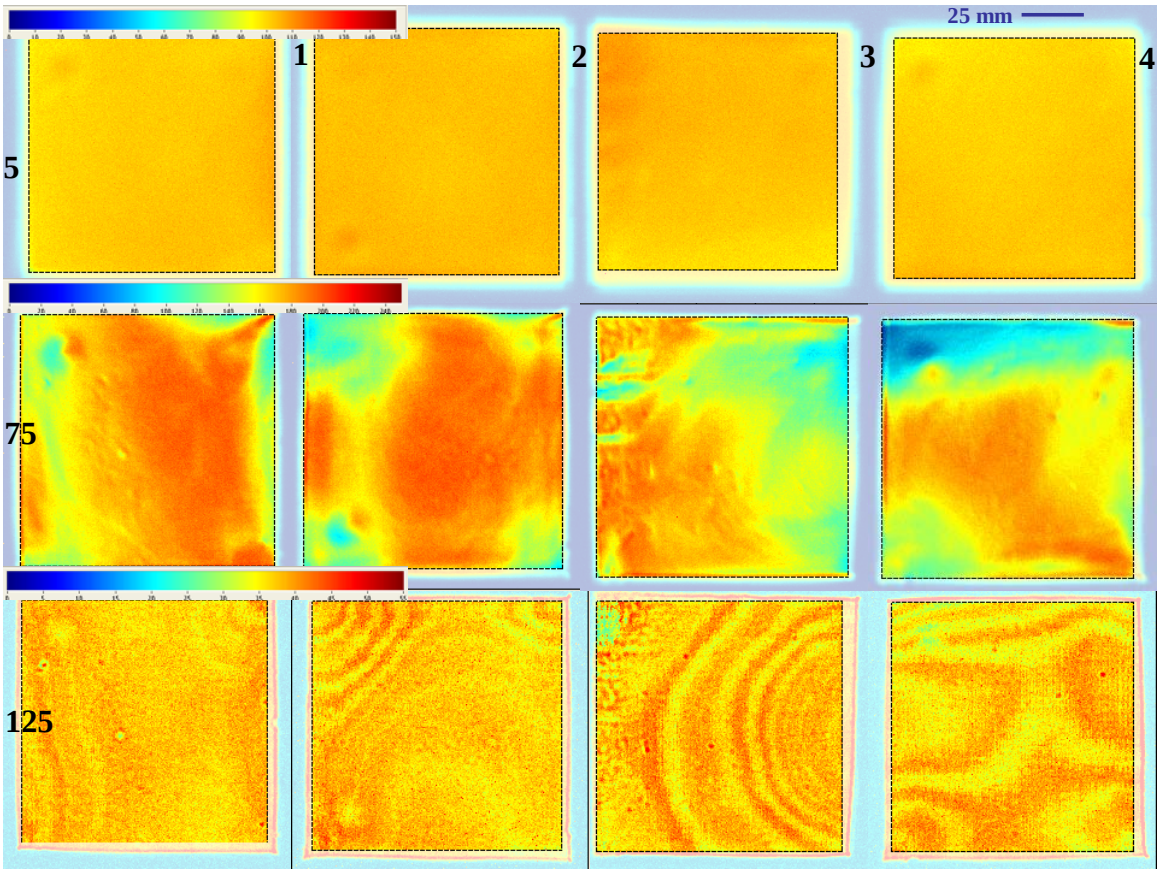

Figure 78. Amplitude C-scan image maps of ST1-ST4 at 5, 75, and 125 MHz.

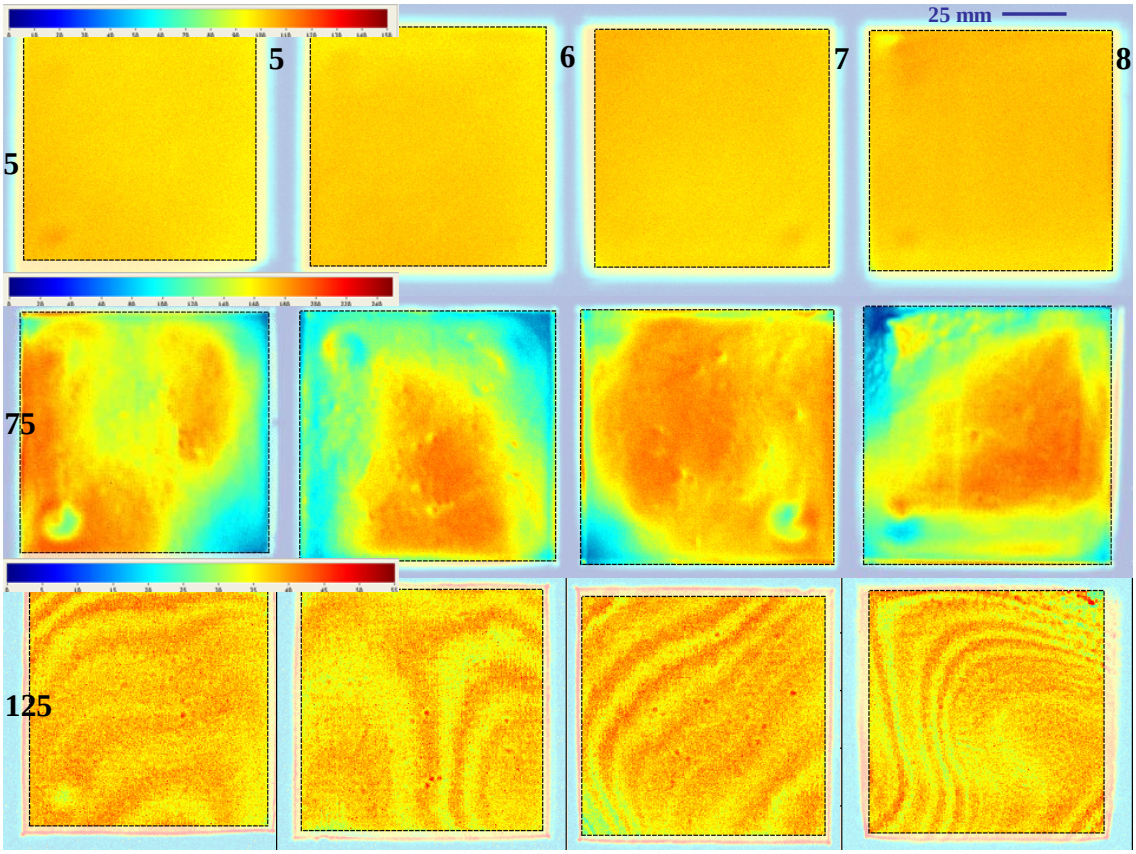

Figure 79. Amplitude C-scan image maps of ST5-ST8 at 5, 75, and 125 MHz.

5MHz

#	Average (mV)	Standard Deviation (mV)
1	109	2.853
2	112	1.938
3	111	3.676
4	109	2.680
5	107	2.915
6	108	2.843
7	108	2.700
8	110	3.060

75MHz

#	Average (mV)	Standard Deviation (mV)
1	186	25.35
2	184	31.58
3	163	29.84
4	158	40.78
5	159	35.58
6	146	39.11
7	177	28.07
8	158	37.82

125MHz

#	Average (mV)	Standard Deviation (mV)
1	40	2.722
2	40	3.167
3	41	3.683
4	40	3.728
5	40	2.985
6	39	3.231
7	40	3.418
8	39	3.560

Table XXXIX. Average and standard deviation amplitude C-scan image data for samples ST1-ST8 at various frequencies.

At 5 MHz, there was a specific cause of variation among the eight ST samples over the 0-150 mV reflected surface amplitude range. While table XXXIX showed a very similar average range of amplitude values between 107 - 112 mV, an average difference of only 14 dB among the eight samples, variations were visible. These reflected signal amplitude changes were noticeable in at least one of the corners of each of the samples. These regions were of similar size (5-10 mm), shape (circular), and location (corners) to those found when evaluating the SA samples. In the SA section it was hypothesized that this may have been due to handling of the green samples before firing. The plates may have been placed or stacked in or on top of containers that contained raised circular regions on the corners. If this were the case, more pressure would have been induced on the corners of the samples before firing, creating high density regions of high pressure next to circular low density regions of low pressure where the material was displaced from. In any case, these reflected signal amplitude variations were found in the upper left, bottom left, upper left, upper left, bottom left, upper left, bottom right, and bottom left corners of ST1-ST8, respectively. While the TOF C-scan images collected at 5 MHz were only sensitive to slight thickness differences and could not detect these defects, the amplitude scans detected the variations caused by scattering from material inhomogeneities and defects. In this way, it was shown that the TOF and amplitude scans were justifiably different for determining specific material changes, and that both were necessary for comprehensive ultrasound evaluation.

The 75 MHz reflected signal amplitude C-scan images showed a great deal of variation over the 0-250 mV range. This was due to acoustic wave scattering of a large

number of material inhomogeneities at the associated wavelength for this frequency. When compared to the TOF C-scan images, many of the same high TOF regions that were identified in ST2, ST4, ST7, and ST8 matched the regions of lowest reflected signal amplitude. For example, the upper left corner of ST4 in which there was a complete loss of signal in the TOF scan was also representative of the highest degree of attenuation in the amplitude scan. However, instead of more definitive contrast between two distinct regions as observed in the TOF scans, the amplitude scans showed more detailed variations corresponding to minor changes throughout each sample. The circular defects pointed out in the 5 MHz scans were also observed in greater detail at 75 MHz. Regions that appeared to be textured with high amplitude points were also found in many of the amplitude scans. These were most noticeable in areas that were not overshadowed by high loss in reflected signal amplitude. As opposed to the larger low loss regions, these high amplitude point regions were believed to be representative of isolated TiB_2 additives, which possessed higher Z values than the SiC bulk. While these features could be identified in all of the ST samples, they were most readily apparent in ST3, ST6, and ST7. The ability to detect TiB_2 regions within the bulk provided an important distinction between the features observed at 5 MHz and those found at 75 MHz.

The 125 MHz reflected signal amplitude images showed pressing patterns, defects, and other material inhomogeneities that were not detected at 75 MHz or in any of the TOF C-scan images. The detection of microstructural inhomogeneities in this size range was a result of acoustic wave scattering from smaller features at 125 MHz as compared to the larger features at 75 MHz. Most noticeably, the pressing patterns were clearly identified in each of the samples, whereas they could not be detected at 75 MHz,

demonstrating the importance of successfully achieving higher frequency imaging. The circular defects of lower reflected signal amplitude were imaged in more detail in all of the ST samples. In addition, individual defects that were not detectable at other frequencies were also found in all of the images. For example, in samples ST1, ST3, ST7, and ST8, isolated circular features of both lower and higher amplitude as small as 75-125 μm were identified throughout the sample. The regions of higher reflected signal amplitude were most likely representative of TiB_2 additives as opposed to the lower reflected signal amplitude regions which were most likely representative of low acoustic impedance defects and pores. ST1 showed examples of isolated high and low amplitude features, in which the smaller higher amplitude features were distributed throughout the sample and a distinct lower amplitude feature was observed near the center of the sample. One unique regional trend detected at 125 MHz occurred in sample ST3, in which the left side of the sample showed distinct high amplitude regions which were most likely representative of inhomogeneous TiB_2 distribution. The normally isolated high amplitude features appeared to be grouped more in this particular sample, and a corresponding high loss area occurred at the upper left hand corner as well. These defect and feature types were only resolved in the 125 MHz reflected signal amplitude C-scan images since the 75 MHz scans were overwhelmed by larger regions of high signal loss.

5.5.5. Reflected Signal Amplitude Quantitative Analysis of ST1-ST8

Reflected signal normalized amplitude histograms were plotted in Figures 80, 81, and 82. At 5 MHz, the C-scan images were very similar with little noticeable variability, and the normalized amplitude histograms reflected this trend. The histogram curves were similar for all eight samples, with ST3, ST6, and ST8 demonstrating slightly extended

tails. The presence of the circular defects did not have a noticeable effect on the histogram data. Upon observation of the AUTC and FWHM data, ST5 had the highest values of 612 and 5.7 while ST2 had the lowest values of 404 and 3.7, respectively. These trends matched those of the TOF data, but unlike the TOF results, these values were much closer to the AUTC and FWHM data from the rest of the samples. It was important to note that despite the different types of information that the TOF and reflected signal amplitude data provided, the interpretation of the most homogeneous and inhomogeneous samples remained the same.

At 75 MHz, the normalized amplitude histograms showed the highest degree of variation due to the drastic changes in reflected signal amplitude. Wide distributions and tails of significant area were present for all of the samples, demonstrating the large amplitude variations throughout each sample, both from low amplitude defects and high amplitude isolated features. Once again, sample ST2 had the narrowest distribution due to a high degree of homogeneity, but the sample with the broadest distribution was ST6 which had the largest low amplitude region among all the samples. The C-scan image for ST6 demonstrated the wide horseshoe-shaped area of low reflected signal amplitude. The same trends corresponded to the AUTC data, in which the highest value was from ST6 at 4,424 and the lowest value was from ST2 at 1,711. ST6 also had the highest FWHM value of 53 while ST2 exhibited the lowest FWHM value of 9. These trends were consistent for reflected signal amplitude data at 75 MHz.

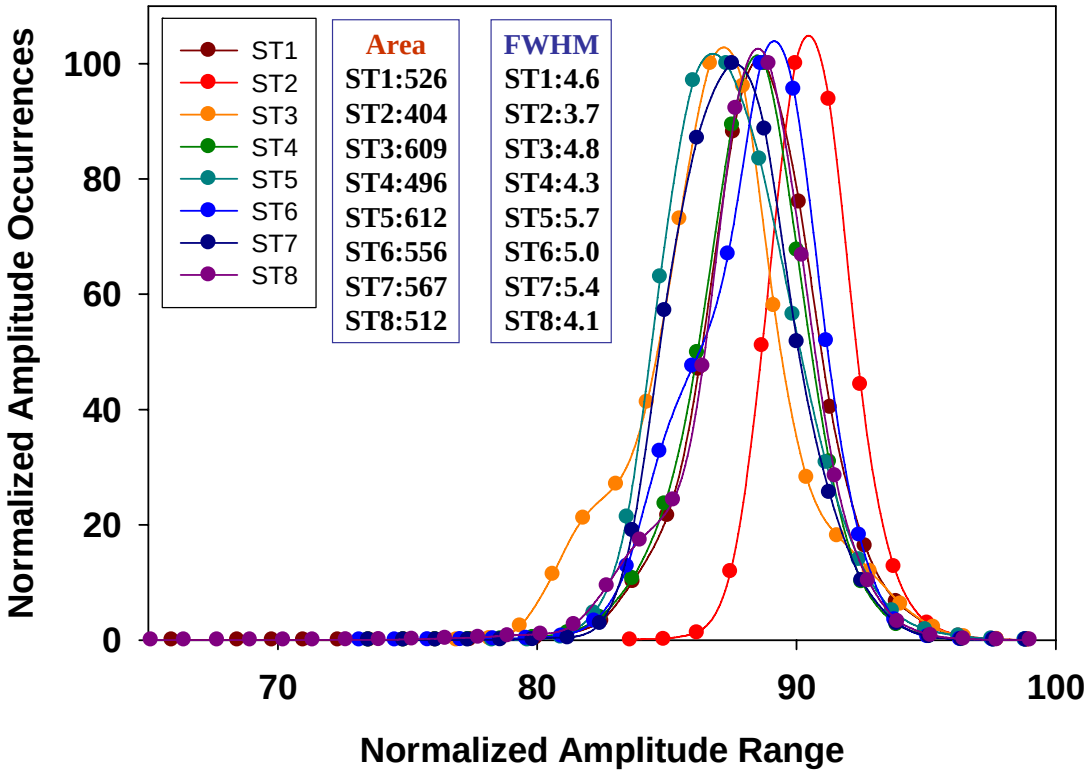

Figure 80. Reflected signal amplitude histogram curves for ST1-ST8 at 5 MHz.

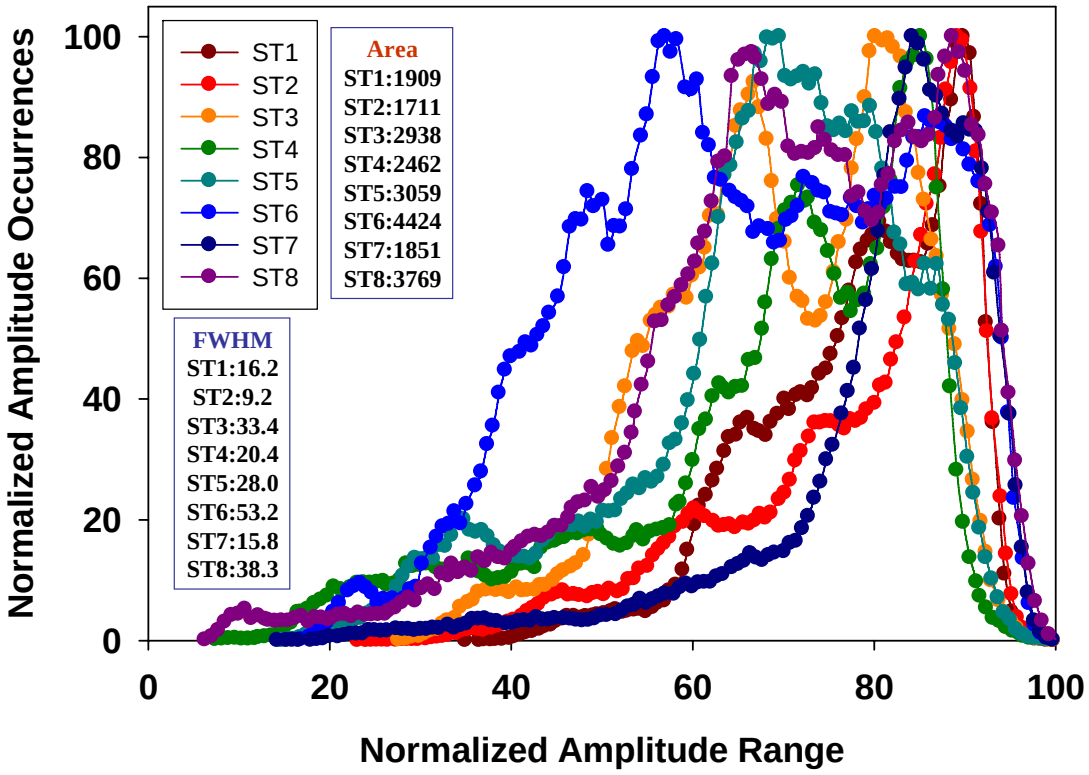

Figure 81. Reflected signal amplitude histogram curves for ST1-ST8 at 75 MHz.

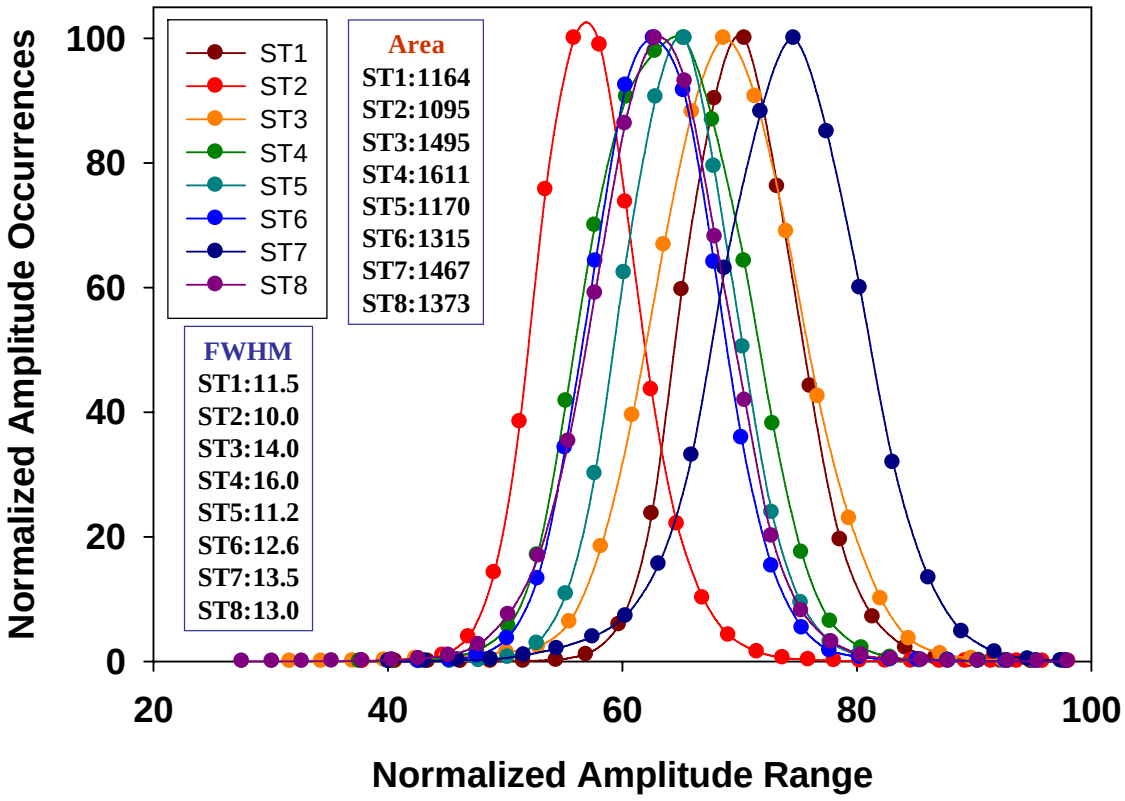

Figure 82. Reflected signal amplitude histogram curves for ST1-ST8 at 125 MHz.

At 125 MHz, the normalized amplitude histograms were not as broad as the ones obtained at 75 MHz. The distinguishing features in the 125 MHz reflected signal amplitude C-scan images were the pressing patterns, which dominated the scans, and therefore the quantitative data. The trends were primarily indicative of the homogeneity of the pressing patterns while the secondary factor seemed to be the presence and distribution of isolated defects and additives. Pressing patterns and 75-125 μm defects provided more detail of minor differences among samples. For this reason, the sample with the highest AUTC and FWHM values (which was ST5 according to the 5 MHz data and ST6 according to the 75 MHz data) was ST4 at 125 MHz. Sample ST4 had the highest AUTC value of 1611 and the highest FWHM value of 16. While the sample with the highest values changed at each frequency for the reflected signal amplitude data, the sample with the minimum values remained the same throughout. Sample ST2 had the lowest AUTC value of 1095 and the lowest FWHM value of 10. This sample was the most consistent as far as maintaining the same trend for both TOF and amplitude scans at all frequencies. For these scans, the identification of the most inhomogeneous sample was highly dependent on frequency. The 5 MHz trends were dictated by the presence of circle defects while the 75 MHz trends were dictated by the area of low amplitude regions and the 125 MHz trends were dictated by the homogeneity of pressing patterns. The significance of this data was highly dependent on which features are most highly correlated to mechanical property, elastic property, and ballistic performance. If the circle defects were determined to be most critical, sample ST5 would most likely be red-flagged. If high attenuation areas were determined to be most important, sample ST6

would be red-flagged. If pressing pattern and additive distribution were deemed critical, sample ST4 would most likely be red-flagged.

5.5.6. Schematics of Test Specimens ST1-ST8

The TOF and reflected signal ultrasound C-scan image data were utilized to put together schematics of general regions of interest detected throughout the eight sintered ST SiC samples, as shown in Figures 83-86. As described earlier, the regions of interest were characterized by inhomogeneous TOF or reflected signal amplitude values as compared to the average values for each sample. Again, approximate areas were traced by overlaying scans of varying frequency (5, 75, 125 MHz) and type (TOF, amplitude) and outlining the regional patterns. The resulting areas were labeled accordingly. Just as for the SA samples, the regions were separated in terms of degree of difference from the sample average, with red representing the largest change in TOF or amplitude, blue representing a subtle but definitive change in TOF or amplitude, and green representing an intermediate change in TOF or amplitude falling somewhere between the two. The features were categorized according to the same six factors used to define the SA samples. The schematics were designed to provide a clue as to which areas would be important to test for each sample.

The schematics were evaluated sample by sample. Sample ST1 showed amplitude defect regions in the top right corner and several significant inclusions, including a very large one with a large amplitude difference near the center of the sample. Sample ST2 showed low amplitude regions in all four corners, with the most prominent being the bottom left where a circle defect was also present and the top left in which pressure gradients were located. Sample ST3 showed a distribution of inclusions along

the left side of the sample and a large inclusion near the center of the sample. The right side of the sample contained significant regions of lower amplitude in each of the corners. Pressing patterns were also prominent over most of the sample area. Sample ST4 was characterized by low amplitude and high TOF regions in the upper left corner and several large inclusions. It also contained a pressing pattern that ran through the center of the sample. Sample ST5 showed large regions of lower amplitude along the right side and several small inclusions scattered throughout the center. Sample ST6 showed lower amplitude regions over most of the perimeter with small inclusions and several pressing patterns through the center of the sample. Sample ST7 showed low amplitude regions along the left side with dispersed pressing patterns and inclusions throughout the rest of the sample. Sample ST8 was characterized by low amplitude regions along the top of the sample and pressing patterns around the perimeter. To summarize, the most inhomogeneous regions were in samples ST3, ST4, ST5, ST6 and ST8, the largest individual inclusions were present in ST1, ST3, and ST4, circle defects were most prominent in ST1, ST2, ST5, and ST7, distinct pressing patterns existed in samples ST3, ST4, ST6, ST7, and ST8, and large numbers of inclusion areas were evident in ST3 and ST7. It was evident that a significant number of defects and features were detected in the sintered ST samples.

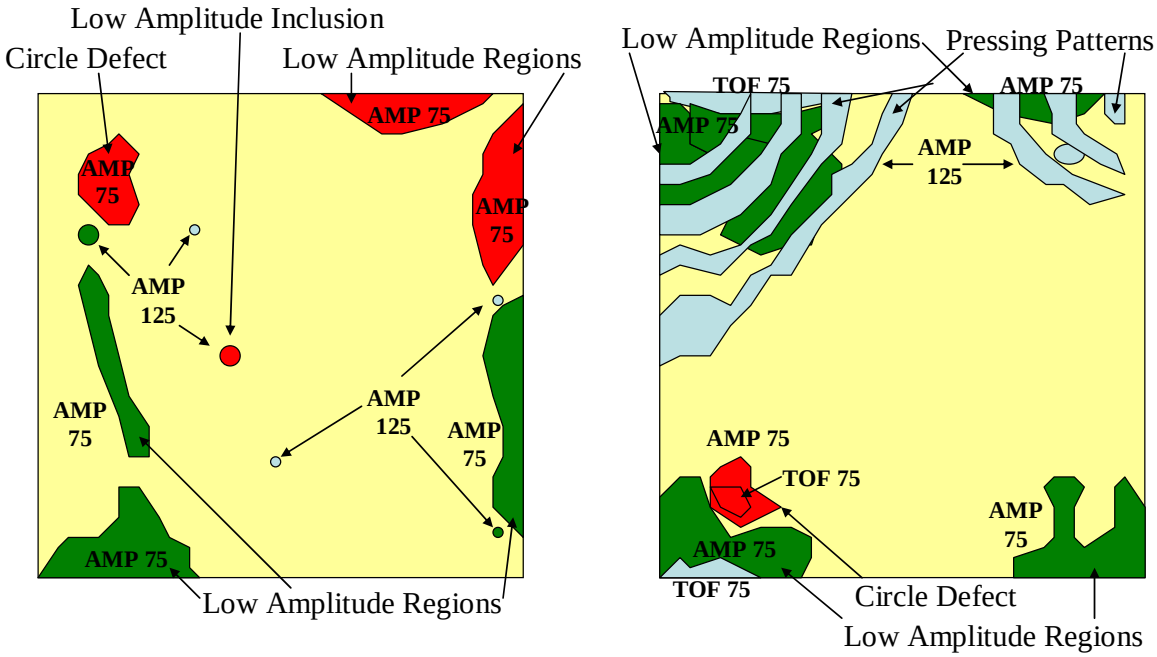

Figure 83. Schematic representations of samples ST1 and ST2.

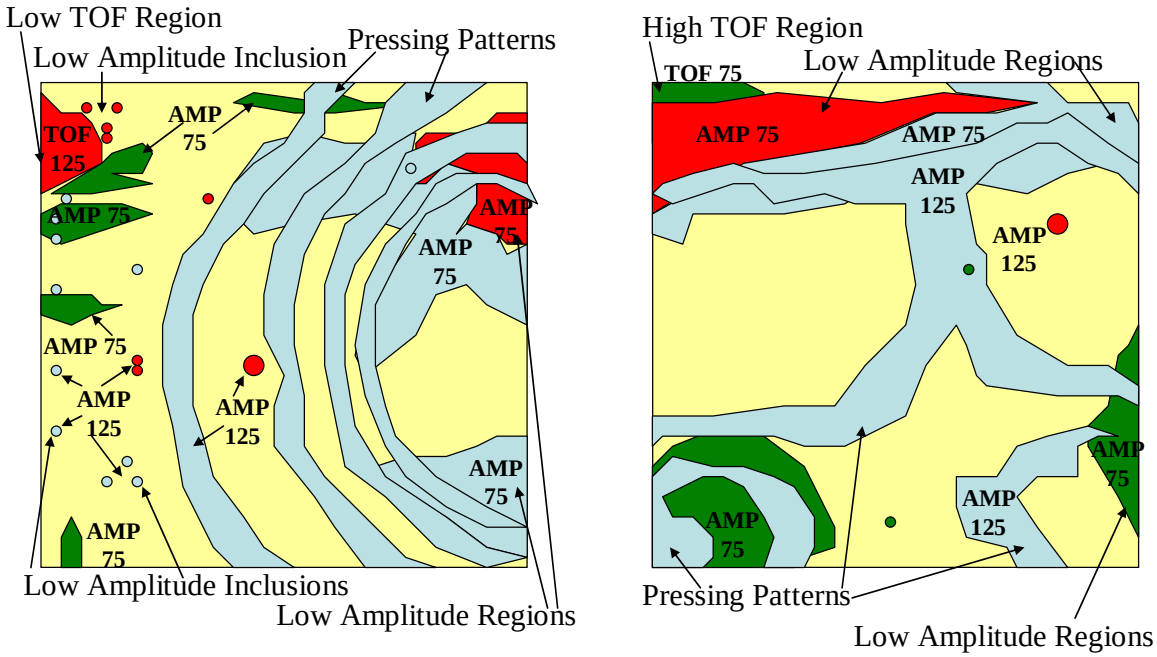

Figure 84. Schematic representations of samples ST3 and ST4.

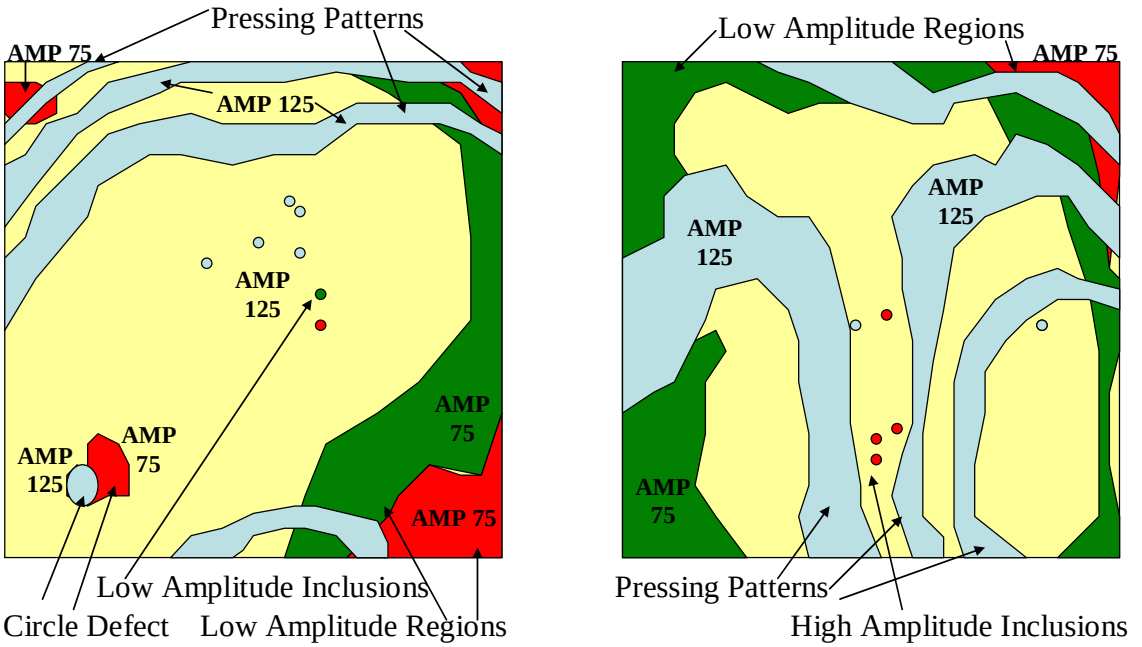

Figure 85. Schematic representations of samples ST5 and ST6.

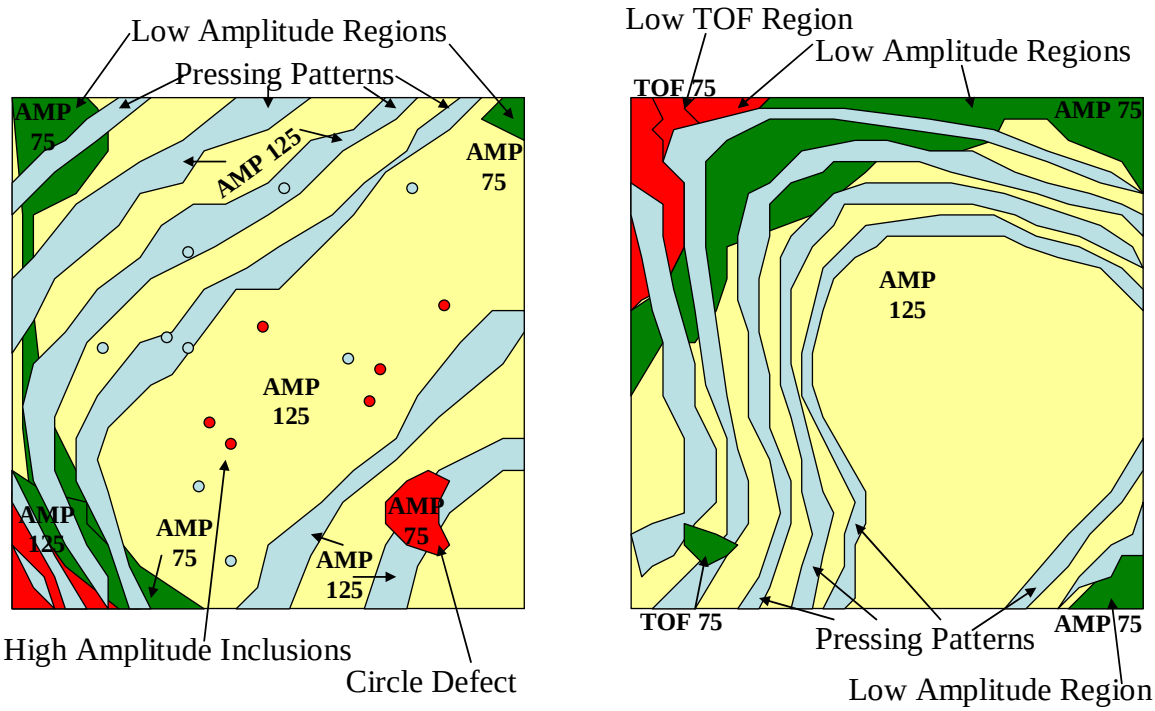

Figure 86. Schematic representations of samples ST7 and ST8.

5.6. Sintered SiC ESC Test Specimens with Correlational Ballistic Data

Another unique set of three sintered SiC samples was evaluated using reflected signal amplitude ultrasound C-scan imaging and quantitative histogram analysis. Not only was each of these samples processed differently, making them useful for effective ultrasound comparison, but they also came from batches of armor ceramic plates that underwent extensive ballistic testing so that correlations could be derived between the ultrasound results and ballistic properties. The first sample, denoted ESC-1, was a sintered SiC armor plate with a length and width of 101.60 mm, an average density of 3.143 g/cm^3 as reported by the manufacturer, and an average thickness of 12.75 mm. Other reported properties of this grade of material included an average grain size of less than 5 μm, a density of greater than 3.100 g/cm^3, a Vicker's hardness of 25.5 GPa, a Knoop hardness of 24.5 GPa, a four-point flexural strength of 400 MPa, a Poisson's ratio of 0.17, and an elastic modulus of 410 GPa [120-122]. Since ESC-1 was much denser than its listed density of 3.100 g/cm^3, these properties were most likely higher than the listed values. The second sample, denoted ESC-2, was fabricated in the same way as ESC-1, except an additional hot isostatic pressing (HIP) was added to increase the sample density. This sample had a length and width of 101.60 mm, an average density of 3.163 g/cm^3 as reported by the manufacturer, and an average thickness of 12.75 mm. Other reported properties of this grade of material included an average grain size of less than 5 μm, a density of greater than 3.160 g/cm^3, a Vicker's hardness of 25.5 GPa, a Knoop hardness of 24.5 GPa, a four-point flexural strength of 510 MPa, a Poisson's ratio of 0.17, and an elastic modulus of 420 GPa [120-122]. Compared to the ESC-1 sample, the post-HIP step showed significant improvements in density, flexural strength, and elastic

modulus while the other properties were identical. The third sample, denoted ESC-3, was a liquid phase sintered (LPS) material with a second phase of yttrium-aluminum garnet (YAG) and, therefore, was much different in composition than ESC-1 and ESC-2 [52,122]. This sample had a length and width of 101.60 mm, an average density of 3.199 g/cm^3 as reported by the manufacturer, and an average thickness of 12.74 mm. Other reported properties of this grade of material included an average grain size of less than 2 μm, a density of greater than 3.210 g/cm^3, a Vicker's hardness of 22.5 GPa, a Knoop hardness of 21.0 GPa, a four-point flexural strength of 550 MPa, a Poisson's ratio of 0.16, and an elastic modulus of 420 GPa [120-122]. Compared to the other sample grades, ESC-3 had a higher density most likely due to the high density of YAG at approximately 4.56 g/cm^3 as reported in the literature (though the added amount was not specifically known) and a smaller grain size [123]. This sample also had lower hardness values and higher flexural strength likely due to the second phase addition.

Ultrasound point analysis was conducted on the three samples to get an idea of the acoustic impedance, material velocity, and elastic properties as shown in Tables XL-XLII. Sample ESC-1 had an average longitudinal velocity of 12,057 m/s and an average shear velocity of 7,644 m/s, which led to average calculated $Z = 37.89 \times 10^5$ g/cm^2s, average $\nu = 0.16$, average E = 428 GPa, average G = 184 GPa, and average K = 212 GPa. The ESC-1 sintered SiC sample had values that were very similar to those measured for the sintered SA SiC samples reported earlier. Sample ESC-2, which added the post-HIP step to increase the density, had an average longitudinal velocity of 12,140 m/s and an average shear velocity of 7,680 m/s, which led to average calculated $Z = 38.40 \times 10^5$ g/cm^2s, average $\nu = 0.17$, average E = 435 GPa, average G = 187 GPa, and average K =

217 GPa. The post-HIP step successfully enhanced the elastic properties above all previous reported sintered SiC samples, with values that started to approach those reported for the hot pressed samples. The elastic properties reported for hot pressed SiC sample A were an average $\nu = 0.17$, average E = 444 GPa, average G = 190 GPa, and average K = 225 GPa. Depending on the elastic property requirements, the sintering and post-HIP fabrication method for SiC could be considered as an alternative to hot pressing. Sample ESC-3, which was liquid phase sintered and contained the YAG second phase showed lower properties than ESC-1 and ESC-2 due to the second phase addition. This sample had an average longitudinal velocity of 11,906 m/s and an average shear velocity of 7,508 m/s, which led to average calculated $Z = 38.09 \times 10^5$ g/cm^{2}s, average $\nu = 0.17$, average E = 423 GPa, average G = 181 GPa, and average K = 214 GPa. While the reported values showed an increase in flexural strength due to the YAG addition, this also resulted in an increase in density, a reduction in hardness, and a reduction in calculated elastic properties.

The three samples underwent reflected signal amplitude ultrasound C-scan imaging and quantitative evaluation at transducer frequencies of 5, 75, and 125 MHz. The C-scan images are shown in Figures 87-89, and the average and standard deviation values for each sample at each frequency are shown in Table XLIII. Just as in previous studies, the ESC samples scanned at 5 MHz showed few noticeable differences among the three test specimens. However, reflected signal amplitude differences were evident in distinct patterns which could have been the result of improper surface finish. The standard deviation values at the lowest frequency were 5.16 mV for ESC-1, 4.62 mV for ESC-2, and 4.08 mV for ESC-3. At 75 MHz, the patterns in the scans were much clearer

as the higher frequency was more sensitive to the reflected signal amplitude differences. The standard deviation values at this frequency were 34.01 mV for ESC-1, 43.84 mV for ESC-2, and 40.71 mV for ESC-3. At 125 MHz, the high sensitivity of the transducer was much closer to the scale of the patterns and therefore less representative of minor material differences. The standard deviation values at this frequency were 27.31 mV for ESC-1, 36.74 mV for ESC-2, and 27.50 mV for ESC-3. Since there were other noticeable reflected signal amplitude differences within each sample that were not influenced by the patterns, quantitative evaluation was conducted.

#	ρ (g/cc)	t (mm)	TOF_l (μs)	TOF_s (μs)	c_l (m/s)	c_s (m/s)	Z (*10^5 g/cm^{2}s)	ν	E (GPa)	G (GPa)	K (GPa)
1	3.143	12.75	2.116	3.336	12,051	7644	37.88	0.16	428	184	212
2	3.143	12.75	2.115	3.336	12,057	7644	37.89	0.16	428	184	212
3	3.143	12.75	2.116	3.336	12,051	7644	37.88	0.16	428	184	212
4	3.143	12.75	2.116	3.336	12,051	7644	37.88	0.16	428	184	212
5	3.143	12.75	2.115	3.336	12,057	7644	37.89	0.16	428	184	212
6	3.143	12.75	2.116	3.337	12,051	7642	37.88	0.16	427	184	212
7	3.143	12.75	2.115	3.336	12,057	7644	37.89	0.16	428	184	212
8	3.143	12.75	2.115	3.336	12,057	7644	37.89	0.16	428	184	212
9	3.143	12.75	2.115	3.336	12,057	7644	37.89	0.16	428	184	212
Avg	**3.143**	**12.75**	**2.115**	**3.336**	**12,057**	**7644**	**37.89**	**0.16**	**428**	**184**	**212**

Table XL. Point analysis data for sample ESC-1.

#	ρ (g/cc)	t (mm)	TOF_l (μs)	TOF_s (μs)	c_l (m/s)	c_s (m/s)	Z (*10^5 g/cm^{2}s)	ν	E (GPa)	G (GPa)	K (GPa)
1	3.163	12.75	2.099	3.320	12,149	7681	38. 43	0.17	436	187	218
2	3.163	12.75	2.099	3.320	12,149	7681	38. 43	0.17	436	187	218
3	3.163	12.75	2.110	3.331	12,085	7655	38.23	0.16	432	185	215
4	3.163	12.75	2.104	3.320	12,120	7681	38.33	0.16	435	187	216
5	3.163	12.75	2.100	3.315	12.143	7692	38.41	0.16	436	187	217
6	3.163	12.75	2.099	3.320	12,149	7681	38. 43	0.17	436	187	218
7	3.163	12.75	2.098	3.319	12,154	7683	38.44	0.17	436	187	218
8	3.163	12.75	2.098	3.319	12,154	7683	38.44	0.17	436	187	218
9	3.163	12.75	2.098	3.319	12,154	7683	38.44	0.17	436	187	218
Avg	**3.163**	**12.75**	**2.101**	**3.320**	**12,140**	**7680**	**38.40**	**0.17**	**435**	**187**	**217**

Table XLI. Point analysis data for sample ESC-2.

#	ρ (g/cc)	t (mm)	TOF_l (μs)	TOF_s (μs)	c_l (m/s)	c_s (m/s)	Z (*10^5 g/cm^{2}s)	ν	E (GPa)	G (GPa)	K (GPa)
1	3.199	12.74	2.144	3.393	11,884	7510	38.02	0.17	422	181	211
2	3.199	12.74	2.144	3.398	11,884	7499	38.02	0.17	421	180	212
3	3.199	12.74	2.138	3.392	11,917	7512	38.12	0.17	423	181	214
4	3.199	12.74	2.144	3.398	11,884	7499	38.02	0.17	421	180	212
5	3.199	12.74	2.138	3.392	11,917	7512	38.12	0.17	423	181	214
6	3.199	12.74	2.138	3.393	11,918	7510	38.12	0.17	423	181	214
7	3.199	12.74	2.138	3.392	11,917	7512	38.12	0.17	423	181	214
8	3.199	12.74	2.138	3.392	11,917	7512	38.12	0.17	423	181	214
9	3.199	12.74	2.138	3.393	11,918	7510	38.12	0.17	423	181	214
Avg	**3.199**	**12.74**	**2.140**	**3.394**	**11,906**	**7508**	**38. 09**	**0.17**	**423**	**181**	**214**

Table XLII. Point analysis data for sample ESC-3.

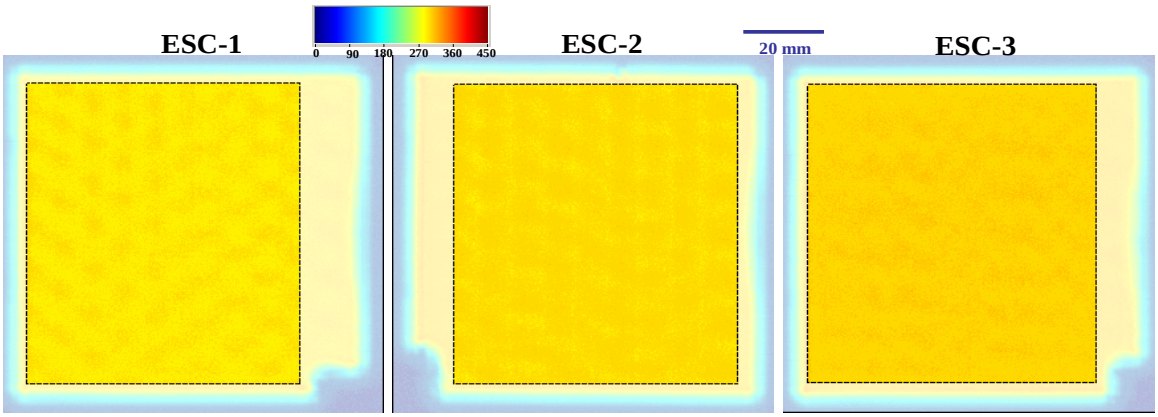

Figure 87. Reflected signal amplitude scans of ESC-1, ESC-2, and ESC-3 at 5 MHz.

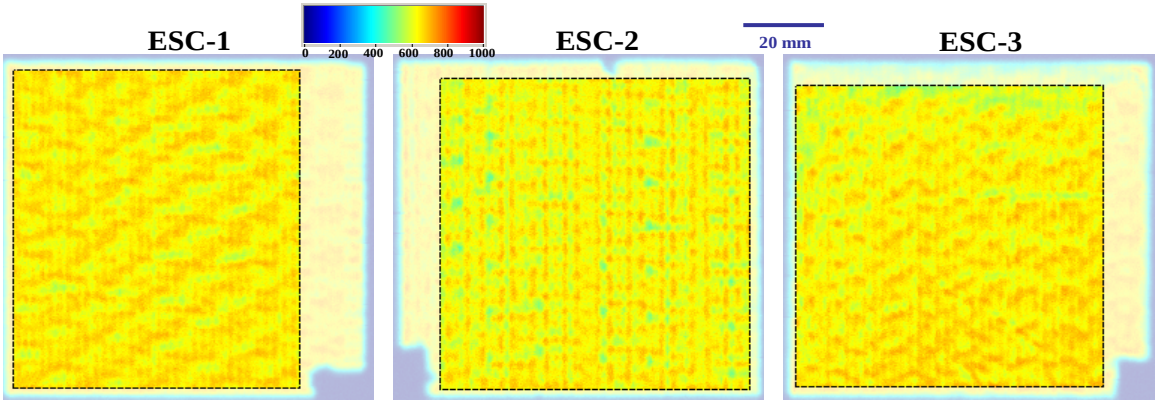

Figure 88. Reflected signal amplitude scans of ESC-1, ESC-2, and ESC-3 at 75 MHz.

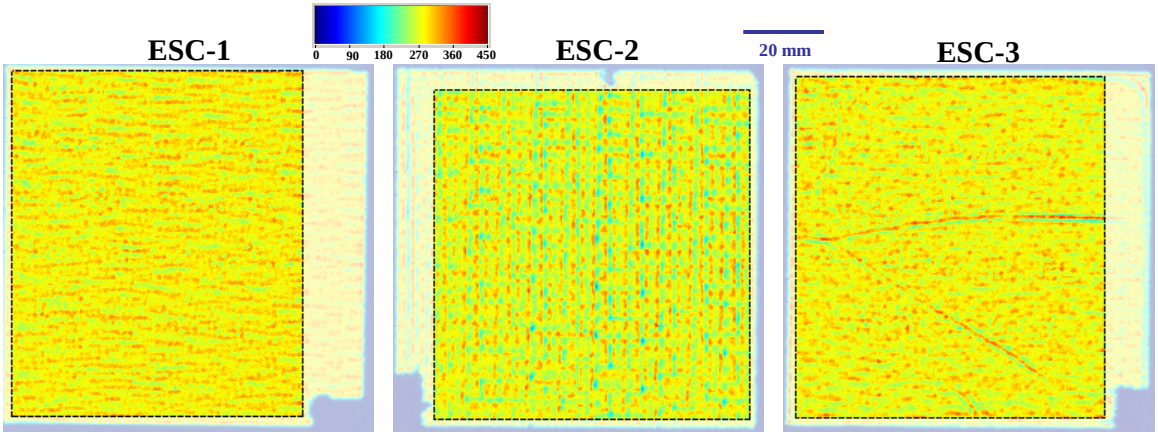

Figure 89. Reflected signal amplitude scans of ESC-1, ESC-2, and ESC-3 at 125 MHz.

5MHz

#	Average (mV)	Standard Deviation (mV)
1	309	5.16
2	317	4.62
3	323	4.08

75MHz

#	Average (mV)	Standard Deviation (mV)
1	688	34.01
2	665	43.84
3	680	40.71

125MHz

#	Average (mV)	Standard Deviation (mV)
1	334	27.31
2	285	36.74
3	315	27.50

Table XLIII. Average and standard deviation amplitude values for ESC samples.

Reflected signal amplitude normalized histogram comparison at 5 MHz showed the amplitude differences in the form of tail regions on the right side of each of the ESC-1 and ESC-3 curves and on the left side of the ESC-2 curve. These histograms are shown in Figure 90. The AUTC values were 520, 442, and 424 for samples ESC-1, ESC-2, and ESC-3, respectively, but these variations reflected little more than surface differences at this low frequency. The regional variations at 75 MHz were also heavily influenced by the patterns. The AUTC values of 453, 762, and 456 for samples ESC-1, ESC-2, and ESC-3, respectively, again provided little insight. These histograms are shown in Figure 91. It wasn't until the evaluation of the 125 MHz normalized histogram curves that some of the variations that were not influenced by the patterns started to show meaningful differences. At this highest frequency, the AUTC values were 1776, 1768, and 1419 for samples ESC-1, ESC-2, and ESC-3, respectively. These histograms are shown in Figure 92. The values indicated that the ESC-3 sample had a significantly narrower distribution than the ESC-1 and ESC-2 which were very acoustically very similar to one another despite the additional post-HIP step and higher properties for ESC-2.

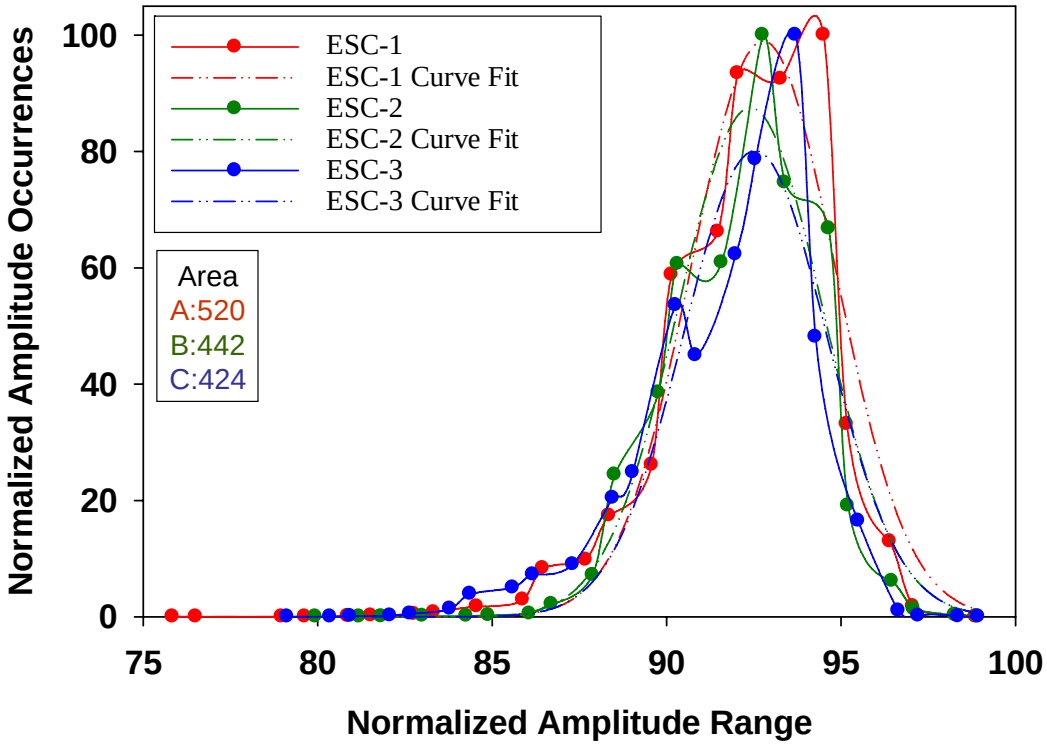

Figure 90. Reflected signal amplitude histogram curves of ESC samples at 5 MHz.

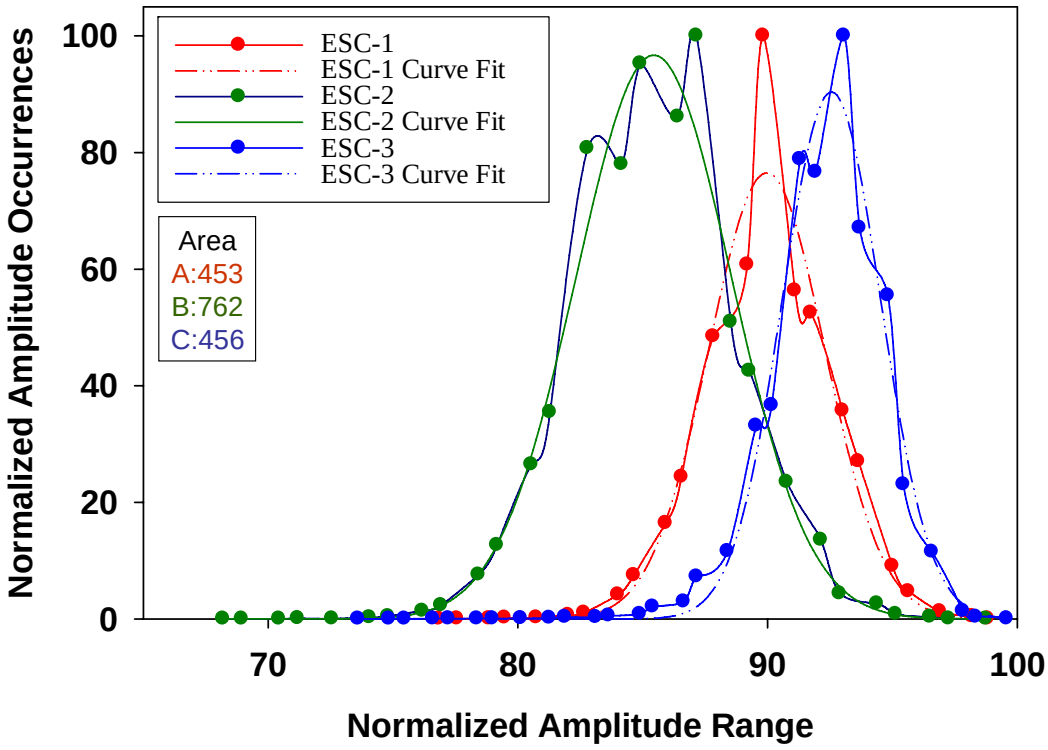

Figure 91. Reflected signal amplitude histogram curves of ESC samples at 75 MHz.

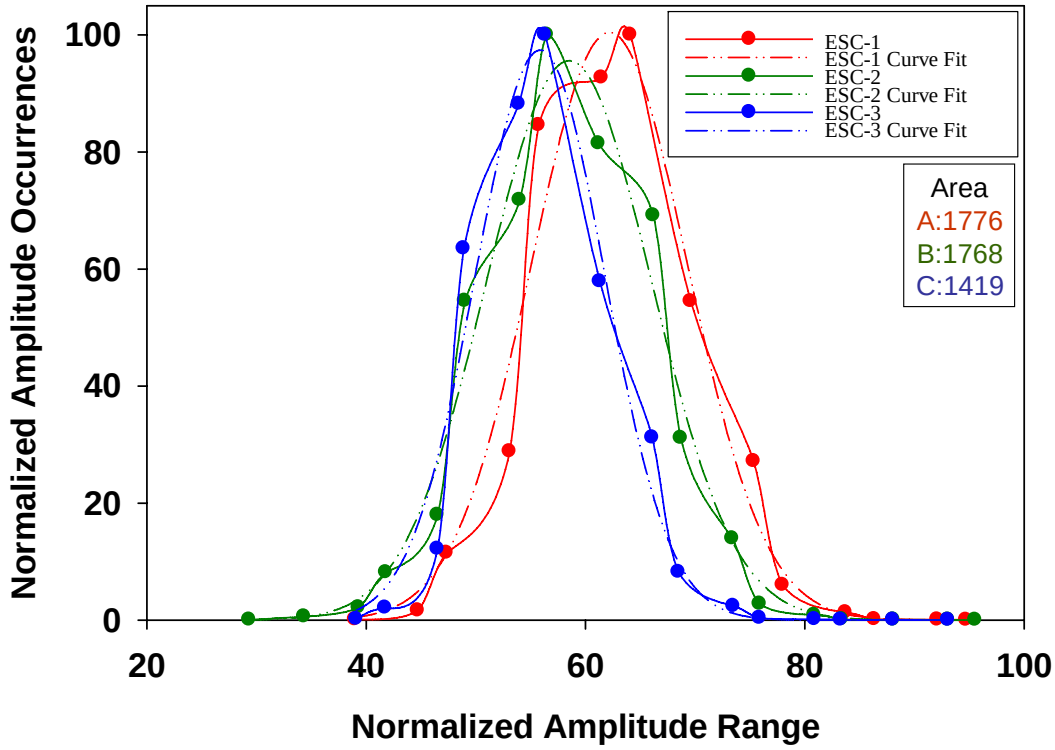

Figure 92. Reflected signal amplitude histogram curves of ESC samples at 125 MHz.

The ballistic data for the three samples were communicated after ultrasound C-scan imaging and quantitative analysis data for the ESC samples were conducted. Both V50 and DOP ballistic testing data which were described in the armor background section were provided. The ESC-1 sample had a V50 value of 625 m/s and a depth of penetration of 27 mm. The ESC-2 sample had a V50 value of 700 m/s and a depth of penetration of 16 mm. The ESC-3 sample had a V50 value of 725 m/s and a depth of penetration of 12 mm. The better armor materials exhibited higher V50 data, meaning that a higher projectile velocity was required to penetrate through half of the thickness of the armor plate. The better armor materials also exhibited lower DOP data, meaning that the projectile did not penetrate as deep into the armor plate under the same ballistic conditions. This showed that the ESC-3 sample had the best ballistic data followed by ESC-2 and ESC-1. These data followed the same trend as the AUTC data, with the most narrow normalized amplitude histogram distribution and smallest AUTC value corresponding to the sample with the highest V50 and lowest depth of penetration. While the ESC-1 and ESC-2 samples also followed this trend, the area values were much more similar to one another than the ballistic data indicated. Despite the fact that the ballistic data were well correlated to the ultrasound data at the highest frequency of 125 MHz, the issue of the influence of the surface patterns still remained. For this reason, a technique was developed to offset the effect of surface inhomogeneities and the quantitative analysis study was conducted again to ensure that the ESC samples followed the ballistic property trends, as was indicated in the initial study.

In order to minimize the effect of surface features without going through additional surface grinding or polishing steps, two separate ultrasound C-scan images

were collected. The bottom surface reflected signal was gated to collect the peak amplitude variations over the selected area, just as in the majority of the ultrasound C-scan image data presented thus far. In addition, a separate scan was run to collect the top surface reflected signal peak amplitude variations without changing the position of the sample. This ensured that the two scanned areas were identical in x and y positions for effective comparison. Both sets of reflected signal amplitude data were imported into Origin Pro 7.0 and converted into matrices so that visual maps could be plotted and contrasted. Any variations from the top surface reflected signal amplitude plot represented surface roughness and surface or near surface inhomogeneities, and these were the critical features that needed to be removed for proper bulk evaluation. Since the ultrasound beam first passed through the top surface before reaching the bulk and eventually the bottom surface of the sample, any features on the top surface that were within the transducer detection limits showed up in the bottom surface reflected signal C-scan image. To offset the top surface features, the top surface reflected signal amplitude values were first divided by the bottom surface reflected signal amplitude values. This difference was averaged to determine a single weighted value to describe the difference between these amplitudes. Since the bottom surface reflected signal amplitude data always had a lower amplitude than the top surface amplitude due to attenuation, the average weighted value was always greater than one. This constant was then multiplied by each bottom surface reflected signal amplitude value so that the majority of the new values would be very similar to the top surface reflected signal amplitude values at matching x and y positions. By subtracting the new values from the original top surface reflected signal amplitude values, most of the values would either cancel out to zero or

result in positive or negative numbers very close to zero. Any resulting values that showed large variations from the new data represented features that were not influenced by the surface features since the majority of the surface features were either completely eliminated or very close to zero. The new amplitude data were plotted with the original x and y positions to observe any variations. This technique was applied to both the 75 MHz and 125 MHz ESC samples to determine if the surface patterns could be offset or eliminated to reveal the true sample features and to determine whether or not the adjusted results followed the ballistic data trends.

The new method was first applied to the 75 MHz reflected signal amplitude C-scan images. Two separate scans were run for each ESC sample, one with the bottom surface reflected signal gated to collect amplitude variations and the other with the top surface reflected signal gated to collect amplitude variations. The top reflected signal amplitude, bottom reflected signal amplitude, and amplitude difference maps from the 75 MHz ultrasound data are shown for each of the ESC sample in Figures 93-95. The top surface scan revealed a heavy pattern that resulted from poor surface grinding and polishing. The top surface reflected signal amplitude data were divided by the bottom surface reflected signal amplitude data to determine the average weighted values. The average weighted values were multiplied by the bottom surface reflected signal amplitude data. The two data columns were next subtracted and the resulting images plotted based on the original x and y positions. The new images were more uniform, as the large amplitude variations were offset. There were still signs of some of the patterns since the top surface effects were often much stronger than the bottom surface features, but the images were drastically improved. A bottom right corner feature in ESC-1 and an upper

middle feature in ESC-2 stood out because they were the result of cracks and pits on the bottom surface of the samples that had no influence on the top surface scans. While these showed the largest differences, more subtle features that were characteristic of previous features detected in SA and ST sintered SiC were also found. These followed no specific patterns and were believed to be representative of the desired critical features that differentiated the three ESC samples from one another. Without applying the amplitude offset method, these features would not have been found.

The same method was applied to the 125 MHz scans. The top surface reflected signal amplitude, bottom surface reflected signal amplitude, and amplitude difference maps from the 125 MHz ultrasound data are shown for each of the ESC sample in Figures 96-98. The most interesting results came from the ESC-3 sample in which distinct lines were detected which extended from one side of the sample to the other and also existed along the perimeter of the sample. At first, these lines were believed to be markings or etchings on the sample surface, but no visual evidence could be found. Another possibility was that these features were the result of a liquid phase sintering-related mechanism, but this would be difficult to ascertain in such a high density sample. In any case, they showed up most clearly in the corrected images. The next step was to perform quantitative histogram analysis on the new adjusted image data to compare to the ballistic data.

For the 75 MHz data, normalized histograms were plotted as shown in Figure 99. The AUTC values were 1449, 1576, and 1152 and the FWHM values 10, 9, and 8 for ESC-1, ESC-2, and ESC-3, respectively. The ESC-1 and ESC-2 AUTC values were much larger and showed broader distributions as compared to the ESC-3 AUTC value.

The FWHM trend also showed the most narrow distribution for sample ESC-3. These trends correlated to the ballistic data in which sample ESC-3 showed the best performance. The trends also followed much better than the previous ESC AUTC data which appeared to be greatly influence by surface features rather than the critical bulk features. For the 125 MHz data shown in Figure 100, all of the samples followed the ballistic trends. The AUTC values were 1280, 1269, and 1191 and the FWHM values 13, 13, and 12 for ESC-1, ESC-2, and ESC-3, respectively. The values were more similar to each other, as was the case for all of the 125 MHz data shown up to this point since more subtle microstructural variations were detected at this highest frequency. The quantitative ultrasound data also followed the ballistic trend, just as it did before the correction was applied. The narrowest distribution which resulted in the lowest AUTC and FWHM values can from ESC-3, which also showed the highest V50 value of 725 m/s and the lowest DOP value of 12 mm. As the ballistic performance decreased for ESC-2 and ESC-1, the distribution of reflected signal amplitude values increased, resulting in higher AUTC and FWHM values. While these trends must be directly tested by correlating quantitative ultrasound data to ballistic data, the intial results appeared to be a good indication that a correlation does exist.

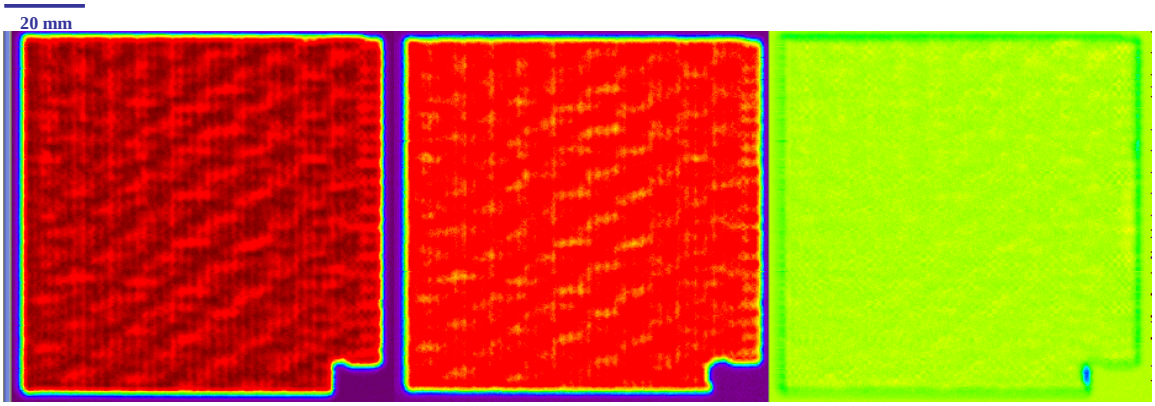

Sample ESC-1 Top **Sample ESC-1 Bottom** **Sample ESC-1 Difference**

Figure 93. Surface roughness adjusted images of ESC-1 sample at 75 MHz.

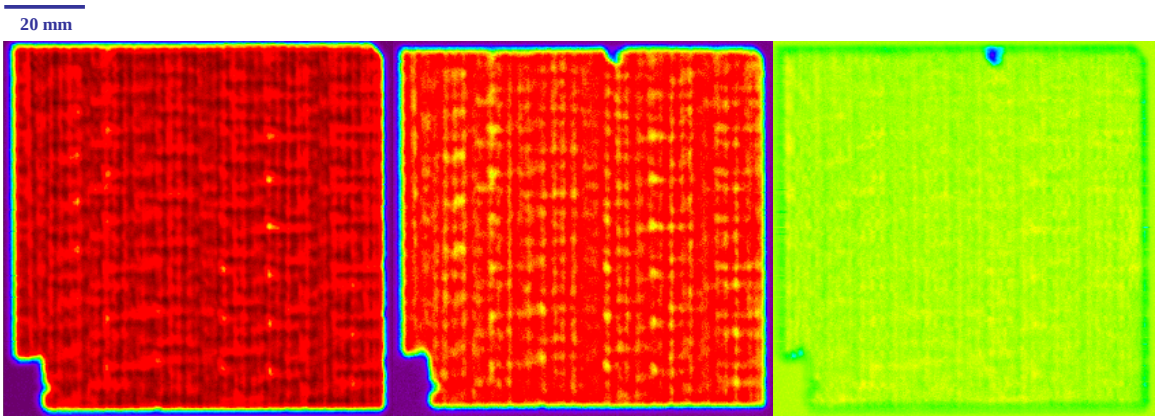

Sample ESC-2 Top **Sample ESC-2 Bottom** **Sample ESC-2 Difference**

Figure 94. Surface roughness adjusted images of ESC-2 sample at 75 MHz.

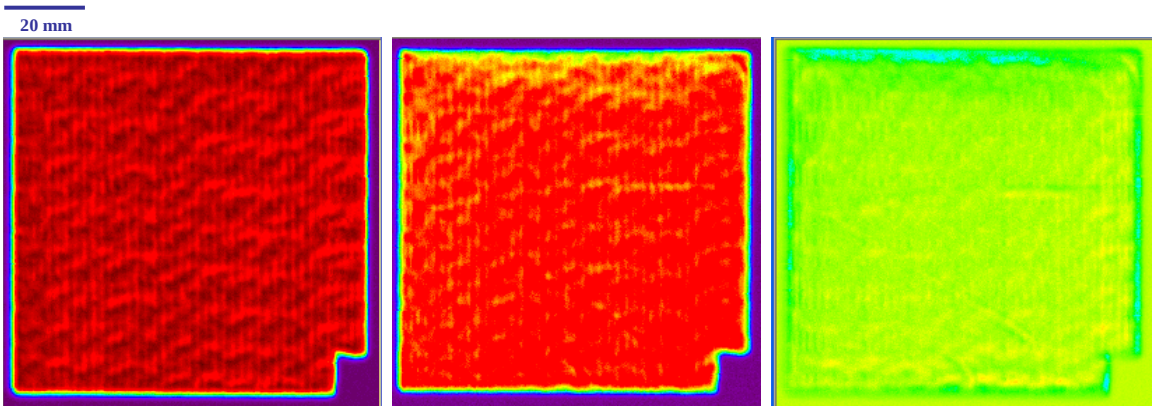

Sample ESC-3 Top **Sample ESC-3 Bottom** **Sample ESC-3 Difference**

Figure 95. Surface roughness adjusted images of ESC-3 sample at 75 MHz.

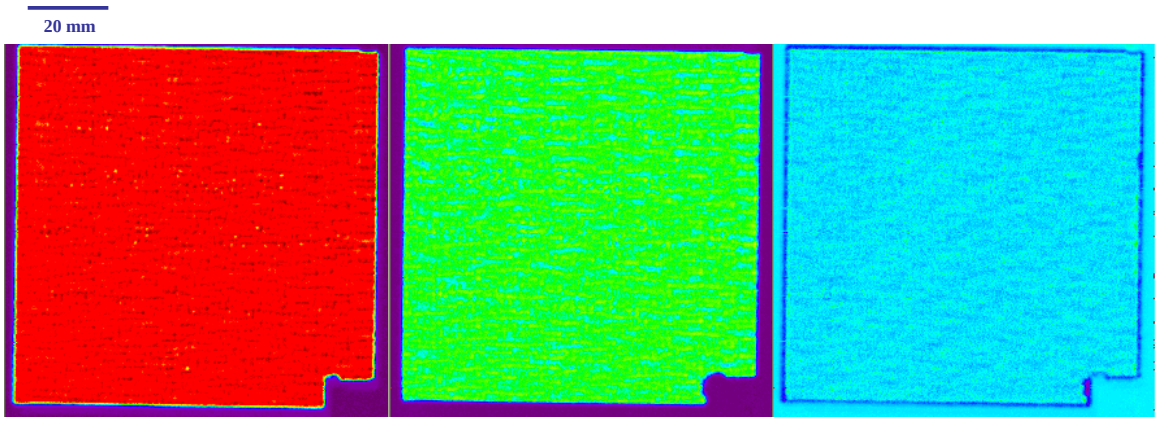

Sample ESC-1 Top **Sample ESC-1 Bottom** **Sample ESC-1 Difference**

Figure 96. Surface roughness adjusted images of ESC-1 sample at 125 MHz.

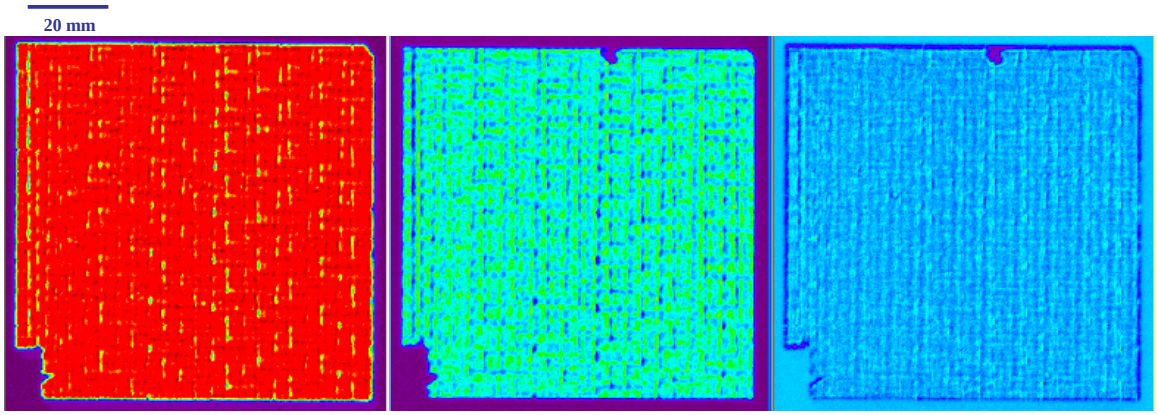

Sample ESC-2 Top **Sample ESC-2 Bottom** **Sample ESC-2 Difference**

Figure 97. Surface roughness adjusted images of ESC-2 sample at 125 MHz.

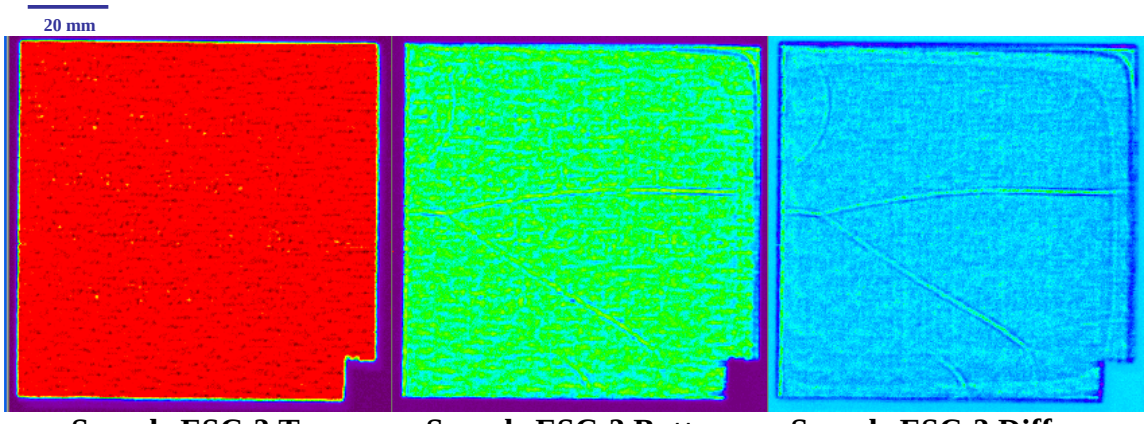

Sample ESC-3 Top **Sample ESC-3 Bottom** **Sample ESC-3 Difference**

Figure 98. Surface roughness adjusted images of ESC-3 sample at 125 MHz.

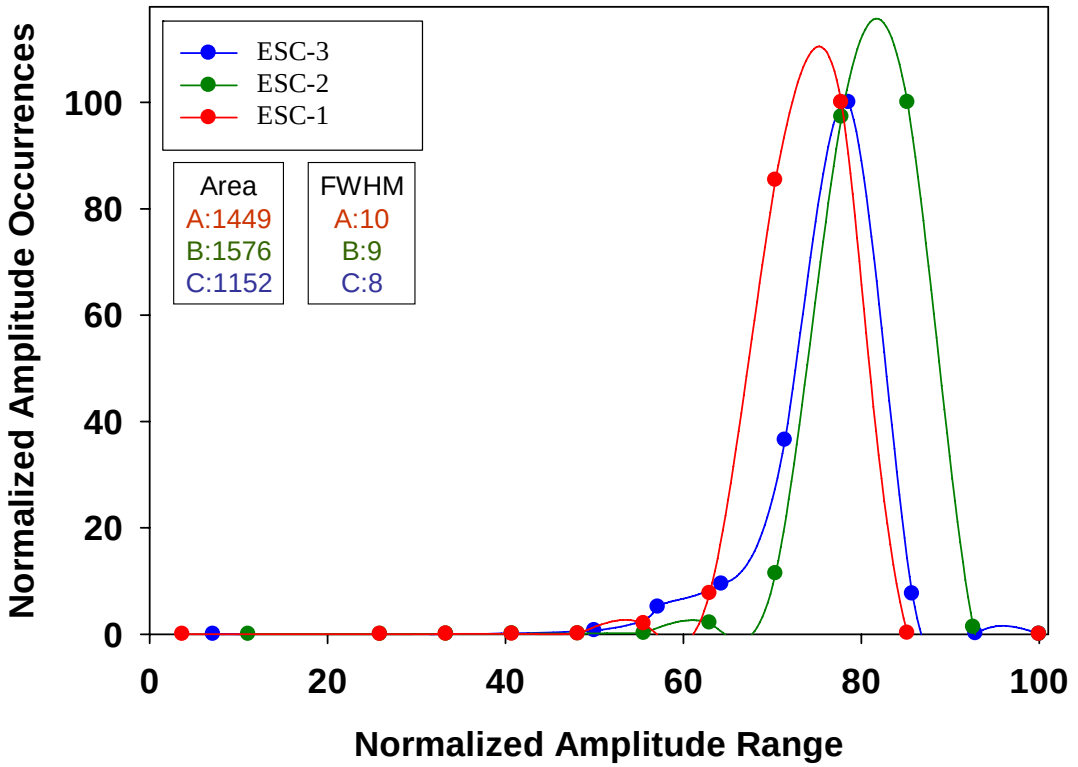

Figure 99. Surface roughness adjusted histogram curves for ESC samples at 75 MHz.

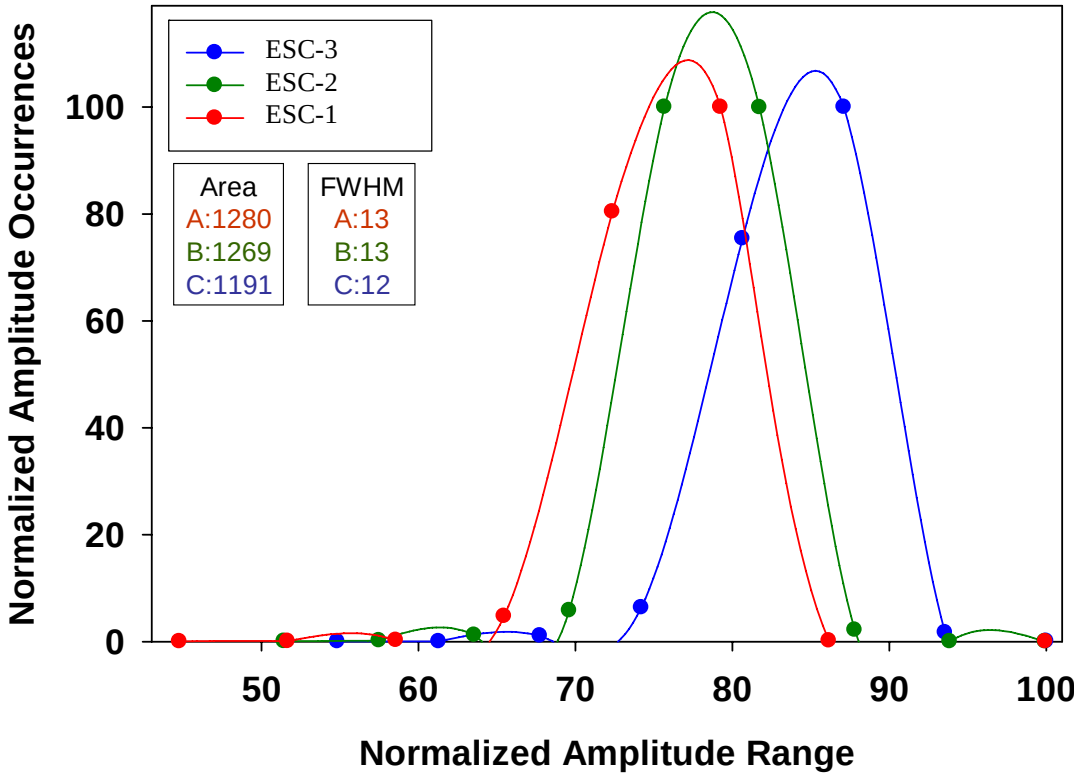

Figure 100. Surface roughness adjusted histogram curves for ESC samples at 125 MHz.

5.7. Fabricated Test Specimens

While commercial armor ceramic SiC ultrasound C-scan imaging and quantitative analysis have exclusively been discussed up to this point, there was also a need to evaluate similar ceramic materials fabricated with specific features. These samples contained bulk features of specific sizes and concentrations which were placed in specific locations. The fabricated samples were ultrasonically tested to gauge ultrasound transducer and system parameters and to develop new techniques for improving quantitative analysis of commercially manufactured materials.

5.7.1. Bulk Reflected Signal Amplitude C-Scan Imaging

For reflected signal amplitude C-scan imaging, the two common gating methods that have been described so far have included top surface and bottom surface reflected signal amplitude imaging. In top surface amplitude imaging, the reflected signal from the top surface of the sample was gated, and the amplitude of the peak was monitored to evaluate the effect of attenuation on or near the surface of the sample. In the most commonly used bottom surface amplitude imaging, the reflected signal from the bottom surface was gated, and the changes in amplitude over the sample area were collected to identify internal defects based on an increase in attenuation. In both of these cases, a decrease in the amplitude of the signal indicated the presence of inhomogeneities and defects in the sample bulk. Another technique, referred to as bulk C-scan imaging, operated on the opposite principle. Instead of gating the reflections from the top and bottom surfaces, the region between the top and bottom signals was gated. When the ultrasound transducer was placed over a fully dense area of the sample, there was no signal over the gated bulk region since there were minimal changes in the material as

shown in Figure 101. If the transducer was placed over an area containing one or more inhomogeneities with different acoustic impedance values from the matrix, there was a characteristic reflected signal from each defect in the inspected region as shown in Figure 102. In this case, the presence of a reflected signal signified a bulk sample feature, and the amplitude of the reflected signal indicated the degree of acoustic impedance mismatch to the matrix. Instead of detecting a loss from the gated signal to identify features, as was the case with top and bottom surface reflected signal imaging, in bulk C-scan imaging, the gain of a reflected signal enable detection of a feature.

5.7.2. Partially Sintered SiC Fabricated Test Specimens

As a first attempt at examining samples with defects, SiC was partially sintered to determine the effect of a high degree of attenuation on the identification of large pores and pore distributions. Samples were fabricated by dry pressing SiC powder and partially sintered to 1300^{o}C to form extremely low density, highly porous samples [124]. Since these samples were only 55 to 60 volume percent dense, they were believed to be suitable for studying pore distribution in a partially sintered body via ultrasound. However, due to the high pore volume in these samples, the signal intensity was greatly reduced at transducer frequencies higher than 10 MHz. While the top surface reflected signal was detectable at frequencies greater than 10 MHz, the high degree of attenuation prevented detection of the bottom surface reflected signal. For this reason, transducers with frequencies of 2-10 MHz were used to perform the scans.

Bulk reflected signal amplitude scans were performed on the partially sintered SiC samples at 10 MHz, as shown in Figure 103. In these scans, high reflected signal amplitudes representing pores within the sample bulk were evident, in contrast to lower

reflected signal amplitude features from the rest of the SiC matrix. As different gated regions of the bulk of the sample were evaluated, different pore distributions were identified at different sample thicknesses. In this way, the gates were used to map the locations of pores at selected thicknesses throughout the sample. While the partially sintered SiC samples provided valuable results as far as detectability of larger pores and pore distributions, the fabrication of these samples did not enable any control over the size and location of the defects that were produced. Although this scanning method was demonstrated effectively with the partially sintered SiC samples, it was not able to directly confirm the integrity of the ultrasound system. For this reason, other types of fabricated samples were developed in which defect size, location, and distribution could be controlled.

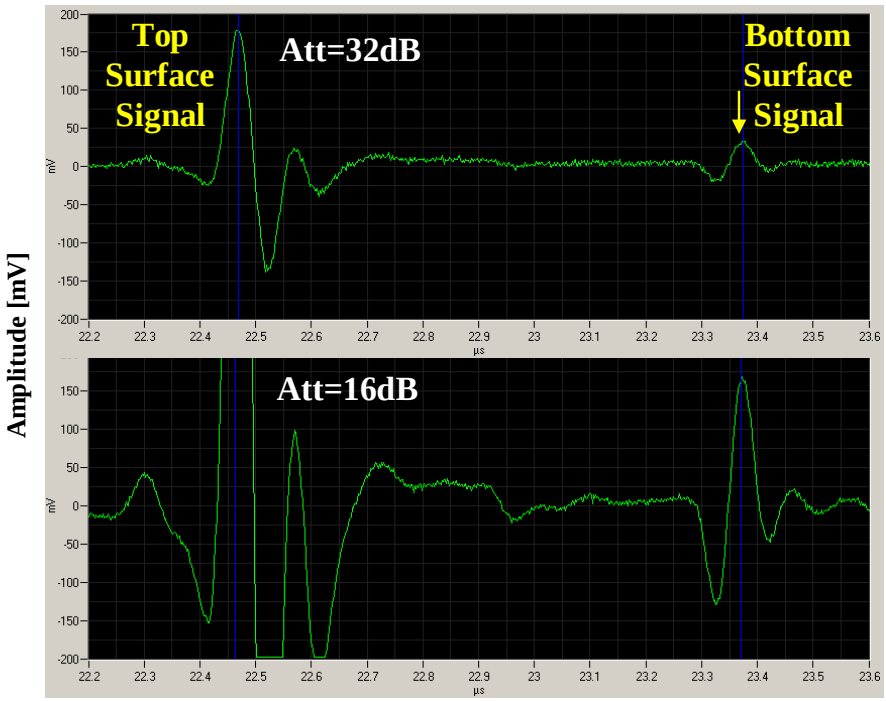

Figure 101. Reflected signals from high density region of defect engineered sample at receiver attenuation values of 32 dB and 16 dB.

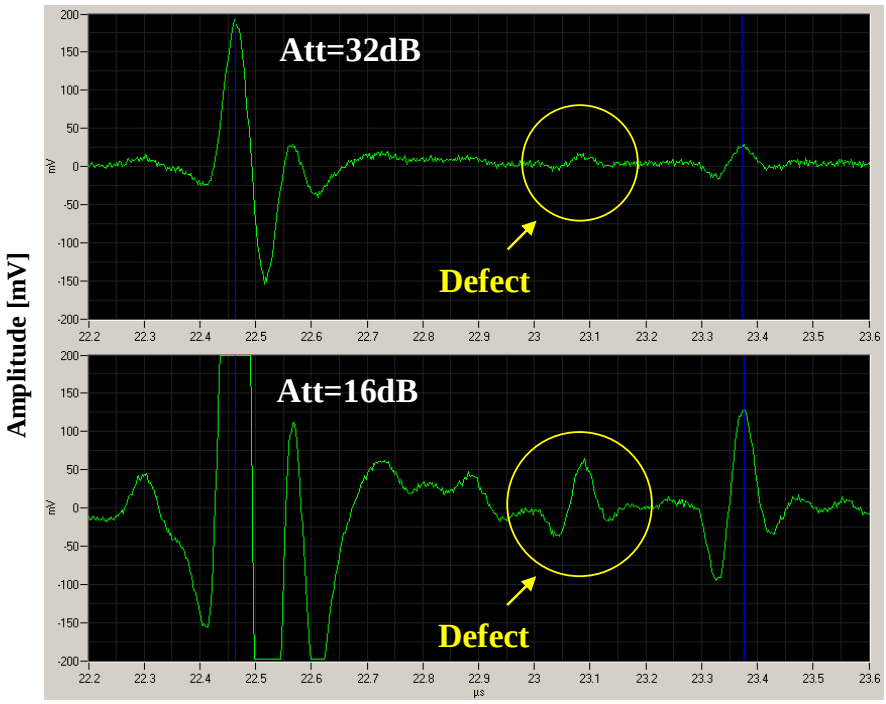

Figure 102. Reflected signals from pore in defect engineered sample at receiver attenuation values of 32 dB and 16 dB.

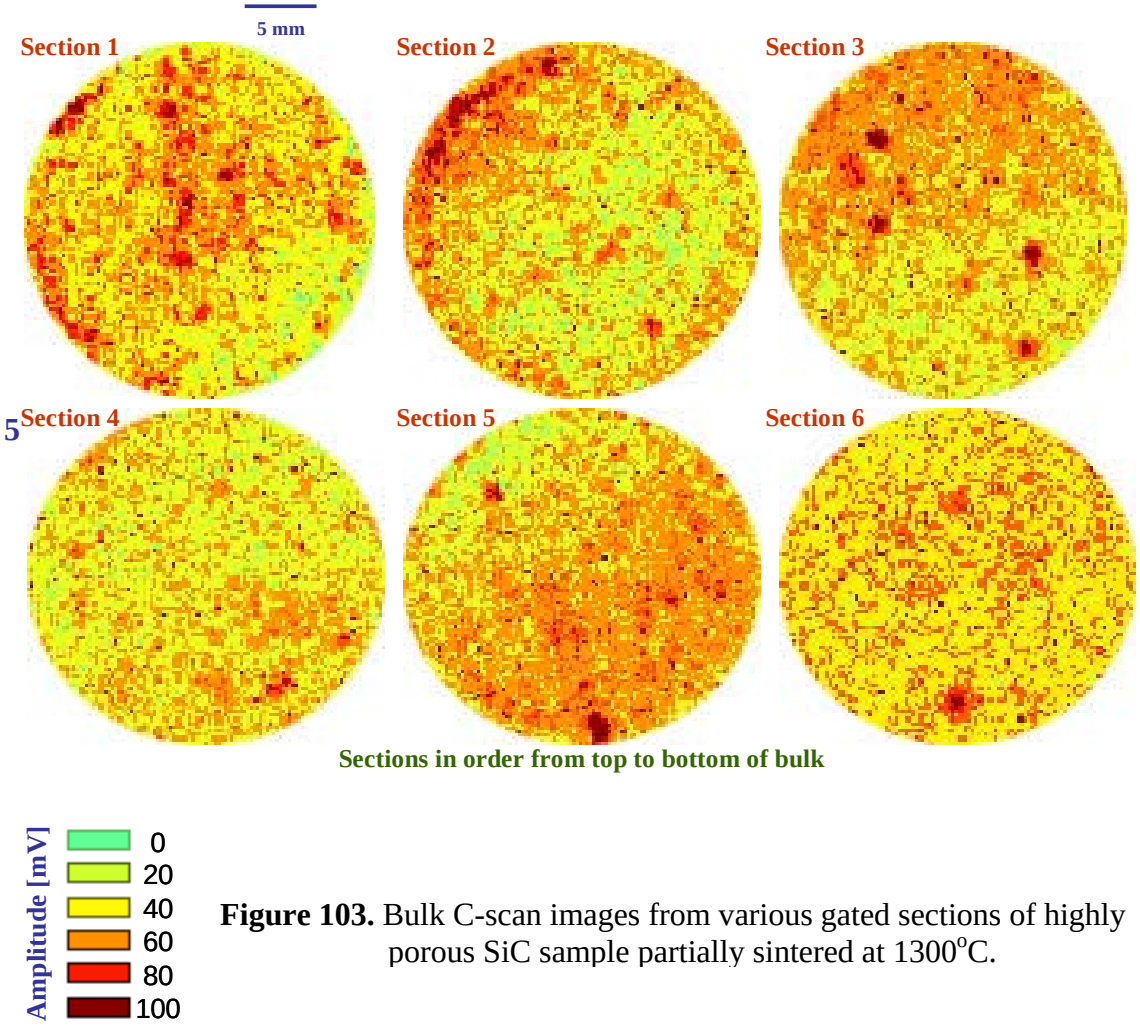

Figure 103. Bulk C-scan images from various gated sections of highly porous SiC sample partially sintered at 1300^{o}C.

5.7.3. Al_2O_3 and Polymer Sphere Fabricated Test Specimens

The next type of fabricated sample utilized a high density bulk matrix rather than a partially sintered matrix. Polymer spheres of known size were embedded in the matrix during the pressing step, and the burn out of these spheres during sintering resulted in controlled porosity. Two different sizes of hollow polymer spheres were obtained from Akzo Nobel [125] in order to fabricate bulk defects of various sizes in known locations. The first set of spheres, referred to as Sphere Type A, was reported to have a particle size between 20 and 40 μm, and the second set of spheres, referred to as Sphere Type B, was reported to have a particle size between 60 and 90 μm. The spheres were characterized by scanning electron microscopy (SEM) and thermal gravimetric analysis (TGA) in order to confirm sphere size distributions and to determine the temperature at which the spheres would burn out of the matrix. Figure 104 shows SEM micrographs of Sphere Type A and Sphere Type B. Both micrographs demonstrated the spherical morphology and confirmed the sizes of the hollow polymer spheres. The micrograph of Sphere Type A showed a majority of spheres within the 15 to 25 μm size range, with several spheres as small as 5 μm and several spheres as large as 35 μm. The micrograph of Sphere Type B showed a majority of spheres within the 60 to 75 μm size range, with several spheres as small as 50 μm and several as large as 90 μm. TGA data were collected up to 700^{o}C for Sphere Type A and Sphere Type B to study the temperature at which there was no longer any weight fraction percent of spheres remaining, as shown in Figure 105. For Sphere Type A, the weight fraction percent reached a minimum at ~475^{o}C. For Sphere Type B, the weight fraction percent reached a minimum at ~525^{o}C. This study showed that the

polymer spheres would burn out at these respective temperatures, resulting in bulk spherical pores at these locations.

To test the ability of the ultrasound C-scan system to detect specific defects placed within a bulk armor material sample, Al_2O_3 samples containing the Type B hollow polymer spheres were fabricated. Twenty five grams of Alcoa A16SG [126] alumina powder, which is a grade commonly utilized in ceramic armor, was used to fabricate the sample using a one-inch diameter cylindrical die. Half of the powder was first added to the die, and a controlled amount of polymer spheres was dispersed over the powder bed. Since the polymer spheres were in the μm-size range, they had to be added and controlled very carefully so they could be properly dispersed within the center of the powder bed. The remaining amount of A16SG powder was then added to fill the die, and the sample was dry pressed at a pressure of 100 MPa. The green samples were sintered at 1600^oC for three hours in order to reach full densification. During sintering, a baseline sample referred to as AO was also fired under the same conditions for comparison. The samples went through a series of polishing steps, with the final step utilizing a 125-grit diamond wheel to provide flat, parallel surfaces before ultrasound evaluation.

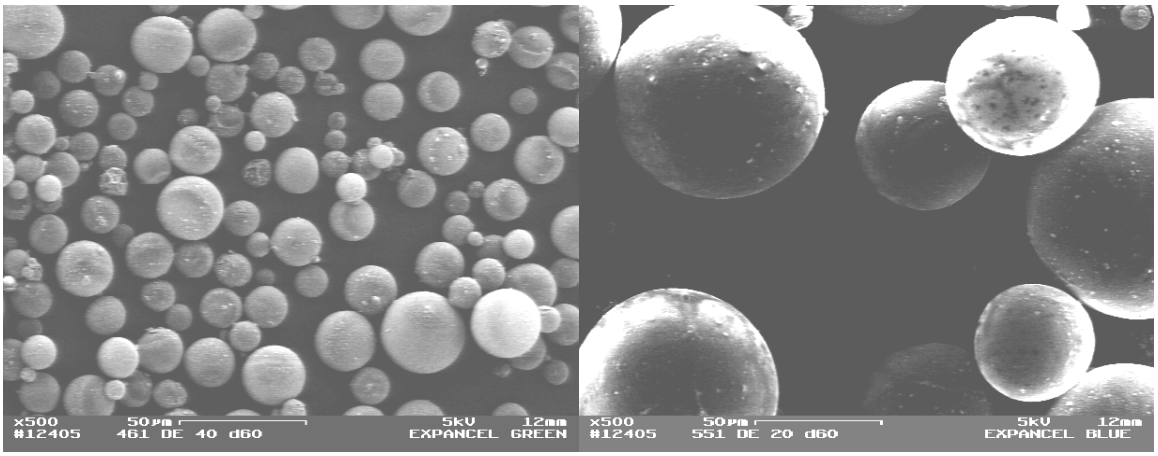

Figure 104. SEM micrographs of polymer sphere types A (left) and B (right).

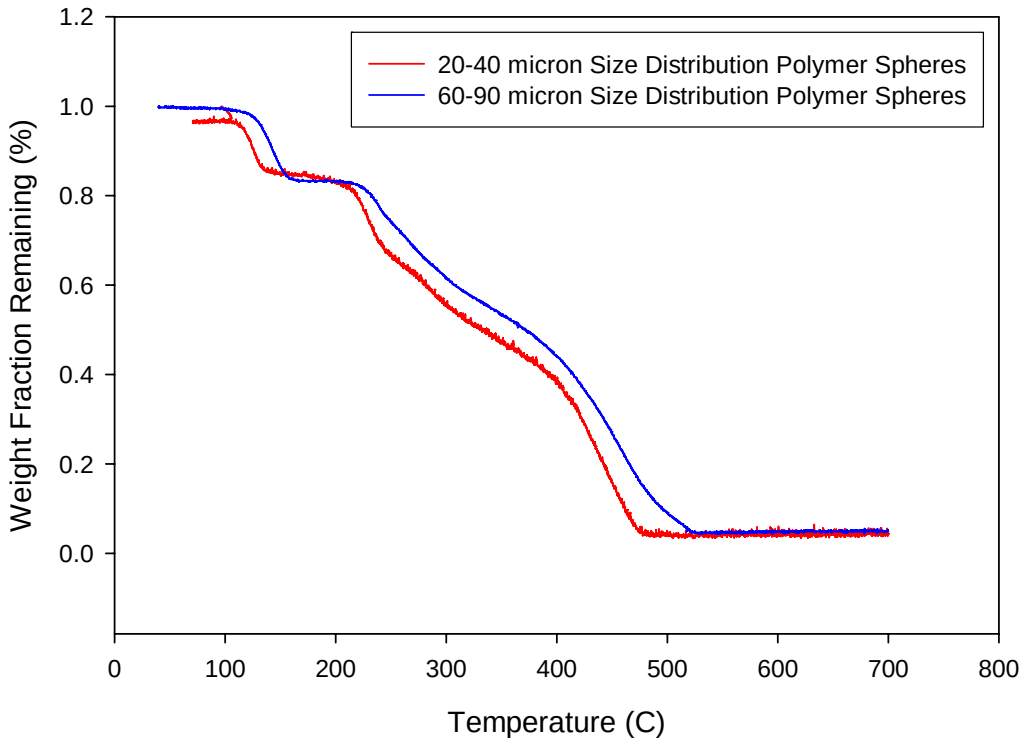

Figure 105. TGA analysis of sphere types A (left) and B (right).

One of the resulting fabricated Al_2O_3 samples that utilized Type B spheres, denoted as AO-EXP, was scanned using a 10 MHz longitudinal immersion transducer. First, the top and bottom surface reflected signals were identified, and a total of five different scans were run over five separate gated regions. First, the top surface reflected signal was gated so that the variation in reflected signal amplitude could be collected over the surface and near surface of the sample. For the top surface reflected signal scan, the amplitude distribution was very uniform, with amplitude changes over a very small range as evident in Figure 106. This was the expected result for the polished top surface of the sample. Next, the bottom surface reflected signal was gated, demonstrating a significant number of amplitude variations throughout the bulk of the sample. The C-scan image revealed two low amplitude lines extending from the perimeter toward the center of the sample which were believed to be radial cracks. While there were no indications of cracking on the surface of the sample, internal cracks may have occurred during sintering due to the addition of the polymer sphere second phase. Low amplitude circular features were also observed in the bottom surface reflected signal C-scan image. These features were believed to show evidence of the spherical pores from the burn out of polymer spheres as shown in Figure 106. These larger low amplitude circular regions appeared to be characteristic of agglomerates of polymer spheres that formed much larger pores within the matrix.

The next three gated regions were set up to conduct bulk C-scan imaging. The first gate was set in the upper region of the bulk, closest to the top surface reflected signal. The second gate was set directly in the center of the bulk. The third gate was set in the lower region of the bulk, closest to the bottom surface reflected signal. The gated

regions are shown in the A-scan of the AO-EXP sample in Figure 106. For these scans, any change in acoustic impedance between the Al_2O_3 bulk material and a spherical pore, for example, would result in a reflected signal with an amplitude representative of the degree of difference from the matrix. In this case, a large difference in acoustic impedance from the presence of a pore would result in higher intensity reflected signal amplitude. As mentioned previously, instead of a loss in reflected signal from the pore, which would be the case for top and bottom surface C-scan images, the bulk C-scan images would result in a gain in reflected signal amplitude. Figure 106 shows the three gated bulk C-scan images from an alumina sample containing bulk pores formed from the burn out of Type B Spheres (60-90 μm). The upper bulk scan showed a distribution of high reflected signal amplitude regions within that thickness of the sample. The middle bulk scan showed even more high amplitude variations in a different distribution than the upper bulk region. The lower bulk scan showed yet another distribution of high reflected signal amplitudes throughout the thickness gated toward the bottom of the sample. In the lower bulk region scan, the high amplitude region at the bottom right seemed to indicate that the bottom surface signal entered into the gate. This explained the saturation of the signal over the given amplitude range. The high amplitude features in the bulk C-scan images were believed to be the fabricated spherical pores from the burn out of polymer spheres at ~525^{o}C because they show the greatest amplitude difference and, therefore the greatest change in acoustic impedance, as compared to the Al_2O_3 matrix. They were also characteristic of the expected pore sizes, shapes, and locations within the bulk.

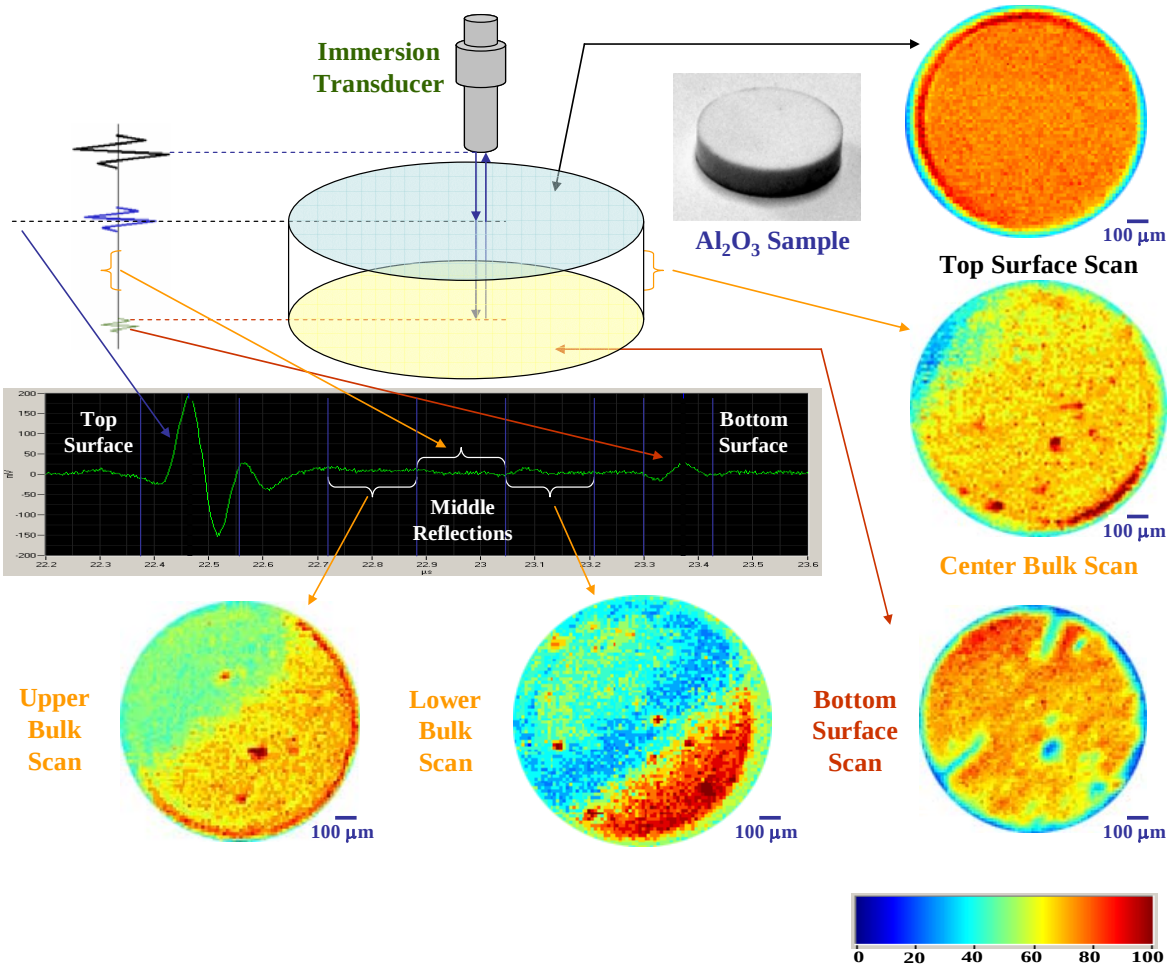

Figure 106. Top, bottom, and bulk reflected signal amplitude C-scan images from defect engineered Al_2O_3 sample containing polymer spheres.

Quantitative histogram analysis was performed on the reflected signal amplitude C-scan images to compare the top and bottom surface scans to one another and the three bulk scans to one another. The normalized amplitude histograms from the top and bottom surface reflected signal data are shown in Figure 107. For the top surface reflected signal, the distribution of amplitudes was narrow, which was expected for the polished surface. In contrast, the bottom surface reflected signal had a much broader distribution at a lower normalized amplitude range. The broadening of the curve was characteristic of the presence of the fabricated low amplitude pores that were embedded in the bulk and the lower normalized amplitude range was characteristic of lower amplitude reflected signals as the ultrasound beam was transmitted through the sample. A tail region was also observed on the left side of the bottom surface normalized histogram curve which was representative of the lowest amplitude pores and cracks. The AUTC and FWHM data supported these trends, as the top surface curve had a lower AUTC of 693 and FWHM of 6 as compared to the higher AUTC of 1557 and FWHM of 12 for the bottom surface histogram curve. The normalized amplitude histograms from the bulk regions are shown in Figure 108. These histogram curves were generally characterized by lower normalized amplitude ranges in which any tails on the right side, or higher amplitude side, of the curve were critical since these cumulative features represented bulk defects. The upper bulk region had a bimodal distribution characteristic of the two distinct amplitude regions over the C-scan image while a small peak on the right side indicated the presence of pores. The middle bulk region was more homogeneous and showed a smaller tail on the right side of the curve. Since the bottom surface reflected signal appeared to enter part of the gate, the tail region on the right side

of the curve for the lower bulk region had an uncharacteristically high tail. The AUTC values were 2174, 1542, and 1578 and the FWHM values 24, 15, and 11 for the upper, middle, and lower bulk regions, respectively. However, it appeared as though the histogram curve shapes and quantitative data were dominated by large regions of varying amplitude rather than the individual embedded defects. The bimodal distribution in the upper bulk scan and the large tail in the lower bulk region were indicative of these effects and this dictated the AUTC and FWHM values. The bulk C-scan image analysis could also be conducted over smaller gated regions and focused more on the tail areas to extract additional data for sample comparison.

To confirm that the detected defects were the result of the fabricated pores, a cross-section of sample AO-EXP was cut in an attempt to locate any spherical pores within the dense alumina matrix, and the region was examined using SEM. Figure 109 shows a micrograph displaying one of the spherical pores that was found in the sample. The pore was approximately 20 μm in diameter as compared to the 60-90 μm diameters of the added polymer spheres. The smaller diameter was the result of either shrinkage during sintering or the fact that the cross-section may not have been cut directly through the center of the pore. Since the low density polymer spheres were very difficult to disperse in the bulk Al_2O_3 matrix, the defects that were observed in the scans were believed to be agglomerates of a multitude of spheres that burned out to form larger pores. In either case, the SEM micrograph did support the fact that spherical pores were successfully fabricated in the Al_2O_3 matrix.

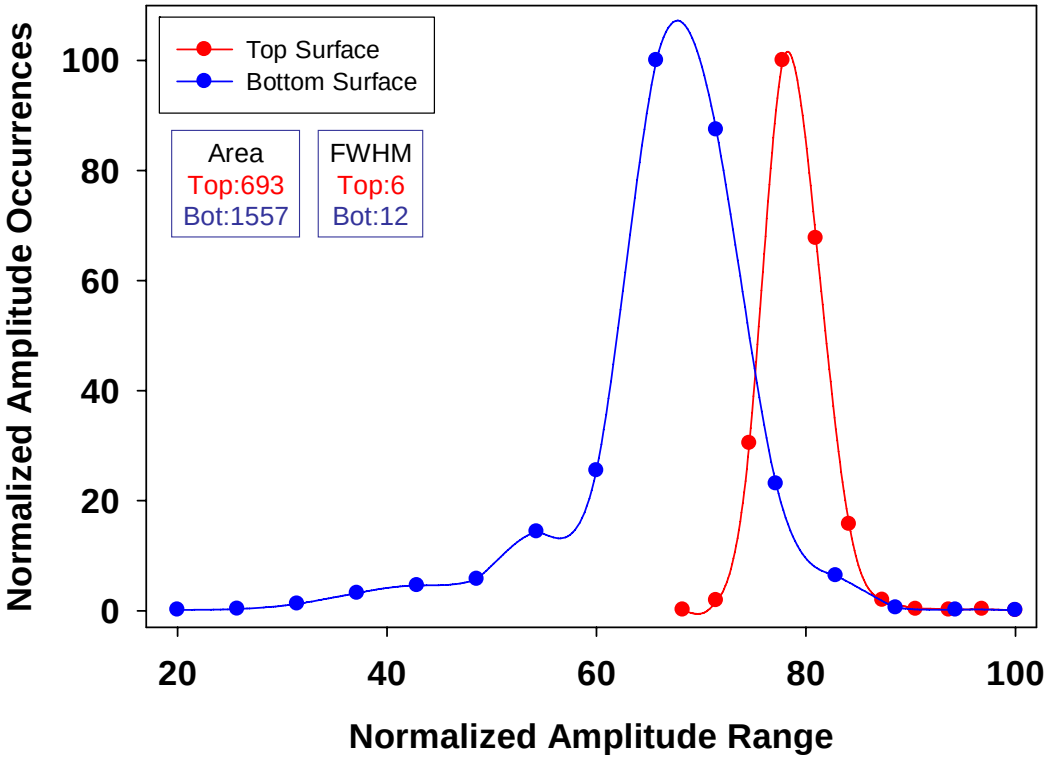

Figure 107. Top and bottom reflected signal amplitude histogram curves of AO-EXP sample at 10 MHz.

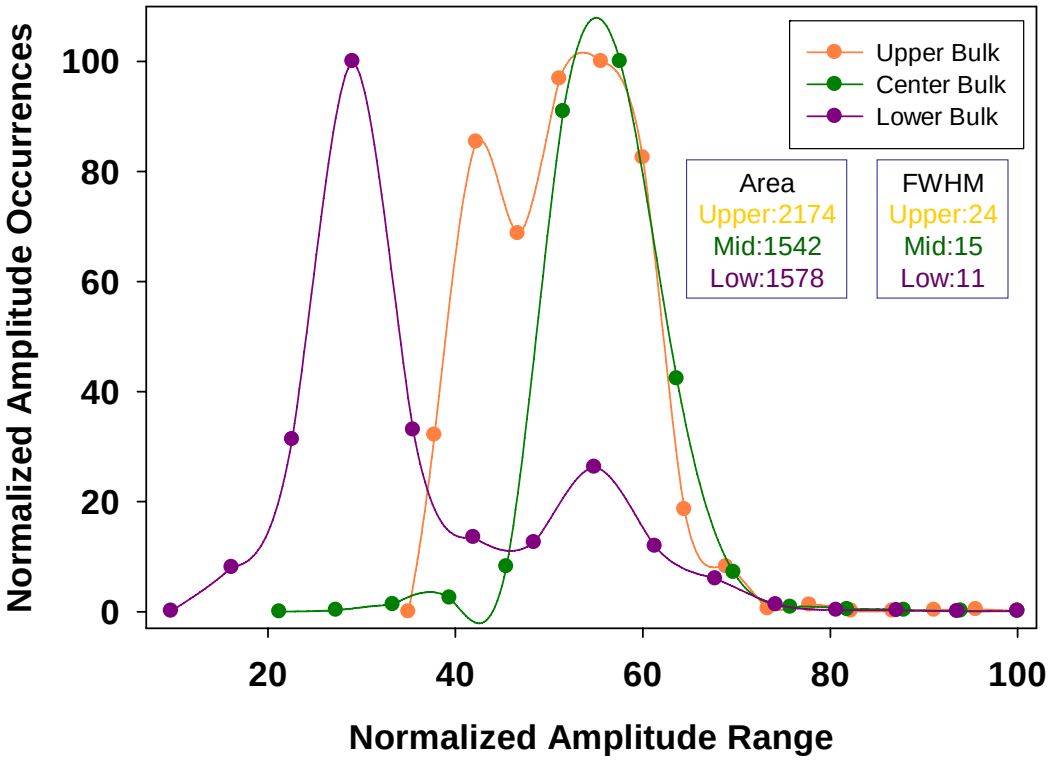

Figure 108. Upper, middle, and bulk reflected signal amplitude histogram curves of AO-EXP sample at 10 MHz.

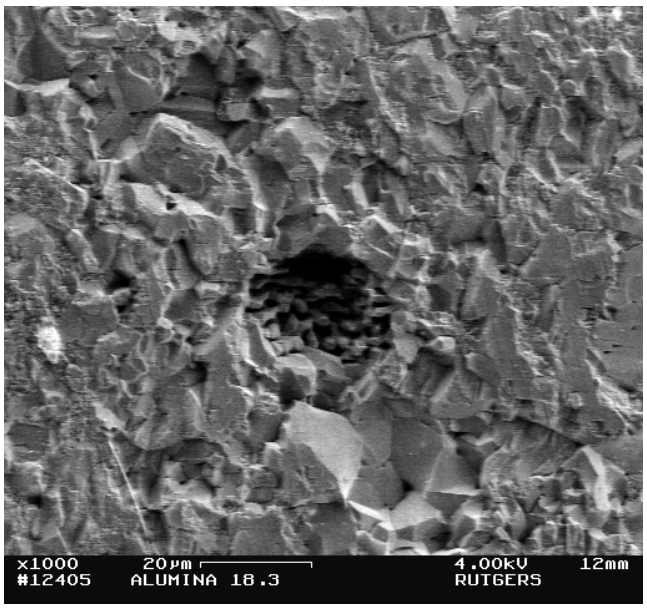

Figure 109. SEM micrograph of spherical pore from cross section of sample AO-EXP.

While initial fabrication of the samples involved randomly pressing the polymer spheres into the center of the bulk, various masking and placement techniques were also used to demonstrate control over placing spheres of a chosen size into desired locations. In these cases, two types of masks were developed so that the polymer spheres could be placed in specific patterns within the bulk of each sample. The first mask was cut in the shape of an "X" pattern while the second was cut in the shape of an "ru" pattern. These masks were used during the polymer sphere addition step after half of the Al_2O_3 powder was added to the die. The goal was to place polymer spheres in this layer only where the mask was cut so that the desired pattern of spheres could be formed. After applying the polymer spheres, the rest of the powder was added, the powder compact formed, and the green sample fired. Top surface, bottom surface, and bulk reflected signal amplitude scans were performed on these fabricated samples at 10 MHz to determine the success of creating the desired patterns.

The first sample that was scanned and evaluated was the sample with the "X" pattern, referred to as AO-X. The top and bottom reflected signal amplitude scans demonstrated the effectiveness of the technique as shown in Figure 110. While the top surface showed some degree of variation in amplitude, the bottom surface showed a low amplitude pattern in the shape of the "X". While the shape of the "X" could be distinguished, the upper part of the shape was filled more clearly due to non-uniform placement of the polymer spheres. The shape was also slightly warped during the pressing and densification steps. Another observation was that individual defects could not be distinguished, since the addition of the spheres to the pattern resulted in an even higher degree of agglomeration that the randomly placed spheres from sample AO-EXP.

Three bulk C-scan images were collected to show the distribution of fabricated bulk features at different thicknesses. In the center of sample AO-X, several defects stood out including one concentrated region of high amplitude and several that were located at the points of the "X" shape. This showed that within this thickness slice of the bulk, only a few of the defects that comprised the "X" were present. By looking at the lower bulk scans, more of the defects contributing to the "X" were detected. This demonstrated that although the defects were deposited in the center of the bulk, the dry pressing step compressed them below the center of the sample, as more defects were found in the lower bulk regions. Since the bulk scans were more uniform that for sample AO-X, the normalized amplitude histogram curves were more representative of the bulk of the sample. According to quantitative analysis results in Figure 111, the top and bottom surface scans again showed a more uniform amplitude distribution for the top surface as compared to the bottom surface, which showed large regions from both the low amplitude "X" pattern as well as a higher amplitude region at the bottom right. The AUTC values of 1881 and 3491 and the FWHM values of 20 and 25 for the top and bottom surface scans, respectively, demonstrated these trends. The bulk scans from the middle and lower regions were also compared in Figure 112. At first, the same bulk comparison used for the AO-X sample was also used. While the bulk histogram curves were more comparable than for sample AO-X, the AUTC values of 1419, 854, and 1153 and FWHM values of 14, 8, and 10 for the middle, low, and lower full scan areas, respectively, were dominated by the low amplitude regions rather than the high amplitude defects. For this reason, the tail areas were instead evaluated. The tail region comparison showed AUTC values of 48, 65, and 70 for the middle, low, and lower bulk scans,

respectively. These values were directly related to the respective features and showed an increase in the number of defects as scans were conducted on deeper sample regions. This followed the same trend that was observed in the scans, as the “X” pattern showed more defects in the lower bulk regions. The tail area evaluation was much more effective than the full area since only the critical defect areas were targeted.

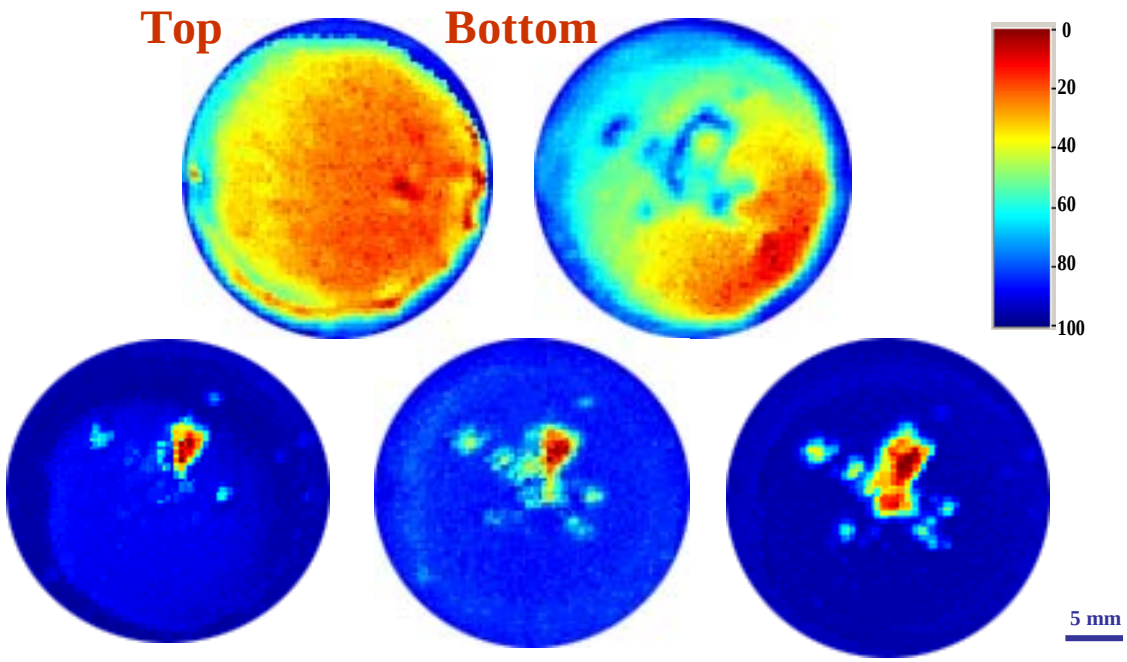

Figure 110. Reflected signal amplitude top, bottom, and bulk scans of sample AO-X.

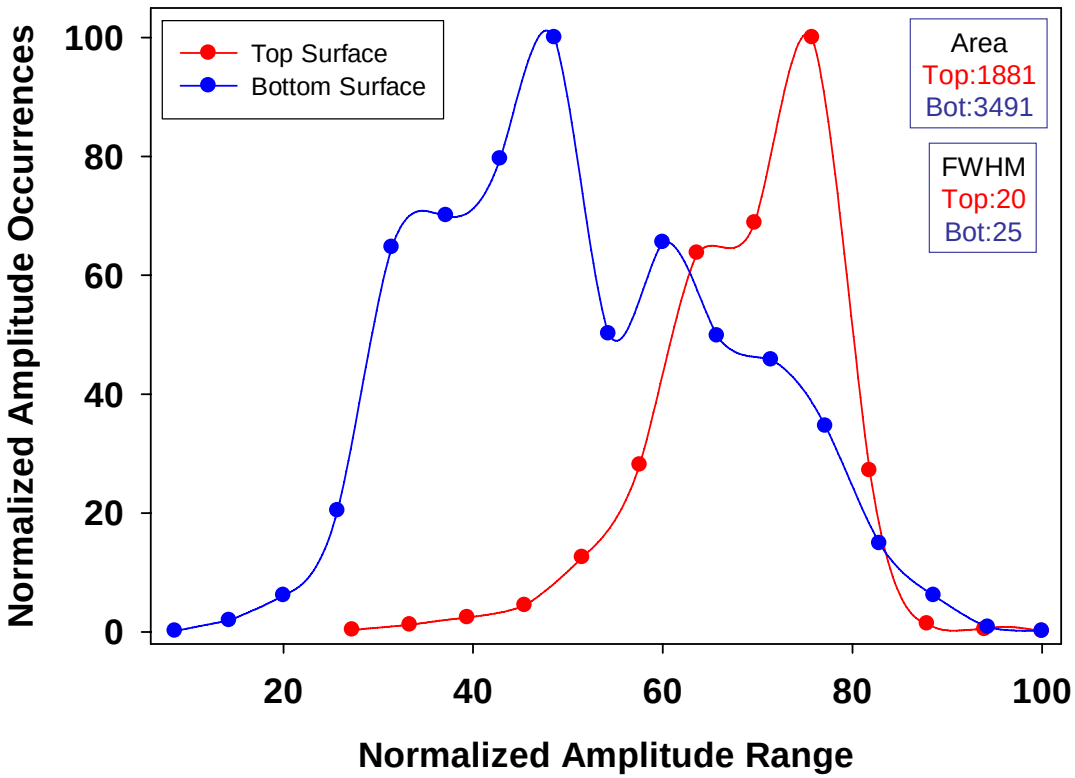

Figure 111. Top and bottom reflected signal amplitude histogram curves of AO-X sample at 10 MHz.

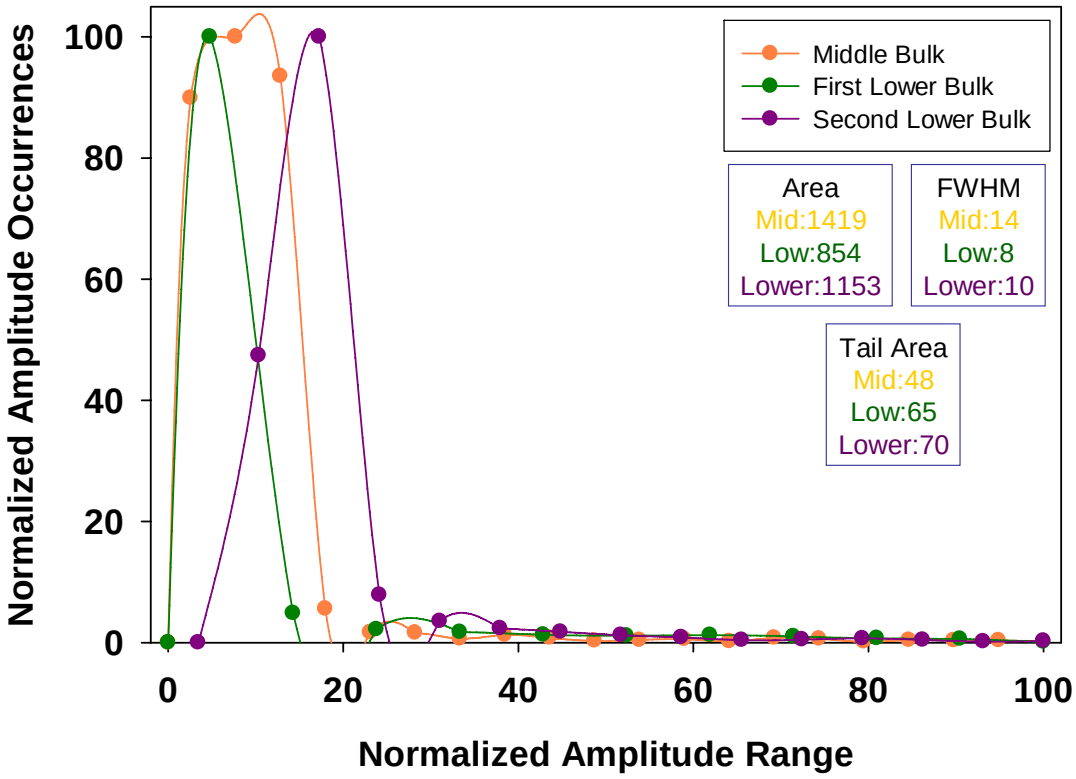

Figure 112. Bulk reflected signal amplitude histogram curves of AO-X sample at 10 MHz.

The same evaluation was conducted on the sample with the “ru” pattern, referred to as AO-RU, as shown in Figure 113. Just as in the AO-X sample, the top surface scan showed no indication of the fabricated pores while the bottom surface scan showed a low amplitude pattern in the shape of an “ru”. While the “r” stood out clearly, uneven dispersion during polymer sphere addition caused the shape of the “u” to change. Three bulk scans were collected for the middle region and two of the lower bulk regions. In the middle bulk scan, the upper tip of the “u” showed a high amplitude region, and the shape of the “u” could be made out while the “r” was not distinguishable. In the first lower bulk region, the defects in the shape of the “r” were present. In the second lower bulk region, the defects from the bottom region of the “r” showed a higher amplitude while the defects from the “u” began to fade. These trends demonstrated the different depths at which the defects within the “ru” were present, most likely due to pressing and warping during densification. The quantitative histogram data in Figure 114 were consistent for top and bottom surface scan evaluation, as the top surface showed a more narrow distribution with an AUTC value of 1572 and FWHM of 13 as compared to the broader distribution and higher AUTC of 2648 and FWHM of 23. For the bulk comparison in Figure 115, since it was established that the lower amplitude regions that covered the majority of the scans were not critical, the comparison of the tail area values was emphasized. The AUTC values were 11 for the middle bulk region, 44 for the first lower bulk region, and 30 for the lowest bulk region. This was consistent with the bulk C-scan images which showed only the defects from the “u” in the middle region. The first lower bulk region appeared to show more defects from both the “r” and the “u” while the lowest bulk region showed fewer and lower amplitude defects from the “u”. The bulk region tail

comparisons for samples AO-X and AO-RU supported the expected trends from observing the bulk C-scan images.

In a final quantitative evaluation, the bottom surface reflected signal amplitude histogram curves were compared for the baseline AO sample, the AO-EXP sample with random addition of polymer spheres, the AO-X sample, and the AO-RU sample as shown in Figure 116. This histogram comparison was similar to the common bottom surface reflected signal amplitude comparisons made for the majority of the commercial samples up to this point. The baseline AO sample histogram curve was a normal curve with a narrow distribution that was similar to a Gaussian distribution, and the corresponding AUTC value was 1275 with an FWHM value of 10. The next broadest curve was the AO-EXP sample which was the first sample in which polymer spheres were added to create pores within the bulk. This sample had a higher AUTC of 1557 and a higher FWHM of 12 as compared to the baseline. Sample AO-X and AO-RU had the highest amount of added polymer spheres to accommodate the defect patterns that were created, and this resulted in the highest AUTC and FWHM values among the four samples as well. Sample AO-X had an AUTC of 3089 and an FHWM of 15 while sample AO-RU had an AUTC of 2669 and an FWHM value of 21. The higher AUTC and FWHM values represented the broadest histogram curves from the samples with the largest numbers of fabricated pores while the baseline Al_2O_3 sample had the most narrow distribution and lowest AUTC and FWHM values. Ultrasound evaluation of the fabricated Al_2O_3 samples demonstrated the ability to nondestructively detect features of known location within a high material velocity bulk matrix.

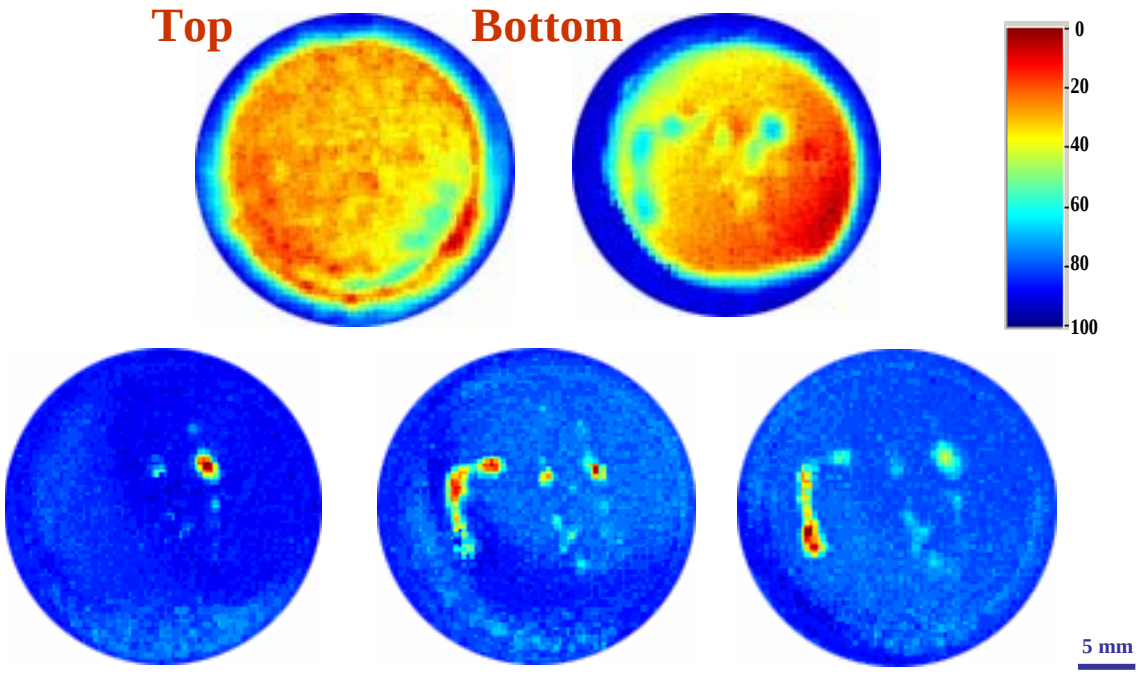

Figure 113. Reflected signal amplitude top, bottom, and bulk scans of sample AO-RU.

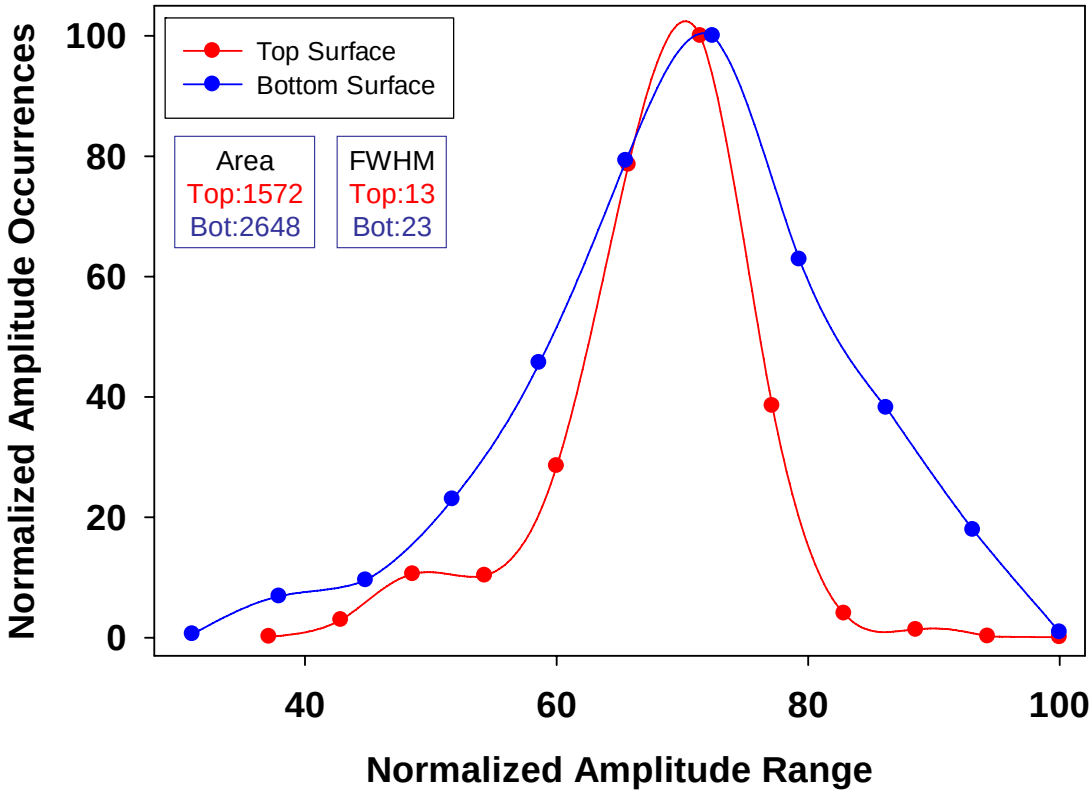

Figure 114. Top and bottom reflected signal amplitude histogram curves of AO-RU sample at 10 MHz.

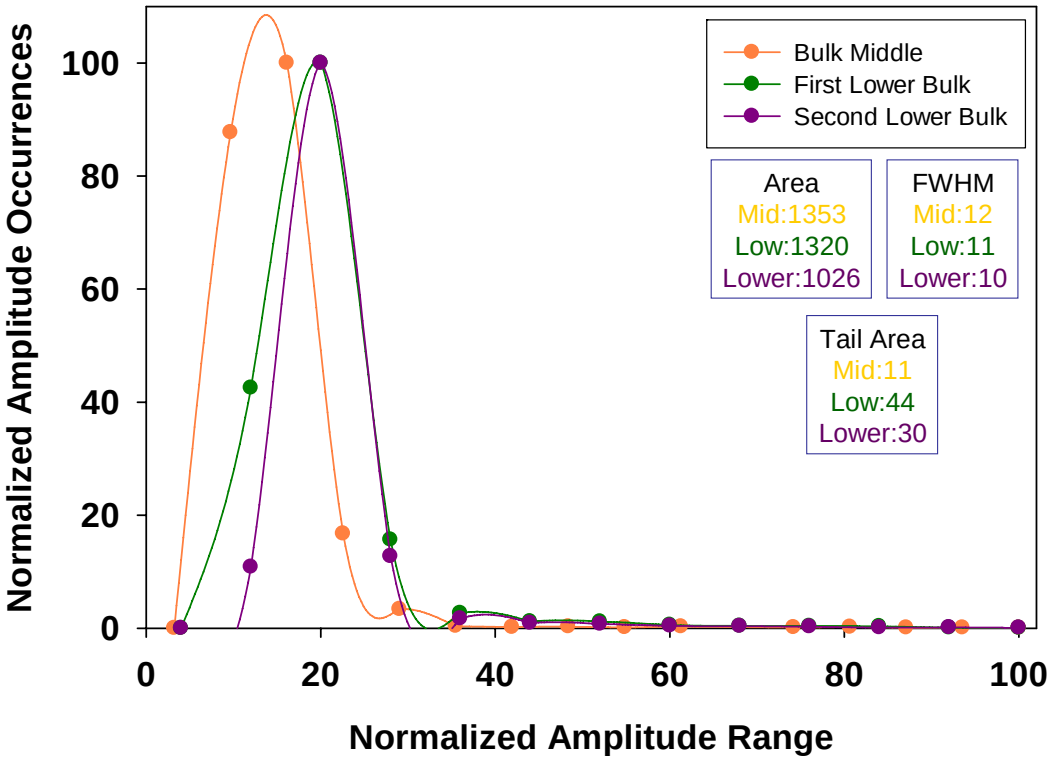

Figure 115. Bulk reflected signal amplitude histogram curves of AO-RU sample at 10 MHz.

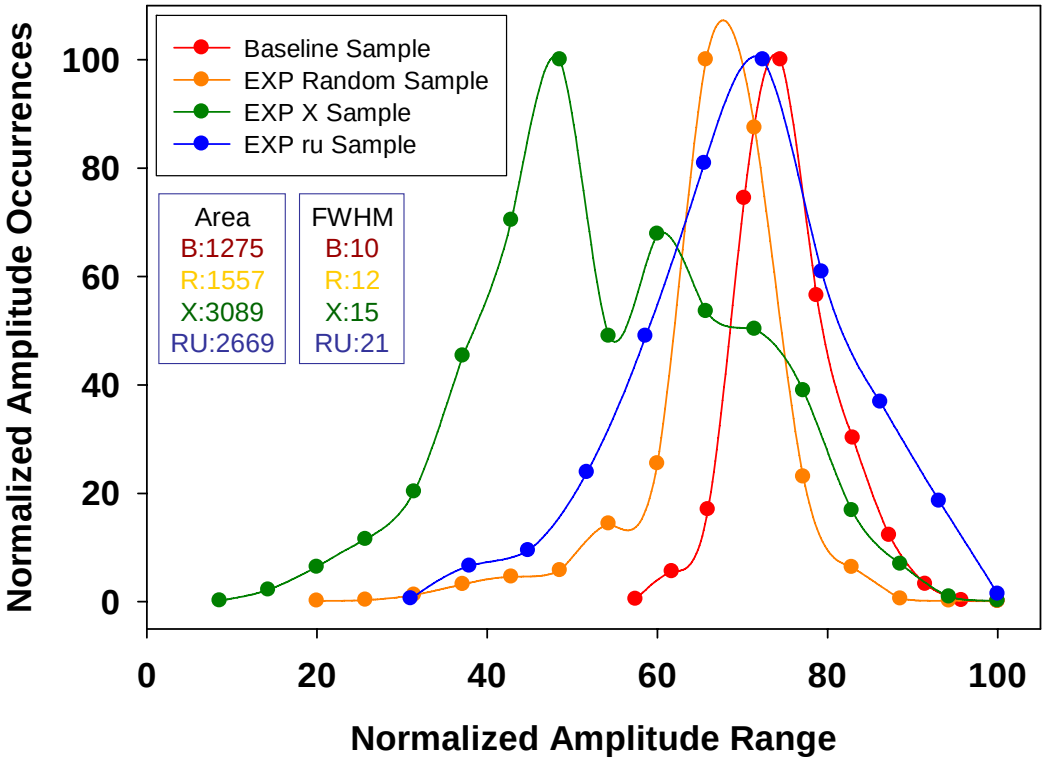

Figure 116. Bottom surface reflected signal amplitude histogram curve comparison of AO-EXP, AO-X, and AO-RU samples at 10 MHz.

5.7.4. Epoxy and WC Sphere Fabricated Test Specimens

In contrast to the addition of a small number of defects to the bulk of a sample, another set of fabricated samples introduced larger features that were more representative of anomalous defects. In this case, one of the considerations was the transparency of the material so that effective optical imaging could be performed to visually evaluate the defects within the matrix in addition to performing ultrasound evaluation. Bulk amplitude C-scan imaging was performed on fabricated two-phase samples composed of an epoxy matrix and tungsten carbide (WC) spheres of various sizes. Sample EPX-1 contained WC spheres with average diameters of ~0.84 mm. Sample EPX-2 contained WC spheres with average diameters of ~1.35 mm. Sample EPX-3 contained WC spheres with average diameters of ~2.08 mm. For each sample, WC spheres were added during the epoxy curing step. Two spheres were specifically placed in the center of each sample. Since the samples were transparent, they were also imaged by optical microscopy and compared to the ultrasound C-scan imaging results. An optical micrograph comparison of the baseline and large WC sphere samples is shown in Figure 117. A magnified optical micrograph comparison of the baseline, small WC sphere, medium WC sphere, and large WC sphere samples is shown in Figure 118. The inhomogeneous features in the baseline sample were due to trapped air during the curing stage. Bottom surface reflected signal amplitude C-scan images were collected at 10 MHz, as shown in Figure 119, and the presence of the WC spheres was identified as a loss in the bottom surface signal in each case. Bulk amplitude C-scan imaging was also performed at 10 MHz as shown in Figure 120, and the presence of spheres was indicated by reflected signals in the bulk, characteristic of each sphere. All of the detectable

spheres and air bubbles were located by this method since each one resulted in a unique reflection due to the high acoustic impedance mismatch with the epoxy matrix. Their locations were confirmed by optical microscopy. In addition to detecting small amounts of fabricated pores in an Al_2O_3 matrix as shown in the previous study, the bulk C-scan technique also proved to be a good way to detect the second phase of the two-phase system.

A separate sample referred to as EPX-4 was fabricated to include a number of WC spheres at various depths within the epoxy. An optical micrograph of the WC spheres in the bulk of this sample is shown in Figure 121. This sample was analyzed at 10 MHz using the bulk amplitude C-scan technique to study the depth of detected features. In the first scan, the entire bulk region of the sample was gated over 6 μs, so all of the internal features were identified as shown in Figure 121. In the next series of scans in Figure 122, 1 μs increments were gated for each scan from the top to the bottom of the sample to determine the depth of each WC sphere. The bulk amplitude C-scan series showed the progression of spheres in terms of depth through the sample. The defects closer to the top appeared in the first few μs while there were only two spheres that could be identified towards the bottom of the sample. The amplitude changes were also observed for a single feature over several scans. For a large feature that was more prominently within one μs slice, the amplitude was higher for that feature. If part of the feature was also in the next μs slice, it appeared in the same position but with a lower amplitude. This technique was a useful way of determining the size and position of defects within the bulk of a sample.

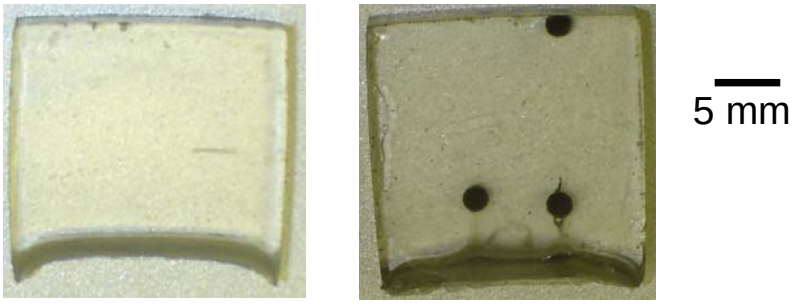

Figure 117. Optical micrograph images of baseline epoxy and epoxy sample with large embedded WC spheres.

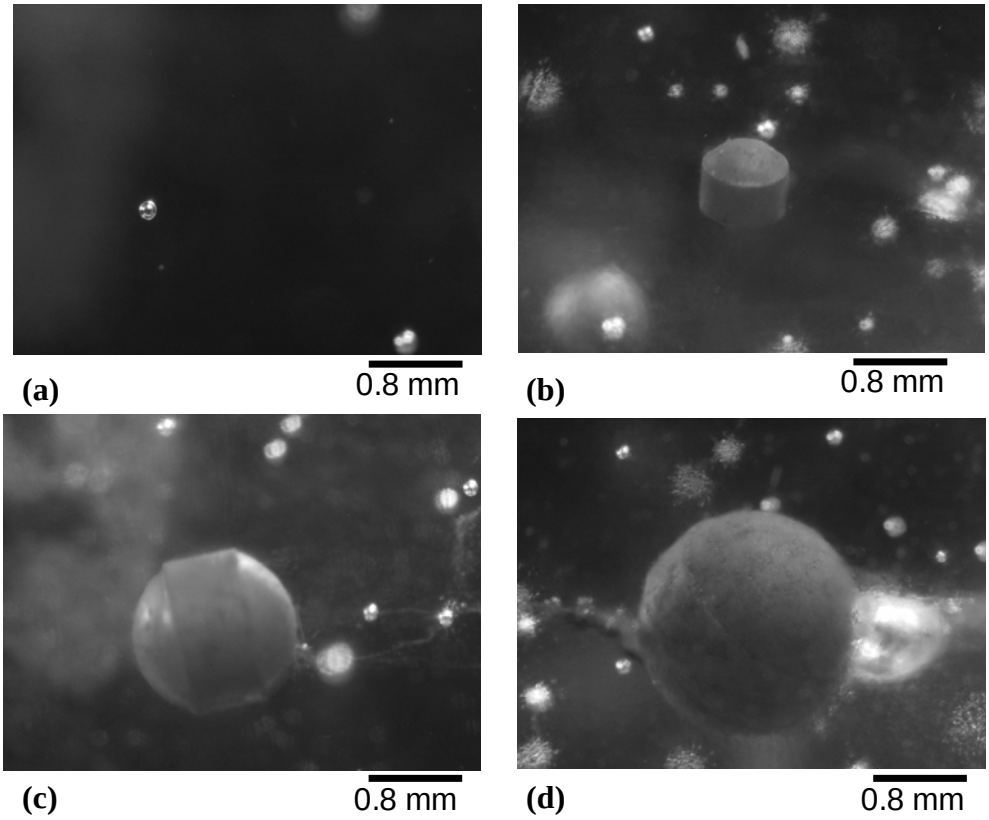

Figure 118. Magnified optical images of (a) baseline epoxy (b) EPX-1 (c) EPX-2 (d) EPX-3 samples with embedded WC spheres.

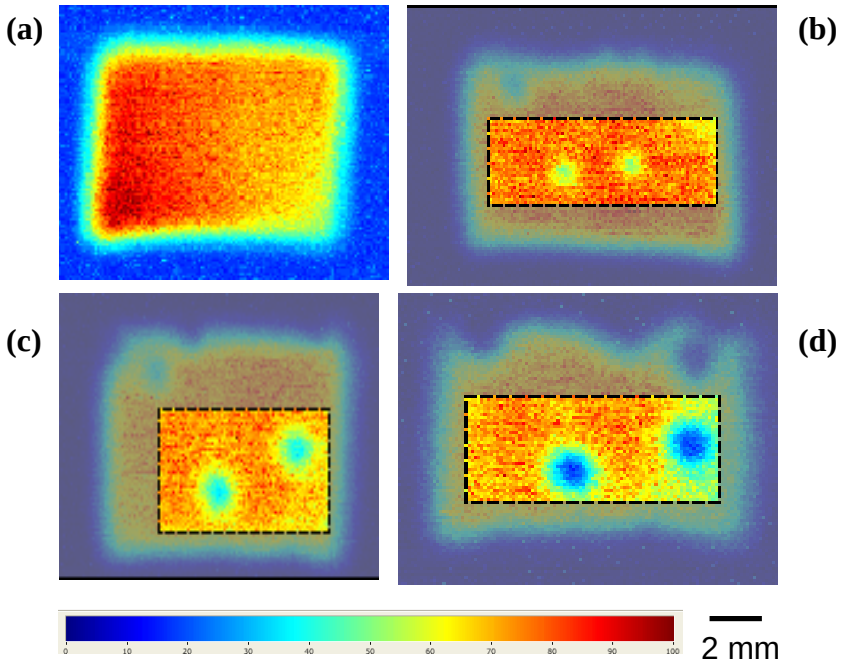

Figure 119. Amplitude C-scan images of (a) baseline epoxy (b) EPX-1 (c) EPX-2 (d) EPX-3 samples with embedded WC spheres.

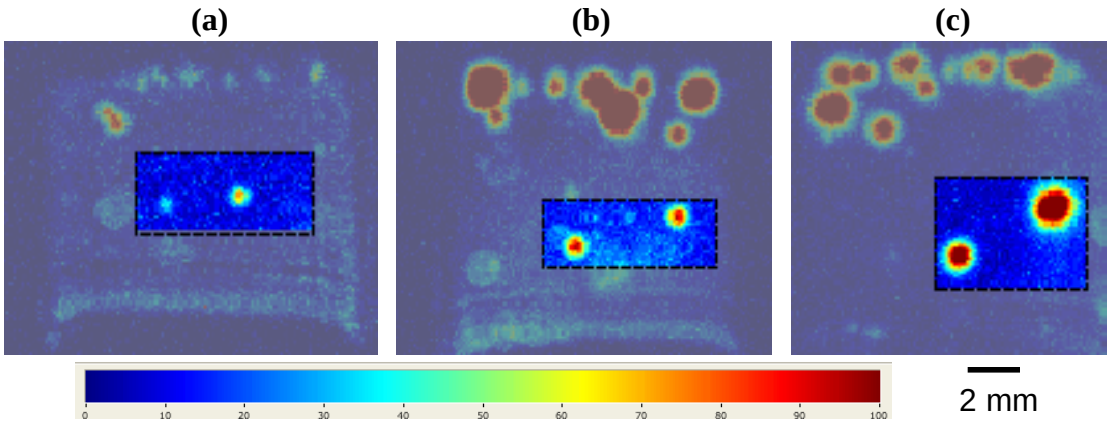

Figure 120. Bulk C-scan images of (a) EPX-1 (b) EPX-2 (c) EPX-3 samples.

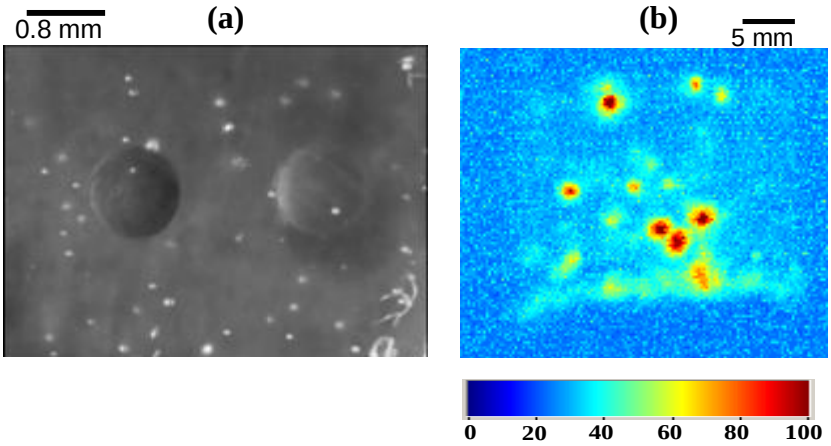

Figure 121. (a) Optical image and (b) full bulk C-scan images of EPX-4.

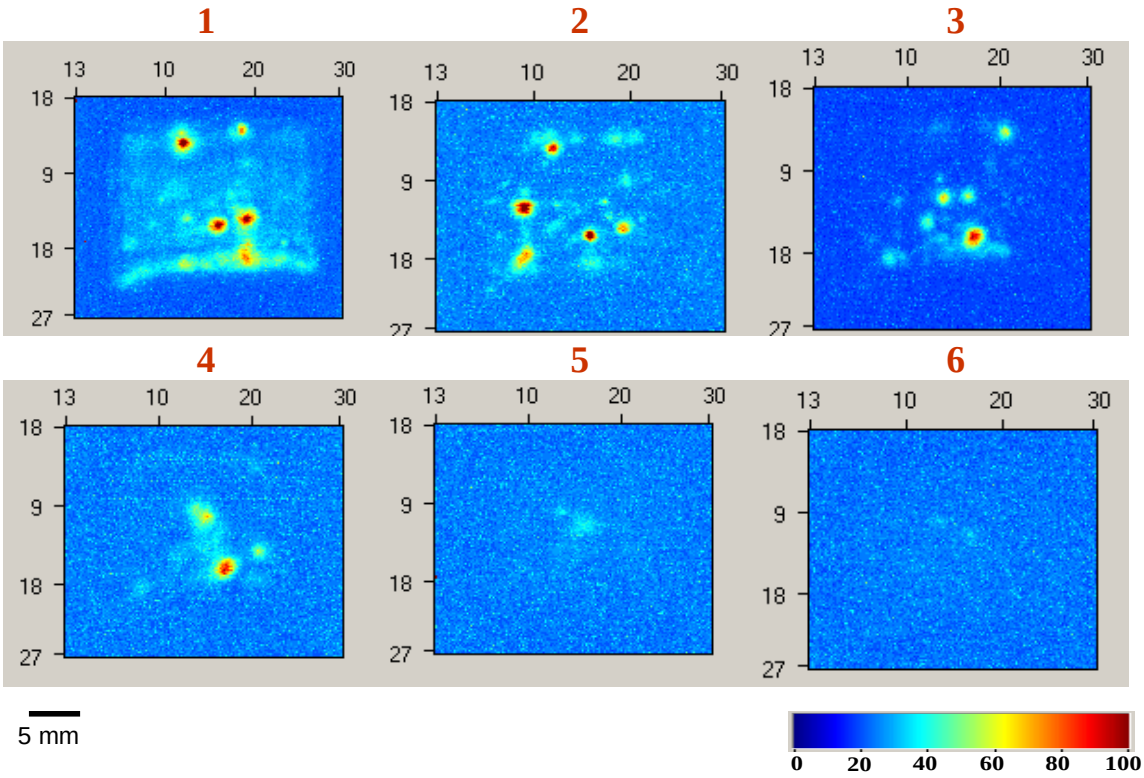

Figure 122. Bulk C-scan imaging in 1 μs increments from top (1) bulk region to bottom bulk region (6) for sample EPX-4.

Bottom surface reflected signal amplitude C-scan images of samples EPX-1, EPX-2, and EPX-3 were compared to a baseline sample of epoxy with no WC spheres, denoted as EPX. The bottom surface C-scan images showed the expected low amplitude regions where the WC spheres were located. The WC spheres in the images not only increased in size from smaller to larger, but also decreased in amplitude for the larger features. This was a result of the larger diameters of the spheres through which a higher degree of attenuation occurred. Bulk C-scan images were also performed on the same regions, but the sizes of the WC spheres appeared to be smaller than for the bottom surface reflected signal amplitude scans. Since the bottom surface reflected signal amplitude C-scan images contained the results through the entire bulk of the sample, they were more accurate in terms of overall size of the second phase features as compared to the bulk scans. The bulk scan second phase features were accurate in size only if the entirety of the features fell within the thickness range that was selected.

The normalized amplitude histograms were collected for the baseline epoxy sample EPX in addition to the three samples containing WC spheres of various sizes as shown in Figure 123. The histogram curve for the baseline epoxy sample showed a narrow distribution of amplitude values and the curve shape was similar to a Gaussian distribution. For the three EPX samples containing WC spheres, the main part of the curve was similar to the baseline histogram curve, but the main difference was the low amplitude tail regions on the left side of each curve. As the size of the WC spheres increased from small to medium to large for the EPX-1, EPX-2, and EPX-3 samples, respectively, there was a corresponding increase in the low amplitude tail region. For the two-phase sample in which the acoustic impedance mismatch was large between the two

phases and the base material was acoustically uniform, two distinct histogram regions were present. The first was the larger main histogram region and the second was the critical tail region. Together these two regions formed a two-phase histogram which will later be used for peak deconvolution and histogram simulations. The AUTC and FWHM values of the three samples containing WC spheres were compared to the epoxy baseline which had an AUTC of 1275 and an FWHM of 11. For sample EPX-1 which contained the smallest diameter WC spheres, the AUTC value increased to 1514 and the FWHM to 14. For sample EPX-2 which contained the medium diameter WC spheres, the AUTC value increased to 1535 while the FWHM value was 13. For sample EPX-3 which contained the largest diameter WC spheres, the AUTC value increased to 1635 while the FWHM was 12. While the FWHM values were very similar to one another and demonstrated a similar main histogram curve for each sample, the AUTC values increased with the size of the WC spheres. The AUTC increase was due to the larger tail region which resulted from an increase in WC sphere size. These areas were calculated separately. The tail AUTC for EPX-1 was found to be 37 and increased to 77 for EPX-2 and 159 for EPX-3. As the area of the second phase region increased for each sample due to the difference in size of WC spheres, the overall AUTC and FWHM also increased due to larger tail regions.

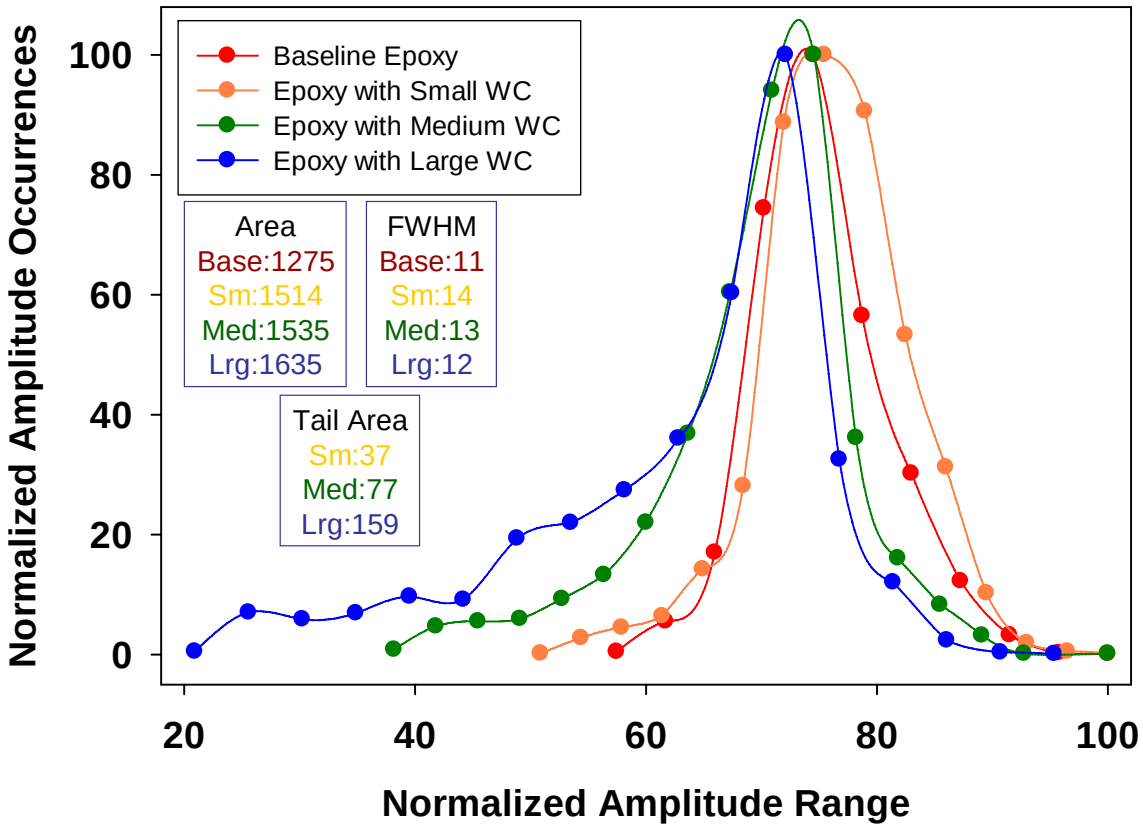

Figure 123. Bottom surface reflected signal amplitude histogram curve comparison of EPX samples at 10 MHz.

The normalized amplitude histogram results were effective in distinguishing sphere sizes and second-phase volumes from one another, as this was directly correlated to the corresponding AUTC values. The distinction of a one-phase or two-phase histogram was established by observing the trends in these different types of fabricated samples. While the addition of a small number of fabricated pores into a dense matrix primarily resulted in one-phase histograms, the addition of a significant amount of second phase resulted in two-phase histograms with distinct tail regions. The other development from the fabricated samples was the ability to utilize bulk C-scan images to characterize sizes and depths of defects within a bulk matrix. The fabrication and ultrasound evaluation of the samples allowed more control and flexibility for determining these trends in contrast to the commercial samples in which many of the determining factors could not be altered. This study shed more light on the detection of defects in a bulk matrix which was used to more effectively evaluate the results from the commercial armor ceramic samples.

5.7.5. Hot Pressed SiC Test Specimens Containing Fabricated Bulk Defects

A set of three hot pressed SiC samples containing three different types of embedded defects was evaluated using reflected signal amplitude C-scan imaging and quantitative histogram analysis. All three were commercial hot pressed samples to which various defects of different sizes were purposely added to the SiC matrix. The first sample, which will be denoted SD-1, contained 1-3 millimeter milling inclusions which were distributed throughout the bulk of the sample. The sample had a length of 101.58 mm, a width of 101.56 mm, an average thickness of 19.08 mm, and an average density of 3.220 g/cm^3 as reported by the manufacturer. The second sample, which will be denoted

SD-2, contained a small percentage of 50 μm Al_2O_3 flakes that were dispersed in the SiC matrix. The sample had a length of 101.55 mm, a width of 101.56 mm, an average thickness of 19.08 mm, and an average density of 3.220 g/cm^3 as reported by the manufacturer. The third sample, which will be denoted SD-3, contained 20-25 μm carbon defects which were dispersed in the matrix. The sample had a length of 101.60 mm, a width of 101.63 mm, an average thickness of 19.00 mm, and an average density of 3.220 g/cm^3 as reported by the manufacturer. Since the embedded defects were added in small amounts, all three hot pressed samples maintained a high density of 3.220 g/cm^3 which was close to the reported theoretical density of SiC [24].

Ultrasound point analysis was conducted to evaluate the material velocities and elastic properties of the three samples, and the data are shown in Tables XLIV-XLVI. For sample SD-1, the TOF values were very consistent as the longitudinal TOF measured at each of the nine points was 3.116 μs and the shear TOF measured at each of the nine points was either 4.936 μs or 4.937 μs with an average of 4.936 μs. The consistency of the TOF values resulted in very similar calculated material velocities and identical acoustic impedance and elastic properties at each measured point. These calculated values included an average longitudinal velocity of 12,246 m/s, an average shear velocity of 7,730 m/s, an average acoustic impedance of 39.43 x 10^5 g/cm^{2}s, an average Poisson's ration of 0.17, an average elastic modulus of 450 GPa, an average shear modulus of 193 GPa, and an average bulk modulus of 226 GPa. Despite the addition of a small number of milling inclusions, sample SD-1 had slightly higher reported SiC values than the hot pressed armor grade SiC sample A which had an average E = 444 GPa, G = 190 GPa, and K = 225 GPa. For sample SD-2, the values were very similar to SD-1, with average TOF_l

= 3.116 μs, average TOF_s = 4.938 μs, average c_l = 12,248 m/s, average c_s = 7,728 m/s, average Z = 39.44 x10^5 g/cm^2s, average ν = 0.17, average E = 450 GPa, average G = 192 GPa, and average K = 227 GPa. For sample SD-3, the TOF values were lower due to the lower sample thickness compared to the other two samples, with an average TOF_l of 3.108 μs and an average TOF_s of 4.910 μs. This resulted in an average c_l = 12,227 m/s, an average c_s = 7,739 m/s, and an average Z = 39.37 x 10^5 g/cm^2s. The average calculated elastic properties over the nine points were similar to SD-1 and SD-2, with values of E = 450 GPa, G = 193 GPa and K = 225 GPa. In general, the addition of small amounts of embedded defects in the hot pressed SiC samples did not affect the overall material properties. There were no significant property variations that could be found when comparing the samples to one another despite the different defect types and sizes.

Reflected signal amplitude C-scan imaging was performed on all three samples at frequencies of 5, 75, and 125 MHz, as shown in Figures 124-126. At 5 MHz, the three SD samples appeared to show the same type of amplitude variation patterns characteristic of surface roughness due to surface grinding and polishing. All of the samples appeared to demonstrate a similar checkerboard pattern with slight reflected signal amplitude differences. In addition, sample SD-2 showed some additional amplitude variations in the form of a higher amplitude region at the bottom right of the sample. The standard deviation values reflected this difference, as SD-2 had the highest value of 8.28 mV followed by SD-1 at 5.15 mV and SD-3 at 4.74 mV. The average amplitude and standard deviation values for the three samples at all three frequencies are shown in Table XLVII. The histogram curve comparison for the 5 MHz scans also reflected this difference, as SD-2 had an extended region on the right side representing higher amplitude values. The

5 MHz histogram data are shown in Figure 127. Sample SD-1 also showed a narrower normalized histogram curve distribution as compared to SD-2. The resulting AUTC values matched the trends, as SD-2 had the highest value of 619, followed by SD-3 at 472 and SD-1 at 358. The FWHM values were 3 for SD-1, 5 for SD-2, and 5 for SD-3, as the sample with the lowest AUTC value also had the lowest FWHM value.

Due to the surface patterns observable even at low frequencies, the offset method used for the ESC samples was also applied to the SD samples at 75 MHz and 125 MHz. For each SD sample, both a bottom surface reflected signal amplitude scan and a top surface reflected signal amplitude scan were performed. The average weighted factor was calculated and multiplied by the bottom surface reflected signal amplitude data before being subtracted by the original top surface reflected signal amplitude data. Again, the majority of values affected by the surface patterns were offset while only the most significant bulk differences remained. This technique was used to allow a better chance of detecting the embedded bulk defects while avoiding the influence of surface features.

#	ρ (g/cc)	t (mm)	TOF_l (μs)	TOF_s (μs)	c_l (m/s)	c_s (m/s)	Z (*10^5 g/cm^{2}s)	ν	E (GPa)	G (GPa)	K (GPa)
1	3.220	19.08	3.116	4.937	12,246	7729	39.43	0.17	450	192	227
2	3.220	19.08	3.116	4.936	12,246	7731	39.43	0.17	450	193	226
3	3.220	19.08	3.116	4.936	12,246	7731	39.43	0.17	450	193	226
4	3.220	19.08	3.116	4.937	12,246	7729	39.43	0.17	450	192	227
5	3.220	19.08	3.116	4.936	12,246	7731	39.43	0.17	450	193	226
6	3.220	19.08	3.116	4.937	12,246	7729	39.43	0.17	450	192	227
7	3.220	19.08	3.116	4.937	12,246	7729	39.43	0.17	450	192	227
8	3.220	19.08	3.116	4.936	12,246	7731	39.43	0.17	450	193	226
9	3.220	19.08	3.116	4.936	12,246	7731	39.43	0.17	450	193	226
Avg	**3.220**	**19.08**	**3.116**	**4.936**	**12,246**	**7730**	**39.43**	**0.17**	**450**	**193**	**226**

Table XLIV. Point analysis data for sample SD-1.

#	ρ (g/cc)	t (mm)	TOF_l (μs)	TOF_s (μs)	c_l (m/s)	c_s (m/s)	Z (*10^5 g/cm^{2}s)	ν	E (GPa)	G (GPa)	K (GPa)
1	3.220	19.09	3.116	4.945	12,253	7721	39.45	0.17	450	192	228
2	3.220	19.09	3.116	4.937	12,253	7733	39.45	0.17	450	193	227
3	3.220	19.09	3.116	4.945	12,253	7721	39.45	0.17	450	192	228
4	3.220	19.08	3.116	4.937	12,246	7729	39.43	0.17	450	192	227
5	3.220	19.08	3.116	4.937	12,246	7729	39.43	0.17	450	192	227
6	3.220	19.08	3.116	4.936	12,246	7731	39.43	0.17	450	193	226
7	3.220	19.08	3.116	4.936	12,246	7731	39.43	0.17	450	193	226
8	3.220	19.08	3.116	4.937	12,246	7729	39.43	0.17	450	192	227
9	3.220	19.08	3.116	4.936	12,246	7731	39.43	0.17	450	193	226
Avg	**3.220**	**19.08**	**3.116**	**4.938**	**12,248**	**7728**	**39.44**	**0.17**	**450**	**192**	**227**

Table XLV. Point analysis data for sample SD-2.

#	ρ (g/cc)	t (mm)	TOF_l (μs)	TOF_s (μs)	c_l (m/s)	c_s (m/s)	Z (*10^5 g/cm^{2}s)	ν	E (GPa)	G (GPa)	K (GPa)
1	3.220	19.00	3.107	4.910	12,230	7739	39.38	0.17	450	193	225
2	3.220	19.00	3.107	4.910	12,230	7739	39.38	0.17	450	193	225
3	3.220	19.00	3.107	4.910	12,230	7739	39.38	0.17	450	193	225
4	3.220	19.00	3.108	4.911	12,227	7738	39.37	0.17	450	193	224
5	3.220	19.00	3.112	4.911	12,211	7738	39.32	0.16	449	193	223
6	3.220	19.00	3.107	4.910	12,230	7739	39.38	0.17	450	193	225
7	3.220	19.00	3.107	4.910	12,230	7739	39.38	0.17	450	193	225
8	3.220	19.00	3.107	4.910	12,230	7739	39.38	0.17	450	193	225
9	3.220	19.00	3.108	4.911	12,227	7738	39.37	0.17	450	193	224
Avg	**3.220**	**19.00**	**3.108**	**4.910**	**12,227**	**7739**	**39.37**	**0.17**	**450**	**193**	**225**

Table XLVI. Point analysis data for sample SD-3.

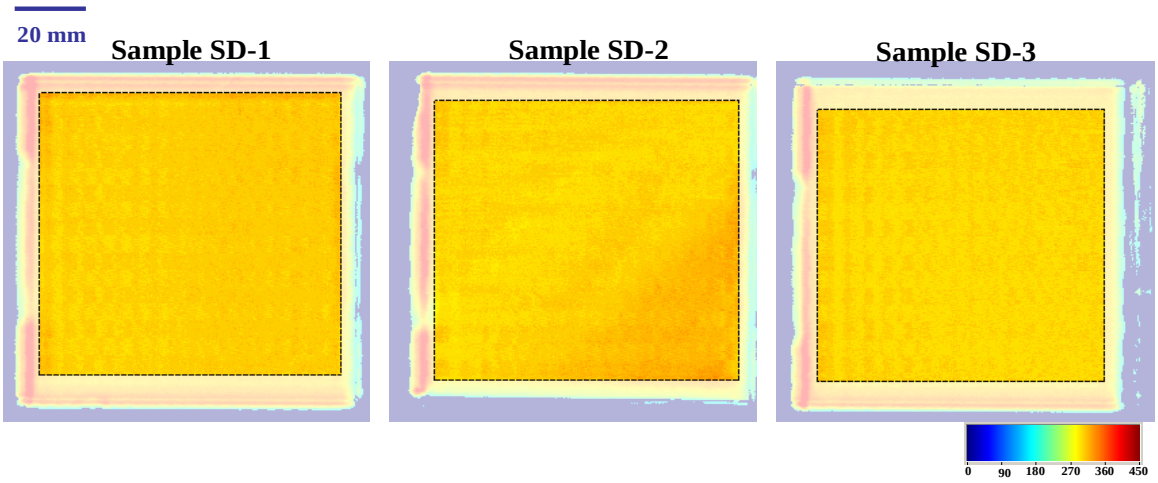

Figure 124. Reflected signal amplitude scans of SD-1, SD-2, and SD-3 at 5 MHz.

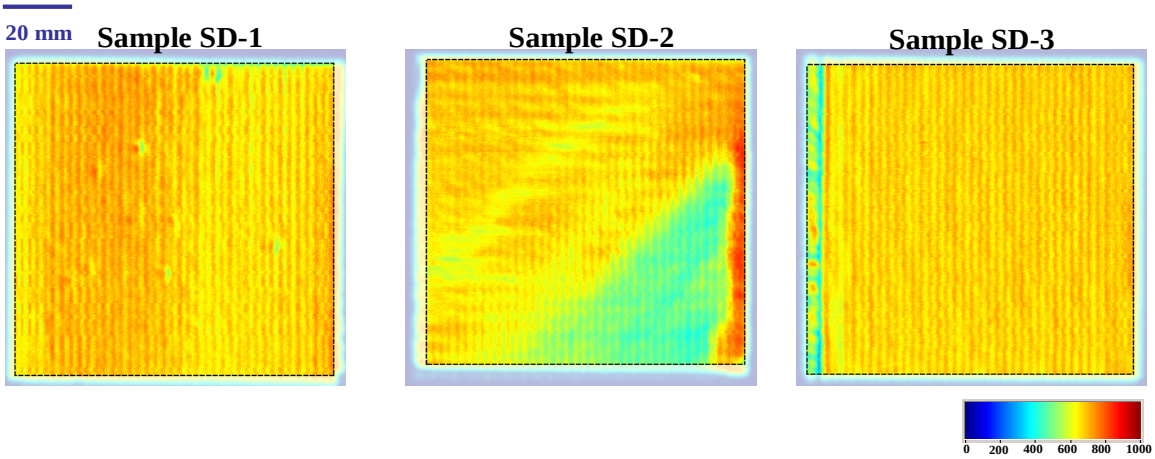

Figure 125. Reflected signal amplitude scans of SD-1, SD-2, and SD-3 at 75 MHz.

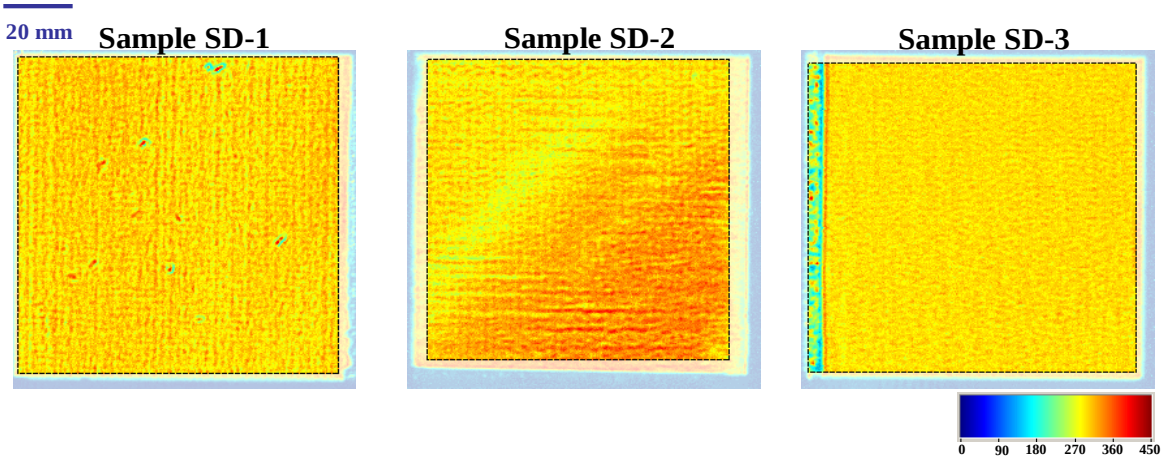

Figure 126. Reflected signal amplitude scans of SD-1, SD-2, and SD-3 at 125 MHz.

5MHz		
#	Average (mV)	Standard Deviation (mV)
1	290	5.15
2	289	8.28
3	285	4.74

75MHz		
#	Average (mV)	Standard Deviation (mV)
1	731	46.58
2	665	104.28
3	715	58.48

125MHz		
#	Average (mV)	Standard Deviation (mV)
1	303	21.79
2	147	13.59
3	156	13.76

Table XLVII. Average and standard deviation amplitude values for SD samples at 5, 75, and 125 MHz.

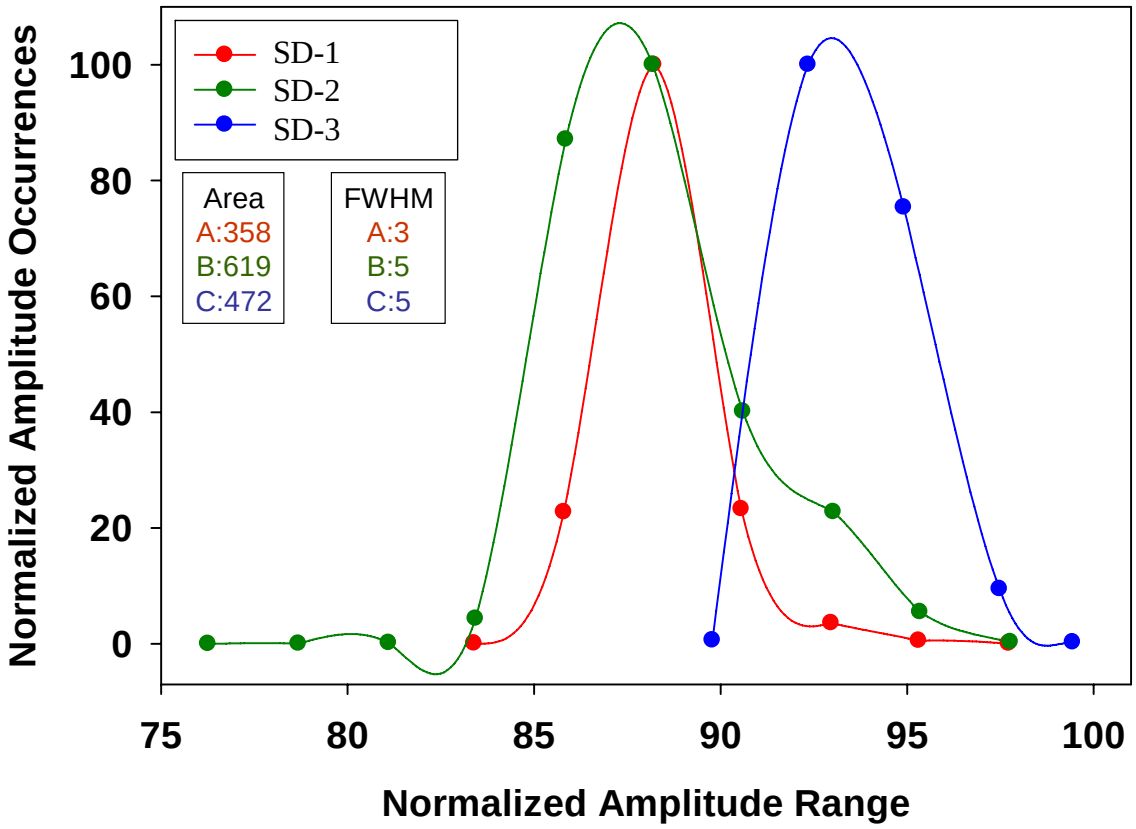

Figure 127. Reflected signal amplitude histogram curves of SD samples at 5 MHz.

At 75 MHz, the offset method was performed on all three SD samples as shown in Figures 128-130. Before applying the method, the C-scan images revealed vertical lines throughout the top surface and bottom surface scans of SD-1 and SD-3. Sample SD-2 revealed both vertical and horizontal lines in addition to a large area of lower reflected signal amplitude in both scans, indicating that there were large surface and/or near surface amplitude variations. After applying the offset technique, the affect of the vertical lines was drastically reduced for samples SD-1 and SD-3. However, while many of the surface features were reduced for SD-2, the offset technique was not able to eliminate all the effects of the surface or near surface features, as some of the patterns were still evident. In SD-1, the 1-3 mm milling inclusions were detected. Two of these inclusions were located next to each other at the top of the sample, while eleven others were detected throughout the central region of the sample. The milling inclusions were characterized by only slightly higher amplitudes than the bulk and some were surrounded by regions of low amplitude compared to the bulk, indicating lower density regions bordering the defect sites. It was believed that the slightly higher amplitudes of the features were an indication that they were either metallic inclusions or hard, high density SiC inclusions within the hot pressed SiC bulk. These types of defects would all have a slightly higher density than the SiC matrix and would be characteristic of higher amplitude features in the ultrasound C-scan images. While the larger defects were detected in SD-1 at 75 MHz, it was much more difficult to detect the smaller features in SD-2 and SD-3. For SD-2, the surface and near surface features had a significant effect on the resulting scans, even after the offset method was applied, and individual defects could not be easily located. For SD-3, while it was difficult to distinguish the smallest

defects at 75 MHz, a large region of varying reflected signal amplitude was found along the left side of the sample. This region, which had a great deal of amplitude variation including several low amplitude regions, seemed to be divided from the rest of the sample by a very low amplitude border. These features were not believed to include the 20-25 μm embedded defects as they covered much larger regions and were concentrated in a very specific area of the scanned SiC sample.

The normalized amplitude histogram curves were plotted and compared in Figure 131. The defects embedded in SD-1 were not significantly high enough in amplitude to create a tail or a lip on the right side of the histogram curve since they were similar to the SiC matrix. This mirrored the trend that even the largest embedded defects in SD-1 had little effect on altering the density and elastic properties measured during point analysis. The low amplitude tail was representative of an edge effect on the right side of the sample and was not believed to be critical. The SD-2 normalized amplitude histogram appeared to have the broadest distribution, as the surface effects were still prevalent and showed the most drastic differences. The low amplitude region appeared as a large tail on the left side of the curve. Sample SD-3 showed the most narrow overall distribution as it was most homogenous over the majority of the bulk. The lower amplitude features from the region along the left side of the sample did result in a tail on the left side of the curve. These curve trends led to the lowest AUTC value of 878 for SD-3, followed by 1173 for SD-2 which was increased due to the detection of the embedded defects, and 1639 for SD-3, which had the highest degree of variability and broadest curve. At 5 MHz, SD-1 had the smallest AUTC since the embedded defects were not detected, but the detection of these defects at 75 MHz resulted in an increase in area while sample SD-

2 instead showed the lowest AUTC value. The FWHM values in this case were also consistent with the same trends, as the values were 8 for SD-3, followed by 11 for SD-1 and 14 for SD-2.

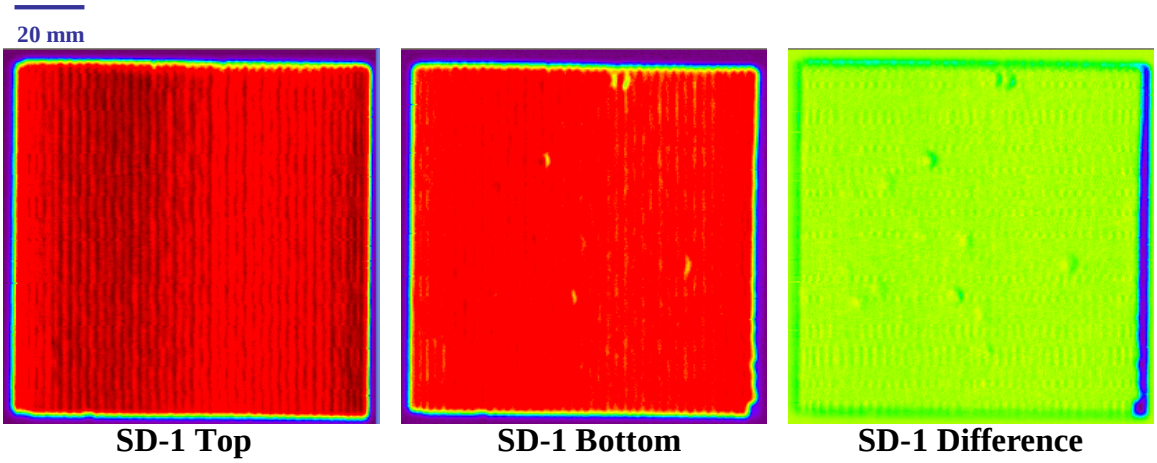

Figure 128. Surface roughness adjusted images of SD-1 sample at 75 MHz.

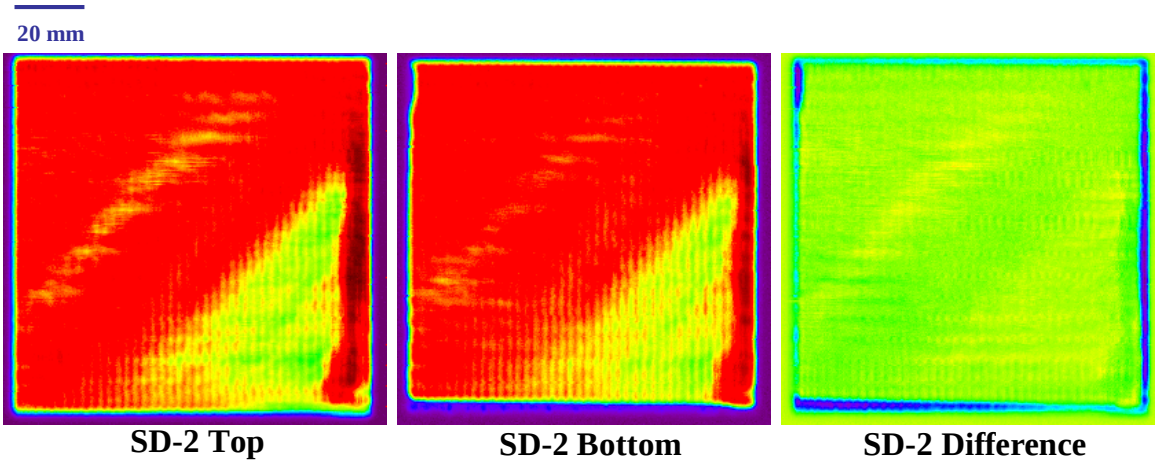

Figure 129. Surface roughness adjusted images of SD-2 sample at 75 MHz.

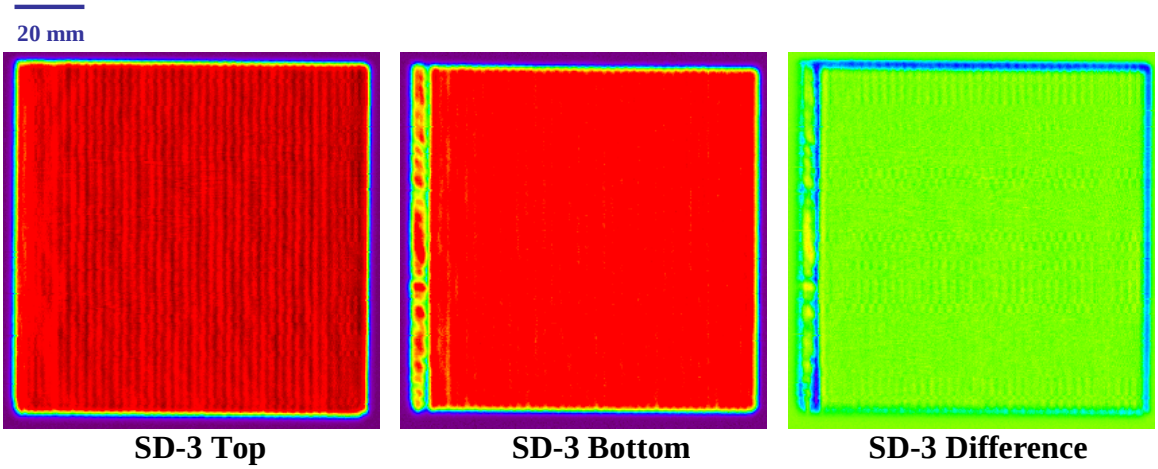

Figure 130. Surface roughness adjusted images of SD-3 sample at 75 MHz.

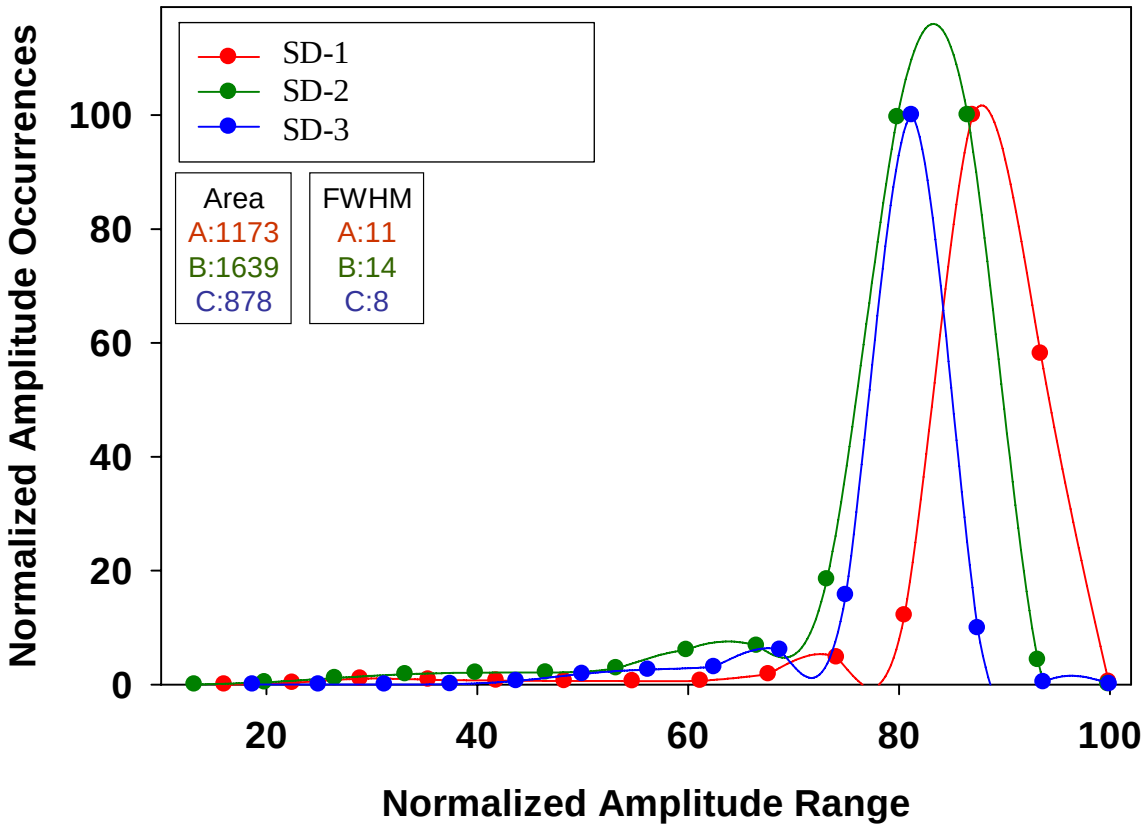

Figure 131. Surface roughness adjusted amplitude histogram curves of SD samples at 75 MHz.

At 125 MHz, the offset method was also applied and the resulting SD images compared as shown in Figures 132-134. For SD-1, the size, shape, and number of embedded defects were much more detailed. Several additional defects that could not be detected at 75 MHz were apparent at 125 MHz. Again, the offset method helped reduce the surface effects so that the embedded defects stood out better. For SD-2, the surface effects were still present, this time in the form of horizontal lines that dragged across the sample. This made it considerably more difficult to detect the small embedded features. While there were some small features present that may have represented the embedded defects, the results were unclear. For SD-3, the main region of the bulk appeared to be very homogeneous as the offset method appeared to remove the presence of any surface features. The region of the left side of the sample was also more detailed, as individual millimeter-size features were found. It was difficult to distinguish the smallest embedded defects in this sample, even at 125 MHz.

A comparison of the normalized amplitude histograms in Figure 135 showed that the SD-1 and SD-2 histogram curves were almost identical while the SD-3 curve was much broader. This was a much different trend than was found at 75 MHz. The low amplitude tails in the SD-1 and SD-2 histogram curves represented the low amplitude edge effects from both samples, which had similar effects on the curve shapes. The detected defects in SD-1 and horizontal lines in SD-2 did not appear to affect the histogram curves greatly at 125 MHz. In contrast, the left side of sample SD-3 instead had a much greater effect at 125 MHz, as the higher frequency was more sensitive to the variations within the region and resulted in broadening of the curve. The AUTC trends reflected this difference as SD-3 showed the highest AUTC value of 935 followed by SD-

1 at 724 and SD-2 at 697. Sample SD-3 also had the highest FWHM value of 10 as compared to a value of 8 for both SD-1 and SD2. This again demonstrated that ultrasound evaluation at different frequencies was characteristic of different sizes and types of features. While the trends were often consistent at higher frequencies, the SD samples showed a case in which a region that was not significant at 75 MHz became much more significant at 125 MHz and resulted in drastically different AUTC values. This also emphasized the point that it is important to choose a transducer frequency based on the sizes and types of features that are desired for evaluation.

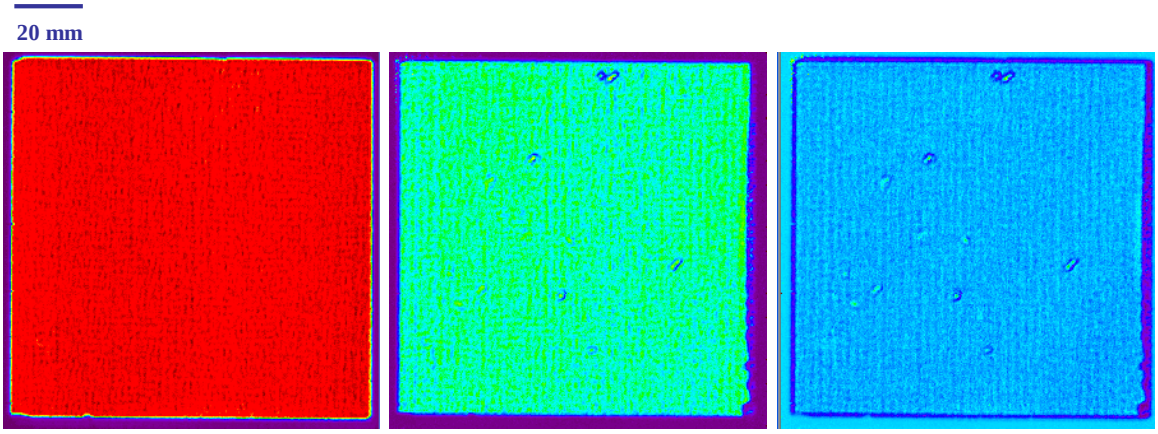

Figure 132. Surface roughness adjusted images of SD-1 sample at 125 MHz.

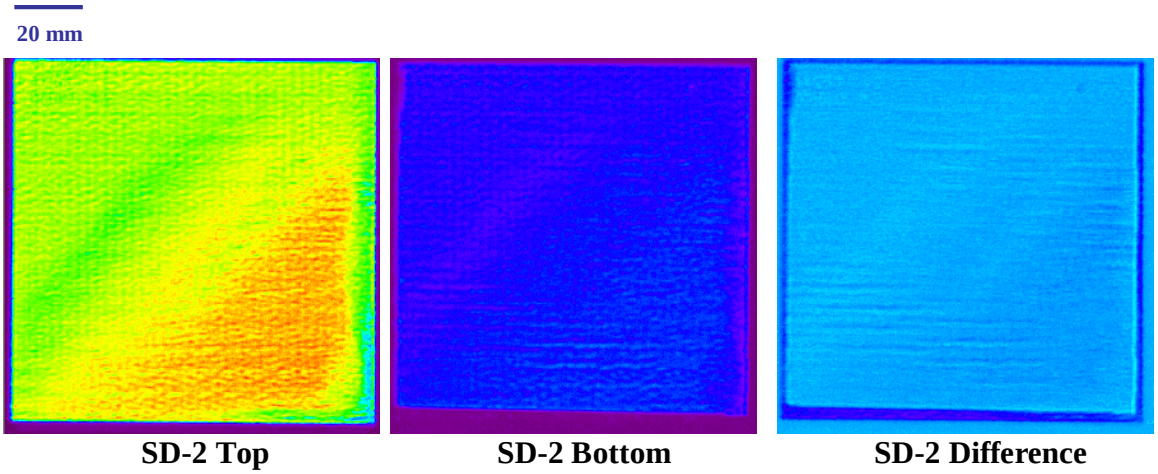

Figure 133. Surface roughness adjusted images of SD-2 sample at 125 MHz.

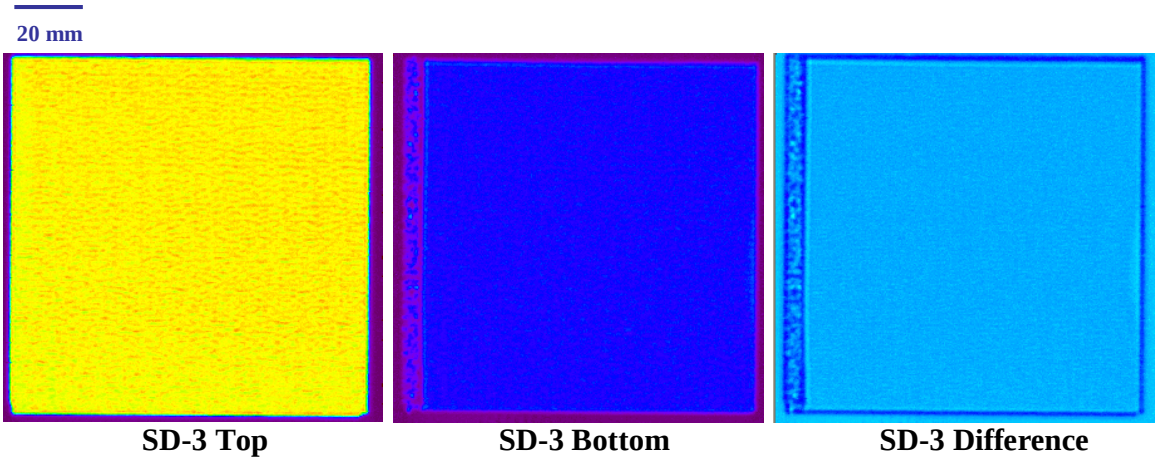

Figure 134. Surface roughness adjusted images of SD-3 sample at 125 MHz.

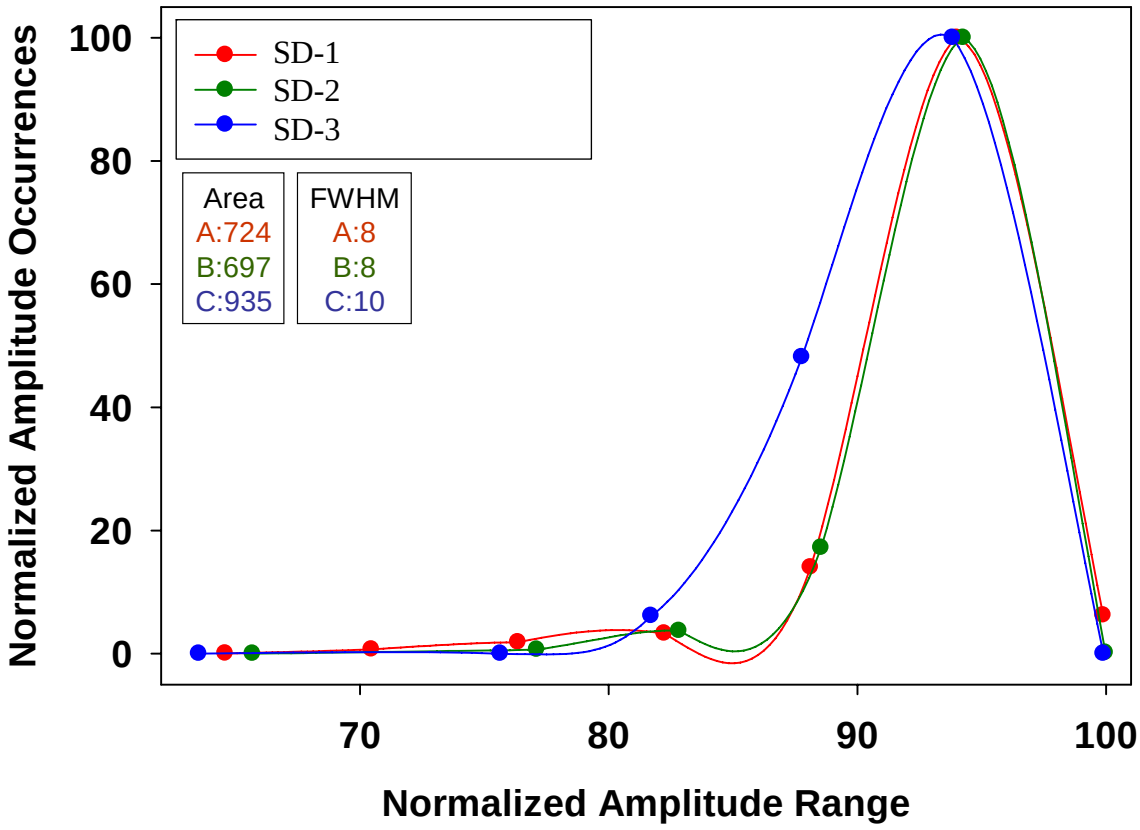

Figure 135. Surface roughness adjusted amplitude histogram curves of SD samples at 125 MHz.

5.8. Sintered Al_2O_3 Test Specimens

A set of three sintered Al_2O_3 plates was evaluated for comparison to the sintered SiC test specimens described earlier. The specimens, referred to as AO-1, AO-2, and AO-3, all came from the same batch. While each of the samples had a length of 90.0 mm and a width of 90.0 mm, samples AO-1 and AO-2 both had an average thickness of 14.84 mm and an average measured density of 3.91 g/cm^3 while sample AO-3 had an average thickness of 14.80 mm and an average measured density of 3.90 g/cm^3. After performing point analysis on the samples at nine separate points, reflected signal amplitude C-scan imaging and quantitative analysis was also conducted at 5, 75, and 125 MHz.

The TOF, material velocity, acoustic impedance, and elastic property values measured during point analysis showed a reasonable degree of variability among the nine points for all three samples, as shown in Tables XLVIII-L. Sample AO-1 showed a longitudinal TOF range of 2.791 μs to 2.823 μs with an average of 2.804 μs while the shear TOF values ranged from 4.749 μs to 4.976 μs with an average of 4.770 μs. This resulted in a longitudinal velocity range of 10,514 m/s to 10,627 m/s with an average of 10,581 m/s and a shear velocity range of 6,188 m/s to 6,246 m/s with an average of 6,221 m/s. The calculated acoustic and elastic properties were Z = 41.37 x 10^5 g/cm^{2}s, ν = 0.24, E = 374 GPa, G = 151 GPa, and K = 236 GPa for AO-1. Sample AO-2, which had the same average thickness and density values, also had identical acoustic and elastic properties with slight variations in average longitudinal TOF at 2.802 μs, average shear TOF at 4.768 μs, and average shear velocity at 6,217 m/s. Sample AO-3, which had slightly lower average thickness and density values, also had lower material velocities, acoustic impedance values, and elastic properties of c_l = 10,562 m/s, c_s = 6,208 m/s, Z =

41.19 x 10^5 g/cm^{2}s, E = 372 GPa, G = 150 GPa, and K = 235 GPa. As expected, the values for all of the Al_2O_3 samples were much lower than the average SA SiC values of c_l = 11,950 m/s, c_s = 7,610 m/s, E = 430 GPa, G = 180 GPa, and K = 210 GPa reported earlier. The lower average Z value of 37.8 x 10^5 g/cm^{2}s for the SA sample showed the greater influence of the higher Al_2O_3 density on the Z calculation as opposed to the higher longitudinal velocity for the SiC sample.

Reflected signal amplitude ultrasound C-scan imaging was first performed at 5 MHz to get a low frequency evaluation of the Al_2O_3 samples, as shown in Figure 136. Unlike the sintered SiC SA test specimens which showed very little reflected signal amplitude variation at the lowest test frequency, the differences among sintered Al_2O_3 samples were much more apparent, with significant low amplitude variations throughout each sample. While the standard deviation values for the SA samples ranged from 1.99 mV to 3.40 mV, the standard deviation values for the Al_2O_3 samples were 11.52 mV for AO-1, 10.41 mV for AO-2, and 11.67 mV for AO-3. The average amplitude and standard deviation values for each sample at each frequency are shown in Table LI. The most distinct features were circular low amplitude regions in the center of samples AO-1 and AO-2, which had much greater relative amplitude differences as compared to the large circular defects from the SA samples detected at the same frequency. The reflected signal amplitude normalized histograms and quantitative analysis data supported these vast differences, as shown in Figure 137. Each of the Al_2O_3 histograms revealed a ledge on the left side of the curve corresponding to the high number of lower amplitude occurrences. The AUTC values were 699, 547, and 616 and the FWHM values were 6, 4, and 4 for samples AO-1, AO-2, and AO-3, respectively. In contrast, the SA SiC

normalized amplitude histograms had AUTC values ranging from 253-388 and FWHM values ranging from 2-3. These results showed a much higher variability for the sintered Al_2O_3 test specimens as compared to the sintered SiC specimens, even at the lowest test frequency. To determine whether or not the relative percent theoretical density was the cause of this difference, average densities of sintered Al_2O_3 at 3.910 g/cm^3 and sintered SA SiC at 3.163 g/cm^3 reported by the manufacturers were compared to average theoretical densities of Al_2O_3 at 3.98 g/cm^3 and SiC at 3.22 g/cm^3 in the literature. The calculations showed that both sets of sintered samples were ~98% of theoretical density, ruling out the possibility that the differences were caused by the amount of porosity alone.

#	ρ (g/cc)	t (mm)	TOF_l (μs)	TOF_s (μs)	c_l (m/s)	c_s (m/s)	Z (*10^5 g/cm^{2}s)	ν	E (GPa)	G (GPa)	K (GPa)
1	3.910	14.84	2.800	4.765	10,600	6229	41.45	0.24	375	152	237
2	3.910	14.83	2.808	4.773	10,563	6214	41.30	0.24	373	151	235
3	3.910	14.83	2.799	4.749	10,597	6246	41.43	0.23	377	153	236
4	3.910	14.83	2.804	4.771	10,585	6221	41.39	0.24	374	151	236
5	3.910	14.84	2.791	4.756	10,627	6236	41.55	0.24	377	152	239
6	3.910	14.83	2.799	4.757	10,597	6235	41.43	0.24	376	152	237
7	3.910	14.84	2.823	4.796	10,514	6188	41.11	0.23	370	150	233
8	3.910	14.84	2.815	4.780	10,544	6209	41.23	0.23	372	151	234
9	3.910	14.84	2.799	4.780	10,604	6209	41.46	0.24	374	151	239
Avg	**3.910**	**14.84**	**2.804**	**4.770**	**10,581**	**6221**	**41.37**	**0.24**	**374**	**151**	**236**

Table XLVIII. Point analysis data for sample AO-1.

#	ρ (g/cc)	t (mm)	TOF_l (μs)	TOF_s (μs)	c_l (m/s)	c_s (m/s)	Z (*10^5 g/cm^{2}s)	ν	E (GPa)	G (GPa)	K (GPa)
1	3.910	14.83	2.800	4.757	10,593	6235	41.42	0.23	376	152	236
2	3.910	14.82	2.800	4.773	10,586	6210	41.39	0.24	373	151	237
3	3.910	14.81	2.792	4. 757	10,609	6227	41.48	0.24	375	152	238
4	3.910	14.83	2.807	4.780	10,566	6205	41.31	0.24	373	151	236
5	3.910	14.82	2.807	4.780	10,559	6201	41.29	0.24	372	150	236
6	3.910	14.81	2.799	4.764	10,582	6217	41.38	0.24	374	151	236
7	3.910	14.83	2.807	4.780	10,566	6205	41.31	0.24	373	151	236
8	3.910	14.82	2.807	4.764	10,586	6222	41.39	0.24	374	151	236
9	3.910	14.81	2.800	4.757	10,579	6227	41.36	0.23	375	152	236
Avg	**3.910**	**14.84**	**2.802**	**4.768**	**10,581**	**6217**	**41.37**	**0.24**	**374**	**151**	**236**

Table XLIX. Point analysis data for sample AO-2.

#	ρ (g/cc)	t (mm)	TOF_l (μs)	TOF_s (μs)	c_l (m/s)	c_s (m/s)	Z (*10^5 g/cm^{2}s)	ν	E (GPa)	G (GPa)	K (GPa)
1	3.900	14.80	2.789	4.772	10,613	6203	41.39	0.24	373	150	239
2	3.900	14.80	2.807	4.772	10,545	6203	41.13	0.24	371	150	234
3	3.900	14.80	2.799	4.764	10,575	6213	41.24	0.24	372	151	236
4	3.900	14.80	2.815	4.772	10,515	6203	41.01	0.23	370	150	231
5	3.900	14.80	2.799	4.757	10,575	6222	41.24	0.24	373	151	235
6	3.900	14.80	2.799	4.764	10,575	6213	41.24	0.24	372	151	236
7	3.900	14.80	2.808	4.781	10,541	6191	41.11	0.24	370	150	234
8	3.900	14.80	2.800	4.772	10,571	6203	41.23	0.24	372	150	236
9	3.900	14.80	2.807	4.757	10,545	6222	41.13	0.23	373	151	232
Avg	**3.900**	**14.80**	**2.803**	**4.768**	**10,562**	**6208**	**41.19**	**0.24**	**372**	**150**	**235**

Table L. Point analysis data for sample AO-3.

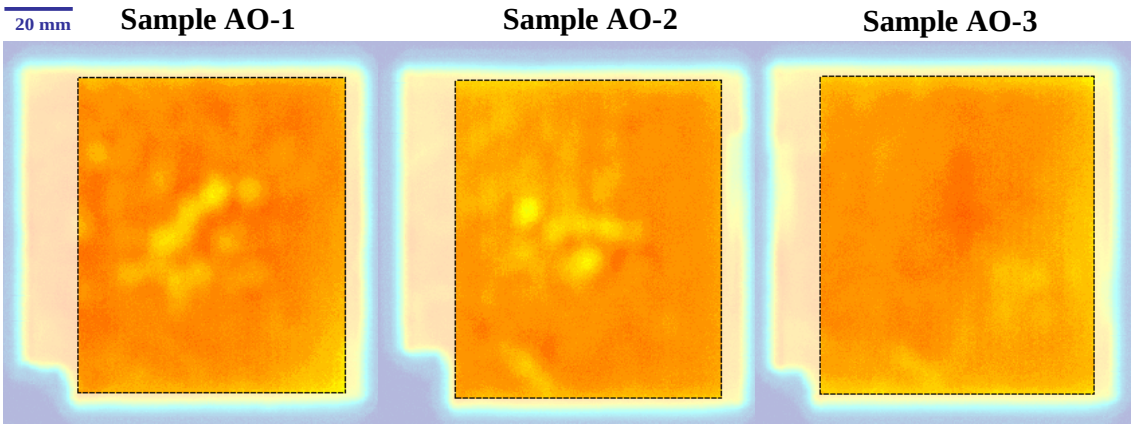

Figure 136. Reflected signal amplitude scans of AO-1, AO-2, and AO-3 at 5 MHz.

5MHz

#	Average (mV)	Standard Deviation (mV)
1	320	11.52
2	315	10.41
3	315	11.67

75MHz

#	Average (mV)	Standard Deviation (mV)
1	559	146.79
2	549	221.11
3	552	257.74

125MHz

#	Average (mV)	Standard Deviation (mV)
1	73	13.64
2	64	14.44
3	71	12.12

Table LI. Average and standard deviation amplitude values for AO samples at 5, 75, and 125 MHz.

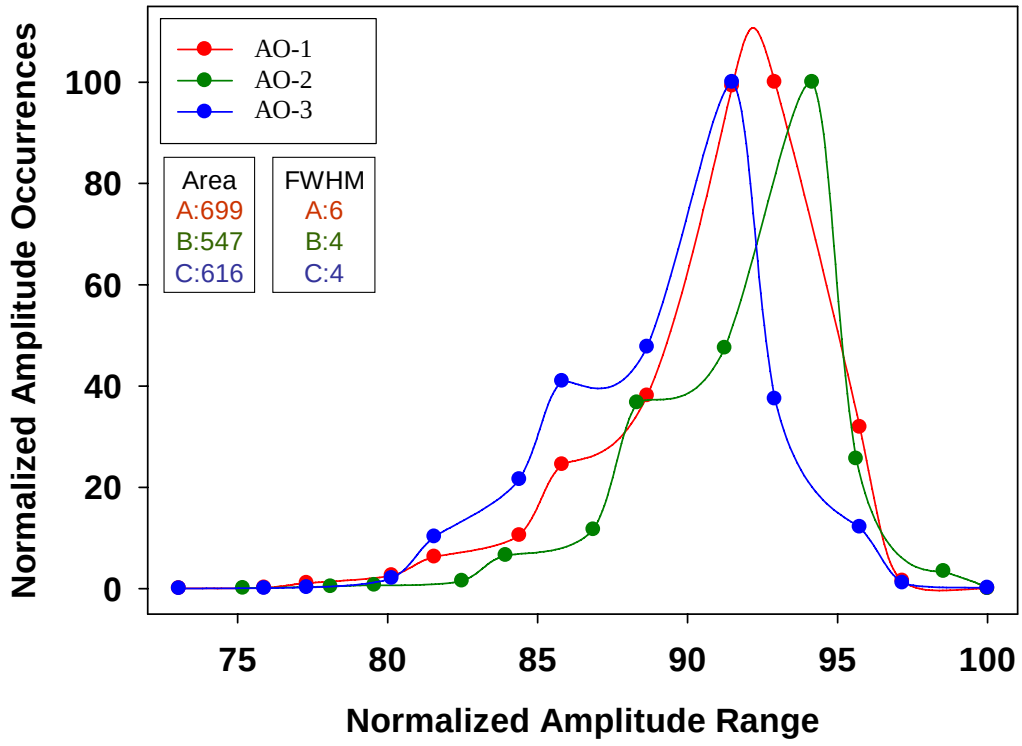

Figure 137. Reflected signal amplitude histogram curves of AO-1, AO-2, and AO-3 at 5 MHz.

Next, the Al_2O_3 samples were evaluated at 75 MHz and the reflected signal amplitude variations were extremely large. The C-scan images in Figure 138 show drastic regional differences from low to high amplitude, especially for samples AO-2 and AO-3, which resulted in high standard deviation differences. The standard deviation values in Table LI were 146.8 mV for AO-1, 221.1 mV for AO-2, and 257.7 mV for AO-3 as compared to SA SiC standard deviation values ranging from 9.8 mV to 50.1 mV at 75 MHz. These large variations resulted in normalized histogram curves that spanned the entire normalized amplitude range for the Al_2O_3 samples, as shown in Figure 139. While sample AO-1 showed more of a normal Gaussian distribution of amplitude values over the scanned area, samples AO-2 and AO-3 showed similar curve shapes with very broad regions extending into the high amplitude range. These differences were apparent in the AUTC values of 3,020 for AO-1, 5,232 for AO-2, and 4,061 for AO-3. Again, these AUTC values were much higher than the SA sample values which were typically below 3000, though sample SA7 had the largest value of 3590 which was higher than sample AO-1. While the FWHM values were representative for two of the samples, with an AO-1 value of 18 and an AO-2 value of 65, the AO-3 value of 19 was deceiving. Since the broad amplitude region for AO-3 fell below the half-maximum value, it was not included in the assessment and fell closer to the AO-1 value as opposed to the AO-2 value which would have described it better. This demonstrated the importance of looking at several key parameters for sample comparison instead of just one, but also showed that the AUTC values tend to be more accurate than the FWHM values if only one parameter is evaluated.

Finally, the 125 MHz ultrasound evaluation was performed on the Al_2O_3 samples, as shown in Figure 140. Rather than large regional differences, the 125 MHz ultrasound scans showed very specific features, the majority of which were round, high reflected signal amplitude inclusions. All three samples showed lower amplitudes and corresponding lower density regions compared to the rest of the bulk - for AO-1 in the bottom right corner, AO-2 in the upper left corner, and AO-3 on the right side of the sample. These appeared to be much more accurate depictions of the differences within each Al_2O_3 sample since the individual features were distinguishable. The standard deviation values in Table LI were 13.64 mV for AO-1, 14.44 mV for AO-2, and 12.11 mV for AO-3. Again, the SA SiC standard deviation values were much lower, ranging from 3.73 mV for SA1 to 8.34 mV for SA2. In the 125 MHz normalized amplitude histogram curves in Figure 141, sample AO-1 again stood out with the most narrow distribution as compared to the other two samples, with sample AO-3 demonstrating the broadest distribution. This trend was reflected in the AUTC and FHWM data, with AO-1 showing values of 1,442 and 12, respectively, AO-2 showing values of 2,025 and 17, respectively, and AO-3 showing values of 2,478 and 22, respectively. These values were still much greater than the SA SiC values, as even the lowest AO-1 AUTC value of 1,442 was slightly higher than the largest SA value of 1,397 for SA7. Among the Al_2O_3 samples, AO-1 was the least variable sample with the lowest AUTC and FWHM values at the highest frequencies. The lower density sample AO-3 had the highest AUTC and FWHM values at the highest frequency, which followed previous trends. Sample AO-1 was also similar to some of the sintered SiC samples such as SA2 and SA7 with the highest AUTC and FWHM values. As far as overall material comparison, the same

trends occurred at all three frequencies, with consistently larger standard deviation, AUTC, and FWHM values for the Al_2O_3 samples as compared to the SiC samples. The elastic property differences were significant when the sample sets were compared, as the average E values of 374 GPa for sintered Al_2O_3 compared to 430 GPa for sintered SiC followed the variability trends determined by ultrasound C-scan imaging and quantitative analysis. In general, SiC is preferred over Al_2O_3 for armor applications due to its higher mechanical and elastic properties, and the ultrasound data and acoustic values also followed this trend.

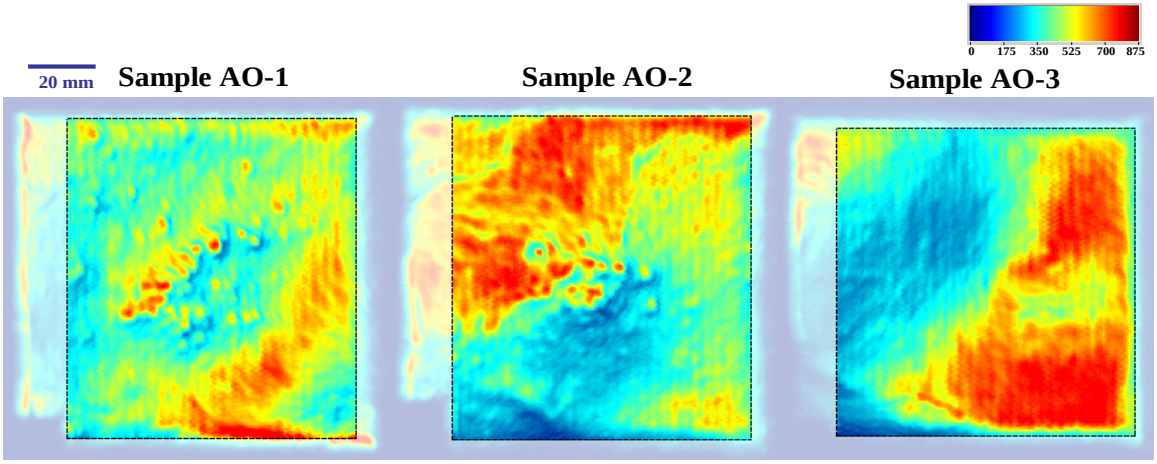

Figure 138. Reflected signal amplitude scans of AO-1, AO-2, and AO-3 at 75 MHz.

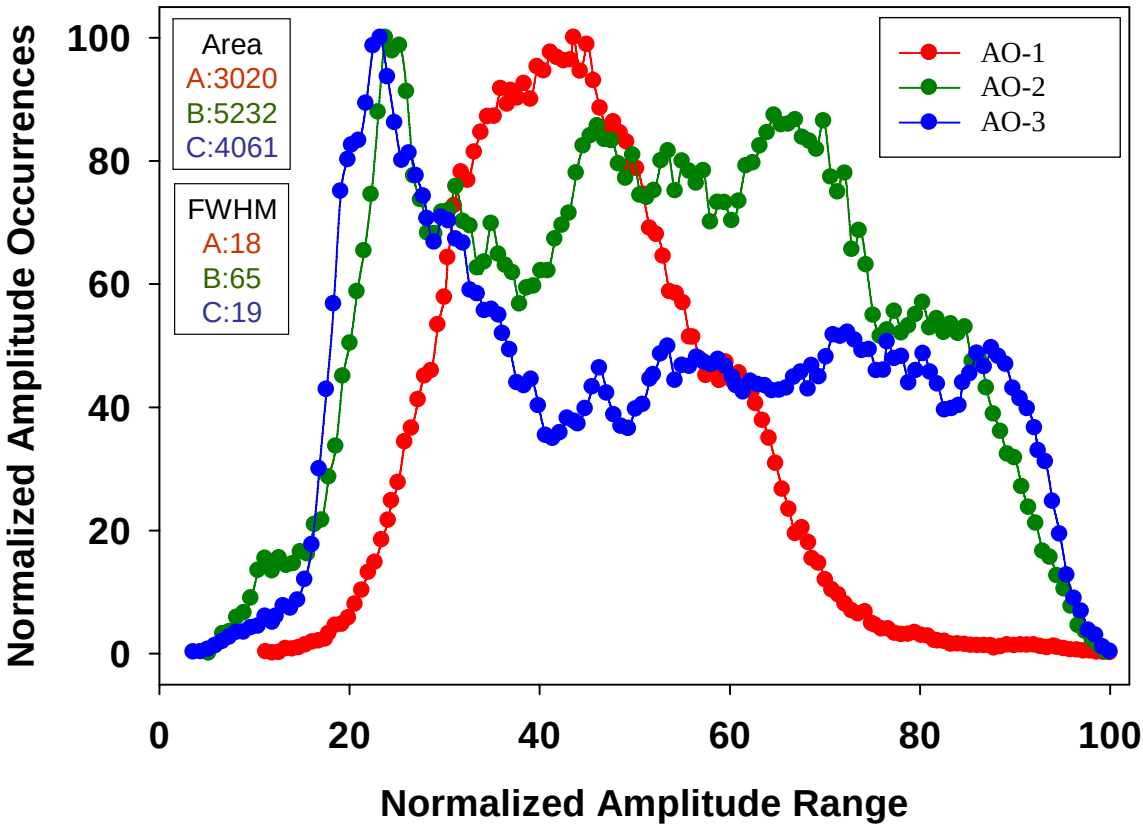

Figure 139. Reflected signal amplitude histogram curves of AO-1, AO-2, and AO-3 at 75 MHz.

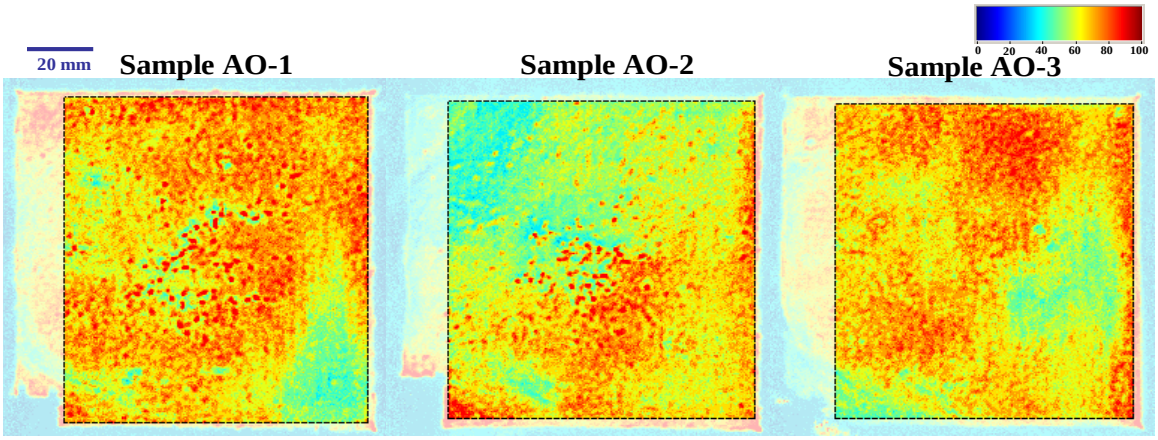

Figure 140. Reflected signal amplitude scans of AO-1, AO-2, and AO-3 at 125 MHz.

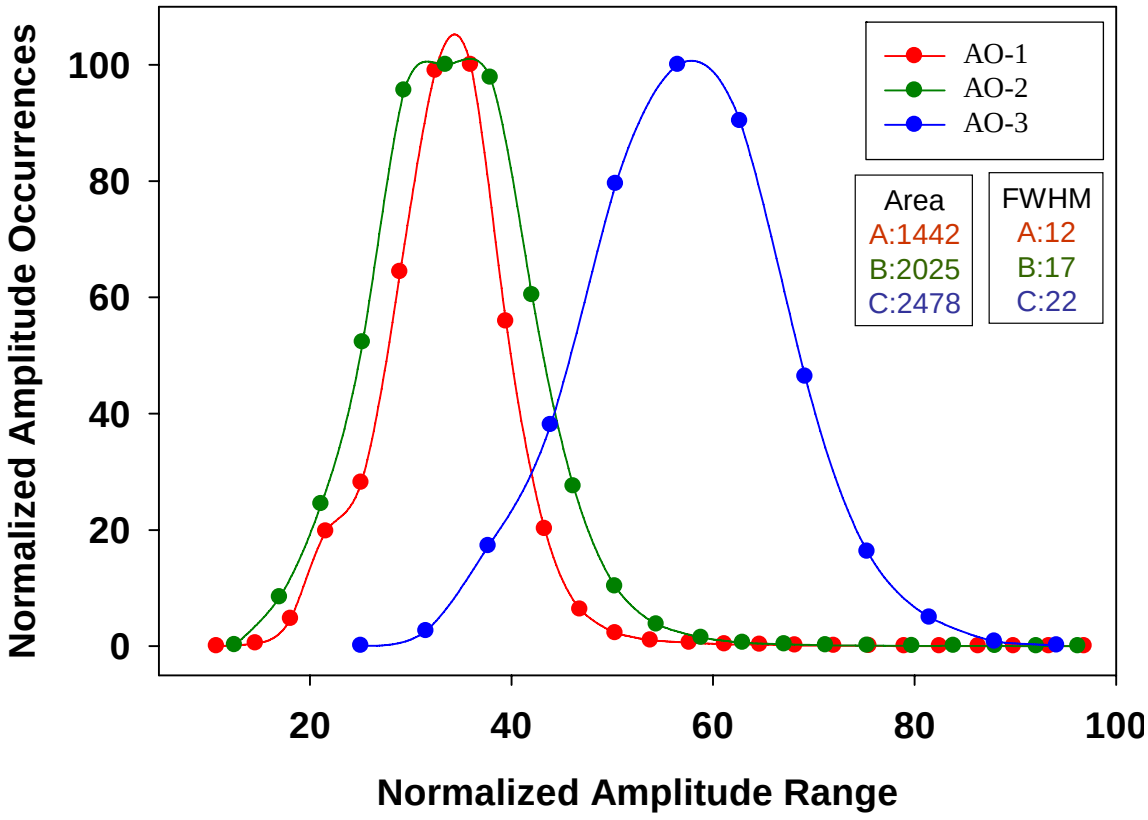

Figure 141. Reflected signal amplitude histogram curves of AO-1, AO-2, and AO-3 at 125 MHz.

5.9. Hot Pressed AlN Test Specimen

While the sintered SiC armor ceramic plates were compared to Al_2O_3 sintered plates, the hot pressed SiC armor ceramic plates were compared to hot pressed yttria-doped aluminum nitride (Y_2O_3-AlN) armor ceramic plates. Ultrasound point analysis, reflected signal amplitude C-scan imaging, and quantitative histogram analysis were applied to the AlN sample, and its properties were compared to the hot pressed SiC values reported for sample A. After measuring the sample length of 102.68 mm and sample width of 102.01, thickness of 15.68 mm, point analysis was conducted over the nine standard points throughout the sample. The average density of the sample reported by the manufacturer was 3.290 g/cm^3. Point analysis data are shown in Table LII. The longitudinal TOF values ranged from 2.919 μs to 2.951 μs with an average value of 2.938 μs while the shear TOF values ranged from 4.993 μs to 5.035 μs with an average value of 5.012 μs. This resulted in an average longitudinal velocity of 10,675 m/s, an average shear velocity of 6,258 m/s, an average Z value of 35.12 x 10^5 g/cm^{2}s, an average ν of 0.24, an average E value of 319 GPa, an average G value of 129GPa, and an average K value of 203 GPa. These measurements compared favorably to values in the literature, as the same type of Y_2O_3-AlN material from the manufacturer was reported to have a density of 3.288 g/cm3, ν = 0.24, and E = 317 GPa along with a flexural strength of 280 MPa and a Vicker's hardness value of 10.3 GPa [127]. An ultrasound study on AlN materials also reported a comparable longitudinal velocity of 10,700 m/s and shear velocity of 6,307 m/s [26]. Other armor ceramic manufacturers that produce both AlN and SiC reported another interesting difference between the two materials. First, the elastic properties were drastically different, with reported values of E for hot pressed SiC

~440 GPa in contrast to AlN values ~320 GPa [128]. Also, for one manufacturer, the average SiC grain size was reported to be 3-5 μm while the same manufacturer reported the average AlN grain size as 5-8 μm [29]. A different manufacturer reported the average grain size to be 10 μm for AlN [28]. Based on the reported data in the literature, the effect of larger average grain size on the ultrasound C-scan results was anticipated.

The first reflected signal amplitude ultrasound scan was conducted at 5 MHz as shown in Figure 142. The resulting image showed a great deal of amplitude variation through the bulk of the sample. In fact, the AlN sample showed more noticeable amplitude differences at 5 MHz than the previously discussed sintered Al_2O_3 test specimens, with a standard deviation value of 21.36 mV as compared to the Al_2O_3 samples which ranged from 12.12 mV to 14.44 mV. The reflected signal amplitude differences were characterized by both high and low amplitude circular regions throughout the scanned sample area. The data were plotted into a normalized amplitude histogram shown in Figure 143, where the low amplitude features stood out as two distinct ledges on the left side of the curve. The AUTC value for the AlN sample at 5 MHz was 758 and the FWHM value was 6. The overall area was much higher than the hot pressed SiC sample A AUTC value of 583, but the FWHM value was the same at 6. The FWHM values were identical because the low amplitude ledges from the AlN sample fell below the half maximum value of the histogram curve. These low amplitude regions led to a higher AUTC for AlN than for SiC sample A.

When high frequency C-scan imaging was attempted, there were several issues that arose that were not a problem for any of the previously reported scans on armor ceramic materials. Even though the average sample thickness was 15.68 mm which was

comparable to other materials, the bottom surface reflected signal could not be resolved at the highest frequency of 125 MHz. There were two major factors that differentiated the hot pressed AlN sample from the hot pressed SiC material and contributed to signal reduction at high frequencies. Not only was there a second phase which led to additional acoustic impedance mismatch between the AlN and the Y_2O_3, but the AlN average grain size was approximately double that of SiC, causing a higher degree of scattering which resulted in an increase in attenuation. These factors reduced the bottom surface reflected signal enough so that the amplitude was too low to separate from the noise floor. While the signal could be resolved to conduct scans at 75 MHz as shown in Figure 144, it was also apparent that the near-surface amplitude variations resulted in large variations in the bottom surface reflected signal amplitude C-scans. For this reason, a similar approach was taken to the ESC sample technique in which the effect of near-surface features was offset to look for the most significant amplitude differences from individual features. This method was applied by collecting both the standard bottom surface reflected signal data as well as the top surface reflected signal data which also included the near-surface features, as shown in Figure 145. The top surface AlN scan demonstrated a series of overlaid circular features while the rest of the sample was saturated with high amplitude values. The bottom surface reflected signal AlN scan showed the circular features even more clearly, with a higher amplitude region in the middle. By determining the average weighted factor, multiplying by the bottom surface reflected signal amplitude data and subtracting from the top surface reflected signal amplitude data as described earlier, the heavy influence of the near surface features was offset. The resulting image was much more uniform overall, with distinct high amplitude features distributed throughout the

sample which were believed to represent a Y_2O_3-Al_2O_3 or Y_2O_3 second phase with a density as high as 4.472 g/cm^3 compared to the measured AlN density of 3.290 g/cm^3 reported by the manufacturer [127]. This higher density second phase effect was similar to the effect that the TiB_2 additive had on the sintered ST SiC samples, as there were circular high amplitude features throughout the ultrasound C-scan images. While these circular high amplitude features were concentrated in the top left corner and throughout the bottom of the sample, the left side of the sample showed low amplitude circular regions that were likely the result of large grains which caused higher scattering and reduced the amplitude. The standard deviation for the hot pressed AlN sample was 111.80 mV as compared to the value of 44.00 mV for hot pressed SiC sample A. The corrected 75 MHz AlN data were plotted as a normalized amplitude histogram in Figure 146, and although the histogram curve was very broad, the correction method reduced the effect of any distinguishing tail characteristics, instead highlighting the presence of individual features. The AUTC value for the AlN sample was 1922 and the FWHM value was 19. These were much higher than the high frequency SiC sample A values of 1143 for AUTC and 2 for FWHM. These quantitative ultrasound histogram trends were consistent with the acoustic and elastic property trends which showed higher values for hot pressed SiC samples as compared to AlN samples. The hot pressed Y_2O_3-AlN sample was the most difficult to evaluate ultrasonically, as it could not be imaged at 125 MHz. While useful data were collected, the AlN sample managed to expose some of the features of armor ceramic plates that are most difficult to handle when performing ultrasound C-scan imaging, especially at high frequencies.

#	ρ (g/cc)	t (mm)	TOF_l (μs)	TOF_s (μs)	c_l (m/s)	c_s (m/s)	Z (*10^5 g/cm^{2}s)	ν	E (GPa)	G (GPa)	K (GPa)
1	3.290	15.68	2.935	5.002	10,685	6269	35.15	0.24	320	129	203
2	3.290	15.68	2.935	5.002	10,685	6269	35.15	0.24	320	129	203
3	3.290	15.68	2.919	4.993	10,743	6281	35.35	0.24	322	130	207
4	3.290	15.68	2.943	5.018	10,656	6250	35.06	0.24	318	129	202
5	3.290	15.68	2.951	5.035	10,627	6228	34.96	0.24	316	128	201
6	3.290	15.68	2.943	5.026	10,656	6240	35.06	0.24	318	128	203
7	3.290	15.68	2.943	5.010	10,656	6259	35.06	0.24	319	129	202
8	3.290	15.70	2.943	5.017	10,669	6259	35.10	0.24	319	129	203
9	3.290	15.70	2.934	5.009	10,702	6269	35.21	0.24	320	129	204
Avg	**3.290**	**15.68**	**2.938**	**5.012**	**10,675**	**6258**	**35.12**	**0.24**	**319**	**129**	**203**

Table LII. Point analysis data for sample AlN.

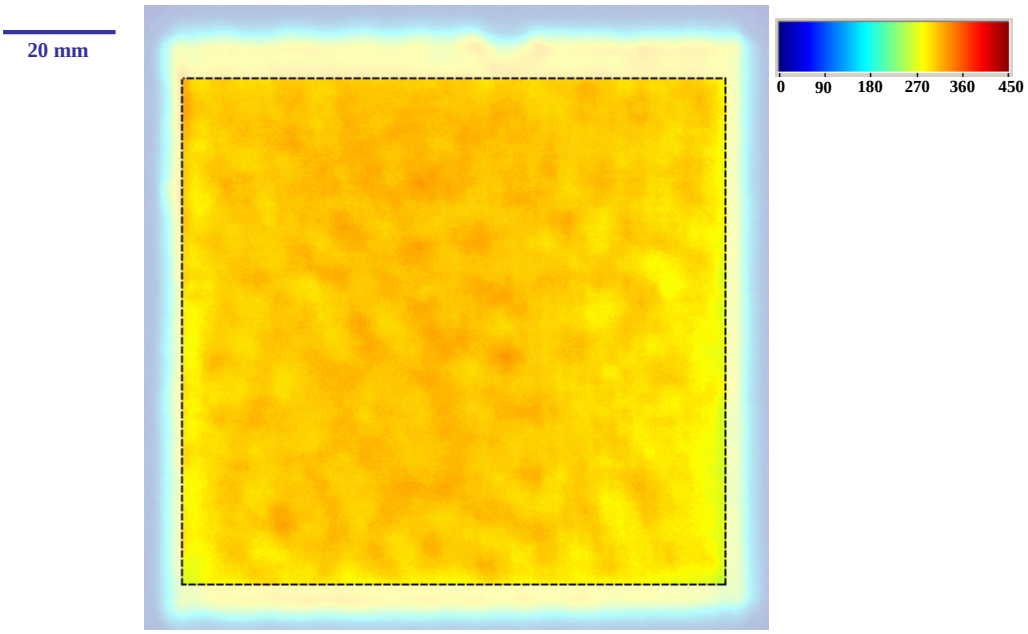

Figure 142. Reflected signal amplitude C-scan image of AlN at 5 MHz.

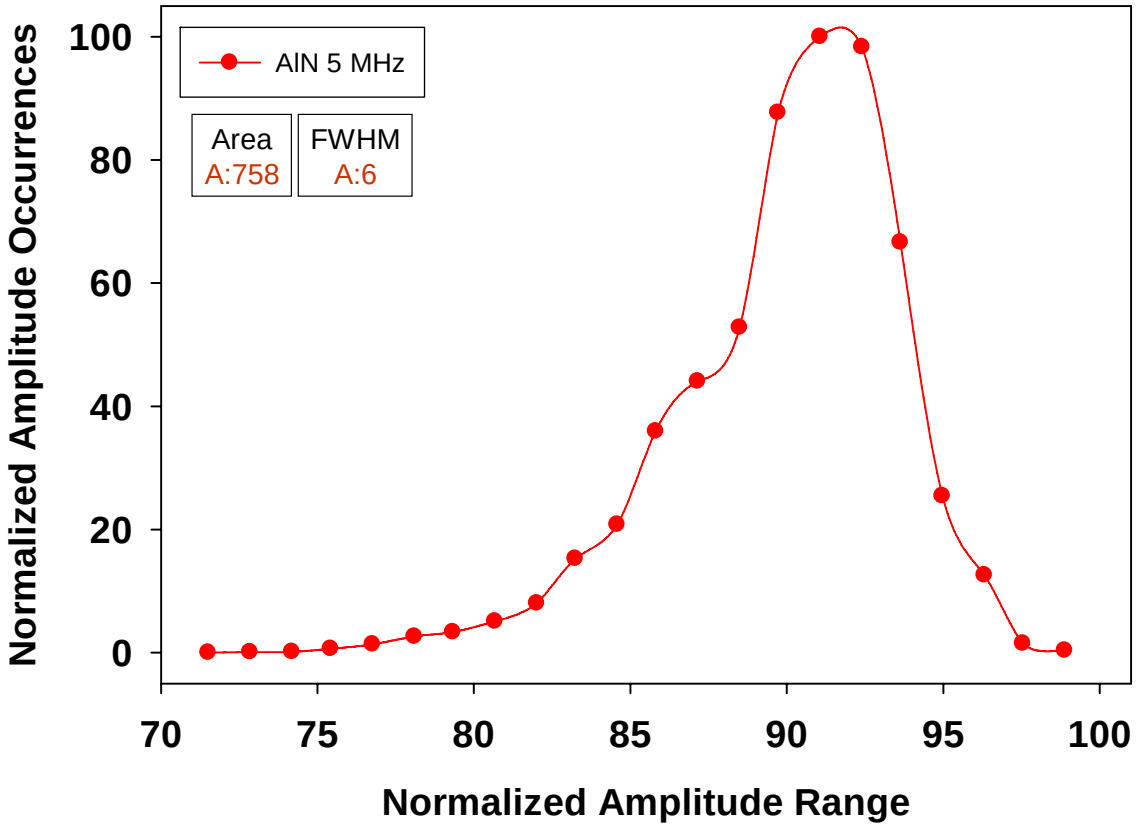

Figure 143. Reflected signal amplitude histogram curve of AlN at 5 MHz.

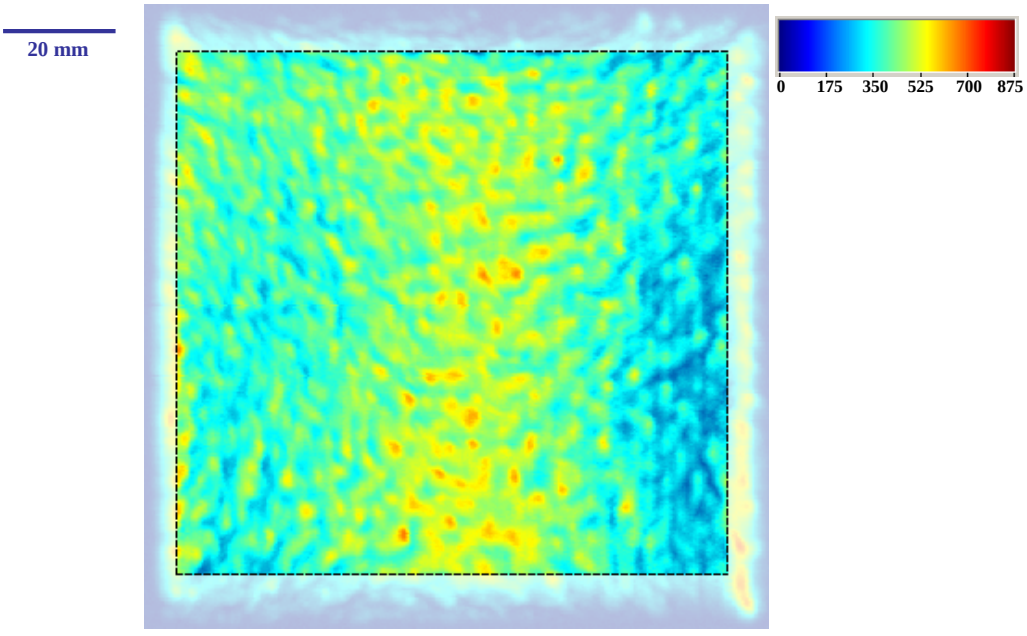

Figure 144. Reflected signal amplitude C-scan image of AlN at 75 MHz.

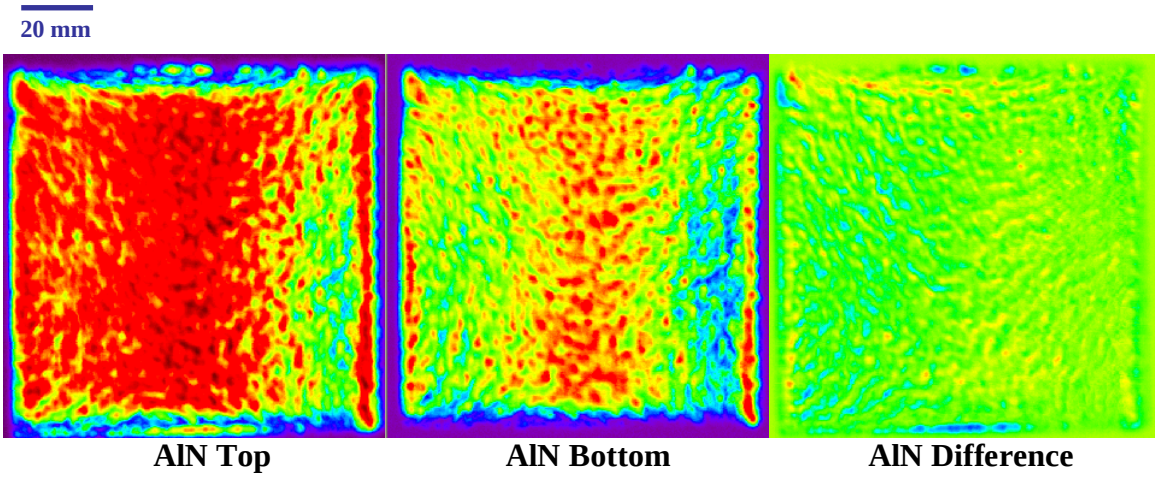

Figure 145. Surface roughness adjusted images of AlN sample at 75 MHz.

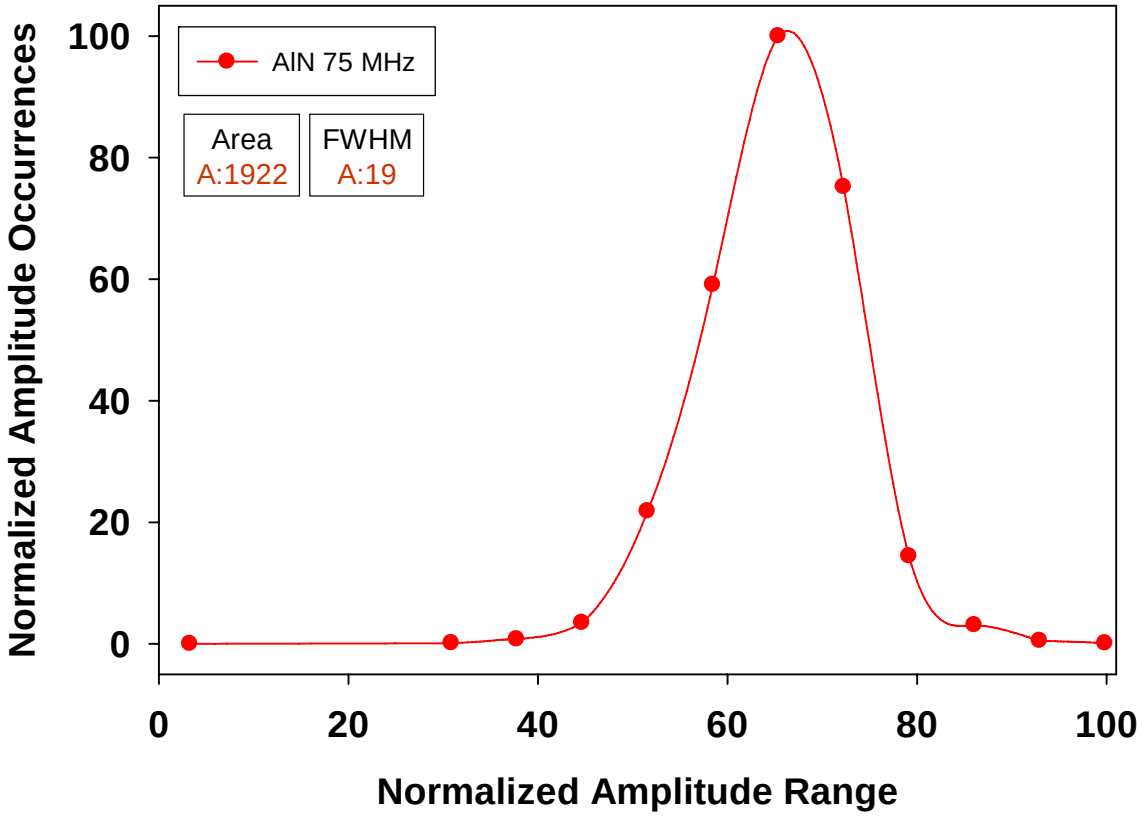

Figure 146. Surface roughness adjusted amplitude histogram curve of AlN sample at 75 MHz.

5.10. Ultrasound Fingerprints

A variety of ultrasound C-scan imaging and quantitative analysis methods have been applied to armor ceramic materials up to this point. In order to summarize and compare the key acoustic parameters and important quantitative values among different samples, an ultrasound fingerprint has been developed. Ultrasound fingerprints have been established for given test specimens at specified frequencies to include reflected signal amplitude and TOF C-scan image maps, reflected signal amplitude, TOF, and material velocity histogram curves, and vital acoustic statistics. The statistics included average density, average sample thickness, average acoustic impedance, average TOF, average TOF standard deviation, average reflected signal amplitude, average reflected signal amplitude standard deviation, TOF AUTC, TOF FWHM, material velocity AUTC, material velocity FWHM, reflected signal amplitude AUTC, reflected signal amplitude FWHM, average longitudinal velocity, average shear velocity, average elastic modulus, average shear modulus, and average bulk modulus. These data highlighted some of the most valuable information that was generated from ultrasound imaging and evaluation and was potentially useful for application to armor ceramic property, design, and performance optimization. Since no two test specimens were exactly the same, the unique set of data, images, and histograms has been described as a representative materials fingerprint. By collecting a series of ultrasound fingerprints for numerous test specimens, a database can be put together for further sample comparison.

The first step in assembling an ultrasound fingerprint involved selecting a test specimen and choosing the frequency or frequencies that would describe the defects or features of interest. As mentioned earlier, different transducer frequencies have been

used to describe different types of features based on their level of sensitivity and theoretical detection limits. If the critical features dictating performance were the microstructural-range defects, the highest frequency ultrasound transducers that could handle the sample thickness without excessive attenuation could be chosen. If the critical features were regional variations in density characterized by TOF and reflected signal amplitude differences, a medium frequency transducer could be used that was sensitive to those variations. If large, anomalous defects were of critical importance for screening materials, a low frequency transducer could be used to detect large variations. In this case, ultrasound fingerprints were established based on high frequency C-scan imaging and data for evaluating microstructural differences at a high sensitivity. The 125 MHz reflected signal amplitude and 75 MHz TOF images and the quantitative data from each sample were utilized. The 75 MHz TOF images were chosen rather than the 125 MHz TOF images because some of the samples at 125 MHz showed a high degree of noise since the reflected signals were gated very close to the noise floor. These ultrasound fingerprints were generally referred to as high frequency ultrasound fingerprints, and were established for hot pressed SiC samples A, B, and C as shown in Figures 147-149, sintered SiC samples SA1-SA8 in Figures 150-157, and sintered SiC samples ST1-ST8 in Figures 158-165. These fingerprints were valuable for side-by-side comparison among armor ceramic test specimens.

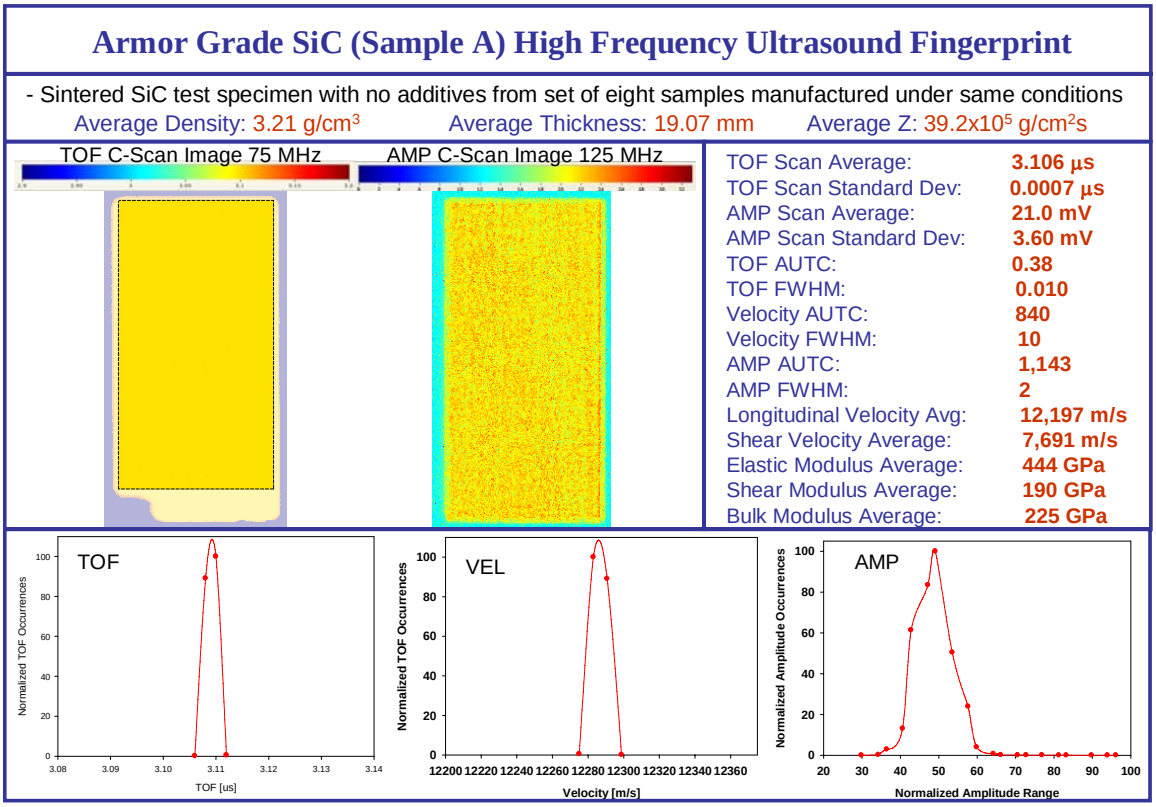

Figure 147. High frequency ultrasound fingerprint of sample A.

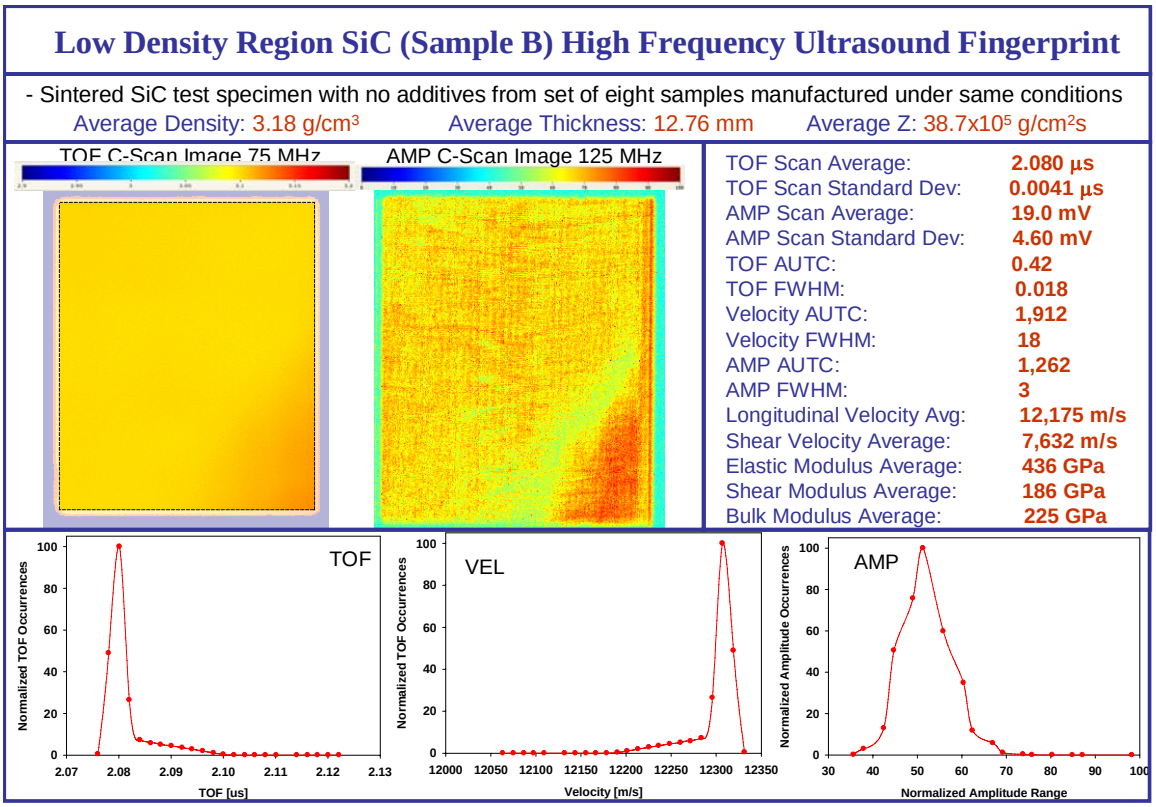

Figure 148. High frequency ultrasound fingerprint of sample B.

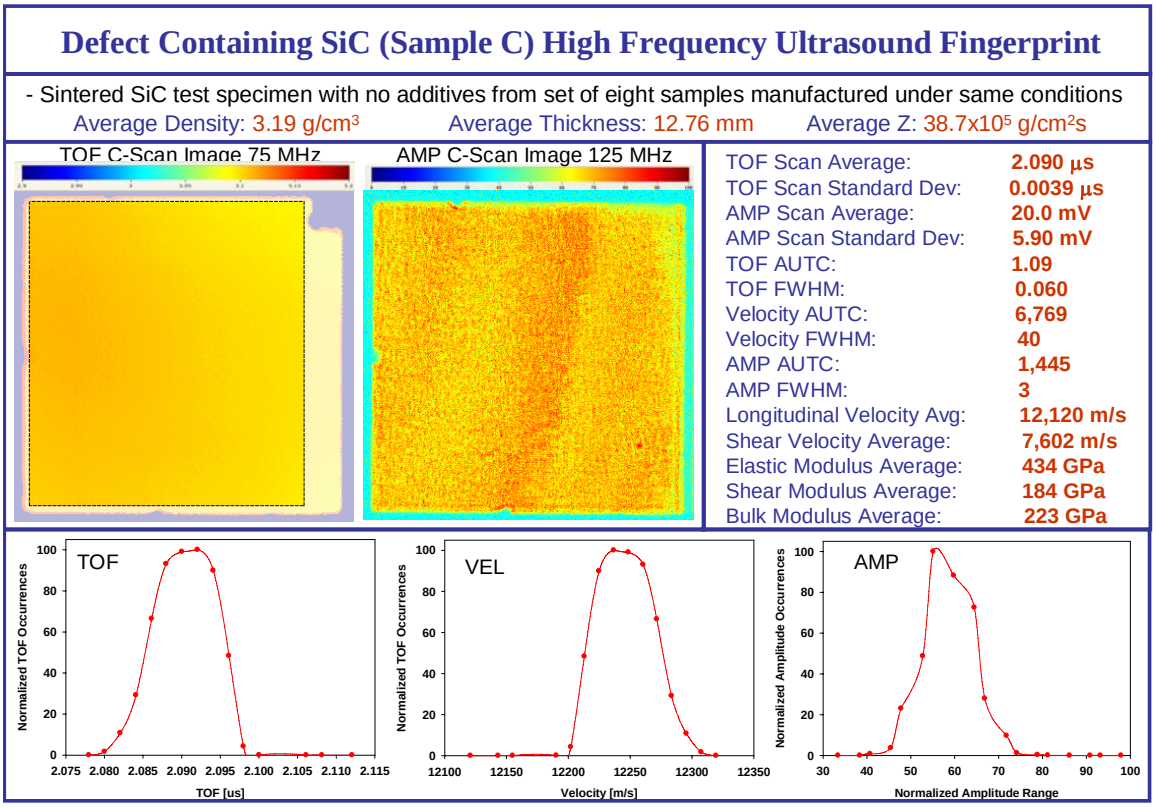

Figure 149. High frequency ultrasound fingerprint of sample C.

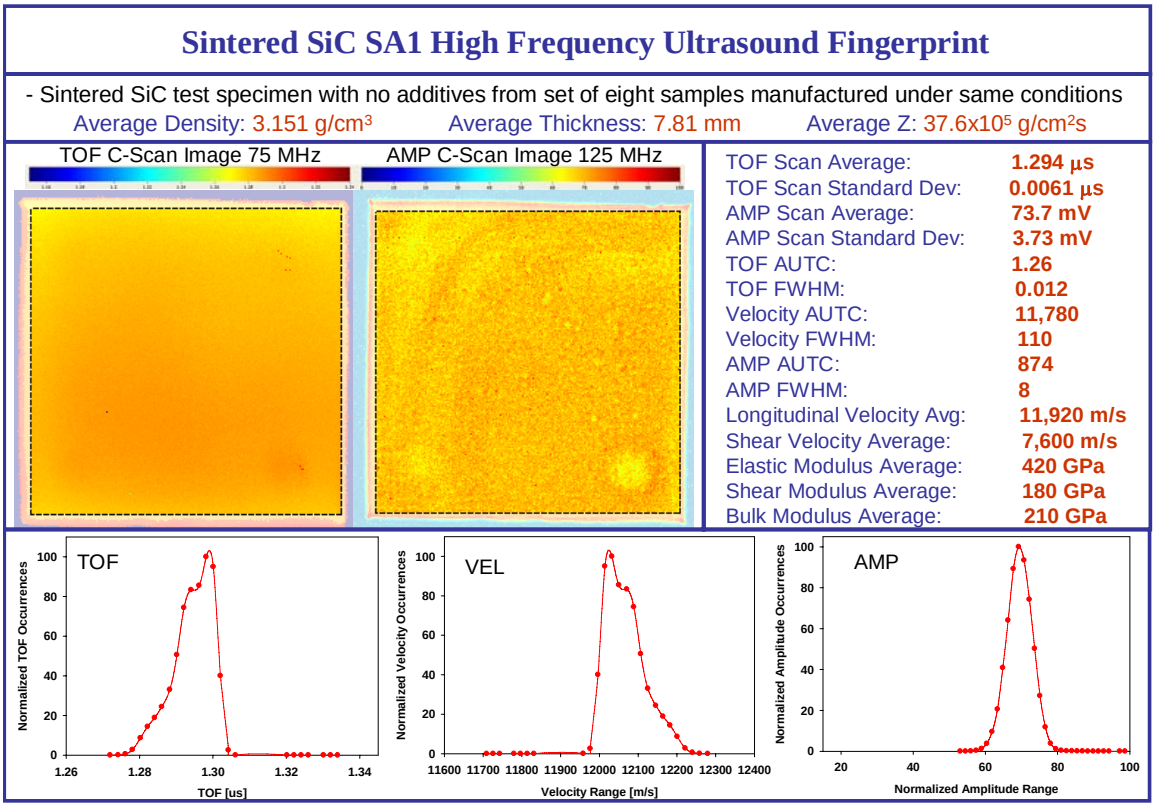

Figure 150. High frequency ultrasound fingerprint of sample SA1.

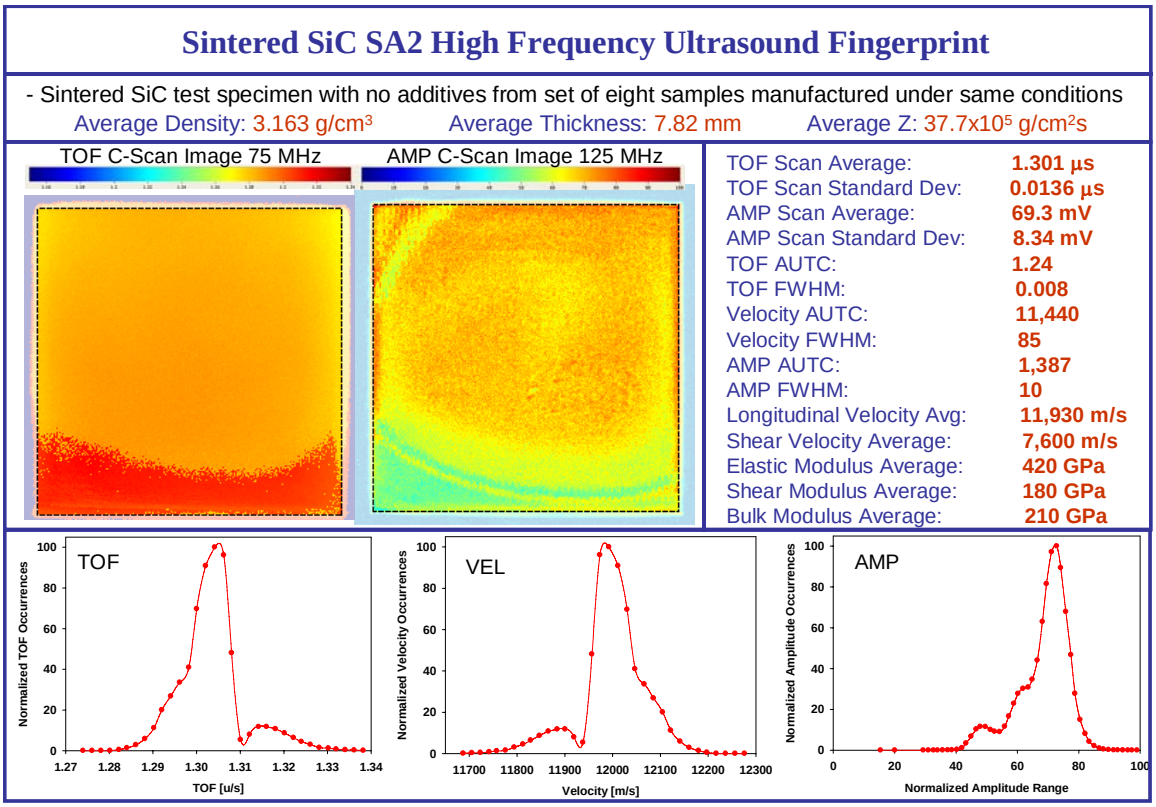

Figure 151. High frequency ultrasound fingerprint of sample SA2.

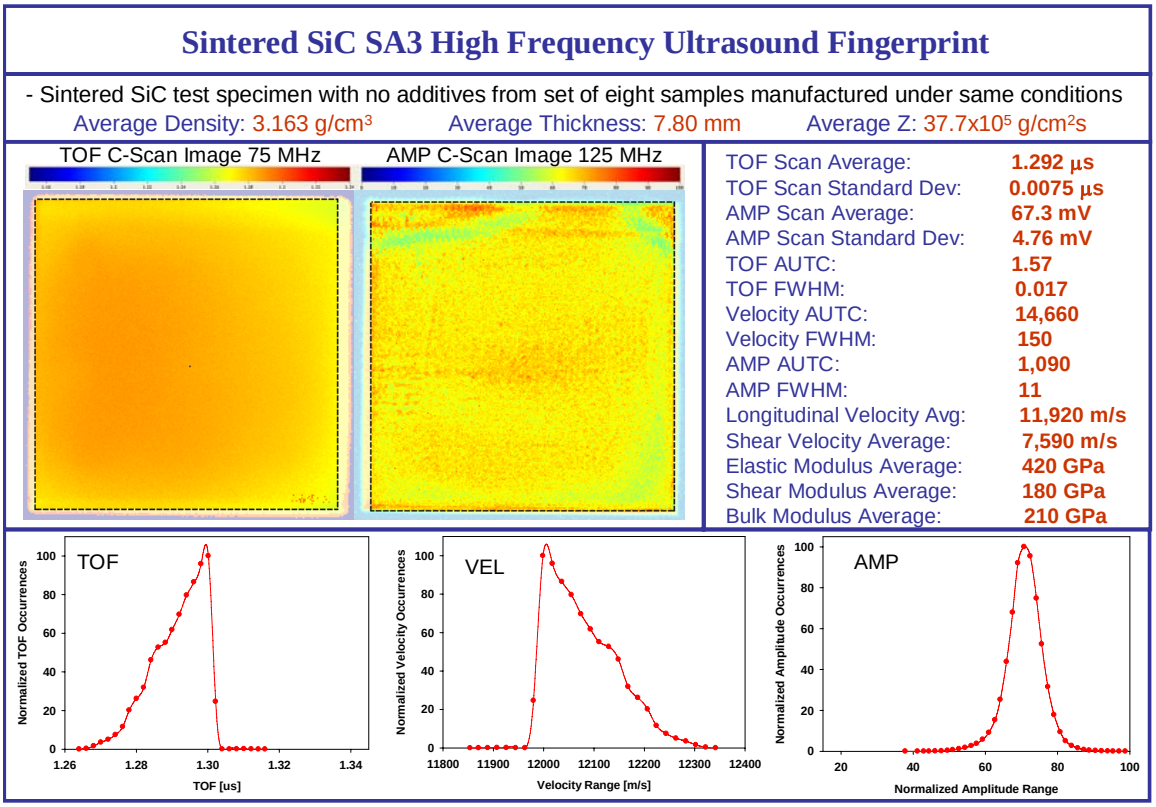

Figure 152. High frequency ultrasound fingerprint of sample SA3.

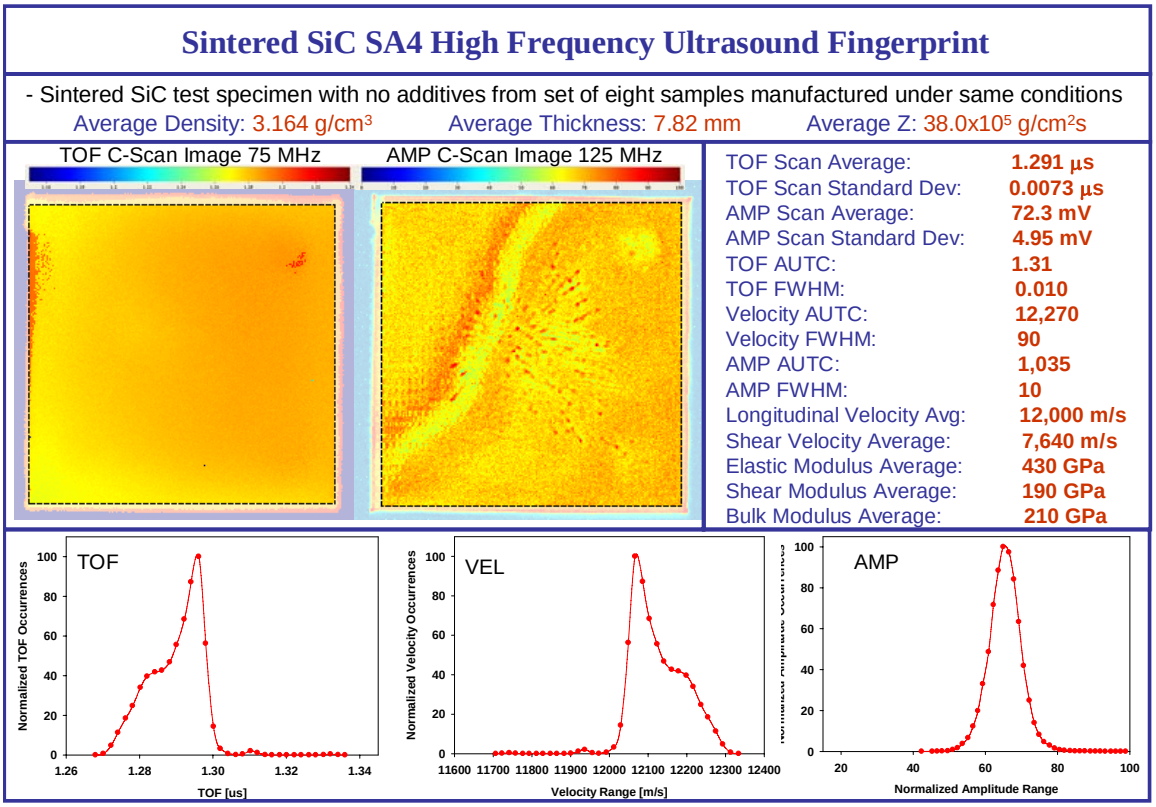

Figure 153. High frequency ultrasound fingerprint of sample SA4.

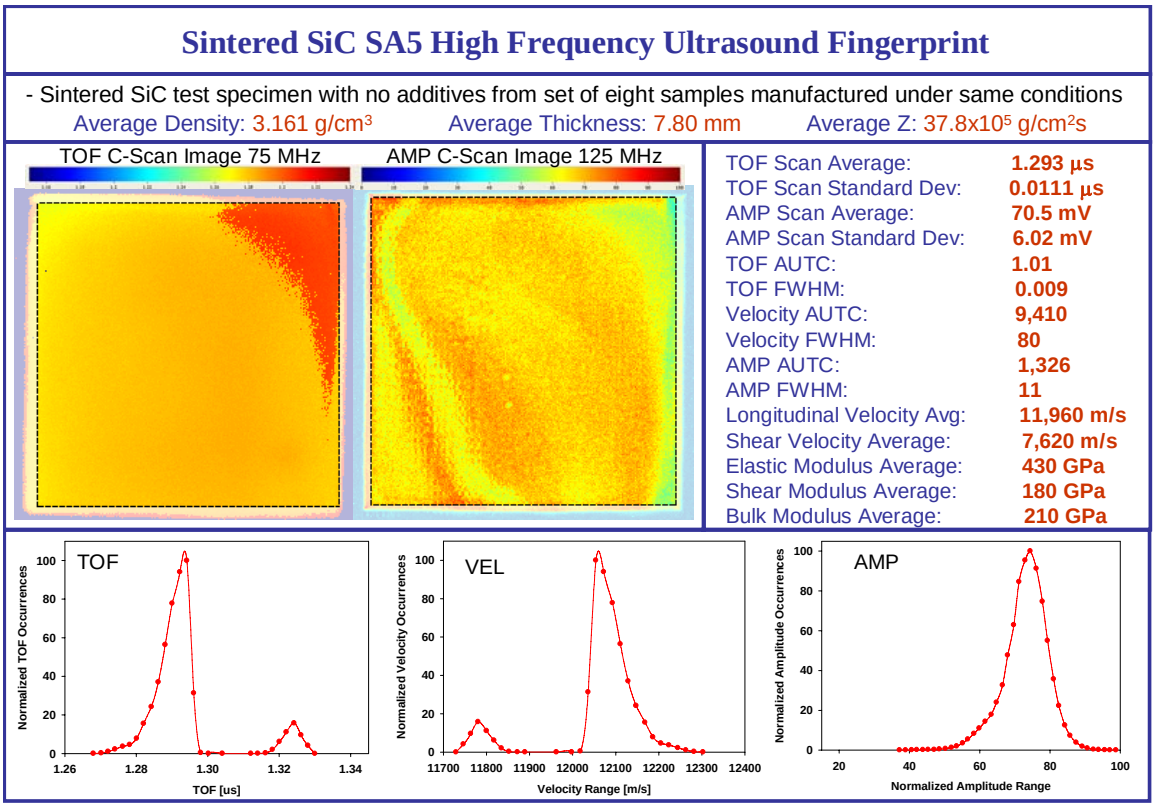

Figure 154. High frequency ultrasound fingerprint of sample SA5.

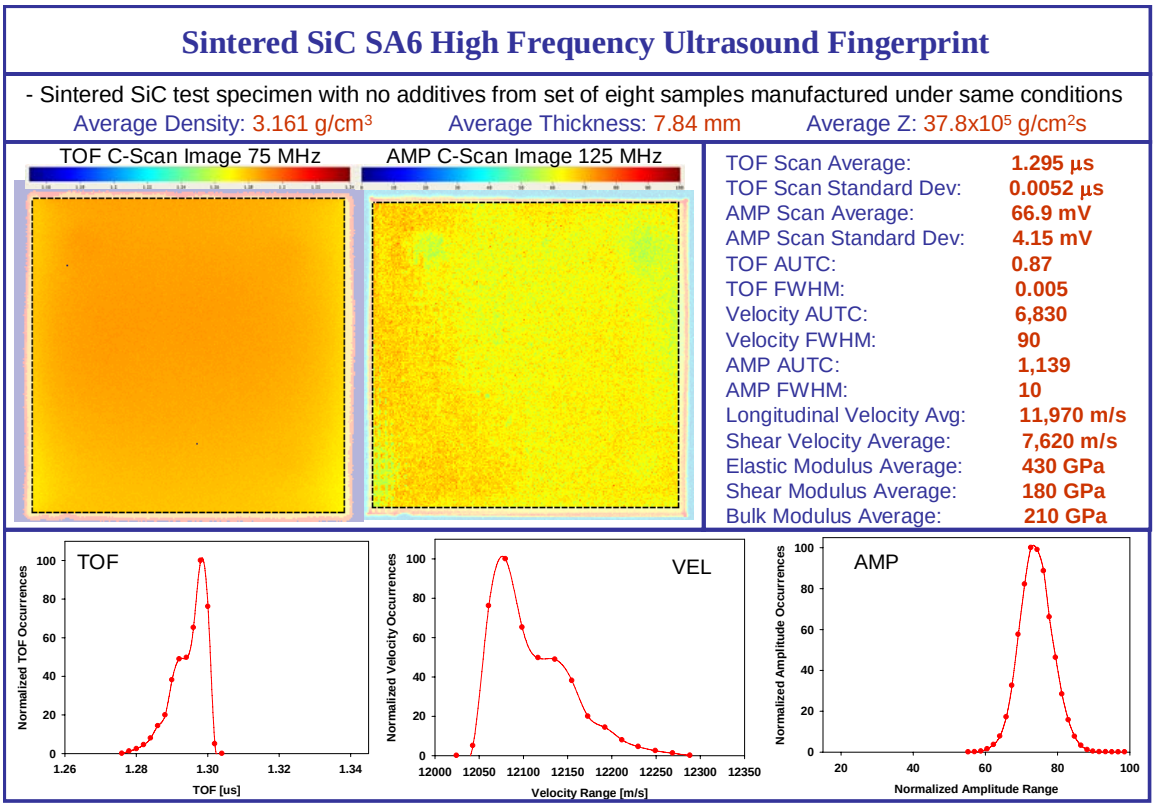

Figure 155. High frequency ultrasound fingerprint of sample SA6.

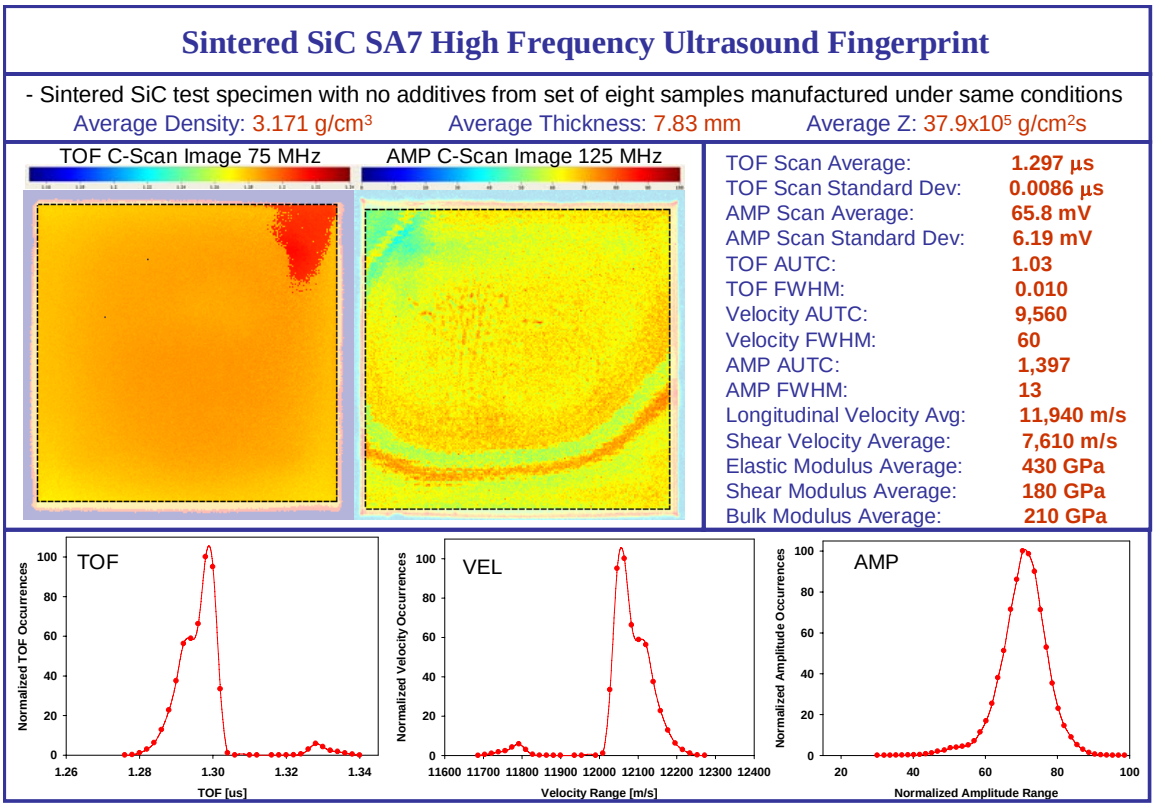

Figure 156. High frequency ultrasound fingerprint of sample SA7.

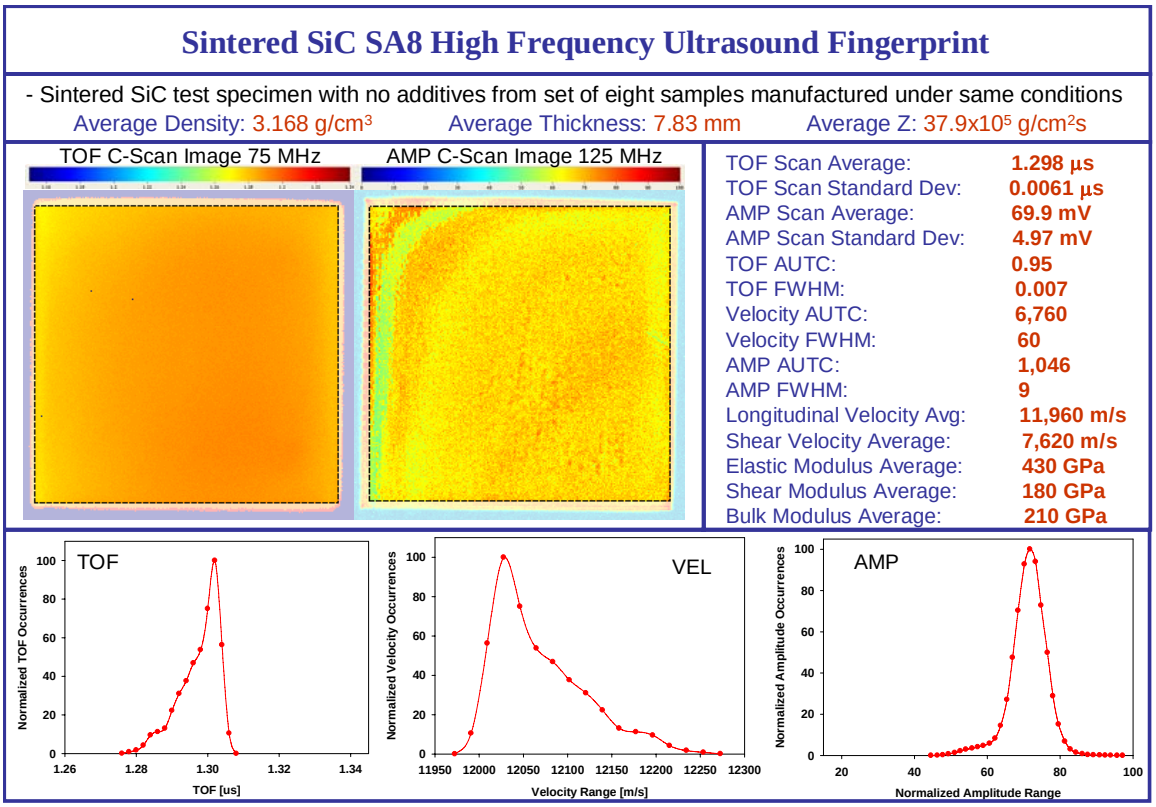

Figure 157. High frequency ultrasound fingerprint of sample SA8.

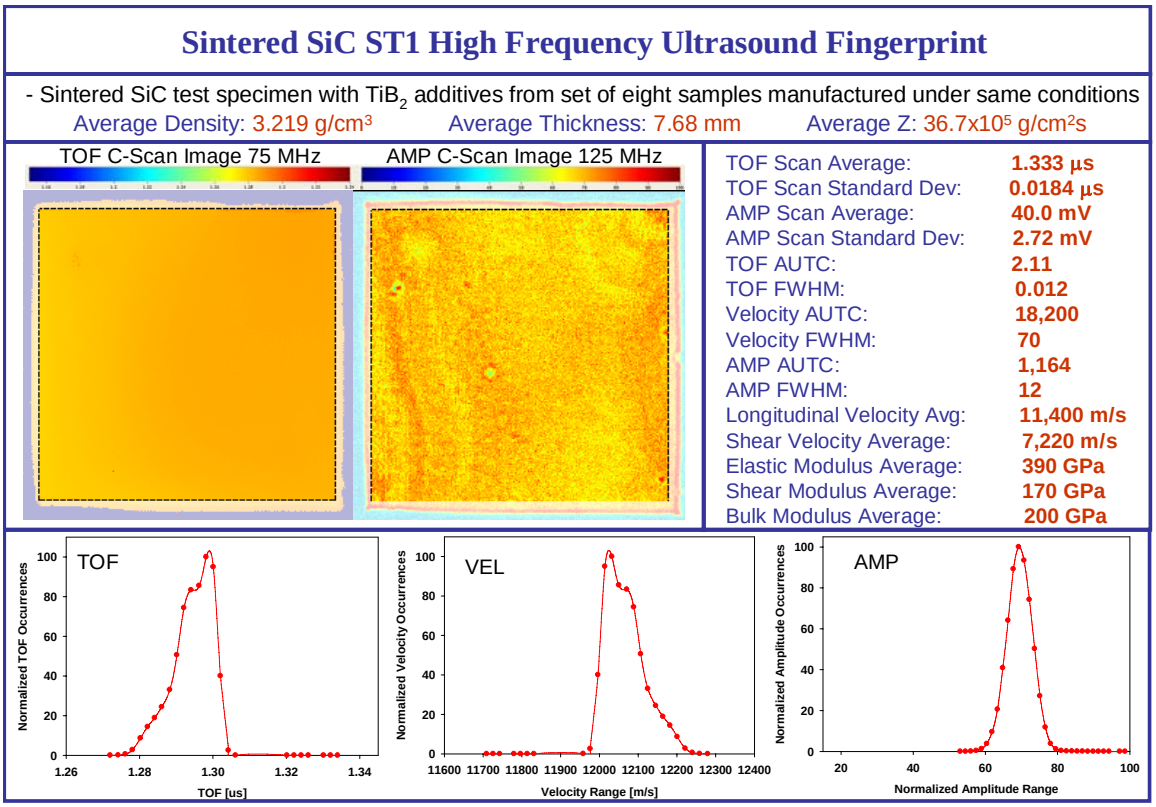

Figure 158. High frequency ultrasound fingerprint of sample ST1.

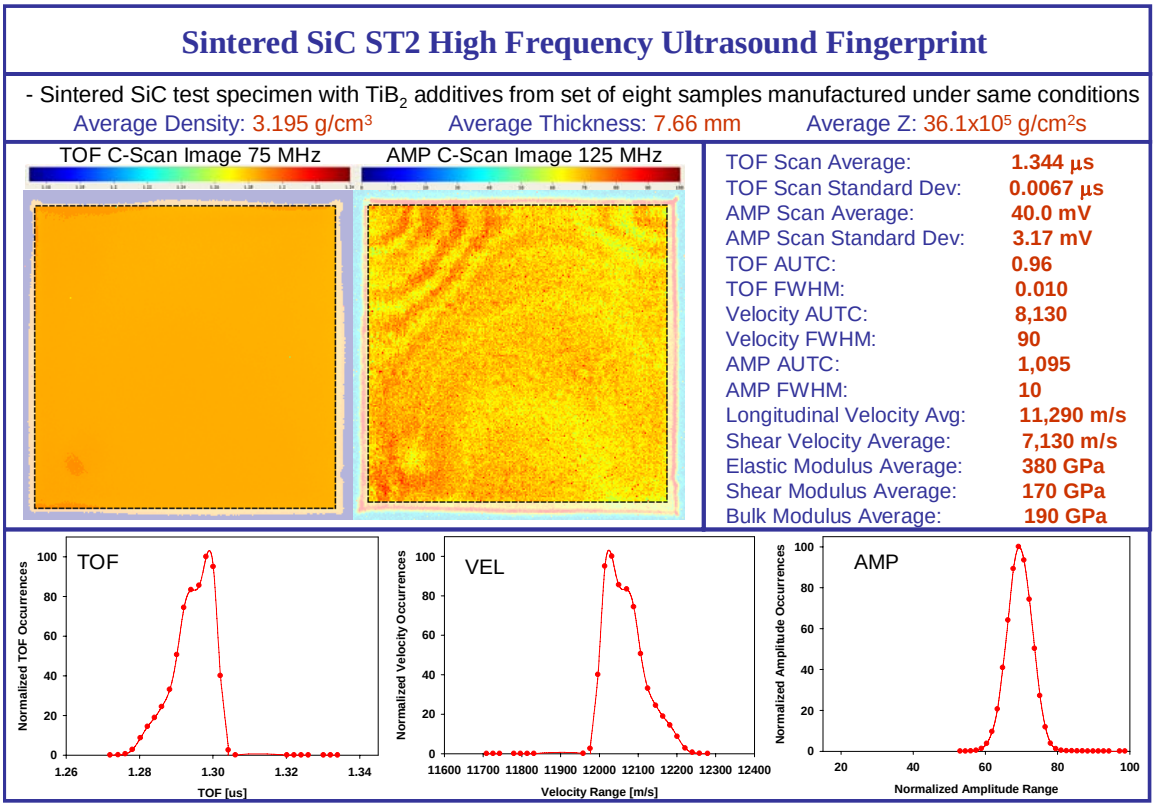

Figure 159. High frequency ultrasound fingerprint of sample ST2.

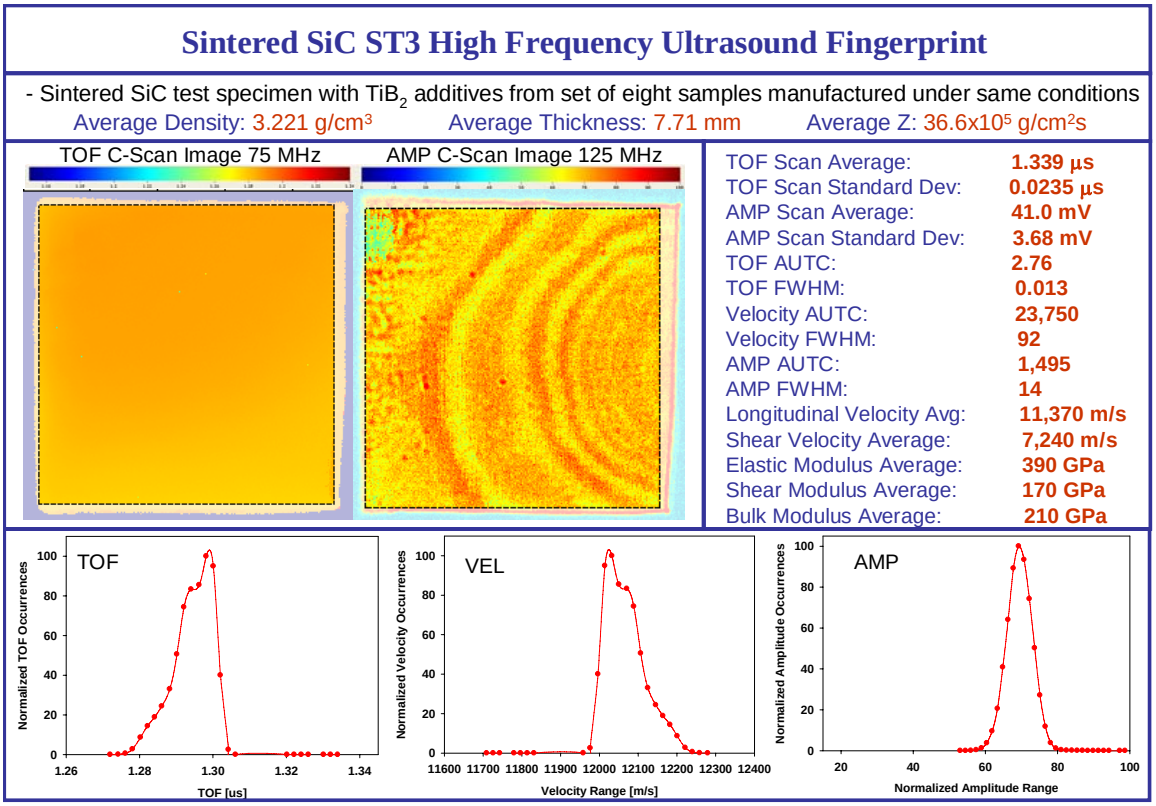

Figure 160. High frequency ultrasound fingerprint of sample ST3.

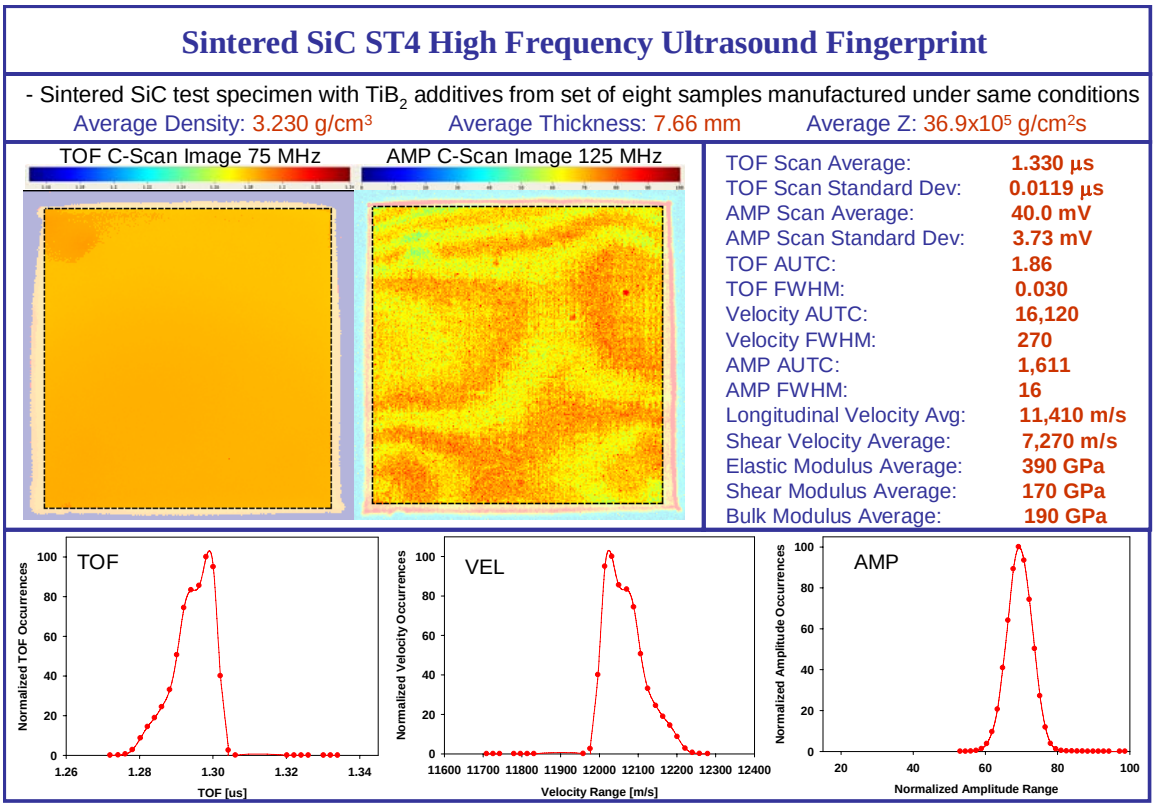

Figure 161. High frequency ultrasound fingerprint of sample ST4.

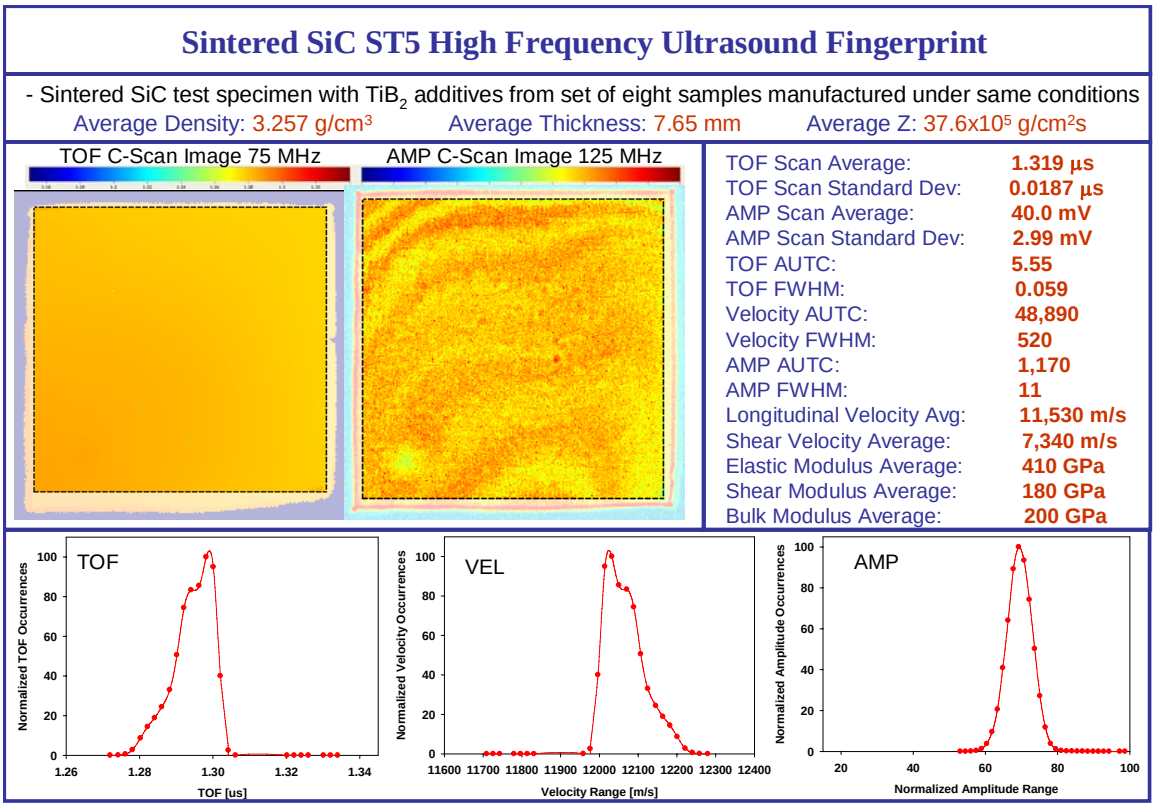

Figure 162. High frequency ultrasound fingerprint of sample ST5.

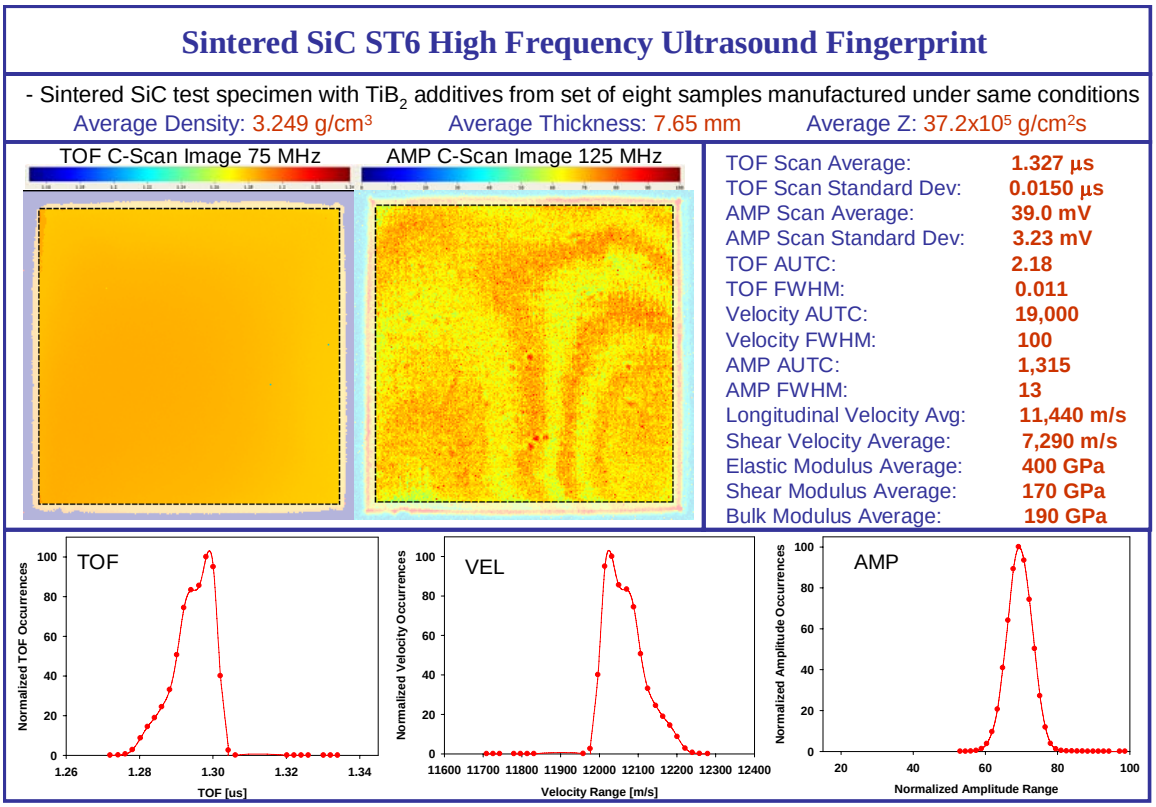

Figure 163. High frequency ultrasound fingerprint of sample ST6.

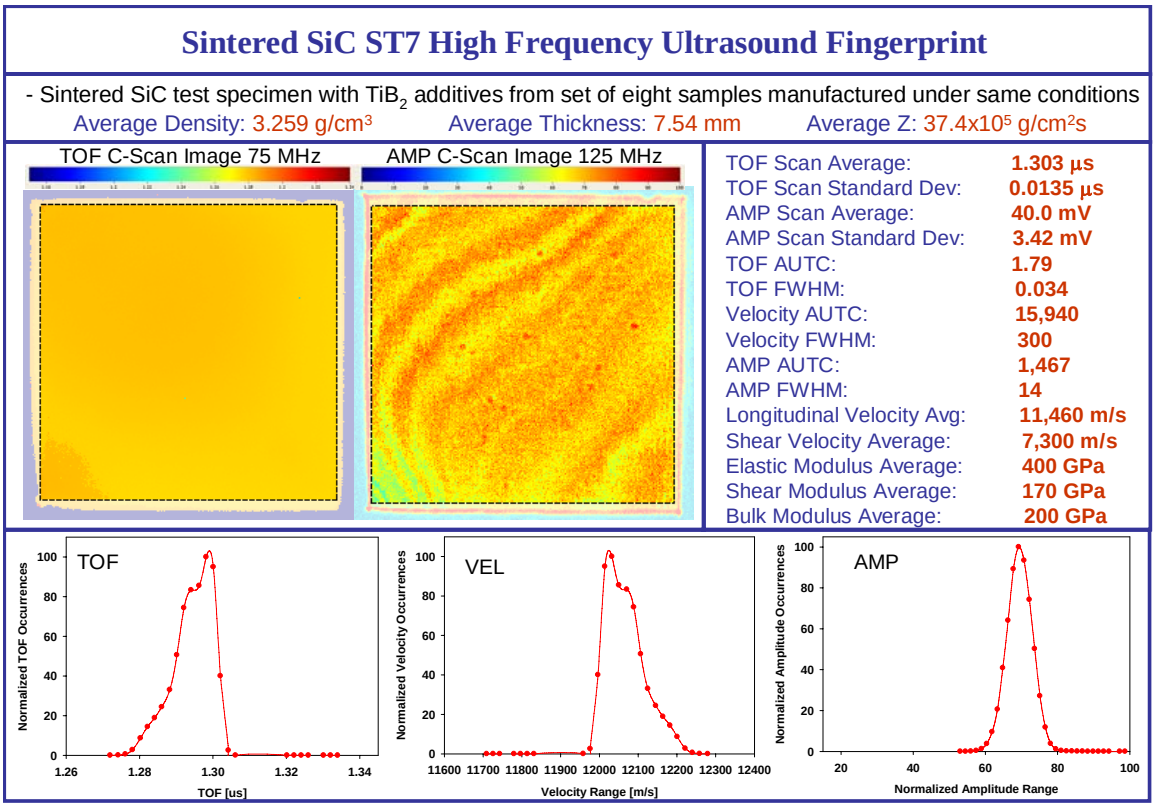

Figure 164. High frequency ultrasound fingerprint of sample ST7.

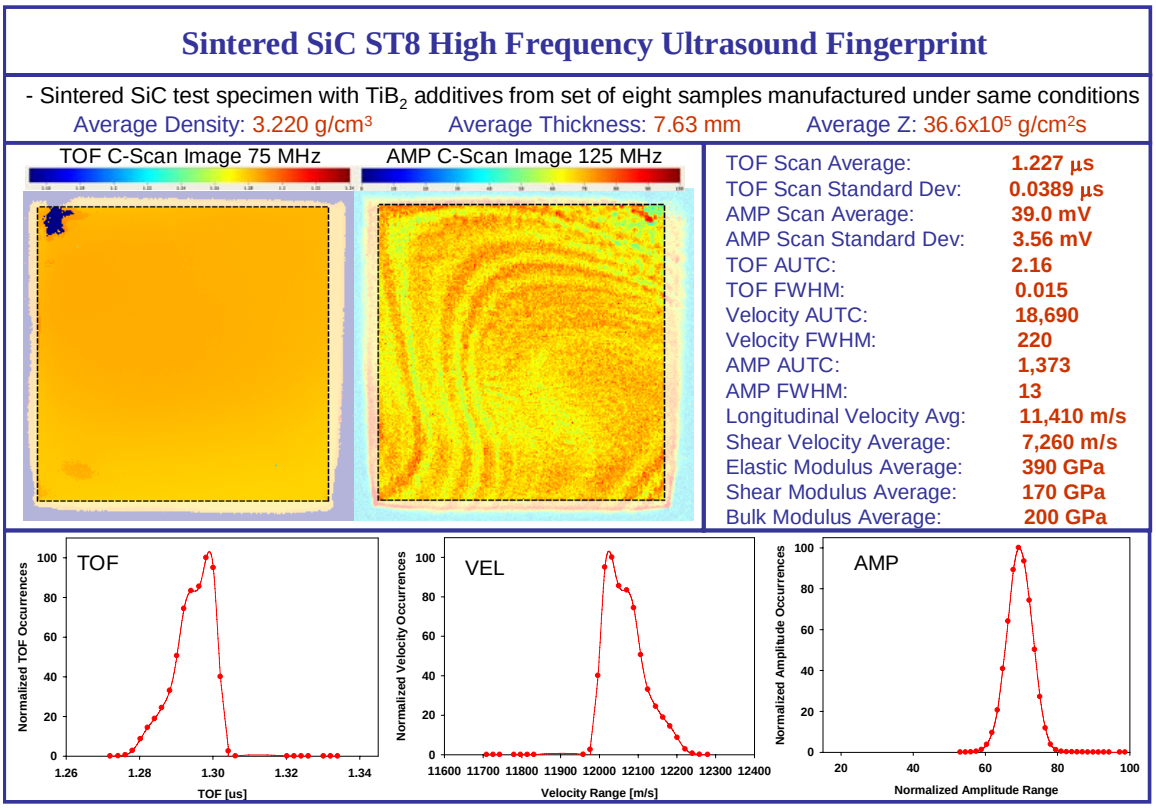

Figure 165. High frequency ultrasound fingerprint of sample ST8.

After putting together high frequency ultrasound fingerprints for the listed test specimens, comparisons were made among the samples. The first two comparisons were made between samples within the same set while the third comparison was made among samples in different sets. Hot pressed SiC samples B and C were compared first, as B was the test specimen pulled from the production line for failing to meet the density specifications and C was the test specimen pulled from the production line when a discoloration on the surface was noticed. Side-by-side comparison of the ultrasound fingerprints first showed that the average thickness and Z values were identical at 12.76 mm and 39.2 x 10^5 g/cm^{2}s, respectively, while the measured average density value was slightly lower for sample B at 3.18 g/cm^3 as compared to 3.19 g/cm^3 for sample C. Comparison of the TOF images showed high TOF regions in the bottom right corner for sample B and on the left side for sample C. Comparison of the reflected signal amplitude images showed a low amplitude region and high amplitude region for sample B in the bottom right corner while sample C showed some high amplitude inclusions and a high amplitude band running through the center of the sample. While the TOF and velocity histograms for sample B showed a long tail due to the high TOF/low velocity region, sample C showed a smaller tail but a much wider distribution of values. The reflected signal amplitude histograms were both one-phase with slight tails on the right sides of the curves representing the high amplitude regions. Since visual comparison indicated only some of the trends, the quantitative data was also compared. The average and standard deviation TOF and amplitude values were very similar for both samples, with sample B having a slightly higher TOF deviation of 0.0041 μs and sample C having a slightly higher amplitude deviation of 5.90 mV. The main differences came from the AUTC and

FWHM values. The wide histogram curve distributions for sample C were apparent from the data, with AUTC values of 1.09, 6769, and 1445 and FWHM values of 0.060, 40, and 3 for TOF, velocity, and amplitude, respectively, as compared to AUTC values of 0.42, 1912, and 1262 and FWHM values of 0.018, 18, and 3, respectively. These values quantitatively described the wide distribution of acoustic values and were reflected in slight differences in average material velocities and elastic properties. While sample C had average longitudinal velocity, shear velocity, elastic modulus, shear modulus, and bulk modulus values of 12,120 m/s, 7,602 m/s, 434 GPa, 184 GPa, and 223 GPa, respectively, sample B showed consistently higher values of 12,175 m/s, 7,632 m/s, 436 GPa, 186 GPa, and 225 GPa, respectively. Ultrasound fingerprint analysis provided a detailed acoustic comparison of two samples that were previously not distinguished other than the fact that neither of them met manufactured specifications.

A second comparison was made between two samples, SA2 and SA6, which were fabricated from the same batch under the same conditions as sintered SiC test specimens. While the average density, thickness, and Z values were comparable, the main distinction was observed when comparing the TOF and reflected signal amplitude scans. Sample SA6 appeared to be much more homogeneous than sample SA2 which showed a large high TOF/low amplitude region at the bottom of the C-scan image. The TOF and velocity histograms revealed a significant shoulder in SA6 that showed some variations while sample SA2 had a separate tail region characteristic of a two-phase material. The standard deviation and AUTC demonstrated these differences quantitatively. Sample SA6 had a TOF deviation of 0.0052 μs, an amplitude deviation of 4.15 mV, a TOF AUTC of 0.87, a velocity AUTC of 6,830, and an amplitude AUTC of 1,139. The values

were consistently higher for SA2 which had a TOF deviation of 0.0136 μs, an amplitude deviation of 8.34 mV, a TOF AUTC of 1.24, a velocity AUTC of 11,440, and an amplitude AUTC of 1,387. Despite these differences, the average material velocities were not very different, with SA2 showing only slightly lower values of longitudinal velocity by 40 m/s and shear velocity by 20 m/s. The biggest difference was in the elastic modulus in which SA2 was lower by 10 GPa, but the shear modulus and bulk modulus values were identical. The variations that were believed to be highly significant between the two samples did not show very high variations according to the ultrasound fingerprints. Further destructive and ballistic testing could indicate whether these differences are significant for armor ceramic performance.

In another study, samples from three different sets were compared. Two of the samples which were utilized for the last two fingerprint comparison studies, sample B and sample SA2, were compared to each other as well as sample ST3. Sample B was the only hot pressed sample out of the three while samples SA2 and ST3 were both sintered, with ST3 containing TiB_2 inclusions. These three samples were all chosen for comparison since they all showed distinct features or critical regions that were different from the rest of the bulk SiC materials. Comparing average reported densities, ST3 was the highest at 3.221 g/cm^3 due to the addition of the TiB_2 second phase, since TiB_2 has a higher density than SiC. Sample B was the thickest of the three samples at 12.76 mm compared to 7.82 mm for SA2 and 7.71 mm for ST3. Sample B also had the highest acoustic impedance value of 38.7 x 10^5 g/cm^2s while SA2 had a Z value of 37.7 x 10^5 g/cm^2s and ST3 had a Z value of 36.6 x 10^5 g/cm^2s. Even though ST3 had the highest density among the three samples, it also had the lowest longitudinal velocity of 11,370

m/s as compared to 11,930 m/s for SA2 and 12,120 m/s for B, which explained why it also had the lowest Z value. Comparison of the C-scan images showed high TOF regions in the bottom right corner of B and the bottom of SA2 while ST3 showed a lower TOF region at the bottom of the sample. This resulted high TOF one-phase tail for B, a high TOF two-phase tail for SA2, and a low TOF two-phase tail for ST3 according to the histograms. The reflected signal amplitude histograms showed slight tails at the lower and higher ends for sample B, a large low amplitude tail for SA2, and a wide normal distribution for ST3. The large amplitude variations accounted for the wide distribution, but also appeared to level out the overall histogram curve as the distribution was more normal and did not favor tails on either side. While TOF and velocity values were difficult to compare since they were not normalized, amplitude AUTC and FWHM values were normalized for the samples and compared to one another. The hot pressed sample B showed the lowest AUTC and FWHM values of 1,262 and 3 while the values increased to 1,387 and 10, respectively, for SA2, and increased again to 1,495 and 14, respectively, for ST3. These reinforced the general histogram trend that armor ceramic materials with the highest overall degree of variation are more likely to have the largest AUTC and FWHM values. The elastic properties also scaled accordingly, with elastic modulus values of 434 GPa, 420 GPa, and 390 GPa for samples B, SA2, and ST3, respectively, shear modulus values of 184 GPa, 180 GPa, and 170 GPa, respectively, and bulk modulus values of 223 GPa, 210 GPa, and 210 GPa, respectively. This comparison of acoustically variable materials from three different sample sets showed a distinct increase in material velocities and elastic properties for the hot pressed armor ceramic material. Since samples SA2 and ST3 were identical in their method of fabrication other

than the addition of TiB_2 to ST3, the presence of TiB_2 accounted for lower overall material velocity and elastic properties despite a higher sample density. While the hot pressed SiC materials appeared to have the overall edge, destructive and ballistic testing are important to determine whether or not these differences are critical. If they were not critical differences in terms of armor ceramic performance, the lower cost of manufactured sintered SiC would hold the advantage. If the differences in material velocity and elastic properties were critical, the higher performance of hot pressed SiC materials would justify the higher cost of production. Once the critical parameters were determined, the ultrasound fingerprint comparisons could serve as an even more important tool in terms of armor ceramic performance evaluation.

5.11. Ultrasound C-Scan Imaging Alternative Visualization Methods

There are three alternative methods that have been used to display C-scan image data in different forms including schematic overlay, regional mapping, and three-dimensional mapping. Schematic overlay has been discussed in the sections on sintered SA and ST SiC, in which the features observed at each frequency were overlaid onto a single map. The degree of difference from the bulk was taken into account for each of these features, as light blue was used to represent a small degree of difference in reflected signal amplitude or TOF from the bulk, green was used to represent a stronger variation, and red was used to represent the features with the highest reflected signal amplitude and TOF differences as compared to the bulk. The advantage of displaying the maps in this format was that the features from both reflected signal amplitude and TOF at all frequencies could be displayed together. This was important since different types of variations were detected at different frequencies. For example, the features detected at

125 MHz were closer to the microstructural-range of the armor ceramic material and gave a lot more detail, such as providing minor density gradient variations in the sintered samples. On the other hand, the features detected at 75 MHz did not provide as much detail but showed broader regional differences over the sample area. Features detected at 5 MHz provided insight into the largest defects, since they could be distinguished despite the lower detection limit. This made it important to choose a transducer frequency based on the sizes and types of defects that were critical. Sometimes it was important to detect features on the microstructural level, making a 125 MHz transducer desirable, while at other times this provided too much detail and a 50 or 75 MHz transducer was selected for distinguishing regional differences. The schematic overlay was advantageous because it allowed visualization of all of these features simultaneously.

For the regional mapping method, Origin Pro Version 7.0 proved to be a valuable software program for providing a unique form of visualization of the C-scan images. First, the raw data collected from the C-scan image including the x-position, y-position, and corresponding bottom surface reflection amplitude signals were imported into an Origin data sheet. The data were converted into a matrix so that each value was placed on a data map according to its x and y coordinates. Based on these values, a color contour fill map was plotted to obtain a regional map. For the typical C-scan image maps that were collected using the iPass software and analyzed using the iniView software, the data were displayed in the same way, but in its raw form. The advantage of using Origin was the degree of control that was gained for mapping the data. The reflected signal amplitude ranges and number of intervals or levels were chosen to create unique regional maps. In this way, regions with similar reflected signal amplitude values were grouped

together. The number of levels was selected to either expand the range of values within a single group for less contrast and fewer regions or tighten the range of values within a single group for more contrast and more regions. Examples of regional maps are shown for 125 MHz scans of samples A-C in Figure 166, SA1-SA3 in Figure 167, and ST1-ST3 in Figure 168. The number of levels chosen for these maps was an average range of 15. If this was changed to 25, the number of regional variations increased, whereas a value of 5 only isolated the most distinctly different regions. For samples A-C in Figure 166, while the armor grade sample A appeared to show variation throughout the sample, the degree of variation fell within a narrow range. On the other hand, the variation was much greater for samples B and C, which showed more drastic differences in the bottom right corner of sample B and throughout sample C. The regional maps of the SA and ST samples in Figures 167 and 168 were effective for distinguishing the lower reflected signal amplitude regions including the top right corner of ST1, the top right and left corners of ST2, and the bottom of SA2. Of the six samples, the regional maps indicated that SA1 appeared to be the most homogeneous. These maps provided an alternate method for extracting regional variations from C-scan images.

For conducting three-dimensional mapping of C-scan imaging, Sigma Plot 8.0 was used. The raw data collected from the C-scan image, including the x-position, y-position, and corresponding bottom surface reflection amplitude signals were imported into a Sigma Plot data sheet. These three columns of data were selected as the input for the 3D Smooth Data Transform function. While there were many data smoothing options, the Negative Exponential default with a sampling proportion of 0.1 and a polynomial degree of one was chosen for its ability to accurately represent the resulting

visual data. Just as for the regional maps, the sampling proportion could have been altered to change the number of levels that were used for displaying the data. Three-dimensional reflected signal amplitude maps of 125 MHz scans are shown for samples A-C in Figure 169, SA1-SA3 in Figure 170, ST1-ST3 in Figure 171, and AO, AO-X, and AO-RU in Figure 172. The unique aspect of these maps was their ability to visualize low and high reflected signal amplitude features based on their depth, or z-position. These maps could also be rotated and tilted to visualize interesting features from a variety of different angles. For samples A-C in Figure 169, sample A showed the highest degree of uniformity, as expected, whereas sample B showed a depth variation from high to low in the critical corner region and the high amplitude inclusion and high amplitude central region in sample C stood out, as they were raised above the rest of the matrix. The variations in the SA and ST samples in Figures 170 and 171 were also evident, with sample SA1 again showing a high degree of uniformity and SA2 showing a drastic drop in amplitude in the critical corner region. The 3D maps of the fabricated AO-X and AO-RU samples in Figure 172 effectively displayed the low amplitude “X” and “ru” porosity patterns, which appeared to be indented within the average amplitude bulk region. These were shown next to a baseline AO sample without any added polymer spheres. In addition, a full set of 3D maps was collected for sample SA2 in Figure 173, including both reflected signal amplitude and TOF maps at 5 MHz, 75 MHz, and 125 MHz. These showed the highest degree of variation at 75 MHz in which the low reflected signal amplitude appeared below the rest of the bulk while the corresponding high TOF area appeared above the rest of the bulk. The 5 MHz 3D maps showed the least amount of variation while the 125 MHz 3D maps showed some specific features of interest. Again,

this was a unique alternate method for displaying visual C-scan image data. The importance of displaying the C-scan images in these ways was to emphasize and enhance variations and features that could not easily be visualized using the standard raw C-scan image maps.

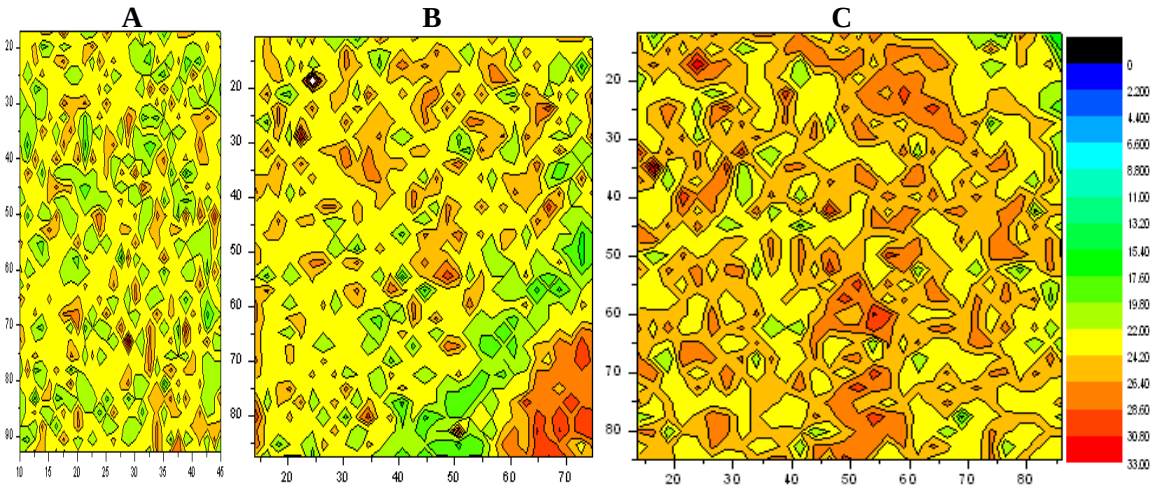

Figure 166. Regional amplitude mapping plots of samples A, B, and C.

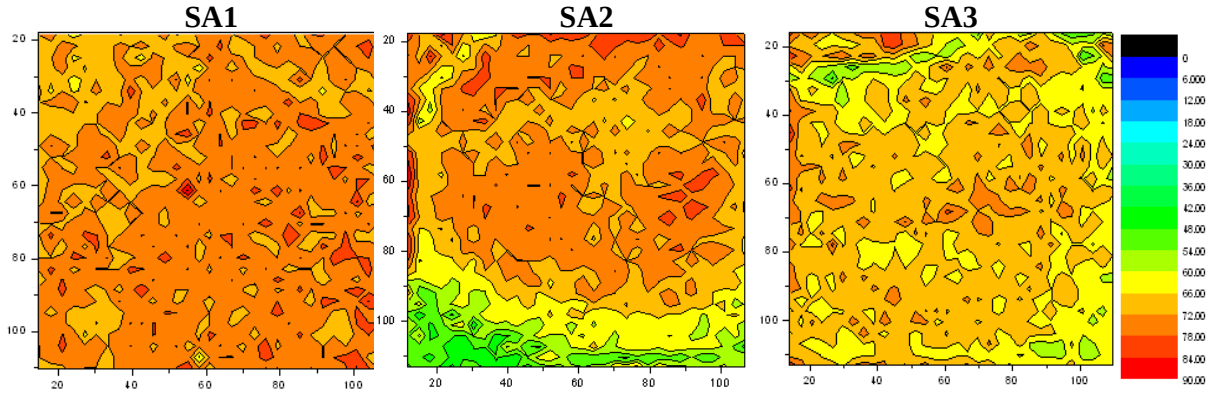

Figure 167. Regional amplitude mapping plots of samples SA1, SA2, and SA3.

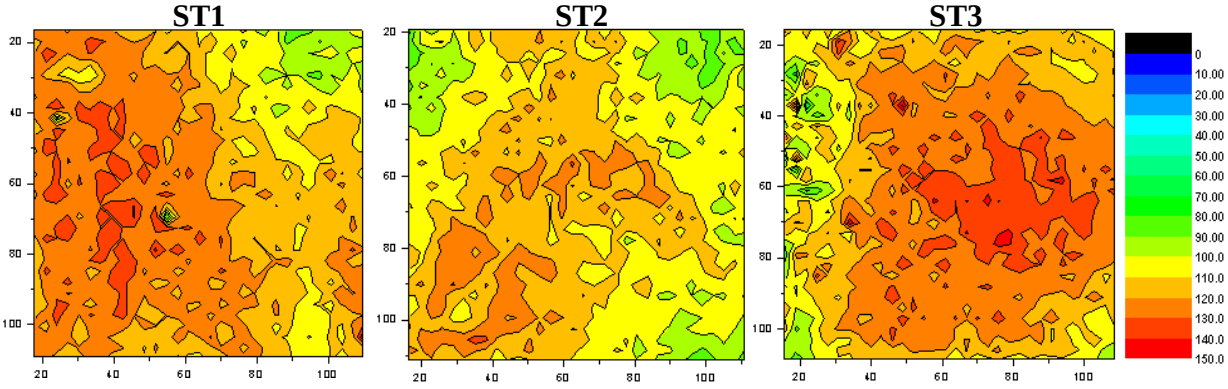

Figure 168. Regional amplitude mapping plots of samples ST1, ST2, and ST3.

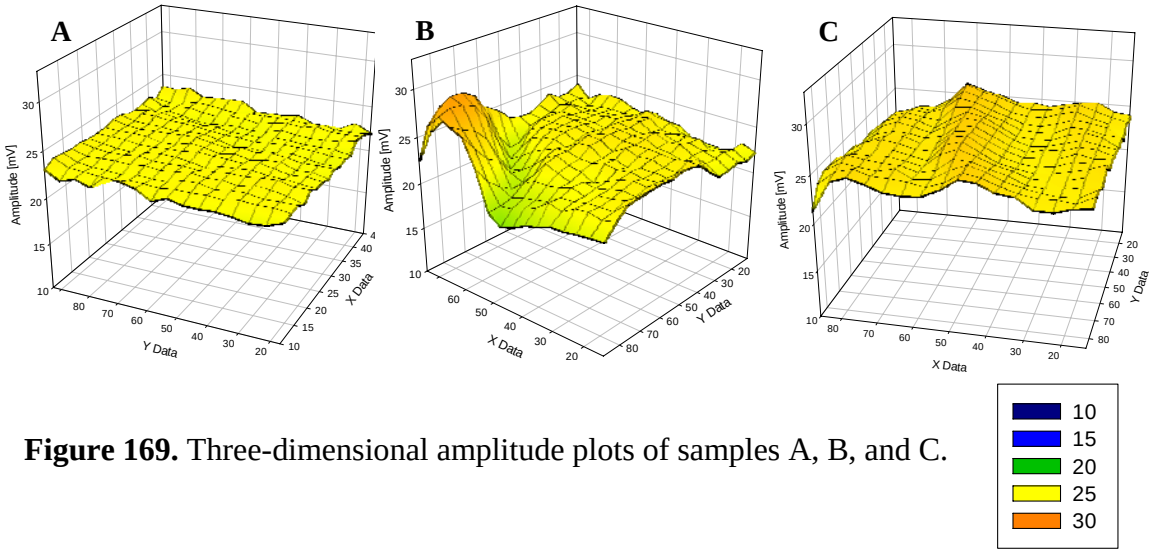

Figure 169. Three-dimensional amplitude plots of samples A, B, and C.

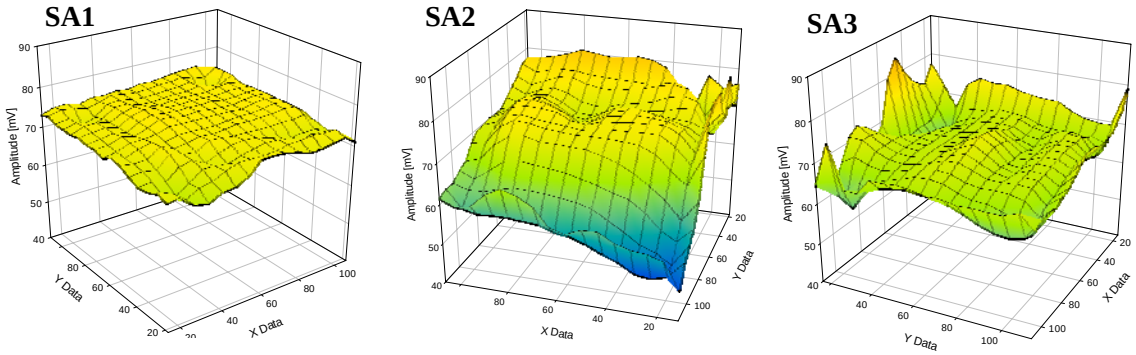

Figure 170. Three-dimensional amplitude plots of samples SA1, SA2, and SA3.

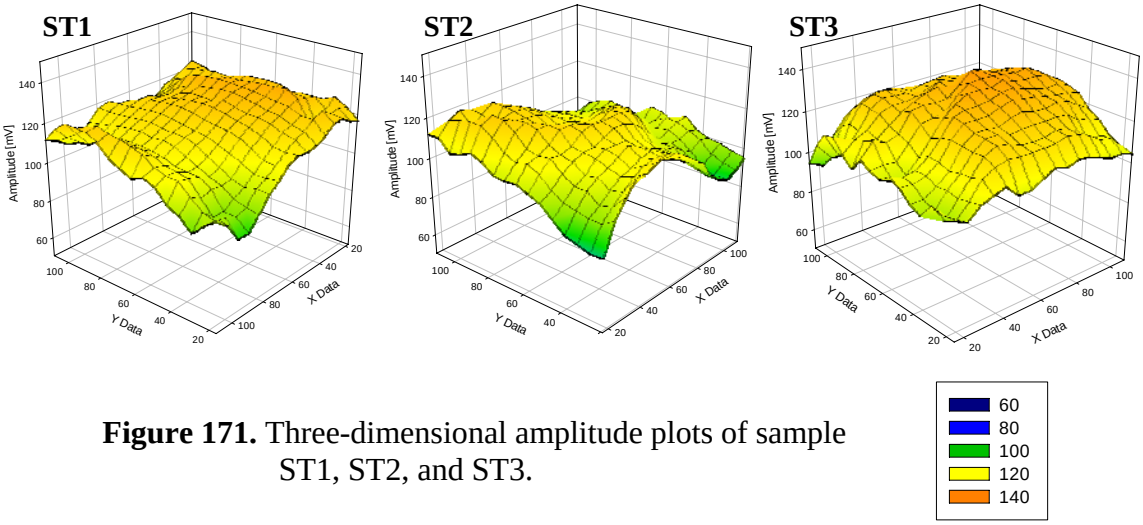

Figure 171. Three-dimensional amplitude plots of sample ST1, ST2, and ST3.

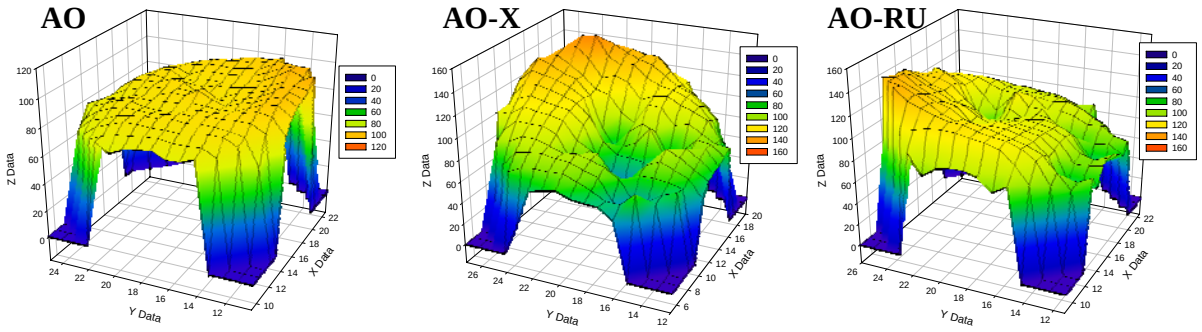

Figure 172. Three-dimensional amplitude plots of samples AO, AO-X, and AO-RU.

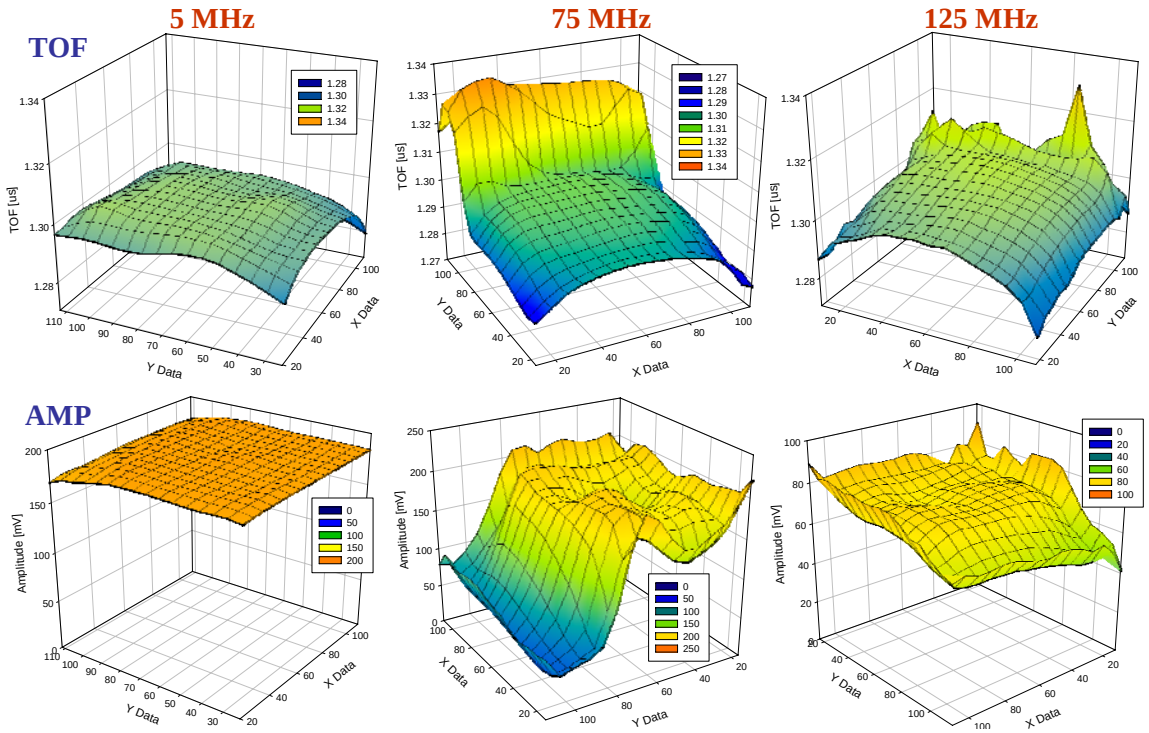

Figure 173. Three-dimensional amplitude and TOF plots of sample SA2 at 5, 75, and 125 MHz.

5.12. Line Scan and Reflected Signal Amplitude Distribution Image Processing

There were several image processing techniques that were used to extract useful quantitative data from ultrasound C-scan image maps, and two of them will be covered in this section. The first method was line scanning in which the iniView software program was used to analyze pixel-to-pixel changes over specific lines selected over a given C-scan image. In this way, reflected signal amplitude or TOF changes were evaluated and compared for multiple C-scan regions. Examples of line scanning are shown for samples A-C in Figures 174-176 in addition to samples SA1-SA3 in Figures 177-179 and samples ST1-ST3 in Figures 180-182. For each of the 125 MHz bottom surface reflected image scans, five lines were selected and the data was overlaid onto a single plot with position in millimeters on the x-axis and amplitude in millivolts on the y-axis.

For samples A-C, which were thicker than the SA and ST samples, the bottom surface reflected signals were more highly attenuated and closer to the noise floor as shown in Figures 174-176. For this reason, the line scans appeared to be much more variable, but this was due to the lower amplitude scale. When comparing these three samples, the lines from bottom to top were represented by black, red, orange, yellow, and green line scans, respectively. For sample A, the reflected signal amplitude variations range between 17-27 mV for the most part. The only significant deviations were a 16 mV point in the yellow line, which was second from the top, and a 30 mV point in the red line, which was second from the bottom. Otherwise, there were minimal changes over each of the lines. For sample B, the variations were much more drastic, especially over the three lines that ran through the critical region that consisted of a low density region with low reflected signal amplitude next to a high density region with high reflected

signal amplitude. The black and red lines that ran directly through this region were characterized by amplitude values as low as 17 mV in the low density region followed by an increase in amplitude to as high as 33 mV in the high density region. There was also a high degree of variation in the green line closest to the top of the sample which varied from 20-31 mV. For sample C, the values appeared to fall consistently between 20 and 30 mV, with a general increase near the center of each line where that intersected the higher amplitude region in the center. There were two separate points of 33 mV which stood out compared to the bulk. The first was from the black line where the line scan ran through the high amplitude inclusion that was isolated for the manufacturer. This feature was also present as a surface discoloration and was the reason why the sample was pulled from the production line. Another feature with the same high amplitude of 33 mV was found in the center of the orange line. Although the line scan results identified the presence of the high density inclusion, there were other areas within the bulk of the sample where similar defects were also detected using this method.

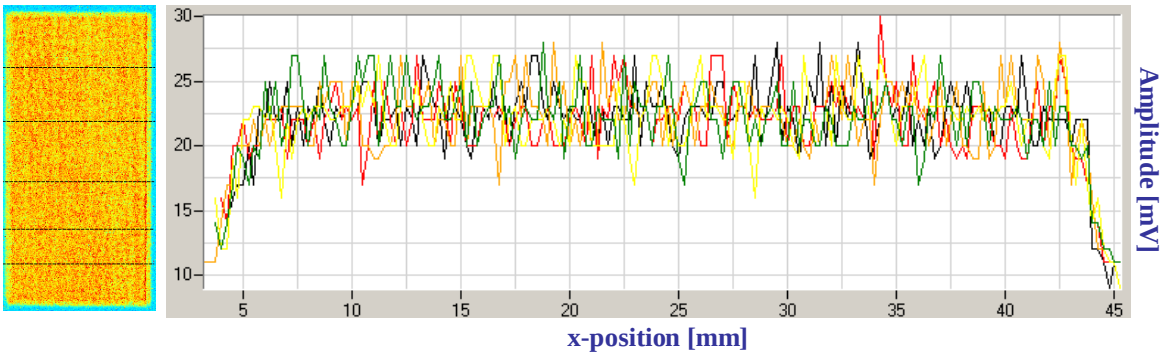

Figure 174. A collection of five horizontal amplitude line scans from sample A.

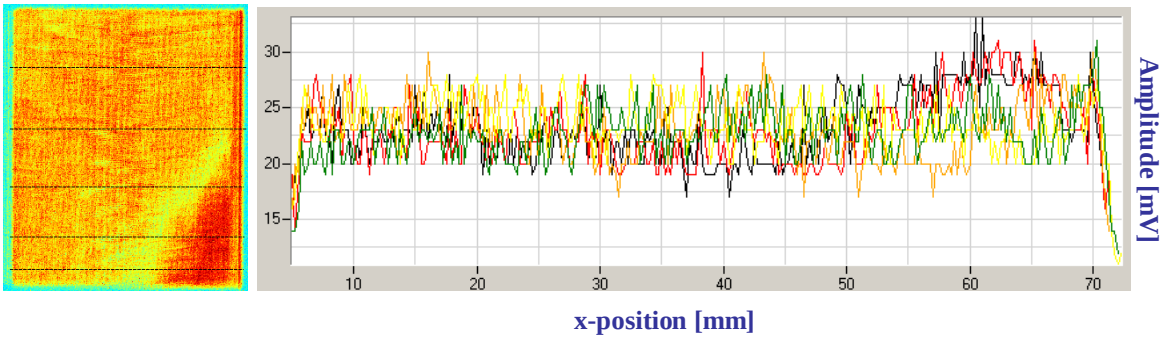

Figure 175. A collection of five horizontal amplitude line scans from sample B.

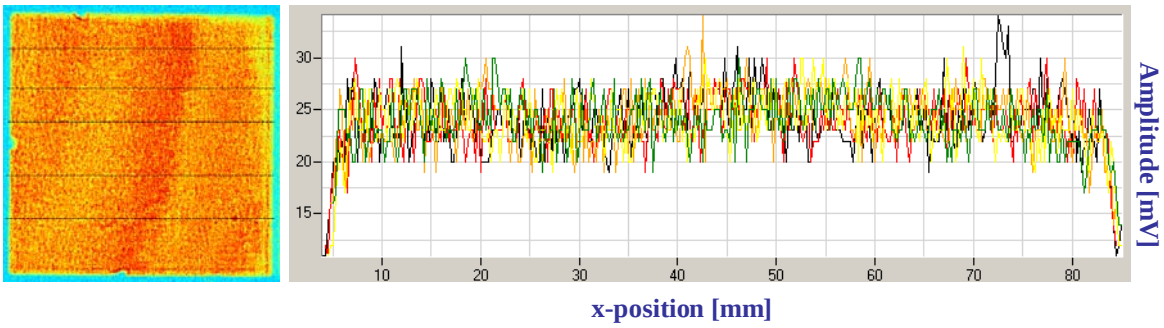

Figure 176. A collection of five horizontal amplitude line scans from sample C.

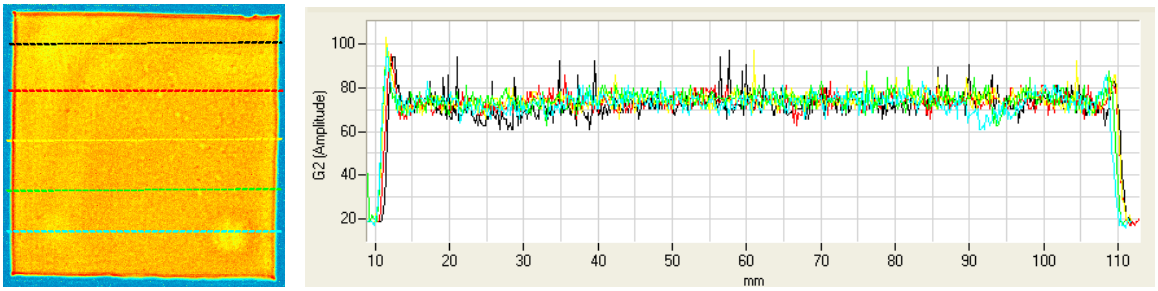

Figure 177. A collection of five horizontal amplitude line scans from sample SA1.

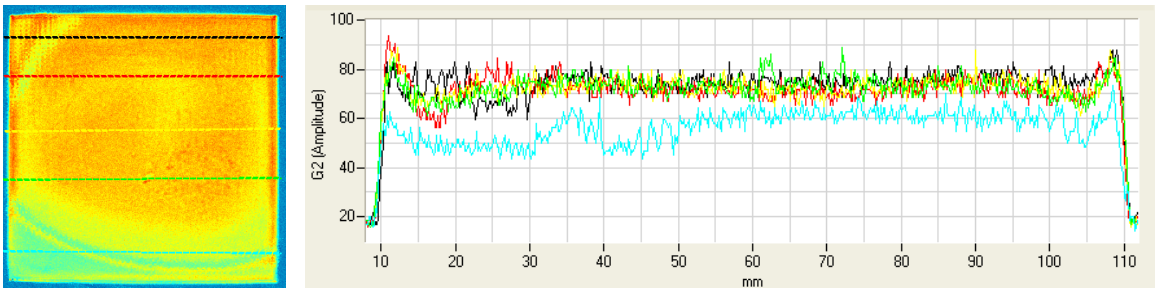

Figure 178. A collection of five horizontal amplitude line scans from sample SA2.

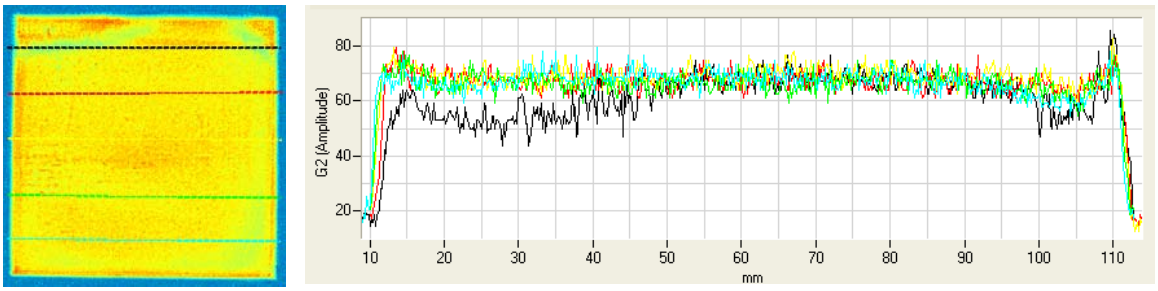

Figure 179. A collection of five horizontal amplitude line scans from sample SA3.

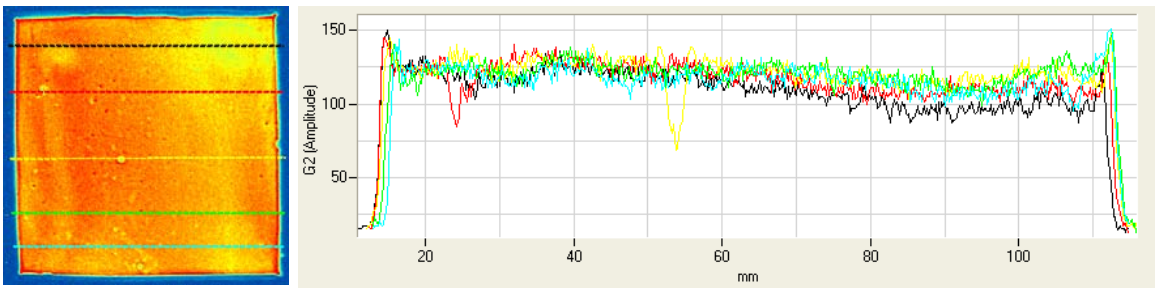

Figure 180. A collection of five horizontal amplitude line scans from sample ST1.

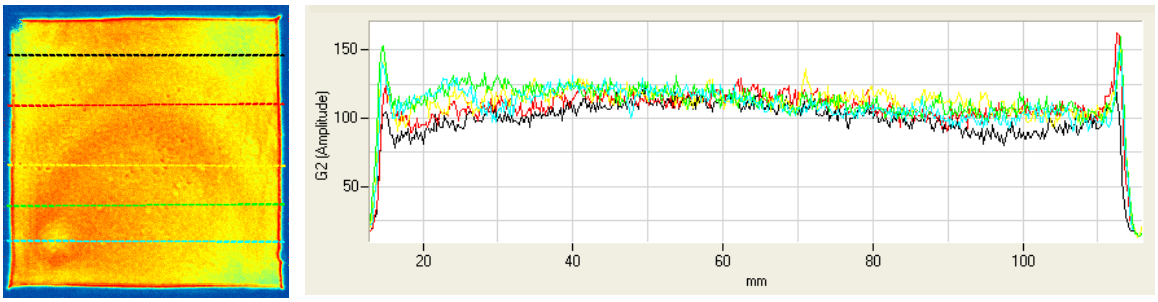

Figure 181. A collection of five horizontal amplitude line scans from sample ST2.

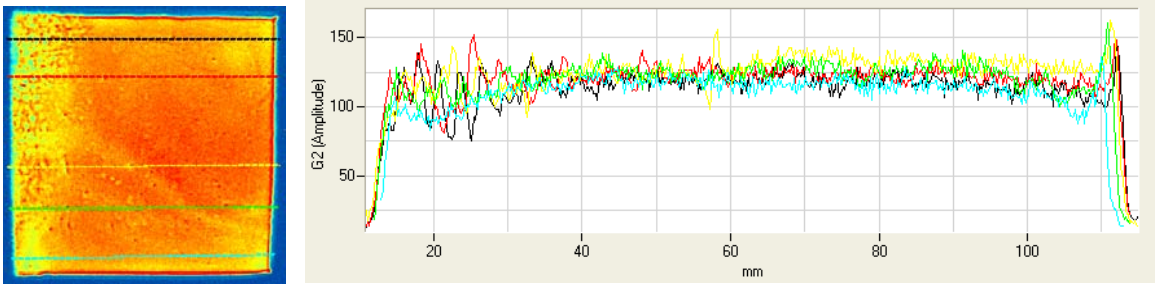

Figure 182. A collection of five horizontal amplitude line scans from sample ST3.

For the SA and ST samples in Figures 177-182, the overall bottom surface reflected signal values were higher, and there were several individual features and regions that stood out by observing the line scans. In these images, the colors of the lines drawn over each sample corresponded to the same colors in the line scan plots. Of the SA samples, SA1 was again the most homogeneous, with values generally ranging from 60-80 mV. The only features that stood out were the higher amplitude peaks up to about 98 mV that were observed in the black and yellow lines. These higher amplitude spikes were caused by high amplitude inclusions that intersected the lines. SA2 and SA3 each had significant low amplitude regions with completely different line scan patterns compared to the rest of the bulk. For SA2, the blue line ranged between 40 and 70 mV, and for SA3, the black line ranged between 43 and 70 mV. The ST materials containing the TiB_2 additives showed some significantly high amplitude spikes from the detected inclusions. In sample ST3, the red and yellow lines showed several high amplitude spikes over 150 mV in amplitude. At the same time, some significant pores stood out in the red and yellow lines of ST1, with amplitude reductions down to 85 and 72 mV, respectively. Both ST1 and ST2 showed the lower amplitude values corresponding to the large features in the upper right corners of the samples, while ST3 showed a highly variable region on the left side of the sample.

These line scans were useful for revealing not only the obvious regional changes, but the pixel-to-pixel variations that were not always evident. The best example may have come from sample C, in which the expected spike from the inclusion was apparent in the black line scan, but another spike of equally high amplitude was found in the center of the orange line scan. While this could not easily be picked up visually, the line scan

revealed it quantitatively. Just as in the other alternative visualization methods, the line scans provided a different way of looking at and quantifying the data so that more useful information could be extracted.

Another image processing method that utilized the iniView software program was reflected signal amplitude distribution mapping. Starting with the standard bottom surface reflected signal amplitude C-scan image map, a range of amplitude values was selected to highlight the pixels falling within the specified range. By illuminating the desired amplitude values, all of the occurrences of either low amplitude or high amplitude were viewed simultaneously. In addition, the quantitative feature of this method was the ability to show the percent area of the selected amplitude range. This method was applied to samples A-C in Figures 183-185, samples SA1-SA3 in Figures 186-188, and samples ST1-ST3 in Figures 189-191.

For samples A-C in Figures 183-185, four separate amplitude ranges were chosen, the first which accounted for the lowest amplitude background signals. For all three samples, a range of 0-16 mV was used to separate background values that included 17.6-24.6% of each scan area. The 17-22 mV and 23-27 mV ranges for sample A covered almost equivalent values of 38.0% and 36.2%, respectively, while the high amplitude range only accounted for 1.2%. This showed a relatively even distribution for the armor grade sample. A similar trend was found for sample C, in which the middle ranges accounted for 41.1% and 40.3%, respectively, while the high amplitude features above 31 mV including high density inclusions amounted to 0.4% of the total area. The ranges were changed for this sample to isolate the high amplitude features, which included the surface discoloration feature and several other features detected in the line scan data. In

contrast to these samples, sample B showed an area of 33.7% in the 17-22 mV range which increase to 43.9% in the 23-27 mV range while the higher amplitude features including the critical bottom right corner region covered 4.8% of the scan area. These percentages were valuable for describing the percentage of critical features present in each scan.

For the SA and ST samples in Figures 186-191, a series of four ranges was chosen for comparing the SA samples while another series of four ranges was chosen for comparing the ST samples. The first range for all samples from 0-40 mV described the reflected amplitude signals from the background. These were similar for all samples, ranging from 19.0% to 21.0% of the total area. For the SA samples, the most critical region for comparison was the low reflected signal amplitude range describing the low density regions in the sintered samples, and this range was chosen as 41-55 mV. For sample SA1, the most homogeneous sample, there were very few occurrences in this range, as the area covered only 0.8%. For SA2, with the large low amplitude region at the bottom of the sample, this increased to 7.7% while the upper region in SA3 accounted for 2.5%. The majority of amplitude values for SA1 and SA2 fell into the 71-94 mV high amplitude range, with percentages of 59.7% and 40.1%, respectively, while the majority of amplitude values for SA3 fell into the 56-70 mV amplitude range at 54.3%. These differences were less important than determining the percentage of low amplitude, low density features in the 41-55 mV range.

A similar method was used for determining the critical low amplitude region for the ST samples, but the ranges were changed to account for the higher average amplitude values of these samples. In this case, the critical region was from 41-100 mV, with ST1

showing the lowest percentage of 5.8% followed by ST3 at 7.3% and the ST2 at 16.4%. Sample ST2 stood out with several low amplitude regions in addition to the large low amplitude defects that were present in each sample. For samples ST1 and ST2, the majority of amplitude distributions fell within the 101-120 mV range, with percentages of 35.4% and 50.8%, respectively. For sample ST3, the majority of amplitude distributions fell within the 121-150 mV range, with a percentage of 39.4% total area. Again, the lower amplitude 41-100 mV range was most important for sample comparison. If a critical range can be definitively determined, these amplitude distribution maps may be utilized to correlate armor performance by quantifying which test specimens have higher and lower percentages of amplitude values within the critical ranges. This was another example of a quantitative method that was used to generate critical information from standard ultrasound C-scan images.

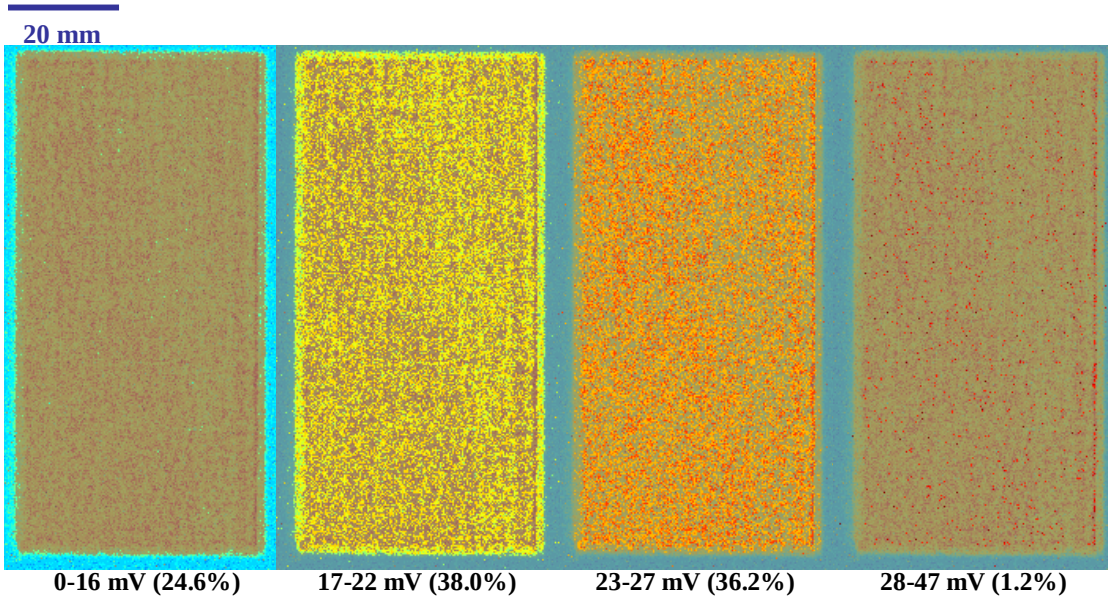

Figure 183. Reflected signal amplitude distribution maps and percentages for sample A.

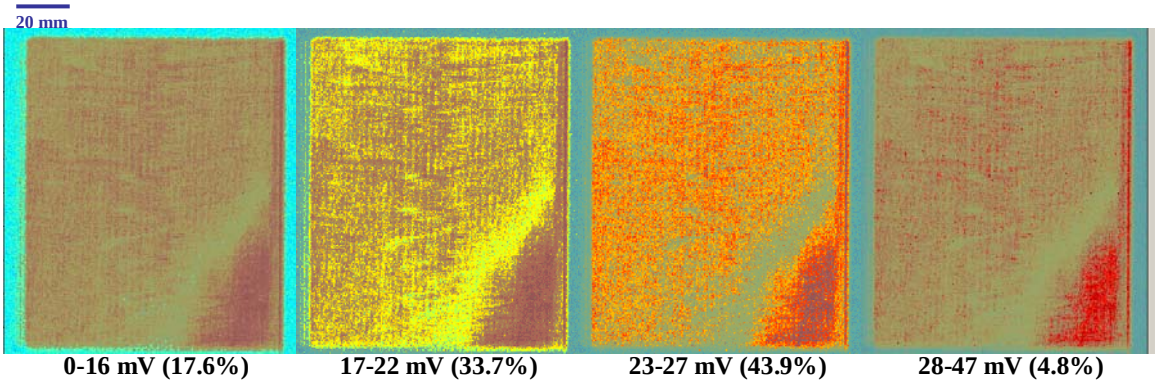

Figure 184. Reflected signal amplitude distribution maps and percentages for sample B.

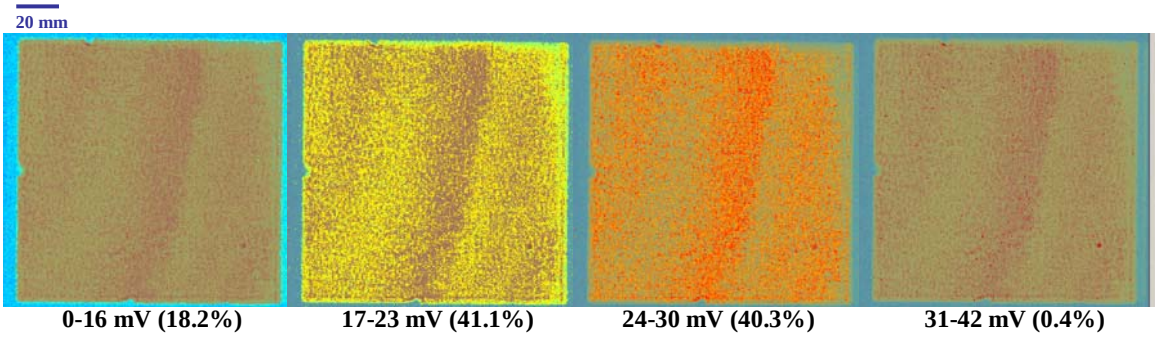

Figure 185. Reflected signal amplitude distribution maps and percentages for sample C.

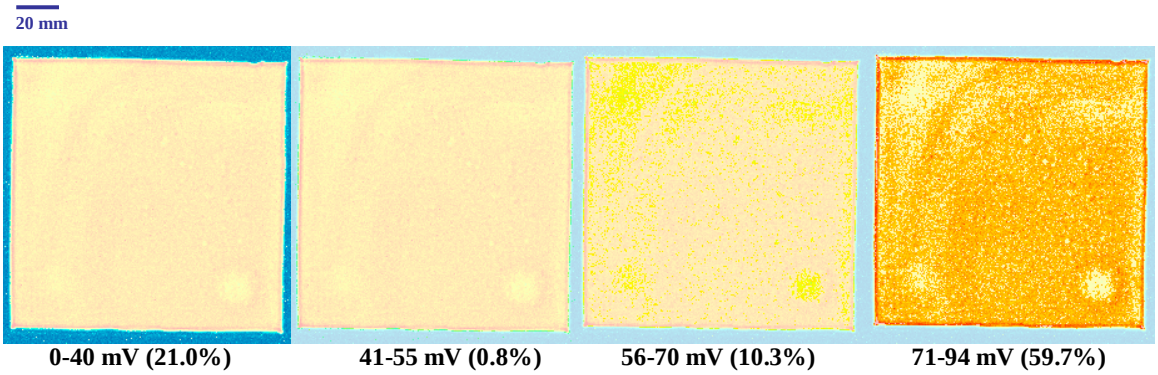

Figure 186. Reflected signal amplitude distribution maps and percentages for sample SA1.

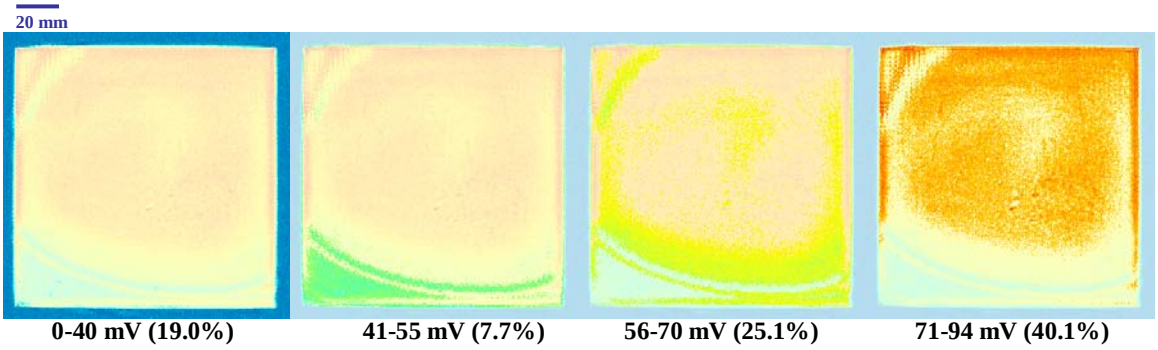

Figure 187. Reflected signal amplitude distribution maps and percentages for sample SA2.

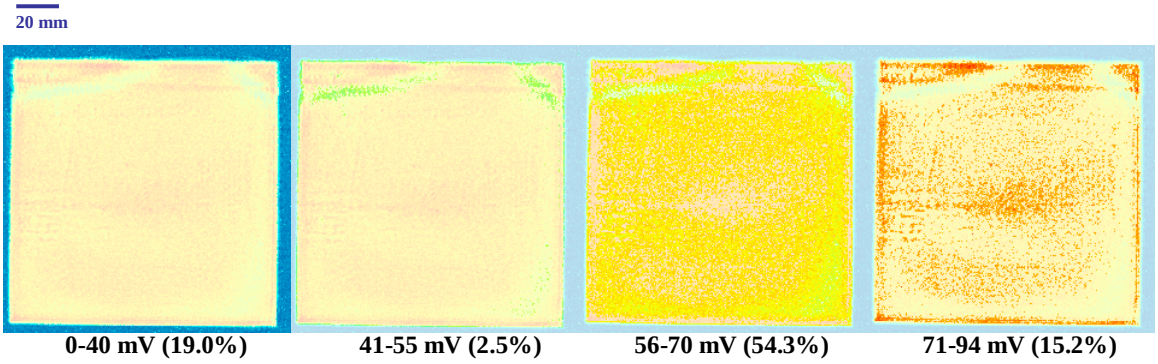

Figure 188. Reflected signal amplitude distribution maps and percentages for sample SA3.

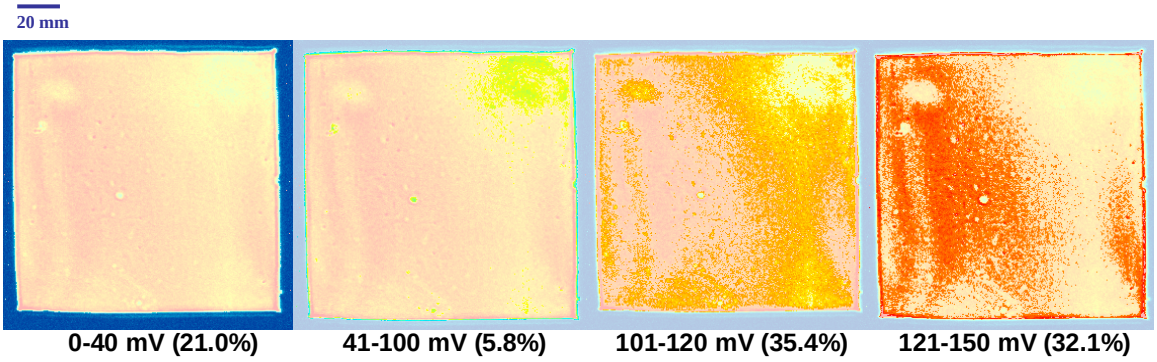

Figure 189. Reflected signal amplitude distribution maps and percentages for sample ST1.

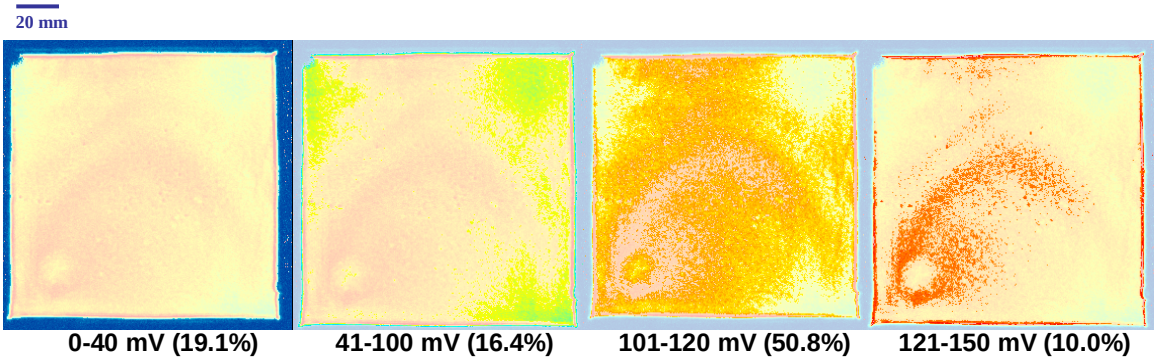

Figure 190. Reflected signal amplitude distribution maps and percentages for sample ST2.

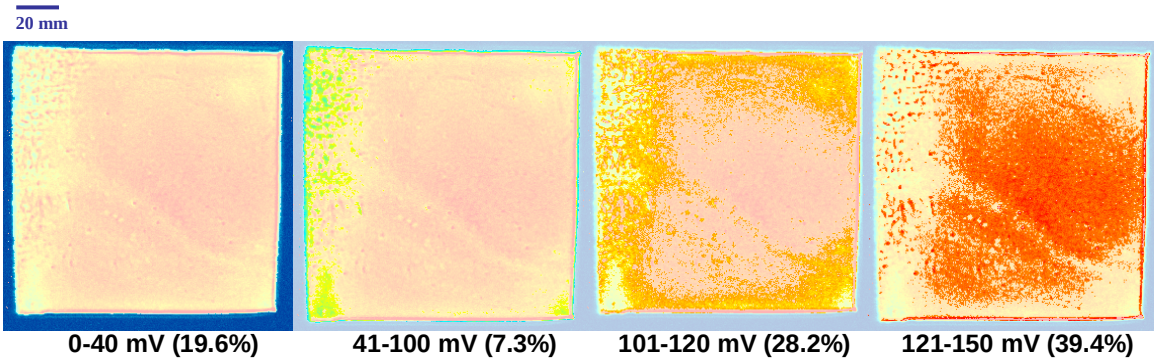

Figure 191. Reflected signal amplitude distribution maps and percentages for sample ST3.

5.13. Tail Analysis Using Peak Deconvolution and Curve Fitting

Throughout the results and discussion section, the importance of critical tail regions in normalized histogram curves has been emphasized. These regions have been used to define the distributions of the lowest reflected signal amplitude or highest TOF values representing low density regions and defects within the bulk of the armor ceramic test specimens. Depending on the number of occurrences of these low amplitude or high TOF regions, the normalized histogram curves have been described as either one-phase or two-phase curves. One-phase curves have been most common for C-scan images that either do not have significantly large variations from the bulk or contain features with close acoustic impedance matching to the bulk material. Some examples included armor grade hot pressed materials such as samples A and E which had narrow normalized distributions with little variation. Low frequency scan histogram curves which also commonly exhibited narrow distributions were also typically one-phase curves. Two-phase curves were most evident for C-scan images with significantly large variations from the bulk, especially when the features showed a drastic acoustic impedance mismatch or attenuation difference and, therefore, a drastic reflected signal amplitude or TOF change from the rest of the bulk. These curves were characterized by distinct second curves, or tails, in addition to the main distribution curves. Two-phase histogram curves were found primarily in sintered armor ceramic materials with large areas of low reflected signal amplitude or high TOF. They were also found in fabricated samples such as the epoxy/WC sphere test specimens in which there was a large acoustic impedance mismatch between the two materials that brought about two separate phases. Two-phase histogram curves were also more common for 75 MHz scans which were sensitive to

minor regional variations and were more likely to demonstrate a distinct second phase. In order to study the effect of critical second phase histogram curve tail regions, the 75 MHz reflected signal amplitude scans of samples SA1-SA8, which were likely candidates for two-phase phenomena, were analyzed.

To analyze these second phase tails, a series of peak deconvolution and curve fitting steps were used. First, the normalized bottom surface reflected signal amplitude histogram curve data were imported into Origin Pro Version 7.0. The data were converted into a scatter plot of normalized amplitude occurrences on the y-axis and normalized amplitude range on the x-axis. Depending on the anticipated shape of the curve based on the scatter plot, a curve fit was chosen. For a curve in which no significant tail peak was found, a non-linear curve fit was chosen. For a curve in which a large distinct tail region or multiple tail regions were found, a multiple peak fit was chosen based on either Gaussian or Lorentzian distributions. Since the majority of the 75 MHz histogram curves for the SA samples showed a great deal of variability, the multiple peak fit was applied in most cases. This method entailed peak deconvolution in which two or three Gaussian or Lorentzian curves were used to describe the main bulk distribution, the tail distribution, and any additional distributions where necessary. This enabled assignment of a unique curve to describe the tail region. Once these curves were established, the AUTC values of each curve were calculated. Based on the percent area of each curve in relation to the total sample area, percentages were calculated and used to plot reflected signal amplitude distribution maps such as the ones described earlier. However, instead of assigning arbitrary values to the amplitude ranges as was done earlier, the ranges were mapped based on the percentages of critical tail regions

characterized by the second phase tail curves. This method will be described in great detail for sample SA2 and more briefly for the other samples. The data for samples SA1-SA8 will also be summarized in terms of the type of curve fit chosen, the R^2 correlation of the fit, the percent area of each curve, and the AUTC of each curve.

The 75 MHz reflected signal amplitude scan of sample SA2 was a good example of a two-phase histogram curve, due to the large low amplitude region at the bottom of the sample which was significantly different than the average amplitude of the bulk. When the normalized amplitude histogram data were imported into Origin and plotted, the scatter plot showed a curve with two distinct peaks representing the bulk and tail regions as shown in Figure 192. The multiple peak fit was chosen, and while the majority of the multiple peak fits showed the highest R^2 correlation for Gaussian distributions, the unique shape of the curve was more suited to a Lorentzian distribution. The approximate maximum value for each curve was estimated and the individual curve fit data for each peak as well as an overall peak to fit the entire data set were fit to the scatter plot. The R^2 correlation value was found to be 92.1%, which was actually the lowest fit among the eight samples, which had correlations ranging from 95% to 99%. The reason for the slightly poorer fit was most likely due to the nature of the Lorentzian distribution fit which did not account for the lower scatter plot data points. The histogram curve data from the overall curve fit, bulk curve fit, and tail curve fit were imported into SigmaPlot version 8.0 for AUTC and percent area analysis. The individual and combined histogram curves are shown in Figure 193. The overall curve fit had an AUTC value of 2662, while the individual curves were broken down into AUTC values of 2065 for the bulk curve and 597 for the tail curve. This translated into a tail area of

22.4% of the sample and a bulk area of 77.6%. These data was used to create amplitude distribution maps using the iniView software program that reflected the amplitude range values corresponding to the tail and bulk regions, as shown in Figure 194. By first eliminating the background amplitude values which ranged from 0-29 mV, the full range of amplitude values was determined to range from 30-228 mV, which was a total range of 198 mV. The 22.4% tail area was used to calculate a range of 30-74 mV representing the tail and 75-228 mV representing the rest of the bulk. Both of these amplitude distribution maps were plotted, with the tail map confirming that the majority of the second phase histogram tail curve corresponded to the low amplitude region near the bottom of the sample. Since the amplitude distribution maps had their own percentage values based on the selected mV ranges, they were scaled to eliminate the background amplitude and compared to the percentages from the AUTC values. The 30-74 mV range represented 19.4% of the amplitude distribution map, compared to 22.4% of the AUTC histogram curve data. This 3.0% difference was a close match between the two sets of data, adding to the validity of the technique.

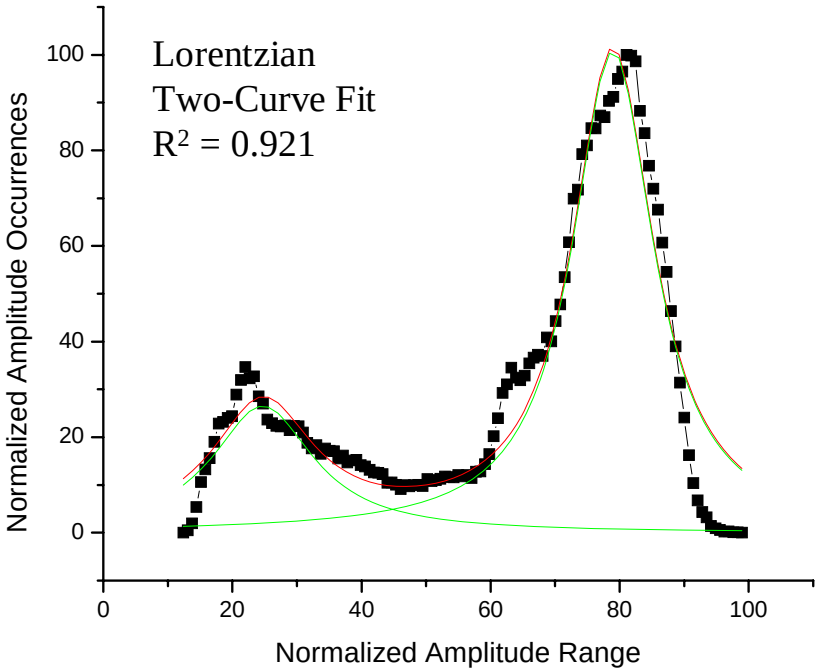

Figure 192. Lorentzian curve fits for amplitude distribution data of SA2 at 75 MHz.

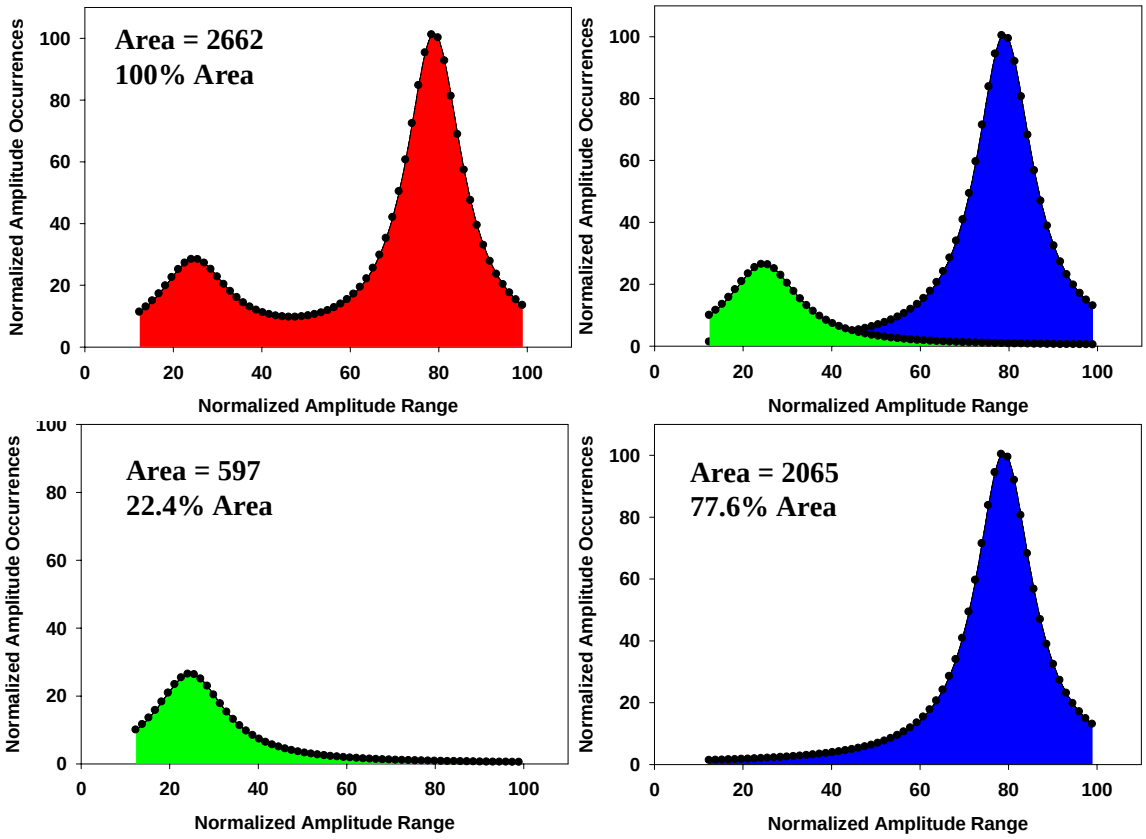

Figure 193. Main and tail histogram curve fits and AUTC values for SA2 at 75 MHz.

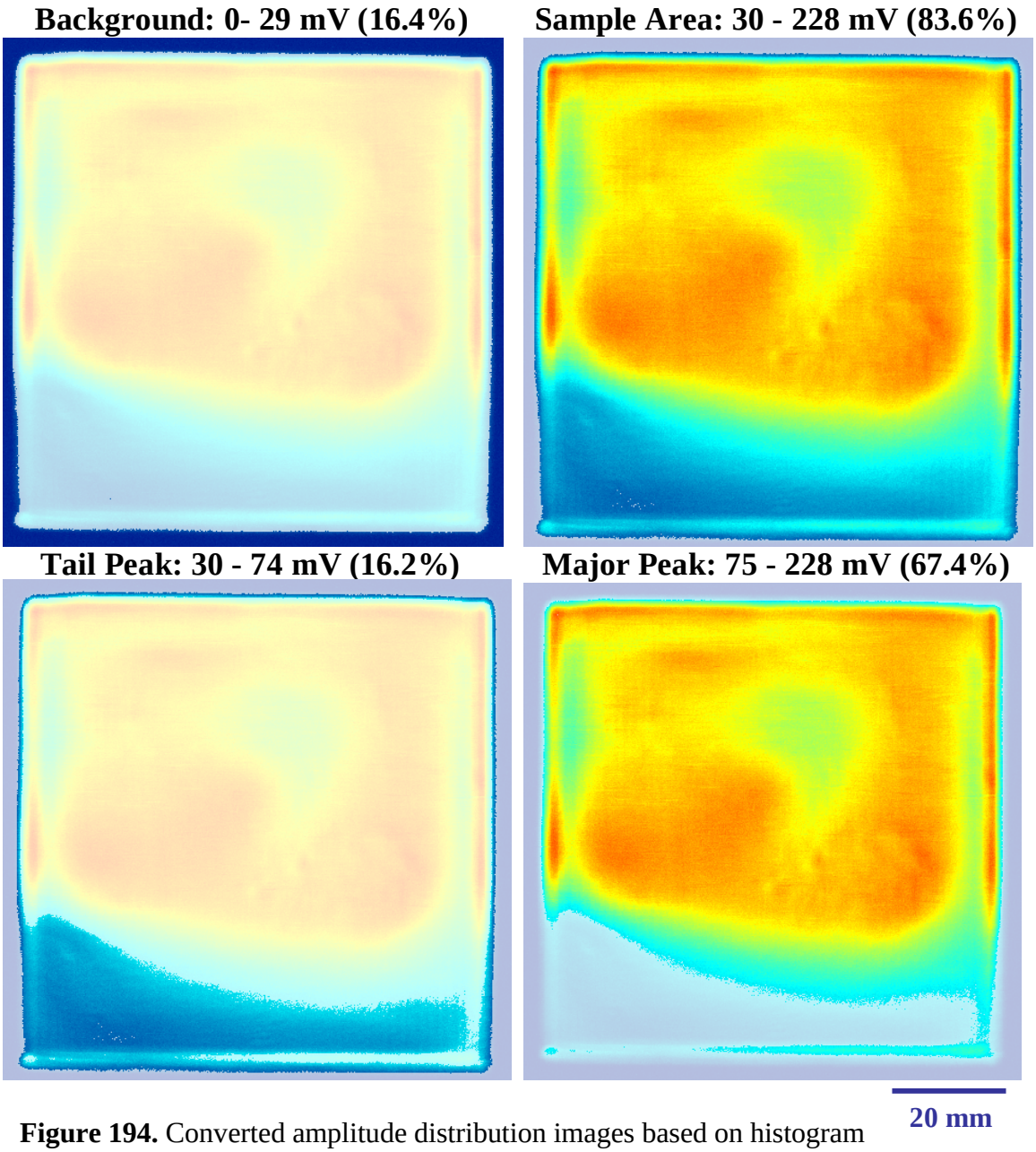

Figure 194. Converted amplitude distribution images based on histogram curve fits for SA2 at 75 MHz..

Similar data analysis and mapping were performed for the other SA samples, as summarized in Table LIII. The combined and deconvoluted peaks for all of the SA samples are shown in Figures 195-201. The two samples in which more than two peaks were deconvoluted were samples SA3 and SA7. These samples showed both high amplitude and low amplitude regions of significance. One unique sample was SA4 in which the tail occurred at the high amplitude side of the curve. Samples SA5, SA3, and SA2 had the highest histogram tail AUTC values of 890, 757, and 597, respectively, while the two highest tail percentages were from samples SA5 and SA3 at 32.5% and 32.4%, respectively. The samples with the highest percentage of low amplitude critical regions that corresponded to either low density or defect regions showed the highest AUTC tail curve values and the highest tail peak percentages, which was useful for sample comparison. However, the other factor that was considered when comparing this data was the proximity of the deconvoluted peaks to one another. When the two peaks were close together such as in sample SA1, the differences between low and high amplitude regions were not as drastic. On the other hand, the deconvoluted peaks for samples SA2 and SA5 were much further apart since the low amplitude region values for these samples were much different from the bulk values.

Out of the eight samples, only sample SA6 was homogeneous enough to be characterized by a one-phase histogram curve. By using the nonlinear curve fit function in Origin, the curve fit that was found to show the highest R^2 correlation fit of 99.8% was the asymmetric double sigmoidal power law function. This function was found to be very useful for describing one-phase normalized histogram curves with either low amplitude or high TOF tails as compared to the Gaussian and Lorentzian curve fits.

Overall, the combination of peak deconvolution, curve fitting, and amplitude distribution mapping was effective for comparing the most critical tail regions of two-phase samples by quantifying the tail data and visually mapping it.

Sample	Fit	R^2	Total Area	Main Peak Area	Main Peak %	Secondary Peak Area	Secondary Peak %	Tail Peak Area	Tail Peak %
SA1	G	0.988	1795	1401	78.1	-	-	394	21.9
SA2	L	0.921	2662	2065	77.6	-	-	597	22.4
SA3	G	0.993	2328	998	42.9	573	24.6	757	32.5
SA4	G	0.989	1972	1538	78.0	-	-	434	22.0
SA5	G	0.951	2748	1858	67.6	-	-	890	32.4
SA6	A	0.998	696	696	100.0	-	-	-	-
SA7	G	0.966	3628	2624	72.3	892	24.6	112	3.1
SA8	L	0.968	918	560	61.0	-	-	358	39.0

Table LIII. Peak deconvolution, curve fit, and tail analysis data for samples SA1-SA8.

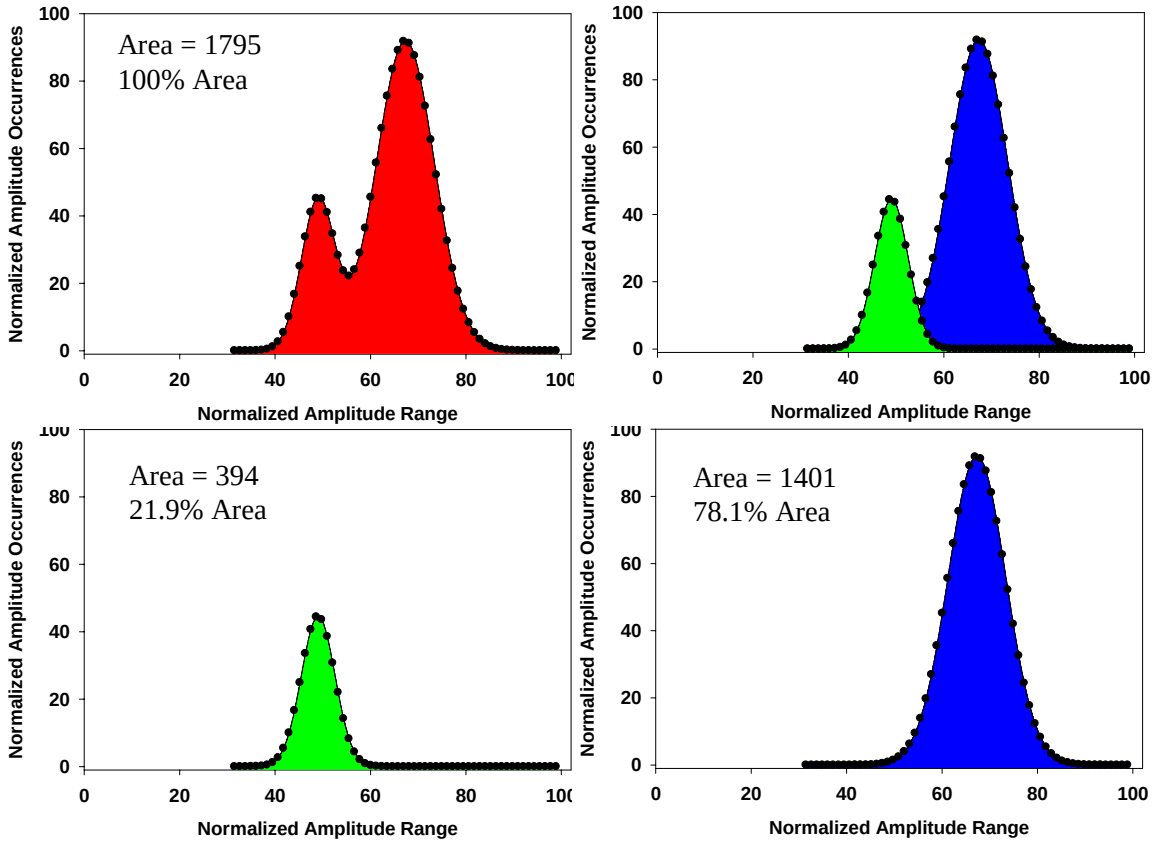

Figure 195. Main and tail histogram curve fits and AUTC values for SA1 at 75 MHz.

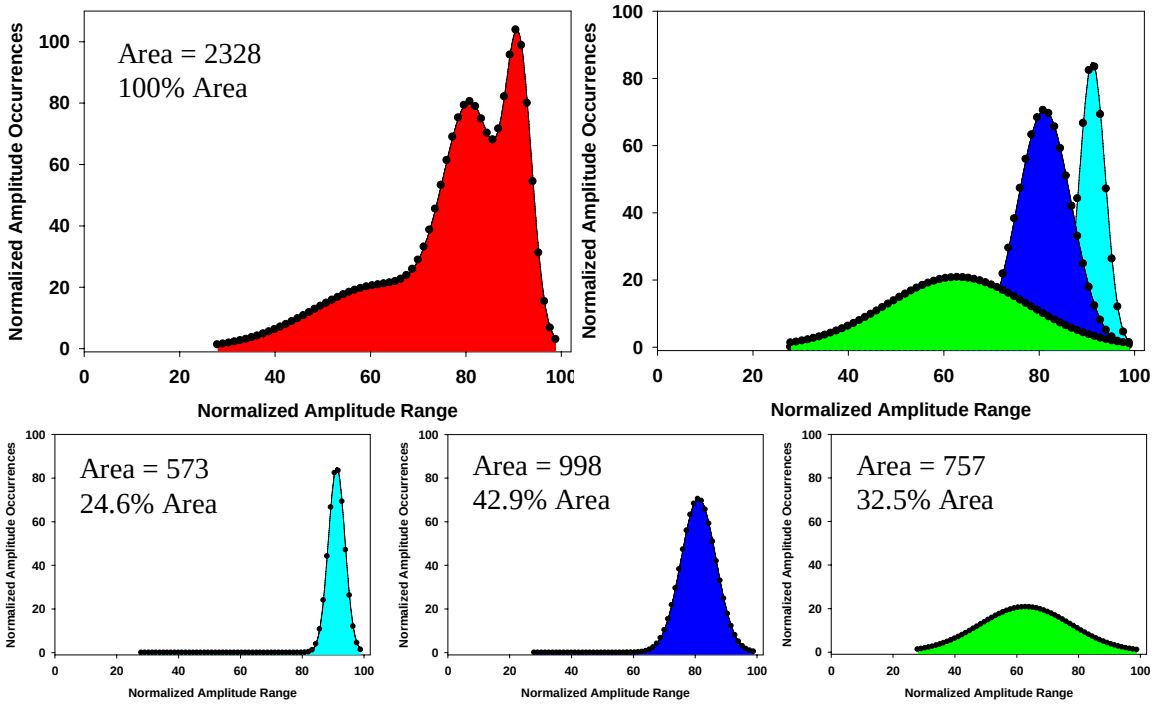

Figure 196. Main and tail histogram curve fits and AUTC values for SA3 at 75 MHz.

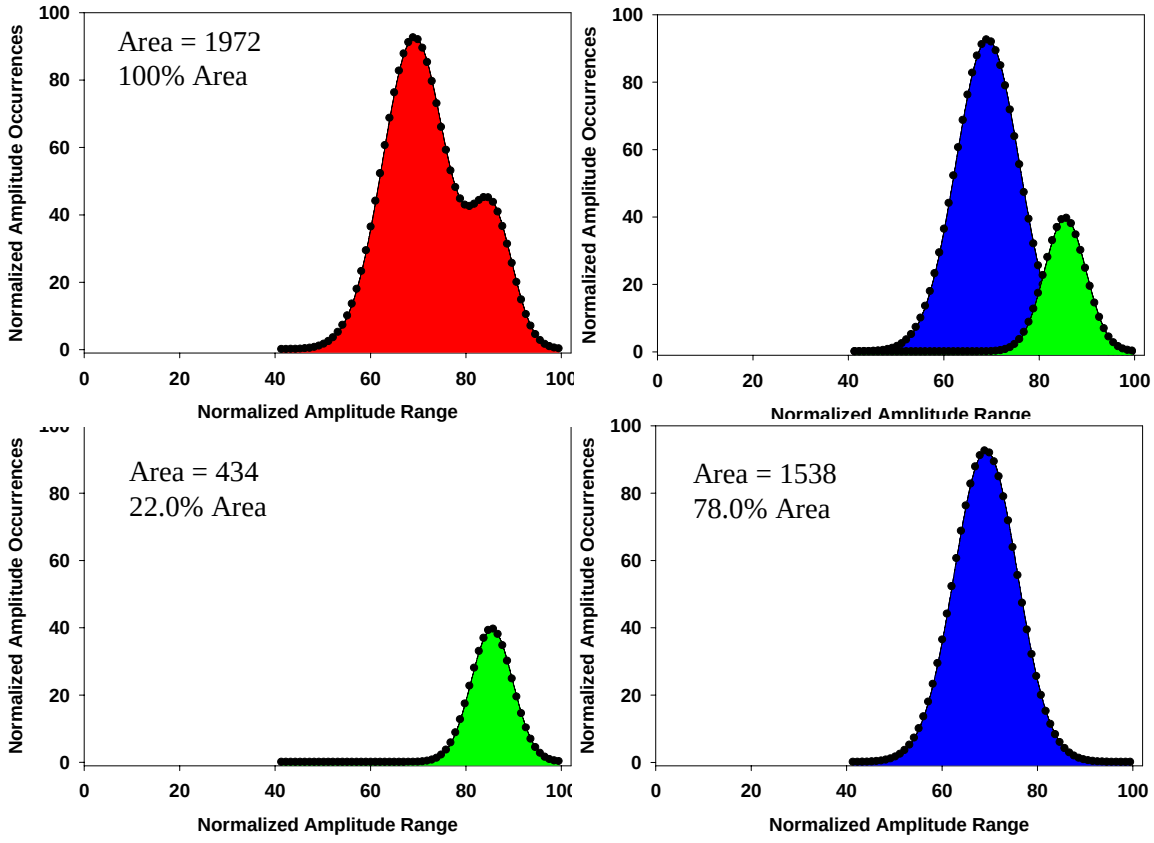

Figure 197. Main and tail histogram curve fits and AUTC values for SA4 at 75 MHz.

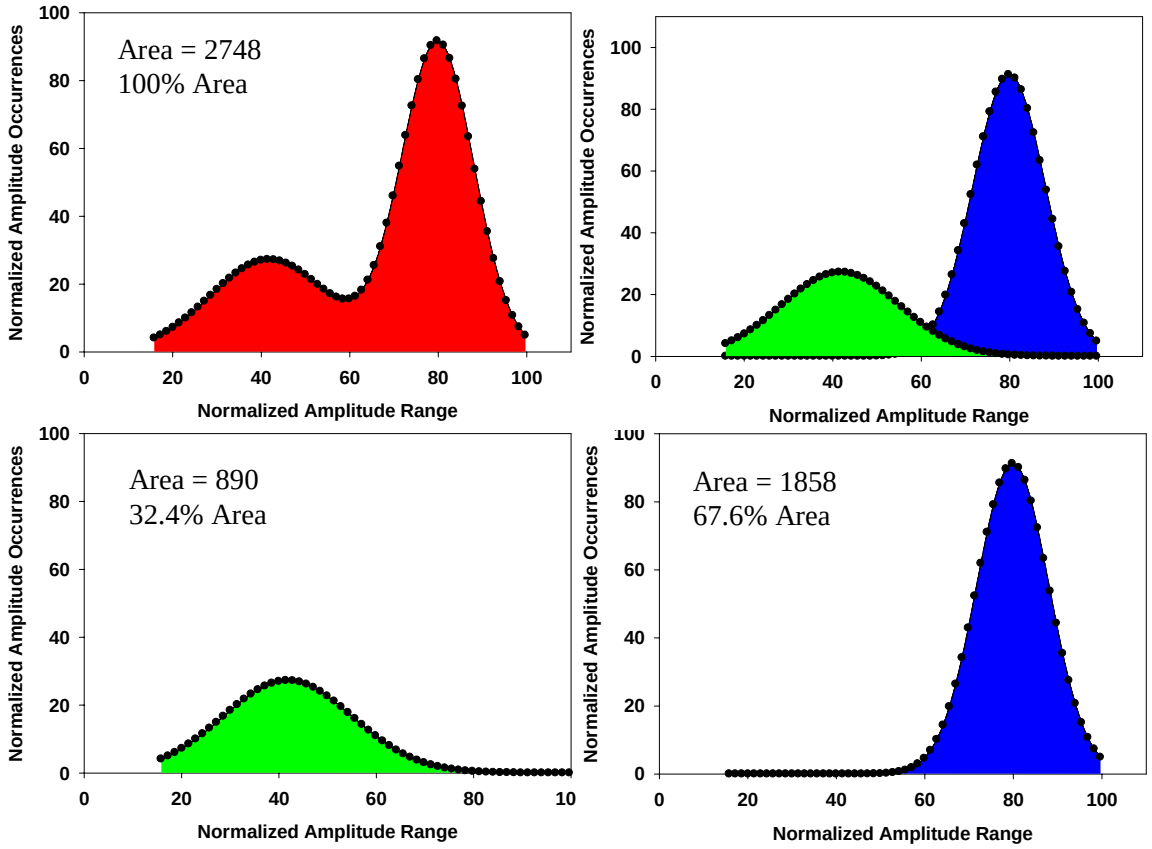

Figure 198. Main and tail histogram curve fits and AUTC values for SA5 at 75 MHz.

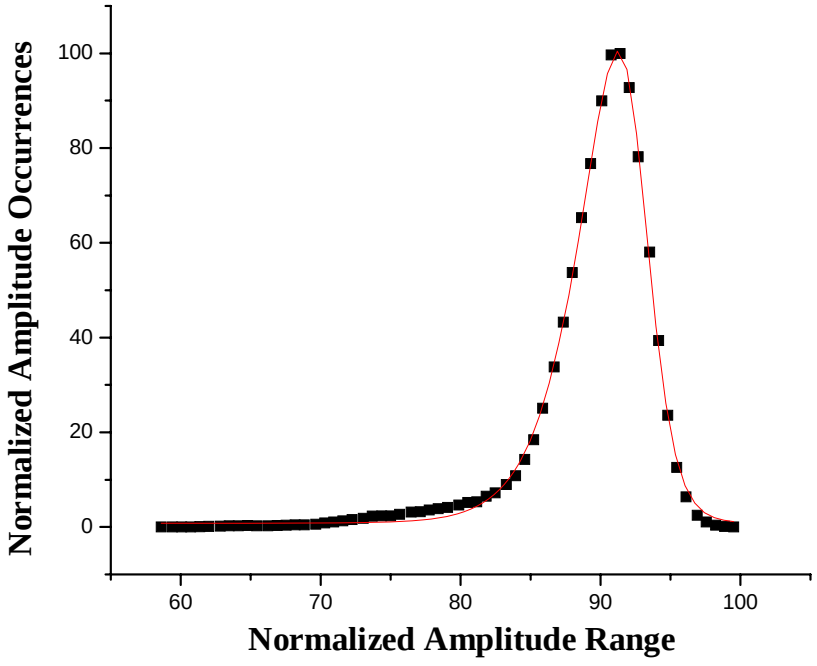

Figure 199. Histogram curve fit for SA6 at 75 MHz.

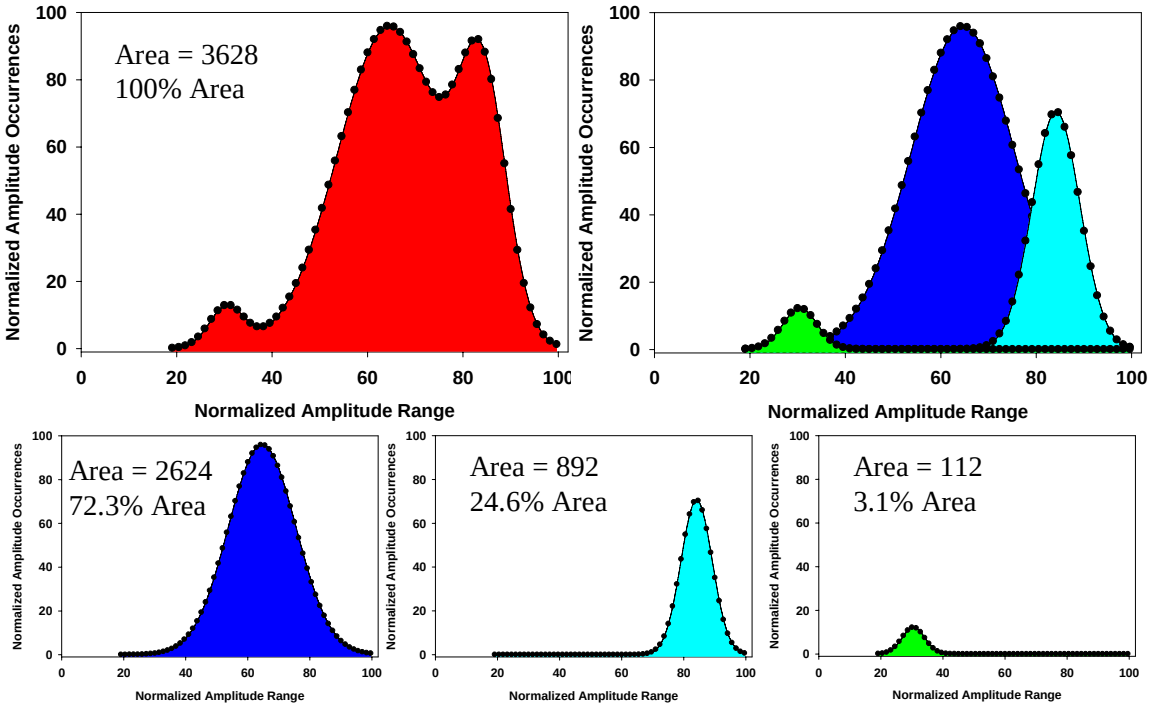

Figure 200. Main and tail histogram curve fits and AUTC values for SA7 at 75 MHz.

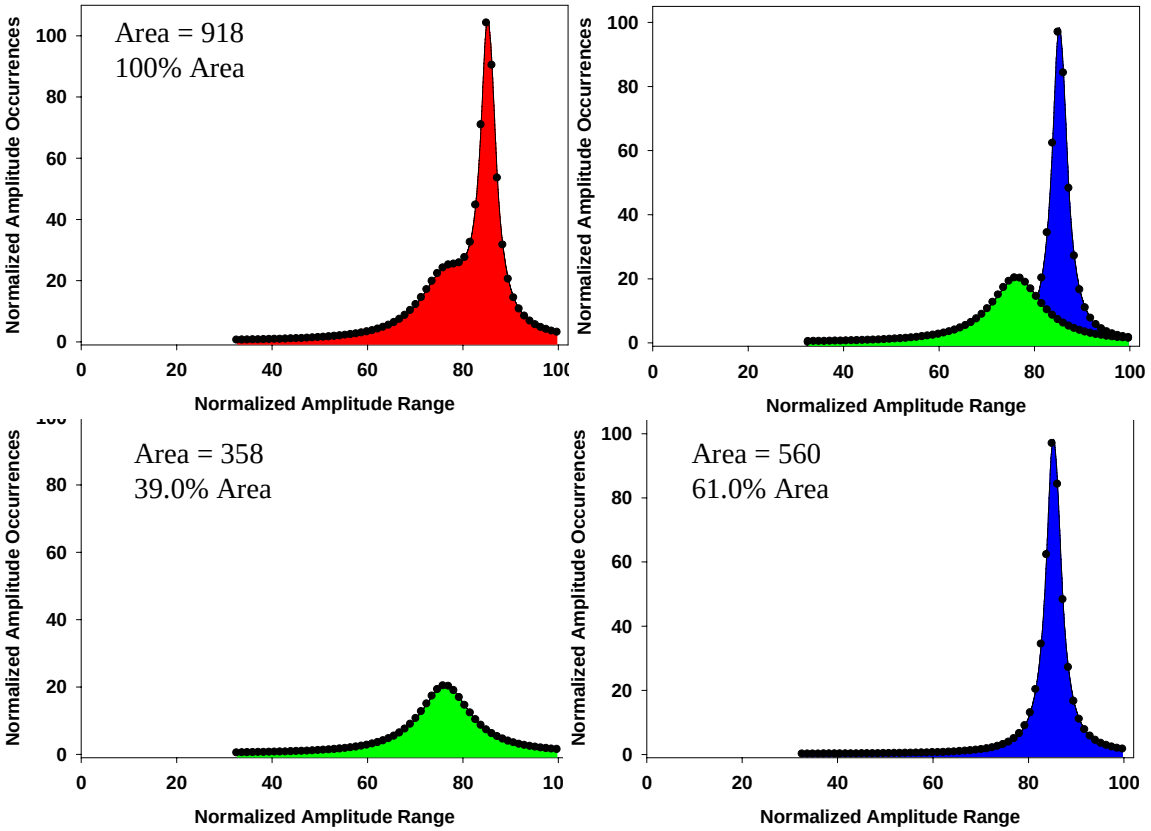

Figure 201. Main and tail histogram curve fits and AUTC values for SA8 at 75 MHz.

5.14. Material Velocity and Elastic Property Mapping

It has been stated in the ultrasound background section that ultrasonic, or acoustic, waves travel by exerting oscillating pressure on particles of a medium, generally corresponding to the frequency of the incident wave [75]. Since acoustic waves must displace a volume of material against the elastic constraints of its bonds in order to propagate, the ease of propagation of the wave is a function of density, which is related to the amount of material that must be moved, and a function of the elastic constraints, or how difficult it is to move the material [66]. For this reason, the interactions between the acoustic waves and the medium can be used to provide density and elastic property measurements, which has only been shown in point analysis data up to this point.

Also stated in the ultrasound background section, the two most common modes of ultrasound wave propagation through a medium are longitudinal waves in which the particle motion of the medium occurs in the same direction as the direction of propagation and shear waves in which the particle motion of the medium occurs at a right angle to the direction of propagation [25,73,76]. Longitudinal waves are unique in that they are the only type that can travel through a liquid while shear waves can only be transmitted through a solid material [25]. By using a proper longitudinal ultrasonic transducer, both longitudinal and shear wave reflected signals can be collected due to mode conversion in which the longitudinal waves change their mode of vibration at a material interface [25]. During immersion testing methods such as C-scan imaging, mode conversion occurs when the longitudinal waves in the water are partially converted to shear waves in the material due to refraction of the acoustic waves at the interface [25]. Shear waves are not refracted as much as longitudinal waves because they travel slower

through a medium [66]. They are also reflected at a smaller angle than longitudinal waves since shear velocity is approximately half of the longitudinal velocity within a given material [75]. Consequently, the shear TOF is approximately 1.5 to 1.7 times greater than the longitudinal TOF due to the inverse relationship between TOF and velocity [116].

The longitudinal and shear wave modes are critical for measuring elastic properties in solids. Just as in point analysis evaluation, longitudinal and shear TOF values can be used to calculate longitudinal and shear velocities when thickness variations are known. These velocities can then be used to calculate density as well as isotropic elastic properties such as Poisson's ratio, elastic modulus, shear modulus, and bulk modulus according to the equations described in the background section. Each of the equations uses either the longitudinal or shear velocity component to determine acoustic and elastic properties.

5.14.1 Material Velocity and Elastic Property Mapping of A, B, and C

While TOF and reflected signal amplitude maps are common forms of C-scan imaging that have been discussed in detail, the next generation of image mapping is focusing on visually depicting minute variations in material velocities and elastic properties directly. While previous studies have demonstrated velocity mapping, either assumptions have been made to presume a constant sample thickness, contact scanning has been conducted in which the transducer was damaged, or the necessary density and thickness changes were not accounted for to directly achieve elastic property mapping [111-115,129]. The novelty of this work was the ability to conduct both longitudinal and shear TOF immersion C-scan imaging which was used to map material velocity and

elastic property variations by accounting for both thickness and density variations throughout the sample.

Through the use of a specialized broadband ultrasound transducer (LS18-15-P75) with a nominal frequency of 15 MHz and a frequency range extending from 8 to 30 MHz, sharp, high intensity reflected signals were generated with sufficient signal-to-noise ratio for evaluation of not only longitudinal reflected signals, but shear wave reflected signals as well. This elastic image mapping technique was applied to the hot pressed samples A, B, and C. The reflected signals used for measuring longitudinal and shear TOF values are shown in Figure 202. By using a C-scan imaging system to collect enough data points for effective mapping, over 200,000 TOF values exhibiting the changes in longitudinal and shear TOF were measured and mapped, as shown in Figures 203-205. While the top and bottom surfaces of samples A, B, and C demonstrated high intensity reflected signals for measuring the longitudinal TOF, the shear peak was more highly attenuated than the longitudinal peak, and the capabilities of the broadband transducer for detecting the mode-converted shear wave reflected signal from the specimen were necessary.

In addition, thickness variations and density variations over the scanned regions were also critical for obtaining the necessary parameters for calculating the elastic properties. By running low frequency TOF ultrasound scans at 1 MHz (MDS25-1) for each sample, a map of the thickness variations over each sample area was also collected. This was possible due to the fact that the specimen was a high density plate with relatively minor inhomogeneities compared to the wavelength of the low frequency transducer. Since it was demonstrated in some sintered SiC samples that differences

unrelated to thickness were detected at 5 MHz, lower frequency transducers were used on samples A, B, and C to ensure that the collected variations were solely due to changes in thickness. In general, if there were anomalous defects or regions with drastic density changes or inhomogeneities that could be detected at low frequencies, this would have affected the strict evaluation of thickness and even lower frequencies would have been used. However, since the hot pressed SiC materials were relatively homogeneous and did not contain millimeter-sized or larger anomalous inclusions or pores, the thickness variation was obtained.

In the shear TOF image maps, several data points were found to be the result of electrical signal interference and were not representative of the sample in any way. They appeared in the scans since the shear wave reflected signals were highly attenuated and had to be scanned and gated close to the noise floor. Although these interference points appeared in the images, they were eliminated before performing further data analysis. The number of interference points was small for samples A and B at about 10 points each, while there were a greater number of occurrences for sample C, as evident in the image maps.

The longitudinal TOF, shear TOF, and thickness variation plots were used to map longitudinal and shear velocities using the equations from the ultrasound background section. The velocity maps are shown in Figures 206-208. Density variations were obtained by using the collected longitudinal velocity values in addition to the material property of acoustic impedance, which was assumed to be constant for the same type of hot pressed SiC material. In the ultrasound background section, the acoustic impedance was defined as a material property determined by the product of density and longitudinal

velocity. As a material property, the acoustic impedance was assumed to be the same for each specimen manufactured using the same materials, processing methods, and conditions. In this case, the acoustic impedance value used for sample A was the average value of 39.2×10^5 g/cm^{2}s while the average value of 38.7×10^5 g/cm^{2}s was used for samples B and C. By using these material properties as Z values in addition to measured changes in c_l, densities changes were calculated over each scanned area. With a full set of data including c_l, c_s, t, and ρ values at each x/y position on the map, elastic properties were calculated at each of the more than 200,000 data points using the aforementioned equations. These values were mapped at each x/y position and color scaled based on minimum and maximum values to obtain image maps of each respective elastic property, as shown in Figures 209-214. The C-scan image maps were qualitatively and quantitatively evaluated, with statistics collected on each data set. Statistics including means, standard deviations, standard errors, 95% confidence intervals, 99% confidence intervals, minimum values, and maximum values for the thickness, density, TOF_l, TOF_s, c_l, c_s, ν, E, G, and K values from each data set are shown in Tables LIV-LVI for samples A, B, and C.

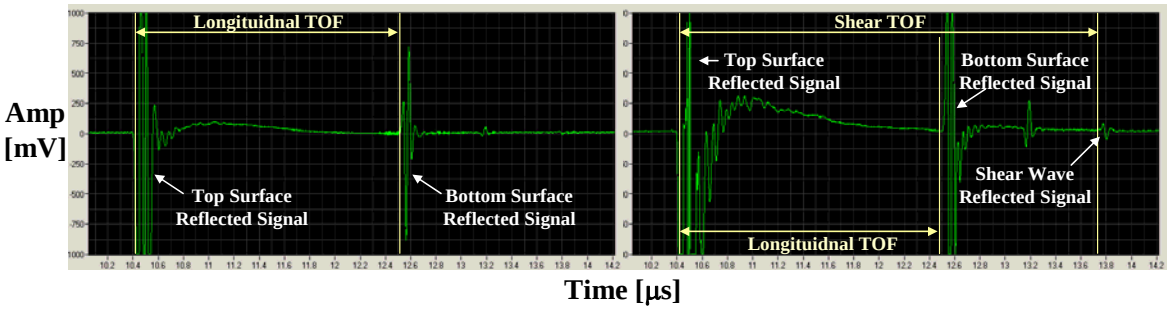

Figure 202. Top, bottom, and shear wave reflected signals for sample C at two different gains demonstrating longitudinal and shear TOF measurements.

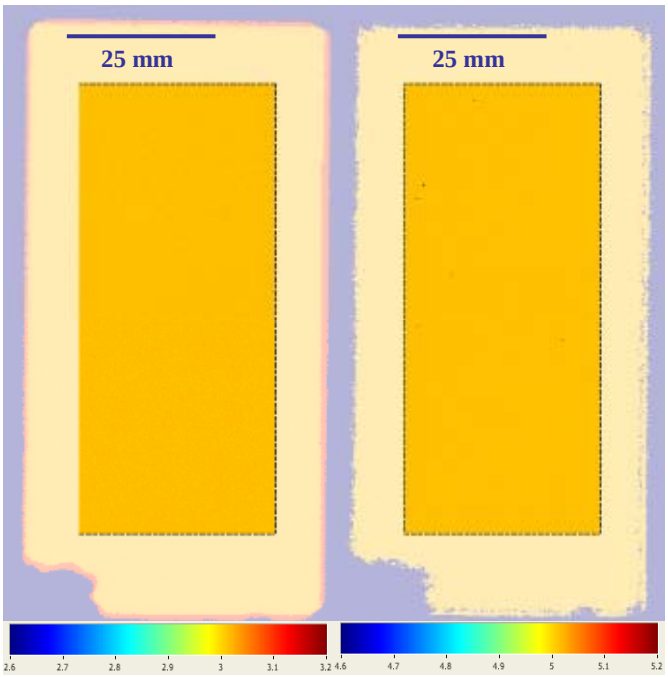

Figure 203. Longitudinal (left) and shear (right) TOF image maps for sample A.

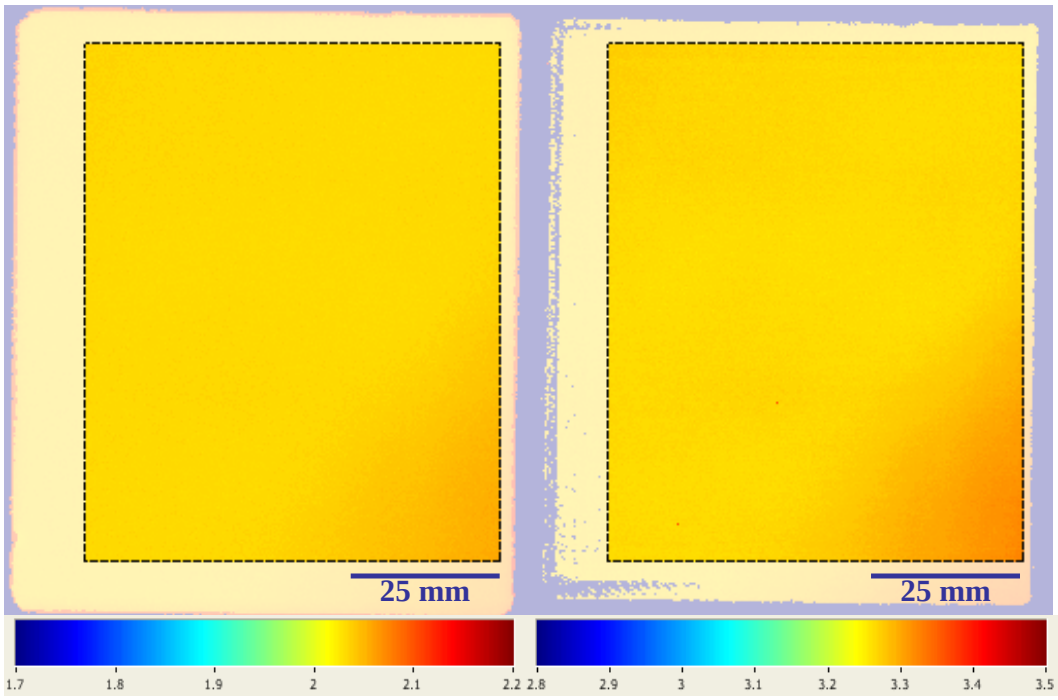

Figure 204. Longitudinal (left) and shear (right) TOF image maps for sample B.

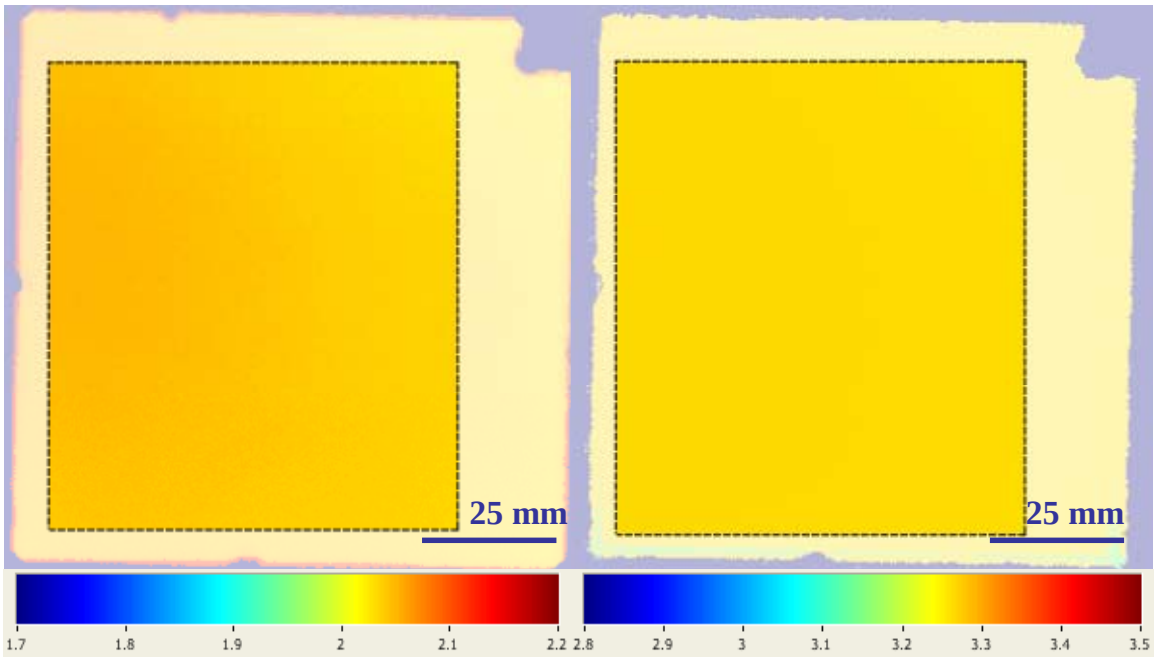

Figure 205. Longitudinal (left) and shear (right) TOF image maps for sample C.

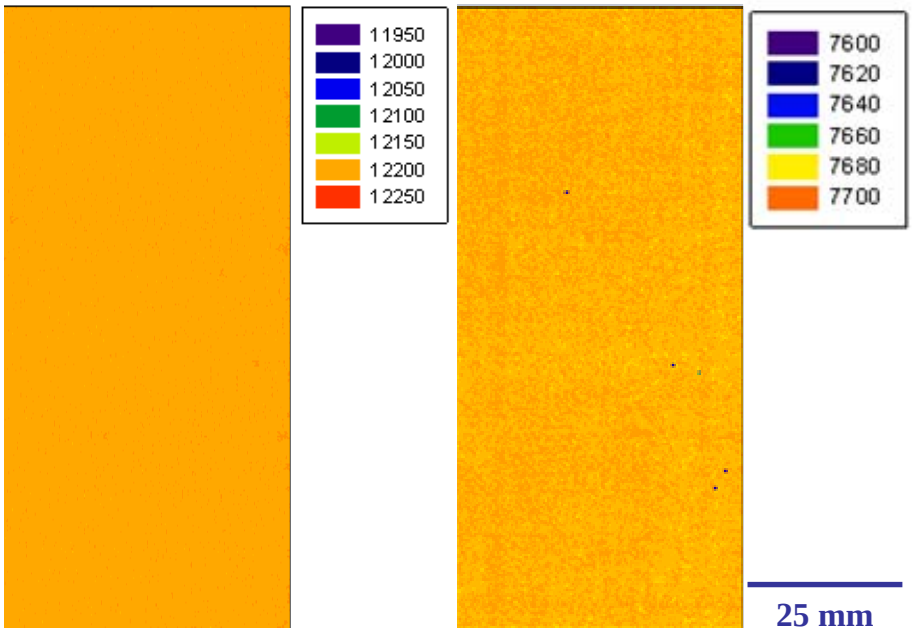

Figure 206. Longitudinal (left) and shear (right) velocity image maps for sample A.

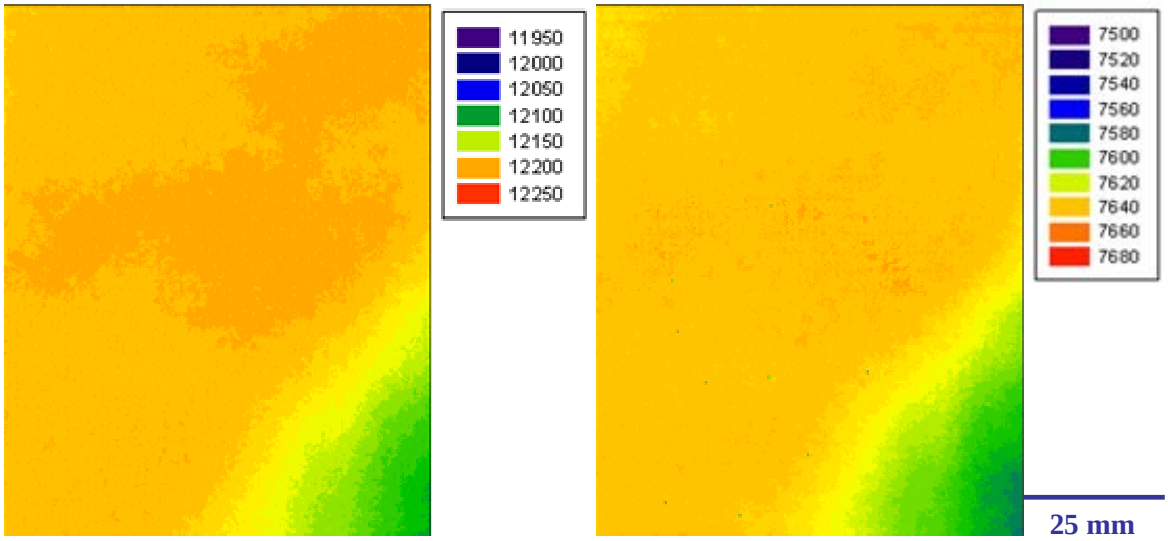

Figure 207. Longitudinal (left) and shear (right) velocity image maps for sample B.

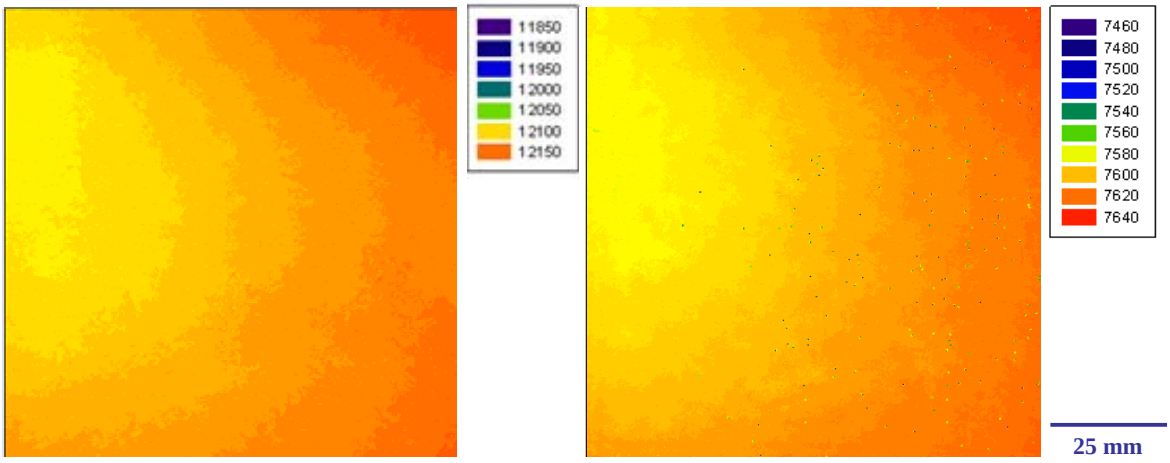

Figure 208. Longitudinal (left) and shear (right) velocity image maps for sample C.

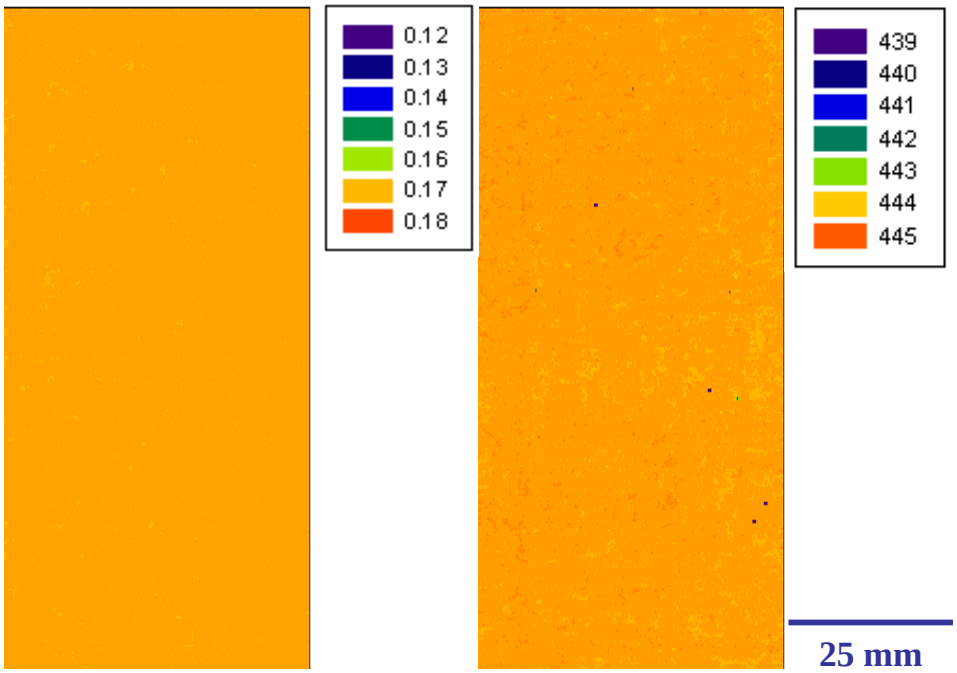

Figure 209. Poisson's ratio (left) and elastic modulus (right) image maps for sample A.

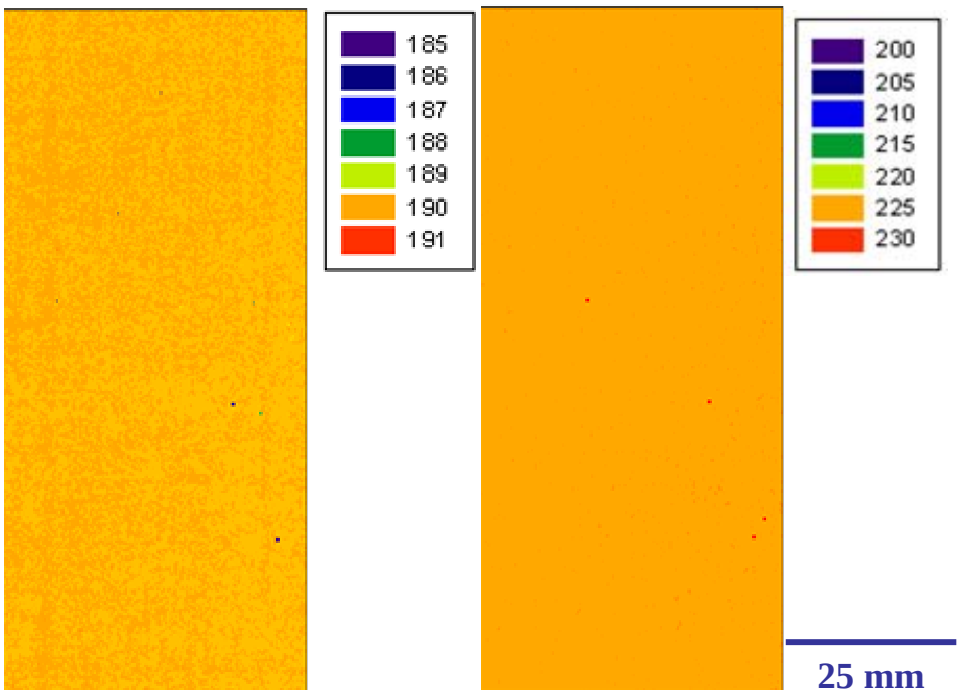

Figure 210. Shear modulus (left) and bulk modulus (right) image maps for sample A.

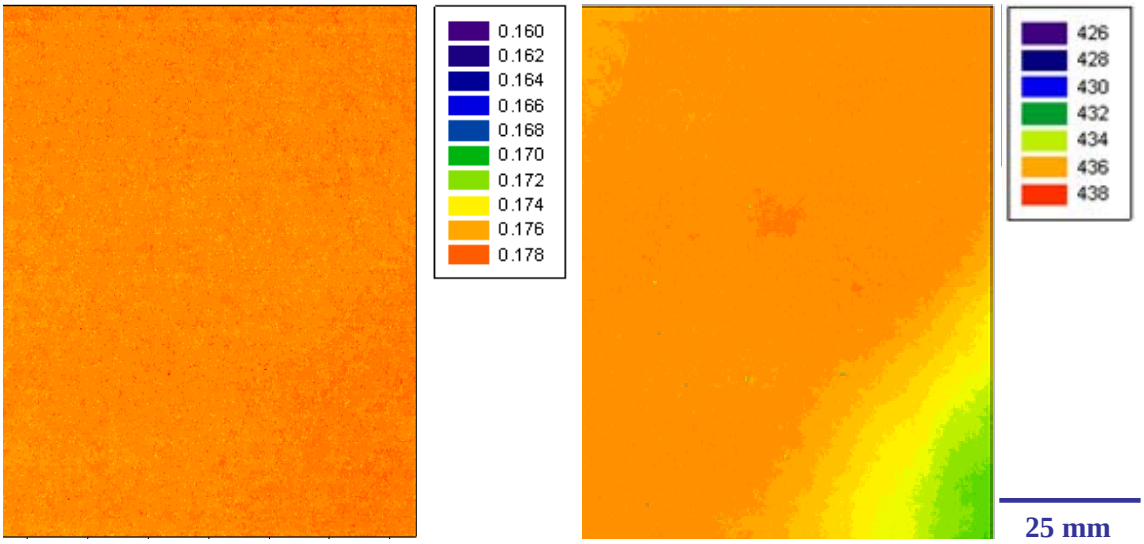

Figure 211. Poisson's ratio (left) and elastic modulus (right) image maps for sample B.

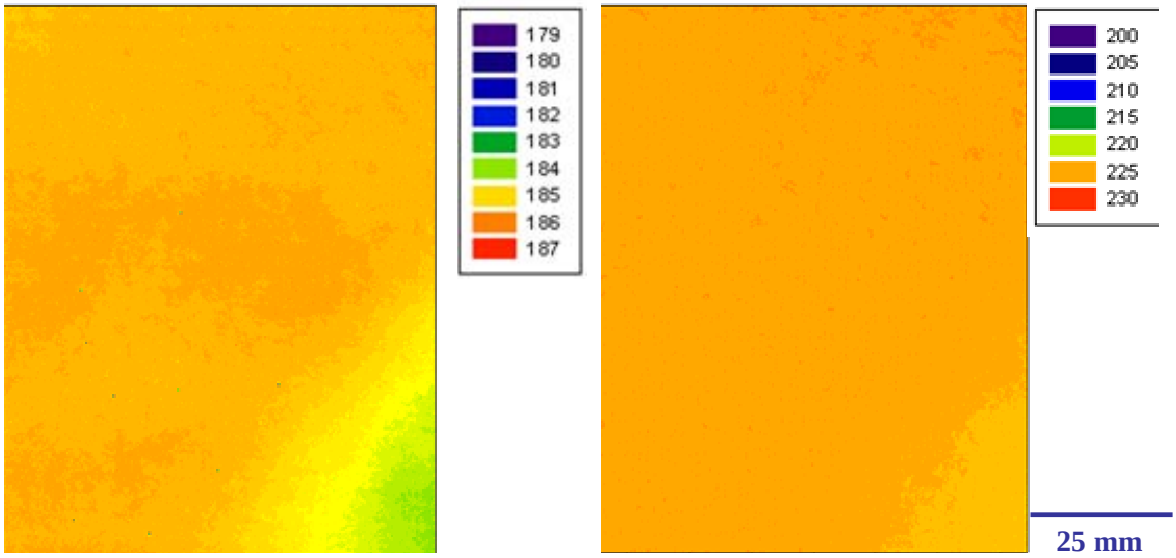

Figure 212. Shear modulus (left) and bulk modulus (right) image maps for sample B.

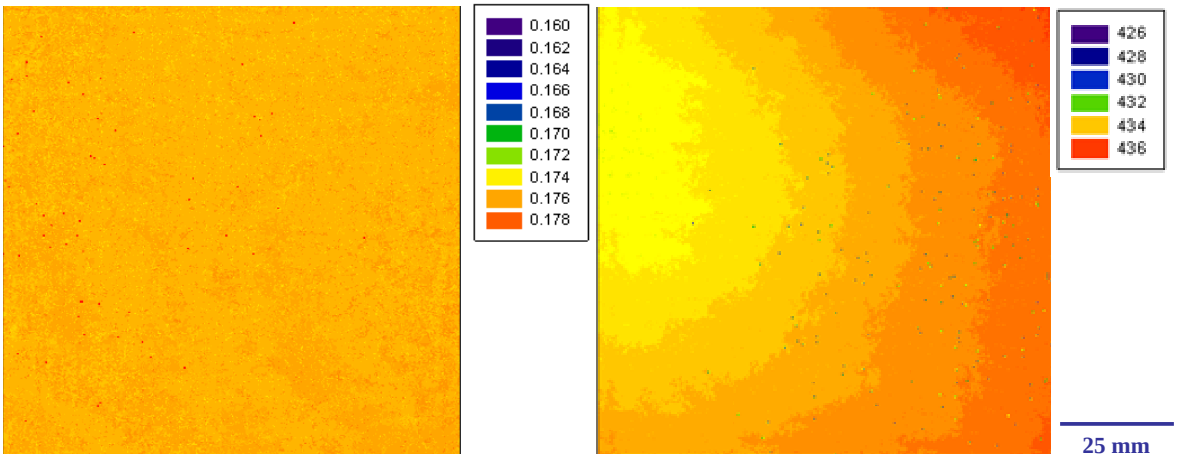

Figure 213. Poisson's ratio (left) and elastic modulus (right) image maps for sample C.

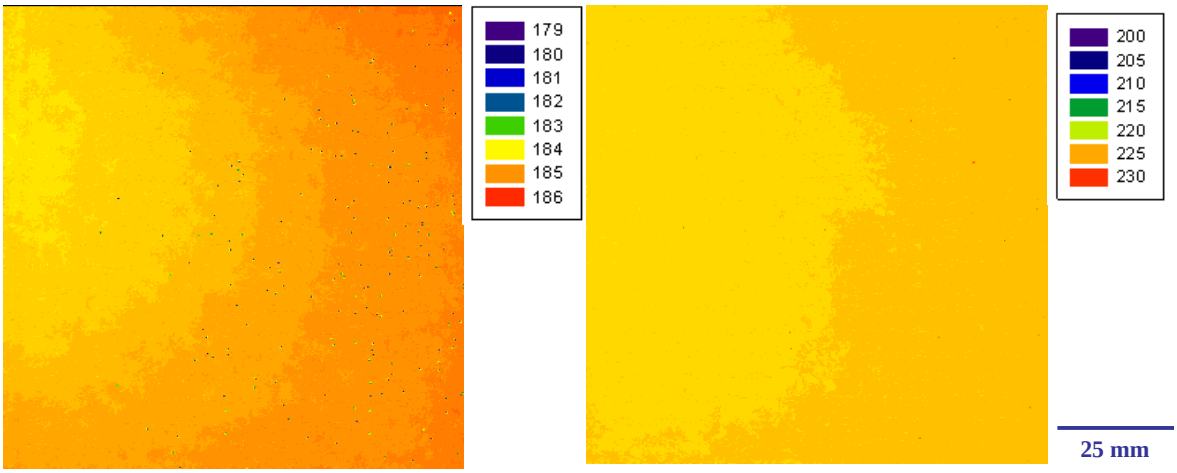

Figure 214. Shear modulus (left) and bulk modulus (right) image maps for sample C.

Parameter	t (mm)	ρ (g/cc)	TOF_l (μs)	TOF_s (μs)	c_l (m/s)	c_s (m/s)	ν	E (GPa)	G (GPa)	K (GPa)
Mean	19.070	3.210	3.127	4.961	12,197	7,688	0.170	444	190	225
Std Dev	1.2E-3	1.1E-3	1.0E-3	1.6E-3	4.113	2.477	5.0E-4	0.1528	0.1367	0.2922
Std Error	4.7E-3	4.3E-6	4.1E-6	6.3E-6	0.0163	0.0098	2.0E-6	6.1E-4	5.4E-4	1.2E-3
95% Conf	9.2E-6	8.4E-6	8.1E-6	1.2E-5	0.0319	0.0192	3.9E-6	1.2E-3	1.1E-3	2.3E-3
99% Conf	1.2E-5	1.1E-5	1.1E-5	1.6E-5	0.0420	0.0253	5.1E-6	1.6E-3	1.4E-3	3.0E-3
Min	19.067	3.206	3.123	4.953	12,186	7,599	0.168	439	185	224
Max	19.075	3.213	3.129	5.019	12,212	7,699	0.183	445	190	230

Table LIV. Quantitative analysis statistics for sample A.

Parameter	t (mm)	ρ (g/cc)	TOF_l (μs)	TOF_s (μs)	c_l (m/s)	c_s (m/s)	ν	E (GPa)	G (GPa)	K (GPa)
Mean	12.760	3.177	2.095	3.343	12,182	7,634	0.177	436	185	225
Std Dev	3.2E-3	5.0E-3	3.8E-3	6.2E-3	19.143	12.278	6.9E-4	0.7088	0.3492	0.5126
Std Error	8.3E-6	1.3E-5	9.7E-6	1.6E-5	0.0493	0.0316	1.8E-6	1.8E-3	9.0E-4	1.3E-3
95% Conf	1.6E-5	2.5E-5	1.9E-5	3.1E-5	0.0967	0.0620	3.5E-6	3.6E-3	1.8E-3	2.6E-3
99% Conf	2.1E-5	3.3E-5	2.5E-5	4.1E-5	0.1271	0.0815	4.6E-6	4.7E-3	2.3E-3	3.4E-3
Min	12.754	3.167	2.088	3.334	12,084	7,505	0.174	428	179	222
Max	12.780	3.203	2.114	3.400	12,221	7,654	0.195	437	186	234

Table LV. Quantitative analysis statistics for sample B.

Parameter	**t (mm)**	**ρ (g/cc)**	**TOF_l (μs)**	**TOF_s (μs)**	**c_l (m/s)**	**c_s (m/s)**	**ν**	**E (GPa)**	**G (GPa)**	**K (GPa)**
Mean	12.760	3.194	2.106	3.357	12,118	7,602	0.176	434	185	223
Std Dev	3.5E-3	5.1E-3	3.3E-3	5.6E-3	19.338	12.741	8.7E-4	0.7428	0.3877	0.5794
Std Error	8.8E-6	1.3E-5	8.4E-6	1.4E-5	0.0485	0.0319	2.2E-6	1.8E-3	9.7E-4	1.5E-3
95% Conf	1.7E-5	2.5E-5	1.6E-5	2.7E-5	0.0950	0.0626	4.3E-6	3.6E-3	1.9E-3	2.8E-3
99% Conf	2.3E-5	3.3E-5	2.2E-5	3.6E-5	0.1248	0.0823	5.6E-6	4.8E-3	2.5E-3	3.7E-3
Min	12.751	3.178	2.096	3.341	12,065	7,456	0.173	425	175	221
Max	12.767	3.208	2.114	3.421	12,178	7,638	0.195	436	186	233

Table LVI. Quantitative analysis statistics for sample C.

For sample A, the longitudinal velocity image map appeared to be very homogeneous while the shear velocity map showed slight variations over the sample area, as shown in Figure 206. The interference points described earlier were evident in the maps due to their distinctly dark colors since they did not have values that fall within the range of the scale. According to Table LIV, the longitudinal TOF values ranged between 12,186 m/s and 12,212 m/s, with an average value of 12,197 m/s while the shear values ranged between 7,599 m/s and 7,699 m/s with an average value of 7,688 m/s. The standard deviation for longitudinal velocity was 4.113 m/s while the shear velocity standard deviation was 2.477 m/s. By assuming the material property Z was constant at 39.2×10^5 g/cm^{2}s, the density range was found to go from 3.206 g/cm^3 to 3.213 g/cm^3 with an average value of 3.210 g/cm^3. The elastic property maps for sample A also appeared to be relatively homogeneous, with the E and G maps showing the most distinct variations, as shown in Figures 209 and 210. Even when there were slight variations, the distribution of the minor differences appeared to be dispersed homogeneously throughout each image map. The ν values ranged from 0.168 to 0.183 with an average of 0.170 and a standard deviation of 5.0×10^{-4}. The E values ranged from 439 GPa to 445 GPa with an average of 444 GPa and a standard deviation of 0.1528 GPa. The G values ranged from 185 GPa to 190 GPa with an average of 190 GPa and a standard deviation of 0.1367 GPa. The K values ranged from 224 GPa to 230 GPa with an average of 225 GPa and a standard deviation of 0.2922 GPa. The ranges for each of the elastic properties for sample A was very narrow, which was consistent with the homogeneous image maps. Even the apparently larger variations in E and G translated to overall differences of 6 GPa and 5 GPa, respectively, over each sample area.

For sample B, the critical region in Figure 207 was again found to be the bottom right corner of the sample which had previously shown low reflected signal amplitude and high longitudinal TOF value. While the rest of sample B appeared to be more homogeneous in previous studies, the longitudinal and shear velocity image maps showed some degree of variation in those regions as well. The critical region was characterized by c_l and c_s values of 12,084 m/s and 7,505 m/s while the average values for the rest of the sample were 12,182 m/s and 7,634 m/s, respectively. The standard deviations were 19.143 m/s for c_l and 12.278 m/s for c_s, which were both about five times higher than the standard deviation value for sample A. By assuming the material property Z was constant at 38.7 x 10^5 g/cm^{2}s, the density range was found to vary between 3.167 g/cm^3 and 3.203 g/cm^3 with an average value of 3.177 g/cm^3. The elastic properties changed most drastically for E, which had a small central region of 437 GPa that was slightly above average, and for G, which showed several regional variations apart for the critical low G area in the bottom right corner. The ν values showed slight variations throughout the sample area without a major change in the critical area while K showed changes in a smaller region in the bottom right corner. These parameters did not appear to vary as drastically as E and G, as shown in Figures 211 and 212. The ν values ranged from 0.174 to 0.195 with an average of 0.177 and a standard deviation of 6.9 x 10^{-4}. The E values ranged from 428 GPa to 437 GPa with an average of 436 GPa and a standard deviation of 0.7088 GPa. The G values ranged from 179 GPa to 186 GPa with an average of 185 GPa and a standard deviation of 0.3492 GPa. The K values ranged from 224 GPa to 235 GPa with an average of 225 GPa and a standard deviation of 0.5126 GPa. All of the elastic

properties for sample B had wider overall ranges and higher standard deviations than sample A, which was a consistent as compared to previous results.

For sample C, the gradient in properties was readily apparent, appearing similar to concentric rings of values that increased from the left side to the right side of the sample, as shown in Figure 208. The longitudinal and shear velocity image maps demonstrated the trend well, but the shear map suffered from a high number of interference points scattered throughout the map. Again, these points, which were not representative of the sample, were eliminated before conducting the quantitative summary found in Table LVI. The longitudinal TOF values ranged from 12,065 m/s and 12,178 m/s, with an average value of 12,118 m/s while the shear values ranged between 7,456 m/s and 7,638 m/s with an average value of 7,602 m/s. These values were the lowest among the three samples. The standard deviation for longitudinal velocity was 19.338 m/s while the shear velocity standard deviation was 12.741 m/s, both of which were slightly higher than sample B and approximately five times greater than sample A. By assuming the material property Z was constant at 39.2 x 10^5 g/cm^{2}s, the density range was found to go from 3.178 g/cm^3 to 3.208 g/cm^3 with an average value of 3.194 g/cm^3. These values were higher than for sample B, which had a much lower average, most likely due to the large low density area of approximately 3.167 g/cm^3 in the bottom right corner of the sample. In Figures 213 and 214, elastic property trends in sample C were found to be similar to sample C, as the E and G maps showed the most noticeable variations while ν showed consistent variations and K showed a gradient distinguishing two specific regions. The ν values ranged from 0.173 to 0.195 with an average of 0.176 and a standard deviation of 8.7 x 10^{-4}. The E values ranged from 425 GPa to 436 GPa with an average of 434 GPa

and a standard deviation of 0.7428 GPa. The G values ranged from 175 GPa to 186 GPa with an average of 185 GPa and a standard deviation of 0.3877 GPa. The K values ranged from 221 GPa to 233 GPa with an average of 223 GPa and a standard deviation of 0.5794 GPa. All of the elastic properties for sample C were similar in overall range and average to sample B, but the standard deviations were slightly higher. Ranked from lowest to highest overall standard deviations, sample A showed the lowest deviation by far while samples B and C were similar, with sample C showing a slightly higher deviation. Again, the results were consistent throughout the reflected signal amplitude, TOF, velocity, and elastic property image map studies described earlier.

By utilizing the specialized broadband transducers, shear TOF C-scan images were collected in addition to the common longitudinal TOF C-scan images. These results were used to directly map both shear velocity and longitudinal velocity data for samples A, B, and C based on over 200,000 points of data. By using a low frequency scan to extract thickness variations over each sample area and assuming the material property Z to be constant for each set of samples to calculate density variations over each sample area, all of the necessary components were available for mapping elastic properties. Isotropic elastic equations were used to construct image maps of Poisson's ratio, elastic modulus, shear modulus, and bulk modulus. The image maps were effective for showing elastic property variations, which were minimal for sample A and more pronounced for samples B and C. Sample B showed its characteristic critical bottom right corner region which had the lowest elastic properties, while sample C showed a clear gradient in elastic properties that increased from left to right. The E and G image maps consistently showed distinctive elastic property variations while ν and K image maps showed smaller degrees

of variation. Overall, the novel technique for elastic property image mapping proved to be effective for showing differences among hot pressed SiC samples that were manufactured under the same processing conditions.

5.14.2. Material Velocity and Elastic Property Mapping of ST1

In addition to exploring material velocity and elastic property mapping for the hot pressed A, B, and C samples, the same mapping techniques were also applied to the sintered SiC sample ST1 which contained the TiB_2 additive. Again, the TOF values exhibiting the changes in longitudinal and shear TOF were measured using the reflected signals shown in Figure 215 and plotted in Figure 216. Thickness variations and density variations were collected over the scanned regions. Thickness changes were obtained by running a low frequency TOF ultrasound scan at 1 MHz, as shown in Figure 217. The longitudinal TOF, shear TOF, and thickness variation plots were used to map longitudinal and shear velocities using the aforementioned equations. The velocity maps are shown in Figure 218. The density variations were obtained by using the collected longitudinal velocity values in addition to the material property of acoustic impedance, which were assumed to be constant for the same type of sintered SiC materials. By taking an average of eight sintered SiC samples manufactured under the same conditions, the acoustic impedance for these tiles was found to be 36.9×10^5 g/cm^{2}s. By using this material property as the Z value in addition to measured changes in c_l, densities changes were calculated over the scanned area. Elastic property values were then calculated, mapped at each x/y position, and color scaled based on minimum and maximum values to obtain image maps of each respective elastic property, as shown in Figures 219 and 220.

From the image maps for the sintered SiC plate, regional variations and changes in elastic properties from isolated defects were found. In the TOF images, multiple isolated areas with different average TOF values as compared to the rest of the bulk were located. The two largest areas in which this occurred were in the top left corner of the sample, which had a lower TOF value, and the bottom right corner of the sample, which had a higher TOF value than the average. Besides these isolated features, the TOF images showed a slight gradient of lower to higher TOF values from the left to the right side of the sample. These were the same trends found during point analysis of the sample, with TOF values on the left side averaging 1.327 μs for longitudinal and 2.083 μs for shear as compared to 1.359 μs for longitudinal and 2.134 μs for shear over the rest of the sample area. By applying the thickness correction factor, these patterns were accounted for so that any remaining differences were not due to changes in thickness, but changes in the bulk properties.

The same trends found in the TOF maps were analyzed using the velocity and elastic property maps. In the velocity maps, the low TOF area in the top left corner corresponded to the area of highest longitudinal and shear velocity, ranging between 11,800 to 12,000 m/s for longitudinal velocity as compared to the average velocity of 11,400 m/s, and between 7,400 and 7,500 m/s for shear velocity as compared to the average velocity of 7,220 m/s. The high TOF area in the bottom right corner corresponded to the area of lowest longitudinal and shear velocity, ranging between 10,800 and 11,000 m/s for longitudinal velocity as compared to the average velocity of 11,400 m/s, and between 6,900 m/s and 7,000 m/s for shear velocity as compared to the average velocity of 7,220 m/s. Even after accounting for the change in thickness, the

overall velocity trend for the sample decreased from left to right, which correlated to the point analysis data trends. For points 1, 4, and 7 on the left side of the sample, the average longitudinal velocity was 11,560 m/s, which decreased to an average of 11,340 m/s for points 2, 5, and 8 down the center of the sample, and further decreased to an average of 11,300 m/s for points 3, 6, and 9 on the right side of the sample. Similar trends were found for the shear velocity map.

Evaluation of the elastic property maps showed a more narrow range of variability, but evidence of similar trends was found as compared to the longitudinal and shear TOF and velocity maps. In the Poisson's ratio point analysis data, the values at all nine points were found to be 0.16. The majority of the ν map matched this value as well, though there were some areas containing slight deviations. There were a few areas of higher ν with values above 0.18 scattered throughout the sample, including the isolated features in the top left and bottom right corners. In the center of the bottom right feature, ν dropped to about 0.14. In the elastic modulus map, there were three distinct regions from left to right that represented E values ranging from 400 to 410 GPa on the left edge, 390 to 400 GPa through most of the center, and 380 to 390 GPa on the right side. While the isolated feature in the top left corner was not detectable, the one on the bottom right showed an E value ranging between 370 and 380 GPa. The shear modulus maps showed more of a gradient from left to right, with higher G values around 180 GPa on the left side of the sample and lower G values of 160 GPa on the right side of the sample. The isolated feature in the bottom right had a G value of approximately 150 GPa. The bulk modulus map displayed a very narrow range, with the majority of K values falling between 190 and 200 GPa over the sample area. As expected, the bottom right feature

had a lower K value of approximately 150 GPa, but there were two additional regions with K values ranging between 160 and 170 GPa above the bottom right feature and in the top right corner. Overall, the elastic property trends were consistent with point analysis measurments, with values decreasing from left to right. Another important trend was that the feature at the bottom right of the sample consistently had the lowest elastic properties. The image map data were collected and summarized in terms of the mean, standard deviation, standard error, and 95% and 99% confidence interval for each data set, representing thickness, density, longitudinal TOF and velocity, shear TOF and velocity, Poisson's ratio, elastic modulus, shear modulus, and bulk modulus, respectively. These data are shown in Table LVII. When compared to the hot pressed elastic property mapping data for samples A, B, and C, the data from the sintered sample ST1 showed a much higher degree of variability, as expected according to previous results. The material velocity and elastic property mapping technique was shown to be effective for evaluating property variations for both hot pressed and sintered SiC armor ceramic plates.

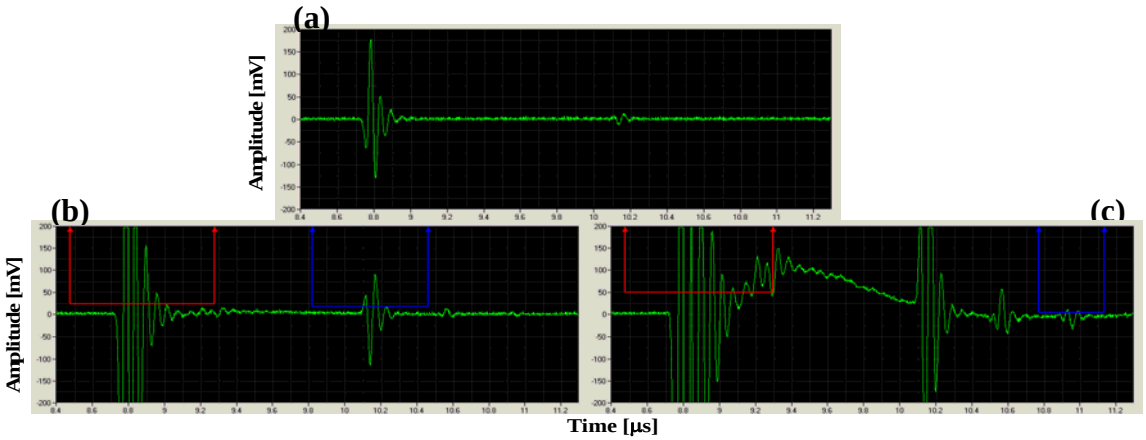

Figure 215. Amplitude scans of (a) reflected signals and gated (b)longitudinal TOF and (c) shear TOF peaks for ST1

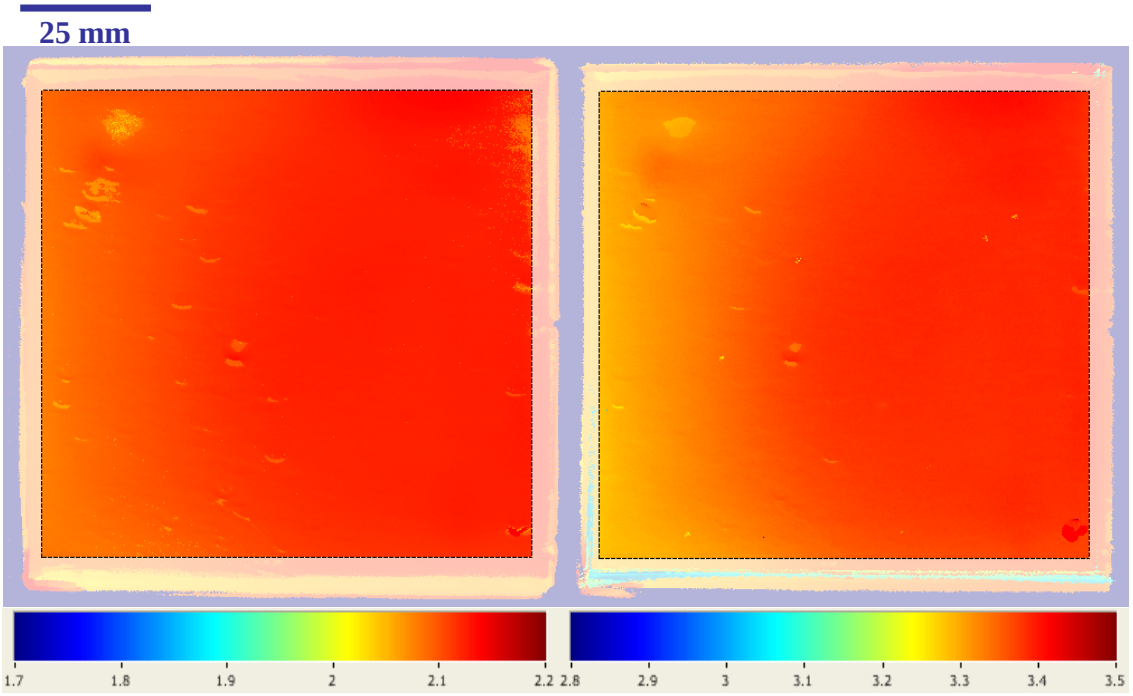

Figure 216. Longitudinal TOF (left) and shear TOF (right) C-scan image maps for ST1.

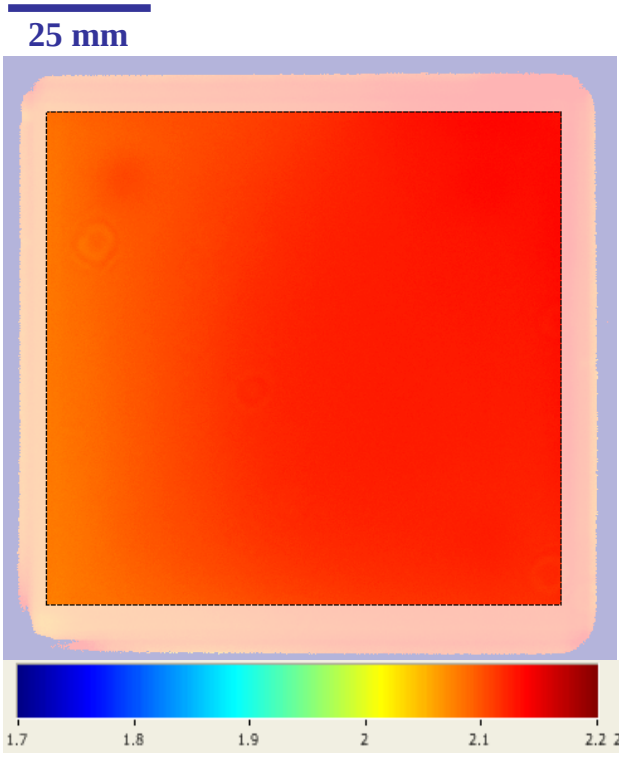

Figure 217. Low frequency scan for assessing thickness variations of ST1.

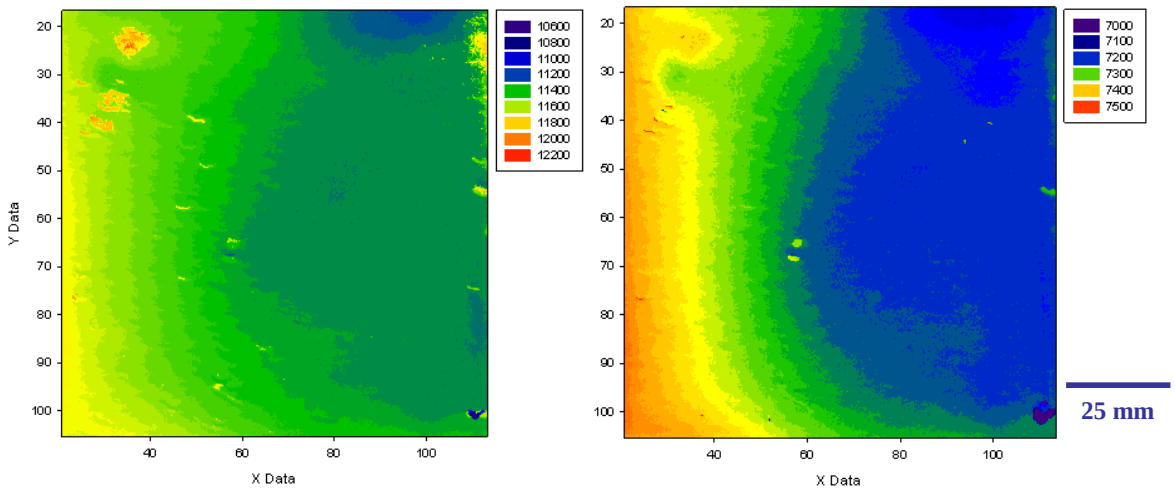

Figure 218. Longitudinal (left) and shear (right) velocity image maps for sample ST1.

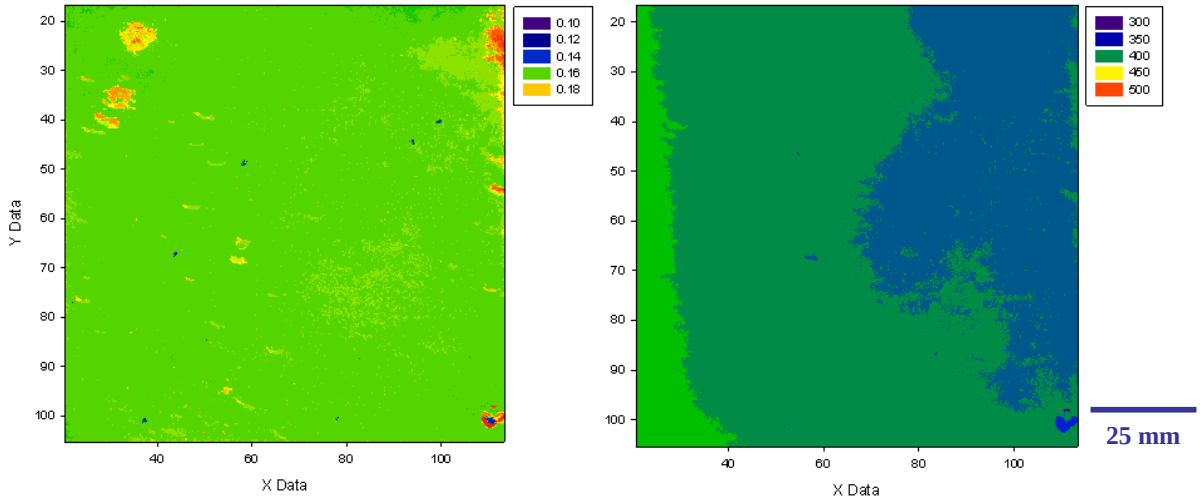

Figure 219. Poisson's ratio (left) and elastic modulus (right) image maps for sample ST1.

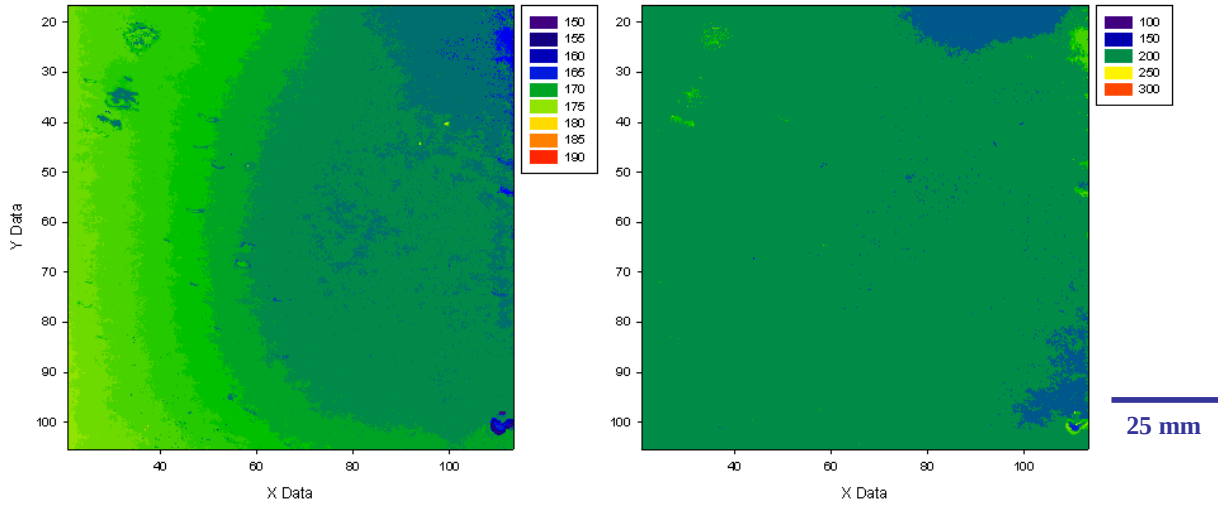

Figure 220. Shear modulus (left) and bulk modulus (right) image maps for sample ST1.

Parameter	**t (mm)**	**ρ (g/cc)**	**TOF_l (μs)**	**TOF_s (μs)**	**c_l (m/s)**	**c_s (m/s)**	**ν**	**E (GPa)**	**G (GPa)**	**K (GPa)**
Mean	7.68	3.221	1.348	2.117	11,400	7,260	0.16	393	170	192
Std Dev	0.017	0.035	0.017	0.027	123.57	76.20	0.004	4.14	1.96	3.08
Std Error	3.8E-5	7.6E-5	3.8E-5	5.9E-5	0.272	0.168	9.3E-6	9.1E-3	4.3E-3	6.7E-3
95% Conf	7.4E-5	1.5E-4	7.4E-5	1.2E-4	0.532	0.328	1.8E-5	0.018	0.008	0.013
99% Conf	9.7E-5	2.0E-4	9.8E-5	1.5E-4	0.700	0.432	2.4E-5	0.023	0.011	0.017

Table LVII. Quantitative analysis statistics for sample ST1.

5.15. Individual Feature Properties and Size Distributions

A technique was developed for separating the most distinct individual features from an ultrasound C-scan image and measuring key properties that could be categorized for determining size distributions. This was important for figuring out the number of distinguishable features in an armor ceramic test specimen. The Adobe Photoshop Image Processing Tool Kit 4.0 was utilized for this purpose.

Starting with a reflected signal amplitude C-scan image, the color scale was converted to grayscale and the brightness and contrast were optimized to generate the starting image. Next, the histogram curve of amplitude occurrences over the full grayscale range was used to choose the appropriate threshold value. In order to characterize high amplitude and low amplitude features separately, thresholds were chosen from the left side of the curve to highlight the low amplitude features and from the right side of the curve to highlight the high amplitude features. Low reflected signal amplitude features were defined as features with lower densities and significant acoustic impedance mismatch compared to the bulk of the test specimen. Another consideration was the depth of the feature, since features farther away from the sample surface had slightly lower reflected signal amplitude values. On the other hand, high reflected signal amplitude features were a more rare case that included significant sized features of higher density than the bulk of the test specimen. Since these features had higher density and therefore a higher degree of ultrasound transmission, the bottom surface reflected signal amplitude values over these features was higher than the average amplitude values. Some examples of high amplitude features within sintered SiC ($Z \sim 37.5 \times 10^5$ g/cm^{2}s) were Al_2O_3 ($Z \sim 43.0 \times 10^5$ g/cm^{2}s), iron ($Z \sim 45.4 \times 10^5$ g/cm^{2}s), and TiB_2 ($Z \sim 51.3 \times 10^5$ g/cm^{2}s)

inclusions. Low and high reflected signal amplitude features were thresholded and mapped separately.

If there were large regions of either low or high reflected signal amplitude, the grayscale image was sectioned and analyzed separately. In this case, if the full image was evaluated without sectioning, wash out or saturation occurred that prevented distinction of individual features within specific regions. Since the main goal was to distinguish features over the full area of the image, the presence of low or high reflected signal amplitude regions was less important than locating specific individual features. If the image was sectioned and thresholded separately, the sections were reassembled before advancing to the next step. Erosion, or shrinking, and dilation, or expanding, image processing steps were used on each image to remove image noise and enhance the distinguishable features for further evaluation [130]. More specifically, an opening step, which consisted of erosion followed by dilation, or a closing step, which consisted of dilation followed by erosion, was utilized to enhance the features while maintaining their characteristic properties.

The resulting map of high reflected signal amplitude features was inverted and all of the features colored red. Next, these red features were overlaid on the low reflected signal amplitude feature map, which had low amplitude features that were black in color. This combined feature map showed all of the distinct features that could be detected and the identification of low or high reflected signal amplitude features were characterized by their black or red coloration, respectively. The next step was to number each individual feature and determine their properties. This was accomplished by the labeling function of the Image Processing Toolkit, which assigned a value to each unique feature that was

detected. After calibrating the scale of the image, the “Measure All” function was selected to measure the properties of each feature including the area, perimeter, equivalent diameter, length, width, aspect ratio, symmetry, roundness, nearest neighbor distance, and minimum separation distance among others. Out of these parameters, the equivalent diameter was the most important for determining the size of each feature. These were collected and plotted in histogram form based on the number of occurrences of each size (y-axis) over the feature size range (x-axis). Different curve fit equations were plotted to find the highest correlation to the data to look for a representative equation that described the size distribution. Additional maps of features with varying size ranges were also displayed by using the Image Processing Toolkit “Select” function. These maps displayed only the features within the chosen size range and provided a count of the number of distinct individual features within each range.

This technique was applied to two different four by four-inch armor ceramic test specimens to determine the number of distinct features and their properties including size distributions. Each of the samples was run at a step size of 0.05 mm, so the high resolution images included data sets of approximately 3.6 million data points. The first sample that was analyzed was sample D, which was the hot pressed armor grade SiC specimen described in detail earlier, while the other was sample ST1, which was one of the sintered SiC specimens containing the TiB_2 additive.

For evaluation of sample D, the 125 MHz bottom surface reflected signal amplitude C-scan image was utilized. The color image was converted to grayscale and the brightness and contrast were optimized to bring out any distinct features as shown in Figure 221. Since there were no large regions of either low or high reflected signal

amplitude, the sectioning step was unnecessary. The full range of grayscale values on the histogram curve went from approximately 50 to 250. Three different thresholds denoted low, medium, and high were selected for the low amplitude features as well as the high amplitude features, where a low threshold collected a small sample of the most distinct features and a high threshold collected a large sample of features. For the low amplitude features, thresholds of 120, 130, and 140 were chosen as low, medium, and high as shown in Figure 222 while thresholds of 231, 201, and 171 were chosen as low, medium, and high for high amplitude features at the other end of the spectrum as shown in Figure 223. The medium thresholds for each amplitude range were chosen to represent each sample, since the low thresholds showed too few individual features and the high thresholds showed too many. The map of high amplitude features was inverted and the individual features colored red before they were overlaid on the low amplitude feature map as shown in Figure 224. Erosion and dilation were then performed on the combined image map in Figure 225. This screening method ensured that only the most prominent features were being evaluated. Next, the features were numbered individually as shown and the properties were measured for the low amplitude map, high amplitude map, and combined feature map. The individual numbering of the combined feature map is shown in Figure 226.

The data sheet revealed that 131 low amplitude features and 16 of the more rare high amplitude features were distinguished for a total of 147 total features in the combined feature map. The average individual feature properties for the combined feature image map included an average area of 29,510 μm^2, an average perimeter of 684 μm, an average equivalent diameter of 159 μm, an average length of 246 μm, an average

width of 156 μm, an average aspect ratio of 1.457, an average symmetry of 0.937, an average roundness of 0.497, an average nearest neighbor distance of 2781 μm, and an average minimum separation distance of 2553 μm. The average parameters from each map are shown in Table LVIII. The smallest feature size detected was 56 μm while the largest was 538 μm. The minimum and maximum parameters from each map are shown in Table LIX. The "Select" function was used to create maps based on feature size range, and according to the breakdown in Figure 227, there were 62 features between 56-99 μm, 43 features between 100-199 μm, 22 features between 200-299 μm, 7 features between 300-399 μm, 6 features between 400-499 μm, and 3 features between 500-550 μm.

The equivalent diameter values were used to construct a feature size distribution curve. Since various forms of the power law function were commonly used to describe defect size distributions [46,131-132], these functions were explored. Using the nonlinear curve fit function from Origin version 7.0, the best fit to the data was found to be the Extended Freundlich power law function, which had an R^2 correlation of 96.9% to the data set for sample D. The size distribution curve and fit are shown in Figure 228. The AUTC value for the size distribution curve was calculated as 8,363. The feature size distribution curve was compared to the work of Bakas et al. in which size distribution curves were found for defects detected on the fracture surfaces of ballistically tested hot pressed SiC. A different variation of the power law was used for the Bakas et al. curve fit and the shapes of the distribution curves were similar. The main difference was that the distribution from Bakas et al. was from defects found on the fracture surface after destructive testing, which means that the original defect sizes may have been larger. On the other hand, the data shown in this study was from intact features found in the bulk of

the material after nondestructive testing, which were much more representative in actual defect size and may also provide further insight into the affect of defects on armor ceramic failure.

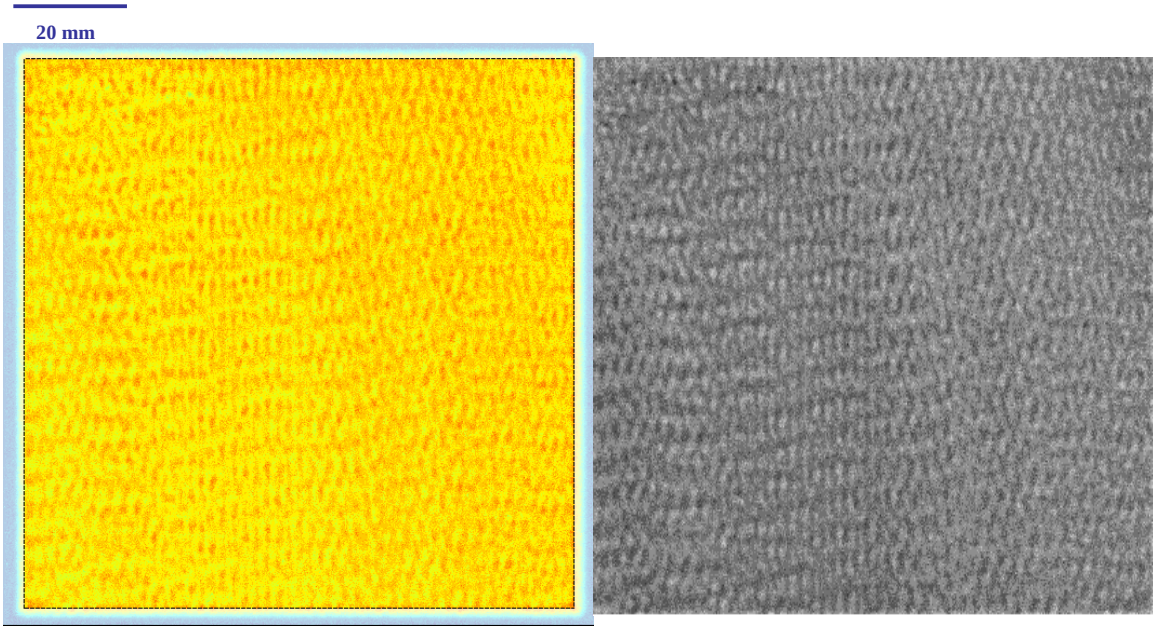

Figure 221. Reflected signal amplitude color and gray scale images from sample D.

Figure 222. Threshold selections of low amplitude grayscale features from sample D.

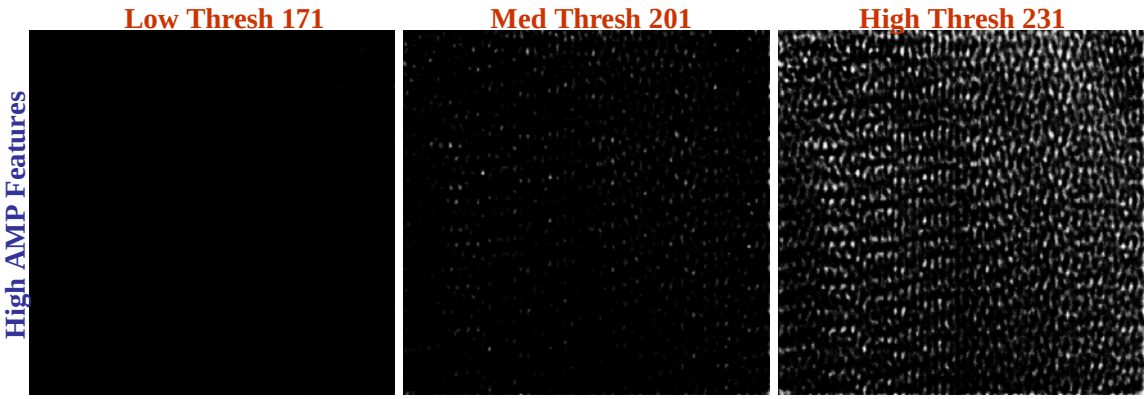

Figure 223. Threshold selections of high amplitude grayscale features from sample D.

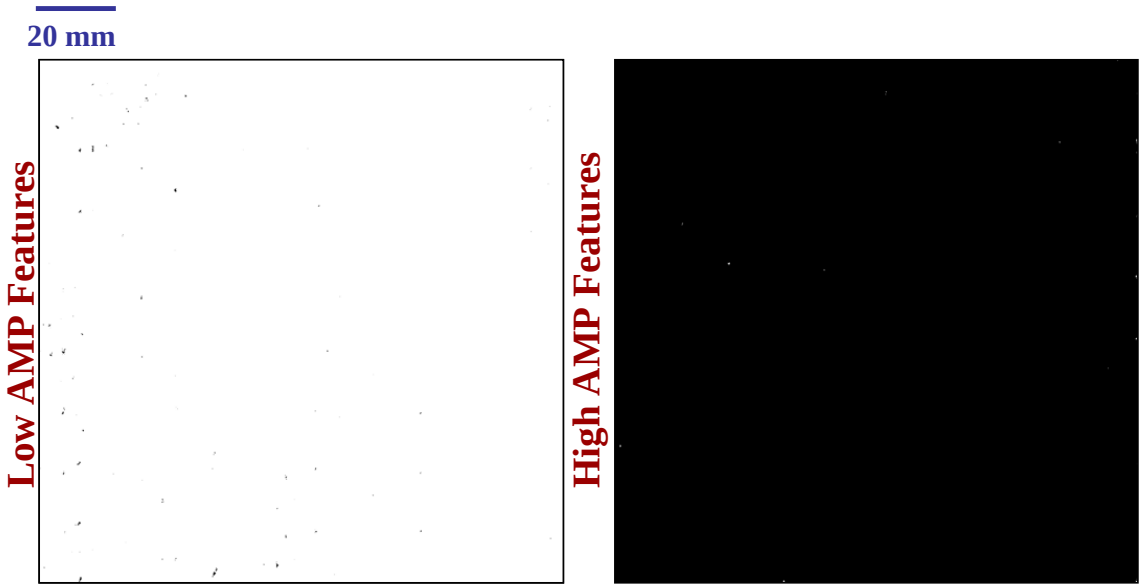

Figure 224. Threshold image selections featuring most distinct high and low amplitude features from sample D.

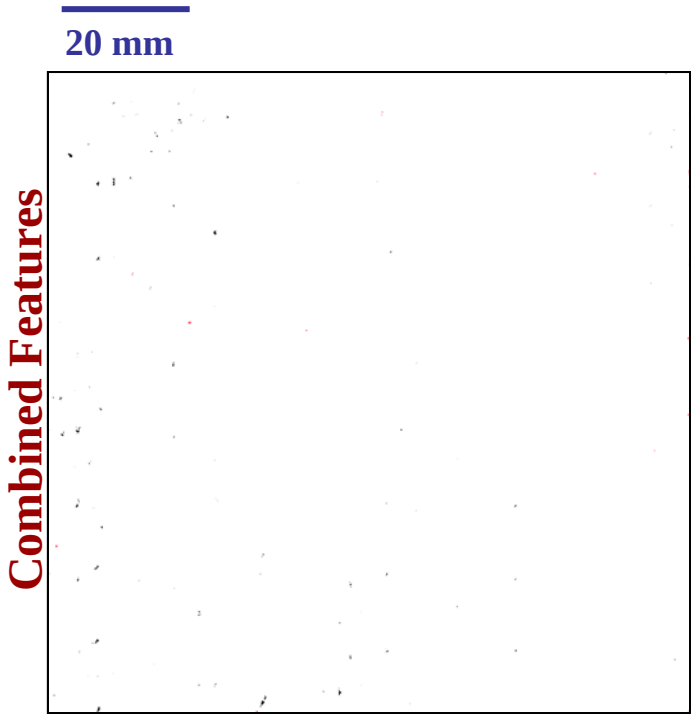

Figure 225. Threshold image of combined high and low amplitude features from sample D.

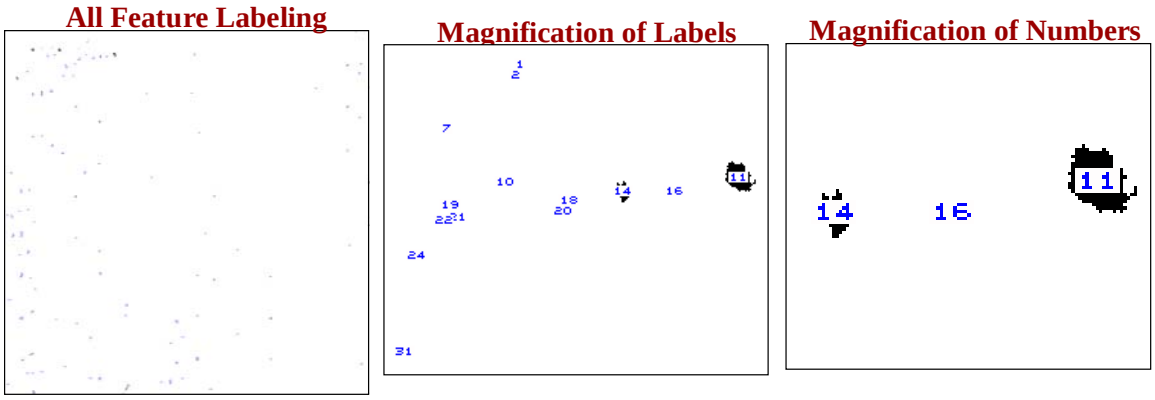

Figure 226. Individual feature labeling from combined map of sample D including magnification of labels and numbers.

Average Feature Parameters

Image	Area [µm²]	Perimeter [µm]	Equivalent Diameter [µm]	Near. Neighb. Dist. [µm]	Min. Sep. Dist. [µm]
Low AMP	29,542	685	157	2676	2502
High AMP	29,375	669	182	9564	8082
Full	29,510	684	159	2781	2553

Additional Average Feature Parameters

Image	Length [µm]	Width [µm]	Aspect Ratio	Symmetry	Roundness
Low AMP	247	153	1.475	0.935	0.486
High AMP	231	186	1.217	0.958	0.630
Full	246	156	1.457	0.937	0.497

Table LVIII. Average low, high, and combined threshold map values from sample D individual features.

Minimum and Maximum Selected Parameters

Image	Min. Area [µm²]	Max. Area [µm²]	Equ. Diam. Min. [µm]	Equ. Diam. Max. [µm]
Low AMP	2500	227,500	56	538
High AMP	12,500	80,000	126	319
Full	2500	227,500	56	538

Table LIX. Minimum and maximum low, high, and combined threshold map values from individual features of sample D.

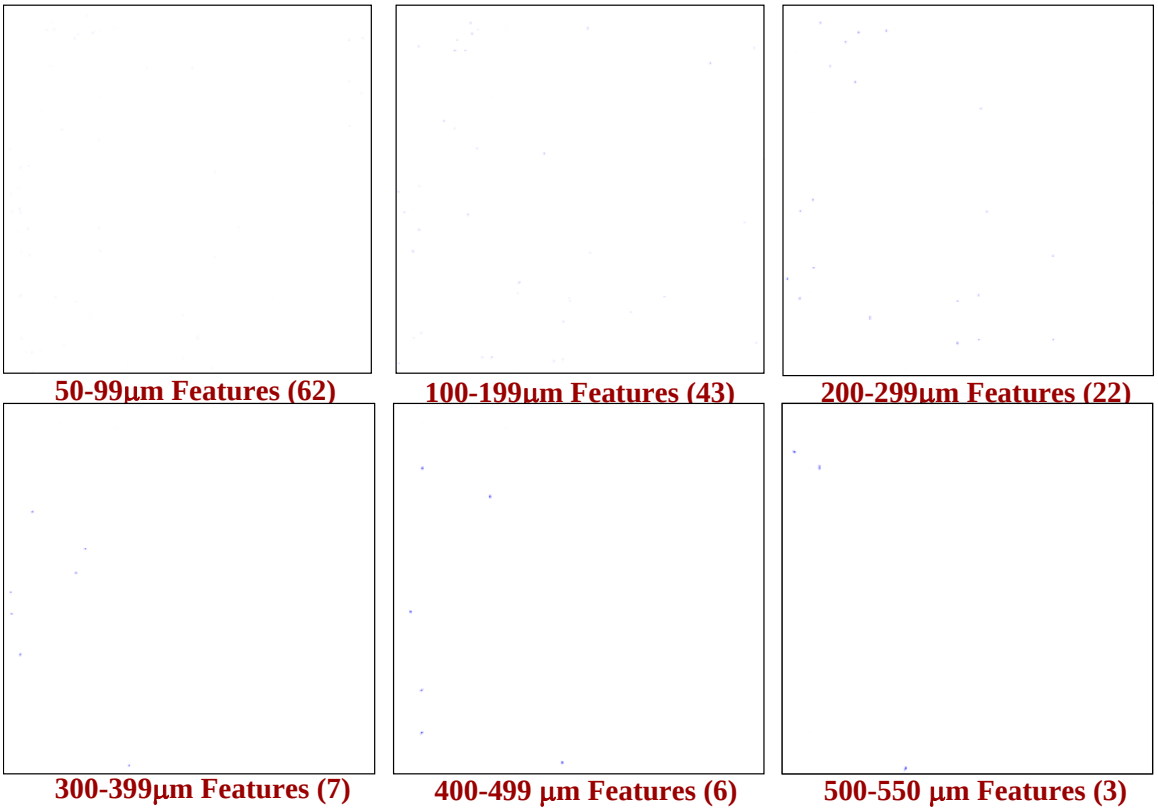

Figure 227. Individual feature size range maps of sample D and number of features.

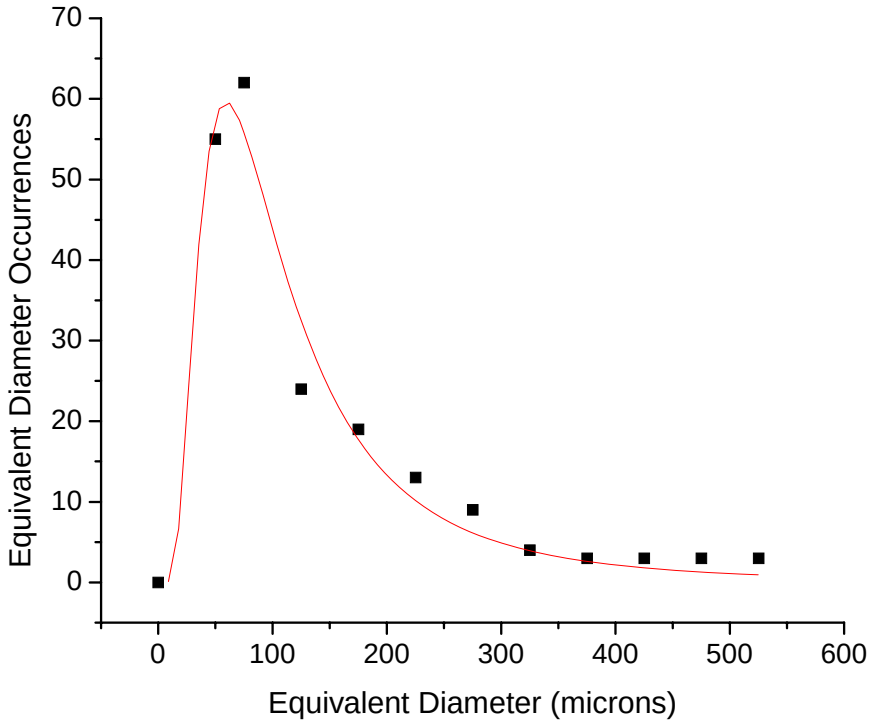

Figure 228. Individual feature size distribution curve and extended Freundlich curve fit for sample D.

For evaluation of sample ST1, one of the sintered SiC samples containing TiB_2 additives, the 125 MHz bottom surface reflection signal amplitude C-scan image was also used. Again, grayscale conversion and brightness and contrast adjustments were implemented as shown in Figure 229. In this case, however, the sintered SiC material containing inclusions of higher density than the bulk material did reveal some low amplitude regions that had to be sectioned and evaluated separately. The full range of grayscale values on the histogram curve went from approximately 50 to 250. When initial thresholding was attempted, the low reflected signal amplitude region in the top right corner and some other smaller regions of lower amplitude were saturated so that no individual features could be found. For this reason, the grayscale image was sectioned into three parts including the lower amplitude region from the top right corner (Section 1), the section of smaller regions with lower amplitude (Section 3), and the rest of the sample (Section 2), as shown in Figure 230. Thresholds for each of the sections were chosen in terms of both low and high reflected signal amplitude evaluation. For section 1, the low amplitude feature thresholds were chosen as 120, 130, and 140 while the high amplitude feature thresholds were chosen as 155, 150, and 145. For section 2, the low amplitude feature thresholds were chosen as 137, 147, and 157 while the high amplitude feature thresholds were chosen as 195, 185, and 170. For section 3, the low amplitude feature thresholds were chosen as 134, 137, and 140 while the high amplitude feature thresholds were chosen as 160, 158, and 156. The medium thresholds were selected for each section as shown in Figures 231 and 232 since they provided sufficient individual feature data without either drowning out too many features or resulting in an excess of features. After choosing the proper thresholds, the sections were merged to provide a

single low amplitude image and a single high amplitude image, and erosion and dilation were performed, as shown in Figure 233. Due to the high number of overall features in the sintered SiC sample as compared to the hot pressed sample, the feature size cutoff was changed to 99 μm as opposed to the previous minimum of 56 μm. The high amplitude feature map was inverted and the features colored red before being overlaid onto the low amplitude feature map. The combined feature map in Figure 234 was much different than for the hot pressed sample, with a greater number of overall features, many of which were large in size. While thresholding of Section 1 helped bring out more individual features, the corner still appeared to be somewhat saturated, but it was still a major improvement over thresholding the entire image without sectioning.

The features were numbered individually in Figure 235 and properties measured. The data sheet revealed that 769 low amplitude features and 66 of the more rare high amplitude features were distinguished for a total of 835 features in the combined feature map. The average individual feature properties for the combined feature image map included an average area of 1.96×10^5 μm^2, an average perimeter of 1615 μm, an average equivalent diameter of 332 μm, an average length of 472 μm, an average width of 316 μm, an average aspect ratio of 1.427, an average symmetry of 0.933, an average roundness of 0.566, an average nearest neighbor distance of 807 μm, and an average minimum separation distance of 411 μm. The full list of average values from low amplitude, high amplitude, and combined images is shown in Table LX. The smallest low amplitude feature size detected was 99 μm while the largest was 5.53 mm. The full list of minimum and maximum values from low amplitude, high amplitude, and combined images is shown in Table LXI. The smallest high amplitude feature size

detected was 99 μm while the largest was 1.56 mm. These millimeter-range features greatly increased the average area, perimeter, equivalent diameter, length, and width values as compared to the hot pressed SiC sample. The large number of high amplitude features was attributed to higher density TiB_2 additives that were dispersed throughout the sintered SiC test specimen. The "Select" function was used to create maps based on feature size ranges, and according to the breakdown, there were 276 features between 99-150 μm, 254 features between 151-250 μm, 79 features between 251-350 μm, 57 features between 351-500 μm, 134 features between 500-999 μm, and 34 features between 1-6 mm. The images representing each of these ranges are found in Figure 236. The 834 distinct individual features found in the sintered SiC sample was much higher than the 147 found in the hot pressed SiC sample despite the fact that the hot pressed SiC data included 50-99 μm features that the sintered SiC data did not. Also, the 34 millimeter-range features detected in the sintered ST1 sample were a major contrast to the hot pressed sample D which had no features larger than 538 μm.

The equivalent diameter values were once again used to plot a defect size distribution curve as shown in Figure 237. Using the nonlinear curve fit function from Origin version 7.0, the Extended Freundlich power law function was applied to the data set and showed an R^2 correlation of 96.3% for sample ST1. The AUTC for the size distribution curve of sample ST1 was calculated as 177,840 which was more than 20 times greater than for sample D. The power law function demonstrated high correlations for the size distribution data from both samples, which were also similar to the curves from the work of Bakas et al. The histograms from sample D and sample ST1 were both characterized by curves with the highest number of occurrences within the 150-350 μm

range and long tails that represented few occurrences of the largest defects. While the major difference was the range of values, since the tail for sample ST1 extended much longer into the millimeter-range, the shapes were still comparable. This technique proved to be valuable for describing large volumes of armor ceramic test specimens in terms of the sizes and properties of detectable features and should prove to be valuable for further correlation to destructive testing for determination of the relationship between defects and dynamic failure.

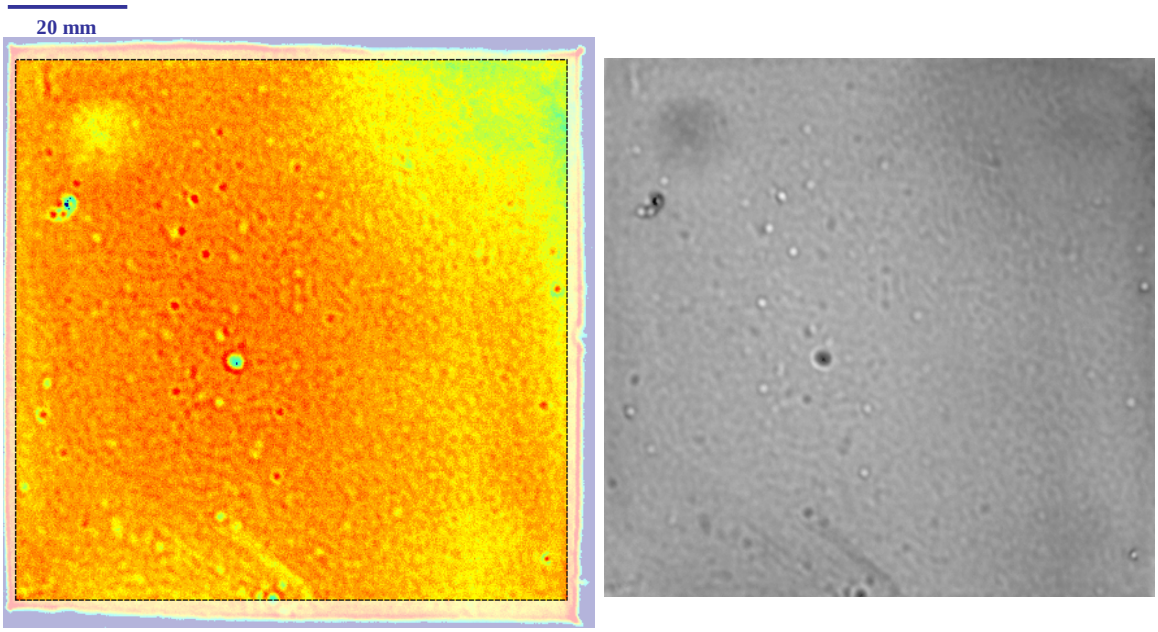

Figure 229. Reflected signal amplitude color and gray scale images from sample ST1.

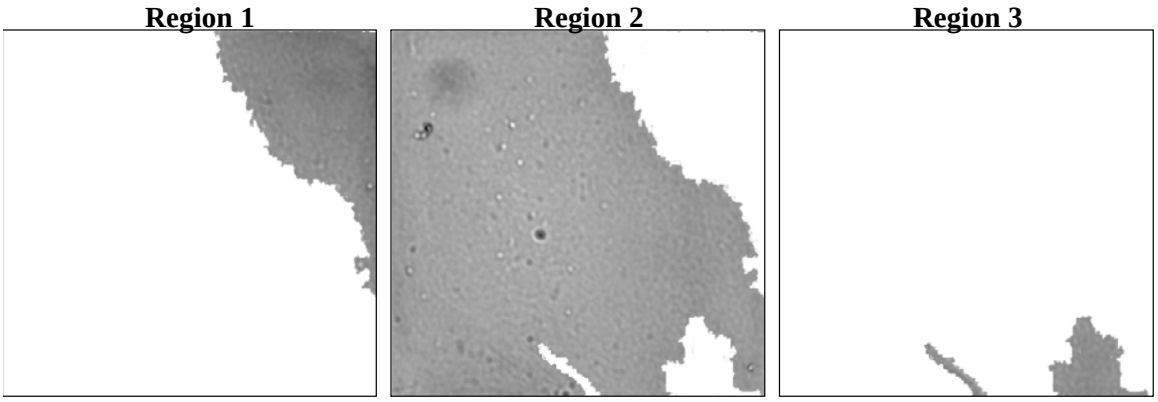

Figure 230. Three regions chosen for separate threshold evaluation of sample ST1 to avoid saturation of individual features.

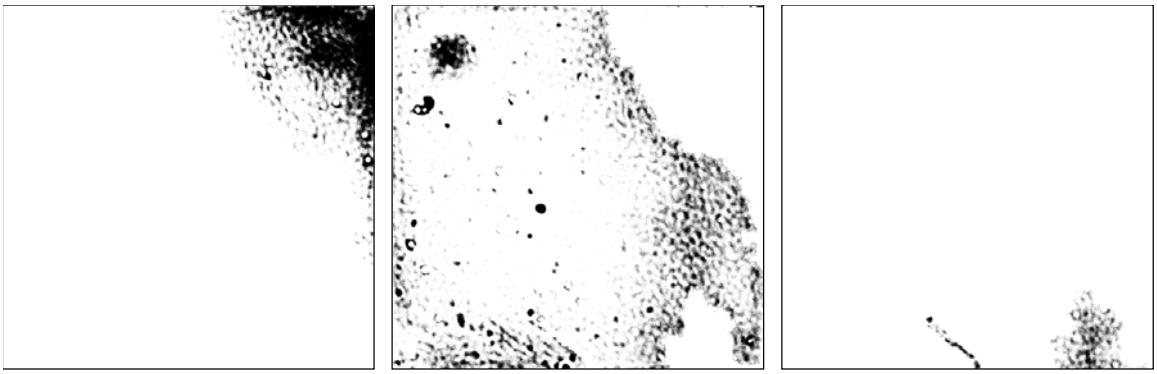

Figure 231. Selected low amplitude feature threshold images from separate regions of ST1.

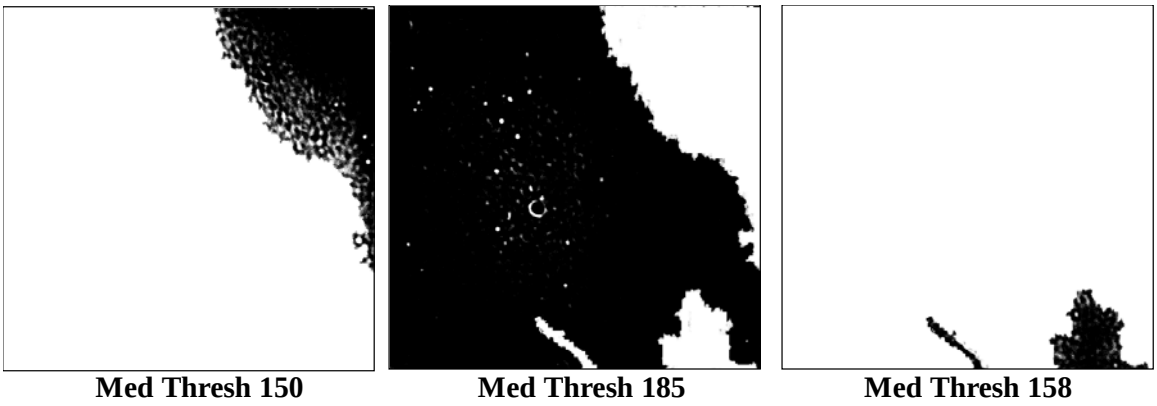

Figure 232. Selected high amplitude feature threshold images from separate regions of ST1.

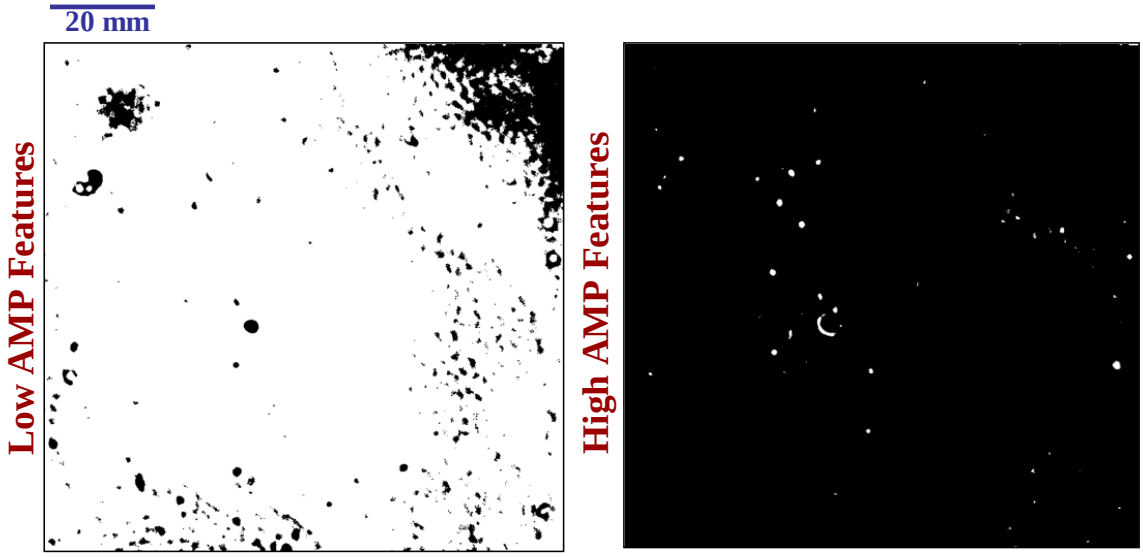

Figure 233. Threshold image selections of high and low amplitude features from sample ST1.

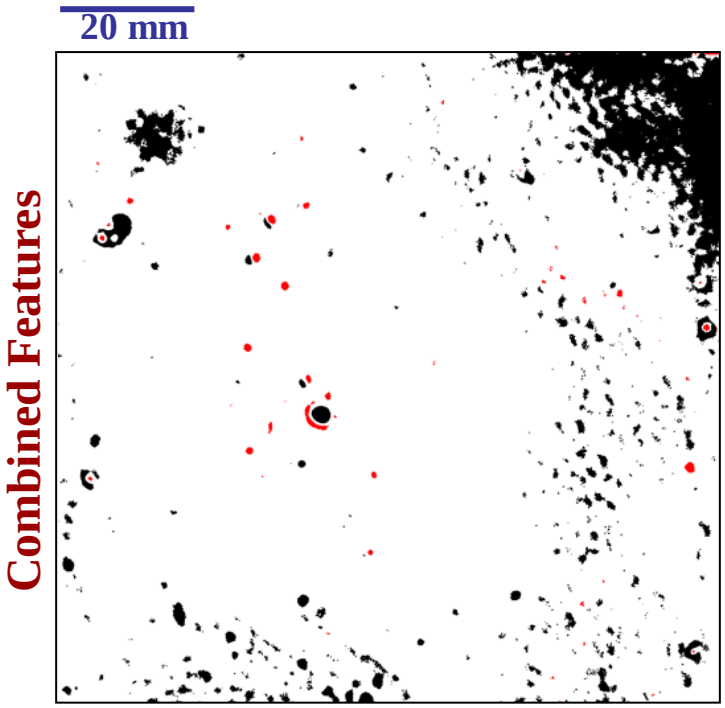

Figure 234. Threshold image of combined high and low amplitude features from sample ST1.

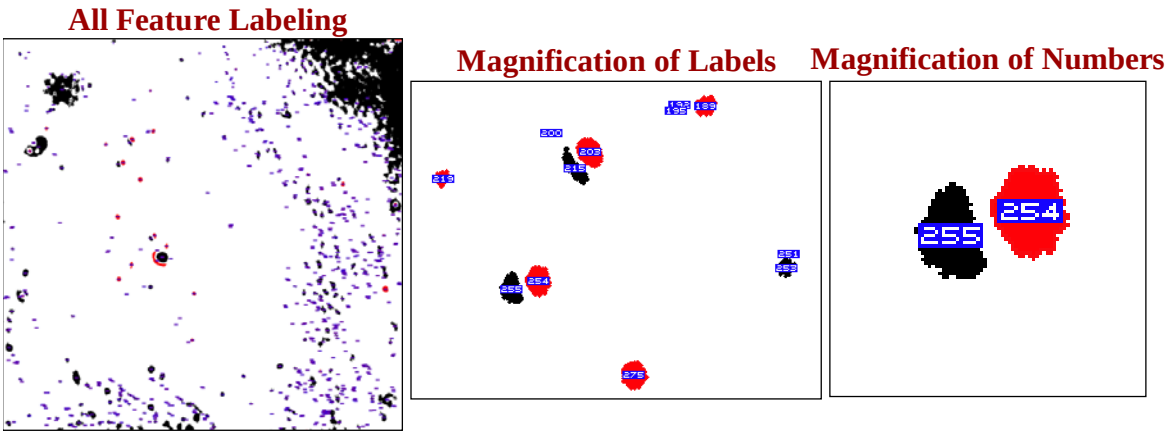

Figure 235. Individual feature labeling from combined map of sample ST1 including magnification of labels and numbers.

Average Feature Parameters

Image	Area [µm²]	Perimeter [µm]	Equivalent Diameter [µm]	Near. Neighb. Dist. [µm]	Min. Sep. Dist. [µm]
Low AMP	1.97E5	1620	327	826	427
High AMP	1.90E5	1560	388	3319	2872
Full	1.96E5	1615	332	807	411

Additional Average Feature Parameters

Image	Length [µm]	Width [µm]	Aspect Ratio	Symmetry	Roundness
Low AMP	467	311	1.430	0.933	0.567
High AMP	523	371	1.397	0.934	0.595
Full	472	316	1.427	0.933	0.566

Table LX. Average low, high, and combined threshold map values from sample ST1 individual features.

Minimum and Maximum Selected Parameters

Image	Min. Area [µm²]	Max.Area [µm²]	Equ. Diam. Min. [µm]	Equ. Diam. Max. [µm]
Low AMP	7801	2.40E7	100	5525
High AMP	7801	1.91E6	100	1557
Full	7801	2.40E7	100	5525

Table LXI. Minimum and maximum low, high, and combined threshold map values from individual features of sample ST1.

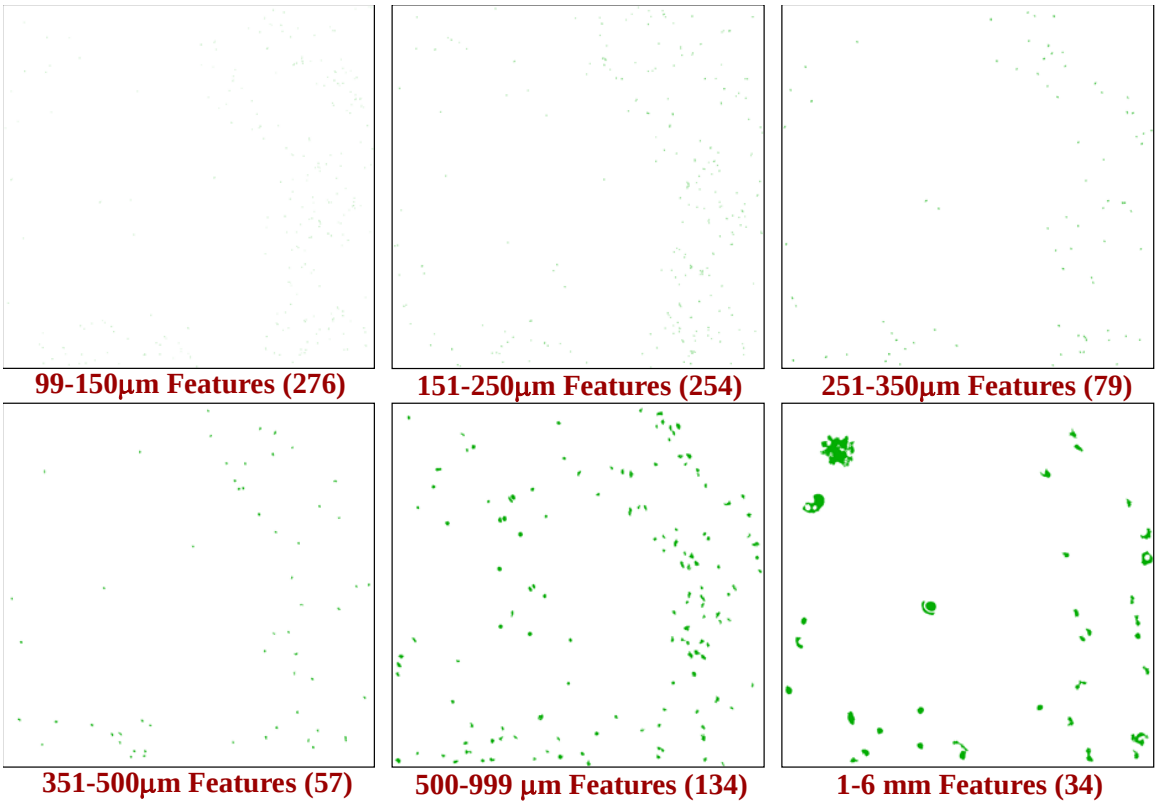

Figure 236. Individual feature size range maps of sample ST1 and number of features.

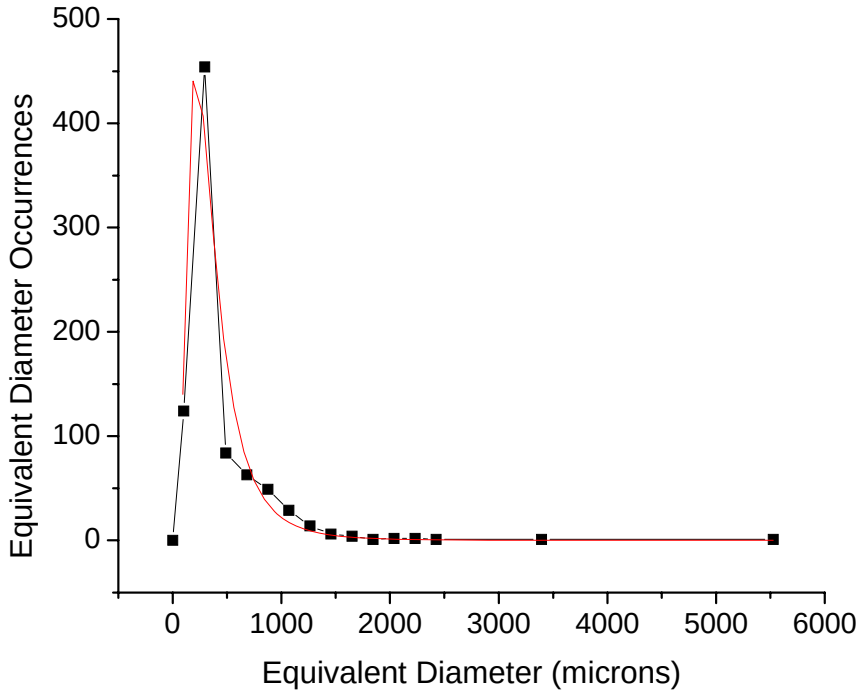

Figure 237. Individual feature size distribution curve and extended Freundlich curve fit for sample ST1.

5.16. One and Two-Phase Histogram Simulations

The quantitative analysis techniques used for evaluating ultrasound C-scan images have highlighted the importance of normalized histograms which provide valuable information about overall amplitude or TOF distributions that can be utilized to compare armor ceramic materials. Some of the key features described by these histograms have included the types of defects and their acoustic impedance mismatch to the bulk material, the defects sizes, and the number of defects. Another factor, the defect distribution, has also been described using thresholding techniques to characterize nearest neighbor distributions and minimum separation distances. While some of these factors such as defect size and type have been addressed by studying the fabricated samples, they have been limited in their ability to comprehensively describe these trends. For this reason, a method has been developed for simulating the effect of defects within a simulated armor ceramic matrix. This method has also been used to address the resulting histogram curve and tail shapes which have been categorized up to this point as either one-phase or two-phase histograms.

The first attempt at providing simulations was based on the influence of different numbers and sizes of simulated features in a simulated bulk material that could be described by Gaussian distribution estimates. The simulated bulk material was extracted from an actual bottom surface reflected signal amplitude C-scan image of a typical SiC material. This material was comparable to a high density region from one of the hot pressed SiC materials with a similar distribution of reflected signal amplitude values. The simulated defects were extracted from low amplitude regions of bottom surface reflected signal amplitude C-scan images of SiC materials. Adobe Photoshop version 7.0

was utilized to change the size of the defects and overlay them onto the simulated baseline SiC matrix. Two different defects sizes denoted as “small” or “large” were used to compare the size effect. The number of defects was altered by overlaying one, two, three, or four defects onto the simulated baseline matrix. The baseline, four small defect, and four large defect simulated images are shown in Figure 238. In this early attempt, the baseline histogram curve was plotted based on the actual range of C-scan image data. This curve was converted into a typical Gaussian distribution and the AUTC calculated as 617. The Gaussian distribution equation was changed based on the percent area of defects within each simulated sample. For the small defects, the percent areas were 0.9%, 1.9%, 2.8%, and 3.7% for one, two, three, and four defects, respectively. For the large defects, the percent areas were 3.5%, 6.9%, 10.4%, and 13.9% for one, two, three, and four defects, respectively. These percentages were used to estimate the Gaussian histogram curves in Figure 239, all of which were assumed to be one-phase curves. Since the major effect of dissimilar features in the bulk material caused histogram curve broadening in previous one-phase histogram results, the center position and amplitude of 100% were held as constants, and the curve width was changed based on the different percent areas. This led to histogram curve broadening and an increase in AUTC values with more defects and large size defects. For the smaller defects, the baseline AUTC of 617 was increased to 922, 1132, 1312, and 1467 for one, two, three, and four defect additions, respectively. For the larger defects, the baseline AUTC of 617 was increased to 1481, 1957, 2316, and 2596 for one, two, three, and four defect additions, respectively. These data were plotted for AUTC comparison among simulations as shown in Figure

240. However, this simulation made a lot of assumptions and characterized the differences in a simplified manor, so an improved technique was necessary.

When the epoxy/WC sphere samples were fabricated, the sample set consisted of four different types – a baseline sample of just epoxy (EPX), an epoxy sample containing small WC spheres with average diameters of ~0.84 mm (EPX-1), an epoxy sample containing medium WC spheres with average diameters of ~1.35 mm (EPX-2), and an epoxy sample containing large WC sphere with average diameters of ~2.08 mm (EPX-3). The resulting histogram curves from epoxy regions with equal areas each containing two defects started to show examples of two-phase histogram curves. These two-phase histogram curves were later found in some of the 75 MHz and 125 MHz sintered SiC samples as well. Based on these data, two-phase histogram curve simulations were put together in contrast to the one-phase simulations described in the first simulation method. In this case, the simulated baseline was once again extracted from the actual C-scan image of a SiC material and the simulated defects from actual defects in the epoxy/WC sphere samples, as shown in Figure 241. Four simulations including the baseline with no defects, a one-defect simulation, a two-defect simulation, and a three-defect simulation also shown in Figure 241 were analyzed. The baseline histogram curve in Figure 242 was again estimated as a Gaussian distribution from the actual SiC sample data which has an AUTC value of 1228. The defect areas were estimated as separate Gaussian curves that doubled and tripled as the number of defects was increased. These tail curves were placed at the left side of each baseline curve in the same locations where they were located in the actual epoxy/WC sphere histogram curves. The two-phase histogram simulations are shown in Figure 243. The AUTC values for the one-defect, two-defect,

and three-defect simulated tail histograms were calculated as 38, 78, and 116, respectively. While this two-phase histogram simulation method showed the expected trends, it was also simplified and based solely on Gaussian distributions. The assumptions and simplifications used to describe the one and two-phase simulations shown up to this point were addressed in the final simulation technique.

The most sophisticated simulation technique was developed to account for both one and two-phase simulations. The initial baseline simulation was extracted from the bottom surface reflected amplitude C-scan image of a typical SiC material, just as in the other techniques. In this method, the simulated baseline image was converted into grayscale and the range of values was determined to be 116-141 in terms of differential grayscale shades, with a center value of 129. Next, the simulated defects were created. Since the first goal was to establish that the simulation technique was able to differentiate one-phase from two-phase tail simulations, two basic defect simulations were created. The first was a circular defect with a series of concentric rings that had grayscale values ranging from 114-123, which was a large range in relation to the scale. The second was a circular defect with a series of concentric rings with grayscale values ranging from 114-118 which was a more narrow and concentrated range. The first type with the larger range was expected to result in a gradual difference characteristic of a one-phase histogram curve tail while the concentrated range at lower values was expected to result in a more drastic difference characteristic of a two-phase histogram curve tail.

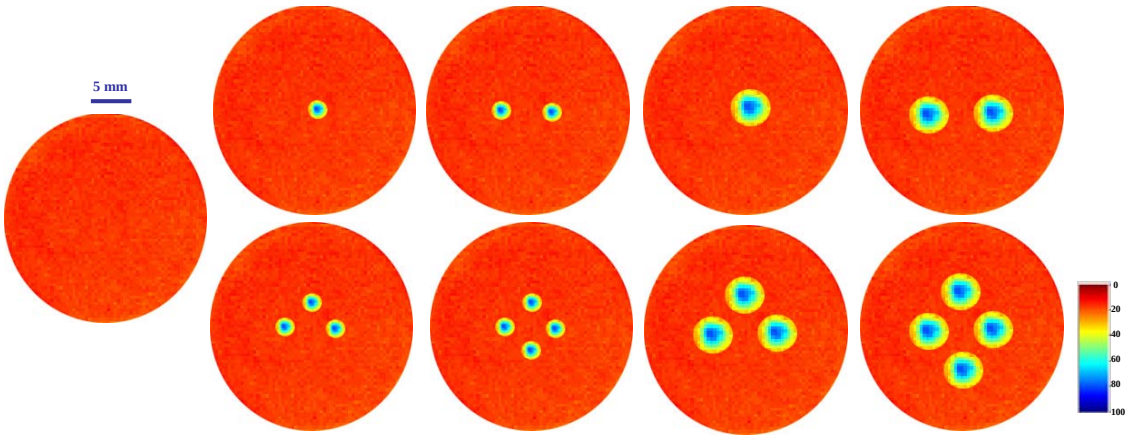

Figure 238. One-phase simulation images with (a) small and (b) large defects.

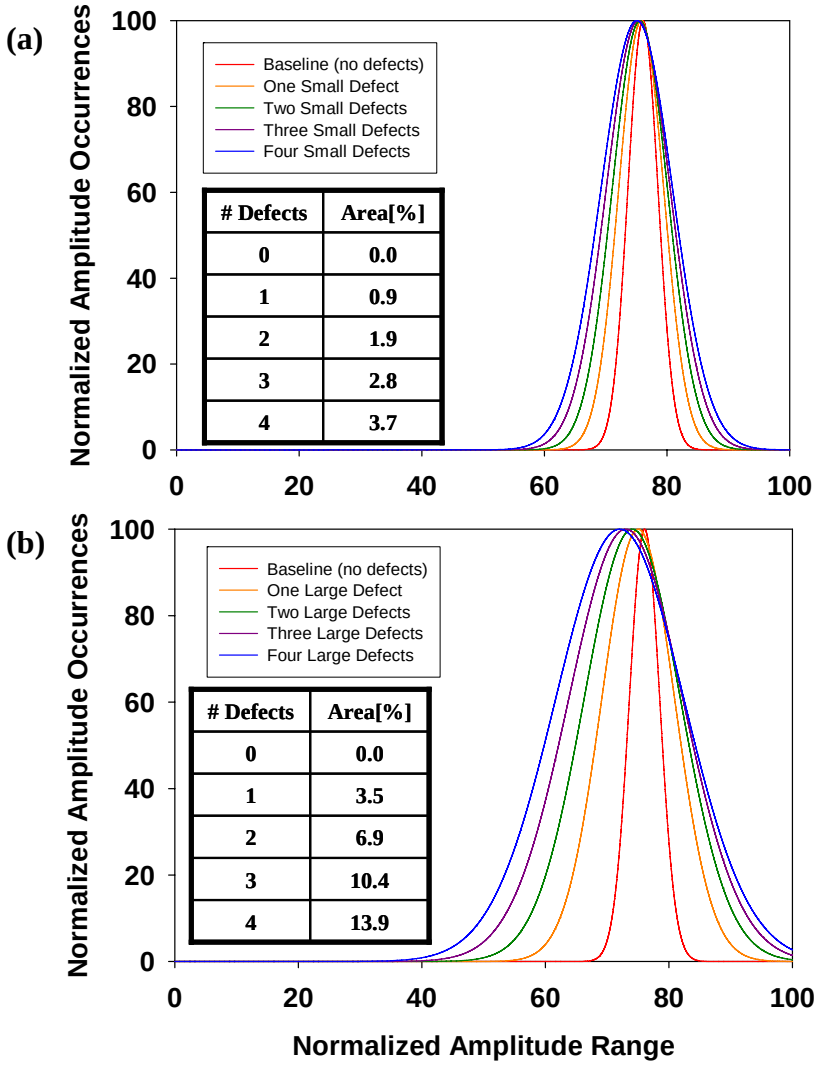

Figure 239. Simulated one-phase histogram curves for (a) smaller and (b) larger defects.

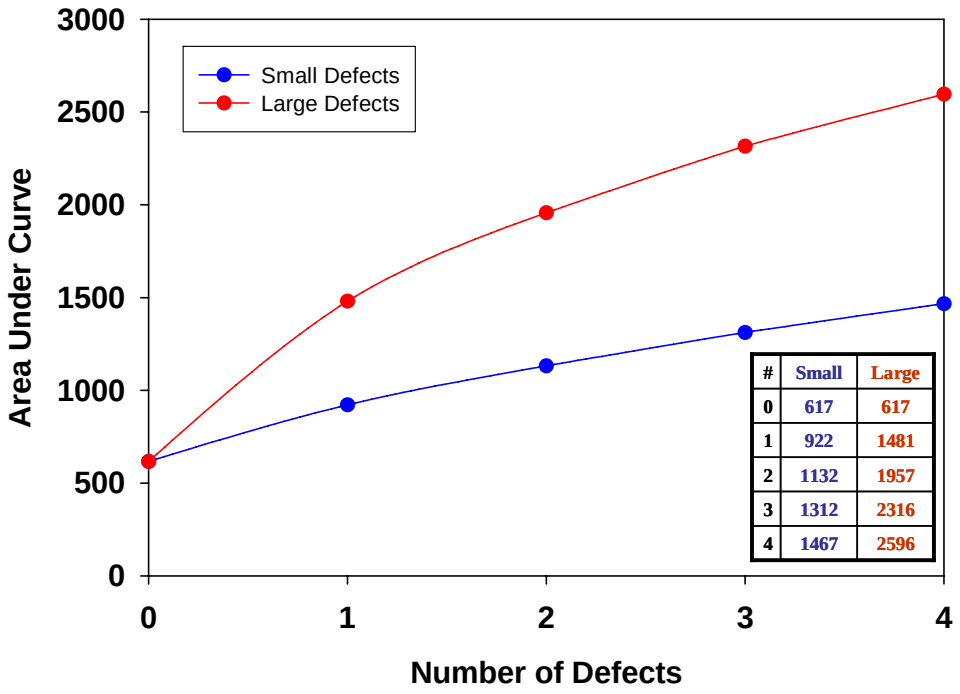

Figure 240. Simulated one-phase histogram curve AUTC values and comparisons of small and large defects.

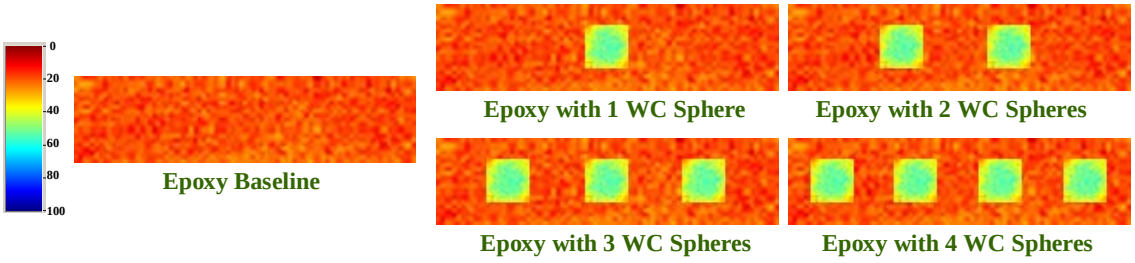

Figure 241. Two-phase simulation images based on defect engineered epoxy samples containing WC spheres.

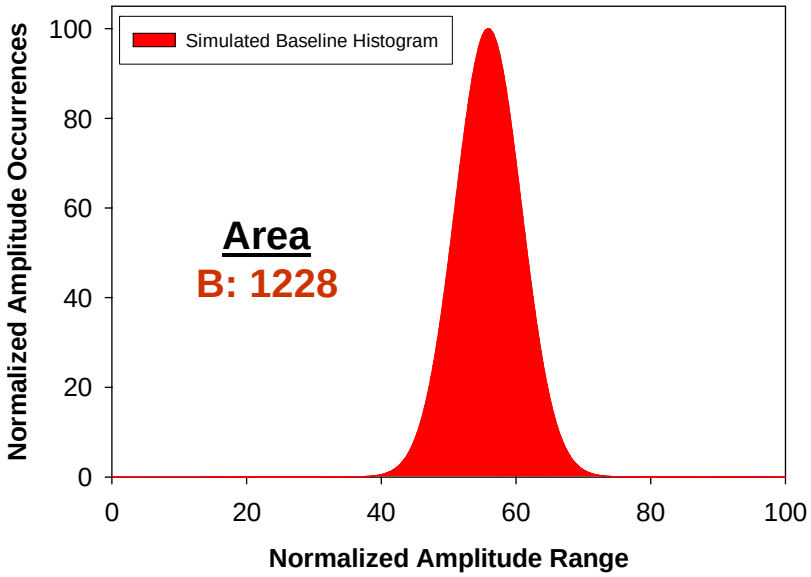

Figure 242. Two-phase histogram simulation curve and AUTC value for baseline epoxy sample.

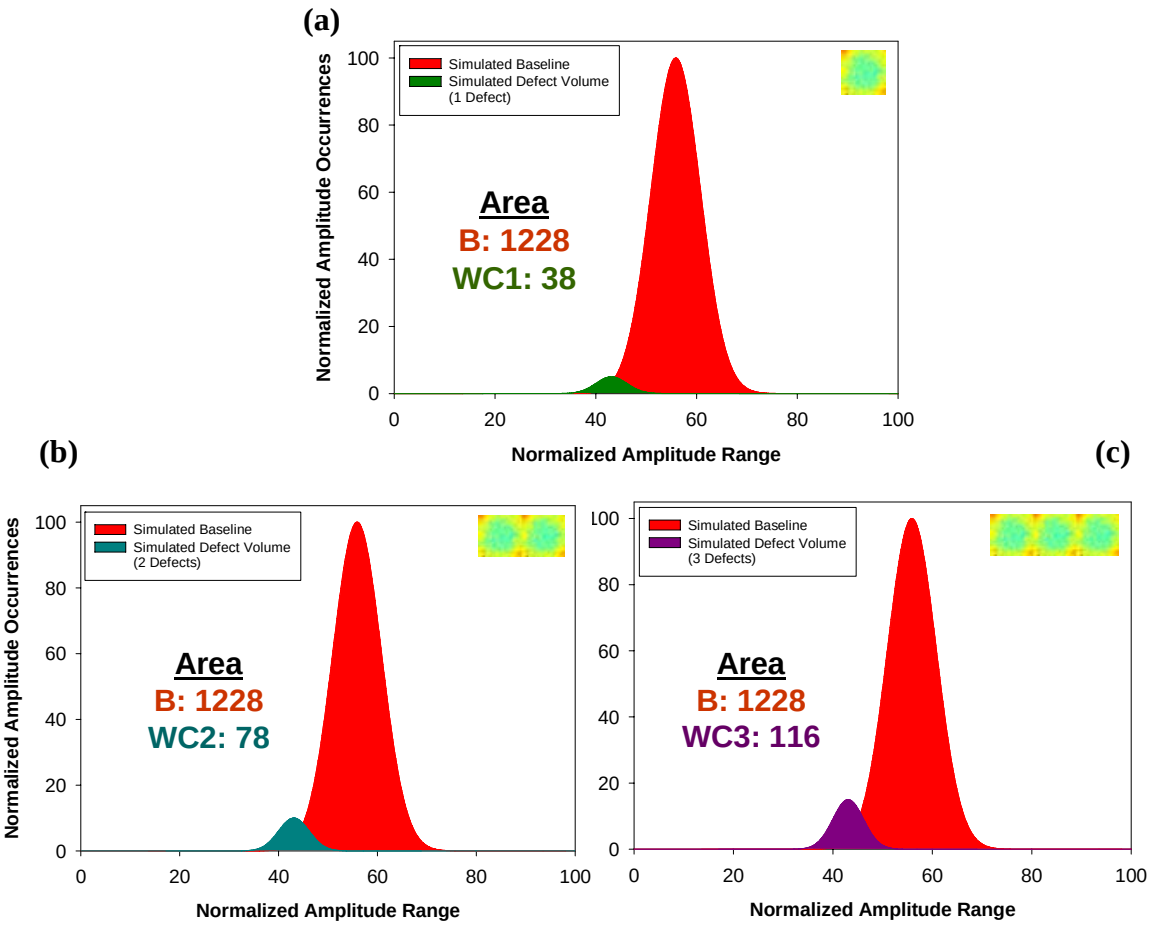

Figure 243. Two-phase histogram simulation curves and AUTC values for epoxy samples with (a) one (b) two (c) three WC spheres.

In a more advanced method, different defects were simulated based on acoustic impedance mismatch to the baseline matrix. In order to accomplish this, the baseline matrix acoustic impedance was attributed to a sintered SiC material with Z equal to 37.5 x 10^5 g/cm^{2}s. The mismatch between the sintered SiC matrix was then compared to common defects found in SiC. The materials that were chosen for simulated defects were carbon inclusions (Z = 6.3 x 10^5 g/cm^{2}s), Al_2O_3 inclusions (Z = 43.0 x 10^5 g/cm^{2}s), boron inclusions (Z = 22.7 x 10^5 g/cm^{2}s), B_4C inclusions (Z = 34.3 x 10^5 g/cm^{2}s), pores (Z = 0.0 x 10^5 g/cm^{2}s), SiO_2 inclusions (Z = 12.4 x 10^5 g/cm^{2}s), residual Si (Z = 8.3 x 10^5 g/cm^{2}s), AlN inclusions (Z = 41.6 x 10^5 g/cm^{2}s), cast iron inclusions (Z = 33.2 x 10^5 g/cm^{2}s), and TiB_2 inclusions (Z = 51.3 x 10^5 g/cm^{2}s). The acoustic impedance mismatch of each of these materials to the sintered SiC matrix was calculated while applying negative values for lower density defects and positive values for higher density defects, as described in the threshold and defect size distribution section. These Z differences were calculated as -83%, +15%, -39%, -9%, -100%, -78%, -67%, +11%, -11%, and +37% for C, Al_2O_3, B, B_4C, pores, SiO_2, residual Si, AlN, cast iron, and TiB_2, respectively. Based on the full grayscale range of 116-141, with sintered SiC associated with the center value of 129, all of the Z percent differences were estimated. The assigned grayscale values were 118, 130, 124, 127, 116, 119, 120, 130, 127, and 133 for C, Al_2O_3, B, B_4C, pores, SiO_2, residual Si, AlN, cast iron, and TiB_2, respectively. Circular defects were created based on these values, but rather than just using the assigned grayscale values, the edge effect currently found in actual defects detected from ultrasound C-scan imaging was accounted for. By creating narrow outer rings of grayscale values about and below the average values, the edge effect was simulated. For example, a simulated C defect with a

grayscale value of 118 would have narrow outer rings with grayscale values of 116 and 120.

In the first simulation study, the two basic defect types were used to differentiate one and two-phase histogram curve tails. The baseline image, which had a full grayscale range of 116-141, was a 300 by 300 pixel square image representing a high density region from a sintered SiC matrix as shown in Figure 244. The resulting histogram curve in Figure 245 was based on grayscale occurrences over the given range. This curve was normalized and plotted using the same method that was utilized for plotting normalized amplitude and TOF histograms from ultrasound C-scan images. The nonlinear curve fit in Origin was found to have the best R^2 correlation of 99.8% using the asymmetric double sigmoidal power law function which was first used in the peak deconvolution tail analysis section. The AUTC value for the baseline curve was found to be 317. The first defect simulation image in Figure 244 overlaid ten 20 by 20 pixel 114-123 grayscale range defects on the 300 by 300 pixel image. The resulting histogram curve in Figure 245 was similar to the baseline curve except for the presence of a long tail on the left side of the curve that represented the added defects. This was very similar in shape to the tail regions found in many of the one-phase histogram curves of actual sintered and hot pressed SiC samples. The asymmetric double sigmoidal power law function fit showed a correlation of 99.7%. However, the AUTC value of 317 was identical to the baseline curve, showing the relatively minor effect of these added defects. The second defect simulation image in Figure 244 overlaid ten 20 by 20 pixel 114-118 grayscale range defects on the 300 by 300 pixel image. The resulting histogram simulation in Figure 245 showed a curve similar to the baseline curve in addition to a separate distinct tail curve on

the left side of the baseline curve. This was also very similar in histogram shape to the two-phase histogram curves found in the epoxy/WC sphere samples and many of the sintered SiC samples. Origin was used to conduct a Gaussian multiple peak fit as used in the peak deconvolution tail analysis section. The R^2 correlation was found to be 98.9% and the AUTC value increased to 327 as compared to the baseline and one-phase histogram curves with values of 317. This simulation technique was successful in describing both the one-phase and two-phase histogram curves and tail shapes found in the actual armor ceramic ultrasound C-scan image data.

The next set of simulations utilized the simulated defects based on acoustic impedance mismatch from the sintered SiC baseline matrix. Eight simulated images were created by adding ten 20 by 20 pixel defects to the 300 by 300 pixel baseline image. The simulated defects had average grayscale values of 116 for the pores, 118 for carbon inclusions, 120 for SiO_2 inclusions and residual Si, 124 for boron inclusions, 127 for B_4C and cast iron inclusions, 130 for AlN and Al_2O_3 inclusions, and 133 for TiB_2 inclusions. A final simulation used two each of the pores, boron inclusions, and TiB_2 inclusions with one each of the rest of the simulated defects for a total of ten. The first set of four simulations covering pores, carbon inclusions, SiO_2 inclusions/residual Si, and boron inclusions is shown in Figure 246. The second set of four simulations covering B_4C/cast iron inclusions, AlN/Al_2O_3 inclusions, TiB_2 inclusions, and mixed defects is shown in Figure 247. Histogram scatter plots were established for each of the simulated images, the appropriate curves were fit to the plots based on whether they were one-phase or two-phase histograms, and the AUTC values were calculated. The histogram curves corresponding to each simulation are also found in Figures 246 and 247. Two-phase

histogram curves were found for the simulations with pores, carbon inclusions, SiO_2 inclusions, residual Si, and TiB_2. All of these curves were fit using multiple Gaussian distribution peak fits. The defects with the largest acoustic impedance mismatch from the bulk were furthest away from the baseline curves. The simulated pore second phase curves were furthest away from the baseline SiC curve while the SiO_2 inclusion and residual Si second phase curves very close to the left side of the baseline curves. Since the TiB_2 defects had a higher density than the baseline matrix, the second phase curve was on the right side of the baseline curve. The rest of the simulated histogram curves were one-phase, with the boron, B_4C, and cast iron inclusion simulation curves very similar to the baseline curve since the defects were encompassed within the main baseline peak. All of the one-phase curves were fit using asymmetric double sigmoidal power law functions. The one-phase histogram curve simulations for the AlN and Al_2O_3 defects were characterized by a slightly different shape, with a lip on the right side of the curve representing the higher density defects. The mixed histogram simulation containing at least one of each type of defect showed histogram curve shape features on both sides, with a long tail on the left side of the curve from the lower amplitude features and a lip on the right side of the baseline curve similar to the one found for the AlN and Al_2O_3 defect simulations. In terms of AUTC values, the difference between the values was not as large as expected. While the pore and carbon inclusion simulations had AUTC values of 305 each, the rest of the AUTC values ranged from 298-300. While the second phases increased the overall area compared to the rest of the simulations, the other defects had a minimal effect in comparison to the baseline simulation containing no defects. This detailed simulation study was effective for observing the effect of common defects found

in SiC. Two additional sample sets were also simulated to look at the effect of defect size and number of defects.

For looking at the effect of defect size, ten 10 by 10 pixel simulated defects were overlaid on the 300 by 300 pixel baseline image as opposed to the 20 by 20 pixel simulated defects used in the previous study. The simulations are shown in Figures 248 and 249. As expected with the reduction in size, similar trends were found, but the effect of the simulated defects was reduced. The corresponding histogram curves from the eight simulations are also shown in Figures 248 and 249. The pore, carbon inclusion, SiO_2 inclusion, residual Si, and TiB_2 simulated defect curves all showed a small second phase corresponding to the acoustic impedance differences from the sintered SiC matrix. Again, the low amplitude inclusion features were on the left side of the baseline curve while the high amplitude TiB_2 inclusion features were on the right side. All of the other simulated defect histogram curves could not be clearly distinguished from the baseline sintered SiC curve. The influence of these 10 by 10 pixel defects in the 300 by 300 pixel matrix, which accounted for 8.7% of the total area, had much less of an effect as compared to the 20 by 20 pixel defects which accounted for 34.9% of the total area. In this study, all of the AUTC values were the same at 317, reinforcing the fact that the effects on the histograms were minimal.

For looking at the effect of number of defects, a different number of 10 by 10 pixel simulated defects were overlaid on the 300 by 300 pixel baseline image. These simulations are shown in Figures 250 and 251. This was studied for both the carbon inclusions as well as the TiB_2 inclusions. Either one, five, ten, or twenty defects representing 0.9%, 4.4%, 8.7%, or 17.5% of the total area, respectively, were analyzed

for each material. The corresponding simulated histogram curves are also shown in Figures 250 and 251. For the simulated carbon inclusion histogram curves, the second phase tail peak increased in size as the number of defects is increased. Since these were 10 by 10 pixel defects which were shown to have a minimal effect on the overall AUTC value, the AUTC was the same for simulations with one, five, and ten defects at 317 and increased to 318 when twenty carbon inclusions were present. Similar results were found for the TiB_2 inclusions, as the second phase tail on the right side of the SiC baseline curve visibly increased in size for the ten and twenty simulated defect histogram curves. Again, the AUTC values were the same at 317 for one, five, and ten defects and increased to 318 when twenty TiB_2 inclusions were present.

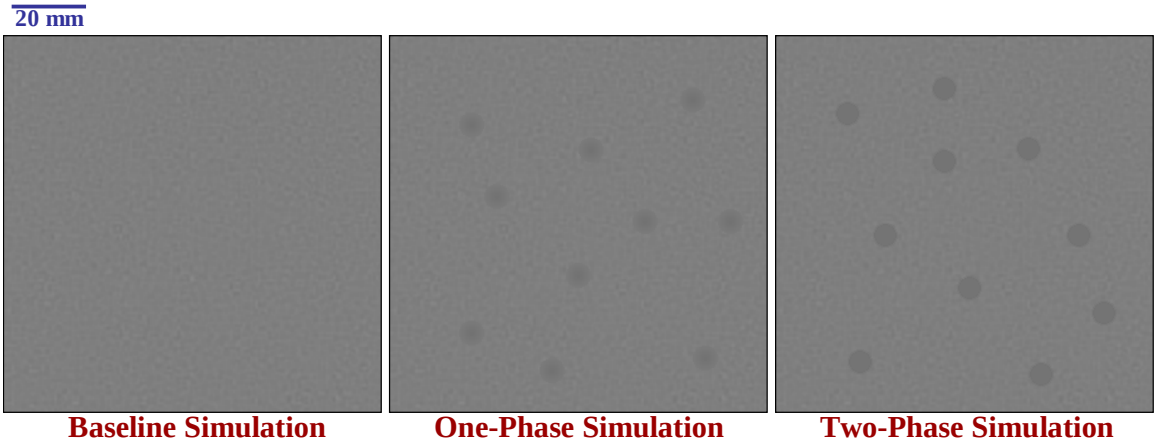

Figure 244. Advanced baseline, one-phase, and two-phase simulations based on sintered SiC material.

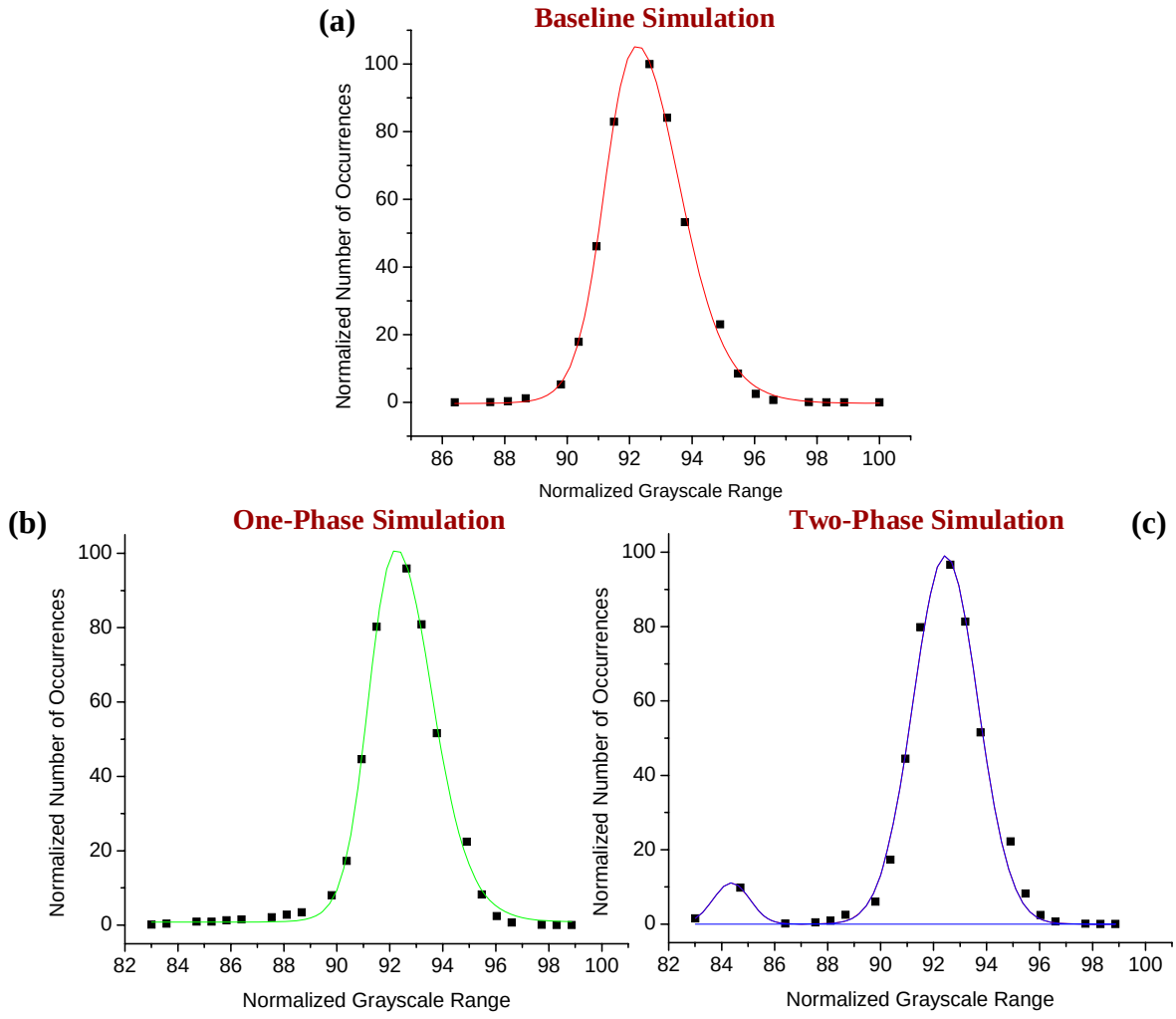

Figure 245. (a) Baseline (b) one-phase and (c) two-phase histograms from simulated images.

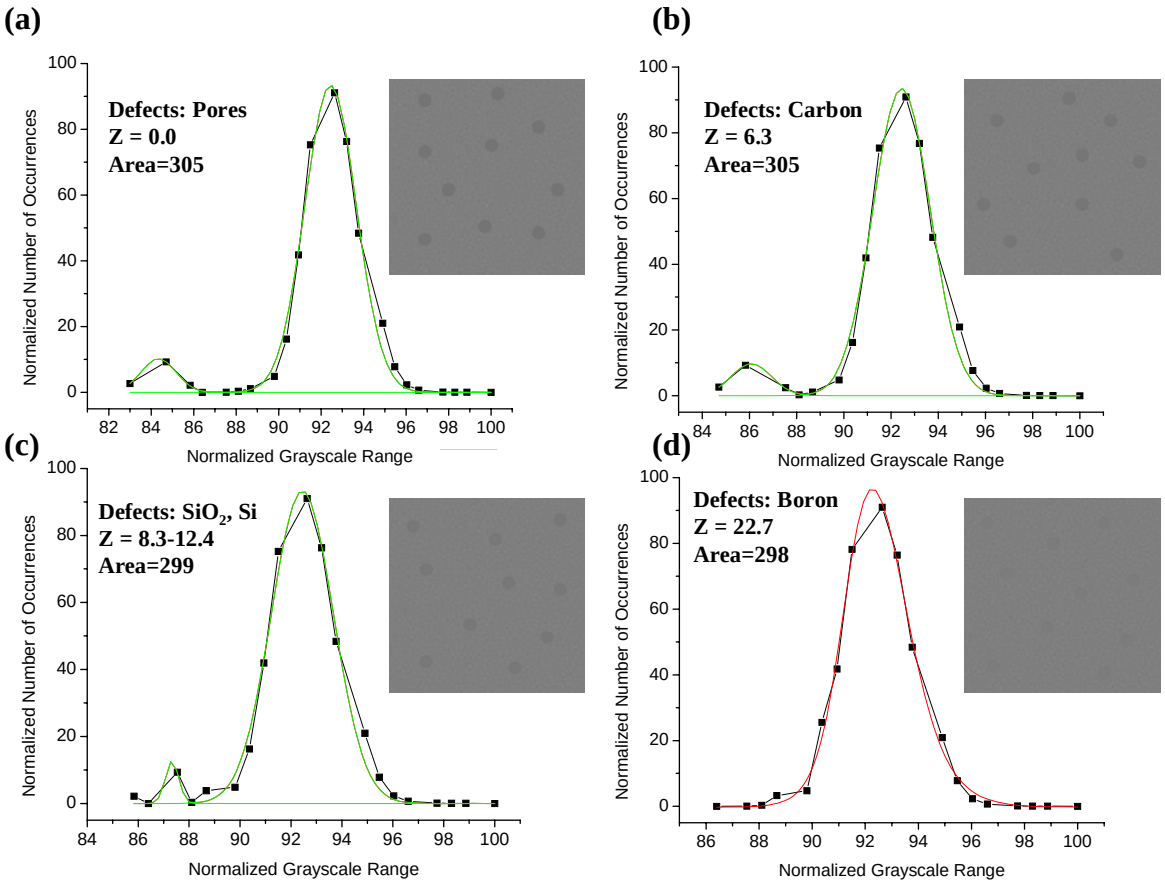

Figure 246. Simulated images and histograms based on acoustic impedance mismatch between sintered SiC and 20 by 20 pixel (a) pores (b) carbon (c) SiO_2 and Si and (d) boron.

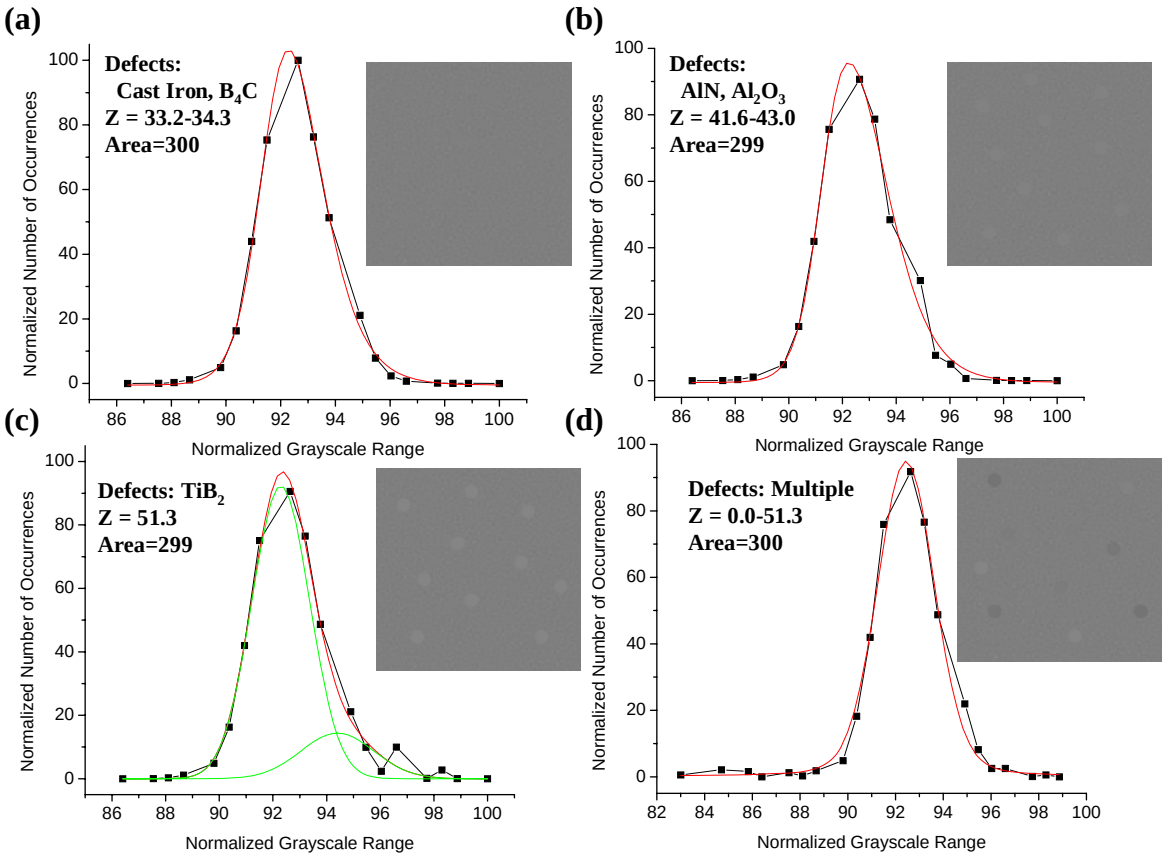

Figure 247. Simulated images and histograms based on Z mismatch between sintered SiC and 20 by 20 pixel (a) iron and B_4C (b) AlN and Al_2O_3 (c) TiB_2 and Si and (d) random defects.

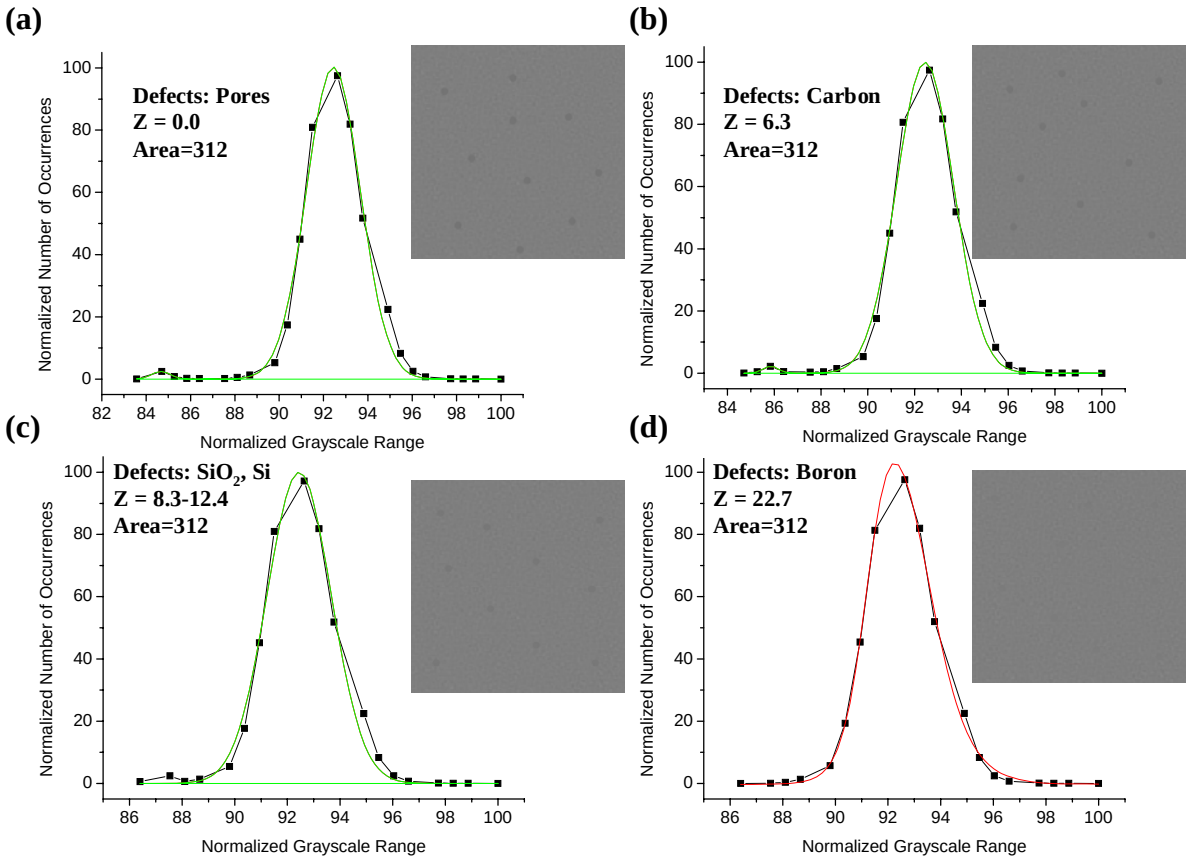

Figure 248. Simulated images and histograms based on acoustic impedance mismatch between sintered SiC and 10 by 10 pixel (a) pores (b) carbon (c) SiO_2 and Si and (d) boron.

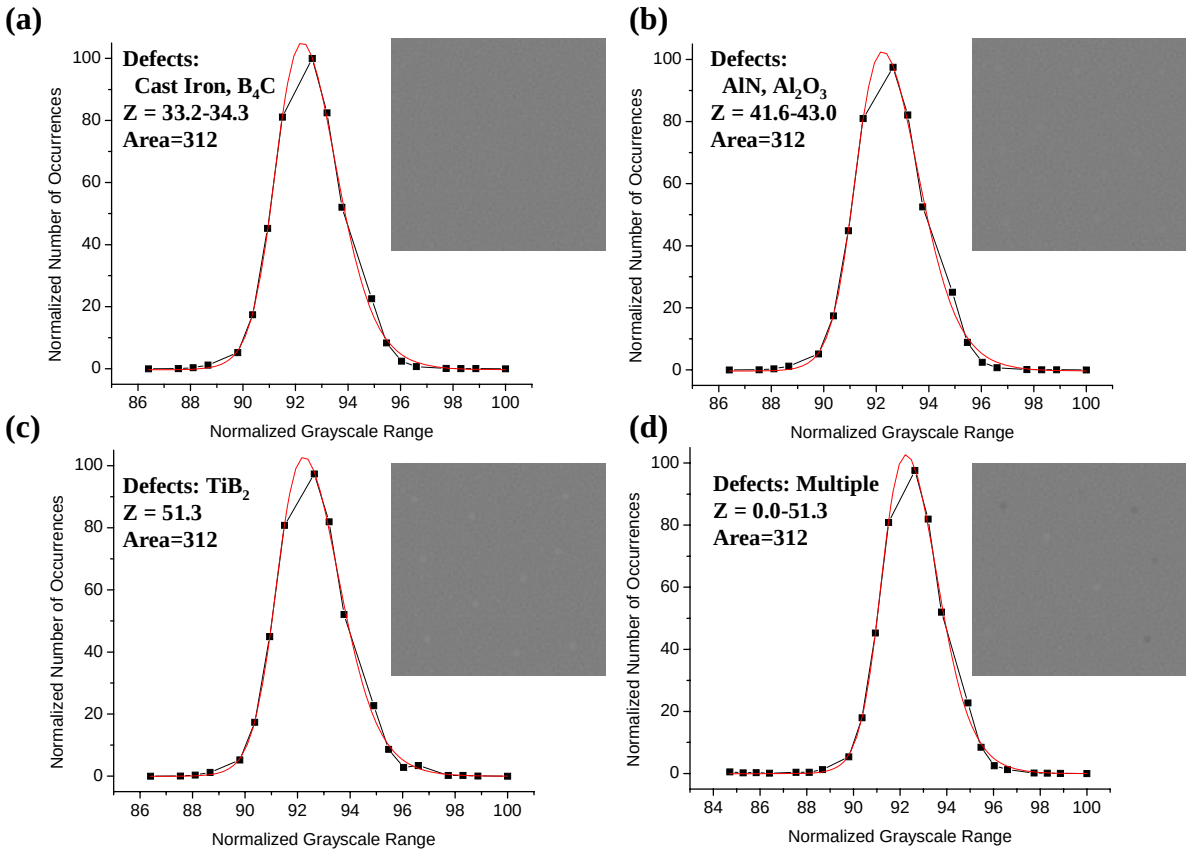

Figure 249. Simulated images and histograms based on Z mismatch between sintered SiC and 10 by 10 pixel (a) iron and B_4C (b) AlN and Al_2O_3 (c) TiB_2 and Si and (d) random defects.

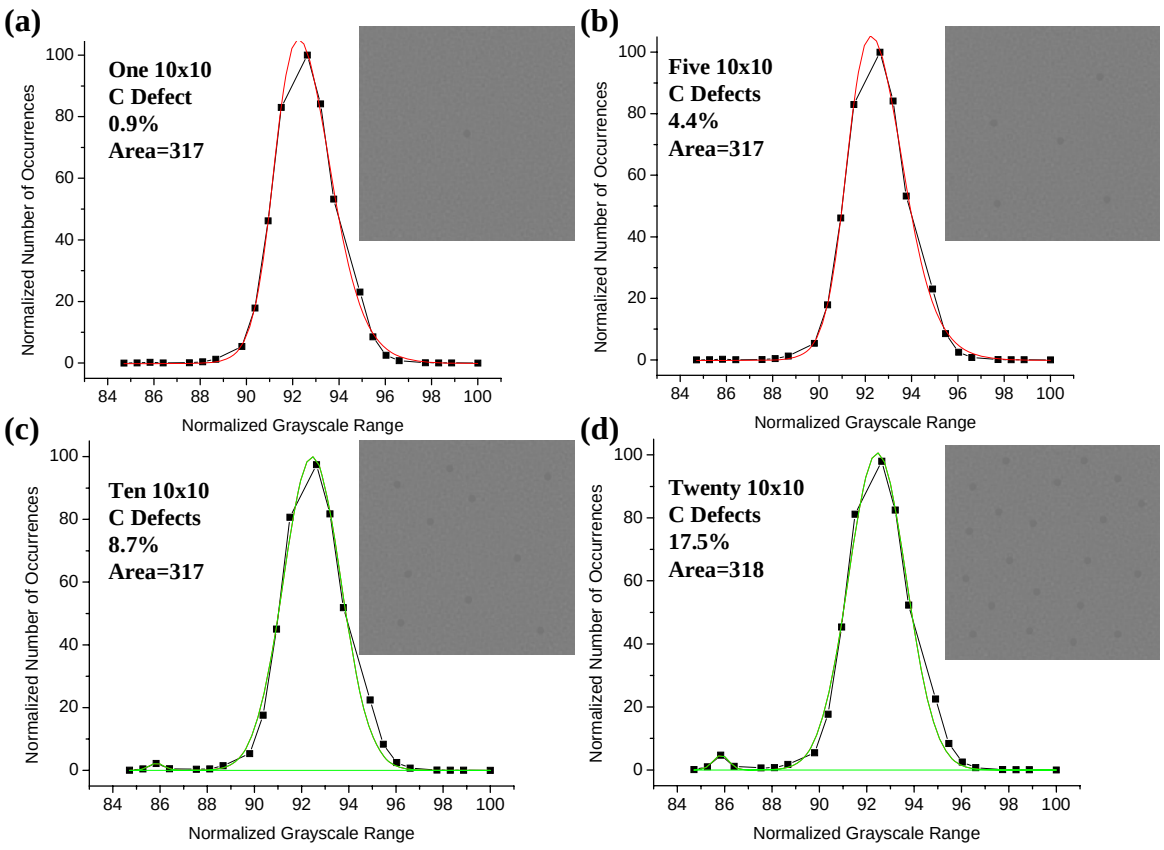

Figure 250. Simulated images and histograms based on Z mismatch between sintered SiC and (a) one (b) five (c) ten or (d) twenty 10 by 10 pixel carbon defects.

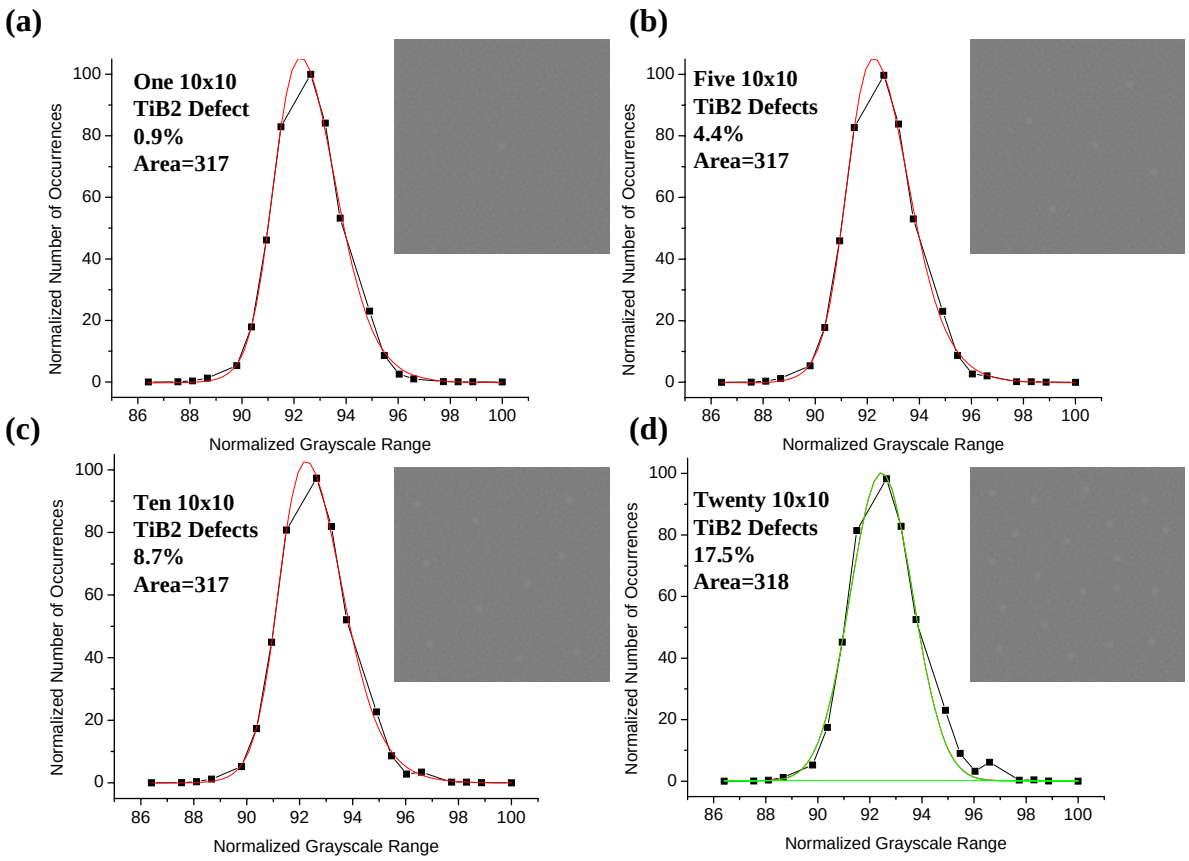

Figure 251. Simulated images and histograms based on Z mismatch between sintered SiC and (a) one (b) five (c) ten or (d) twenty 10 by 10 pixel TiB_2 defects.

While the first two histogram simulation techniques were based on many assumptions and simplifications, accounting separately for one-phase and two-phase simulations and applying only Gaussian curve fits, the new simulation technique proved to be much more effective. By applying more accurate curve fits with extremely high R^2 correlation values, both one-phase and two-phase histogram simulations were accounted for. Taking into account the effect of different defects based on acoustic impedance mismatch to the bulk matrix, the simulation of common defects in sintered SiC were accurately and reliably accomplished. Factors such as defect type, defect size, and number of defects were also simulated using this technique. While many examples are given, this simulation method can also be expanded to include additional defect types and sizes of different amounts as well as different types of bulk materials with varying properties.

5.17. B-Scan Imaging of Hot Pressed and Sintered SiC Armor Ceramics

As mentioned previously, B-scan imaging involved collecting a cross-section or slice of A-scan data over a selected plane and mapping it in terms of the horizontal intensity of the reflected amplitude signals. In order to visualize this in terms of a C-scan image, a horizontal or vertical line was first selected over the desired area of the C-scan. Since each point in the C-scan represented the gated reflected signal amplitude or TOF of an A-scan, this was insufficient, as the entire A-scan and not just the gated value was necessary to generate a B-scan image. For this reason, a specialized scan known as a full wave scan was collected. The full wave scans were set up in the same way as a C-scan, except instead of only collecting the gated values, the entire A-scan spectrum was collected over the range of time from the top to the bottom surface reflected signal for

each C-scan image point. In this way, when the horizontal or vertical line was selected for the B-scan, the full A-scan spectrum data were available for constructing the image. The advantage of the B-scan image was that the cross-sectional data gave depth and size information for any features within the selected plane. This type of imaging was performed using selected lines from reflected signal amplitude full wave scans of both sintered and hot pressed SiC samples. Quantitative histogram analysis and AUTC and FWHM data were also collected to compare the selected slices for each sample.

First, three categories of hot pressed samples including samples A, B, C, D, SD-1, SD-2, and SD-3 were evaluated. Each of the samples was first re-scanned as a reflected signal amplitude full wave scan by choosing the time range from the top surface reflected signal to the bottom surface reflected signal and performing the C-scan with the broadband LS18-15 transducer. The reason why this transducer was chosen was that unlike with the higher frequency transducers, there were fewer interfering peaks in the A-scans, even at relatively lower receiver attenuation, or high gain, values. This was crucial since the A-scan spectra were used for the B-scan imaging and any additional peaks resulted in collection of data that were not representative of the sample. After collecting the full wave scans, representative horizontal lines were selected for B-scan imaging. These lines were chosen through regions that were characteristic of the features of the samples. For samples A, D, SD-2, and SD-3, lines were selected through the center of each sample since there were no specific distinguishing features. For sample B, the lines were chosen through the low density region while for samples C and SD-1, the lines were chosen through detected inhomogeneities.

The B-scan image maps were first evaluated through the selected cross-sections of samples A, B, and C, as shown in Figure 252. Since no significant variations were visually evident over the full range of amplitudes including the highest values from the top surface reflected signal, the amplitude range was reduced to look for slight variations. Since the B-scan images were cross-sections, the thickness differences among the samples were apparent, as the thickness for sample A was 19.09 mm compared to samples B and C at 12.78 mm. There were also some different patterns of horizontal amplitudes among the samples, but nothing that specifically stood out as an individual feature. Upon reducing the amplitude range, one thing that was evident was the line patterns across the sample from the reflected signals. There were higher amplitude signals closer to the top surface signal reflection for all of the samples and these were reduced as the bottom surface reflected signal was approached. This was consistent with the higher degree of attenuation and reduction in the signal amplitude as the ultrasound beam penetrated further into each sample. Since there were no major distinguishable differences that could be found during visual comparison of the B-scan images, the data were quantified to see if the B-scan was an effective method for comparison of hot pressed SiC samples of varying integrity.

Normalized amplitude histogram data were collected for samples A, B, and C as shown in Figure 253, and a large difference was found. While the main peaks of amplitude occurrences appeared to be quite similar, the number of higher amplitude occurrences was much greater for samples B and C as compared to sample A. The resulting AUTC values were 2405 for sample A compared to much higher values of 4848 for sample B and 4119 for sample C. The FWHM values also followed the same trend as

sample A had a value of 18 as compared to 37 for sample B and 30 for sample C. Just as in the other normalized histogram comparisons for samples A, B, and C, the higher AUTC values represented a higher degree of variability for samples B and C, which did not meet manufactured specifications, as compared to sample A which was a commercial armor grade hot pressed SiC sample. However, despite the thicker dimension of sample A, the overall areas of samples B and C were larger, so more samples had to be evaluated to ensure that these results were not solely due to the greater number of values. In order to explore this further, sample D was used as a better comparison to B and C since it was a hot pressed armor grade sample with an even larger area. If the AUTC and FWHM values were influenced only by the area of the B-scan image, sample D would have larger values. Again, the B-scan image for sample D in Figure 254 did not show any individual features that could be distinguished, but it did show the same type of reflected signal amplitude trends found in the B-scans of A, B, and C. When the normalized amplitude histogram was collected in Figure 255, the pattern had a close resemblance to that of sample A. The AUTC value was calculated as 2946 with an FWHM value of 20. Not only were the normalized histogram curves similar between the two commercial hot pressed SiC samples A and D, but despite the vast differences in the B-scan areas, the AUTC and FWHM values were also consistent as they were both much lower than the values for samples B and C. While the visual evidence was not overwhelming for distinguishing the representative B-scan images, the quantitative data demonstrated the expected cumulative trends.

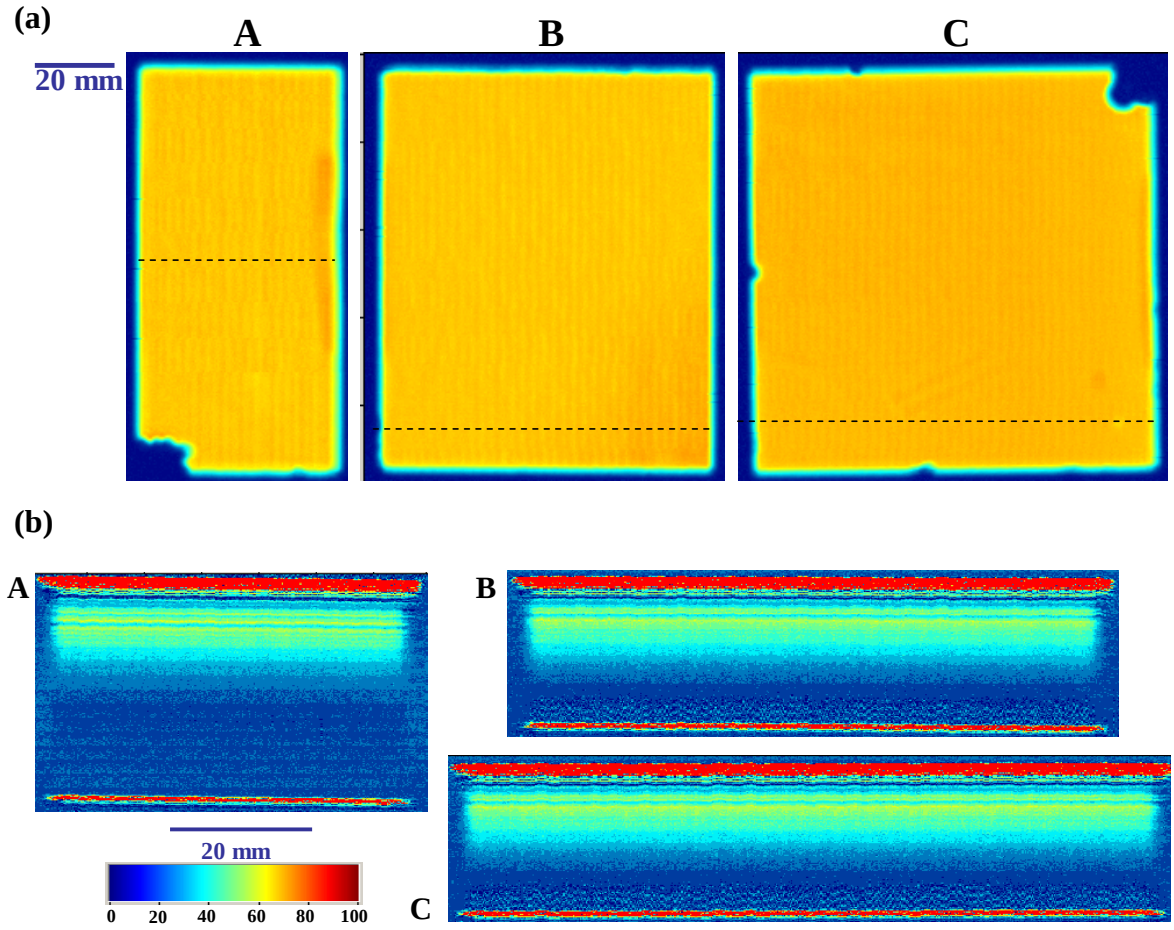

Figure 252. (a) C-scan images with representative lines and (b) corresponding B-scan cross-sectional images of samples A, B, and C.

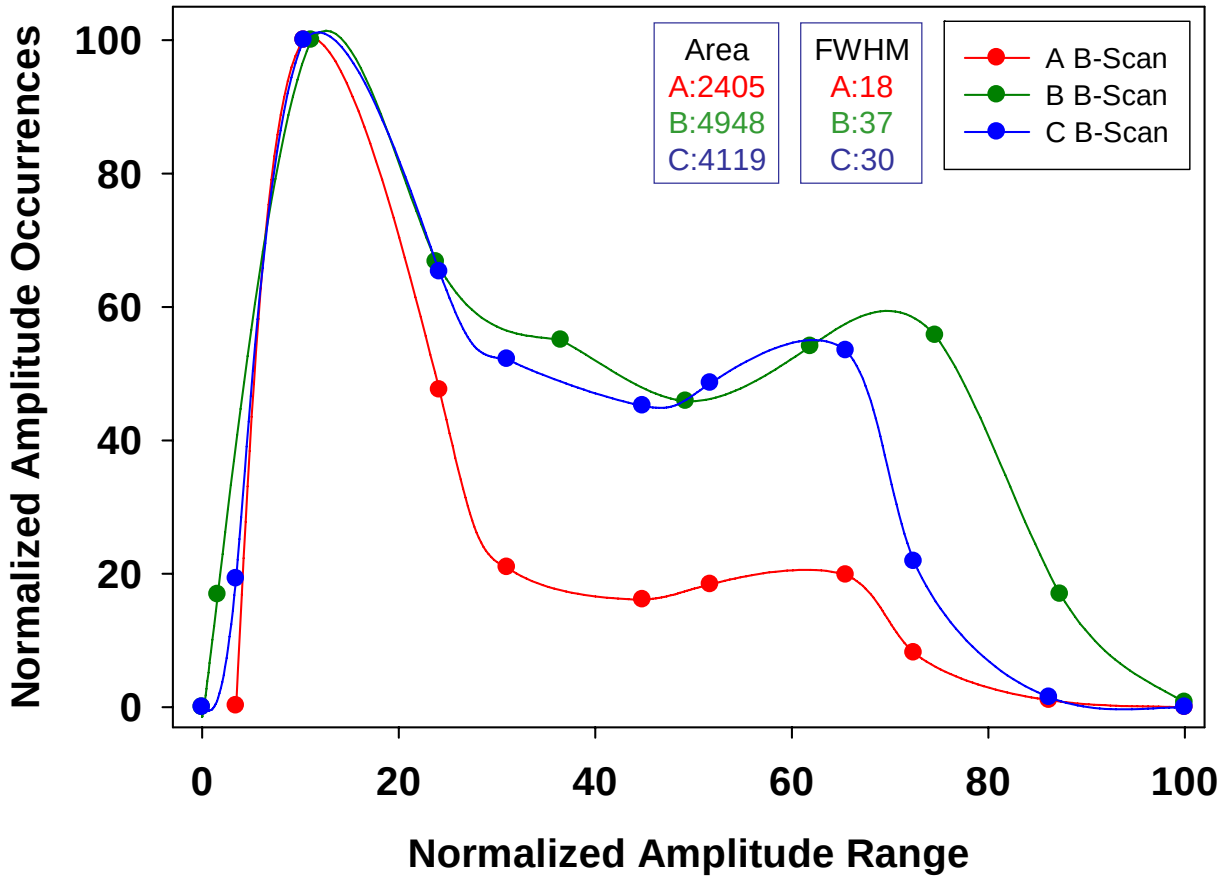

Figure 253. B-scan image histogram curves, AUTC values, and FWHM values for samples A, B, and C.

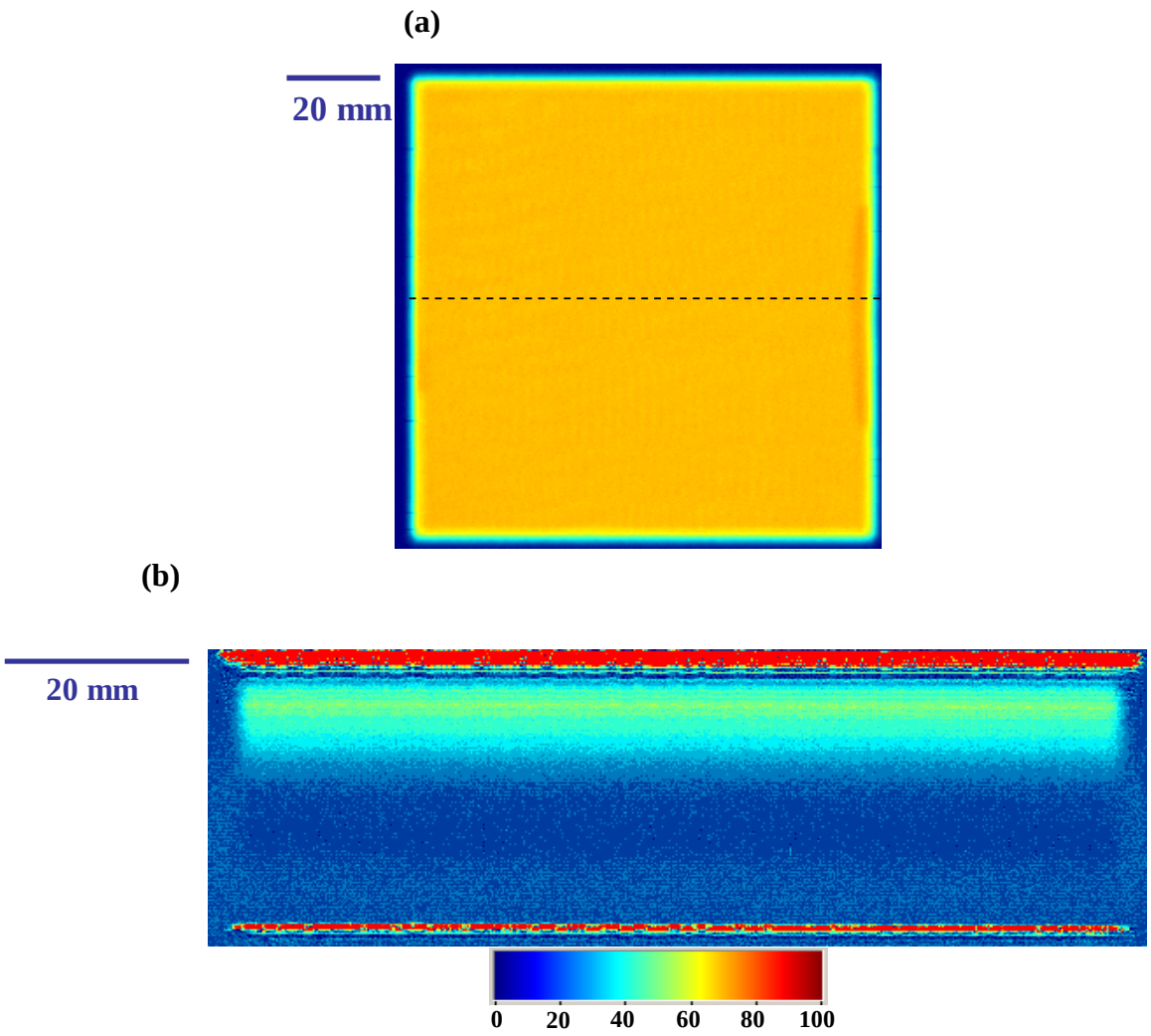

Figure 254. (a) C-scan image with representative line and (b) corresponding B-scan cross-sectional image of sample E.

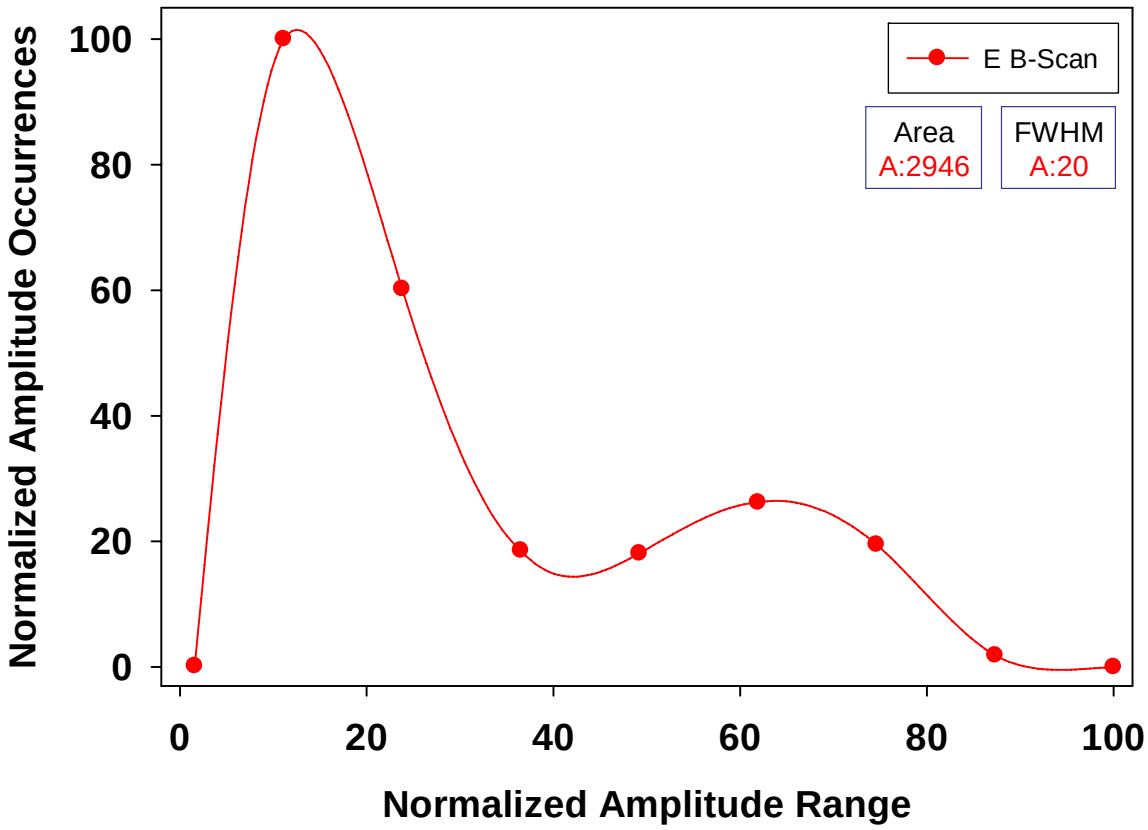

Figure 255. B-scan image histogram curves, AUTC values, and FWHM values for sample E.

Next, samples SD-1, SD-2, and SD-3 underwent the same type of evaluation. Since these three hot pressed SiC samples had the same dimensions and the only differences were the types of embedded defects, they were valuable for B-scan image comparison. Upon evaluation of the three B-scan images in Figure 256, there were some interesting differences. For sample SD-3, the C-scan image had shown a region on the left side of the sample with varying reflected signal amplitude, making the overall amplitude in that region lower than the rest of the sample, which was very homogeneous with no detectable defects or features. The B-scan image showed this variable amplitude region as a raised line representing the bottom surface signal amplitude. It appeared as though this signified a physical cut through the side of the sample at the depth indicated in the B-scan, and upon further inspection of the sample, this was the case. While it was not noticed previously, there was a thin cut into the sample along its left side. This was the reason why the amplitude varied in the C-scan and why the B-scan image seemed to end abruptly at that point. In this case, the depth analysis function of the B-scan image proved to be an advantage. Another interesting difference came in the SD-1 and SD-2 B-scan images, which were the two samples that had embedded inclusions of 50 μm or greater. Unlike the B-scans from any of the other samples that were analyzed, these samples had distinct features along the right side of each B-scan that appeared to represent features within the bulk of each sample. However, it was unexplainable why these features were along the right side of each scan rather than in the bulk regions of the scan where they were expected to be found. It was either just a coincidence that these features appeared only for samples SD-1 and SD-2, or there was some significance with

regard to the way the B-scan data were collected that made these features appear on the right side of the scans.

Just as for the other hot pressed samples, quantitative histogram analysis was used to look for differences among the samples since they were difficult to find through visual inspection of the B-scan images. The SD histogram curves are shown in Figure 257. While the normalized amplitude histograms appeared to be similar for the SD samples, the AUTC values were 2857, 2335, and 2637 while the FWHM values were 20, 19, and 19 for samples SD-1, SD-2, and SD-3, respectively. Just as in the armor grade hot pressed SiC samples A and D, the SD samples all had AUTC values lower than 3000 and FWHM values of 20 or less in contrast to the B and C hot pressed samples which did not meet manufactured specifications and had AUTC values greater than 4000 and FWHM values of 30 or higher. The SD samples, which had very small effective volumes of inclusions added, had quantitative values much closer to the armor grade hot pressed samples than samples B and C which had much larger regions of varying amplitude. Despite the ambiguity of visual evidence in the B-scan images, the quantitative data showed strong AUTC and FWHM trends.

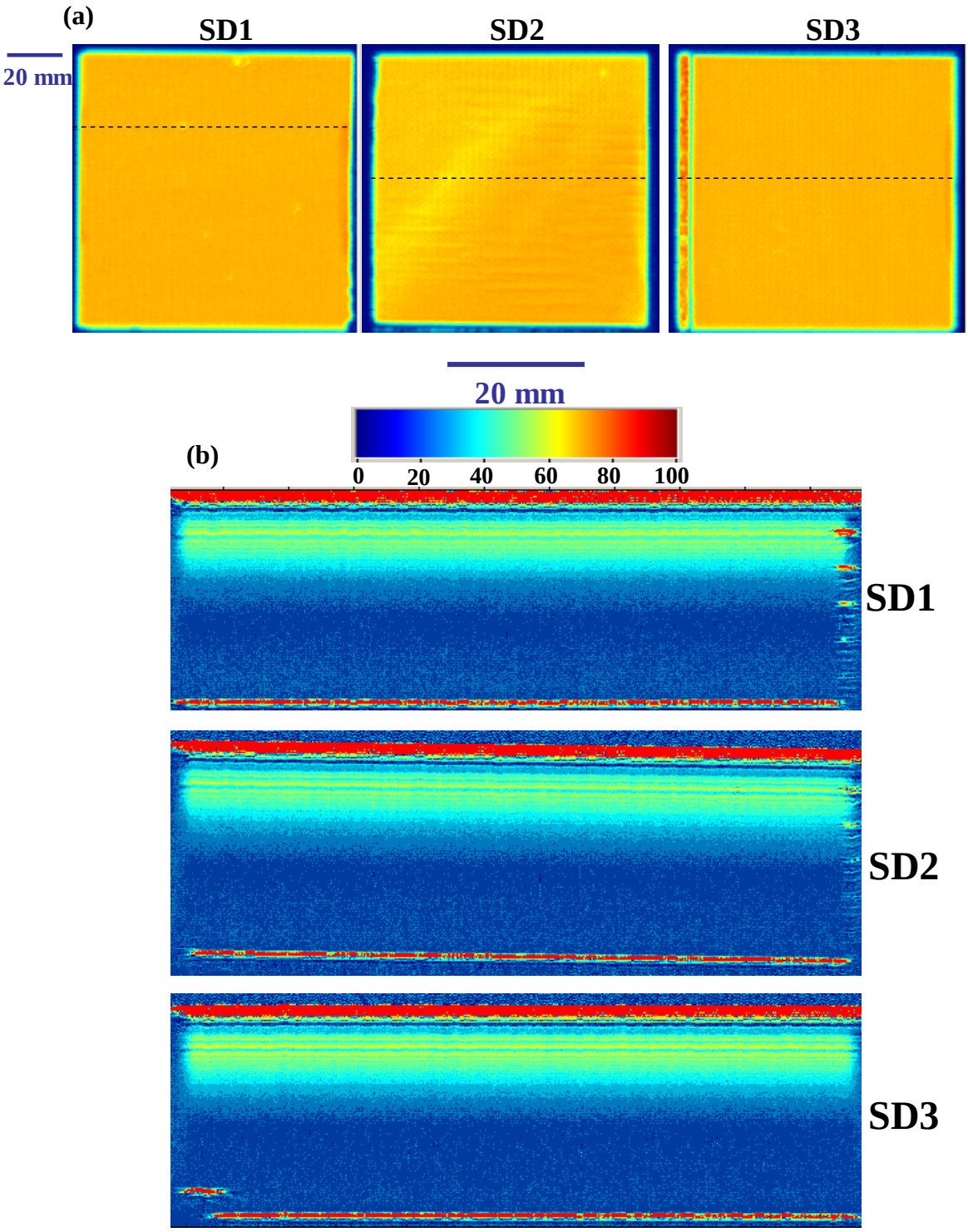

Figure 256. (a) C-scan images with representative lines and (b) corresponding B-scan cross-sectional images of samples SD1, SD2, and SD3.

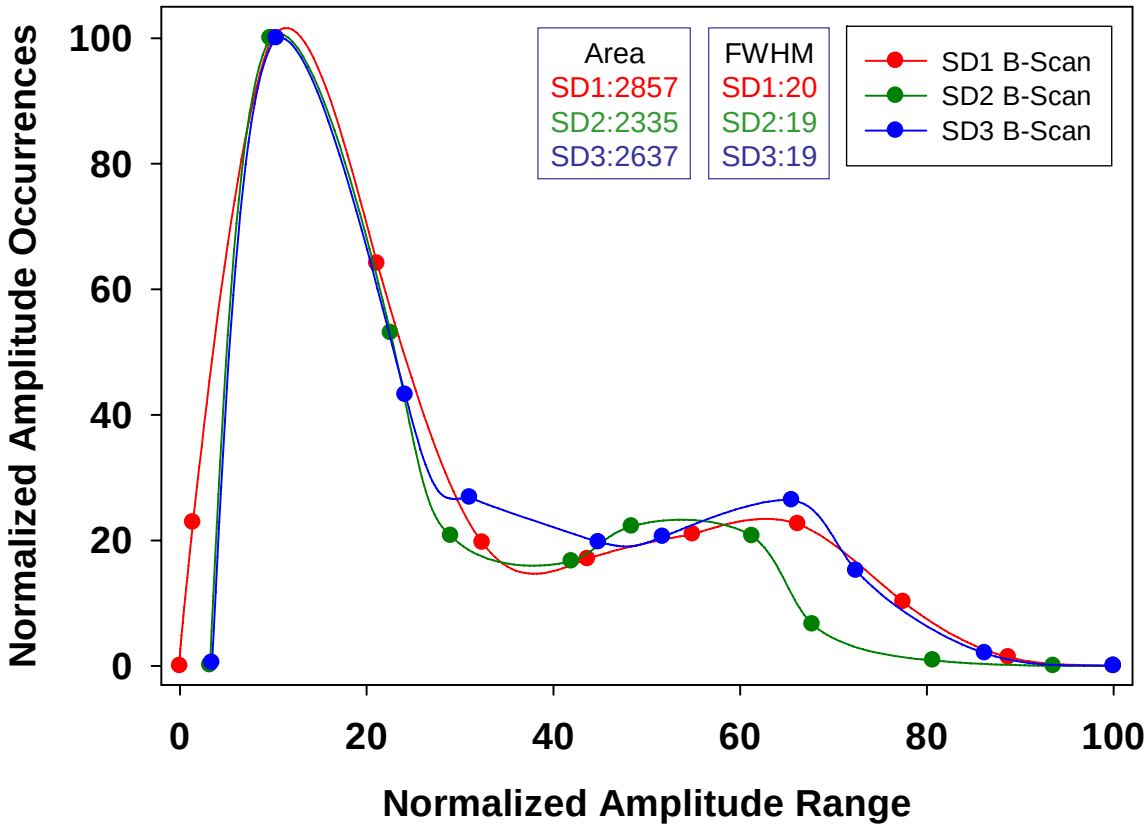

Figure 257. B-scan image histogram curves, AUTC values, and FWHM values for samples SD1, SD2, and SD3.

The next sets of samples that were evaluated using B-scan imaging were sintered SiC samples including three of the ST samples and all three ESC samples. The first samples that were analyzed were ST-1, ST-2, and ST-6. Again, the amplitude range was reduced to look for specific features within the B-scan images as shown in Figure 258. The lines that were selected from the C-scan images of the ST samples went through selected low amplitude regions and features within each of the sintered samples. Upon evaluation of the samples, these features stood out clearly within the B-scan images. The large inclusion from ST-1 showed up in the form of a low amplitude region through the cross-sectional thickness of the sample. This was even more apparent in sample ST-2 in which the B-scan image was collected through one of the circular millimeter-range low amplitude features that was detected near the corners of each of the ST samples. The low amplitude region expanded to a larger size halfway through the sample as it approached the bottom surface reflected amplitude signal. This gave evidence that the feature was present in the lower half of the sample. For sample ST-3, there were two similar regions of lower amplitude that were found, though the reduction in amplitude was not as drastic as it was for samples ST-1 and ST-2. As compared to the hot pressed samples that showed little variation within the bulk regions of the B-scan images, the ST samples did show representative amplitude variations. Quantitative histogram analysis was conducted to look for how these bulk changes affected the AUTC and FWHM values, as shown in Figure 259. The normalized amplitude histogram curves were much more different than for the hot pressed samples in terms of shape, as the regions with a higher number of occurrences were concentrated at lower amplitude values. The resulting AUTC values were 4757 for ST-1, 5409 for ST-2, and 4275 for ST-3 while the FWHM values were 50

for ST-1, 55 for ST-2, and 46 for ST-3. These values were much higher than the armor grade hot pressed A and D samples and SD hot pressed samples, but fell within a similar range to the variable B and C hot pressed samples. The level of variability was also consistent with the features that the B-scan lines were drawn through. The data for ST-2, which went through the cross section of the millimeter-sized feature, had the highest overall AUTC and FWHM values. The next largest feature in ST-1 showed the second highest B-scan values and ST-6 showed the lowest B-scan values. The amplitude variations in the B-scan images of the ST samples translated into higher AUTC and FWHM values. In this case, the visual evidence was also more pronounced.

The last set of sintered SiC samples that were evaluated using B-scan imaging were the ESC samples as shown in Figure 260, which were fabricated under different processing conditions. Horizontal lines were selected from the C-scan images through the center of ESC-1, ESC-2, and ESC-3. The resulting B-scan images showed the same characteristics as many of the other B-scans, as no distinct individual features were specifically detected. The B-scan images of the three samples appeared to be identical, so again the quantitative data were collected to compare the samples in Figure 261. The AUTC values for the ESC samples were 4144 for ESC-1, 4868 for ESC-2, and ESC-3 for 4054 while the FWHM values were 28 for ESC-1, 36 for ESC-2, and 29 for ESC-3. Again, just as with the ST sintered SiC samples all of the AUTC values were above 4000. While the FWHM values were lower than the ST samples, they still had values of 28 or higher, which was higher than all of the hot pressed SiC A, D, and SD samples. Among the ST samples, the lowest AUTC and FWHM values were characteristic of the ESC-3 sample, which also had the highest ballistic properties, as correlated to the reflected

signal amplitude histogram data reported earlier. While this was consistent, the ESC-1 and ESC-2 values were reversed, as the ESC-2 sample had higher AUTC and FWHM values than ESC-1 despite the fact that ESC-2 had higher ballistic properties. It can be stated that in this case, random lines were selected for B-scan evaluation, so the line for ESC-2 may not have been representative and more B-scan evaluations could be collected to determine an average instead of relying on one set of values. However, the trends for hot pressed and sintered samples remained consistent. While the A, D, and SD hot pressed samples all had AUTC values below 3000 and FWHM values of 20 or less, the B and C variable hot pressed samples and all of the sintered samples including ST and ESC had AUTC values greater than 4000 and FWHM values of 28 or higher. This was a distinct trend that separated the samples in terms of integrity, which was important to note since few visual variations in the B-scan image data were found. The only set of samples that showed definitive visual differences was the ST set which took the B-scan cross-sections through features of very large amplitude differences from the bulk. By using higher frequencies for collection of B-scan image data, it is possible that more isolated features can be detected. However, interfering acoustic signals from high frequency transducers will be present that may be mistaken for material inhomogeneities. Even at the given frequency, while visually it appeared as thought the B-scan imaging technique did not provide a means for sample comparison, the quantitative normalized amplitude histogram curves and AUTC and FWHM values were able to extract meaningful differences.

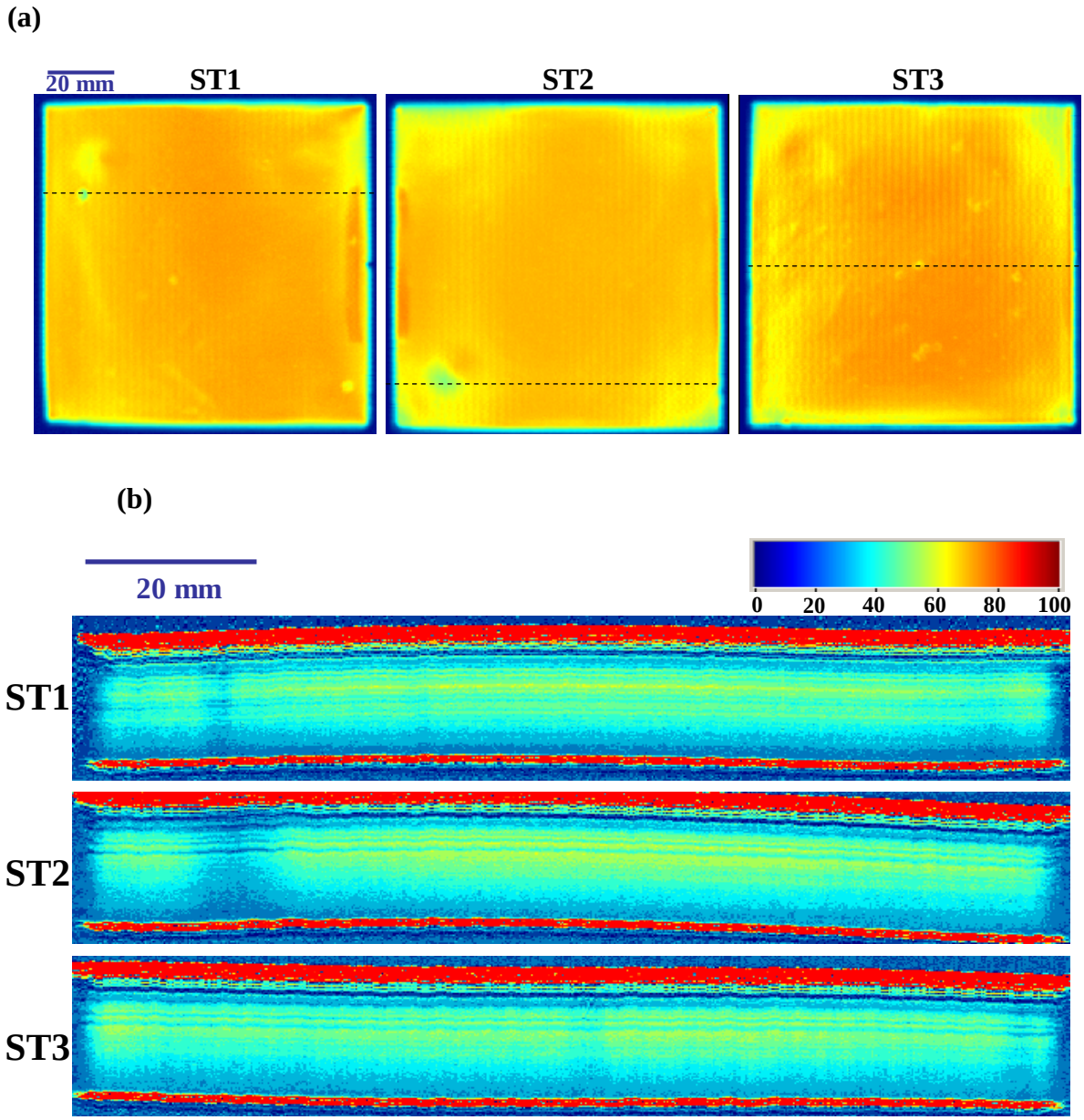

Figure 258. (a) C-scan images with representative lines and (b) corresponding B-scan cross-sectional images of samples ST1, ST2, and ST3.

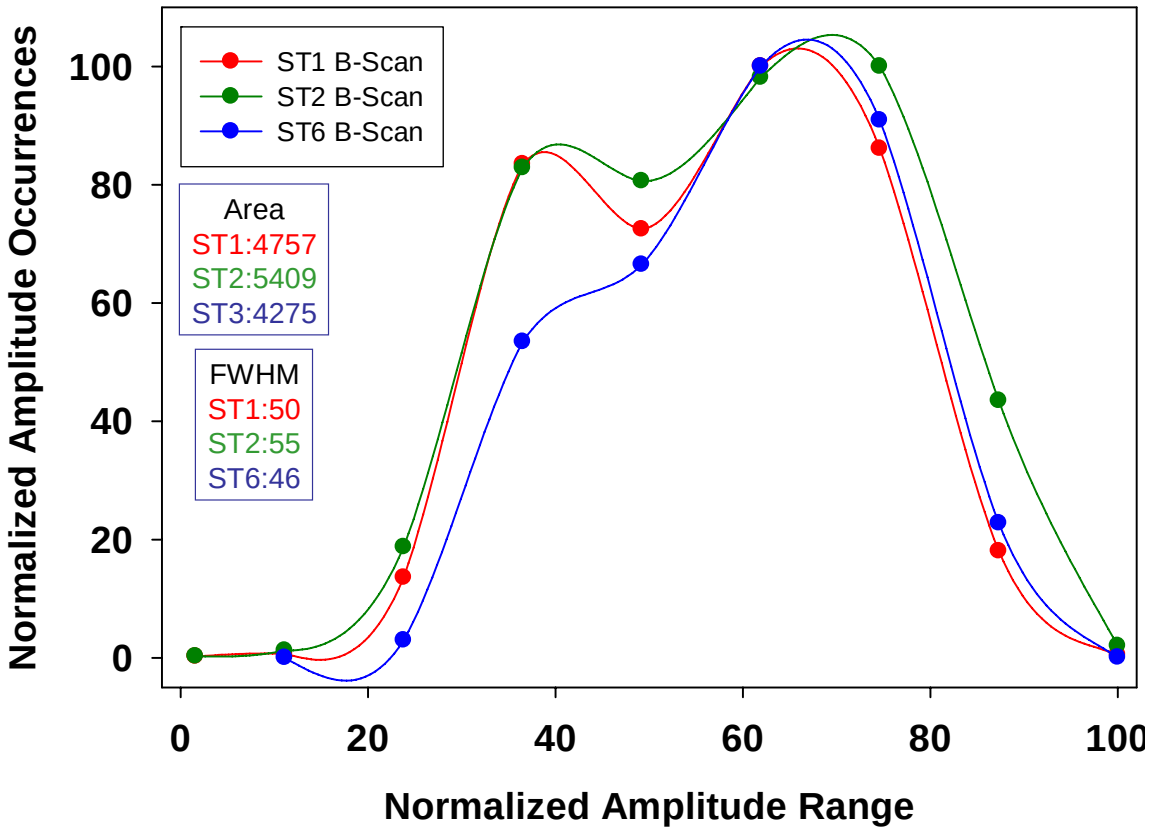

Figure 259. B-scan image histogram curves, AUTC values, and FWHM values for samples ST1, ST2, and ST3.

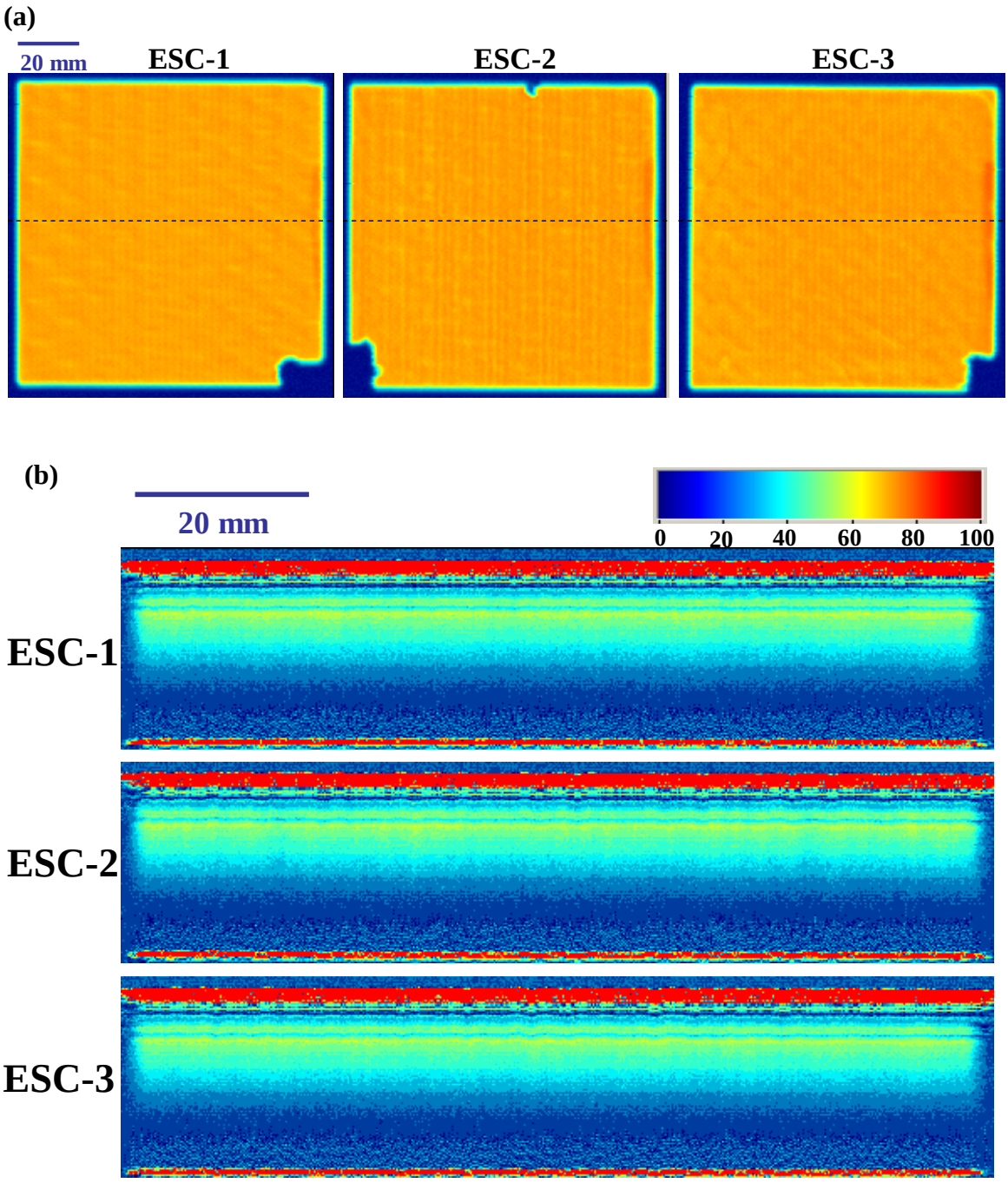

Figure 260. (a) C-scan images with representative lines and (b) corresponding B-scan cross-sectional images of samples ESC-1, ESC-2, and ESC-3.

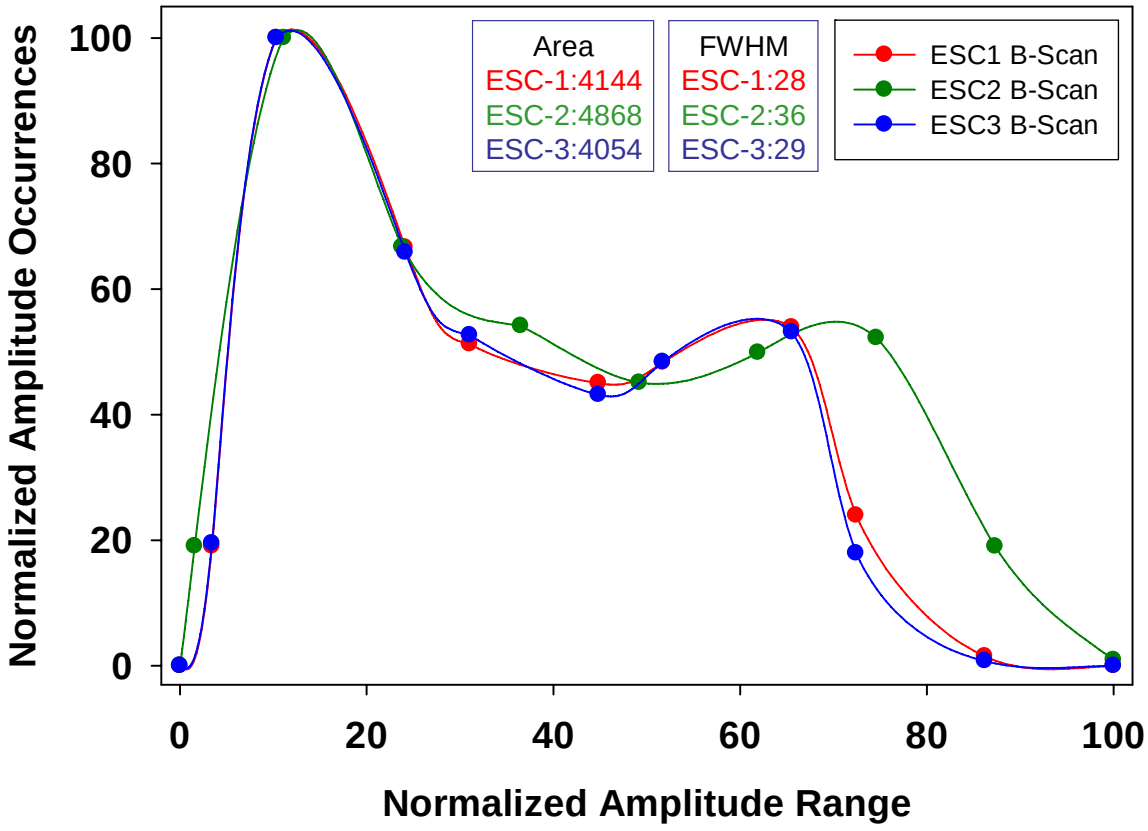

Figure 261. B-scan image histogram curves, AUTC values, and FWHM values for samples ESC-1, ESC-2, and ESC-3.

5.18. Results and Discussion Conclusions

Ultrasound nondestructive evaluation has been established as a method capable of detecting μm-scale and larger size inhomogeneities in armor ceramic test specimens. The utility of ultrasound testing was first confirmed by using point analysis techniques to measure longitudinal and shear TOF values which were used to calculate longitudinal velocity, shear velocity, acoustic impedance, Poisson's ratio, elastic modulus, shear modulus, and bulk modulus values. The measured and calculated acoustic and elastic property values were very similar to values reported in the literature. After measuring individual values from A-scan data, C-scan images were collected by determining changes in either the bottom surface reflected signal amplitude or the TOF over the chosen sample area. The reflected signal amplitude C-scan images proved to be valuable for differentiating attenuation changes due to acoustic wave scattering, demonstrating a high degree of sensitivity for detection of defects and inhomogeneities over the sample bulk. The TOF C-scan images were also valuable for distinguishing more subtle regional changes in TOF, which were used to calculate specific differences in thickness, density, material velocity, and various elastic properties. While the reflected signal amplitude C-scan images were more frequently used for establishing subtle acoustic differences and detecting material inhomogeneities, TOF C-scan images were critical for developing unique material velocity and elastic property maps. Since each method resulted in a distinct set of ultrasound data, the combination of methods was used to extract a meaningful set of acoustic values from the armor ceramic samples.

While the raw data from both reflected signal amplitude and TOF C-scan images were useful for qualitative analysis, a quantitative analysis technique was necessary for

comparison of material integrity between and among sample sets. Normalized reflected signal amplitude, TOF, and material velocity histogram curves were developed for this purpose. By determining the number of occurrences of each amplitude or TOF value and plotting these data over the full amplitude or TOF range, the resulting histogram curve gave a quantitative assessment of the reflected signal amplitude and TOF cumulative distributions. These distributions were characteristic signatures of each test specimen that could be directly compared by extracting tail data, area-under-the-curve values, and full-width at half-maximum values. These individual values gave an indication of not only the homogeneity of each scanned sample area, but an idea of the presence of critical regions of interest as well. Low amplitude and high TOF tail regions identified the cumulative effects of features and inhomogeneities throughout the sample bulk. The broadness of the histogram curve gave a general indication of overall sample homogeneity. Area-under-the-curve and full-width at half-maximum data in addition to average and standard deviation values helped quantify these trends for direct comparison among tested samples. It was determined that a narrow distribution of amplitude or TOF values and, therefore, low values of standard deviation, AUTC, and FWHM, indicated a more uniform and homogeneous sample characteristic of a high density armor grade test specimen with few material inhomogeneities. On the other hand, a broad distribution of amplitude or TOF values and, therefore, high values of standard deviation, AUTC, or FWHM, indicated an inhomogeneous sample containing density variations and/or significant material inhomogeneities. Depending on the degree of difference between the features and the bulk materials, these normalized histogram curves were categorized as either one-phase histogram or two-phase histograms. For a test specimen with slight

amplitude and TOF variations, a one-phase histogram in which there were no distinct tail peaks was common. For a test specimen with large inhomogeneous regions or containing a significant number of features with amplitude or TOF values that were drastically different from the average bulk material values, a second histogram peak characteristic of those cumulative features led to a two-phase histogram. Two-phase histograms containing large tail regions were the most highly variable materials that were associated with the highest probability of failure.

Once the ability to perform ultrasound C-scan imaging and quantitative evaluation was established, ultrasound transducer and system parameters were analyzed to determine the optimum conditions for extracting necessary information from each test specimen. The main parameter that was altered was the transducer frequency, which helped dictate the limits for detecting features of specific sizes. Since higher frequencies produced shorter wavelengths, the theoretical detection limits were improved when the frequency was increased. However, the limitation of using high frequencies was an increase in the effect of attenuation. This, in turn, affected the depth of penetration into the test specimen, as a higher degree of attenuation eventually resulted in a complete loss of signal. It was determined that transducers with frequencies as high as 125 MHz could be used to detect μm-scale features while still being able to evaluate high density test specimens as thick as 50 cm. This frequency was the highest frequency used to detect small reflected signal amplitude and TOF variations within the armor ceramic materials without sacrificing the bottom surface reflected signals. Another impact of transducer frequency related to the types of features that were desired for detection. If only thickness variations were important for evaluation, 1-2 MHz transducers were sufficient.

If only the largest millimeter-size material features were critical for detection, 5-10 MHz transducers were utilized. If large regional variations were important to differentiate without emphasizing the smallest features, 50-75 MHz transducers were used. If the smallest μm-range inhomogeneities in armor ceramics were found to be critical for evaluation, the 125 MHz transducers were used. The nature of the resulting quantitative histogram data was dictated by the initial transducer frequencies, as the lower frequency scans generally showed one-phase Gaussian distributions. Two-phase data in which critical tails were present were more commonly found in the 50-75 MHz frequency range. This type of data was effective for sample evaluation and comparison. The 125 MHz quantitative data did not generally show large regional evaluations, but rather specific individual features and slight amplitude and TOF variations, again characterized more frequently by Gaussian, one-phase distributions. Of course these were generalizations, as samples with large porous regions evaluated at frequencies as low as 5 MHz or as high as 125 MHz might result in a two-phase histogram or uniform armor grade samples evaluated at 75 MHz might show Gaussian distributions. However, the expected frequency trends were predictable for the majority of armor ceramic samples, and transducer frequencies were chosen for detection of specific types of features.

A variety of armor ceramic samples were evaluated using ultrasound techniques to compare differences between hot pressed and sintered SiC materials, commercial and red-flagged hot pressed SiC materials from the same batch, sintered SiC materials from the same batch, hot pressed SiC and AlN materials, sintered SiC and Al_2O_3 materials, and commercial and fabricated materials. Hot pressed SiC test specimens were characterized by fewer distinctly different features at all frequencies as compared to sintered SiC test

specimens. Hot pressed SiC materials generally showed more narrow normalized histogram distributions as well as lower standard deviation, AUTC, and FWHM values when compared to sintered SiC materials. Commercial armor grade hot pressed SiC materials were the most uniform and homogeneous samples that were evaluated, while samples that were red-flagged for their inability to meet manufactured specifications showed large variations, but only at the highest frequency of 125 MHz. On the other hand, sintered SiC test specimens that came from the same batch showed significant variations at all transducer frequencies. Despite the fact that these samples were manufactured under the exact same conditions, regional differences were often highly variable, and the detection of material inhomogeneities was even more important for comparison of sample integrity. Hot pressed AlN samples showed higher acoustic variability as compared to hot pressed SiC samples due to the larger grain size of AlN, which resulted in additional wave scattering, higher attenuation, and lower reflected signal amplitude. Sintered Al_2O_3 test specimens showed more acoustic variability than comparable sintered SiC samples. Fabricated Al_2O_3/polymer sphere and epoxy/WC sphere samples aided in evaluation of the integrity of the ultrasound system itself, since features of known size and location were detected at the predicted frequencies. These studies also confirmed the normalized histogram trends that were determined from evaluation of the armor ceramic samples. The one and two-phase histograms were demonstrated effectively using the epoxy/WC sphere samples to show that a bulk matrix containing a second phase with vastly different acoustic impedance resulted in a large tail region. These types of sample comparisons effectively showed the ability of ultrasound

testing to provide meaningful data for the comparison of armor ceramic material integrity.

After establishing the ultrasound evaluation technique and comparing various armor samples, a variety of post-processing methods were developed in an attempt to extract the maximum amount of meaningful information from the raw ultrasound data. In terms of alternate visualization methods, schematic overlay, regional mapping, and three-dimensional mapping were utilized to represent the ultrasound data visually. For examining C-scan imaging regional variations, line scan and reflected signal amplitude distribution images were developed. These methods showed pixel-to-pixel amplitude variations and selected range amplitude values directly on the image maps. Critical tail analysis was further emphasized by using peak deconvolution and curve fitting techniques to compare tail regions of different test specimens. Material velocity and elastic property mapping were novel techniques developed by utilizing specialized broadband transducers to generate both longitudinal and shear TOF C-scan images. By using low frequency transducers to plot thickness differences and using the acoustic impedance material property to calculate density differences, elastic property equations were used to generate image maps of Poisson's ratio, elastic modulus, shear modulus, and bulk modulus differences. Another novel technique that was developed was individual feature characterization from ultrasound C-scan images. In this method C-scan image thresholding was used to generate maps of the most distinct individual features in comparison to the rest of the bulk. The individual features were further characterized to generate defect size distributions, and power law equations which were commonly used in the literature for curve fitting applications, were applied. There were very high

correlations between the curve fit and the size distribution data from both sintered and hot pressed SiC materials.

One and two-phase histograms were utilized as the basis for developing a series of three types of simulations. The first two, based on simple Gaussian distributions, showed normalized histogram curve broadening with an increase in the number and size of features. The more complex simulations were able to show resulting one and two-phase histograms based on the number of features, the size of features, and the degree of difference between the acoustic impedance of the matrix and the detected features. B-scan imaging, while it was not able to show overwhelming differences in the cross-sections of the samples, did show a strong correlation based on the type of materials being evaluated. Hot pressed and sintered SiC materials showed characteristic quantitative data in terms of AUTC and FWHM values that followed the same trends that were found in the C-scan imaging results.

All of these methods, from the initial normalized histogram results to the most complex peak deconvolution and tail analysis techniques to novel elastic property mapping, resulted in a set of ultrasound data that effectively characterized armor ceramic materials for detailed comparison among different sample sets. The cumulative acoustic signature from each material that was used as the basis of material integrity comparison was collected as the representative ultrasound fingerprint. The fact that no two ultrasound fingerprints were identical enabled material comparison even when two test specimens were manufactured under the same stringent processing conditions. These ultrasound fingerprints can be used not only as a screening technique to detect critical features, but depending on the types of features that are found, they can also be used to

determine the processing and manufacturing steps that can be improved to avoid such problems in the future. Ultrasound technology is not only limited to post-processing evaluation, but can be utilized as a tool for early prevention of the same types of features that it is capable of detecting.

6. Conclusions

There were several important outcomes of this thesis work. The results established that high frequency ultrasound is a useful technique for detecting second phases, low density regions, and other features in armor ceramic materials. Ultrasound C-scan imaging was performed to distinguish changes in reflected signal amplitude and TOF for both hot pressed and sintered armor ceramics, demonstrating that microstructural differences in dense armor test specimens could be determined. Reflected signal amplitude scans at the higher frequencies were sensitive to fine microstructural inhomogeneities due to acoustic wave scattering. This allowed for detection of small changes in reflected signal amplitude for effective comparison of hot pressed or sintered test specimens from the same batch manufactured under the same processing conditions. In contrast, TOF scans commonly demonstrated only larger regional variations that included thickness differences over each tested sample. For this reason, material velocity mapping was more valuable than TOF mapping for sample comparison as the effect of changes in thickness was eliminated. Increasing the transducer frequency above 5 MHz to higher frequencies (50, 75, 125 MHz) enabled detection of isolated individual features as small as 50 μm while maintaining a signal-to-noise ratio acceptable for evaluation of high density samples as thick as 50 cm at the highest frequency of 125 MHz. Quantitative analysis of reflected signal amplitude and TOF variations was accomplished

by utilizing normalized histograms to compare critical tail regions, area-under-the-curve values, and full-width at half-maximum values among armor ceramic test specimens. Normalized histogram simulations were also developed to differentiate one and two-phase distributions and to account for acoustic impedance mismatch variations. A comprehensive ultrasound fingerprint method was established for direct comparison of critical acoustic parameters among armor samples. Elastic property mapping of Poisson's ratio, elastic modulus, shear modulus, and bulk modulus differences was accomplished for potential application as input data for effective ballistic modeling. A grayscale threshold imaging analysis technique was established to extract isolated microstructural features from high resolution C-scan images and determine their resulting feature size distributions. These techniques and methods were developed to utilize ultrasound nondestructive detection for effective evaluation and comparison of armor ceramic materials.

7. Future Work

Since the ground work has been laid for establishing nondestructive ultrasound evaluation as a feasible technique for analyzing bulk high density armor ceramics, future work will concentrate on further exploration of optimum conditions and parameters as well as further correlation to ballistic data. It will be vital to establish which feature sizes, shapes, types, concentrations, and distributions are critical to the performance of armor ceramics. Once this is determined, the ultrasound evaluation methods can be modified to specifically target only the critical features. If it is determined that the more common 20-80 μm features are not detrimental to the dynamic failure of the armor ceramics, lower frequency transducers can be utilized to focus on the more rare

anomalous features. Since the shock wave from the ballistic event affects pre-existing features of all sizes within the armor ceramic material, if it is determined that features even smaller than 20 μm are critical to ballistic performance, higher frequency transducers may need to be utilized to detect these critical features. The advantage of first conducting ultrasound nondestructive evaluation is that a vast amount of meaningful data can be collected on an armor ceramic material without causing any degree of damage. Next, ballistic testing such as V50 or depth of penetrations methods can be applied to the nondestructively evaluated test specimens and strong correlations can be established based on performance. Another option is to cut up the test specimens after ultrasound evaluation and to perform individual testing of density, hardness, strength, and other mechanical properties on the smaller samples. The data on individual samples can be correlated to regional variations that may be present in B-scan and C-scan images from previous ultrasound evaluation. Once these critical parameters are effectively established, they can be integrated into the ultrasound fingerprint data to compare samples and predict the probability of failure. This will be facilitated by utilizing the characteristic single value ultrasound data from quantitative analysis studies such as standard deviation, AUTC, and FWHM values for comparison. Since the normalized histogram curve trends have already been established, the values can be directly correlated to critical ballistic data. By determining which ultrasound quantitative analysis values are directly related to ballistic failure data, these results can help assess the probability that an armor ceramic test specimen will either succeed or fail.

Ultrasound data from elastic property mapping and individual feature size distributions may be applied as input data for improved ballistic modeling. Many current

ballistic models do not account for variations in material velocities or elastic properties within a bulk armor ceramic plate, using only a single average value as input. Many models do not account for material inhomogeneties and the few that incorporate these differences do not utilize representative size distribution data. By applying ultrasound data that describes differences in both elastic properties and feature size distributions, more accurate and realistic ballistic models may be developed.

Through intensive and comprehensive ultrasound and ballistic studies of various armor ceramic materials, a cutoff may eventually be established to directly predict performance. This cutoff may indicate the critical average standard deviation values, AUTC values, FWHM values, or a combination of these values in which there is a high probability of ballistic failure. As a first step, this method can be used as a screening technique to categorize armor materials in terms of the cumulative distribution of features and material inhomogeneities that describe overall plate-to-plate variability. Eventually, this type of method may be established as a go/no-go system for acceptance and rejection of armor ceramic materials. Ideally, this system could be applied online as a manufacturing step to screen materials as they are fabricated. Since one of the limitations of single element transducer scanning is a slower speed of evaluation, phased arrays can be utilized for electronic scanning, reducing or eliminating the need for mechanical manipulation of the transducer. If the critical feature sizes are too small for evaluation, phased array technology, which is currently limited to 20-25 MHz frequencies, may be improved in terms of piezoelectric crystal fabrication and, therefore, feature size detection. With the enhancement of phased array evaluation and a natural progression toward the improvement of computer memory and processing technologies, the scanning

speed can eventually be overcome and general ultrasound analysis applied as an online manufacturing step.

Another way of ensuring the integrity of ultrasound as an evaluation technique is to correlate the data to other comparable nondestructive methods. Techniques such as resonant ultrasound spectroscopy and x-ray computed tomography can be used to evaluate the same sets of samples to make sure that the same features are detected. Just as some of the post-processing ultrasound methods were more useful for showing the data in different ways to pick up on things that may not have been as clear using basic methods, other nondestructive evaluation techniques may be useful for showing armor ceramic data in different ways that ultrasound is not able to.

With the establishment of ultrasound evaluation of armor ceramics as an important technique, the next step is to move forward to continue and advance these studies in any way possible. Since the preservation and protection of the lives of soldiers is at stake in this vital application, the most effective advancements must be made by any means necessary – whether through the continued development of ultrasound or any other methods. The bottom line is that something must be done, and nondestructive evaluation of armor ceramics may be one small step in achieving that ultimate goal.

REFERENCES

1. M.J. Normandia, J.C. LaSalvia, W.A. Gooch, J.W. McCauley, A.M. Rajendran, “Protecting the Future Force: Ceramics Research Leads to Improved Armor Performance”, AMPTIAC Quarterly, 8(4), pages 21-27, 2004.
2. R.J. Clifton, “Response of Materials Under Dynamic Loading”, International Journal of Solids and Structures, 37(1-2), pages 105-113, 2000.
3. American Society for Nondestructive Testing: Definition of NDT http://www.asnt.org/ndt/primer1.htm/
4. J. Kim and P.K. Liaw, “The Nondestructive Evaluation of Advanced Ceramics and Ceramic-Matrix Composites”, JOM, 50(11), 1998.
5. Armadillo Armory and Collectibles: History of Armour http://www.armadilloarmory.com/hxarmour.htm/
6. National Park Service: History of Armour and Weapons Relevant to Jamestown http://www.nps.gov/archive/colo/Jthanout/HisArmur.html/
7. Global Security: Body Armor History http://www.globalsecurity.org/military/systems/ground/body-armor2.htm/
8. E. Medvedovski, “Alumina Ceramics for Ballistic Protection Part I”, American Ceramic Society Bulletin, 81(3), pages 27-32, 2002.
9. M. Jacoby, “Science Transforms the Battlefield”, Chemical and Engineering News, 81(32), pages 28-34, 2003.
10. J. Shih, “Dynamic Deformation of Silicon Carbide”, Ph.D. Thesis, University of California, San Diego, 1998.
11. D.J. Sandstrom, “Armor/Anti-Armor Materials by Design”, Los Alamos Science, pages 36-50, 1989.
12. M.A.G. Silva, C.G. Chiorean, C. Cismasiu, “Ballistic Simulation of Impact on Composite Laminates”, The International Conference Construction: Cluj-Napoca, Romania, page 8, 2003.
13. S.R. Martin, “Experimental Characterization of the Effect of Microstructure on Dynamic Behavior of SiC”, Ph.D. Thesis, Georgia Institute of Technology, 2004.
14. B.A. Gama, J.W. Gillespie, T.A. Bogetti, B.K. Fink, H. Mafuz, “Study of Through-Thickness Wave Propagation in Multi-Layer Hybrid Lightweight Armor”, Proceedings of the 13th Annual Technical Conference on Composite Materials, September 21-23, Baltimore, MD, 1998.
15. L.R. Vyshnyakov, A.V. Mazna, A.V. Neshpor, V.A. Kokhanyi, O.N. Oleksyuk, “Influence of Structural and Technological Factors on the Efficiency of Armor Elements Based on Ceramics”, Strength of Materials, 36(6), pages 643-648, 2004.
16. W.A. Gooch, “An Overview of Ceramic Armor Applications”, Ceramic Transactions: Ceramic Armor Materials by Design, 134, pages 3-21, 2002.

17. C.J. Shih, V.F. Nesterenko, M.A. Meyers, “High-Strain-Rate Deformation and Comminution of Silicon Carbide”, Journal of Applied Physics, 83(9), pages 4660-4671, 1998.
18. R.C. McCuiston, “Fabrication and Simulation of Random and Periodic Composites for Reduced Stress Wave Propagation”, Ph.D. Thesis, Rutgers University, 2005.
19. H. Luo, W.W. Chen, A.M. Rajendran, “Dynamic Compressive Response of Damaged and Interlocked SiC-N Ceramics”, Journal of the American Ceramic Society, 89(1), pages 266-273, 2006.
20. E. Medvedovski, “Alumina Ceramics for Ballistic Protection Part II”, American Ceramic Society Bulletin, 81(4), pages 45-50, 2002.
21. A.E. Brown, “Rationale and Summary of Methods for Determining Ultrasonic Properties of Materials at Lawrence Livermore National Laboratory”, Technical Report UCRL-ID-119958, Lawrence Livermore National Laboratory, pages 1-45, 1997.
22. J.D. Achenbach, “Quantitative Nondestructive Evaluation”, International Journal of Solids and Structures, 37, pages 13-27, 2000.
23. National Institute of Standards and Technology Property Data Summaries for Advanced Materials
http://www.ceramics.nist.gov/srd/summary/advmatdb.htm/
24. S.J. Schneider, *Engineered Materials Handbook: Ceramics and Glasses, Vol. 4*, ASM International, 1991.
25. P.E. Mix, *Introduction to Nondestructive Testing*, Publisher: John Wiley & Sons, New York, 1987.
26. S.P. Dodd, G.A. Saunders, M. Cankurtaran, B. James, “Ultrasonic Study of the Elastic and Nonlinear Acoustic Properties of Ceramic Aluminum Nitride”, Journal of Materials Science, 36, pages 723-729, 2001.
27. S.P. Dodd, G.A. Saunders, B. James, “Temperature and Pressure Dependences of the Elastic Properties of Ceramic Boron Carbide”, Journal of Materials Science, 37, pages 2731-2736, 2002.
28. *Materials Data Book*, Cambridge University Engineering Department, 2003.
29. BAE Systems: Armor Materials Properties
http://www.cercomceramics.com/material.htm/
30. W.D. Callister, *Materials Science and Engineering: An Introduction*, Publisher: John Wiley and Sons, Inc., New York, 1994.
31. M. Chheda, J. Normandia, J. Shih, “Ceramic Defense: Improving Ceramic Armor Performance”, Ceramic Industry, pages 124-126, 2006.
32. M. Flinders, D. Ray, R.A. Cutler, “Toughness-Hardness Tradeoff in Advanced SiC Armor”, Ceramic Transactions: Ceramic Armor and Armor Systems, 151, pages 37-48, 2003.
33. D.E. Grady, “Shock Wave Compression of Brittle Solids”, Mechanics of Materials, 29, pages 181-203, 1998.
34. D. Sherman, “Impact Failure Mechanisms in Alumina Tiles on Finite Thickness Support and the Effect of Confinement”, International Journal of Impact Engineering, 24, pages 313-328, 2000.

35. D. Sherman, T. Ben-Shushan, “Quasi-Static Impact Damage in Confined Ceramic Tiles”, International Journal of Impact Engineering, 21(4), pages 245-265, 1998.
36. V. Madhu, K. Ramanjaneyulu, T.B. Bhat, N.K. Gupta, “An Experimental Study of Penetration Resistance of Ceramic Armour Subjected to Projectile Impact”, International Journal of Impact Engineering, 32(1-4), pages 337-350, 2005.
37. P. Lundberg, B. Lundberg, “Transition Between Interface Defeat and Penetration for Tungsten Projectiles and Four Silicon Carbide Materials”, International Journal of Impact Engineering, 31, pages 781-792, 2005.
38. T.J. Holmquist, G.R. Johnson, “Characterization and Evaluation of Silicon Carbide for High-Velocity Impact”, Journal of Applied Physics, 97, 2005.
39. D.A. Shockey, D.R. Curran, R.W. Klopp, L. Seaman, C.H. Kanazawa, J.T. McGinn, “Characterizing and Modeling Penetration of Ceramic Armor”, Technical Report PYU-3673, U.S. Army Research Office, pages 1-85, 1995.
40. M.B. Karamis, F. Nair, A. Tasdemirci, “Analyses of Metallurgical Behavior of Al-SiCp Composites After Ballistic Impacts”, Composite Structures, 64, pages 219-226, 2004.
41. Y.V. Milman, S.I. Chugunova, I.I. Timofeeva, “The Resistance of Silicon Carbide to Static and Impact Local Loading”, International Journal of Impact Engineering, 26, pages 533-542, 2001.
42. R. Feng, G.F. Raiser, Y.M. Gupta, “Material Strength and Inelastic Deformation of Silicon Carbide under Shock Wave Compression”, Journal of Applied Physics, 83(1), pages 79-86, 1998.
43. T.J. Holmquist, A.M. Rajendran, D.W. Templeton, K.D. Bishnoi, “A Ceramic Armor Materials Database, Technical Report No. 13754, U.S. Army Tank-Automotive Research Development and Engineering Center (TARDEC), 1999.
44. First Defense Armor Systems
http://www.firstdefense.com/
45. D. Ray, R.M. Flinders, A. Anderson, R.A. Cutler, J. Campbell, J.W. Adams, “Effect of Microstructure and Mechanical Properties on the Ballistic Performance of SiC-Based Ceramics”, Advances in Ceramic Armor II, 27(7), 2006.
46. M.P. Bakas, “Analysis of Inclusion Distributions in Silicon Carbide Armor Ceramics”, Ph.D. Thesis, Rutgers University, 2006
47. M.P. Bakas, V.A. Greenhut, D.E. Niesz, G.D. Quinn, J.W. McCauley, A.A. Wereszczak, and J.J. Swab, “Anomalous Defects and Dynamic Failure of Armor Ceramics”, International Journal of Applied Ceramic Technology, 1(3), pages 211-218, 2004.
48. S. Somiya, Y. Inomata, *Silicon Carbide Ceramics 1*, Publisher: Elsevier Applied Science, New York, 1991.
49. W. van Rijswijk, D.J. Shanefield, “Effects of Carbon as a Sintering Aid in Silicon Carbide”, Journal of the American Ceramic Society, 73(1), pages 148-149, 1990.

50. P.T.B. Shaffer, “A Review of the Structure of Silicon Carbide”, Acta Crystallographica, B25, pages 477-488, 1969.
51. G. Schwier, I. Teusel, M.H. Lewis, “Characterization of SiC Powders and the Influence of Powder Properties on Sintering”, Pure and Applied Chemistry, 69(6), pages 1305-1316, 1997.
52. K. Biswas, “Liquid Phase Sintering of SiC Ceramics with Rare Earth Sesquioxides”, Ph.D. Thesis, Stuttgart University, 2002.
53. C. Ziccardi, V. Demirbas, R. Haber, D. Niesz, J. McCauley, “Means of Using Advance Processing to Eliminate Anomalous Defects in SiC Armor”, Advances in Ceramic Armor, 26(7), 2005.
54. R. Nab, M. Aslan, R. Nonninger, H. Schmidt, P. Matje, “New Processing Techniques for the Production of Pressureless Sintered SiC Parts”, Proceedings of the International Conference of Ceramic Processing Science and Technology, pages 433-437, 1995.
55. M.S. Datta, A.K. Bandyopadhyay, B. Chaudhuri, “Sintering of Nano-Crystalline α Silicon Carbide by Doping with Boron Carbide”, Bulletin of Materials Science, 25(3), pages 181-189, 2002.
56. S.M. McMillan, R.J. Brook, “Synthesis of Silicon Carbide Ceramics at Low Temperatures”, Ceramic Transactions, 51, pages 187-191, 1994.
57. J.S. Reed, *Principles of Ceramic Processing*, Publisher: John Wiley and Sons, Inc., New York, 1995.
58. B. Chelluri, E. Knoth, E. Schumaker, J. Barber, L.P. Franks, “High Rate Manufacturing Process for Silicon Carbide Tiles”, Proceedings of the American Ceramic Society, pages 1-4, 2006.
59. M. Aslan, R. Nonninger, R. Nab, R. Rein, H. Schmidt, “Relations Between Microstructure and Mechanical Properties of Pressureless Sintered SiC”, Ceramic Transactions, 51, pages 757-761, 1995.
60. S. Obata, H. Asano, O. Sakurada, M. Hashiba, Y. Nurishi, “Fabrication of Dense Silicon Carbide through Aqueous Slurries Containing Well-Dispersed Carbon as a Sintering Aid”, Journal of Materials Science, 40, pages 757-760, 2005.
61. J.B. Hurst, S. Dutta, “Simple Processing Method for High-Strength Silicon Carbide”, Journal of the American Ceramic Society, 70(11), pages C-303-C-308, 1987.
62. Olympus: Ultrasonic Transducers for Nondestructive Testing
http://www.olympusndt.com/data/File/panametrics-UT.pdf/
63. A Summary of the Early Development of Ultrasonics Prior to the 1950s Leading to Medical Applications
http://www.ob-ultrasound.net/ultrasonics_history.html/
64. A.D. Pierce, *Acoustics: An Introduction to Its Physical Principles and Applications*, Publisher: Acoustical Society of America, Woodbury, NY, 1991.
65. A Short History of the Development of Ultrasound in Obstetrics and Gynecology, by J. Woo
http://www.ob-ultrasound.net/history1.html/

66. NDT Resource Center: Collaboration for NDT Education
http://www.ndt-ed.org/
67. EDinformatics: Medical Ultrasonography
http://www.edinformatics.com/inventions_inventors/ultrasound.htm/
68. Wikipedia
http://www.wikipedia.com/
69. A. Shoh, "Industrial Applications of Ultrasound – A Review: I. High Power Ultrasound", IEEE Transactions on Sonics and Ultrasonics, SU-22(2), pages 60-71, 1975.
70. L. Lynnworth, *Ultrasonic Measurements for Process Control: Theory, Techniques, Applications*, Academic Press, Inc., Boston, MA, 1989.
71. L.C. Lynnworth, "Industrial Applications of Ultrasound – A Review: II. Measurements, Tests, and Process Control using Low-Intensity Ultrasound", IEEE Transactions on Sonics and Ultrasonics, SU-22(2), pages 71-101, 1975.
72. R.D. Finch, *Introduction to Acoustics*, Publisher: Pearson Prentice Hall, Upper Saddle River, NJ, 2005.
73. J. Krautkramer, H. Krautkramer, *Ultrasonic Testing of Materials*, Springer-Verlag, Berlin, Germany, 1990.
74. Acoustic and Vibration Animations, by D. Russell, Kettering University
http://www.kettering.edu/~drussell/demos.html/
75. M.C. Bhardwaj, "Evolution, Practical Concepts and Examples of Ultrasonic NDC", Ceramic Monographs – Handbook of Ceramics, 41, pages 1-7, 1992.
76. D.E. Bray, R.K. Stanley, *Nondestructive Evaluation: A Tool in Design, Manufacturing, and Service*, CRC Press, Inc., Boca Raton, FL, 1997.
77. J.L. Rose, *Ultrasonic Waves in Solid Media*, Publisher: Cambridge University Press, Cambridge, UK, 1999.
78. L.W. Schmerr, *Fundamentals of Ultrasonic Nondestructive Evaluation*, Plenum Press, New York, 1998.
79. M.G. Silk, *Ultrasonic Transducers for Nondestructive Testing*, Publisher: Adam Hilger Ltd, 1984.
80. M. Prasad, "Mapping Impedance Microstructures in Rocks with Acoustic Microscopy", The Leading Edge, 20, pages 172-179, 2001.
81. J.T. Bushberg, J.A. Seibert, E.M. Leidholdt, J.M. Boone, *The Essential Physics of Medical Imaging: Second Edition*, Publisher: Lippincott, Williams, and Wilkins, Haggerstown, MD, 2001.
82. N. Kulkarni, B. Moudgil, M. Bhardwaj, "Ultrasonic Characterization of Green and Sintered Ceramics: II, Frequency Domain", American Ceramic Society Bulletin, 73(7), pages 83-85, 1994.
83. J. Zhao, P.A. Gaydecki, F.M. Burdekin, "A Numerical Model of Ultrasonic Scattering by a Defect in an Immersion Test", Ultrasonics, 33(4), pages 271-276, 1995.
84. J. Lewandowski, "Acoustic and Dynamic Properties of Two-Phase Media with Non-Spherical Inclusions", Ultrasonics, 33(1), pages 61-68, 1995.
85. T.A. Bigelow, M.L. Oelze, W.D. O'Brien, "Estimation of Total Attenuation and Scatterer Size from Backscattered Ultrasound Waveforms", Journal of the Acoustical Society of America, 117(3), pages 1431-1439, 2005.

86. A.B. Bouda, S. Lebaili, A. Benchaala, “Grain Size Influence on Ultrasonic Velocities and Attenuation”, NDT&E International, 36, pages 1-5, 2003.
87. I.H. Sarpun, M.S. Kilickaya, S. Tuncel, “Mean Grain Size Determination in Marbles by Ultrasonic Velocity Techniques”, NDT&E International, 38, pages 21-25, 2005.
88. I.H. Sarpun, M.S. Kilickaya, “Mean Grain Size Determination in Marbles by Ultrasonic First Backwall Echo Height Measurements”, NDT&E International, 39, pages 82-86, 2006.
89. G.S. Kino, *Acoustic Waves: Devices, Imaging, and Analog Signal Processing*, Prentice Hall, Inc., Englewood Cliffs, NJ, 2000.
90. S. Dumond, “Ultrasound Technology for Small Animal Imaging”, Animal Lab News, November/December 2006.
91. F. Gomez, K. Althoefer, L.D. Seneviratne, “Simulation of Ultrasound Imaging Inside Fully Charged Pipes”, Automation in Construction, 15, pages 355-364, 2006.
92. Sonix
http://www.sonix.com/
93. K. Raum, A. Ozguler, S.A. Morris, W.D. O’Brien, “Channel Defect Detection in Food Packages using Integrated Backscatter Ultrasound Imaging”, IEEE Transactions on Ultrasonics, Ferroelectrics, and Frequency Control, 45(1), pages 30-40, 1998.
94. BME355 Lab, Yale University
http://noodle.med.yale.edu/~staib/bme355/ultrasound/prep.htm/
95. E.P. Papadakis, *Ultrasonic Instruments and Devices: Reference for Modern Instrumentation, Techniques, and Technology*, Publisher: Academic Press, San Diego, CA, 1999.
96. M.C. Bhardwaj, “High-Resolution Ultrasonic Nondestructive Characterization”, Ceramic Bulletin, 69(9), pages 1490-1496 (1990).
97. B.A.J. Angelsen, *Ultrasound Imaging Volume I: Waves, Signals, and Signal Processing*, Emantec, Norway, 2000.
98. B.R. Thompson, “Elastic-Wave Propagation in Random Polycrystals: Fundamentals and Application to Nondestructive Evaluations”, Topics in Applied Physics, 84, pages 233-256, 2002.
99. M. Bhardwaj, The Ultran Group, personal communications
100. R.B. Thompson, “Ultrasonic Measurement of Mechanical Properties”, IEEE Ultrasonics Symposium, pages 735-744, 1996.
101. B.W. Drinkwater, P.D. Wilcox, “Ultrasonic Arrays for Non-Destructive Evaluation: A Review”, NDT&E International, 39(7), pages 525-541, 2006.
102. S. Mahaut, O. Roy, M. Serre, “An Adaptive System for Advanced NDT Applications using Phased Arrays”, Ultrasonics, 36, pages 127-131, 1998.
103. Obstetetric Ultrasound: A Comprehensive Guide, by J. Woo
http://ob-ultrasound.net/
104. M. Moles, A. Lamarre, “Phased Array Ultrasonic Inspection of Friction Stir Welds”, 4th International Symposium on Friction Stir Welding, Park City, UT, May 14-16, 2003.
105. J.-F. Cyr, “Ultrasound Phased Array”, NDT.net, 7(5), 2002.

106. JSR Ultrasonics
http://www.imaginant.com/pulsereceivers.html/
107. Techno Isel
http://www.techno-isel.com/
108. Gage
http://www.gage-applied.com/
109. Ultran
http://www.ultrangroup.com/
110. Fisher Scientific
http://www.fishersci.com/
111. D.J. Roth, J.D. Kiser, S.M. Swickard, S.A. Szatmary, D.P. Kerwin, "Quantitative Mapping of Pore Fraction Variations in Silicon Nitride using an Ultrasonic Contact Scan Technique", NASA Technical Paper 3377, pages 1-33, 1993.
112. D.J. Roth, J.L. Hendricks, M.F. Whalen, J.R. Bodis, K. Martin, "Commercial Implementation of Ultrasonic Velocity Imaging Methods via Cooperative Agreement between NASA Lewis Research Center and Sonix, Inc.", NASA Technical Memorandum 107138, pages 1-35, 1996.
113. E.R. Generazio, D.J. Roth, D.B. Stang, "Ultrasonic Imaging of Porosity Variations Produced During Sintering", Journal of the American Ceramic Society, 72(7), pages 1282-1285, 1989.
114. W.M.D. Wright, D.A. Hutchins, G. Hayward, "Ultrasonic Velocity Imaging of Slip-Cast Silicon Nitride Ceramics", Acoustic Sensing and Imaging, 369, pages 245-250, 1993.
115. L.-S. Chang, T.-H. Chuang, W.J. Wei, "Characterization of Alumina Ceramics by Ultrasonic Testing", Materials Characterization, 45, pages 221-226, 2000.
116. N. Kulkarni, B. Moudgil, M. Bhardwaj, "Ultrasonic Characterization of Green and Sintered Ceramics: I, Time Domain", American Ceramic Society Bulletin, 73(6), pages146-153, 1994.
117. M.-J. Pan, P.A. Hoffman, D.J. Green, J.R. Hellmann, "Elastic Properties and Microcracking Behavior of Particulate Titanium Diboride-Silicon Carbide Composites", Journal of the American Ceramic Society, 80(3), pages 692-698, 1997.
118. R.G. Munro, "Material Properties of Titanium Diboride", Journal of Research of the National Institute of Standards and Technology, 105, pages 709-720, 2000.
119. S.G. Seshadri, M. Srinivasan, "Liquid Corrosion and High-Temperature Oxidation Effects on Silicon Carbide/Titanium Diboride Composites, Journal of the American Ceramic Society, 71(2), pages C-72-C-74, 1998.
120. Sanyo Trading Co., Ltd.: Silicon Carbide
http://www.sanyo-trading.co.jp/kagaku/kaga_20.html/
121. EKasic Silicon Carbide
http://www.esk.com/materials/siliconcarbide.asp/

122. J.C. LaSalvia, “Recent Progress on the Influence of Microstructure and Mechanical Properties on Ballistic Performance”, Ceramic Transactions: Ceramic Armor Materials by Design, 134, pages 557-570, 2002.
123. S. Ramanathan, S.K. Roy, Y.J. Bhat, “Transparent YAG from Powder Prepared by Homogeneous Precipitation Reaction – $Al(NO_3)_3$+$Y(NO_3)_3$+$(NH_4)_2SO_4$+$CO(NH_2)_2$”, Journal of Materials Science Letters, 20(23), pages 2119-2121, 2004.
124. A. Kaza, “Gas Phase Composition in Pores During Initial Stages of Sintering”, Ph.D. Thesis, Rutgers University, 2006.
125. Akzo Nobel
http://www.akzonobel.com/
126. Alcoa
http://www.alcoa.com/
127. G. Subhash, S.M. Beesley, R.K. Govila, W. Rafaniello, “Fatigue Crack Propagation in Aluminum Nitride Ceramics under Cyclic Compression”, Journal of Materials Science, 34, pages 4645-4652, 1999.
128. Ceradyne, Inc.: Materials
http://www.ceradyne.com/materials/materials.aspx/
129. J.J. Gruber, J.M. Smith, R.H. Brockelman, “Ultrasonic Velocity C-Scans for Ceramic and Composite Material Characterization”, Materials Evaluation, 46(1), pages 90-96, 1988.
130. C.-H.H. Chu, E.J. Delp, “Impulsive Noise Suppression and Background Normalization of Electrocardiogram Signals using Morphological Operators”, IEEE Transactions on Biomedical Engineering, 36(2), pages 262-273, 1989.
131. A.M. Korsunsky, K. Kim, L.R. Botvina, “An Analysis of Defect Size Evolution”, International Journal of Fracture, 128, pages 139-145, 2004.
132. H. Abe, M. Naito, T. Hotta, N. Shinohara, K. Uematsu, “Flaw Size Distribution in High-Quality Alumina”, Journal of the American Ceramic Society, 86(6), pages 1019-1021, 2003.

Curriculum Vita

Raymond Edwin Brennan IV

EDUCATION:

- Rutgers University, New Brunswick, NJ
  Ph.D., Materials Science and Engineering, October 2007
- Rutgers University, New Brunswick, NJ
  M.S., Ceramic and Materials Engineering, May 2003
- Rutgers University, New Brunswick, NJ
  B.S., Ceramic and Materials Engineering, **B.A. Psychology,** May 2000

EXPERIENCE:

Institute of Electrical and Electronics Engineers, Piscataway, NJ
IEEE-UFFC Senior Student Representative, March 2001 to October 2002
Graduate Housing Office, Rutgers University, Piscataway, NJ
Resident Graduate Hall Director, May 2001 to May 2002
Center for Ceramic Research, Rutgers University, Piscataway, NJ
Teaching Assistant, Engineering Laboratory III, September 2001 to December 2001
Center for Ceramic Research, Rutgers University, Piscataway, NJ
Undergraduate Technician, January 1998 to June 2000

PUBLICATIONS:

1. E.K. Akdogan, R.E. Brennan, M. Allahverdi, and A. Safari; "Effects of Molten Salt Synthesis (MSS) Parameters on the Morphology of $Sr_3Ti_2O_7$ and $SrTiO_3$ Seed Crystals"; *Journal of Electroceramics*; 16 [2], pp.159-165 (March 2006).
2. R.E. Brennan, R. Haber, D. Niesz, and J. McCauley; "Defect Engineering of Samples for Non-Destructive Evaluation (NDE) Ultrasound Testing"; *Ceramic Armor and Armor Systems II: Ceramic Transactions*, 178, pp.103-108 (2005).
3. R.E. Brennan, R. Haber, D. Niesz, J. McCauley, and M. Bhardwaj; "Non-Destructive Evaluation (NDE) of Ceramic Armor: Fundamentals"; *Advances in Ceramic Armor*, 26 [7], pp.223-230 (2005).
4. R.E. Brennan, R. Haber, D. Niesz, and J. McCauley; "Non-Destructive Evaluation (NDE) of Ceramic Armor: Testing"; *Advances in Ceramic Armor*, 26 [7] pp.231-238 (2005).
5. R.E. Brennan, M. Allahverdi, and A, Safari; "Templated Grain Growth (TGG) of PMN-PT Textured Components Using $SrTiO_3$ Templates"; *Proceedings of ISAF 14th IEEE International Symposium on Applications of Ferroelectrics*, pp.270-273 (2004).
6. R.E. Brennan, S. Turcu, A. Hall, N.M. Hagh, and A. Safari; "Layered Manufacturing for Prototyping of Novel Transducers"; *Ferroelectrics*, 293, p. 3-17 (2003).
7. M. Allahverdi, A. Hall, R. Brennan, M.E. Ebrahimi, N. Marandian Hagh, and A. Safari; "An Overview of Rapidly Prototyped Piezoelectric Actuators and Grain-Oriented Ceramics"; *Journal of Electroceramics*; 8; pp. 129-137 (August 2002).

8. R.E. Brennan, M. Allahverdi, M.E. Ebrahimi, and A. Safari; “Growth of Net-Shape PMN-PT Single Crystal Components by Fused Deposition of Ceramics (FDC) and Templated Grain Growth (TGG) Techniques”; *Proceedings of IFFF-ISAF*; Nara, Japan (May 2002).